MONASH University

# *Deformation Processing of Lead-Free Duplex Brass*

*Michael Moriarty*

*B.E. (Hons) (Materials Engineering)*

A thesis submitted for the degree of Doctor of Philosophy at

Monash University in March 2020

Department of Materials Science and Engineering

Victoria, Australia

# Copyright Notice

© The author 2020. Except as provided in the Copyright Act 1968, this thesis may not be reproduced in any form without the written permission of the author.

*I certify that I have made all reasonable efforts to secure copyright permissions for third-party content included in this thesis and have not knowingly added copyright content to my work without the owner's permission.*

# Abstract

Duplex brasses (Cu-Zn) are used extensively for the large-scale production of plumbing fittings, valves, and water control products. The ease with which these alloys are processed and their in-service characteristics, namely good mechanical strength and excellent corrosion resistance, are major advantages compared with other alloy families such as steel and aluminium.

As a result of nationwide legislation implemented in the United States in 2014, the brass industry is currently under a state of major transition from traditional alloys containing up to 8 wt. % Pb to 'lead-free' alloys that contain no more than 0.25 wt. % Pb. Pb is widely known for its ability to significantly improve the machinability of brass while remaining neutral to the other manufacturing processes. As a direct result, the removal of Pb has led to a dramatic increase in cycle times and/or rejection rates at various stages of the manufacturing process, not only during machining.

The legislated reduction on Pb has paved the way for several new brass compositions to emerge, each with various alloying additions. These new alloys each claim that a degree of machinability has been restored. However, the conditions under which they are processed, for example during forging, heat treating, or cold working, is not well defined. The Pb-free alloy grade to employ is also a matter of contention, with different manufacturing companies and many countries at odds over the most suitable grade/s.

This research examines in detail the processing-structure-properties relationships for several commercial Pb-free brass alloys on the market. The comparison will focus on their processing and in-service characteristics. It is the first objective of this thesis to assess the effects of alloy composition on duplex brass phase equilibria through the use of thermodynamic descriptions and neutron diffraction techniques. Of particular interest is characterisation of Si-bearing brasses.

The second section of this thesis contains a study on the effect of alloying additions and fabrication mode on elevated temperature plasticity using uniaxial hot compression. This is inclusive of the development of a forgeability index and semi-empirical model using the 'law of mixtures' to predict steady-state flow stress at a given temperature and strain rate.

The third section of this thesis contains a systematic study of the relationship between key microstructural parameters (grain size, phase fraction, grain morphology and interconnectivity) and the dezincification resistance of duplex brass. This is followed by a discussion on the effect of cooling rates and interpretation of the microstructure effects on dezincification in the context of percolation theory.

The final part of this thesis uses drilling operations to explore the microstructural and particle size and distribution effects on machining properties of duplex brass. The feed forces, drilling torques, swarf morphology and resulting surface roughness of 10 different duplex brasses are all incorporated into this analysis.

*Keywords: Duplex brass; 'lead-free'; machinability; phase equilibria; dezincification; hot workability.*

# Declaration of Authorship

This thesis is an original work of my research and contains no material which has been accepted for the award of any other degree of diploma at any university or equivalent institution and that, to the best of my knowledge and belief, this thesis contains no material previously published or written by another person, except where due reference is made in the text of the thesis.

Michael Moriarty

6 / 3 / 2020

# Acknowledgements

This PhD was conducted part-time whilst working full-time in operations at Reliance Worldwide Corporation (RWC). It would not have been possible without the support and guidance of an incredible group of people. I've been fortunate enough to be involved in a long and highly collaborative academic-industry partnership between Monash University and RWC and I'm sincerely appreciative of the assistance provided on both sides of this partnership.

At the forefront of this group has been Professor Christopher Hutchinson, a constant source of encouragement from day one, his enthusiasm is infectious. From cold winter mornings on campus discussing ideas to scorching summer days proofing work at his home, I could not have asked for a better supervisor to guide my development in metallurgy and provide continued support in my experiments and writing.

Thanks go out to my various equipment trainers at Monash University over the journey, including Mr. Silvio Mattievich, Dr. Wenwen Sun, Mr. Ireneusz Kozicki, Ms. Yeannette Lizama and Mr. Rod Mackie. A special mention to one man in particular, Mr. Daniel Curtis, who has consistently gone above and beyond in ensuring the laboratories run smoothly, equipment training is conducted with ease and most importantly we have fun doing what we do! His technical assistance over the years and training in hot compression was outstanding. An additional thanks to Mr. Brett Williams at the Monash Instrumentation Facility who has done a great job helping me design and create the samples for the hot compression and machining trials.

Many thanks to Dr. Cong Qui for his assistance in the development of the thermodynamic descriptions for various Cu-Zn alloy systems using ThermoCalc, Dr. Sasha Wilson, Ms. Vanette Tran and Mr. Lingyu Wang for their assistance in the XRD experiments, Dr. Mark Styles of CSIRO for his insight into the use of Topas software for the Rietveld refinement of XRD results, and Dr. Yuxiang Wu for his extensive time and effort in assisting with the Neutron diffraction experiment and corrosion percolation theory.

I gratefully acknowledge the collaboration with our colleagues at Deakin University (Waurn Ponds), Dr. Junior Nomani and Mr. Craig McGill, who provided not only the necessary laboratory equipment and support for the machining trial, but additionally the guidance from their own learnings with duplex stainless steels. My sincere thanks for their support.

I would like to additionally express my gratitude to Mr. Timothy Murray for his assistance in the sample preparation and testing throughout the dezincification studies of this thesis. It has been a pleasure to work with him.

None of this work would be possible without the ongoing support of my colleagues at RWC. First and foremost, thank you to the man who introduced me to the industry, Dr. Greg Morwood, and who encouraged me to take my first steps in post-graduate research. In addition, thanks to Mr. John Boyle, Mr. William (Bill) Kluss and Mr. Brad Reid. Each have played an enormous role in my professional development, both from an academic and industry perspective and I am humbled to have the opportunity to work with these leaders of the industry. Finally, thanks to Ms. Gabrielle Dinsdale and Ms. Vanette Tran for their continual support and never-yielding enthusiasm.

To my family; Marna, Peter, Emily and Adrian, thank you for the encouragement throughout. I always know you're there to provide an ear and keep me sane outside of study. A special thanks to Dr. Paul Firbas, who's friendship throughout has been incredible, a cheeky coffee, caramel slice and chat about the footy never goes astray. Finally, to my wife Samantha, her support and constant positivity to the point of making up songs about brass provided the energy to keep persevering and eventually complete this work. Thank you all for putting up with this crazy rollercoaster of a thesis.

# Contents

**Copyright Notice** ..... **i**

**Abstract** ..... **ii**

**Declaration of Authorship** ..... **iv**

**Acknowledgements** ..... **v**

**Contents** ..... **vii**

**List of Figures** ..... **xi**

**List of Tables** ..... **xxvi**

**1 Introduction** ..... **1**

1.1 Brass Manufacturing ..... 1

1.2 The Emergence of 'Lead-Free' ..... 3

**2 Literature Review** ..... **6**

2.1 Introduction ..... 6

2.2 Brass (Cu-Zn) Alloys and Phase Equilibria ..... 6

2.2.1 Alloy Families and Designations ..... 6

2.2.2 Brass (Cu-Zn) Alloys ..... 7

2.2.3 Characteristics of the α and β Phase ..... 11

2.2.4 Effect of Alloying Additions on Phase Equilibria ..... 16

2.3 Elevated Temperature Plastic Deformation ..... 22

2.3.1 High Temperature Processing of Duplex Cu-Zn Alloys ..... 22

2.3.2 Hot Workability ..... 23

2.3.3 The Pre-Heating and Forging Process ..... 24

2.3.4 Assessment of Forgeability ..... 31

2.3.5 Influence of Chemical Composition on Forgeability of Duplex Brasses ..... 32

2.4 Intermediate Heat Treatments ..... 36

2.4.1 Post-Forging Intermediate Heat Treatment ..... 36

2.4.2 Dezincification Resistance ..... 38

2.4.3 Effect of Alloying Additions on Dezincification Resistance ..... 39

2.5 Machinability ..... 42

2.5.1 Machining Operations ..... 42

2.5.2 Measures of Machinability of Duplex Cu-Zn Alloys ..... 43

2.5.3 The Role of Lead (Pb) in Machining Processes ..... 46

2.5.4 Alternatives to Pb for Improved Machinability ..... 48
2.6 Post-Machining Processes ..... 54
2.6.1 Introduction ..... 54
2.6.2 Crimping (Cold Working) ..... 55
2.6.3 Stress Corrosion Cracking (SCC) ..... 56
2.6.4 Effect of Alloying Additions on SCC Resistance ..... 60
2.7 Summary, Gaps in Knowledge and Objectives of Research ..... 63
2.7.1 Summary ..... 63
2.7.2 Gaps in Knowledge and Objectives of Research ..... 64

**3 Experimental Method ..... 68**
3.1 Thermal Treatments ..... 68
3.2 Mechanical Testing ..... 68
3.2.1 Vickers Hardness ..... 68
3.2.2 Tensile Testing ..... 69
3.2.3 Hot Compression ..... 69
3.2.4 Machining Experiments ..... 71
3.3 Electrochemical Testing ..... 73
3.3.1 Dezincification Testing ..... 73
3.4 Microstructural Characterisation ..... 75
3.4.1 Metallography ..... 75
3.4.2 X-Ray Diffraction (XRD) ..... 77
3.4.3 High Intensity *In-Situ* Neutron Diffraction ..... 79
3.4.4 Scanning Electron Microscopy (SEM) with Energy-Dispersive X-Ray Spectroscopy (EDS) and Backscattered-Electron (BSE) Imaging ..... 79

**4 Phase Equilibria ..... 80**
4.1 Alloy Selection ..... 80
4.2 Phase Equilibria ..... 82
4.2.1 CALPHAD Calculations ..... 82
4.2.2 X-Ray Diffraction ..... 85
4.2.3 High Intensity *In-Situ* Neutron Diffraction ..... 88
4.3 Summary and Conclusions ..... 109

**5 Elevated Temperature Plasticity ..... 111**
5.1 Alloy Selection ..... 111
5.2 Experimental Results ..... 113
5.2.1 Leaded Brasses ..... 114
5.2.2 Bismuth Brasses ..... 116
5.2.3 Silicon Brasses ..... 118

5.2.4 Alternative Brasses – Binary, Al-, Sn-bearing ..... 119
5.3 Forgeability Index ..... 122
5.3.1 Leaded Brasses ..... 124
5.3.2 Bismuth Brasses ..... 129
5.3.3 Silicon Brasses ..... 132
5.3.4 Alternative Brasses – Binary, Al-, Sn-bearing ..... 133
5.4 Constitutive Modelling ..... 136
5.4.1 Methodology ..... 136
5.4.2 Rule of Mixtures ..... 138
5.5 Summary and Conclusions ..... 145

**6 Dezincification Behaviour ..... 146**
6.1 Alloy Selection and Thermal Treatments ..... 147
6.2 Effect of Fabrication Anisotropy ..... 150
6.3 Effect of Phase Fraction, Size and Shape ..... 154
6.3.1 Effect of Fabrication Mode ..... 154
6.3.2 Effect of β' Phase Fraction on Dezincification Resistance ..... 156
6.3.3 Effect of α Grain Size and Shape on Dezincification Resistance ..... 163
6.4 Dezincification of Extruded CuZn37.8BiPAs – Effect of Cooling Rate ..... 172
6.5 Percolation Simulations of the Effect of Phase Fraction, Size and Morphology on Dezincification ..... 180
6.5.1 Percolation-Simulation Methodology ..... 180
6.5.2 Effect of β' Phase Fraction and α Grain Size on Percolation ..... 184
6.5.3 Effect of α Aspect Ratio and Orientation on Percolation ..... 186
6.5.4 Percolation Simulations on Real Microstructures ..... 188
6.5.5 Perspectives on Microstructural Effects on Dezincification ..... 191
6.6 Summary and Conclusions ..... 192

**7 Machinability ..... 193**
7.1 Alloy Selection and Thermal Treatments ..... 194
7.2 Sample Material Properties ..... 197
7.2.1 Leaded Brass ..... 198
7.2.2 Bismuth Brass ..... 201
7.2.3 Silicon Brass ..... 206
7.2.4 Alternative Brasses – Binary, Al-, Sn-bearing ..... 208
7.3 Machining Experimental Results ..... 209
7.3.1 As-Received Experimental Results ..... 209
7.3.2 Swarf Morphology ..... 216
7.4 Microstructure-Machinability Correlations ..... 218

7.4.1 Feed Force ($F_Z$) ..... 218
7.4.2 Drilling Torque ($M_Z$) ..... 221
7.4.3 Surface Roughness ($R_a$) ..... 231
7.5 Summary and Conclusions ..... 236

**8 Conclusions and Future Work ..... 238**
8.1 Conclusions ..... 238
8.2 Future Work ..... 243
8.2.1 Phase Equilibria ..... 243
8.2.2 Elevated Temperature Plasticity ..... 243
8.2.3 Dezincification Behaviour ..... 244
8.2.4 Machinability ..... 245

**Appendix A – U.N.S. Alloy Designations ..... 246**

**Appendix B – CALPHAD .tdb Files ..... 247**
Cu-Zn-Pb .tdb file ..... 247
Cu-Zn-Sn .tdb file ..... 250
Cu-Zn-Al .tdb file ..... 253
Cu-Zn-Pb-Sn .tdb file ..... 256
Cu-Zn-Si .tdb file ..... 260

**Appendix C – TOPAS Macro for Rietveld Refinement of Neutron Diffraction Data ..... 265**
Neutron Diffraction TOPAS Macro ..... 265

**References ..... 271**

# List of Figures


Figure 1.1: Examples of brass plumbing fittings. (a) a 1" straight barb fitting and ½" elbow barb fitting with thread adaptor, (b) a ½" straight push-to-connect (PTC) fitting, and a ½" elbow PTC fitting [3]. ..... 1

Figure 1.2: Examples of more complicated plumbing valves which use a combination of directly machined and forged components. (a) A thermostatic mixing valve, (b) a ball valve [3, 4]. ..... 2

Figure 1.3: A typical processing schedule (time vs. temperature) for a potable water plumbing component utilising a forging step. ..... 2

Figure 1.4: (a) A brass billet workpiece sectioned from a rod for forging, (b) an elbow fitting (with flash) after the forging process, (c) a heat-treated forging after the shot-blasting process, (d) a machined fitting body, and (e) the final machined plumbing fitting with a cartridge crimped into the brass body. ..... 3

Figure 2.1: Engineering stress-strain curves exhibiting the solid solution strengthening effects of a 30 wt. % Zn alloy (Cu-30Zn) against pure copper. Cu-30Zn has a comparatively higher tensile strength, yield strength, and greater elongation to fracture [1]. ..... 8

Figure 2.2: Cu-Zn Binary Phase Diagram [1]. Three regions highlighted to show what are commonly referred to as Red Brasses, Semi-Red Brasses, and Yellow Brasses. ..... 9

Figure 2.3: (a) The Cu-rich corner of the Cu-Zn Binary Phase Diagram calculated using the thermodynamic assessment of Miettinen [12] with the 39Zn wt. % highlighted, and (b) Plot of phase fraction of α (red) and β (black) as a function of temperature for Cu-39Zn (highlighted) and Cu-37.5Zn (wt. %) calculated using the thermodynamic assessment of Miettinen [12]. ..... 10

Figure 2.4: (a-c) Duplex Cu-Zn Microstructures exhibiting the α phase (lighter) and the β' phase (darker). ..... 11

Figure 2.5: (a) Representation of slip in an FCC lattice such as for the α phase along the (111) plane, (b) the dissociation of a perfect dislocation into two partial dislocations. This occurs in the Cu-Zn α phase which has an FCC lattice and low stacking fault energy ($\gamma_{SFE}$) which continues to decrease with increasing Zn composition [16]. ..... 13

Figure 2.6: The ordered BCC β' lattice [1]. ..... 14

Figure 2.7: (a) Hardness and (b) elongation characteristics of Cu-49Zn (100% BCC β phase) with increasing temperature [1]. ..... 15

Figure 2.8: (a) Cu-Zn-2Pb (wt. %) Ternary Isopleth calculated using the thermodynamic assessment of Miettinen [28] and (b) Plot of phase fraction of α and β as a function of temperature for Cu-38.5Zn (grey) and Cu-37.7Zn-2Pb (colour) (wt. %) calculated using the thermodynamic assessment of Miettinen [28]. (c) Cu-Pb and (d) Cu-Bi Binary Phase Diagrams [36]. ..... 17

Figure 2.9: (a) Cu-Zn-1Sn (wt. %) Ternary Isopleth calculated using the thermodynamic assessment of Miettinen [12] and (b) Plot of phase fraction of α, β and γ as a function of temperature for Cu-38.5Zn (grey) and Cu-38.1Zn-1Sn (colour) (wt. %) calculated using the thermodynamic assessment of Miettinen [12]. ..... 18

Figure 2.10: (a) Cu-Zn-1Al (wt. %) Ternary Isopleth calculated using the thermodynamic assessment of Miettinen [12] and (b) Plot of phase fraction of α, β and γ as a function of temperature for Cu-38.5Zn (grey) and Cu-38.1Zn-1Al (colour) (wt. %) calculated using the thermodynamic assessment of Miettinen [12]. ..... 19

Figure 2.11: Microstructural evolution of Cu-Zn with increasing wt. % of Al (a) CuZn38.2Al0.49, (b) CuZn37.9Al1.05, (c) CuZn37.6Al1.6, (d) CuZn35.3Al3.4 [38]. The β' appears as the dark phase in (a) and (b), whilst (c) and (d) are almost entirely β'. ..... 19

Figure 2.12: (a) Cu-Zn-3.4Si (wt. %) Ternary Isopleth calculated using the thermodynamic assessments of Miettinen and Wang et al. [29, 30] and (b) Plot of phase fraction of α, β and γ as a function of temperature for Cu-38.5Zn (grey) and Cu-21Zn-3.4Si (colour) (wt. %) calculated using the thermodynamic assessment of Miettinen and Wang et al. [29, 30]. ..... 21

Figure 2.13: Hot Torsion Stress-Strain curves for a Cu-36.5Zn-2Pb alloy at various temperatures [48]. ..... 23

Figure 2.14: Softening of Cu-Zn alloys as a function of temperature ($^{o}$C) [49]. ..... 24

Figure 2.15: Duplex α + β' cast structure heated to 750$^{o}$C and quenched. The β' phase appears dark against the lighter α phase due to the etchant effect [13]. Note the α phase exhibits no twinning at this stage because it has not undergone any prior deformation process. ..... 26

Figure 2.16: RWC internally-developed FEA simulation using GL Inova of a brass workpiece placed in a forging die at elevated temperature (a) just prior to the forging cycle, and (b) at the end of the forging cycle just prior to the forging pins being withdrawn and die opened. Inset (i): Cross-section of the same workpiece exhibiting the temperature gradient. Inset (ii): A real example of the same workpiece after a forging. ..... 27

Figure 2.17: True stress-strain curves obtained during hot compression of Cu-38Zn at various temperatures and strain rates ((a) 0.01$s^{-1}$, (b) 0.1$s^{-1}$, (c) 1$s^{-1}$, (d) 10$s^{-1}$) by Xiao et al. [18]. ..... 28

Figure 2.18: (a) An example continuous cooling transformation (CCT) diagram indicating the cooling time differential required to form 1. Equiaxed α grains, 2. Widmanstätten α grains, 3. Massive transformation α grains, and 4. Martensitic transformations (very low temperatures) [14]. (b) Example of Massive α formed along β grain boundaries in a Cu-38.7Zn quenched from 850$^{o}$C to 0$^{o}$C in brine [14]. ..... 31

Figure 2.19: Evolution of α and β phases in two common duplex brasses; Cu-38.5Zn-2Pb (grey) and Cu-38.75Zn-0.75Sn (black). The Sn additions stabilise β at lower temperatures and therefore the recommended optimal hot working temperature is lower. 65α/35β phase fraction highlighted in orange for each alloy. ..... 33

Figure 2.20: (a) Example of an as-fabricated duplex brass rod microstructure (Cu-35.9Zn-3.5Pb-0.16Sn-0.08As) and (b) the resulting reduction in β' phase present in the

microstructure with increasing soak time at intermediate temperatures. This is also known as a time-temperature-transformation diagram [45]. (c) Equilibrium phase fraction of α and β against temperature. ..... 37

Figure 2.21: Cu37.5Zn0.75Bi0.3Sn (a) Post-forging microstructure without heat treatment, (b) after the completion of an intermediate heat treatment. The α grains are now fully recrystallised with little to no β' present in the microstructure which is desired for dezincification resistance of the final component. ..... 37

Figure 2.22: (a) The loss of tensile strength in samples of brass for incremental additions of Zn, where the samples have been exposed to a solution of 0.01M ammonium chloride at 45°C for 60 days. It is evident the effect of including more than 15 wt. % Zn. (b) Dezincification will typically only occur for alloys with an excess of 15 wt. % Zn, beneath this value, pitting is more likely to be encountered [1]. ..... 38

Figure 2.23: (a) Schematic of the build-up of zinc carbonate during plug-type dezincification [84]. (b) This occurs more readily when copper piping is used in tandem with a brass fitting and a crevice is created, for example when a pipe is not fully engaged, inserted into or over a brass fitting. ..... 39

Figure 2.24: Layer-type dezincification of two duplex Cu-Zn alloys (a) containing trace amounts of phosphorus (only β' attacked), and (b) without any α phase dezincification inhibitors present in the composition (both α and β' attacked). Depths highlighted in red. ..... 40

Figure 2.25: The negative effect of increasing Fe and Mn wt. % on nullifying the dezincification resistance acquired through the addition of As wt. % as an α dezincification inhibitor [45]. ..... 41

Figure 2.26: Example of intermediate temperature embrittlement in a recrystallised α microstructure causing fracture in a Cu-37.1Zn-0.58Bi-0.37Sn-0.28Pb alloy during machining. Red dotted arrow indicates direction of fracture progression from origin... 43

Figure 2.27: SEM images showing various states of carbide tool wear after completion of a turning operation on 4 different alloys (a) Cu-21Zn-3.4Si, (b) Cu-38Zn, (c) Cu-42Zn, (d) Cu-39Zn-3.3Pb [121]. ..... 44

Figure 2.28: Examples of various classifications of Cu-Zn swarf or 'chip' morphologies attained after a machining operation [122]. Finer swarf, like that observed in no. 1, are generally more desirable. ..... 45

Figure 2.29: (a) Free-cutting C36000 brass microstructure exhibiting dark Pb-globules primarily along the grain boundaries of the α phase [1], (b) The correlation between Pb-additions and improvement in universal machinability rating for brass alloys with a Cu-content between 62 and 65 wt. % [1]. ..... 46

Figure 2.30: Microstructural observations of four different brass alloy chips after a turning operation, (a) Cu-39Zn-3Pb, (b) Cu-42Zn, (c) Cu-38Zn-As, (d) Cu-36Zn [122]. ..... 47

Figure 2.31: A comparison between free-machining brass (C36000, 61.5Cu-35.5Zn-3Pb), a low-Pb brass (C34000, 65Cu-34Zn-1Pb), and a Pb-free brass (C46400, 60Cu-39.2Zn-0.8Sn) for tool life and universal machinability index against some other common materials like 2011-T3 aluminium and 12L14 bright mild steel [1]. ..... 47

Figure 2.32: (a-c) The microstructure of a duplex brass containing 1 wt. % Mg and 0.8 wt. % Sb at various magnifications. The dark particles are intermetallics $Cu_2Mg$ and $Cu_9Sb$ [165]. (d) Loss in mechanical properties (tensile strength and elongation) with increasing Sb additions for machinability [165] ..... 50

Figure 2.33: Microstructures of 60Cu-Zn-0.5Sb-0.5Bi alloys with additions of (a) 1 wt. % Mg, (b) 2 wt. % Mg, (c) 3 wt. % Mg, (d) 4 wt. % Mg [130]. Increasing Mg concentration stabilising additional β' (dark phase) and changing the morphology of α from acicular to spherical. ..... 51

Figure 2.34: Increase in hardness with Si additions [41]. ..... 52

Figure 2.35: A direct comparison of cutting forces (N) for (a) the Si-bearing C69300 vs. (b) the Pb-bearing C38500 at various depths of cut during a turning operation [120]. ..... 53

Figure 2.36: A direct comparison of the accumulated tool wear encountered while machining (a) the Si-bearing C69300 vs. (b) the Pb-bearing C38500 [120]. Far less wear is encountered for the machining tip on the right used to turn Pb-bearing duplex brass while the Si-bearing tip has failed after chipping off a section of the tip due to excessive crater wear. ..... 54

Figure 2.37: Plumbing fittings exhibiting (a) the orange-peel effect without cracking and (b) with extensive cracking. ..... 56

Figure 2.38: Metallographic representation of the Orange peel effect as a result of a dual-grain-morphology. The recrystallised α grains deform preferentially on the surface during cold working/crimping. ..... 56

Figure 2.39: An example of two duplex brass fittings which have suffered from SCC around the crimped (cold worked) ends. ..... 57

Figure 2.40: Microstructural characteristics of SCC in a duplex brass. Cracks can be either intergranular or transgranular and typically have several secondary branches, also known by the industrial term 'Spider-Web' cracking. ..... 58

Figure 2.41: Time to SCC failure of a 70Cu-30Zn brass (a) under the influence of varying engineering stress in an aqueous ammonia environment, and (b) showing the beneficial effects of reducing grain size in a moist ammonia vapour [1]. ..... 59

Figure 2.42: An example of a duplex brass microstructure exhibiting failure via the dual-mechanism of stress corrosion cracking and dezincification. Inset: macroscopic view of the failed fitting surface. ..... 60

Figure 2.43: The crack propagation rate of several brass alloys of varying Zn content [214] and pure copper [215] in 1M $Cu(NO_3)_2$. As the Zn content increases, SCC resistance decreases. ..... 61

Figure 2.44: The average crack velocity (CV) of 70Cu-30Zn as a function of As wt. % in an $NaNO_2$ solution at room temperature [217]. ..... 62

Figure 3.1: Tensile specimen dimensions. Central gauge length of 30 mm used with a 25mm extensometer. ..... 69

Figure 3.2: Instron 5984 setup used for hot compression tests. (1) Load cell, (2) load cell temperature thermocouple, (3) water cooling inlet and thermal protection plate, (4) upper cooling column, (5) furnace (containing sample and two screw-in cylindrical die platens), (6) temperature controller, (7) sample temperature thermocouple, (8) Instron controller, (9) ceramic brick for sample cooling. ..... 70

Figure 3.3: Duplex brass cylindrical samples both before and after the hot compression process. . 71

Figure 3.4: Twin-flute solid carbide drill dimensions used for machining experiments. ..... 72

Figure 3.5: Drilling operation on the 'Spinner U-620' CNC machine; (a) Prior to cycle commencement, (b) during drilling cycle, and (c) the sample post-machining. ..... 72

Figure 3.6: (a) Brass sample mounting schematic and (b) examples of samples that have undergone dezincification testing according to ISO6509-1 (2014). ..... 73

Figure 3.7: Dezincification test rig setup (a) schematic and (b) the 3 laboratory test rigs used for testing in this study. ..... 74

Figure 3.8: Method for recording dezincification depths according to ISO6509-1 (2014). Each of points a), b), and c) represent an individual measurement of a dezincified samples under magnification. ..... 75

Figure 3.9: Example of real dezincification depth measurements according to ISO6509-1 (2014)... 75

Figure 3.10: (a) Superimposed grid (blue points) used to determine the phase fraction of BCC β' and (b) the colour threshold and particle analysis indication % used to determine the number of grid points required. ..... 76

Figure 3.11: (a) Typical continuously cast and heat treated α microstructures can be difficult to measure, and (b) example of over-etching to assist determine grain boundary locations. ..... 77

Figure 3.12: Bruker D8 Advance - XRD powder sample setup. ..... 78

Figure 4.1: (a) Quaternary CuZnPb2.3Sn0.23 isopleth and (b) evolution of equilibrium α (green) and β (red) phase fraction of CuZn36.5Pb2.3Sn0.23 with temperature, calculated using the CALPHAD approach in conjunction with the Cu-Zn-Pb and Cu-Zn-Sn databases developed by Miettinen [12, 28]. ..... 82

Figure 4.2: (a) Ternary CuZnSn0.32 isopleth and (b) evolution of equilibrium α (green) and β (red) phase fraction of CuZn36.9Sn0.32 with temperature, calculated using the CALPHAD approach in conjunction with the Cu-Zn-Sn database developed by Miettinen [12]. ..... 83

Figure 4.3: Ternary isopleths of (a) CuZnSi2.7, (b) CuZnSi3, (c) CuZnSi3.4 and (d) the evolution of equilibrium α (red), β (black) and γ (blue) phase fraction of CuZn22Si2.7, CuZn22Si3, CuZn22Si3.4 with temperature, calculated using the CALPHAD approach in conjunction with the Cu-Zn-Si databases developed by Miettinen [29] and Wang et al. [30]. ..... 84

Figure 4.4: Room temperature powder XRD scan of CuZn36.5Pb2.3Sn. ..... 85

Figure 4.5: Room temperature powder XRD scan of CuZn37.6Bi0.8Sn. ..... 85

Figure 4.6: Room temperature powder XRD scan of CuZn22Si3. ..... 86

Figure 4.7: CuZn37.6Bi0.8Sn0.3 heat treated and subsequently (a) air-cooled from 750°C and (b) quenched from 750°C. The quenched microstructure exhibits both equiaxed and Widmanstätten α grains, the latter forming on the rapid cool. ..... 87

Figure 4.8: Example of an *in-situ* XRD scan of CuZn36.5Pb2.3Sn (powder sample) performed at 700°C using a 150kPa nitrogen atmosphere and identifying several zinc oxide peaks that have formed due to surface oxidation at elevated temperatures. ..... 87

Figure 4.9: The temperature schedule used throughout the neutron diffraction experiments for (a) the CuZn36.5Pb2.3Sn alloy and (b) the CuZn36.9Bi0.8Sn alloy. Highlighted on each figure is a temperature chosen to show an example scan in Figs. 4.10 (750°C) and 4.11 (700°C). ..... 88

Figure 4.10: Example of an ANSTO neutron diffraction pattern taken for the CuZn36.5Pb2.3Sn alloy at 750°C. An additional peak related to furnace setup highlighted with a red arrow. .... 89

Figure 4.11: Example of an ANSTO neutron diffraction pattern taken for the CuZn36.9Bi0.8Sn alloy at 700°C. Examples of peak splitting highlighted with black arrows..... 89

Figure 4.12: Bulk XRD scan of CuZn36.9Bi0.8Sn before (blue scan) and after (black scan) heat treating at 825°C for 1 hour followed by a drop to 725°C for 1 hour and water-quenched. The resulting scan (a) shows the formation of α peak-splitting after heat treatment, and (b) inset view (highlighted by grey box) - increased magnification on higher-angle peaks where this is more easily observed (highlighted with red arrows). . 90

Figure 4.13: Dependence of β phase fraction on temperature for the CuZn36.5Pb2.3Sn alloy using neutron diffraction data, CALPHAD calculations [12, 28] and optical metallography estimates. The temperature range of 650°C – 800°C has been highlighted as the most critical for elevated temperature deformation processing. ..... 91

Figure 4.14: Optical micrographs of continuous cast CuZn36.5Pb2.3Sn taken in the quenched state from (a) 650°C, (b) 700°C, (c) 750°C, (d) 800°C, (e) 850°C after a soak time of 30 minutes. The fine Widmanstätten α grains found upon cooling are highlighted in the 850°C condition. ..... 93

Figure 4.15: Dependence of β phase fraction on temperature for the CuZn36.9Bi0.8Sn alloy using neutron diffraction data, CALPHAD calculations [12] and optical metallography estimates. The temperature range of 650°C – 800°C has been highlighted as the most critical for elevated temperature deformation processing. ..... 94

Figure 4.16: Optical micrographs of continuous cast CuZn36.9Bi0.8Sn taken in the quenched state from (a) 650°C, (b) 700°C, (c) 750°C, (d) 800°C, (e) 850°C (soak 30 minutes). Highlighted are examples of both original α grains that are typically observed around larger β grain boundaries and Widmanstätten α formed during the quenching process and therefore not included in the equilibrium estimations of phase fraction. ..... 95

Figure 4.17: Dependence of β phase fraction on temperature for the CuZn37.6Bi0.8Sn alloy using CALPHAD calculations [12] and optical metallography estimates. ..... 96

Figure 4.18: Optical micrographs of extruded CuZn37.6Bi0.8Sn taken in the quenched state from (a) 650°C, (b) 700°C, (c) 750°C, (d) 800°C, (e) 850°C after a soak of 30 minutes. ..... 97

Figure 4.19: Dependence of β phase fraction on temperature for the CuZn22Si3 alloy using CALPHAD calculations [29, 30] and optical metallography estimates. ..... 98

Figure 4.20: Optical micrographs of extruded CuZn22Si3 taken in the quenched state from (a) 650°C, (b) 700°C, (c) 750°C, (d) 800°C, (e) 850°C after a soak of 30 minutes. Highlighted are abnormalities in the microstructure heat treated to 850°C (bright spot formation and prior β grain boundary film formation). ..... 99

Figure 4.21: Samples of CuZn22Si3 heat treated to 850°C for a soak time of (a-c) 30 minutes and (d-f) 45 minutes (increasing magnification). Incipient melting is occurring throughout the microstructures due to Si in composition. ..... 100

Figure 4.22: (a) Microstructure of CuZn22Si3 heat treated to 850°C for 45 minutes adjacent to a grain boundary and (b) a low magnification BSE image of the same sample area of interest. Highlighted in the BSE image is the EDS line scan region (in white) chosen to evaluate the levels of Cu, Zn, and Si shown in Fig. 4.23 as well as the key grain boundary regions showing depleted levels of Zn (in blue). ..... 101

Figure 4.23: SEM-EDS line scan of the sample in Fig. 4.22 showing the quantitative presence of (a) Zn and (b) Si. The region near the grain boundary is shown to be depleted in Zn, with higher than normal levels of Zn immediately adjacent to this region. ..... 102

Figure 4.24: (a) Evolution of phase fraction with temperature showing equilibrium formation of liquid for homogenous CuZn22Si3 at ~890°C, (b) CuZn22 Isopleth showing liquid formation at 850°C commences for Si content in excess of ~3.8 wt. %, (c) Increase in Si content for liquid formation, (d) decrease in Zn content for liquid formation. ..... 103

Figure 4.25: Room-temperature bulk-specimen XRD scans (Co Kα Source – λ = 0.1789nm) of CuZn22Si3 after intermediate heat treating at (a) 300°C for 60 minutes and water-quenched, (b) 400°C for 60 minutes and water-quenched, (c) 500°C for 60 minutes and water-quenched with Rietveld refinement completed using TOPAS software. ..... 104

Figure 4.26: Stabilisation of equilibrium ε (highlighted with a blue arrow) for CuZn22Si3 when γ is suspended in CALPHAD. ..... 105

Figure 4.27: Sample metallography of CuZn22Si3 heat treated at (a) 300°C, (b) 400°C, and (c) 500°C after a 1-hour soak time followed by water-quenching. (d) magnified SEM-EDS Si-map of the sample heat treated at 500°C in (c). ..... 106

Figure 4.28: Room-temperature bulk-specimen XRD scans (Co Kα Source) of CuZn22Si3 after elevated temperature heat treating at (a) 600°C for 60 minutes and water-quenched and (b) 700°C for 60 minutes and water-quenched with Rietveld refinement completed using TOPAS software. ..... 107

Figure 4.29: Sample metallography of CuZn22Si3 heat treated at (a) 600°C and (e) 700°C after a 1-hour soak time followed by water-quenching. ..... 108

Figure 5.1: Stress-strain curves as a function of temperature for continuous cast CuZn39Pb2 with average applied strain rates of (a) $0.35s^{-1}$, (b) $0.64s^{-1}$ and (c) $0.85s^{-1}$. Multiple tests are performed at each temperature to show reproducibility. ..... 114

Figure 5.2: Stress-strain curves as a function of temperature for extruded CuZn39Pb3 with average applied strain rates of (a) $0.35s^{-1}$, (b) $0.64s^{-1}$ and (c) $0.85s^{-1}$. ..... 114

Figure 5.3: As-fabricated (a) continuous cast CuZn39Pb2 and (b) extruded CuZn39Pb3 microstructure with highlighted grain directionality. ..... 115

Figure 5.4: Stress-strain curves as a function of temperature for (a) continuous cast CuZn37Pb2 and (b) extruded CuZnPb2SnFe with an average applied strain rate of $0.85s^{-1}$. ..... 116

Figure 5.5: Stress-strain curves as a function of temperature for continuous cast CuZnBi0.7 with average applied strain rates of (a) $0.35s^{-1}$, (b) $0.64s^{-1}$ and (c) $0.85s^{-1}$. ..... 117

Figure 5.6: Stress-strain curves as a function of temperature for extruded CuZnBi0.8 with average applied strain rates of (a) $0.35s^{-1}$, (b) $0.64s^{-1}$ and (c) $0.85s^{-1}$. ..... 117

Figure 5.7: Stress-strain curves as a function of temperature for extruded CuZnBi2Sn with average applied strain rates of (a) $0.35s^{-1}$, (b) $0.64s^{-1}$ and (c) $0.85s^{-1}$. ..... 118

Figure 5.8: Stress-strain curves as a function of temperature for extruded CuZnSi with average applied strain rates of (a) $0.35s^{-1}$, (b) $0.64s^{-1}$ and (c) $0.85s^{-1}$. ..... 119

Figure 5.9: Stress-strain curves as a function of temperature for extruded CuZn37 with average applied strain rates of (a) $0.35s^{-1}$, (b) $0.64s^{-1}$ and (c) $0.85s^{-1}$. ..... 120

Figure 5.10: Stress-strain curves as a function of temperature for extruded CuZnSn with average applied strain rates of (a) $0.35s^{-1}$, (b) $0.64s^{-1}$ and (c) $0.85s^{-1}$. ..... 121

Figure 5.11: Stress-strain curves as a function of temperature for extruded CuZnAl with average applied strain rates of (a) $0.35s^{-1}$, (b) $0.64s^{-1}$ and (c) $0.85s^{-1}$. ..... 121

Figure 5.12: Uniaxially hot compressed sample stacks of the continuous cast CuZn39Pb2 in the temperature range of 550-800°C and average strain rate of $0.85s^{-1}$. Peak stress ($\sigma_p$) for each 50°C increment additionally labelled. ..... 124

Figure 5.13: Uniaxially hot compressed sample stacks of the extruded CuZn39Pb3 in the temperature range of 550-750°C and average strain rate of $0.85s^{-1}$. Peak stress ($\sigma_p$) for each 50°C increment additionally labelled. ..... 125

Figure 5.14: Uniaxially hot compressed sample stacks of the continuous cast CuZn37Pb2 in the temperature range of 550-800°C and average strain rate of $0.85s^{-1}$. Peak stress ($\sigma_p$) for each 50°C increment additionally labelled. ..... 126

Figure 5.15: Uniaxially hot compressed sample stacks of the extruded CuZnPb2SnFe in the temperature range of 550-800°C and average strain rate of $0.85s^{-1}$. Peak stress ($\sigma_p$) for each 50°C increment additionally labelled. ..... 127

Figure 5.16: (a) SEM-BSE image and (b) associated Cu mapping, (c) Fe mapping, (d) As mapping, (e) Pb mapping, (f) Sn mapping of CuZnPb2SnFe. There is a clear presence of intermetallic particles in the microstructure which will affect the mechanical properties of the alloy. ..... 128

Figure 5.17: Uniaxially hot compressed sample stacks of the continuous cast CuZnBi0.7 in the temperature range of 550-800°C and average strain rate of $0.85s^{-1}$. Peak stress ($\sigma_p$) for each 50°C increment additionally labelled. ..... 129

Figure 5.18: Uniaxially hot compressed sample stacks of the extruded CuZnBi0.8 in the temperature range of 550-800°C and average strain rate of 0.85$s^{-1}$. Peak stress ($\sigma_p$) for each 50°C increment additionally labelled. ..... 130

Figure 5.19: Uniaxially hot compressed sample stacks of the extruded CuZnBi2Sn in the temperature range of 550-800°C and average strain rate of 0.85$s^{-1}$. Peak stress ($\sigma_p$) for each 50°C increment additionally labelled. ..... 131

Figure 5.20: Bi-particle-rich microstructure of CuZnBi2Sn after hot compression at 550°C. After initiation (blue arrows), the fracture paths have a tendency to propagate in directional preference to these particles (red arrows). ..... 131

Figure 5.21: Uniaxially hot compressed sample stacks of the extruded CuZnSi in the temperature range of 550-800°C and average strain rate of 0.85$s^{-1}$. Peak stress ($\sigma_p$) for each 50°C increment additionally labelled. ..... 132

Figure 5.22: Uniaxially hot compressed sample stacks of the extruded CuZn37 in the temperature range of 550-800°C and average strain rate of 0.85$s^{-1}$. Peak stress ($\sigma_p$) for each 50°C increment additionally labelled. ..... 133

Figure 5.23: Uniaxially hot compressed sample stacks of the extruded CuZnSn in the temperature range of 550-800°C and average strain rate of 0.85$s^{-1}$. Peak stress ($\sigma_p$) for each 50°C increment additionally labelled. ..... 134

Figure 5.24: Uniaxially hot compressed sample stacks of the extruded CuZnAl in the temperature range of 550-800°C and average strain rate of 0.85$s^{-1}$. Peak stress ($\sigma_p$) for each 50°C increment additionally labelled. ..... 135

Figure 5.25: Comparison of the steady-state flow stress determined experimentally at an average strain-rate of 0.85$s^{-1}$ against the calculation according to the rule of mixtures for (a) CuZn39Pb2 and (b) CuZn37 using the Class 1 activation energy values $Q_\alpha$ and $Q_\beta$ calculated by Spigarelli et al. [48] (solid blue line). This is compared against a recalculated rule of mixtures using the Class 2 activation energy values (dotted line). 138

Figure 5.26: Activation energy ($Q_{Zn}$) and frequency factor ($D_{0Zn}$) data for diffusion of Zn in brass (a) in total (b) after Class 1 selection by Spigarelli [48], and (c) Class 2 data selected for this study. ..... 139

Figure 5.27: Variation of Qc and $D_{0c}$ as (a) interpolated by Spigarelli [48] using Class 1 data and (b) as interpolated using the Class 2 data. ..... 140

Figure 5.28: Comparison of the steady-state stress determined experimentally at an average strain rate of 0.85$s^{-1}$ against the calculation according to the rule of mixtures for (a) CuZn39Pb2 and (b) CuZn39Pb3. ..... 141

Figure 5.29: Comparison of the steady-state stress determined experimentally at an average strain rate of 0.85$s^{-1}$ against the calculation according to the rule of mixtures for (a) CuZn37Pb2 and (b) CuZnPb2SnFe. ..... 142

Figure 5.30: Comparison of the steady-state stress determined experimentally at an average strain rate of 0.85$s^{-1}$ against the calculation according to the rule of mixtures for (a) CuZnBi0.7, (b) CuZnBi0.8 and (c) CuZnBi2Sn. ..... 143

Figure 5.31: Comparison of the steady-state stress determined experimentally at an average strain rate of 0.85$s^{-1}$ against the calculation according to the rule of mixtures for CuZnSi. .... 143

Figure 5.32: Comparison of the steady-state stress determined experimentally at an average strain rate of 0.85$s^{-1}$ against the calculation according to the rule of mixtures for (a) CuZn37, (b) CuZnSn and (c) CuZnAl. ..... 144

Figure 6.1: Schematic representation of major experimental work undertaken in Chapter 6. ..... 149

Figure 6.2: Example of the transverse and longitudinal view for a brass rod sample. ..... 150

Figure 6.3: (a) Transverse view of the as-extruded CuZn37.2BiAs microstructure and (b) resulting dezincification of this microstructure after ISO6509-1 test conditions. (c) Transverse view of the extruded CuZn37.2BiAs microstructure after 60 minutes at ~508°C and (d) resulting dezincification of this microstructure after ISO6509-1 test conditions with inset of the β 'stringer'. ..... 151

Figure 6.4: Evolution of dezincification depths of extruded CuZn37.2BiAs as a function of intermediate heat treatment (508°C) length. Depths measured in the transverse direction (blue) and longitudinal direction (gold). ..... 152

Figure 6.5: (a) Longitudinal view of the as-extruded CuZn37.2BiAs microstructure and (b) resulting dezincification of this microstructure after ISO6509-1 test conditions. (c) Longitudinal view of the extruded CuZn37.2BiAs microstructure after 60 minutes at ~508°C and (d) resulting dezincification of this microstructure after ISO6509-1 test conditions. ..... 153

Figure 6.6: Optical micrographs of a) as-received continuous cast CuZn37.4BiAs brass microstructure, and (b) as-received extruded CuZn37.6BiPAs brass microstructure. .... 154

Figure 6.7: Observation of the tendency for dezincification to follow prior β grain boundaries in the continuous cast CuZn37.4BiAs, likely due to orientation of acicular α grains. ..... 155

Figure 6.8: (a) CuZn37.4BiAs microstructure post-heat treatment at 450°C for 15 minutes, (b) CuZn37.4BiAs microstructure post-heat treatment at 500°C for 30 minutes, (c-d) resulting dezincification of these microstructures after testing to ISO6509-1. ..... 156

Figure 6.9: Average α grain length (μm) vs. aspect ratio of continuously cast CuZn37.4BiAs samples annealed between 450-675°C. ..... 157

Figure 6.10: Continuous cast CuZn37.4BiAs Dezincification (ISO6509-1) dependency on (a) β' phase fraction while (b) α grain size is maintained. ..... 158

Figure 6.11: (a) Hot compressed CuZn37.4BiAs microstructure post-heat treatment at 550°C for 30 minutes, (b) Hot compressed CuZn37.4BiAs microstructure post-heat treatment at 750°C for 30 minutes, (c-d) resulting dezincification of these microstructures after testing to ISO6509-1. ..... 159

Figure 6.12: Hot compressed continuous cast CuZn37.4BiAs Dezincification (ISO6509-1 average depth) dependency on (a) β' phase fraction while (b) α grain size is maintained. ..... 160

Figure 6.13: (a) CuZn37.6BiPAs microstructure in the longitudinal direction post-heat treatment at 500°C for 15 minutes, (b) CuZn37.6BiPAs microstructure in the longitudinal direction

post-heat treatment at 625°C for 30 minutes, and (c-d) the resulting dezincification of these microstructures after ISO6509-1 test conditions. ..... 161

Figure 6.14: Extruded CuZn37.6BiPAs Dezincification (ISO6509-1 average depth) dependency on (a) β' phase fraction while (b) α grain size is maintained..... 162

Figure 6.15: (a) CuZn37.4BiAs microstructure post-heat treatment at 700°C for 30 minutes, (b) at 700°C for 180 minutes, (c) at 850°C for 60 minutes and ramped down to 700°C for 10 minutes, and (d-f) resulting dezincification of these microstructures after testing to ISO6509-1. ..... 163

Figure 6.16: Average α grain length (μm) vs. aspect ratio of continuously cast CuZn37.4BiAs samples annealed between 700-800°C. The self-coarsening trend is highlighted (black curves A and B). ..... 164

Figure 6.17: Continuous cast CuZn37.4BiAs Dezincification (ISO6509-1) dependency on (a) α grain size while (b) β' phase fraction is maintained. ..... 165

Figure 6.18: (a) Hot compressed CuZn37.4BiAs microstructure post-heat treatment at 700°C for 180 minutes, (b) at 850°C for 60 minutes and ramped down to 700°C for 15 minutes, and (c-d) the resulting dezincification of these microstructures after ISO6509-1 test conditions. ..... 166

Figure 6.19: Hot compressed continuous cast CuZn37.4BiAs Dezincification (ISO6509-1 average depth) dependency on (a) α grain size while (b) β' phase fraction is maintained. ..... 167

Figure 6.20: (a) CuZn37.6BiPAs microstructure in the longitudinal direction post-heat treatment at 700°C for 30 minutes, (b) CuZn37.6BiPAs microstructure in the longitudinal direction post-heat treatment at 700°C for 180 minutes, (c) CuZn37.6BiPAs microstructure in the longitudinal direction post-heat treatment at 850°C for 60 minutes and ramped down to 700°C for 10 minutes, (d-f) the resulting dezincification of these microstructures after ISO6509-1 test conditions. ..... 168

Figure 6.21: Extruded CuZn37.6BiPAs Dezincification (ISO6509-1 average depth) dependency on (a) α grain size while (b) β' phase fraction is maintained..... 169

Figure 6.22: Observation of Widmanstätten α forming along β grain boundaries in CuZn37.6BiPAs post-quenching from 700°C after a soak time of 120 minutes. ..... 170

Figure 6.23: Dezincification results of: (a) as-received CuZn37.6BiPAs and (b) CuZn37.6BiPAs heat treated at 850°C for 60 minutes and ramped down to 700°C for 10 minutes after being subject to ISO6509-1 conditions for 120 hours (5 days). Results in longitudinal direction. ..... 171

Figure 6.24: β' phase fraction (calculated using ImageJ analysis) of extruded CuZn37.8BiPAs brass after either water-quenching (orange) or air cooling (blue) from elevated temperatures as well as the estimated equilibrium β phase fraction at temperature using the CALPHAD approach [12]. ..... 173

Figure 6.25: Extruded CuZn37.8BiPAs microstructures post-heat treatment annealing for 30 minutes soak and quenched (column 1), and 20 minutes soak and air-cooled (column 2) from (a-b) 650°C, (c-d) 700°C, (e-f) 750°C, (g-h) 800°C, and (i-j) 850°C. All images at same magnification. ..... 174

Figure 6.26: The evolution of average dezincification depth of extruded CuZn37.8BiPAs to ISO6509-1 as a function of heat treatment temperature. Samples have been either air-cooled or water quenched from elevated temperatures. Depths measured in transverse direction. ..... 176

Figure 6.27: The evolution of maximum dezincification depth of extruded CuZn37.8BiPAs to ISO6509-1 as a function of heat treatment temperature. Samples have been either air-cooled or water quenched from elevated temperatures. Depths measured in transverse direction. ..... 176

Figure 6.28: ISO6509-1 Dezincification micrographs for the (a) 650$^{o}$C quenched, (b) 700$^{o}$C quenched, (c) 750$^{o}$C quenched, (d) 800$^{o}$C quenched, (e) 850$^{o}$C quenched conditions after 30-minute soak and for the (f) 800$^{o}$C air-cooled condition after 20 minutes soak. Dezincification depths shown in the transverse direction. ..... 178

Figure 6.29: Average dezincification depth results of extruded CuZn37.8BiPAs to ISO6509-1 as a function of β' phase fraction. Depths measured in transverse direction. ..... 179

Figure 6.30: Square lattice model initialised based on microstructural variables f (β vol. fraction), d (α grain size), θ (tilt angle) and k (α aspect ratio) – (a) spherical shape, (b) elliptical shape and (c) the lattice evolution of dissolved β' (red circles), undissolved β' (blue circles) and resistant α (black circles) phases in the first 5 time-steps in the simulation. The magnified region shown in (c) is highlighted in (b). ..... 181

Figure 6.31: Probability of percolation occurrence (determined from 100 repeats) as a function of β' phase fraction for 3 different α grain sizes. The site percolation threshold at 0.593 for the case of nearest neighbour in square lattice is labelled (red). ..... 183

Figure 6.32: Percolation depth at the 99$^{th}$ step as a function of β' phase fraction for 2 different α grain sizes. Error bars represent the 95% confidence interval calculated from 100 repeats. ..... 184

Figure 6.33: Percolation depth at the 99$^{th}$ step as a function of α grain size (pixel$^{-1}$) for 3 different β' phase fractions. Error bars represent the 95% confidence interval calculated from 100 repeats. ..... 185

Figure 6.34: Contour plot showing the dependence of percolation depth at the 99$^{th}$ step on the β' phase fraction and α grain size. The colour bar (right) shows the extent of the percolation depth. ..... 186

Figure 6.35: Percolation depth at the 99$^{th}$ step as a function of aspect ratio for 4 different tilt angles. Error bars represent the 95% confidence interval calculated from 100 repeats. ..... 187

Figure 6.36: Contour plot showing the dependence of percolation depth at the 99$^{th}$ step on aspect ratio and tilt angle. The colour bar (right) shows the extent of the percolation depth. 188

Figure 6.37: (a) Hot compressed CuZn37.4BiAs microstructure post heat treatment at 750$^{o}$C for 30 minutes, (b) in binary form, (c) converted to a 297 x 225 grid lattice model, and (d) the resulting percolation after the 297$^{th}$ time-step. ..... 189

Figure 6.38: (a) Hot compressed CuZn37.4BiAs microstructure post heat treatment at 550°C for 30 minutes, (b) 297 x 225 grid lattice model and resulting percolation after the 297th time-step. ..... 190

Figure 6.39: (a) Hot compressed CuZn37.4BiAs microstructure post heat treatment at 700°C for 180 minutes, (b) inset 297 x 225 grid lattice model and resulting percolation after the 297th time-step, (c) hot compressed CuZn37.4BiAs microstructure post heat treatment at 850°C for 60 minutes and ramped down to 700°C for 15 minutes, and (d) inset 297 x 225 grid lattice model and resulting percolation after the 297th time-step. ..... 191

Figure 7.1: The as-received microstructures and average Vickers hardness values for (a) CuZn39Pb3, (b) CuZnPb2SnFe, (c) CuZn37Pb2, and (d) their respective tensile stress-strain curves (x2). ..... 198

Figure 7.2: The evolution of (a) Vickers hardness and (b) α grain size and phase fraction with applied heat treatment temperature for CuZn37Pb2. ..... 200

Figure 7.3: CuZn37Pb2 microstructures post heat treatment at (a) 800°C for 30 minutes followed by air-cooling and (b) 800°C for 30 minutes followed by water-quenching. ..... 200

Figure 7.4: The as-received microstructures and average Vickers hardness values for (a) CuZnBi0.8, (b) CuZnBi2Sn, (c) CuZnBi0.7, and (d) their respective tensile stress-strain curves (x2). ..... 201

Figure 7.5: The evolution of (a) Vickers hardness and (b) α grain size and phase fraction with applied heat treatment temperature for CuZnBi0.8. ..... 202

Figure 7.6: CuZnBi0.8 microstructures post heat treatment at (a) 700°C for 30 minutes followed by water quenching, (b) 800°C for 30 minutes followed by air-cooling, and (c) 800°C for 30 minutes followed by water quenching. ..... 203

Figure 7.7: The evolution of (a) Vickers hardness and (b) α grain size and phase fraction with applied heat treatment temperature for CuZnBi2Sn. ..... 204

Figure 7.8: CuZnBi2Sn microstructure post heat treating at 800°C for 30 minutes followed by air-cooling. ..... 205

Figure 7.9: The evolution of (a) Vickers hardness and (b) α grain size and phase fraction with applied heat treatment temperature for CuZnBi0.7. ..... 205

Figure 7.10: (a) The as-received microstructure and average Vickers hardness value for CuZnSi and (b) the resulting tensile stress-strain curves (x2) for this same alloy. ..... 206

Figure 7.11: The evolution of (a) Vickers hardness and (b) α grain size and phase fraction with applied heat treatment temperature for CuZnSi. ..... 207

Figure 7.12: CuZnSi microstructures post heat treatment at (a) 700°C for 120 minutes followed by air-cooling and (b) 700°C for 30 minutes followed by water quenching. ..... 207

Figure 7.13: The as-received microstructures and average Vickers hardness values for (a) CuZnSn, (b) CuZnAl, (c) CuZn37 and (d) their respective tensile stress-strain curves (x2). ..... 208

Figure 7.14: An example of drilling feed force ($F_Z$) measurement as a function of time for as-received CuZnSi for the program set on the Spinner U-620. Segment A – Drill positioning, Segment B – Full Testing. ..... 209

Figure 7.15: An example of drilling torque ($M_Z$) measurement as a function of time for as-received CuZnSi for the program set on the Spinner U-620. Segment A – Drill positioning, Segment B – Full Testing. ..... 210

Figure 7.16: (a) Average feed force ($F_Z$) and (b) drilling torque ($M_Z$) for each of the CuZn alloys tested in the as-received condition. ..... 210

Figure 7.17: Correlations observed between (a) Vickers hardness and feed force, (b) UTS and feed force, (c) Vickers hardness and drilling torque and (d) UTS and drilling torque for each of the alloys in the 'as-received' condition. The feed forces ($F_Z$) are significantly more affected by the mechanical properties of the alloy, whilst there are only weak or negligible correlations for drilling torque ($M_Z$). ..... 212

Figure 7.18: Correlations observed between (a) elongation and feed force and (b) elongation and drilling torque. An increase in the ductility of the alloy is shown to be detrimental to both forms of machinability. ..... 213

Figure 7.19: Average drilled surface roughness ($R_a$) for each of the CuZn alloys tested in the as-received condition. ..... 214

Figure 7.20: Correlations observed between (a) Vickers hardness and (b) elongation and surface roughness for each of the alloys in the 'as-received' condition. Whilst a weak correlation is noted for ductility, the surface roughness does appear to be moderately impacted by the Vickers hardness. ..... 215

Figure 7.21: Swarf morphology of (a) CuZnPb2SnFe, (b) CuZn37Pb2, (c) CuZnBi0.8, (d) CuZnSi, (e) CuZnBi0.7, (f) CuZnBi2Sn, (g) CuZn39Pb3, (h) CuZnSn, (i) CuZn37, (j) CuZnAl and a grading summary of each. ..... 217

Figure 7.22: The evolution of Feed Force ($F_Z$) with increasing Vickers hardness segregated by colour into key groups (Pb-Alloys, each of the individual Bi-Alloys, CuZnSi and other CuZn alloys). ..... 218

Figure 7.23: The evolution of Feed Force ($F_Z$) with increasing FCC α (a) grain size and (b) phase fraction segregated by colour into key groups (Pb-Alloys, each of the individual Bi-Alloys, CuZnSi and other CuZn alloys). ..... 219

Figure 7.24: The evolution of Drilling Torque ($M_Z$) with increasing Vickers hardness segregated by colour into key groups (Pb-Alloys, each of the individual Bi-Alloys, CuZnSi and other CuZn alloys). ..... 221

Figure 7.25: The evolution of Drilling Torque ($M_Z$) with increasing FCC α (a) grain size and (b) phase fraction segregated by colour into key groups (Pb-Alloys, each of the individual Bi-Alloys, CuZnSi and other CuZn alloys). ..... 222

Figure 7.26: Compound composition of Pb + Bi wt. % vs. the average drilling torque ($M_Z$) for all of the brasses tested in the machinability study. ..... 223

Figure 7.27: BSE images (500x) of (a) CuZn39Pb3 as received, (b) CuZn37Pb2 as received, (c) after soaking at 500°C for 120 minutes and air-cooled, (d) after soaking at 700°C for 120 minutes and air-cooled, (e) after soaking at 800°C for 30 minutes and water quenching and (f) CuZnPb2SnFe as received. ..... 225

Figure 7.28: BSE images (500x) of (a) CuZnBi0.7 as received, (b) after soaking at 500°C for 120 minutes and air-cooled, (c) after soaking at 700°C for 120 minutes and air-cooled, (d) after soaking at 800°C for 30 minutes and water quenching and (e-h) as for images a-d but with CuZnBi0.8. ..... 226

Figure 7.29: BSE images (500x) of (a) CuZnBi2Sn as received, (b) after soaking at 500°C for 120 minutes and air-cooled, (c) after soaking at 700°C for 120 minutes and air-cooled, (d) after soaking at 800°C for 30 minutes and water quenching and (e) magnified view of as received sample to show Sn-bearing intermetallics. ..... 227

Figure 7.30: BSE images (500x) of (a) CuZnSi as received, (b) after soaking at 500°C for 120 minutes and air-cooled, (c) after soaking at 700°C for 120 minutes and air-cooled, (d) after soaking at 800°C for 30 minutes and water quenching. ..... 228

Figure 7.31: BSE images (500x) of (a) CuZn37 as received, (b) CuZnSn as received and (c) CuZnAl as received. ..... 228

Figure 7.32: The evolution of drilling torque ($M_Z$) with increasing (a) Pb + Bi particle density and (b) average particle size segregated into the 4 heat-treated alloys (CuZn37Pb2, CuZnBi0.7, CuZnBi0.8, CuZnBi2Sn). ..... 230

Figure 7.33: The evolution of Surface Roughness ($R_a$) with increasing Vickers hardness segregated by colour into key groups (Pb-Alloys, each of the individual Bi-Alloys, CuZnSi and other CuZn alloys). ..... 231

Figure 7.34: The evolution of Surface Roughness ($R_a$) with increasing FCC α (a) grain size and (b) phase fraction segregated by colour into key groups (Pb-Alloys, each of the individual Bi-Alloys, CuZnSi and other CuZn alloys). ..... 232

Figure 7.24: CuZnSi microstructures for the (a) air-cooled and (b) quenched state after soaking at 600°C for 30 minutes. The BCC ε forms at lower temperatures upon air-cooling but does not have adequate time to form during quenching. ..... 232

Figure 7.36: Compound composition of Pb + Bi wt. % vs. the average surface roughness ($R_a$) for all of the brasses tested in the machinability study. ..... 233

Figure 7.37: The evolution of drilling surface roughness ($R_a$) with increasing (a) Pb + Bi particle density and (b) average particle size segregated into the 5 heat-treated alloys (CuZn37Pb2, CuZnBi0.7, CuZnBi0.8, CuZnBi2Sn)..... 234

# List of Tables


Table 1.1: C35330 and C48600; brass alloys traditionally used in the plumbing industry. C46500; A traditional 'lead-free' brass used in Naval applications. C28340, C49340, and C69300; Common 'lead-free' brass alloys designed to replace traditional leaded alloys for use in the plumbing industry [2]. *bismuth (Bi) and silicon (Si) are two elements often added to the composition in place of lead (Pb). 4

Table 2.1: Classification of Cu-alloys according to the North American UNS Designations [1]. 7

Table 2.2: Approximate atom size difference and solubility of various solutes in copper [1]. 8

Table 2.3: Calculated values of the diffusion coefficient of Zn diffusion through BCC β and FCC α at 950K. 12

Table 2.4: Guillet and Portevin Zinc Equivalents [26]. 16

Table 2.5: A comparison of various material properties for both a common Si-bearing brass alloy (C69300) and a Pb-bearing brass alloy (C38500) [120]. 53

Table 3.1: Duplex brass phases, space groups and lattice parameters [1, 223-226]. 78

Table 4.1: Chemical composition (wt. %) of the investigated workpiece materials for microstructural characterisation. 81

Table 4.2: Chemical composition (wt. %) of the investigated workpiece materials for Neutron diffraction experiments. 81

Table 4.3: Phase equilibria assessment methods undertaken for each alloy. 81

Table 5.1: Chemical composition (wt. %) of the investigated workpiece materials for uniaxial hot compression. 112

Table 5.2: Estimated BCC β phase fraction (%) of the investigated workpiece materials for uniaxial hot compression using CALPHAD calculations. 113

Table 5.3: Comparison of peak and steady-state flow stress (MPa) against the estimated β phase fraction (%) for each of the 11 duplex brasses at T = 700°C and $\dot{\varepsilon} = 0.85s^{-1}$. 113

Table 5.4: Summary of temperature conditions vs. observation of fracture (O = No Fracture, X = Fracture, H = Hairline or Very Close to Fracture, W = Wrinkling, - = Not Tested). 122

Table 5.5: Summary of forgeability index ratings for each of the alloys tested under uniaxial hot compression. 123

Table 5.6: Constitutive equation parameters for the α and β phases according to Spigarelli et al. [48, 60] assuming 36 wt. % Zn for FCC α and 44 wt. % Zn for BCC β. 137

Table 6.1: Chemical composition (wt. %) of the investigated workpiece materials for microstructure-dezincification analysis. (CC) = continuous cast rod, (EX) = extruded rod. ..... 147

Table 6.2: Dezincification resistance of the two as-received rod sections according to ISO6509-1. ..... 155

Table 6.3 (a) Heat treatment conditions and microstructural parameters used for extended dezincification testing according to ISO6509-1. ..... 171

Table 6.3 (b) Dezincification results after 24 hours and 120 hours – Longitudinal Direction. ..... 171

Table 7.1: Chemical composition (wt. %) of the investigated workpiece materials for machinability evaluations. ..... 194

Table 7.2: Heat-treatment parameters applied to CuZn37Pb2, CuZnBi0.7, CuZnBi0.8, CuZnBi2Sn and CuZnSi. ..... 196

Table 7.3: Room temperature tensile data for each of the alloy sample compositions shown in Table 7.1. ..... 197

Table 7.4: CuZn alloy samples submitted for BSE analysis and their resulting average particle size and density as measured using ImageJ analysis. ..... 224

Table A1: U.N.S. Chemical Composition Ranges (wt. %) of commonly found alloys in this thesis. 246

# 1 Introduction

## 1.1 Brass Manufacturing

Brass (Cu-Zn) has been the traditional material of choice for the manufacture of plumbing fittings, faucets and valves for use in potable water applications. This is due to the ease with which brass is processed during typical manufacturing steps like casting, forging, and machining while simultaneously satisfying the requisite in-service properties, namely good mechanical strength and corrosion resistance [1]. This is demonstrated by production levels in excess of 900,000 Tonnes of material from brass mills in the U.S. in 2016 [2]. Examples of two types of brass plumbing fittings (barb and push-to-connect) are shown in Fig. 1.1 and the differences in geometry between the straight fittings and the elbow fittings helps to determine the manufacturing process used.

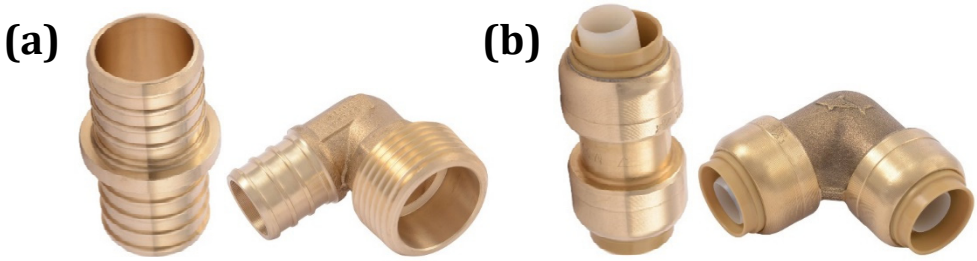


**Figure 1.1: Examples of brass plumbing fittings. (a) a 1" straight barb fitting and ½" elbow barb fitting with thread adaptor, (b) a ½" straight push-to-connect (PTC) fitting, and a ½" elbow PTC fitting [3].**

Due to their simple design, the straight fittings may be directly machined from continuously cast or extruded rod. In these cases, the machinability of the original rod is a key determinant of the efficiency of the process. The elbow fittings are very difficult to directly machine without the correct section or shape of rod, and even then, there would be significant material wastage during machining. Therefore, an elevated temperature forging step and subsequent machining is more commonly utilised in order to efficiently generate the desired geometry.

Many plumbing components, such as the examples shown in Fig. 1.2, use a combination of both directly machined and forged components in order to produce the highest manufacturing efficiencies.

**Figure 1.2: Examples of more complicated plumbing valves which use a combination of directly machined and forged components. (a) A thermostatic mixing valve, (b) a ball valve [3, 4].**

A schematic illustration of a typical processing schedule for the manufacture of a forged brass plumbing component is shown in Fig. 1.3.

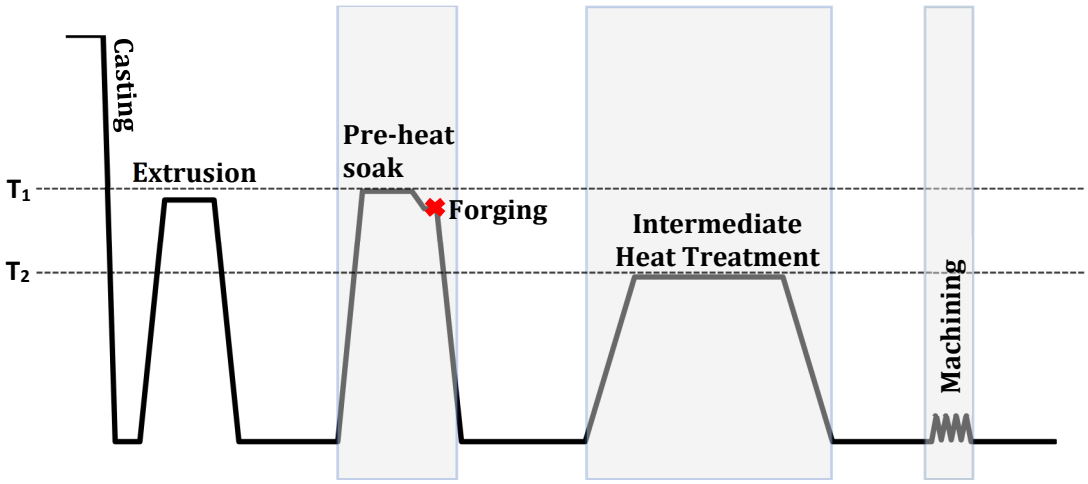


**Figure 1.3: A typical processing schedule (time vs. temperature) for a potable water plumbing component utilising a forging step.**

The alloy begins in the form of a billet workpiece, cut from a length of rod which has been fabricated by either continuous casting or casting then extrusion (Fig. 1.4a). This has the desired dimensions (length and diameter) suitable for the specific forging design. The billet, which is commonly coated in graphite for lubrication and thermal efficiencies, is first heated to elevated temperatures ($T_1$), typically between 700-750$^{o}$C, after which it is forged into the rough design geometry and air-cooled to room temperature (Fig. 1.3, Fig. 1.4b)). The flash is trimmed away and the component is subjected to an intermediate heat treatment (IHT) step ($T_2$), typically between 400-550$^{o}$C (Fig. 1.3). The components are subsequently shot-blast with fine steel pellets to remove surface imperfections, oxidation from the IHT, and any sharp edges (Fig. 1.4c). These shot-blast components are then machined (Fig. 1.3) into their desired internal and external dimensions (Fig. 1.4d) using a combination of drilling, turning, and threading operations. Some types of potable water fittings and valves then have cartridges

inserted into the brass body, which require the edges of the component to be cold worked or 'crimped' to hold the cartridge in place.

Efficient processing of these brass fittings and valves requires a detailed understanding of elevated temperature plastic deformation, the dependence of the corrosion resistance on the microstructure, and the dependence of the machinability and cold workability of these alloys on the chemical composition and microstructure.

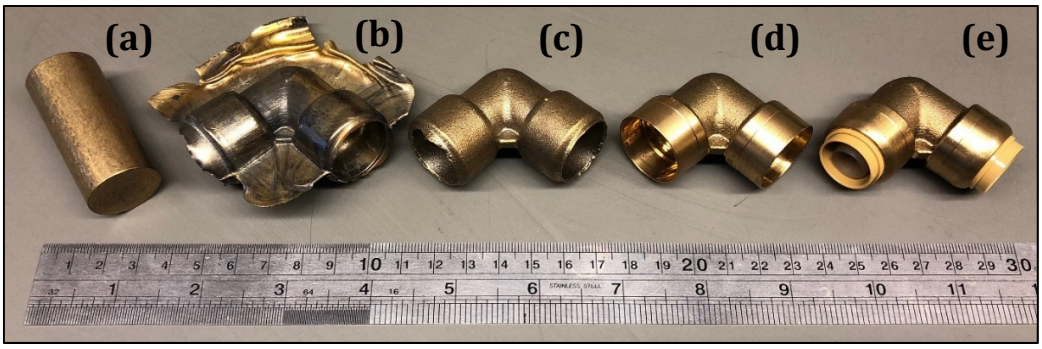


**Figure 1.4: (a) A brass billet workpiece sectioned from a rod for forging, (b) an elbow fitting (with flash) after the forging process, (c) a heat-treated forging after the shot-blasting process, (d) a machined fitting body, and (e) the final machined plumbing fitting with a cartridge crimped into the brass body.**

## 1.2 The Emergence of 'Lead-Free'

Until recently, the favoured brass grades for the types of components shown in Figs. 1.1 and 1.2 were known as dezincification resistant or 'DZR' brass. The two most common are designated according to the North American United Numbering System (U.N.S) as designations C35330 and C48600 listed in Table 1.1. Lead (Pb) is included in these designations largely because it improves the machinability of these alloys [1] and each of the processing steps schematically illustrated in Fig. 1.3 have been optimised in the plumbing industry for these two grades of brass. The industry, however, is currently undergoing a major transition from leaded to 'lead-free' brass. This is inclusive of the author's company, Reliance Worldwide Corporation, which produces in excess of 40 million brass plumbing components each year for a variety of regions around the world.

**Table 1.1: C35330 and C48600; brass alloys traditionally used in the plumbing industry. C46500; A traditional 'lead-free' brass used in Naval applications. C28340, C49340, and C69300; Common 'lead-free' brass alloys designed to replace traditional leaded alloys for use in the plumbing industry [2]. *bismuth (Bi) and silicon (Si) are two elements often added to the composition in place of lead (Pb).**

| Alloy Description | U.N.S. Alloy | Cu wt. % | Zn wt. % | Pb wt. % | Sn wt. % | As wt. % | Bi wt. % | P wt. % | Si wt. % |
|---|---|---|---|---|---|---|---|---|---|
| Leaded (DZR) Plain | C35330 | Rem. | 32.3 – 39.0 | 1.5 – 3.5 | - | 0.02 – 0.25 | - | - | - |
| Leaded (DZR) + Sn | C48600 | Rem. | 33.8 – 38.7 | 1.0 – 2.5 | 0.30 – 1.5 | 0.02 – 0.25 | - | - | - |
| Lead-Free (DZR) As-Inhibited | C46500 | Rem. | 36.6 – 40.5 | 0.20 max. | 0.50 – 1.0 | 0.02 – 0.06 | - | - | - |
| Lead-Free (DZR) Bi-bearing | C28340 | Rem. | 36.4 – 37.8 | 0.17 – 0.25 | 0.30 – 0.40 | 0.07 – 0.17 | 0.65 – 0.75 | *(A) | 0.05 max. |
| Lead-Free (DZR) Bi-bearing | C49340 | Rem. | 33 – 39 | 0.09 max. | 0.50 – 1.5 | - | 0.50 – 2.2 | 0.05 – 0.15 | 0.10 max. |
| Lead-Free (DZR) Si-bearing | C69300 | Rem. | 19.2 – 24.3 | 0.09 max. | 0.20 max. | - | - | 0.04 – 0.15 | 2.7 – 3.4 |

**(A): P may be substituted for As.*

On the 30th September 2006, the Californian state bill AB1953 was passed into law under the CA Health & Safety Code 116875. This state law imposed a new limitation on the use of lead (Pb) in plumbing components in contact with potable drinking water to a maximum 0.25 wt. % and had an effective date of the 1st January 2010. This state law acted as the catalyst for national interest surrounding the legislation into lead-free water fittings and progressed around the United States becoming national law on the 1st January 2014 [5, 6], followed shortly thereafter by Canada [7]. The primary reason for its implementation was due to health concerns surrounding lead leaching from fittings into drinking water [8]. The removal of the vast majority of lead from brass has created numerous challenges in the manufacturing process and particularly in the last 5 years we have seen the emergence of several new 'lead-free' alloys that claim to have equal or similar processability, mechanical strength, and corrosion resistance. A selection of these new grades are shown in Table 1.1.

Each of the 'lead-Free' brasses containing Bi and Si listed in Table 1.1 were originally designed for introduction into low-lead markets and applications, and although they have been assessed to comply with the U.S. legislation on Pb additions, there has been relatively little research conducted on the processing characteristics of these alloys. Many manufacturing companies, and even regions around the world are at odds over which alloy system is the best and, in many cases, older well established

'lead-free' alloys like C46500 (Table 1.1), also known as Naval brass due to its traditional application, have been brought back into use due to their comparative processing simplicity. This has not however slowed down the discussion and eventual progression of other still leaded regions (for example Western Europe, Australia and New Zealand) towards 'lead-free' legislation [9, 10].

The brass industry is still an experience-oriented industry, where until recently the best alloy and processing combinations have been well-known. As a direct result of the removal of Pb (limitation of 0.25 wt. %) from common industrial brass alloys, there is a tendency for rejection rates to increase dramatically during the manufacturing process. The increase in rejection rates, typically in the form of elevated susceptibility to cracking and related machining or cold working defects, is partially due to the clear decrease in machinability associated with the removal of Pb, but it is also because the industry is, in many cases, still attempting to use many of the same processing parameters (e.g. forging temperatures, intermediate heat treatment parameters, machining parameters) without knowledge of the consequences. It is unfortunately, in many cases, a trial and error approach. For high volume manufacturing of simple geometry fittings, for example, rejection rates can more than double if processing parameters are not adjusted appropriately. This is because the limitation of Pb has an effect not only on machining, but also forging, extrusion, heat treatment and casting and each of these steps need to be optimised for 'lead-free' alloy systems in order for the industry to move forward. There is a need to rediscover the metallurgy of brass, in the context of these new Pb-free grades, so that processing may be re-optimised for the fabrication of the types of components shown in Figs. 1.1 – 1.3. This is the topic of this thesis.

# 2 Literature Review

## 2.1 Introduction

This thesis will draw upon several fields related to the processing and service characteristics of duplex (α + β) brass for potable water applications. This includes phase equilibria and transformations, hot working, machining, and cold working, as well as dezincification and stress corrosion cracking resistance. In the following, we summarise the current state of knowledge in these areas as they pertain to duplex brasses. Presented first is an introduction to Cu-Zn alloys, and the designations relevant to this research, followed by an introduction to duplex brasses and their respective phase equilibria. The elevated temperature properties of duplex brass are then summarised including the various factors involved in the forging of this material and the reasoning for its widespread use in the manufacturing industry. The use of intermediate heat treatments post-forging is explored with an emphasis on the benefit to the corrosion properties of duplex brass. This is followed by an examination of the role of lead in brass for improved machining characteristics, common measures of machinability, and lead-free alternative brasses currently utilized in the potable water industry. Finally, cold-working processes post-machining are reviewed with connections made to common defects and stress corrosion cracking resistance of duplex brass.

## 2.2 Brass (Cu-Zn) Alloys and Phase Equilibria

### 2.2.1 Alloy Families and Designations

There are a wide variety of copper alloys available in industry and these are separated into alloy families by two factors: (1) the fabrication method and (2) the chemical composition. Alloy systems are designated as either ‘Cast’ (i.e. directly cast into the desired shape or geometry, for example via sand casting) or ‘Wrought’ (i.e. the material is worked in some way, for example via extrusion or forging). The designation according to chemical composition is typically characterised via the most common alloying additions found in copper alloys, such as lead (Pb), tin (Sn), or nickel (Ni).

There are several copper alloy designation systems available to industry. The system used is often characteristic of the various regions around the world. The most commonly used designation in Europe, is the Comité Européen de Normalisation (CEN) system which utilises a 6-figure code to

describe the alloy [1]. For example, CW509L describes a copper alloy (C), in the wrought state (W), with the reference 509L relating to a binary Cu-40Zn brass alloy [2]. In North America, and many other parts of the world, the most common designation is the Unified Numbering System (UNS) which was designed by the National Institute of Standards and Technology [2]. Table 2.1 shows the general classification of copper alloys in the UNS system where each designation is given a 5-figure code. For example, C37700 describes a copper alloy (C), with a general makeup of Cu-Zn-Pb (3), and a reference of 7700 relating specifically to a common alloy known as 'Forging Brass' with the composition Cu-38Zn-2Pb. For the purposes of this thesis, UNS designations will be used where appropriate.

**Table 2.1: Classification of Cu-alloys according to the North American UNS Designations [1].**

| Generic name | UNS No. | Composition |
|---|---|---|
| **Wrought alloys** | | |
| Coppers(a) | C10100–C15815 | >99% Cu |
| High-copper alloys(b) | C16200–C19900 | >96% Cu |
| Brasses | C20100–C28000 | Cu-Zn |
| Leaded brasses | C31200–C38500 | Cu-Zn-Pb |
| Tin brasses | C40400–C48600 | Cu-Zn-Sn-Pb |
| Phosphor bronzes | C50100–C52480 | Cu-Sn-P |
| Leaded phosphor bronzes | C53400–C54400 | Cu-Sn-Pb-P |
| Copper-phosphorus and copper-silver-phosphorus alloys(c) | C55180–C55284 | Cu-P-Ag |
| Aluminum bronzes | C60800–C64210 | Cu-Al-Ni-Fe-Si-Sn |
| Silicon bronzes | C64700–C66100 | Cu-Si-Sn |
| Other copper-zinc alloys | C66300–C69710 | Cu-Zn-Mn-Fe-Sn-Al-Si-Co |
| Copper nickels | C70100–C72950 | Cu-Ni-Fe |
| Nickel silvers | C73500–C79830 | Cu-Ni-Zn |
| **Cast alloys** | | |
| Coppers(a) | C80100–C81200 | >99% Cu |
| High-copper alloys(d) | C81400–C82800 | >94% Cu |
| Red and leaded red brasses | C83300–C83810 | Cu-Sn-Zn-Pb (82–94% Cu) |
| Semi-red and leaded semi-red brasses | C84200–C84800 | Cu-Sn-Zn-Pb (75–82% Cu) |
| Yellow and leaded yellow brasses | C85200–C85800 | Cu-Zn-Pb |
| Manganese bronzes and leaded manganese bronzes(e) | C86100–C86800 | Cu-Zn-Mn-Fe-Pb |
| Silicon brasses/bronzes | C87300–C87800 | Cu-Zn-Si |
| Copper-bismuth and copper-bismuth-selenium alloys | C89320–C89940 | Cu-Sn-Zn-Bi-Se |
| Tin bronzes | C90200–C91700 | Cu-Sn-Zn |
| Leaded tin bronzes | C92200–C94500 | Cu-Sn-Zn-Pb |
| Nickel-tin bronzes | C94700–C94900 | Cu-Ni-Sn-Zn-Pb |
| Aluminum bronzes | C95200–C95900 | Cu-Al-Fe-Ni |
| Copper nickels | C96200–C96950 | Cu-Ni-Fe |
| Nickel silvers | C97300–C97800 | Cu-Ni-Zn-Pb-Sn |
| Leaded coppers | C98200–C98840 | Cu-Pb |
| Special alloys | C99300–C99750 | Cu-Zn-Mn-Al-Fe-Co-Sn-Pb |

(a) Metals that have a designated Cu content of 99.3% or higher. (b) For wrought products, those alloys with designated Cu contents less than 99.3%, but more than 96% that do not fall into any other copper alloy group. (c) Brazing filler metal alloys. (d) Cast high-copper alloys have designated Cu contents in excess of 94%, to which Ag may be added for special properties. (e) Also referred to as high-strength and leaded high-strength yellow brasses

### 2.2.2 Brass (Cu-Zn) Alloys

Brasses are copper (Cu) based solid-solution alloys that contain zinc (Zn) as the primary alloying element. They are the most widely used Cu-based alloys [2] and Cu alloys are the third most widely used alloys after ferrous and Al alloys [2]. Although Zn has an approximate atom size difference of only -4% compared with Cu (Table 2.2), its high solubility in FCC copper of up to 39% leads to a significant solid-solution-strengthening effect (Fig. 2.1). This solid solution strengthening effect increases with increasing Zn content and occurs whilst maintaining the excellent corrosion resistance of the FCC Cu [1]. The Zn in solid solution also enhances the strain hardening capacity of FCC Cu and this means

single-phase FCC brasses also exhibit greater elongation/formability than pure Cu (Fig. 2.1). This makes them excellent choices for applications requiring good corrosion resistance, medium strength, and good formability [1].

**Table 2.2: Approximate atom size difference and solubility of various solutes in copper [1].**

| Solute | Approximate atom diameter size difference, % $(d_{Cu} - d_M)/d_{Cu}$ | Approximate solubility in Cu, wt% |
|---|---|---|
| Oxygen | +113 | 0 |
| Beryllium | +14 | 2 |
| Aluminum | –11 | 9 |
| Silicon | +9 | 5 |
| Phosphorus | +70 | 2 |
| Nickel | +2 | 100 |
| Zinc | –4 | 39 |
| Arsenic | +2 | 8 |
| Silver | –11 | 8 |
| Cadmium | –14 | 3 |
| Tin | –15 | 15 |
| Antimony | –12 | 11 |
| Gold | –11 | 100 |
| Bismuth | –18 | 0 |
| Lead | –27 | 0 |

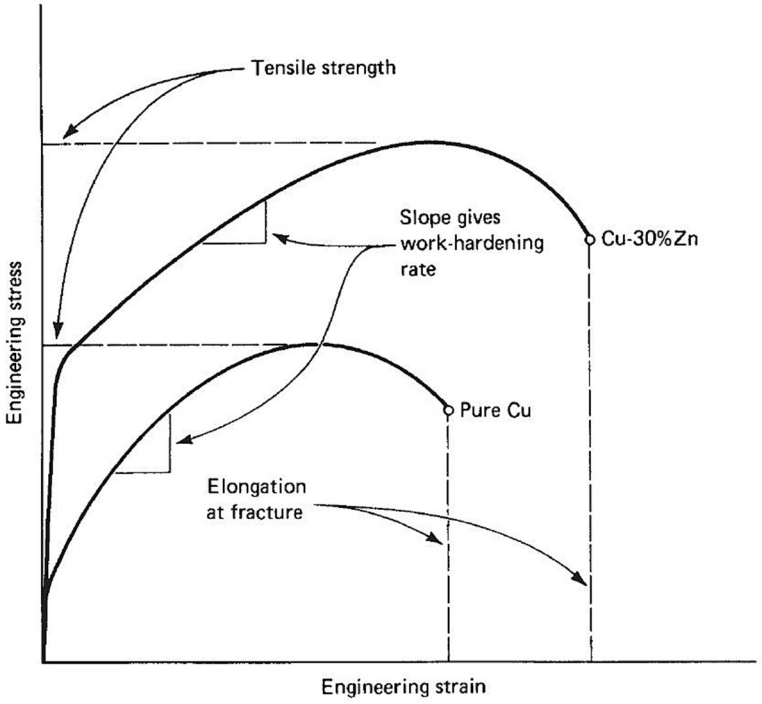


**Figure 2.1: Engineering stress-strain curves exhibiting the solid solution strengthening effects of a 30 wt. % Zn alloy (Cu-30Zn) against pure copper. Cu-30Zn has a comparatively higher tensile strength, yield strength, and greater elongation to fracture [1].**

The Cu-Zn binary phase diagram is shown in Fig. 2.2 [1]. Zn is soluble in FCC Cu up to a maximum of ~39 wt. % at 456°C and ~35 wt. % at room temperature. Beyond these Zn contents a body centred cubic (BCC) crystal structure (intermediate solid solution) is introduced. These are known as the α

(FCC, space group $Fm\bar{3}m$ [11]) and β (disordered BCC, space group $Im\bar{3}m$ [11]), or β' (ordered BCC, space group $Pm\bar{3}m$ [11]) below 456°C, phases and form the basis of the vast majority of brass alloys used in the plumbing industry today.

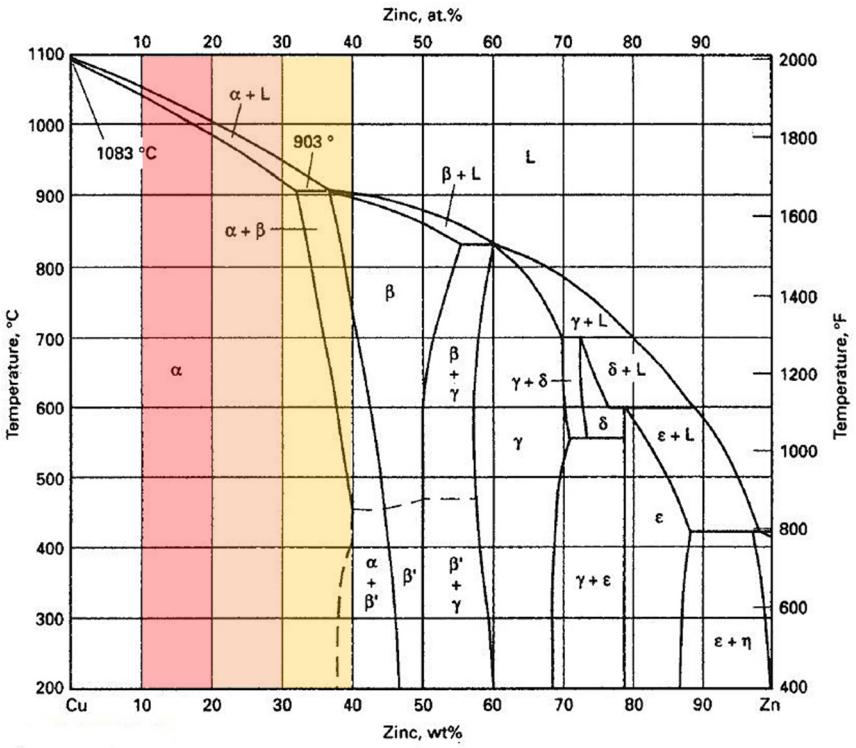


**Figure 2.2: Cu-Zn Binary Phase Diagram [1]. Three regions highlighted to show what are commonly referred to as Red Brasses, Semi-Red Brasses, and Yellow Brasses.**

Brasses that are industrially relevant will rarely exist without some fraction of the α phase due to its inherently high corrosion resistance and ductility [2]. For example, brasses that are designed to be directly cast into near-net shape components typically use Zn additions that will allow the alloy to remain entirely in the α phase field upon solidification. Common 'ounce-metal' or '85-5-5-5' castings (C83600) will use ~5 wt. % Zn along with similar additions of Sn and Pb. Wrought brasses containing ~10-20 wt. % Zn (red region in Fig. 2.2) are 100% α phase alloys that are commonly used for architectural components and jewellery due to their natural aesthetic (commonly referred to as Red Brasses) [1]. Above 20 wt. %, Zn additions become more useful to the overall mechanical and processing properties of the brass. The ability to deep draw components, for example, is far more easily achieved. Cu-30Zn is a commonly utilized α phase brass used to manufacture cartridge cases and heat exchangers.

The plumbing industry tends to increase the Zn content of brass alloys even further, into a region known as Yellow Brasses (Fig. 2.2) in order to take advantage of the unique properties of both the α

and β phases in what are commonly called 'Duplex' or 'Dual-phase' brasses. These two phases are utilised together during processing, taking advantage of the increased workability of the β phase at elevated temperatures, the good room temperature workability of the α phase, and the high stability of the α phase at intermediate temperatures leading to excellent corrosion resistance of the final components. It is the variation in stability of the α and β phases as a function of temperature (Fig. 2.2) which determines the temperatures at which the different processing steps in Fig. 1.3 take place.

The phase diagram in Fig. 2.3a illustrates a closer view of the phase stabilities of the α and β phases in a standard binary Cu-Zn alloy. The (α+β) phase field is very important for the processing of duplex brass alloys into plumbing components, particularly for high temperature processes such as forging and extrusion (Fig. 1.3). It is observed that the slope of the α/(α+β) phase boundary is very steep, so even minor variations in the chemical composition of the alloy will lead to a significant change in the α/β phase fraction in the microstructure at any given temperature. Fig. 2.3b illustrates the change in phase fraction of α and β as a function of temperature for two duplex brasses containing different amounts of Zn (37.5 and 39.0 wt. % respectively). The simple addition of 1.5 wt. % Zn stabilises the β phase at much lower temperatures so the ratio of Cu to Zn is very important in determining both the α/β phase fractions and the subsequent optimal processing parameters of the alloy.

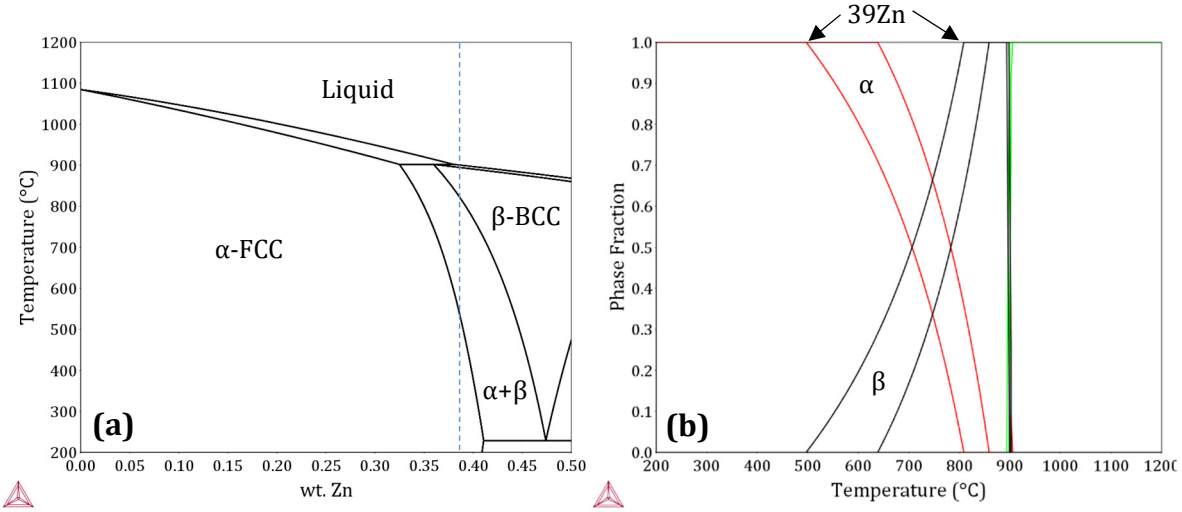


**Figure 2.3: (a) The Cu-rich corner of the Cu-Zn Binary Phase Diagram calculated using the thermodynamic assessment of Miettinen [12] with the 39Zn wt. % highlighted, and (b) Plot of phase fraction of α (red) and β (black) as a function of temperature for Cu-39Zn (highlighted) and Cu-37.5Zn (wt. %) calculated using the thermodynamic assessment of Miettinen [12].**

### 2.2.3 Characteristics of the α and β Phase

Some example microstructures of a typical duplex brass (C28340; Cu-38Zn-0.7Bi-0.3Sn) are shown in the optical micrographs in Fig. 2.4a-c identifying each of the phases present, that is FCC α and ordered BCC β' (each of these microstructure was cooled in air from elevated temperature and the disordered β present at high temperatures has undergone ordering below 450°C to become β'). The β' phase appears dark due to the preferential attack of the etchant (acidic ferric chloride) [13]. In Fig. 2.4a, the α phase has formed in the solid-state during cooling from high temperature, with an initial preference to form along the β grain boundaries. By cooling through the α + β phase field, the alloy avoids the typical dendritic α phase structure common in single-phase as-cast alloys. As the α phase becomes more stable throughout cooling, it forms the majority of the phase percentage in this microstructure. Fig. 2.4b exhibits an extruded microstructure in the transverse direction. The α grains in this state have become equiaxed upon cooling from the hot working extrusion temperatures. Fig. 2.4c shows a forged microstructure after intermediate heat treatment (~500°C). At intermediate temperatures, the α phase is stabilised at the expense of the dark β' phase and thus makes up more than 90% of the phase fraction in this micrograph. This is discussed further in Section 2.4.

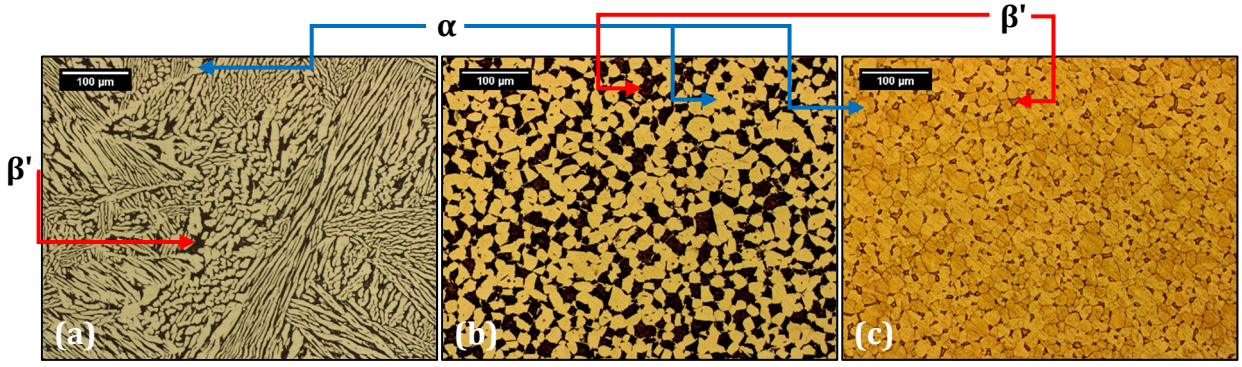


**Figure 2.4: (a-c) Duplex Cu-Zn Microstructures exhibiting the α phase (lighter) and the β' phase (darker).**

Although it is not desirable to retain a 100% phase fraction of β' in a duplex brass microstructure for industrial purposes, if one were to try, it would be very difficult to prevent the nucleation and growth of some FCC α phase in duplex brass, even when very fast cooling rates from the 100% β phase-field are employed [14]. This is because the diffusivity of Zn in the 'open' BCC β phase is very fast, much faster than in the FCC α phase. This means that the Zn redistribution from α to β that needs to occur for α precipitation from β can occur quickly. Diffusion of Zn in the α phase is much slower and as a result, the precipitation and growth of β grains from α requires a longer time period. The diffusivity of Zn is expressed by an Arrhenius equation:

$$D = D_o \exp(-Q/RT) \qquad (2.1)$$

D is the diffusion coefficient, $D_o$ is known as the pre-exponential, Q is the activation energy for diffusion, R is the gas constant, and T is the absolute temperature [1]. The activation energy and pre-exponential for Zn diffusion in the disordered BCC β phase is ~78.6 (kJ $mol^{-1}$) and ~3.5 x $10^{-7}$ ($m^2$ $s^{-1}$) for a T range of 772 – 991K [15]. The activation energy and pre-exponential for Zn diffusion in the FCC α phase is ~135.6 (kJ $mol^{-1}$) and ~5.6 x $10^{-7}$ ($m^2$ $s^{-1}$) for a T range of 907 – 1074K [15]. This results in a diffusivity for Zn in β that is two orders of magnitude greater than for α in the temperature range typically of interest. An example of this is shown at 950K in Table 2.3.

**Table 2.3: Calculated values of the diffusion coefficient of Zn diffusion through BCC β and FCC α at 950K.**

| Zn diffusion in | $D_o$ ($m^2$ $s^{-1}$) | Q (kJ $mol^{-1}$) | D ($m^2$ $s^{-1}$) |
|---|---|---|---|
| BCC β | 3.5 x $10^{-7}$ | 78.6 | 1.7 x $10^{-11}$ |
| FCC α | 5.6 x $10^{-7}$ | 135.6 | 2.0 x $10^{-14}$ |

The FCC α phase of brass exhibits excellent corrosion resistance, good room temperature ductility and is often characterised by the presence of twins that are the result of annealing after deformation [1]. The plasticity of the FCC α phase is very sensitive to grain size as a result of a low stacking fault energy ($\gamma_{SFE}$), estimated to be ~80mJ.$m^{-2}$ in Cu which progressively decreases with increasing Zn content to <10mJ.$m^{-2}$ in α brass [1, 16]. If we were to observe the {111} plane in FCC α (Fig. 2.5a), close packed in an ABC ABC arrangement, faults can be easily created in the stacking sequence during plastic deformation to become ABC AC AB (called a stacking fault). This is an energetically favourable process and is realised in the form of an extended dislocation consisting of a thin hcp region bounded by partial dislocations (Fig. 2.5b) [16]. These partial dislocations are also known as Shockley partials [17]. Although partial dislocations repel each other, they will have a surface tension that pulls them together and this is largely dictated by the stacking fault energy. For low $\gamma_{SFE}$ FCC alloys like α brass, the partial dislocations therefore have a wider fault region which results in banded, linear arrays of dislocations leading to faster strain-hardening and the tendency to twin during annealing. In essence, the low $\gamma_{SFE}$ of FCC α leads greater 'planarity' of slip during deformation [16]. The result is that the linear arrays of dislocations pile up at grain boundaries during deformation which in turn causes high stress concentrations, especially in larger grains. Therefore, as coarsening of α grains occurs during any elevated temperature process, the α phase will simultaneously become more susceptible to cracking due to strain localisation. This is of particular importance during hot working processes such as extrusion and forging where temperatures up to 800°C are utilised. Care needs to be taken to ensure that the workpiece is not kept at elevated temperatures for extended periods of time as the remaining α phase grains present in the microstructure will continue to grow rapidly, with the coarsening rates increasing with temperature [18]. This will affect the forgeability of the material.

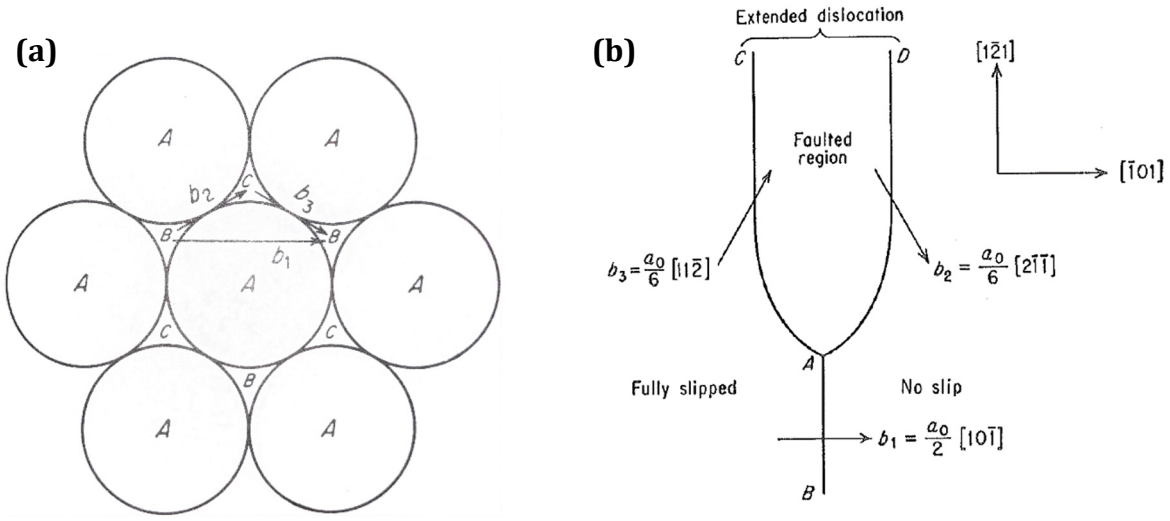


**Figure 2.5: (a) Representation of slip in an FCC lattice such as for the α phase along the (111) plane, (b) the dissociation of a perfect dislocation into two partial dislocations. This occurs in the Cu-Zn α phase which has an FCC lattice and low stacking fault energy ($\gamma_{SFE}$) which continues to decrease with increasing Zn composition [16].**

Compared with the α phase, the β phase shows very different deformation characteristics above and below a critical temperature of approximately 465°C. The β phase has a disordered BCC crystal structure above ~465°C [1, 19, 20] in which the Cu and Zn atoms sit in random lattice sites (and predominantly move around via site vacancies). The β phase in this state exhibits excellent ductility and toughness and is often utilised for this property in elevated temperature deformation processing where the α phase alone is unable to deform to the extent required for the given product application.

As the temperature decreases below ~465°C, the thermal energy and subsequent lattice vibrations that are normally enough to disperse atoms to random lattice sites decrease enough to promote long-range ordering of the Cu and Zn atoms into a CsCl structure (or B2 superlattice [14]). The atoms find preferential positions in the BCC crystal structure causing ordered domains to form and grow rapidly [1, 14]. The resulting ordered domains are comparatively hard and brittle [1] and the β phase is termed β' in this ordered state. An example of the ordered lattice is shown in Fig. 2.6.

An experiment was undertaken by Ayers [20] in which CuZn47.5 alloy samples (100% ordered β') were pulse heated from room temperature to temperatures up to 550°C in order to quantify the kinetics of the disorder transformation to β (acknowledging the previous failed attempts by others investigators to quantify the reverse ordering transformation from high temperature. This is due to the inability to quench and retain disordered beta because the transformation is second order and can occur by a rapid continuous ordering process [14]). It was demonstrated that for all temperatures trialled, the

disordering to β occurred in less than $10^{-4}$s, below which the reaction rate measurements were not possible. The degree of ordering of β' is characterised between S = 0 (completely disordered) to 1 (completely ordered).

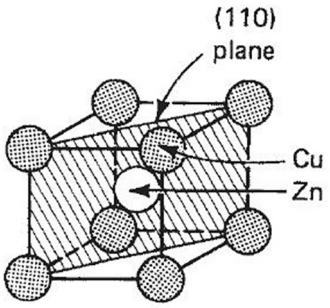


**Figure 2.6: The ordered BCC β' lattice [1].**

Fig. 2.7 shows the evolution of hardness and elongation as a function of temperature around the critical β/β' transition temperature for a 100% β alloy. There is a clear indication that the order/disorder transformation in BCC β leads to vastly different mechanical properties. This ranges from very difficult plastic deformation in the ordered BCC β' (which depends on the motion of superlattice dislocations) to instances in which superplastic elongation (that is elongations in excess of 100%) can be reached during deformation of the disordered BCC β at elevated temperatures ($T > 0.5T_M$) and is the basis for hot forging [16, 21, 22]. Deformation studies were conducted by Khezri et al. [23-25] in which tensile testing of two-phase bicrystals of α-β brass was performed in a temperature range at first between 371-427°C just below $T_C$ and then subsequently between 482-538°C just above $T_C$. The results indicated that below $T_C$, deformation proceeded by a combination of β' grain boundary sliding and deformation of the FCC α phase. Above $T_C$, the primary mode of deformation transitioned as the β phase became disordered and proceeded predominantly via slip in the BCC lattice (in BCC this occurs predominantly on the {110} planes [16]). The FCC α was shown not to deform at all unless the initial yield stress was high enough to initiate slip in this phase.

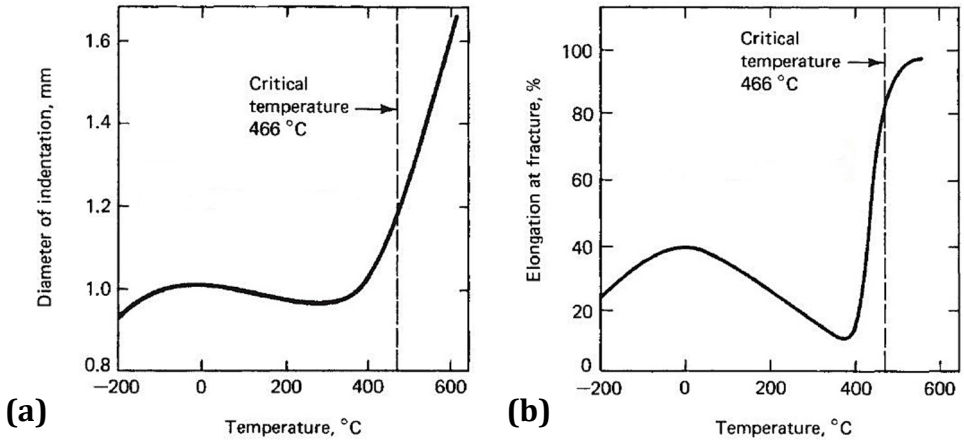


**Figure 2.7: (a) Hardness and (b) elongation characteristics of Cu-49Zn (100% BCC β phase) with increasing temperature [1].**

β’ is not considered to be industrially useful and is known to be susceptible to certain types of corrosion such as the de-alloying phenomenon known as dezincification [1, 26]. As a result, it is often deliberately transformed into the α phase at intermediate temperatures, and this is the objective of the intermediate heat treatment shown in Fig. 1.3, thus improving the final mechanical properties and corrosion resistance of the finished brass component.

### 2.2.4 Effect of Alloying Additions on Phase Equilibria

The Cu-Zn binary phase diagram (Fig. 2.2) is a useful tool for estimating the phase fractions in simple duplex brasses. However, most brasses used in service are not simple binary Cu-Zn alloys but contain other alloying additions. These alloying additions, if soluble within the brass matrix, will alter the α and β phase equilibria and this needs to be well understood in order to appropriately process the alloy. In 1920, Guillet and Portevin designed the now commonly used zinc equivalence system [26, 27] that works by designating certain alloying elements with a value that corresponds to their effect on the phase stability, similar to Zn. For example, magnesium (Mg) is thought to have the effect on phase equilibria of 2 wt. % Zn for every 1 wt. % Mg added to the composition. In other words, Mg is a β stabiliser. Table 2.4 below gives selected Zn equivalents and shows that the strongest β phase stabilisers are Al and Si with values of 6 and 10 respectively [26]. Elements with a value of 1, like lead (Pb), tend to be neutral to the phase stability of brass alloys.

**Table 2.4: Guillet and Portevin Zinc Equivalents [26].**

| Element | Si | Al | Sn | Mg | Pb | Fe | Mn | Ni |
|---|---|---|---|---|---|---|---|---|
| Zinc Equivalent | 10 | 6 | 2 | 2 | 1 | 0.9 | 0.5 | -1.3 |

Although the Guillet/Portevin system is simple to understand and factor into estimations of phase fraction, it can be misleading. The values were generated only for dilute solutions of the alloying additions and can therefore be inaccurate when using larger additions or where multiple alloying additions are present, which is the case for most alloys used today [26]. The use of thermodynamic assessments to calculate more accurate phase fractions (using the CALPHAD approach) are becoming more commonplace in research and industry today, and many Cu-Zn alloys now have this information readily available, including ternary systems containing Pb [28], Sn [12], Al [12], Si [29, 30], Ni [31], Mn [32], and Fe [33]. Four of these thermodynamic assessments (Sn, Al, Pb, and Si – all elements readily found in common industrial duplex brass alloys) have been used to generate databases for the phase diagram calculations found in the figures described below. The Calphad .tdb files used to make the plots are shown in Appendix B. Instead of relying on the old Zn equivalence system, we take advantage of the most recent developments in computational thermodynamics and use calculated phase equilibria for these multi-component brass alloys.

### 2.2.4.1 Effect of Pb Additions

Fig. 2.8a shows the ternary isopleth for the addition of 2 wt. % Pb on the binary Cu-Zn phase diagram using the thermodynamic description of the Cu-Zn-Pb system calculated by Miettinen [28]. Pb is essentially insoluble in brass (Fig. 2.8c) and is most commonly present in the brass microstructure as small globules or particles formed along the grain boundaries [1, 34]. The melting point of Pb is ~327°C [35] and the transition from solid to liquid state is shown clearly (highlighted Pb. (Liq.)) in the isopleth. Being an insoluble element, Pb itself has very little effect on the steepness of the α/(α+β) phase boundary, and as shown in Fig. 2.8a, can only shift the boundary left or right by affecting the final ratio of Cu and Zn in the alloy composition. Therefore, the Guillet/Portevin Zn equivalent of 1 appears to be relatively accurate for this element and would likely carry over to other insoluble elements in Cu-Zn, such as Bi (Fig. 2.8d). This neutrality is shown in Fig. 2.8b in which the evolution of the α and β phase fractions with temperature for a Cu-37.7Zn-2Pb alloy superimposes on the same thermodynamic calculations for binary Cu-38.5Zn, an alloy with the same calculated Cu-Zn ratio.

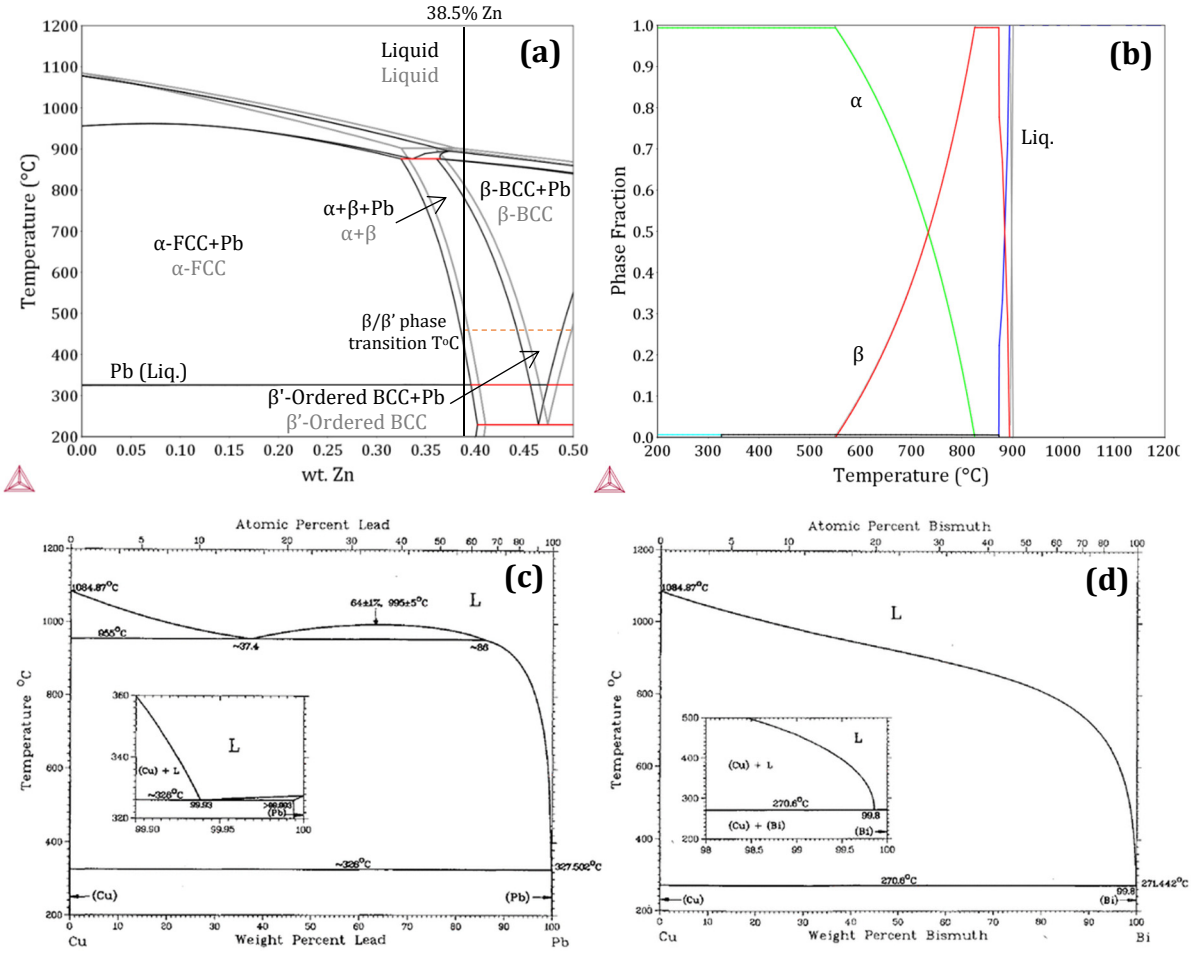


**Figure 2.8: (a) Cu-Zn-2Pb (wt. %) Ternary Isopleth calculated using the thermodynamic assessment of Miettinen [28] and (b) Plot of phase fraction of α and β as a function of temperature for Cu-38.5Zn (grey) and Cu-37.7Zn-2Pb (colour) (wt. %) calculated using the thermodynamic assessment of Miettinen [28]. (c) Cu-Pb and (d) Cu-Bi Binary Phase Diagrams [36].**

### 2.2.4.2 Effect of Sn Additions

Table 1.1 shows the types of Pb-free brasses that are becoming popular in the plumbing industry today and illustrates that Sn additions are amongst the most common alloying elements used not only for ternary alloys, but as additions used in tandem with other elements such as Bi, Si, and Ni [2]. The effect of the addition of 1 wt. % Sn is shown in the ternary isopleth in Fig. 2.9a according to the thermodynamic description for the Cu-Zn-Sn system calculated by Miettinen [12]. The addition of 1 wt. % Sn clearly shows a stabilisation of the β phase in the duplex brass region as the α/(α+β) phase boundary has shifted considerably to the left. Not only has the β phase been stabilised (Fig. 2.9b), but additional phases, commonly referred to as the γ phase ($Cu_5Zn_8$ complex cubic, space group $I\bar{4}3m$) and ε phase ($Cu_3Sn$), have also been stabilised. Vilarinho et al. [37] identified the composition of the γ phase at equilibrium can contain up to ~12 wt. % Sn. This tends to indicate that for significant additions of Sn, the Guillet/Portevin Zn equivalent of 2 probably underestimates the effect Sn has on the Cu-Zn phase equilibria.

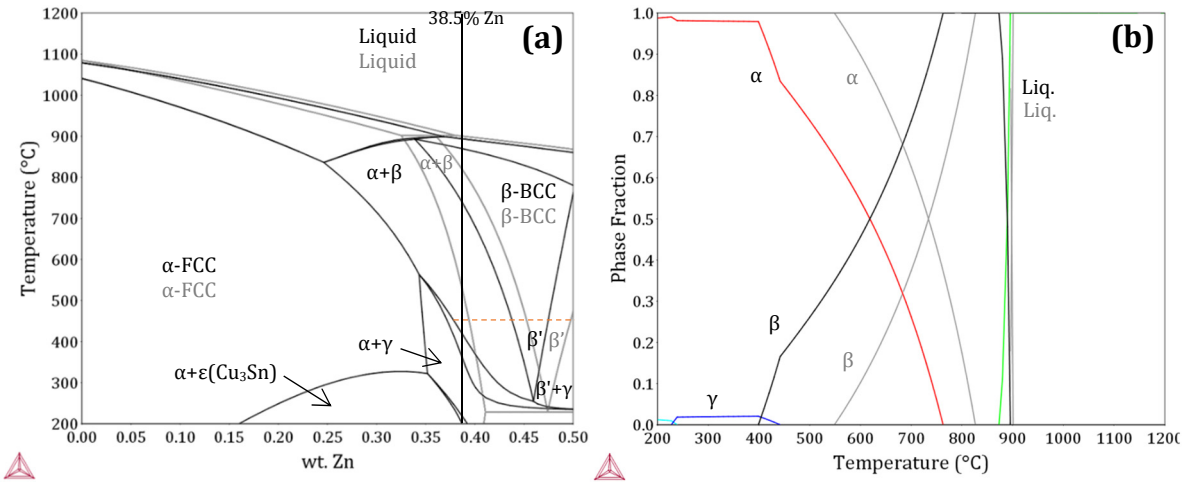


**Figure 2.9: (a) Cu-Zn-1Sn (wt. %) Ternary Isopleth calculated using the thermodynamic assessment of Miettinen [12] and (b) Plot of phase fraction of α, β and γ as a function of temperature for Cu-38.5Zn (grey) and Cu-38.1Zn-1Sn (colour) (wt. %) calculated using the thermodynamic assessment of Miettinen [12].**

### 2.2.4.3 Effect of Al Additions

Another commonly used addition in the plumbing industry is Al. The effect of the addition of 1 wt. % Al on the phase equilibria is shown in the ternary isopleth in Fig. 2.10a according to the thermodynamic description for the Cu-Zn-Al system calculated by Miettinen [12]. Similar to Sn, Al additions are shown to stabilise the β phase in the duplex region by shifting the α/(α+β) phase boundary to the left and this is supported by the work of Sadayappan et al. [34] in which β was more readily produced in cast melts when Al was present at 0.35 wt. %. The evolution of α and β phase fraction with temperature is shown in Fig 2.10b and again at low temperatures we see the presence of the γ phase, similar in structure to Sn-brass γ. It is apparent the stabilising effect Al has on the β

content, stabilising at much lower temperatures than for the simple binary alloy of otherwise equivalent Cu-Zn ratio. Similarly, the work of Vilarinho et al. [38] (Fig. 2.11) shows the gradual increase in stabilisation of the β' phase as additions of Al are increased in a duplex Cu-Zn alloy. A direct comparison between 1 wt. % additions of Al against the binary CuZn α/(α/β) phase-field boundaries tends to indicate that a Guillet/Portevin Zn equivalent of 6 is approximately correct or perhaps a slight overestimation for significant additions of Al based on the ~6% shift in this boundary towards the Cu-rich end of the phase diagram and the essentially unchanged steepness of this same phase-field boundary.

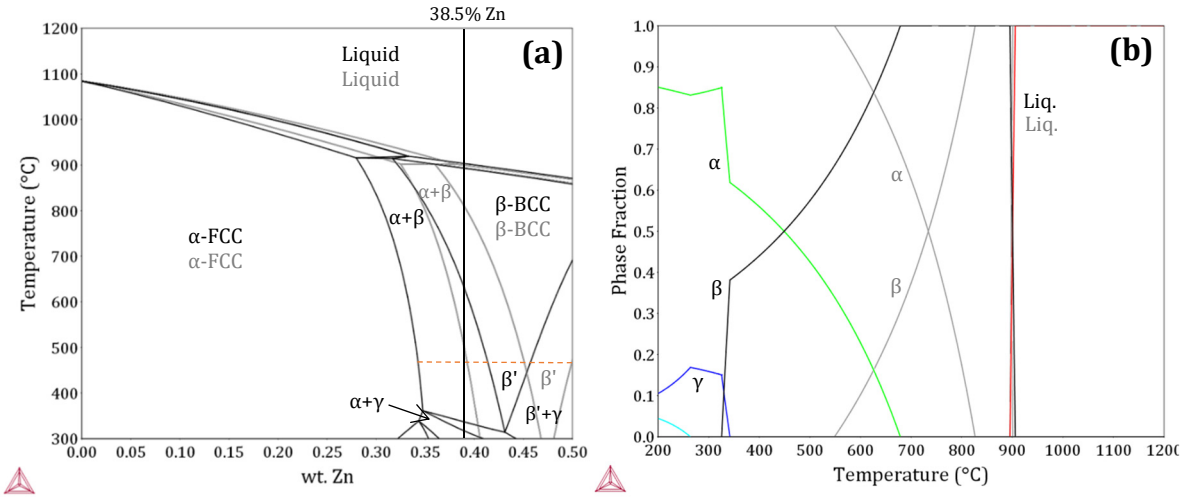


**Figure 2.10: (a) Cu-Zn-1Al (wt. %) Ternary Isopleth calculated using the thermodynamic assessment of Miettinen [12] and (b) Plot of phase fraction of α, β and γ as a function of temperature for Cu-38.5Zn (grey) and Cu-38.1Zn-1Al (colour) (wt. %) calculated using the thermodynamic assessment of Miettinen [12].**

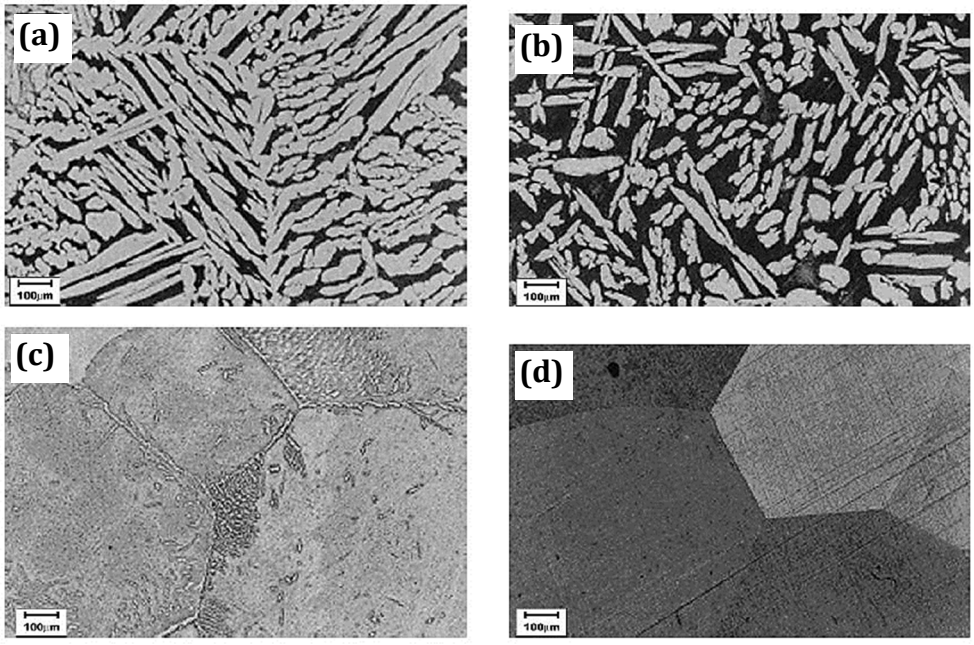


**Figure 2.11: Microstructural evolution of Cu-Zn with increasing wt. % of Al (a) CuZn38.2Al0.49, (b) CuZn37.9Al1.05, (c) CuZn37.6Al1.6, (d) CuZn35.3Al3.4 [38]. The β' appears as the dark phase in (a) and (b), whilst (c) and (d) are almost entirely β'.**

#### 2.2.4.4 Effect of Si Additions

A ternary isopleth for the addition of 3.4 wt. % Si is shown in Fig. 2.12a according to the thermodynamic description for the Cu-Zn-Si system calculated by Miettinen [29] and Wang et al. [30]. It is indicative as to why Si is considered to have the greatest effect on the properties of brass alloys, and why Si-containing brasses are one of the fastest growing areas of research in the plumbing industry. Si is shown to not only stabilise the β phase to large extents at comparatively low concentrations of Zn, but it also has the ability to stabilise several other phases at a variety of compositions and temperatures, including γ, κ, and ε phases. This is supported by the works of Taha et al. [39], Puathawee et al. [40], and Doostmohammadi et al. [41] in which additions of Si are shown to gradually destabilise the α phase in favour of the β and γ phases, particularly around the Cu-Zn ratios traditionally used in duplex brasses in the plumbing industry. The difference here is that for Si additions, the γ (denoted as a complex cubic $Cu_5Zn_8$ structure, space group $I\bar{4}3m$) is supposedly far more stable than for Sn additions, and thus more easily produced in the microstructure in an industrial setting. As such, many companies around the world have explored its potential, and the potential of other phases such as HCP κ ($P6_3/mmc$) and BCC ε ($Cu_{15}Si_4$), for improving various stages of the processing schedule, particularly focussed on machining improvements. For example, a now commonly used Si-brass in industry is 'EcoBrass' which utilises 2.7 – 3.4 wt. % Si [42].

Fig. 2.12b plots the equilibrium phase fraction of the α, β, and γ phases for this same Cu-21Zn-3.4Si alloy (EcoBrass) currently used in the plumbing industry. It shows that the β phase tends to stabilise at similar temperatures to a standard duplex Cu-39Zn binary alloy with no γ present. As such, it is expected that the properties of this brass will be similar at elevated temperatures thus is likely to require similar processing parameters for high temperature stages such as forging and extrusion. As the temperature is decreased, the β phase becomes unstable, primarily transforming to α, but with a minor phase fraction transforming to the γ phase at equilibrium. Klocke et al. observed for CuZn21Si3P as-received from a large European manufacturer the retention of HCP κ after hot working during the extrusion stage which is followed by fairly rapid cooling from temperature ranges between 600-700$^{o}$C [43]. The γ and κ phases are said to have considerably different characteristics to the α phase and can therefore be used to alter processability during other manufacturing steps. This will be explored further in the following sections.

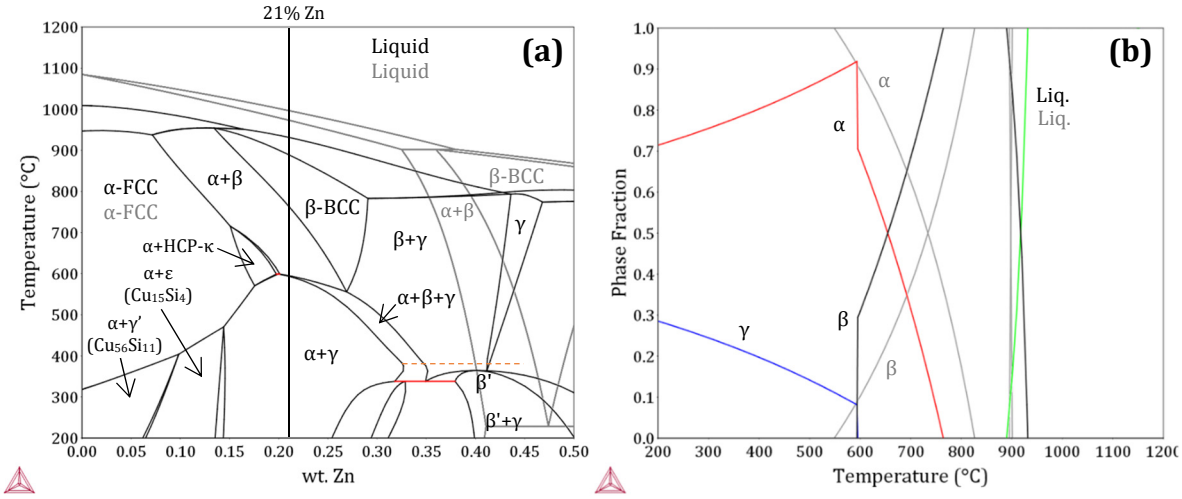


**Figure 2.12: (a) Cu-Zn-3.4Si (wt. %) Ternary Isopleth calculated using the thermodynamic assessments of Miettinen and Wang et al. [29, 30] and (b) Plot of phase fraction of α, β and γ as a function of temperature for Cu-38.5Zn (grey) and Cu-21Zn-3.4Si (colour) (wt. %) calculated using the thermodynamic assessment of Miettinen and Wang et al. [29, 30].**

In comparing the various alloying additions available for duplex brass, one of the major considerations is cost, not only from a raw material point of view, but also from the cost of processing and the degree of risk to the alloy once in the field. Pb is an example of an element exceptional in improving machinability and thus reducing a variety of costs from tooling to improved volume throughput and efficiency. The addition of Pb also has the added benefit of not impacting too heavily on the phase equilibria of the alloy. Sn, Al, and Si, on the other hand, are all different in that they stabilise β (and other phases) to varying degrees and this could potentially be harnessed to derive a positive impact on certain processing steps, or under certain circumstances have the opposite effect. For example, if we elected to include Si additions in a duplex brass to stabilise certain phases for improved machinability, but wanted to maintain forgeability and good corrosion resistance, the phase equilibria indicates we would require significantly greater additions of Cu (which is the most expensive element in duplex brass compositions). So any saving made through improved machining would be partially or completely offset by increased raw material cost.

## 2.3 Elevated Temperature Plastic Deformation

### 2.3.1 High Temperature Processing of Duplex Cu-Zn Alloys

The use of elevated temperatures in the processing of brasses is very common in industry, particularly for duplex brasses which are known to have excellent hot workability [1]. Several stages in a typical processing schedule that utilise elevated temperatures are:

(1) The initial **casting** process from which large ingots or continuously cast rods are produced from molten material.

(2) The **extrusion** process. Large ingots of duplex brass are heated to approximately 650-800$^{o}$C (depending on composition) and uniformly pushed through a smaller die to produce rod of a desired diameter.

(3) The **forging** process in which billets of duplex brass (cut from rod) are heated to approximately 650-800$^{o}$C (depending on composition) and compressed between two die halves to obtain a specific geometrical shape (step shown in Fig. 1.3).

(4) The post-forging or post-extrusion **intermediate heat treatment** in which duplex brass is treated at approximately 400-550$^{o}$C in order to anneal and alter the microstructure of the brass for corrosion resistance purposes (Section 2.4).

(5) Post-machining **low temperature heat treatment** in which the brass is exposed to mildly elevated temperatures (~100-200$^{o}$C) in order to reduce residual stress within the component rather than alter the microstructure (Section 2.6).

The forging process is the most widely used method for creating duplex brass plumbing fittings for potable water applications (e.g. Fig. 1.2). This is because the inherent properties of duplex brass complement high volume forging production very well. Compared with direct machining from rod, forging allows for far more difficult geometrical shapes to be produced, while compared with direct sand-casting, forging allows for high volumes to be produced quickly and economically, with much closer tolerances, once a forging press and tooling is set up. In addition, the forging process also enhances the mechanical and metallurgical properties and therefore reliability of the finished component [1, 44]. Duplex brasses are typically processed using closed-die forging, and these components are subsequently machined into their final dimensions. The closer the forging is to the final weight and dimensions of the finished component, the more material, and in turn cost that is saved.

The forgeability in various directions (anisotropy) of duplex brass is dependent on several factors including the chemical composition, pre-forging microstructure, phase percentages, grain size,

segregation of certain elements, and prior strain history (for example from extrusion or cold drawing) as well as factors directly related to the deformation process including the forging temperature, complexity of the design (relating to the degree of strain), and the strain-rate [44]. In order for the process to be economically attractive, a large number of components need to be produced continuously, and therefore the forging cycle time needs to be as short as possible without creating a significant number of rejects. To give an indication of the cycle time, at the author's company, individual forging presses typically produce components in excess of 20-30 strokes a minute. For commonly used dual-cavity dies, this is more than 60 forgings a minute.

### 2.3.2 Hot Workability

A typical continuously cast duplex brass microstructure, like that shown in Fig. 2.4a, will begin with a given ratio of α and β' phase. Although the FCC structure of the α phase has reasonable room-temperature ductility, the alloy in this state is not forgeable at low or even intermediate temperatures due to a lack of workability [45]. The ordered BCC β' phase is very hard and brittle due to long-range ordering and is unable to deform to any significant extent [1, 46, 47]. At higher temperatures above ~465°C, however, when the ordered β' phase transforms into the disordered BCC β phase, the ductility, toughness, and subsequent workability of the material increases dramatically (Figs. 2.07 and 2.13) [1, 48]. Fig. 2.14 shows an example of the associated drop in hardness with temperature for varying Zn wt. % [49]. Not only do we find the hardness decreases with increasing temperature, but that the decrease is accelerated considerably when the alloy is α+β or simply β phase alone. Therefore, an understanding of the elevated temperature characteristics of duplex brass is necessary in order to maintain a low reject rate during the forging operation.

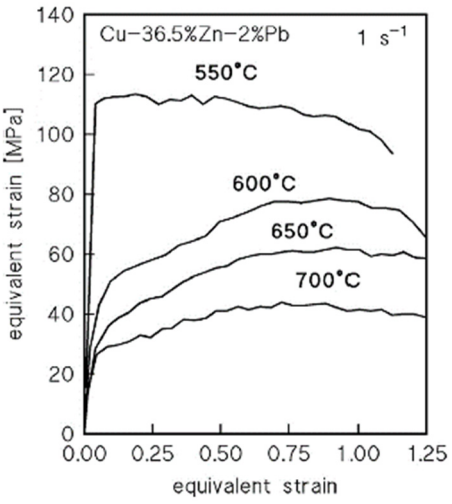


**Figure 2.13: Hot Torsion Stress-Strain curves for a Cu-36.5Zn-2Pb alloy at various temperatures [48].**

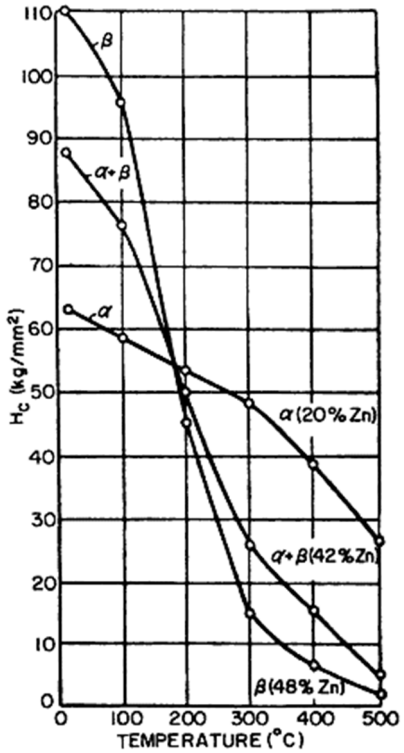


**Figure 2.14: Softening of Cu-Zn alloys as a function of temperature (°C) [49].**

### 2.3.3 The Pre-Heating and Forging Process

The forging process typically relies upon one of two methods for heating billets to elevated forging temperatures. Historically, gas-fired furnaces have been the most popular [1], however, because these can require long heating or soak times and take up a significant amount of floor space, many manufacturing companies now elect to use induction furnaces which are more compact and efficient with today's modern computer numerical control (CNC) forging presses [50, 51]. The furnace will typically utilise an internal conveyor chain for the heating of the brass billets with the length of heating time determined by the dimensions and specific thermal properties of the brass chosen.

As the billets are heated to forging temperatures, several changes occur in the microstructure. As the temperature progresses past the critical ~465°C order/disorder temperature, any hard β' present within the microstructure will transform to the more workable β phase (see Section 2.2.3). Second, as the temperature continues to increase into the α + β phase field, the α phase becomes less stable, gradually transforming to β (as indicated in the binary Cu-Zn phase diagram – Fig. 2.2) [1]. As a general rule of thumb, the manufacturing industry will typically choose a forging temperature based on a phase ratio of approximately 60-75% β phase and 25-40% α phase as the billet exits the furnace just prior to forging. The reason for this is two-fold:

- If there is not enough β phase present within the microstructure at the time of forging, particularly for more complex component designs, higher flow stresses will be required to deform the α grains leading to significant strain partitioning [52]. This in turn leads to reduced ductility and increased chances of either incomplete (cold) forming (and increased tool wear), or fracture initiation in delicate regions of the forging.
- If the billet is heated to too high a temperature, removing most of the α phase within the microstructure, rapid grain growth of the β grains will occur which will lead to a phenomenon known as hot shortness. Hot shortness is the tendency of an alloy to separate along the grain boundaries when deformed at temperatures near the melting point [53] and this is a fairly common occurrence for duplex brass alloys, particularly those containing Pb which segregates along these β grain boundaries and is in the liquid phase at forging (and extrusion) temperatures [1, 54, 55].

Another parameter of importance to the forging process is the soak time required for the duplex brass to reach a suitable forging temperature [1, 44]. For gas-fired furnaces in particular, which can be slower to transfer heat to the brass, it is important not to allow the brass to remain at high temperatures for extended periods of time. Even when using the correct α/β phase ratio, the α grains will coarsen with soak time which is detrimental to the mechanical properties of the material (Section 2.1.3). It is commonly known that one method for improving forgeability is to refine the grains during the initial casting process, thus helping to prevent excessive grain sizes occurring during the pre-heating process [21, 34, 56]. Fig. 2.15 shows the cast microstructure of a typical duplex brass alloy that has been heated to forging temperatures and quenched. This illustrates the change in phase ratio and coarsening of the α phase exhibited at forging temperatures. Many small α grains are present in this microstructure having nucleated during the quenching process. It is very difficult to quench duplex brass without some α grains nucleating from the β phase during the cooling process [14] (See Section 2.2.3).

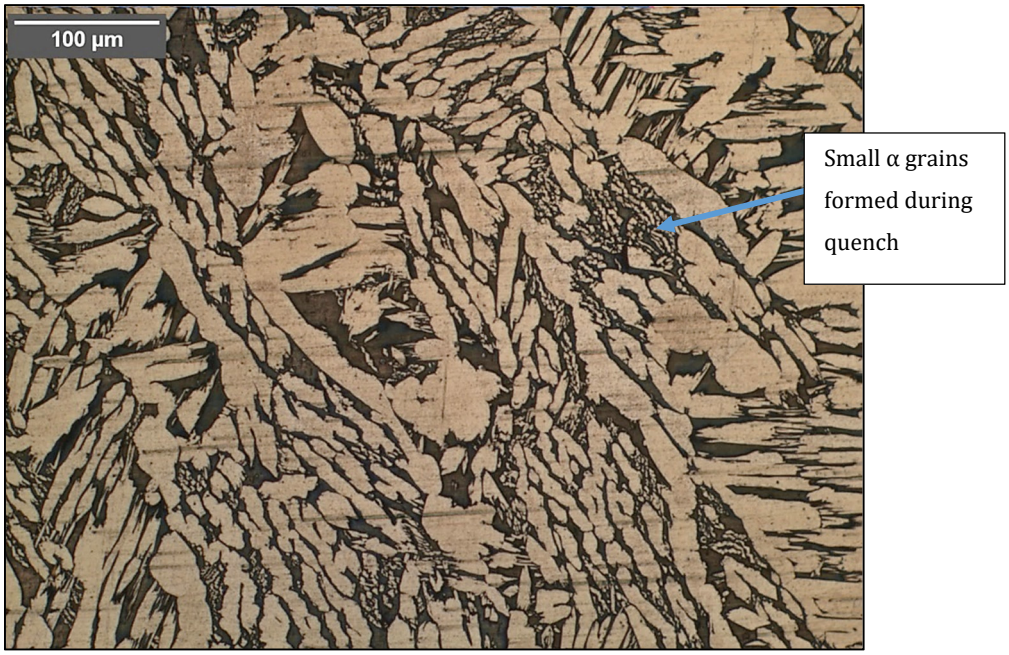


**Figure 2.15: Duplex α + β' cast structure heated to 750°C and quenched. The β' phase appears dark against the lighter α phase due to the etchant effect [13]. Note the α phase exhibits no twinning at this stage because it has not undergone any prior deformation process.**

Figs. 2.16a-b provide examples of the die design from the author's company of a potable water plumbing fitting (elbow). A duplex brass billet which has been heated to uniform forging temperatures, typically 650-800°C depending on the chemical composition, is placed in the die (normally an H13 tool steel [1, 44, 57]) using a robotic arm and subsequently pressed into the die cavity. Fig. 2.16b gives an indication of a typical temperature gradient within the workpiece just prior to ejection from the press. As the workpiece comes into contact with the die and die pins, which are normally pre-heated to 150-315°C [1], the surface is cooled more quickly and as a result the 'receiving end', which doesn't come into contact with the pin until the end of the cycle, retains a higher temperature. Depending on the condition and temperature of the die, this will have an effect on the uniformity of the post-forging microstructure and subsequent machinability and cold formability.

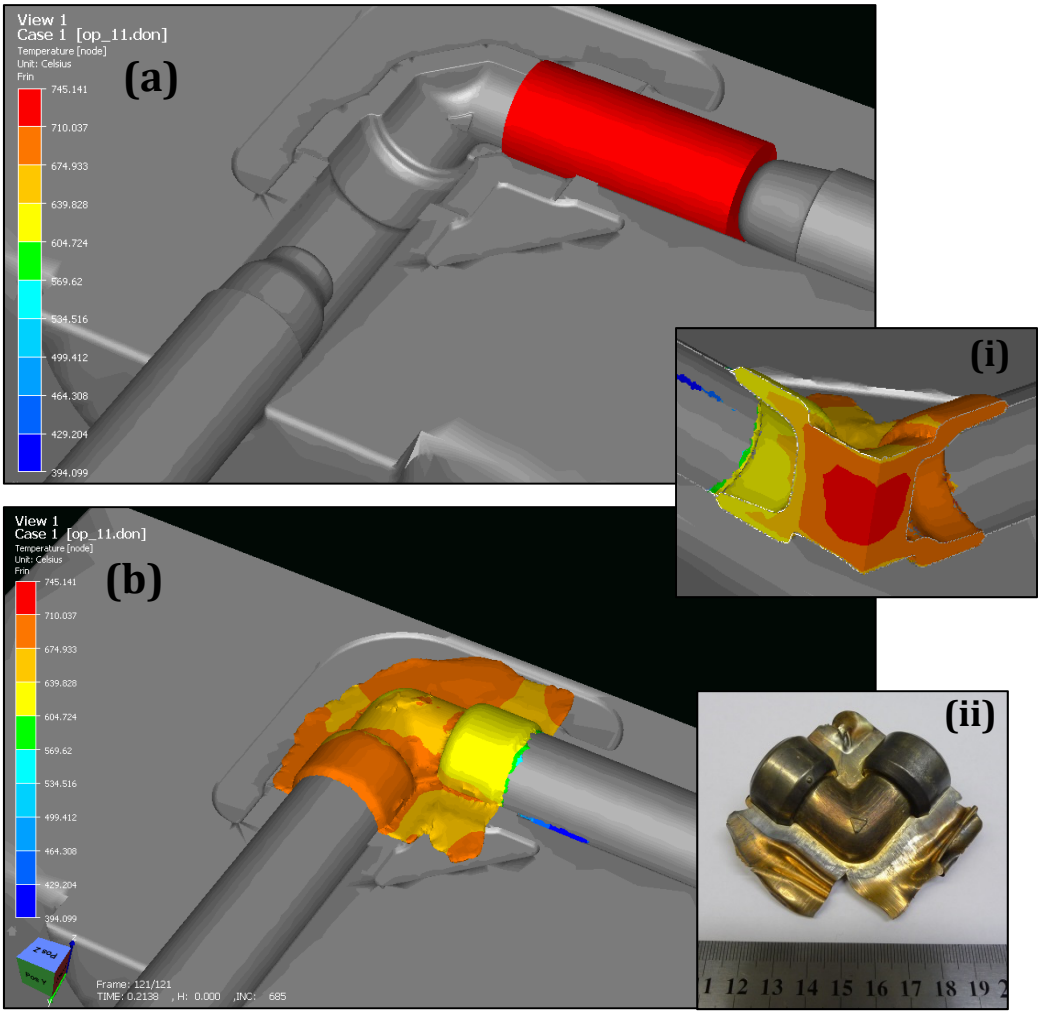


**Figure 2.16: RWC internally-developed FEA simulation using GL Inova of a brass workpiece placed in a forging die at elevated temperature (a) just prior to the forging cycle, and (b) at the end of the forging cycle just prior to the forging pins being withdrawn and die opened. Inset (i): Cross-section of the same workpiece exhibiting the temperature gradient. Inset (ii): A real example of the same workpiece after a forging.**

Fig. 2.17 demonstrates some of the flow stresses required to plastically deform a typical duplex brass alloy (Cu-38Zn) at various temperatures and strain-rates under hot compression [18]. As the temperature is increased for this alloy, a higher phase percentage of β is stabilised, and thus the workability increases, and the flow stress decreases. As the strain-rate increases, however, the flow stress is increased significantly, and this effect is more pronounced at higher temperatures [16, 18] indicating the β phase has a high strain-rate sensitivity. An average contact time between the dies and brass workpiece for potable water fittings is approximately 0.75 seconds [57] so the strain-rate, and thus the flow stress, of forging is very high. The strain-rate for a typical brass forging process could be estimated to be in the range of ~2-10$s^{-1}$ depending on the part size, geometry and variable metal flow. Another characteristic of these curves is the decrease in flow stress after the initial yield point is reached, and this is attributed to dynamic recrystallisation during the hot deformation process [58]. Due to the low SFE of the FCC α phase, the material exhibits only small amounts of dynamic recovery

and therefore undergoes a specific type of dynamic recrystallisation known as discontinuous dynamic recrystallisation (or dDRX) [48, 59].

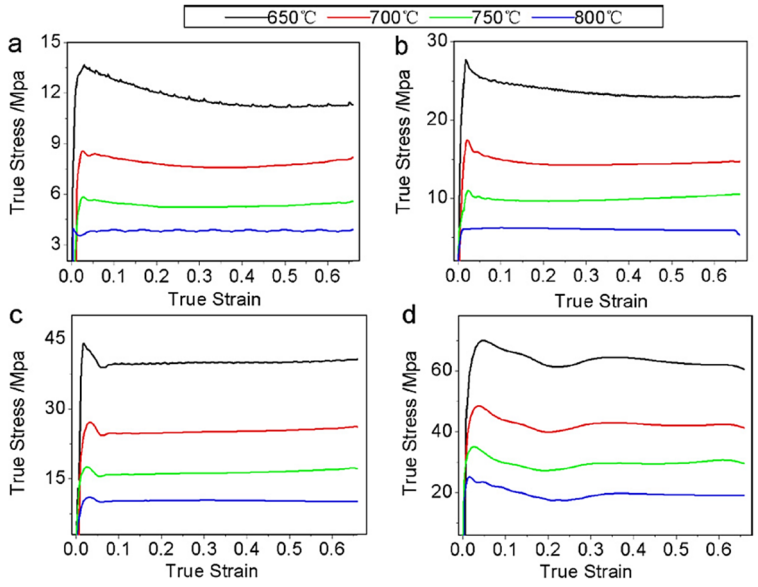


**Figure 2.17: True stress-strain curves obtained during hot compression of Cu-38Zn at various temperatures and strain rates ((a) 0.01s$^{-1}$, (b) 0.1s$^{-1}$, (c) 1s$^{-1}$, (d) 10s$^{-1}$) by Xiao et al. [18].**

The flow stress behaviour of brass alloys can be quite complex depending on the composition of the alloy and the amount of FCC α and BCC β present in the microstructure. Employing modelling techniques to help predict this behaviour can be very useful when designing a hot working process (e.g. forging, hot extrusion) and this is typically achieved through one of two ways:

1) Empirical modelling and curve fitting of experimental data. This has the advantage of usually describing well the existing data, however the resulting model isn't actually based on any physical behaviour, so such empirical models have limited extrapolative capacity.
2) Physically-based modelling which despite being less accurate on average, considers the specific properties of the alloy, its microstructural state, and other common factors which affect the alloy's behaviour. Physically-based models have the advantage of some capability of extrapolating outside the range of the existing data.

Both of the above approaches usually commence with identifying the effects of temperature and strain-rate on the alloy behaviour by calculating the Zener-Hollomon parameter (Z) which is expressed mathematically as follows:

$$Z = \dot{\varepsilon}\exp\left(\frac{Q}{RT}\right) \qquad (2.2)$$

$\dot{\varepsilon}$ is the strain-rate ($s^{-1}$), T is the absolute temperature (K), R is the universal gas constant (8.3145 J/mol.K) and Q is the activation energy of deformation (kJ/mol) [18, 60]. The Zener-Hollomon parameter is then usually related to the flow stress by an Arrhenius-type equation:

$$Z = A[\sinh\left(\frac{\alpha\sigma}{G}\right)]^n \quad (2.3)$$

Rewritten with the original Zener-Hollomon Eq. 2.2 yields the following:

$$\dot{\varepsilon} = A[\sinh\left(\frac{\alpha\sigma}{G}\right)]^n \exp\left(-\frac{Q}{RT}\right) \quad (2.4)$$

σ is the flow stress (MPa), α and A are material parameters, *n* is the stress exponent and *G* is the shear modulus (MPa).

From the experimental data collected in Fig. 2.17 and the above equations, Xiao et al. [18] employed empirical methods to calculate the material constants (A and α), the stress exponent (n) and subsequently the activation energy (Q) by calculating the average slopes in various plots comparing ln[sinh(ασ)] and the inverse temperature (1/T). From these values, curves were fitted to the experimental Cu-38Zn hot compression curves to generate an accurate model for predicting the flow stress at various strain, strain rates, and temperatures, albeit one without any direct reference to the microstructural state.

In order to assess the individual contribution of multiple phases to the plasticity of dual-phase materials as part of a physically-based model, homogenisation routines such as the 'Law of Mixtures' are often used [48, 60-62]. This rule, expressed in Eq. 2.5, simply combines the flow stress contribution of each phase (typically denoted as a hard phase and a softer phase) as a function of their respective phase fraction. In the case of duplex brasses, which contain FCC α (considered the harder matrix phase) and BCC β (considered the soft phase), the overall flow stress can be estimated if the individual flow stress behaviour of each phase is known.

$$\bar{\sigma} = (1 - f_s)\sigma_h + f_s\sigma_s \quad (2.5)$$

Spigarelli et al. [60] were able to successfully describe the flow stress behaviour of Cu-36.5Zn-2Pb using torsion testing by first employing the Arrhenius-type equation (Eq. 2.4) and subsequently applying the 'Law of Mixtures' (Eq. 2.5) to calculate the material constants in the equation. This

information could then be subsequently utilised in future studies to estimate the flow stress behaviour of other similar duplex brass compositions. This will be explored further in Chapter 5 of this thesis.

An assumption that must be noted about the 'Law of Mixtures' is that both the *soft* and the *hard* phases accommodate an equal amount of strain which is not always true and can cause the resulting model to overestimate the predicted flow stress of a duplex alloy. In order to better reflect the strain partitioning between multiple phases, Tomota et al. [63] suggested applying a similar mixture law to strain as well as flow stress (Eqs. 2.6a and 2.6b). However, these require an additional fitting constant, most commonly denoted β, to be successfully implemented (Eq. 2.7).

$$\sigma(\varepsilon) = (1 - f_s)\sigma_h(\varepsilon_h) + f_s\sigma_s(\varepsilon_s) \quad (2.6a)$$

$$\varepsilon = (1 - f_s)\varepsilon_h + f_s\varepsilon_s \quad (2.6b)$$

$$\beta = [(\sigma_s - \sigma_h)/(\varepsilon_s - \varepsilon_h)] \quad (2.7)$$

Another solution was proposed by Bouaziz et al. [64] who suggested applying the so-called 'IsoWork' assumption given in Eq. 2.7 which can be applied in both the elastic and plastic regions of deformation. This approach assumes the strain partitioning is such that equivalent 'work' (σ.dε) is done in each phase. This approach agrees well with more sophisticated self-consistent approaches but there is no strong physical basis for the 'IsoWork' assumption.

$$\sigma_s . d\varepsilon_s = \sigma_h . d\varepsilon_h \quad (2.8)$$

Further improvements can be made to these models by employing additional physically-based constitutive equations, such as the Estrin-Mecking equation (to model behaviour in the work hardening-dynamic recovery stage) and the Avrami equation (to model behaviour in the dynamic recrystallisation stage) [65].

The cooling rate after forging can have a significant effect on the microstructure of the forging. At forging temperatures, the equilibrium phase ratio will be approximately 60-75% β and 25-40% α phase. As the temperature decreases, the α phase becomes more stable and subsequently nucleates in the microstructure. For slow to moderate cooling rates, the α will form in a similar way to ferrite forming from austenite in steels [14]. Slow cooling will result in the formation of reasonably equiaxed α grains. As the cooling rate is increased, a morphological transition occurs and Widmanstätten α

'needles' or 'plates' are more likely to form. Under very fast cooling conditions in which quenching is involved, a massive transformation from β to α can occur if there is no time available for long range diffusion [14] (Fig. 2.18). A typical cooling process for industrial forging is completed in air at room temperature where forgings are either individually cooled along a conveyor or in large steel containers. The latter is more likely to be conducive to slow to moderate cooling rates, particularly for those forgings in the middle of the container (centre of the thermal mass), while those on the edges will cool more quickly and be more likely to produce Widmanstätten α grains. α phase nucleation and growth will be explored further in Chapter 4 of this thesis.

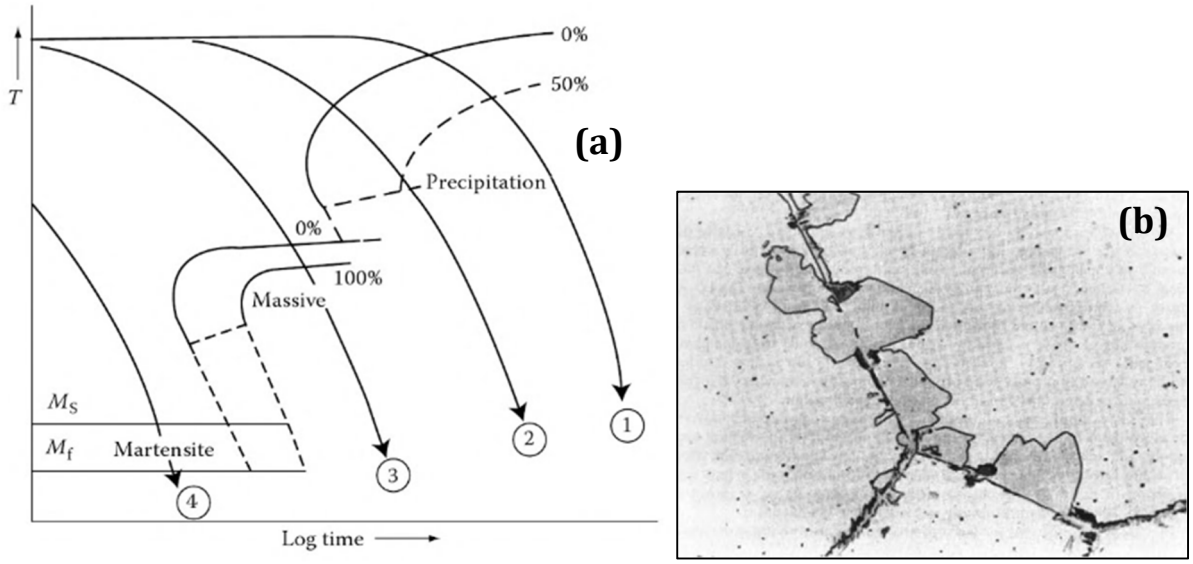


**Figure 2.18: (a) An example continuous cooling transformation (CCT) diagram indicating the cooling time differential required to form 1. Equiaxed α grains, 2. Widmanstätten α grains, 3. Massive transformation α grains, and 4. Martensitic transformations (very low temperatures) [14]. (b) Example of Massive α formed along β grain boundaries in a Cu-38.7Zn quenched from 850°C to 0°C in brine [14].**

### 2.3.4 Assessment of Forgeability

Forgeability is a common term used in the manufacturing industry to describe in general the elevated temperature stability of a metal whilst undergoing some form of plastic deformation. It is a way of benchmarking one metal or alloy against another under otherwise identical hot working conditions that will normally take into account some combination of die pressure, die wear, and plasticity [1]. When a wider array of materials, particularly those within the same base-element family (for example Cu-base alloys) are measured against each other at the same time, a *'forgeability index'* is often used to rank these alloys accordingly. The best available alloy within the group is given a forgeability index rank of 100, from which all other alloys are measured against. In the case of Cu-based alloys, CuZn alloys typically rank very highly in forgeability ratings with C37700 (59.5Cu-38.5Zn-2Pb) the benchmark 100 alloy of choice for hot working. Some other common CuZn ratings include:

- C46400 (60.5Cu-38.8Zn-0.7Sn) – **90**
- C48600 (61Cu-37.2Zn-1.8Pb) – **90**
- C69400 (81.5Cu-14.5Zn-4Si) – **80**

As can be seen in the few examples shown above, duplex brasses will typically yield a standard forgeability rating in the range of 70-100 when compared against all other Cu-based alloys. This can limit the resolution by which duplex brasses are measured against one another and is subsequently a key focus of this thesis (Chapter 5).

There are several common methods available for assessing the hot working behaviour of duplex brasses under controlled conditions. This includes:

1. **Hot tensile testing** [66, 67]. This test, whilst very useful at room temperature and for small plastic strains, is limited at elevated temperatures due to the necking process restricting uniform flow [16, 44, 68].
2. **Hot compression (upset) testing** [18, 47, 52, 56, 61]. This is by far the most common method for measuring the elevated temperature flow behaviour of duplex brasses, and involves uniaxially compressing a cylindrical sample at a given temperature and strain or displacement rate between two platens [16, 44, 68]. Friction between the sample surface and the platens is typically the greatest issue encountered and can be countered with the use of appropriate lubrication.
3. **Hot torsion (twist) testing** [48, 60]. This test, in which a cylindrical sample is clamped on both ends and rotated on its axis at elevated temperature, is effective for producing data at very large strains and as the dimensions of the sample do not change, the strain rate remains constant for a constant rpm of the test [16, 44, 68]. The primary challenge with this test, however, is the varying strain from the outer surface of the sample to the centre.

### 2.3.5 Influence of Chemical Composition on Forgeability of Duplex Brasses

The α/β phase field in the Cu-Zn binary phase diagram (Fig. 2.2) demonstrates how dependent the equilibrium phase ratio is on the forging temperature. This sensitivity is due to the steepness of the α/(α+β) phase boundaries. Any change in chemical composition will likely have a significant effect on the phase equilibria, and thus alter the forgeability at a given temperature. This can occur due to a simple shift in the Cu/Zn ratio [45], or due to an alloying addition shifting the α/(α+β) phase boundary to the left (stabilising the β phase and decreasing the optimal forging temperature), to the right (stabilising the α phase and increasing the optimal forging temperature), or increasing/decreasing the

steepness of the phase boundary, and therefore the sensitivity of the changes to phase equilibria with temperature.

A calculation demonstrating the evolution in equilibrium phase fraction against temperature in Fig. 2.19 shows the effect of various Cu/Zn ratios and alloying additions by comparing the optimal forging temperatures for two common industrial duplex brasses. The two alloys are:

- C37700 (59.5Cu-38.5Zn-2Pb), also commonly known as 'Forging Brass', which is the standard industry alloy by which all other Cu alloys are measured for forgeability [1]. It is typically given an arbitrary rating of 100.
- C46400 (60.5Cu-38.75Zn-0.75Sn), also commonly known as 'Naval Brass'. This alloy has a higher Cu content than C37700, however has an optimal forging temperature range decreased by ~50°C [1] from 730°C to 680°C (Fig. 2.19). The forgeability rating of this alloy is 90 [1].

This recommended change in optimal forging temperature is primarily due to the addition of Sn to C46400 which stabilises the β phase more quickly as temperatures are increased. This allows C46400 to be forged comfortably, that is the temperature window that achieves the best combination of material flow (low flow stress) and minimal defects, at lower-than-normal temperatures compared to C37700.

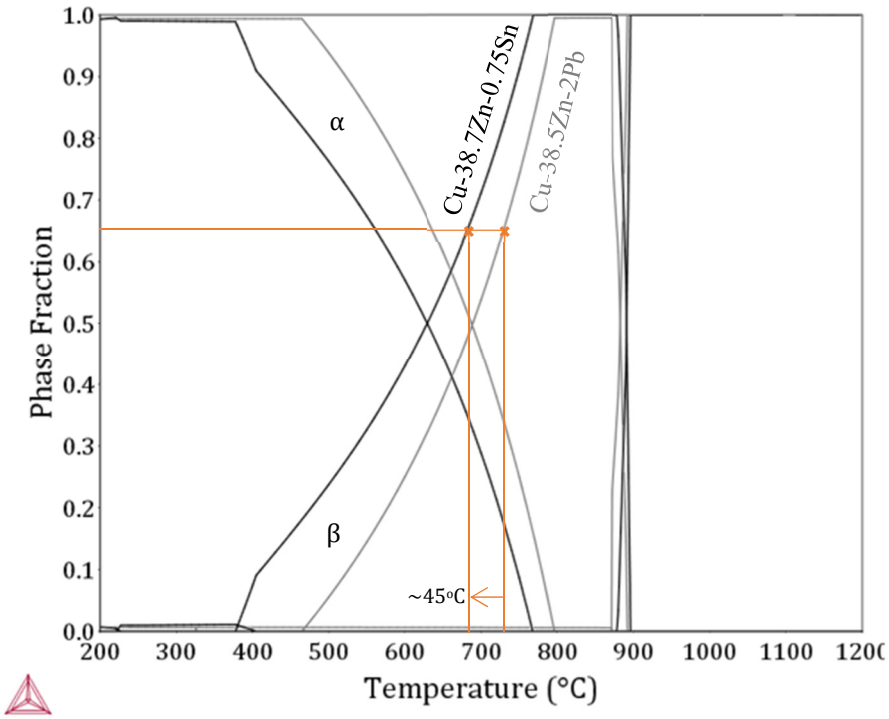


**Figure 2.19: Evolution of α and β phases in two common duplex brasses; Cu-38.5Zn-2Pb (grey) and Cu-38.75Zn-0.75Sn (black). The Sn additions stabilise β at lower temperatures and therefore the recommended optimal hot working temperature is lower. 65α/35β phase fraction highlighted in orange for each alloy.**

Due to its insolubility in the brass matrix, Pb does not have any significant effect on Cu-Zn phase equilibria and is therefore considered to generally have a neutral effect on the optimal forging temperatures [48, 60, 69]. However, it can have other effects on the forgeability. Pb has been found to help improve metal flow through the die, however it can also encourage the formation of cracks in thin-walled or delicate sections of the forging [1, 45], particularly if the brass has been overheated, encouraging instances of hot shortness (Pb is liquid which decreases the cohesive strength between grains) [53, 54]. As a result, a Pb content in excess of 2.5 wt. % is seldom recommended for duplex brasses in order to protect the processing characteristics of the material [1].

An interesting, but not well explored effect of Pb on duplex brasses, is its effect on controlling grain coarsening at elevated temperatures, be it for forging, extrusion, or intermediate heat treatment [70]. It has already been suggested by Sadayappan et al. that this is the case during the initial casting process [34]. The soak time with which a brass billet remains at elevated temperatures is critical, with grain growth rates varying for different alloy compositions [1]. For example, Forging Brass (C37700) has been found to have a lower grain growth rate compared with Naval Brass (C46400), therefore it is more detrimental to keep Naval Brass at elevated temperatures for any longer than is required to bring the billet to uniform temperatures [1]. It is suggested the reduced rate of grain coarsening can be attributed to the phenomenon of Zener pinning where the small Pb particles retard grain boundary migration during recrystallisation and grain growth [70, 71]. It has also been shown that this effect is not limited to spherical particles [72] so Pb can be melted to different morphologies and still have an effect on grain boundary pinning.

Bismuth (Bi), which is similarly insoluble in the brass matrix (Table 2.2) and appears in several of the new Pb-free alloy grades (Table 1.2), is also expected to have a negligible effect on the α/β phase equilibria and may also have an effect on controlling the grain coarsening behaviour through Zener pinning. An additional effect, however, is that Bi is found to expand approximately 3.32 vol. % on solidification [73] and can distribute along grain boundaries in a more film-like manner [74-77], which can lead to embrittlement and/or directionally sensitive ductility in subsequent manufacturing stages. The precise quantities at which this negative effect will be clearly observable for duplex brasses used in the plumbing industry has not yet been discussed in the literature, therefore care should be taken not to use Bi in quantities greater than that required to gain a suitable level of post-hot working machinability.

It has been shown that elements such as Sn and Al will have an effect on the α/β phase equilibria in acting to stabilise the β phase at elevated temperatures (Section 2.2.4), which will therefore alter an alloys' optimal forging temperature. Beyond this effect, assuming optimal forging temperatures are utilised, there will likely also be a mild increase in flow stress due to the solid-solution-strengthening effect of these elements (Table 2.2), and therefore the forgeability rating will drop slightly for controlled additions of these elements [1]. For example, C46400 has a forgeability rating of 90 with the addition of Sn (compared with C37700 at 100). Another secondary effect, observed by Yakovtseva et al. [67], is the ability of Al to help raise the ductility of the β phase by reducing grain boundary sliding, while Lei et al. [74] suggests Al additions are useful for increasing the surface tension of Bi-particles changing their morphology from film-like into more spherical-like particles, thus increasing hot workability. Many other less common alloying elements have been proposed in the past to aid in improving hot workability. Parikh et al. [78] suggested the use of Cr and Sb to reduce the susceptibility of brass to 'edge-cracking', Atsumi et al. [79] suggested a small addition of Ti could be useful to increase the toughness of the alloy during hot working through the formation of fine precipitation particles (thereby controlling β grain size), while Sadayappan et al. [34] employed the addition of Zirconium (Zr) to refine grains in the initial brass casting, which is thought to help prevent excessive grain sizes during the hot working stages of extrusion and forging. Each of these elemental additions though are second order effects to the overriding effect of having the disordered BCC β phase present in suitable quantities at elevated temperatures.

Overall, adjusting the Cu/Zn ratio to compensate for β stability at elevated temperatures is the primary objective for creating a readily forgeable alloy. A perfect example of this is for Si-bearing alloys which have been shown (Section 2.2.4) to dramatically alter the α/β phase equilibria. A normal duplex Cu/Zn ratio in the presence of Si is not ideal because forging would likely take place in the (β+γ) phase field where the alloy would not have the requisite hot workability. In the case of alloy C69400 (Cu-14.5Zn-4Si), the forgeability rating remains high (at 80) because the Cu/Zn ratio has been adjusted toward the Cu-rich end of the phase diagram so that a manageable ratio of α and β (~35/65) are stable at forging temperatures.

## 2.4 Intermediate Heat Treatments

### 2.4.1 Post-Forging Intermediate Heat Treatment

Upon completion of the forging stage, there are several additional steps required before the components are ready for the next processing stage of machining (Fig. 1.3). These include:

(1) **Trimming of the forgings.** After the forging stroke is completed, large amounts of excess material, also known as flash (Fig. 1.4), will have formed around the mid-section of the component where the dies (and pins) have come together, and this needs to be removed prior to machining. The retrieval of flash is also an economical way to recover raw material costs directly after the forging process.

(2) **Intermediate heat treatment.** Upon cooling from the high temperatures utilised during the forging process, each forged brass component will contain a mixture of both the α phase and the β' phase (transformed from β during cooling). The fraction of α and β' will be determined largely by the cooling rate and alloy composition. In most cases, a significant amount of α phase will have stabilised during cooling and any remaining β phase will have transformed into β'. The β' is particularly susceptibility to several forms of corrosion [1] including a de-alloying phenomenon known as dezincification. As a result, a heat treatment is applied at intermediate temperatures of approximately 400-550$^{o}$C for a soak time of between 1-8 hours (the Australian Standard AS2345 (2006) [80] recommends 500$^{o}$C for 4 hours). This is usually undertaken as a batch process and is purposely completed within the all-α phase field in order to simultaneously recrystallise the α phase grains, reduce residual stress in the component, and to transform the remaining β' phase into α [81, 82] thus improving the dezincification resistance of the component. A time-temperature-transformation (TTT) diagram is shown in Fig. 2.20 completed by Bowers et al. [45] for a Cu-35.9Zn-3.5Pb alloy with an example of the change in microstructure both before and after heat treatment shown in Fig. 2.21. Although an all-α structure can be achieved for heat treatments at lower temperatures (<500$^{o}$C), the slower kinetics at these temperatures mean that significantly longer periods are required in order to achieve the desired microstructure. Utilisation of intermediate heat treatments is a very common method for improving dezincification resistance in the brass industry, however the effect of alloying additions in this temperature range is not as commonly discussed in the literature as the effects at the relevant temperatures characteristic of forging (Section 2.4.2). A study of intermediate heat treatments is the topic of Chapter 6.

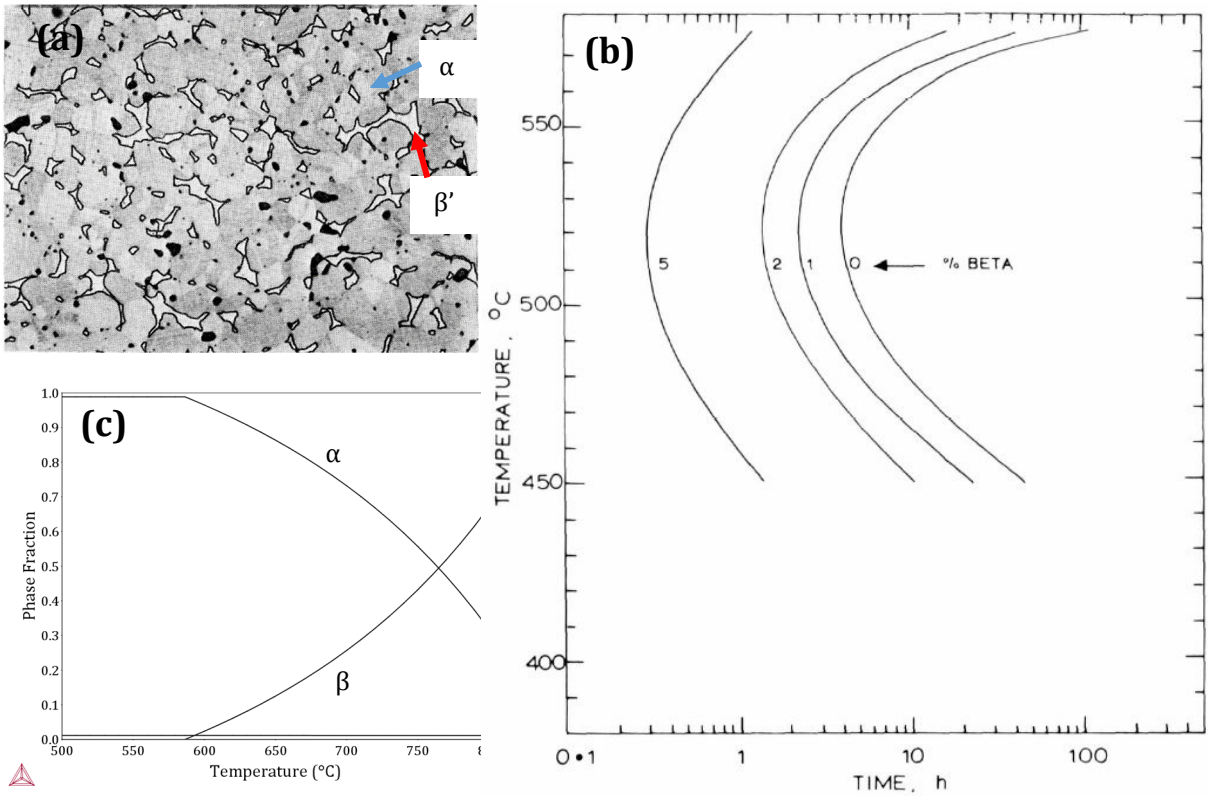


**Figure 2.20: (a) Example of an as-fabricated duplex brass rod microstructure (Cu-35.9Zn-3.5Pb-0.16Sn-0.08As) and (b) the resulting reduction in β' phase present in the microstructure with increasing soak time at intermediate temperatures. This is also known as a time-temperature-transformation diagram [45]. (c) Equilibrium phase fraction of α and β against temperature.**

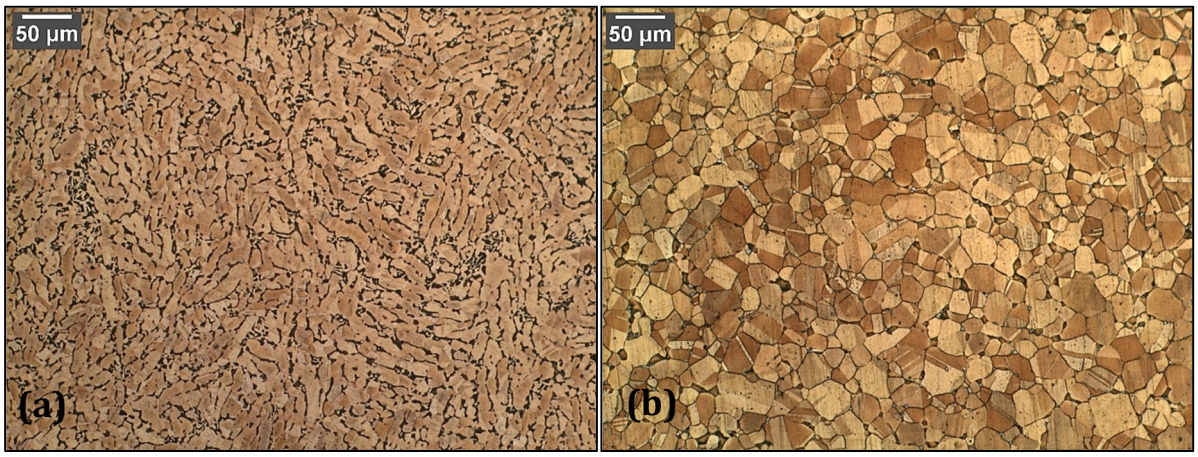


**Figure 2.21: Cu37.5Zn0.75Bi0.3Sn (a) Post-forging microstructure without heat treatment, (b) after the completion of an intermediate heat treatment. The α grains are now fully recrystallised with little to no β' present in the microstructure which is desired for dezincification resistance of the final component.**

(3) **Shot-blasting of the heat-treated components.** This final process before machining is typically desired for both aesthetic and safety reasons. After the intermediate heat treatment is completed, the components have heavily oxidised surfaces with sharp edges remaining as a result of trimming. The shot-blasting process discharges small steel or brass pellets or a

similarly abrasive media (cut from wire [83]) at the brass components, which simultaneously removes the oxidised surfaces and any sharp edges allowing the machining process to be carried out more easily and for the final component to have a better aesthetic appearance.

### 2.4.2 Dezincification Resistance

Although brasses are known to have excellent corrosion resistance in most potable water environments, there are some specific cases in which these alloys will be attacked through a de-alloying process known as dezincification. The dezincification resistance of a brass component is of primary concern throughout processing because it can be a major cause of failure in the field. Dezincification is a process whereby the Zn in the alloy is selectively leached out, leaving behind a weak, porous layer of Cu which is mechanically compromised [1, 81, 84]. This is known to be of concern in waters containing a high concentration of chloride ions, low temporary hardness or alkalinity, increased temperature, and in slow moving or brackish waters [1, 45, 81, 84-86].

The propensity of brass to dezincify increases with increasing Zn content, and it is generally accepted that brasses which contain greater than 15 wt. % Zn are considered vulnerable to dezincification [1, 26, 80, 81, 84-86] (Fig 2.22). This form of corrosion can present as either 'layer' type dezincification, where the brass gradually loses strength and perforates, or 'plug' type dezincification (Fig. 2.23) where zinc carbonate forms white voluminous deposits on the brass surface [84, 85, 87].

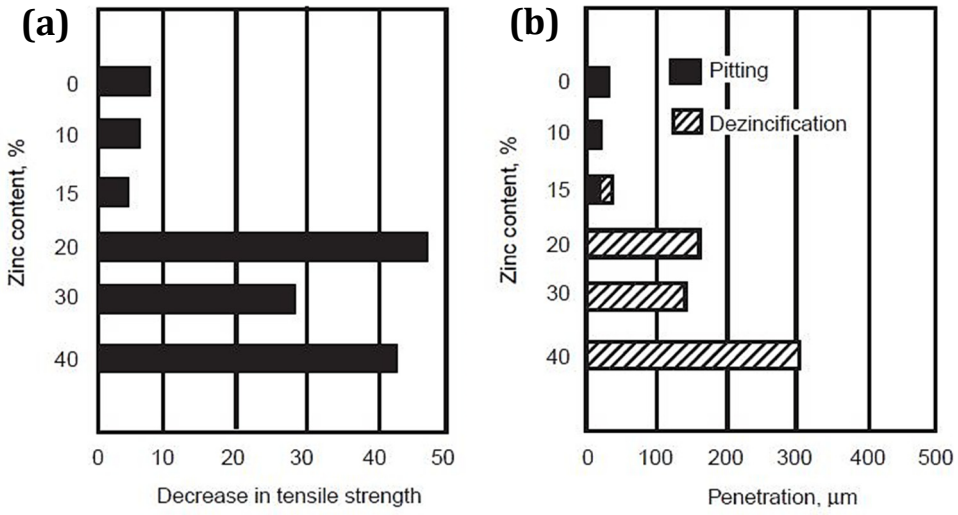


**Figure 2.22: (a) The loss of tensile strength in samples of brass for incremental additions of Zn, where the samples have been exposed to a solution of 0.01M ammonium chloride at 45°C for 60 days. It is evident the effect of including more than 15 wt. % Zn. (b) Dezincification will typically only occur for alloys with an excess of 15 wt. % Zn, beneath this value, pitting is more likely to be encountered [1].**

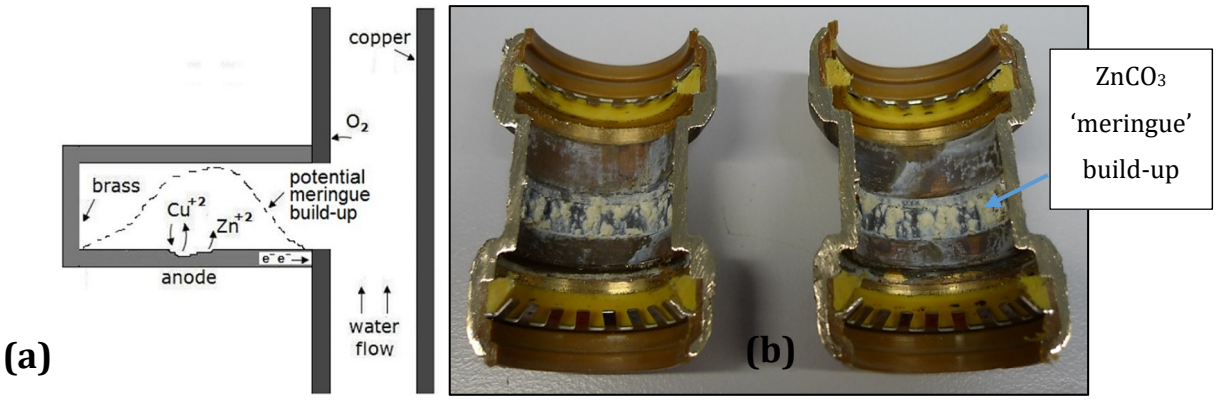


**Figure 2.23: (a) Schematic of the build-up of zinc carbonate during plug-type dezincification [84]. (b) This occurs more readily when copper piping is used in tandem with a brass fitting and a crevice is created, for example when a pipe is not fully engaged, inserted into or over a brass fitting.**

There are two mechanisms commonly invoked when describing the process of dezincification;

1. a process of Zn dissolution, in which the Zn, being less noble than the Cu, undergoes an anodic reaction and will dissolve out of the alloy leaving behind the weak Cu structure [88-90] and
2. a process of Zn and Cu dissolution in which both elements are oxidised and removed from the brass surface, which is then followed by Cu re-deposition when a low oxidation-reduction potential is reached [91-97]. In some instances it has been suggested that both of these processes will occur simultaneously [98, 99], however overall the process remains not well understood and is a current topic of active research, e.g. [93].

Duplex brasses are particularly susceptible to dezincification because not only do they have a much higher Zn content, but the ordered BCC β' phase is preferentially attacked [1, 80-82, 84, 85, 100]. As such, the only methods available to manoeuvre around the problem of dezincification is either through the use of intermediate heat treatments described in Section 2.4.1 to minimise the β' phase fraction, or the utilisation of a dezincification inhibitor/s in the chemical composition.

### 2.4.3 Effect of Alloying Additions on Dezincification Resistance

Certain alloying additions are particularly useful in improving the dezincification resistance of brasses containing more than 15 wt. % Zn, and these are commonly referred to as inhibitors. The most commonly used dezincification inhibitors in the potable water industry are arsenic (As) and phosphorus (P) [26, 45, 82, 84-86, 90, 100-107] (Table 1.1), however antimony (Sb) is also often referred to in the literature [26, 45, 80, 82, 86, 100, 105, 106]. These elements are usually present only in the range of 0.02 – 0.15 wt. % as amounts used in excess of this can increase the alloy's susceptibility to intergranular corrosion/attack (IGA) by the formation of hard intermetallics [81, 100]. It is considered an interesting and perhaps ironic point by the author that arsenic, despite its well-known

negative effects on human health, is still freely usable for alloying with brasses in contact with potable water whilst Pb is heavily legislated. As, P, and Sb have been found to greatly enhance the dezincification resistance of the α phase, however they do not protect any β' phase present in the microstructure (Fig. 2.24). Some work has been performed to suggest Niobium (Nb) might be an effective inhibitor for the β' phase [108]. Hung et al. [109] investigated the effect of adding 0.02 wt. % Nb into duplex brass, however elements such as this are yet to successfully enter the potable water industry either due to cost, lack of supply, or lack of verified results.

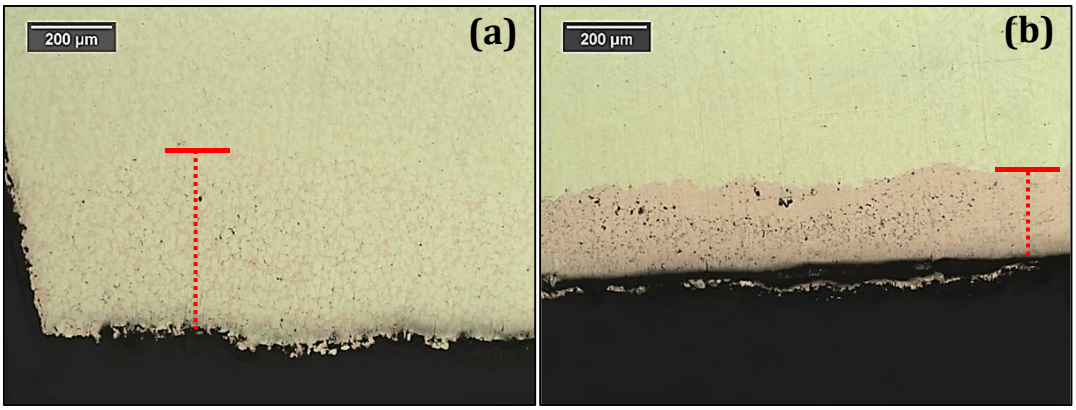


**Figure 2.24: Layer-type dezincification of two duplex Cu-Zn alloys (a) containing trace amounts of phosphorus (only β' attacked), and (b) without any α phase dezincification inhibitors present in the composition (both α and β' attacked). Depths highlighted in red.**

The mechanisms by which As, P, and Sb protect the α phase are still not fully understood. One theory suggested by Lucey [91, 92] indicates that these inhibitors work by suppressing the disproportionation of cuprous chloride into cupric ions. This interference from the inhibitor prevents the dezincification front from advancing into the α phase, but not the β' phase which can additionally be reduced by cuprous ions due to its more negative reduction potential. This is why an intermediate heat treatment is so often used in the potable water industry to remove any residual β' phase remaining in the microstructure.

Several other alloying elements have been investigated for their effects on the dezincification resistance of duplex brass. Sn is generally considered capable of improving both dezincification resistance, and resistance against a variety of other forms of corrosion, particularly when used in higher quantities (~0.3-2.0 wt. %) than the previously mentioned inhibitors [1, 26, 84, 85]. In addition, empirical observations have been made by Karpagavalli et al. [110] who describes the synergistic effect Sn can have with As, and Sohn et al. [82] who describes the synergistic effect Sn has with Ni with these two elements being optimised at approximately 0.7 wt. % Sn and 0.5 wt. % Ni respectively.

An important consideration from the perspective of corrosion is the presence of impurities, such as Fe, Al, Mn, and Mg in brasses because they can serve to decrease the effectiveness of dezincification inhibitors As, P, and Sb, by precipitating these elements from solution to form intermetallic particles, usually along grain boundaries [26, 45, 80, 86, 100, 101, 106, 111-114]. Bowers et al. [45] shows this effect in Fig. 2.25 in which the addition of a combined 0.4 wt. % Fe + Mn can totally nullify the effect of a normal 0.02-0.15 wt. % addition of As inhibitor leading to an increased susceptibility to intergranular attack (also referred to as IGA) [113]. This increased susceptibility to IGA can be of particular concern when it comes to an alloy's propensity to leach Pb into potable water as Pb particles are typically present as small particles along the grain boundaries which are subsequently being attacked during IGA. In cases where a potable water system is leaching Pb due to IGA the only available remedy (other than replacing the system) is to dose the water with phosphate ions [115-117] which can be very invasive and expensive, therefore prevention of excessive impurities in the chemical composition is of utmost importance.

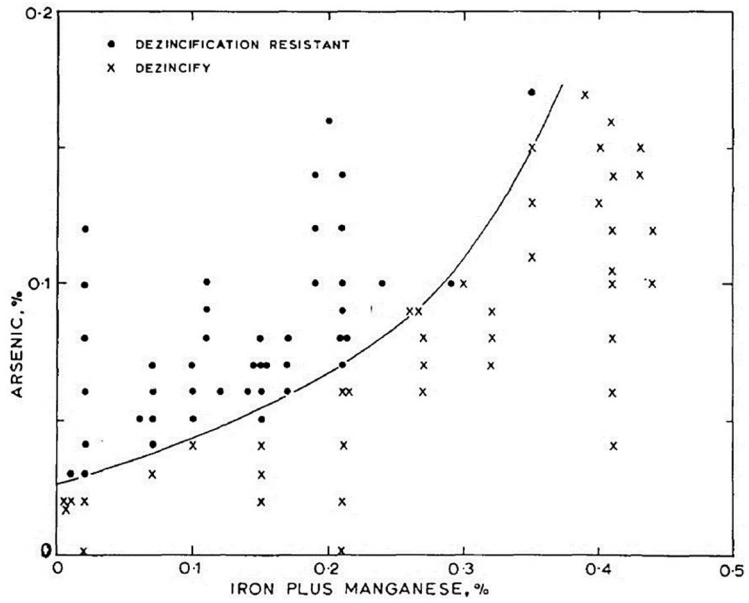


**Figure 2.25: The negative effect of increasing Fe and Mn wt. % on nullifying the dezincification resistance acquired through the addition of As wt. % as an α dezincification inhibitor [45].**

## 2.5 Machinability

### 2.5.1 Machining Operations

Upon completion of the post-forging processes including trimming, intermediate heat treating, and shot blasting discussed in Section 2.4.1, duplex brass components are then typically exposed to a variety of machining operations in order to obtain their final desired dimensions. These operations will include, but are not limited to, a combination of:

- **Turning** operations in which the machining tool is fed into a rotating brass component in order to generate longitudinal profiling or facing.
- **Threading** operations in order to generate a mechanical coupling which may be sealing or non-sealing for potable water applications.
- **Drilling** operations in which a rotating drill is plunged into the brass material in order to generate a channel for bolts or potable water flow.

It is standard practice for turning and drilling operations to use a combination of what are known as roughing and finishing processes. The roughing process removes large amounts of material quickly and close to the final dimension of the component requirements, while the finishing process removes far less material to very close tolerances and produces a much finer surface finish on the duplex brass component.

Throughout industrial-scale machining processes, large amounts of coolant lubrication are sprayed onto the duplex brass in order to prevent over-heating of the workpiece which can cause intermediate temperature embrittlement [118]. This is to additionally help lubricate the machining centre components and tooling. Intermediate temperature embrittlement, also known as 'warm shortness', is the phenomena whereby α grain boundaries slide and form micro-voids at high strain-rates (creep rupture mechanism) between the approximate temperature range of 300 – 500$^{o}$C [118]. This phenomena may be influenced by the presence of Pb and Bi particles which are liquid above 327.5$^{o}$C and 271.4$^{o}$C respectively (or 126$^{o}$C at their eutectic mixing point [11]). An example of this is shown in Fig. 2.26 for a bismuth-bearing duplex brass. The sample microstructure, which comes from a ½" coupling directly-machined from extruded and annealed rod, has experienced fracture originating from the internal bore exposed to a blunt drill. The drill generated excess heat due to being blunt and led directly to warm shortness of the component.

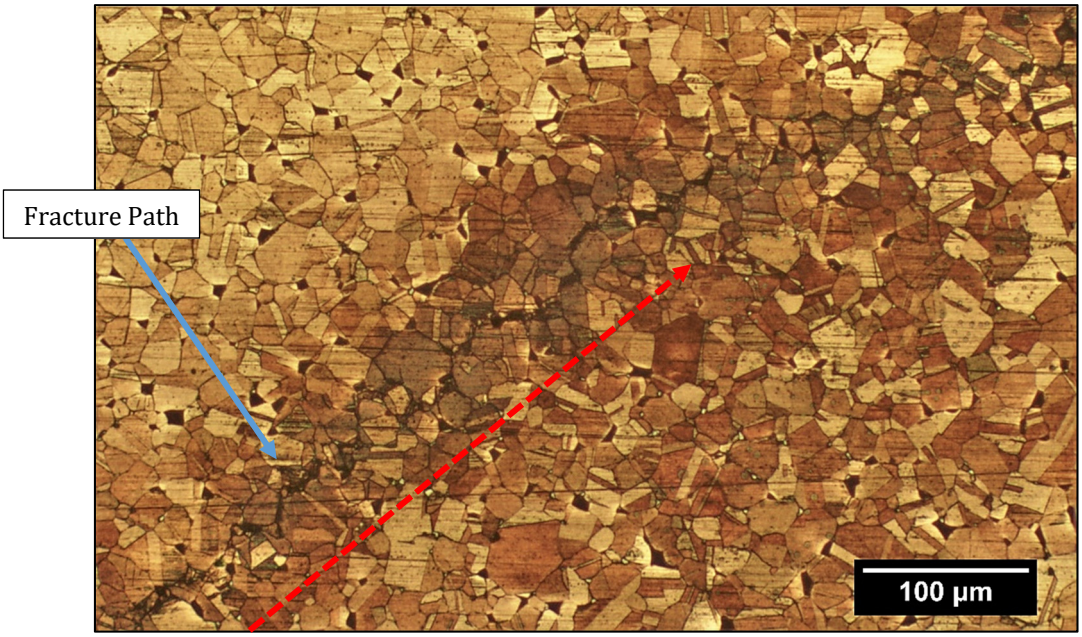


**Figure 2.26: Example of intermediate temperature embrittlement in a recrystallised α microstructure causing fracture in a Cu-37.1Zn-0.58Bi-0.37Sn-0.28Pb alloy during machining. Red dotted arrow indicates direction of fracture progression from origin.**

### 2.5.2 Measures of Machinability of Duplex Cu-Zn Alloys

The machinability of duplex brass (and other metallic materials in general) is often characterised by four key indicators:

1. **Power consumption.** This is the amount of power required by the machining centre to complete the toughest operation. For small components like potable water fittings, this is normally the drilling operation which removes the most material from the workpiece. The power consumption is characterised by evaluating the cutting forces (calculated with the use of a dynamometer) encountered during a standard machining operation such as turning [43, 119-124].
2. **Tooling life.** This is a very important economic factor in which the tool wear is evaluated after a series of repetitive machining operations has occurred [43, 119, 120]. For example, Nobel et al. [121] (Fig. 2.27) shows various degrees of tool wear for a repetitive turning operation on 4 different brass materials. Tool wear is typically characterised as either abrasive or adhesive [125], where the more commonly encountered forms of tool wear during machining are thermal, crater wear, notch wear, flank wear, and built-up-edge (BUE), the latter three of which are often simply due to the use of non-optimal cutting speeds [126]. Pb-bearing brasses typically exhibit the least tool-wear, while Si-bearing brasses tend to significantly increase flank wear due to increased material hardness.

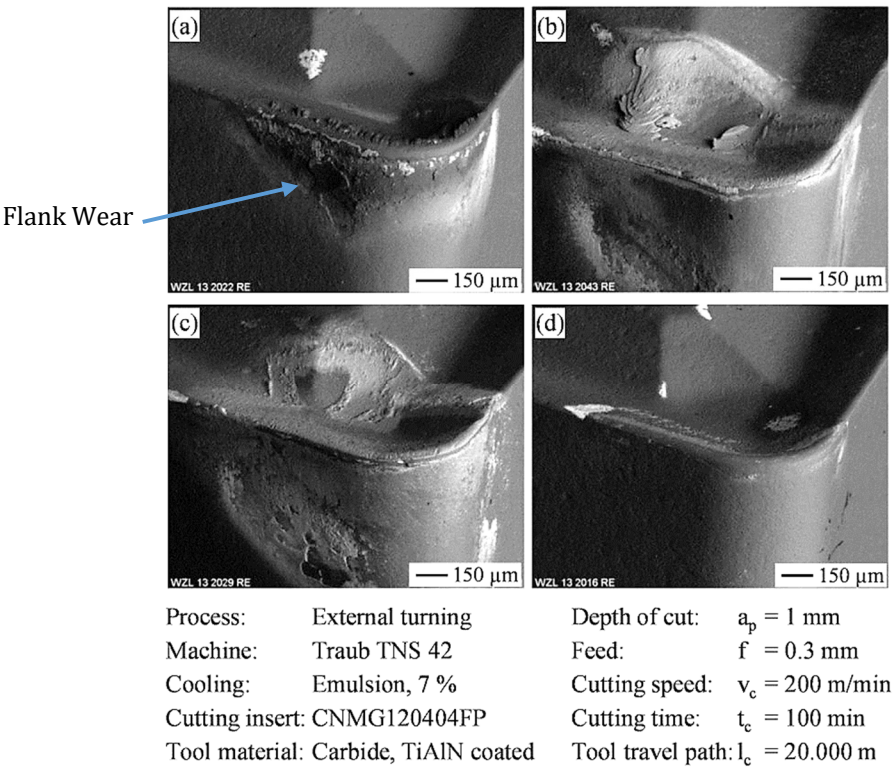


**Figure 2.27: SEM images showing various states of carbide tool wear after completion of a turning operation on 4 different alloys (a) Cu-21Zn-3.4Si, (b) Cu-38Zn, (c) Cu-42Zn, (d) Cu-39Zn-3.3Pb [121].**

3. **Swarf or 'chip' morphology.** The material which is removed from the workpiece is of critical importance to the overall machining operation. This is normally characterised by assessing the morphology of the swarf that is removed and categorising these morphologies into classes [121-123, 127] (Fig. 2.28). Finer classes of swarf are more desirable for the machining process because they are more easily removed from machines and tend not to get tangled in the tooling which can cause damage to the workpiece and shorten tool life.

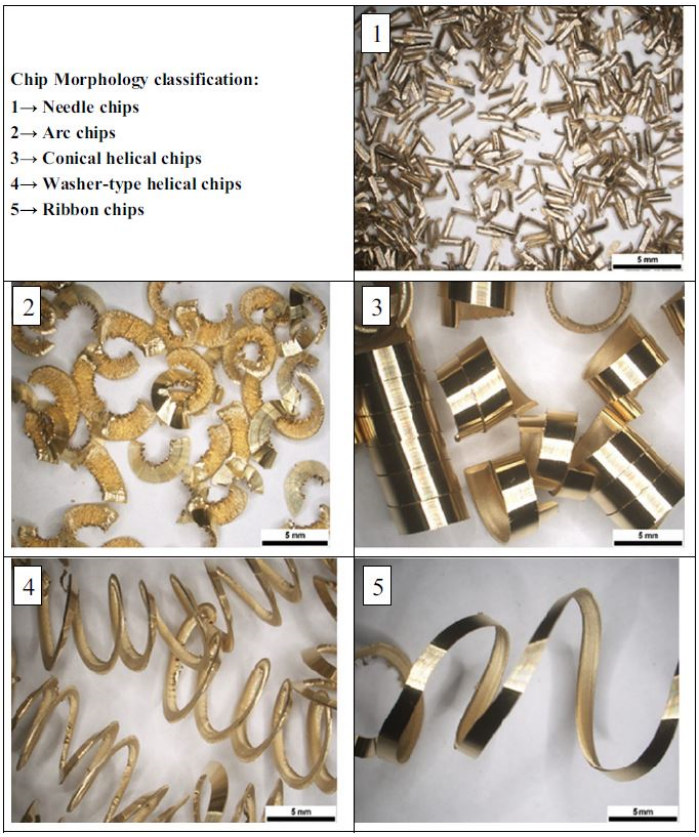


**Figure 2.28: Examples of various classifications of Cu-Zn swarf or 'chip' morphologies attained after a machining operation [122]. Finer swarf, like that observed in no. 1, are generally more desirable.**

4. **Appearance or surface roughness.** This is a key factor for the final aesthetic finish of the component and is usually characterised by the arithmetic mean roughness (Ra) along the surface of the brass [119, 120, 123]. Brass surfaces which exhibit a low Ra are inclined to have a 'shinier' appearance which tends to be more appealing to the customer.

Several other laboratory tests are often used in tandem with the above measures in order to correlate the machinability to other measures of mechanical properties of brass alloys. These include tensile testing [119, 120, 124, 128, 129], torsion testing [124], hardness testing [119, 120, 122, 124, 128, 130], and impact (Charpy V-notch) testing [128].

### 2.5.3 The Role of Lead (Pb) in Machining Processes

In order to improve the fabrication characteristics of traditional duplex brasses, Pb was often introduced into the chemical composition specifically to aid in the machinability of the alloy. Pb is almost completely insoluble in solid Cu-Zn alloys (Fig. 2.8a) and forms as small globules or particles, usually along grain boundaries during the solidification process [1, 34] (Fig. 2.29a). These Pb-particles have several key-effects on the measures of machinability described in Section 2.5.2. Due to the different mechanical properties of these particles, they act as mild stress raisers in the matrix and Pb tends to break up swarf into much finer chips rather than long continuous strands or spirals (Fig. 2.30) [43, 119-123]. This prevents blockages in machines, protects tooling, and decreases heat generation in the brass workpiece which could otherwise lead to intermediate temperature embrittlement [118]. Pb particles are also reported to have a positive effect on both reducing tool wear/friction and cutting forces [43, 119-123, 131]. These positive effects are found even for small additions of Pb as shown in Fig. 2.29b.

Gane et al. [124] showed, using two duplex brasses, one containing ~2.9 wt. % Pb, and the other being Pb-free, that even though the tensile strength, elongation, and hardness of the alloys is unchanged with increased Pb content, a reduction in cutting forces is observed during machining due to the low shear strength at the interface between the brass and the cutting tool. In other words, there is a reduction in localised ductility which results from the low cohesive energy of the Pb particles along the brass grain boundaries which subsequently helps to induce chip breakage and lubrication of the machining tool. It has been postulated that the Pb-particles size and distribution may affect the resulting machinability of the alloy [119, 123], however this is not well explored in the literature.

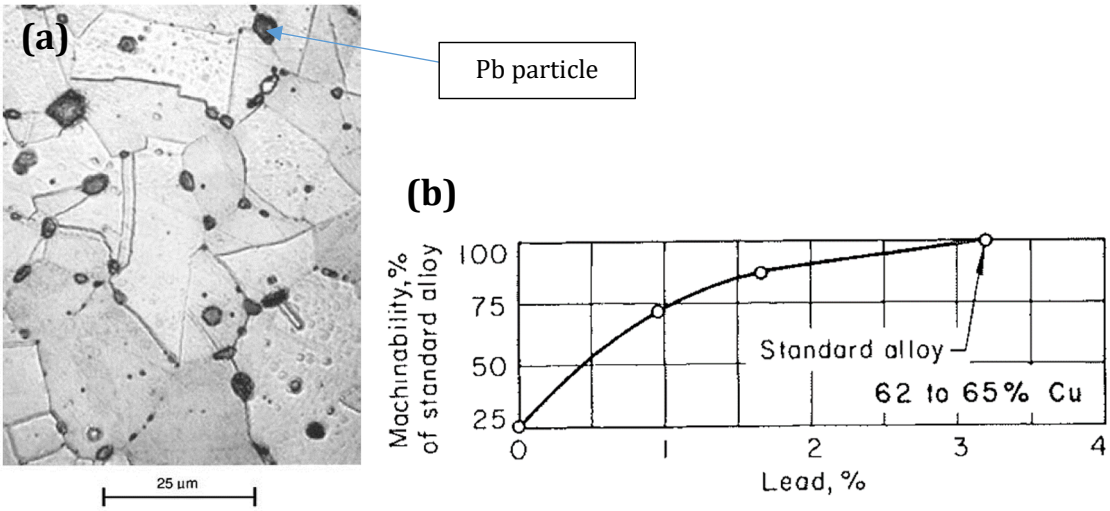


**Figure 2.29: (a) Free-cutting C36000 brass microstructure exhibiting dark Pb-globules primarily along the grain boundaries of the α phase [1], (b) The correlation between Pb-additions and improvement in universal machinability rating for brass alloys with a Cu-content between 62 and 65 wt. % [1].**

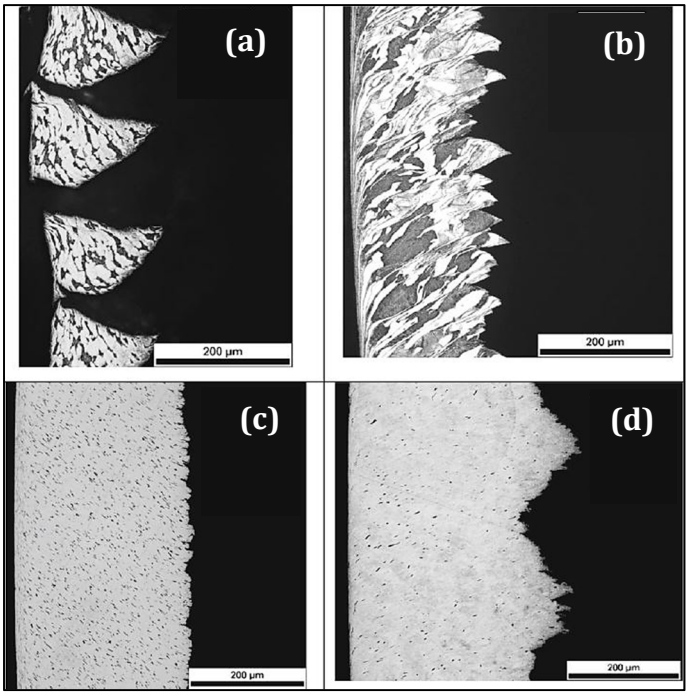


**Figure 2.30: Microstructural observations of four different brass alloy chips after a turning operation, (a) Cu-39Zn-3Pb, (b) Cu-42Zn, (c) Cu-38Zn-As, (d) Cu-36Zn [122].**

A "machinability index" is commonly used in the manufacturing industry in order to gauge the machinability of a given brass against a standard material allocated a rating of 100 [1]. This standard alloy, C36000, also known as 'free-cutting brass', contains ~3.1 wt. % Pb. Levels in excess of this are rarely used due to the plateau in beneficial machining characteristics beyond this point [123]. Fig. 2.31 shows the reduction in machinability index for two other duplex brasses containing ~1 wt. % Pb (C34000) and only trace amounts of Pb (C46400) and their subsequent reduction in tool life under otherwise identical conditions. These results are then compared against other commonly lathe-machined materials, for example 2011-T3 aluminium and 12L14 bright mild steel.

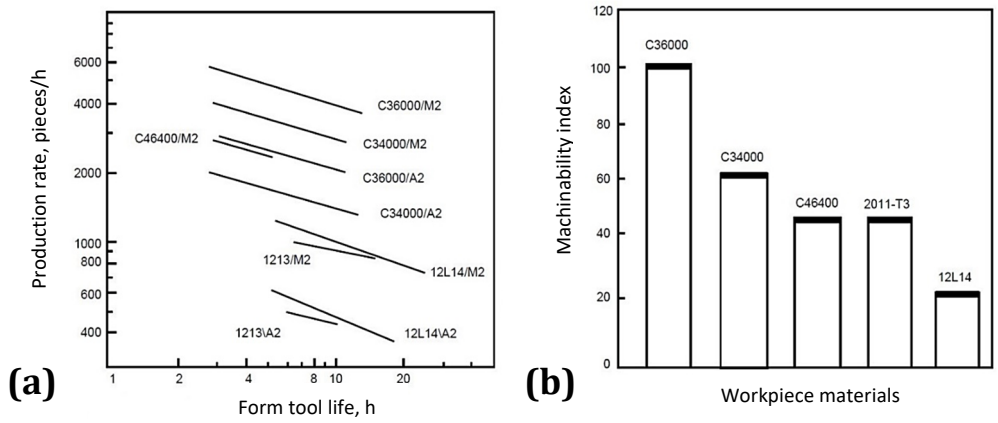


**Figure 2.31: A comparison between free-machining brass (C36000, 61.5Cu-35.5Zn-3Pb), a low-Pb brass (C34000, 65Cu-34Zn-1Pb), and a Pb-free brass (C46400, 60Cu-39.2Zn-0.8Sn) for tool life and universal machinability index against some other common materials like 2011-T3 aluminium and 12L14 bright mild steel [1].**

The introduction of legislation and standardisation around the world which caps Pb content at 0.25 wt. % for brass potable water products [6], or the European 4MS initiative in which Pb leaching rates are strongly evaluated for an approved alloy list [132], has put a new focus on the search for alternatives for Pb in duplex brass components for the purposes of enhanced machinability [43, 119-122, 129]. A difficulty is that not only has Pb been shown to significantly improve the machinability of duplex brass alloys, it is also observed to have an essentially neutral effect on castability, hot workability, corrosion resistance, and mechanical properties like UTS and elongation. This makes it a very difficult element to replace without affecting the final properties of the material and cost of the end-product.

### 2.5.4 Alternatives to Pb for Improved Machinability

Research into Pb-replacement alloys has become an important source of information utilised by the brass industry to design the manufacturing process and keep rejection rates low in the absence of traditional Pb-containing alloys. In order to understand the machining characteristics of Pb-free alloys, a greater emphasis has been placed on the effects of several common alloying additions such as Bi, Sb, P, Mg, Mn, and Si. The addition of these elements aids the machinability of duplex brasses in one of three ways; (1) by replacing Pb with another similarly insoluble element in the brass matrix, such as Bi, (2) by encouraging the formation of intermetallic particles to help emulate the stress raising effect of Pb during chip formation, for example with P, Sb, Mg, or Mn, and (3) by introducing a new phase at room temperature, which behaves in a similar way to Pb during machining, such as the HCP κ, BCC ε or complex cubic γ phases stabilised due to the presence of Sn or Si.

The only other known alternative to these strategies is to simply remove Pb from the brass composition and replace with more Cu and Zn (e.g. remove 2 wt. % Pb and replace with 1 wt. % Cu and 1 wt. % Zn), for example CW511L (Cu-38Zn-As) is a commonly referenced alloy used for potable water products in Europe today [43, 122, 128, 129, 132].

#### 2.5.4.1 The Direct Pb Replacement – Bismuth (Bi)

Since the implementation of Pb-restricting legislation around the world, Bi has become one of the most commonly used Pb-replacement elements for potable water fittings and valves [133-144]. Bi has many similar characteristics to Pb in brass. Bi is insoluble in brass and forms small particles along the grain boundaries [1, 145, 146]. Bi ($T_m$: 270°C) has a relatively close melting point to Pb ($T_m$: 325°C) and similar mechanical properties [35] which allows manufacturers the ability to regain a degree of the machinability they enjoyed with traditional Pb-containing alloys without significantly altering their

tooling parameters. Another important benefit of using Bi as a direct Pb replacement is that it is thought to have a neutral effect on the dezincification resistance of brasses [26].

Subsequent research into the use of Bi has unfortunately uncovered several drawbacks. Bi, more so than Pb, can have a negative effect on the hot workability of brass alloys, specifically encouraging the development of hot tearing because of its tendency to form a film-like morphology along α grain boundaries [74-77, 147, 148]. Bi can also cause significant embrittlement and directionally sensitive ductility when present in significant quantities due to this same film-like formation along grain boundaries [1]. This is also partly due to the expansion of Bi particles by ~3.32% upon solidification [73] which tends to cause high residual stresses. This has led to concerns over other issues such as increased susceptibility to stress corrosion cracking (SCC) [149] which will be discussed in Section 2.6.3. The quantities required to produce a clearly observable negative effect on duplex brasses used in the plumbing industry are yet to be outlined in the literature.

In order to combat the negative effects of embrittlement, concentrations of Bi are rarely seen in excess of 2 wt. % in the more common industrial Bi-bearing U.N.S. alloy designations such as C28340 (0.65 – 0.75% Bi), C49260 (0.5 – 1.8% Bi), C49265 (0.5 – 1.3% Bi), and C49340 (0.5 – 2.2% Bi) [2]. For example, Lansell et al. [150], the co-creators of C28340, recommend a maximum content of 1 wt. % Bi, with an ideal level at 0.7 wt. % in order to generate the best combination of machinability, hot and cold workability. The addition of Sn to Bi-bearing alloys has also been postulated to better distribute Bi-particles throughout the brass matrix by altering the surface tension at the grain boundary and preventing Bi from forming as a film [77, 150, 151]. Another method commonly used to reduce the required concentrations, and therefore drawbacks of Bi in duplex brasses, is the use of selenium (Se) which has been observed to increase the effectiveness of Bi in improving machinability by forming bismuth selenide ($Bi_2Se_3$) particles, thus allowing lower concentrations to be used [1, 133, 152, 153]. A similar effect is also said to be true for additions of tellurium (Te) [1, 154] however this is less well explored in the literature.

The ability to source Bi long-term is an issue as not only is it more expensive than Cu, Zn and Pb as a raw material [35], but its availability is limited as it is a by-product of the production of other elements such as Pb [73, 149, 155]. The separation of Bi-containing brass from other brasses for recycling purposes is also difficult, even more so at the refinery level for extracting Cu via smelting which cannot be done in a pyrometallurgical way due to the low affinity of Bi to oxygen in comparison to other elements like Si [155].

### 2.5.4.2 Precipitation of Intermetallics

Elements such as P and Sb are rarely added to duplex brass in amounts higher than that required to attain suitable dezincification resistance (~0.02-0.15 wt. %) because this can increase susceptibility to intergranular corrosion through intermetallic formation [81, 100, 101, 106]. However, these elements can be deliberately added in much higher concentrations in combination with other alloying elements such as Mg, Mn, Fe, Si, or Al in order to deliberately induce intermetallic formation for the purposes of enhanced machinability [148, 156-163]. The intermetallic particles are thought to have a similar effect to Pb and Bi particles during machining, allowing for finer swarf to be generated. For example, Xu et al. [164] utilised additions of 0.59 – 1.60 wt. % P in order to generate $Cu_3P$ intermetallic particles for increased machinability, while Li et al. (Fig. 2.32a-c) [165], Gan et al. [130] and Zhu et al. [166] each use various Sb and Mg additions to create $Cu_2Mg$ and $Cu_9Sb$ intermetallic particles. For these additions, however, it was observed that the relatively small gain in machinability was offset by an associated loss in tensile strength and elongation (Fig. 2.32d).

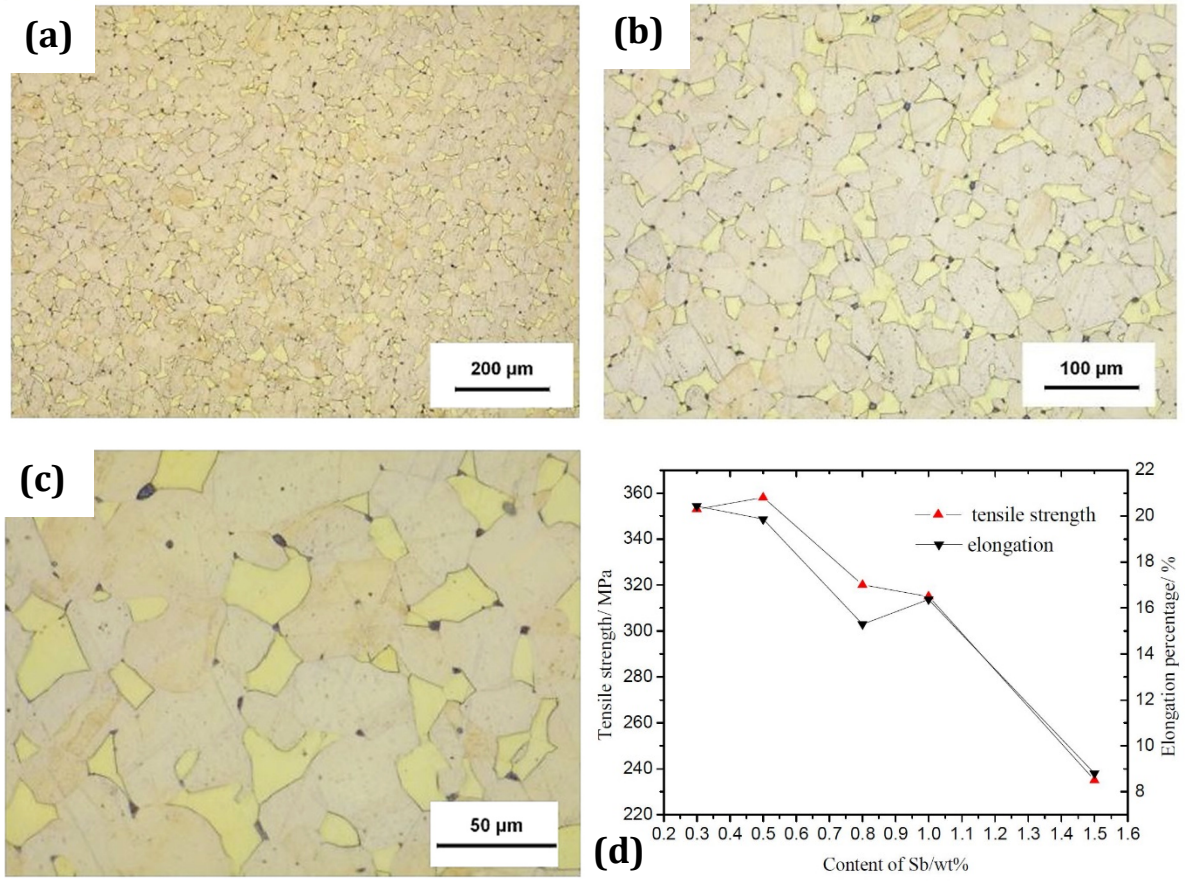


**Figure 2.32: (a-c) The microstructure of a duplex brass containing 1 wt. % Mg and 0.8 wt. % Sb at various magnifications. The dark particles are intermetallics $Cu_2Mg$ and $Cu_9Sb$ [165]. (d) Loss in mechanical properties (tensile strength and elongation) with increasing Sb additions for machinability [165]**

It should be noted that a side-effect to adding Mg (Gan et al. [130]) is the ability to stabilise the β' phase (Fig. 2.33) which, as a result of its own hardness and brittle nature, is able to help break swarf up into a finer chip morphology during machining. This is not the first time an increase in the β' phase fraction has been identified to potentially assist machinability through finer swarf morphology generation. Pantazopoulos et al. [167] proposed that the machinability of a Cu-39Zn-3Pb alloy was superior to a Cu-36Zn-2Pb-As alloy, not only due to its elevated Pb content, but also because it contained ~30% more β' in the microstructure. This was reinforced by Toulfatzis et al. [122, 129] in the evaluation of three Pb-free alloys of varying β' content. However, in spite of the initial characterisation of the three alloys being sound for a wide variety of heat treatments [129] the repeated attempts by Toulfatzis et al. to characterise machining performance while altering several turning operation parameters (depth of cut, cutting speed, and feed rate) [122] meant no two experiments were the same and thus the actual effect of β' phase fraction on machinability remains not well defined in the literature, particularly for power consumption, tool wear, and surface roughness. Of course, the β' also has poor dezincification resistance and hence if it was used to improve machinability, it would be necessary to introduce a new intermediate heat treatment after machining to remove the β'.

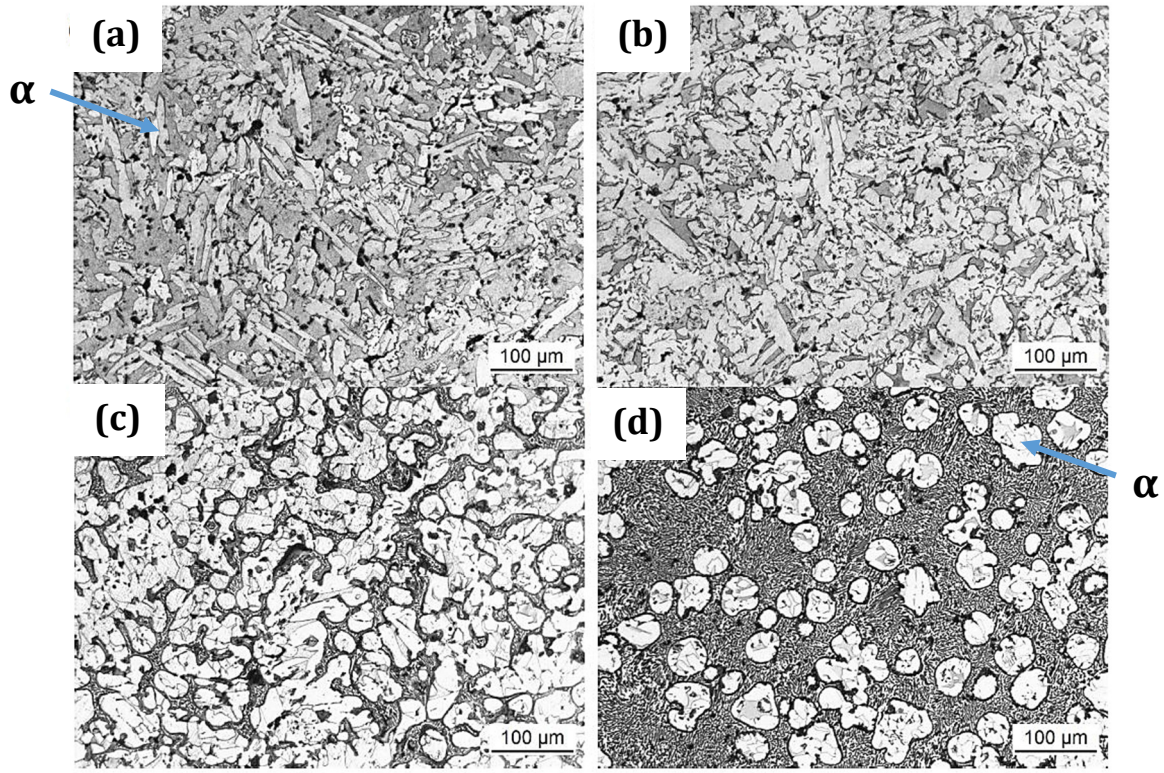


**Figure 2.33: Microstructures of 60Cu-Zn-0.5Sb-0.5Bi alloys with additions of (a) 1 wt. % Mg, (b) 2 wt. % Mg, (c) 3 wt. % Mg, (d) 4 wt. % Mg [130]. Increasing Mg concentration stabilising additional β' (dark phase) and changing the morphology of α from acicular to spherical.**

### 2.5.4.3 Stabilisation of Alternate Phases using Silicon (Si)

As a direct result of its ability to significantly affect the phase equilibria of duplex brass alloys, Si additions have been at the forefront of new Pb-free alloy research and development [168-175]. Identified as early as 1941 [176], Si contents up to 5 wt. % are now commonly used to improve the corrosion resistance, mechanical properties, and the machinability of these alloys. Although these effects can be seen for duplex brasses with standard Cu-Zn ratios, the alloys tend to be too brittle to be industrially useful. For example Fig. 2.34 shows the increase in hardness with increasing Si content for a brass alloy with 60 wt. % Cu [41]. Instead, the Cu-Zn ratio is shifted towards the Cu-rich end of the binary phase diagram in order to stabilise a greater FCC phase fraction and therefore retain a greater degree of ductility throughout processing.

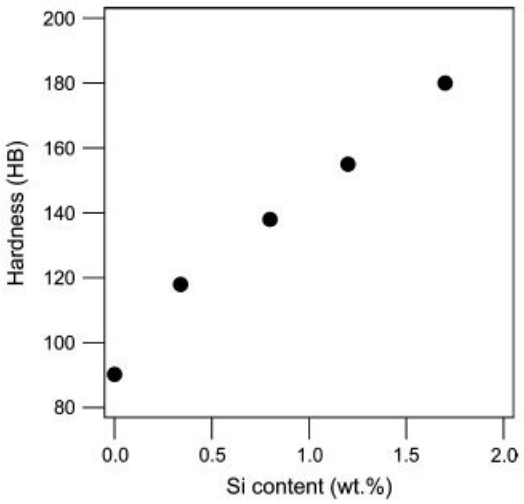


**Figure 2.34: Increase in hardness with Si additions [41].**

The most common Si-bearing alloy used in the potable water industry today is U.N.S. C69300 (Cu-21Zn-3Si-P), also known as EcoBrass. Developed by Oishi [42, 177-180] for Pb-free potable water applications, EcoBrass is currently thought to have the best combination of mechanical properties (Table 2.5), corrosion resistance, and machinability without significantly reducing hot workability. This is primarily due to its optimised Cu content of 73-77 wt. %, with ~3 wt. % Si, which is required to maintain a duplex α/β structure at elevated forging temperatures, while at room temperature there is typically a combination of FCC α, complex cubic γ, HCP κ, and BCC ε [180]. It is the γ, κ, and ε phases that enhance the machining characteristics of the alloy by improving both the swarf morphology and the cutting forces for turning operations compared with simple duplex brasses such as Cu-42Zn (CW510L) and Cu-38Zn-As (CW511L) [43, 121].

**Table 2.5: A comparison of various material properties for both a common Si-bearing brass alloy (C69300) and a Pb-bearing brass alloy (C38500) [120].**

| Material property | CuZn21Si3P | CuZn39Pb3 |
|---|---|---|
| Yield strength, $R_p$ [MPa] | 342 | 201 |
| Tensile strength, $R_m$ [MPa] | 717 | 525 |
| Elongation at rupture, $\varepsilon_b$ [–] | 0.22 | 0.26 |
| Hardness, $H$ [GPa] | 2.97 | 1.86 |
| Thermal conductivity, $k_W$ [W mK$^{-1}$] | 35 | 113 |
| Abrasiveness $W_{ab}$ [GPa] | 3.13 | 1.97 |
| Strain hardening factor, $S_n = R_m/R_p$ | 2.10 | 2.61 |

Compared with traditional Pb-bearing alloys, EcoBrass has its own drawbacks. This is primarily increased tool wear due to a combination of two factors. First, the harder γ, κ, and ε phases present at room temperature will increase the cutting forces (Fig. 2.35) leading to increased abrasive tool wear in turning [43, 119-121]. Second, the thermal conductivity of EcoBrass (Table 2.5) is significantly lower due to the presence of Si-rich phases such as κ and ε. The Si additions promote covalent bonding (Si and Cu both have an electronegativity of 1.90) which simultaneously makes these phases more brittle and significantly lower in thermal conductivity, in turn making it more difficult for heat to transfer away from the machine-face. Their presence means the cutting tool will heat up more quickly compared with traditional Pb-bearing alloys leading to accelerated wear [119, 121]. A direct comparison between two turning tools is shown in Fig. 2.36 in which significant crater wear (on the rake face leading to tool chipping and failure) is encountered for the Si-bearing EcoBrass vs. a traditional Pb-bearing brass.

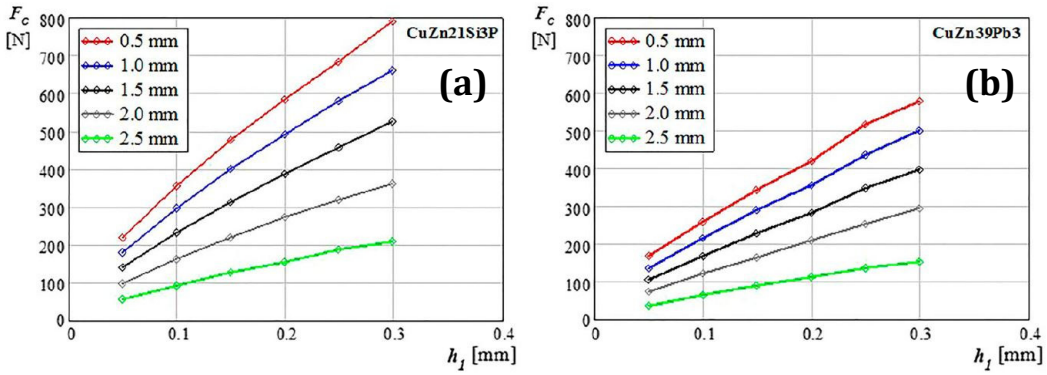


**Figure 2.35: A direct comparison of cutting forces (N) for (a) the Si-bearing C69300 vs. (b) the Pb-bearing C38500 at various depths of cut during a turning operation [120].**

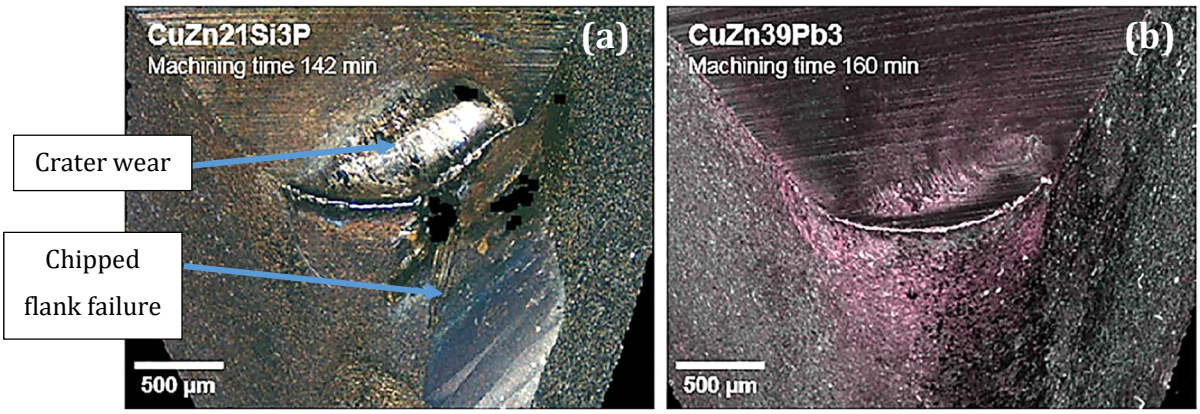


**Figure 2.36: A direct comparison of the accumulated tool wear encountered while machining (a) the Si-bearing C69300 vs. (b) the Pb-bearing C38500 [120]. Far less wear is encountered for the machining tip on the right used to turn Pb-bearing duplex brass while the Si-bearing tip has failed after chipping off a section of the tip due to excessive crater wear.**

Aside from the tool wear affects from adding Si, the two biggest inherent drawbacks of adding Si are:

- Separation of process scrap from Si-free alloy streams. For foundries, forging plants, and machining plants where scrap is mixed, this creates issues when the material is then recycled and becomes contaminated upon melting.
- Cost related to increasing the Cu content up by approximately 15 wt. % [181]. Even for large industrial manufacturers, this makes a significant difference to the cost of the final product which is then passed on to the consumer.

## 2.6 Post-Machining Processes

### 2.6.1 Introduction

Upon completion of the required machining processes, brass components will retain a certain degree of residual stress, with much of this in the form of tensile stresses localised across the exposed surface [1]. This is particularly important around thin-walled sections where there has been significant amounts of material removal, with the remaining section that may need to be subsequently cold worked for the final desired fitting geometry. The level of residual stress may be exacerbated by the presence of hard intermetallic particles, secondary phases (such as the γ or κ phases), or insoluble elements like Bi which expand ~3.32% [73] upon solidification creating stress raisers within the material. There are two primary reasons why the presence of residual stress is undesirable:

- It can promote crack formation during subsequent cold work, such as during coining or crimping.
- It can cause issues in the field such as failure due to stress corrosion cracking (SCC) [1].

In order to relieve residual stresses in machined brass components some manufacturers expose the components to a low-temperature heat treatment at approximately 150-300$^{o}$C for up to 8 hours [1, 81, 182, 183]. This process allows the brass to stress-relieve without any significant change in mechanical properties. The greatest drawback of the process is that the brass surface will tend to oxidise reducing its aesthetic appeal and potentially altering finely set tolerances, for example along a sealing thread section. Deterioration of dimensional tolerances, and damage to delicate wall sections are also the reason why subsequent shot blasting cannot be used to remove any oxide from the surface. It would therefore be useful to understand the post-forging, and post-intermediate heat treatment microstructures of duplex brass, in order to reduce susceptibility to cracking and SCC in post-machining processes. This is not well understood at this time.

### 2.6.2 Crimping (Cold Working)

One of the most common cold working processes used in the plumbing industry today is crimping. Cartridge components made from various polymers (acetyl, nylon, PSU) and metals (usually series 300 austenitic stainless steel) are inserted into the duplex brass component, with a thin-walled brass section subsequently rolled over or 'crimped' in order to hold the cartridge in. The most common type of fitting which employs this mechanism is known as a push-to-connect fitting (Fig. 1.1) [184-186]. At this stage of processing, the aesthetic, in addition to the final mechanical properties and corrosion resistance, is very important. The aesthetic of the brass alloy is affected by several variables including the surface finish from machining and any oxidation from prior heat treatments. However, one factor that is often overlooked in the final part is the 'Orange-Peel' effect (Fig. 2.37). The 'Orange-Peel' (OP) effect is common to deep drawing processes relating to sheet metal [187], in which the material is stretched causing a cosmetic roughening of the surface due to inhomogeneous deformation. One commonly attributed factor to this effect is excessive grain size [188].

For duplex brass alloys in typical manufacturing operations, the 'Orange Peel' effect is difficult to predict due to its dependence on the prior thermo-mechanical processing steps. However, the plastic deformation that occurs during the crimping process can cause the appearance of this defect [182]. 'Orange-Peel' in duplex brass will normally occur via one of two mechanisms during crimping:

- When the final average grain size is significantly higher than normal and deforms locally under cold working conditions.
- When there is more than one grain morphology present in the microstructure which leads to the preferential localised deformation of the weaker grains, typically any recrystallised α grains (Fig. 2.38).

The mechanism by which the latter occurs is not well understood but has become a more common problem since the introduction of Pb-free legislation around the world. It is hypothesised that this may

be the result of increased grain growth in the absence of Pb particles in the microstructure during elevated temperature manufacturing processes (Sections 2.3 and 2.4), however this needs to be explored further in order to verify the origin of this effect.

**Figure 2.37: Plumbing fittings exhibiting (a) the orange-peel effect without cracking and (b) with extensive cracking.**

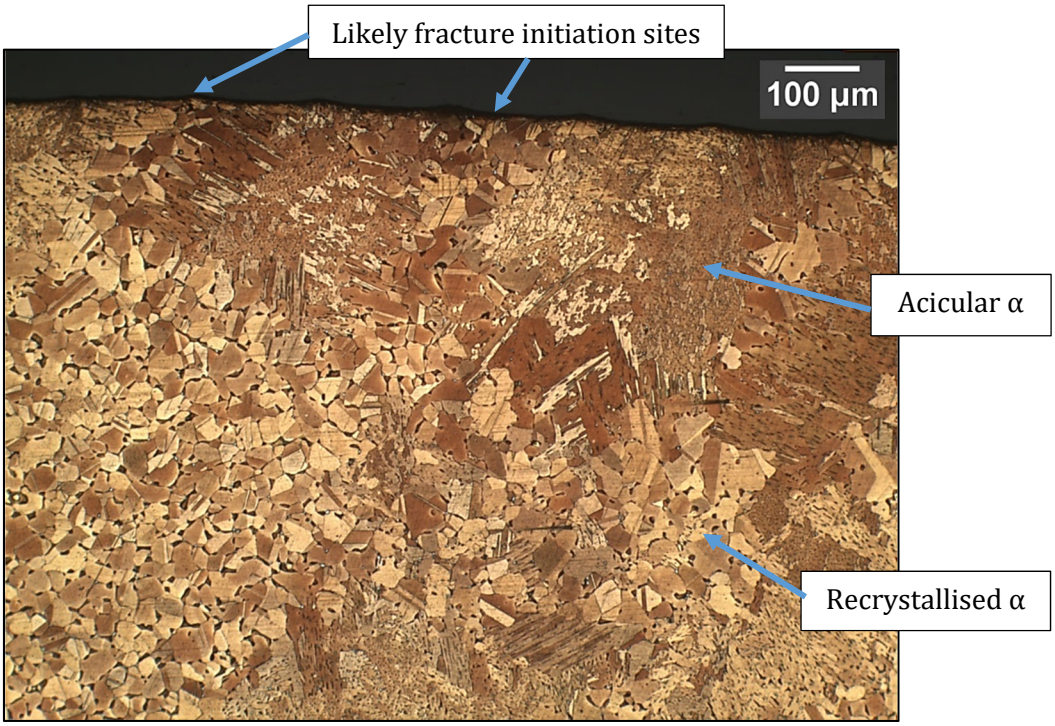


**Figure 2.38: Metallographic representation of the Orange peel effect as a result of a dual-grain-morphology. The recrystallised α grains deform preferentially on the surface during cold working/crimping.**

### 2.6.3 Stress Corrosion Cracking (SCC)

Alongside dezincification, stress corrosion cracking (SCC) is the other commonly occurring failure mechanism of duplex brass in the field (Figs. 2.39-2.40). Failures of this type are normally characterised by severe macroscopic brittle cracking of an otherwise ductile material due to the interaction of the (stressed) component with its surrounding environment. Generally speaking, three specific factors are required for this phenomenon to occur:

- A susceptible material, in this case the duplex brass.

- The presence of stress, either applied mechanically in service or residual (typically from prior manufacturing steps).
- A corrosive compound found in the immediate environment [1, 189, 190].

Also referred to as 'season cracking', the SCC phenomenon was first reported in India in the 1920's when the army's rifle ammunition cases, made from cold drawn cartridge brass, began cracking in storage partly due to exposure to ammoniacal compounds [190, 191]. Ammonia is the most commonly referenced corrosive compound in environments which cause SCC of brass [1, 81, 189, 192-198], however several other compounds such as sulphuric acid [190], chlorides [189, 193, 199, 200], sulphates [189, 193, 194, 199, 200], nitrites [192, 199, 201], nitrates [196, 202], and fluorides [203] have also been identified as effective contributors to the occurrence of SCC. An example of the presence of these compounds in the field was explained by Rao et al. [204] in which brass condenser tubes used in a nuclear power plant underwent SCC due to the presence of Nitrate-reducing bacteria which released ammonia ions into the local environment. Other examples have included the presence of sulphur compounds in heavily built-up industrial areas [190]. The proven ability of the aforementioned compounds towards inducing SCC in Cu alloys is typified by the use of mercurous nitrate [205], ammonium chloride [206, 207], and a combination of copper sulphate, ammonium hydroxide, and ammonium sulphate (also known as Mattsson's solution) [208] in various accelerated SCC test standards around the world. The pH of these solutions is regulated in order to control the level of aggression of the accelerated test.

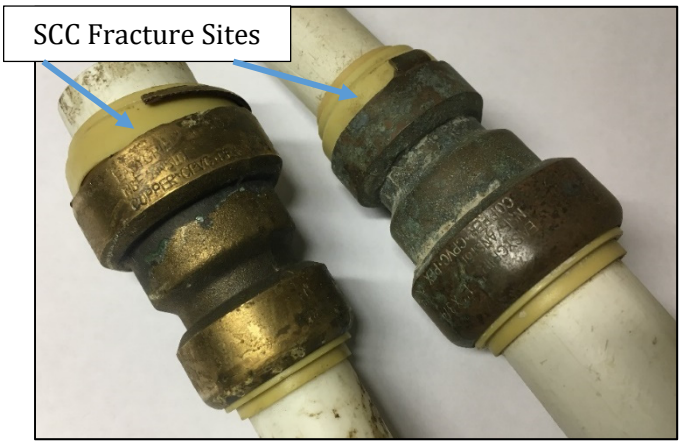


**Figure 2.39: An example of two duplex brass fittings which have suffered from SCC around the crimped (cold worked) ends.**

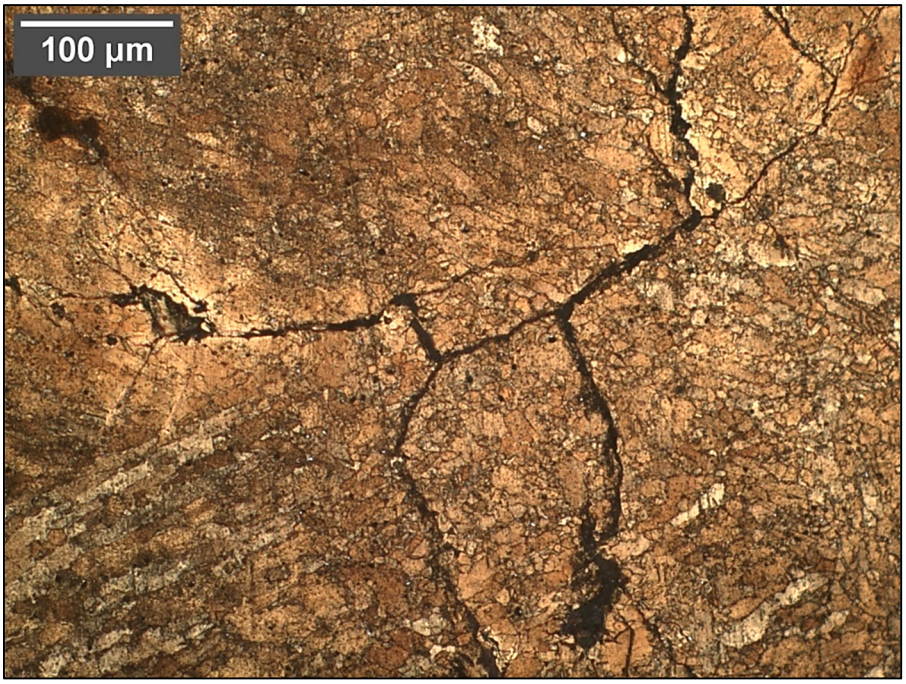


**Figure 2.40: Microstructural characteristics of SCC in a duplex brass. Cracks can be either intergranular or transgranular and typically have several secondary branches, also known by the industrial term 'Spider-Web' cracking.**

The most commonly referenced mechanism of SCC in brass is the passive-film rupture and transient dissolution theory, also known simply as the 'film-rupture' mechanism [191, 193, 197, 203, 209]. In this theory, the brass surface forms a protective/passive layer which, upon exposure to a corrosive medium such as ammonia, will rupture under tensile stress causing the resulting small exposed metal surface to become anodic while the remainder of the surface becomes cathodic. This causes rapid localised dissolution on the exposed metal surface which initiates a crack tip that cannot be repassivated easily due to the ongoing plastic deformation present in this region. As the anodic crack tip propagates into the material, the crack opening acts to channel the SCC-inducing compound, while the walls of the crack become cathodic [191, 193]. Cracking may be intergranular or transgranular depending on a variety of factors, but usually this is attributed to characteristics of the corrosive media such as pH, ion type and concentration [191-194, 201]. Similar to a field remediation method suggested for dezincification, Du et al. [197] suggests that one of the ways to inhibit this corrosion mechanism is by dosing the environment with phosphates which serve to decrease film-induced stress by forming copper phosphate and zinc phosphate in the surface film, allowing repassivation to occur more easily.

The tensile stresses required for SCC to occur in brass may come from either an applied source during service, such as over-torqueing of a mechanical thread [189], or a residual source, such as from prior machining [200] or mechanical crimping upon installation [190]. As these tensile stresses increase, the

time to failure generally decreases (Fig. 2.41a). Under these circumstances the passive-film repair rate tends to fall further behind the rupture rate, therefore the crack progression becomes primarily limited only by the rate of anodic dissolution [193].

Another consideration from a microstructural standpoint is the grain size of the material (Fig. 2.42b). It is widely understood that a reduction of the grain size in Cu-Zn alloys will tend to increase the time to failure because this increases the mechanical (fracture) stress required to propagate a crack [1, 193]. This has been known to follow the Hall-Petch relationship for grain size in:

$$\sigma_f = \sigma_o + KD^{-1/2} \qquad (2.9)$$

$\sigma_f$ is the fracture stress (MPa), $\sigma_o$ and K are constants, and D is the average grain diameter (m) [1].

A recent study by Asabe et al. [210] supports this claim on the positive effects of reducing grain size, however it is suggested that this trend is only found for grain sizes down to 1µm, with a subsequent decrease in SCC resistance found for sub-micron grain sizes in ammonia environments.

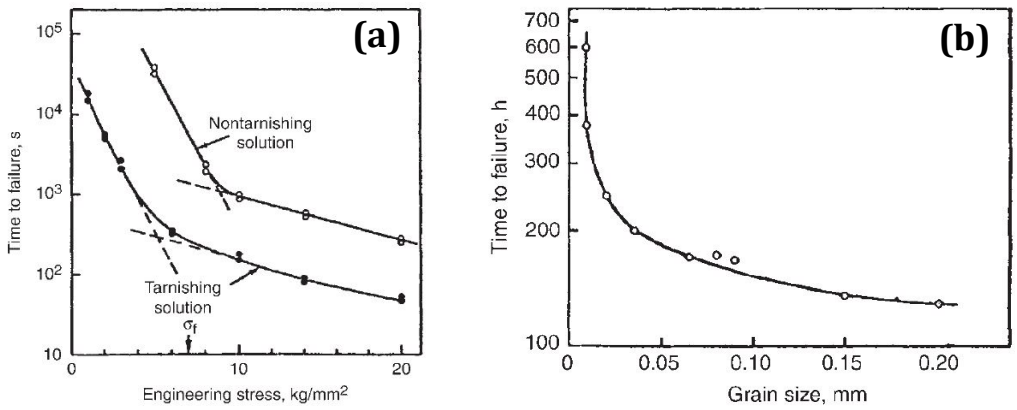


**Figure 2.41: Time to SCC failure of a 70Cu-30Zn brass (a) under the influence of varying engineering stress in an aqueous ammonia environment, and (b) showing the beneficial effects of reducing grain size in a moist ammonia vapour [1].**

There exists a synergistic relationship between stress-induced dezincification and SCC [1, 189, 191, 192, 197, 198, 200, 211, 212]. This was first shown by Leidheiser et al. [213] in 1972 where ongoing cracking through a 70Cu-30Zn alloy in an ammoniacal environment was attributed to dezincification at the crack tip and a consequent weakening of the surrounding matrix. Fig. 2.42 shows an example of this synergistic effect in a duplex brass in which β' grains adjacent to the SCC fracture path have become readily dezincified while they remain unaffected deeper into the brass matrix. As a direct

result of these observations, it is critical that the resistance of the final component to both dezincification and SCC are high.

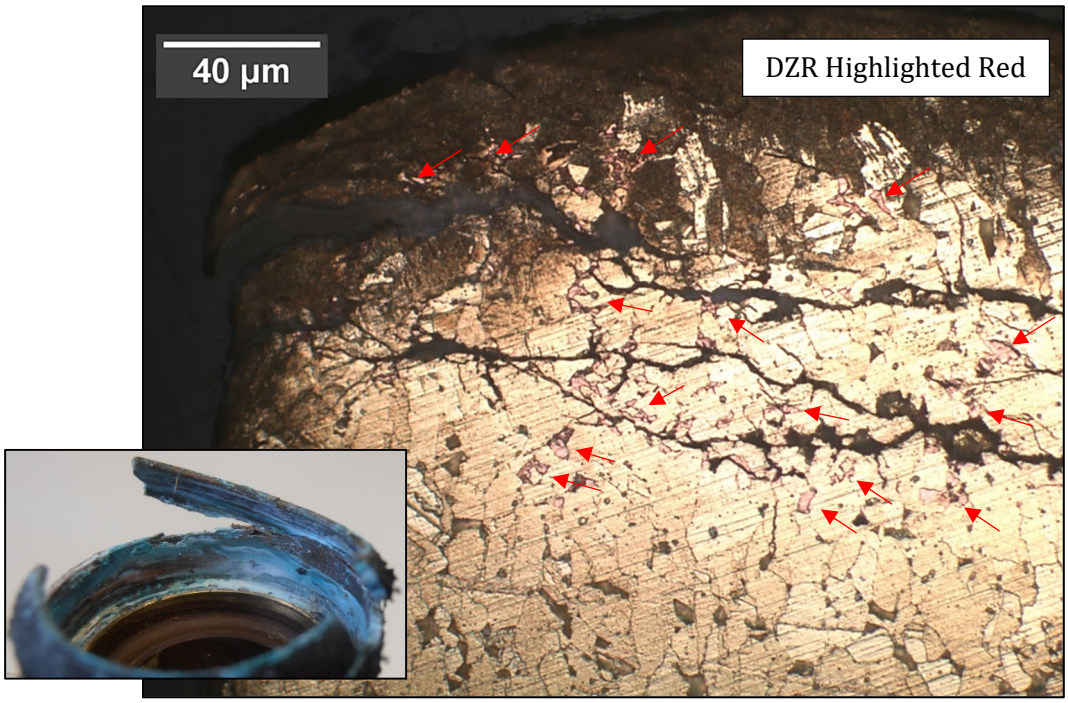


**Figure 2.42: An example of a duplex brass microstructure exhibiting failure via the dual-mechanism of stress corrosion cracking and dezincification. Inset: macroscopic view of the failed fitting surface.**

### 2.6.4 Effect of Alloying Additions on SCC Resistance

Zn has the greatest effect on the stress corrosion cracking resistance of brass with increasing concentrations leading to an increased susceptibility [81, 189-191, 202]. Below 15 wt. % Zn, brass can be considered moderately to highly resistant to SCC (just as it is to dezincification), but above 20 wt. % there is a marked drop in this resistance where they are then considered susceptible to this form of corrosive attack. This is suggested to be due to a change in the dislocation structure as solute addition increases [1]. As Zn additions increase, $\gamma_{SFE}$ decreases leading to an increase in dissociation of perfect dislocations into partial dislocations which results in a greater planarity of slip. This susceptibility only increases marginally as Zn wt. % then increases from 20 wt. % up to 40 wt. % [1]. An example of the gradual deterioration in SCC resistance with increasing Zn wt. % is shown in Fig. 2.43 in which the SCC crack velocity of several Cu-Zn samples in a $Cu(NO_2)_3$ environment increases with increasing Zn content.

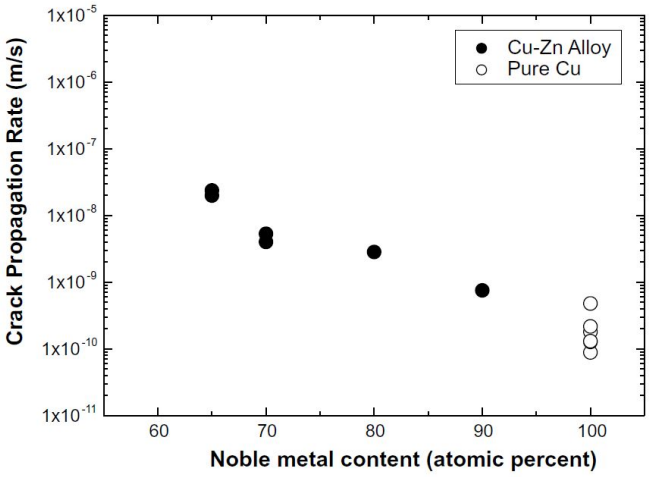


**Figure 2.43: The crack propagation rate of several brass alloys of varying Zn content [214] and pure copper [215] in 1M $Cu(NO_3)_2$. As the Zn content increases, SCC resistance decreases.**

The presence of minor alloying additions in brass have mixed levels of success in affecting the SCC resistance. The degree of their effectiveness can be dependent both upon the level of solute addition, and the severity of other factors such as the type and concentration of the local corrosive media. The most commonly referenced elements in this regard are As, P, and Sn, all of which are typically described as beneficial to the resistance of dezincification (Section 2.4.3). However, these elements are, under some conditions positive [216, 217], and some negative [102, 196, 218, 219], to the resistance of SCC. For example, Luo et al. [217] claims that As is effective as an inhibitor up to 0.1 wt. % for 70Cu-30Zn brasses in Nitrite solutions, however alloying up to concentrations of 0.45 wt. % then causes a deleterious effect (Fig. 2.44). Syrett et al. [216], who studied the effect of As and Sn on 80Cu-20Zn alloys in ammoniacal solutions, claimed that much higher solute levels of these elements (~1.79 and 2.92 wt. % respectively) both produced a positive effect on SCC resistance by affecting the passive film-forming characteristics of the brass. Meanwhile, Torchio [219] and Mazza [102] both claim As and P are detrimental to the SCC resistance of Al-bearing α brass, although admit there is a complicated relationship between de-alloying, IGA, and SCC resistance for brasses containing other alloying elements such as Al and Fe, which in turn makes alloy selection for SCC resistance far more difficult.

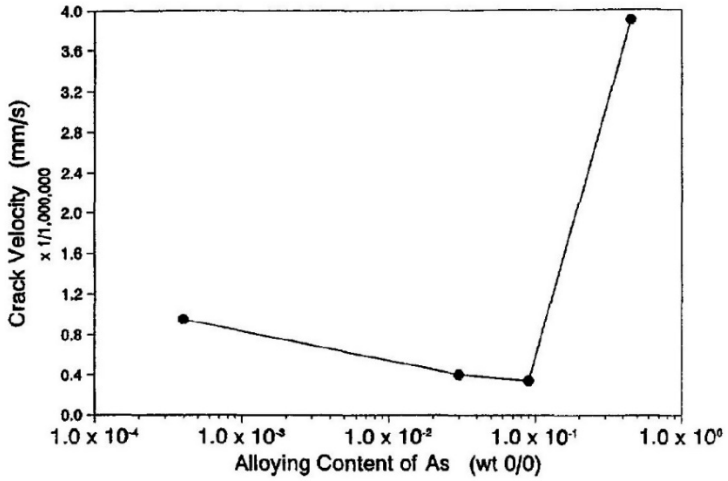


**Figure 2.44: The average crack velocity (CV) of 70Cu-30Zn as a function of As wt. % in an $NaNO_2$ solution at room temperature [217].**

## 2.7 Summary, Gaps in Knowledge and Objectives of Research

### 2.7.1 Summary

Dual-phase Cu-Zn alloys are the most widely used material for the manufacture of potable water components around the world. Many variants of these alloys exist in the market today with additions such as lead, bismuth, tin, aluminium, and silicon. All of them make use of the excellent corrosion resistance and good cold workability of the FCC α phase, and the superior hot workability of the disordered BCC β phase. A duplex brass alloy will typically be required to survive a long manufacturing process of casting, extrusion, drawing, sawing, graphitizing, forging, trimming, heat treatment, shot blasting, machining, and cold working before being exposed to potentially aggressive field conditions. Therefore, the ability to manufacture a high volume of these components with minimal defects, quickly, at a reasonable cost, and with excellent in-service characteristics like mechanical strength and corrosion resistance is of the upmost importance.

Until recently, the duplex brasses used for the production of potable water plumbing fitting and valves were optimised globally to suit high volume production. However, there is now a need for the industry to adjust its position due to the introduction of 'lead-free' legislation originating in California (AB1953, 2006) and progressing to national implementation in the United States in 2014 capping allowable Pb-levels at 0.25 wt. %. In doing so, the traditional Pb-bearing alloys that are simple to produce, particularly during machining, have been replaced with several alternative Pb-free alloys that are comparatively less flexible throughout the manufacturing process. As such, there exists major knowledge gaps in the literature and in industry for several areas of the standard duplex brass processing schedule as companies attempt to optimise the processing conditions for the group of new Pb-free alloys emerging on the market.

The important knowledge gaps that will be addressed in this research include:

1. Identification of the elevated temperature phase stability and transformation characteristics of several Pb-free alloys available in the plumbing market today.
2. Exploration of the hot deformation characteristics of several Pb-free alloys compared with traditional Pb-bearing alloys.
3. The relationship between duplex brass microstructure and dezincification resistance with respect to various heat treatment parameters.
4. Comparison of the machinability of several common Pb-free alloys fabricated via different methods against traditional Pb-bearing alloys under industrial conditions.

## 2.7.2 Gaps in Knowledge and Objectives of Research

### 2.7.2.1 Phase Equilibria and Phase Transformations

The Cu-Zn binary phase diagram is a useful tool for making estimates of the equilibrium phase fractions of FCC α and BCC β at elevated temperatures. These estimations are then critical for fine-tuning the optimal processing parameters used in subsequent duplex brass manufacturing, for example in identifying the equilibrium phase fraction of β at a given temperature and therefore the optimal forging temperatures for a given brass. However, common industrial brasses utilise alloying additions in order to improve various properties such as mechanical, electrochemical, and machining characteristics. These additions will have an impact on the phase equilibria of the alloy, not only affecting the equilibrium phase fraction of α and β, but under some circumstances also stabilising new phases such as κ, γ, and ε. The understanding of the effects of these alloying additions has typically been empirical in nature (for example by using the Guillet-Portevin Zn equivalence system [27]) and has not been well understood for the new grades of Pb-free brass available in the industry, and therefore it is the objective of Chapter 4 to study the phase equilibria of three key groups of brass:

1. Cu-Zn-Pb-Sn (Traditional Pb-bearing brass)
2. Cu-Zn-Bi-Sn (Bi-bearing brass)
3. Cu-Zn-Si (Si-bearing brass)

The use of computational thermodynamics through the CALPHAD approach has been a significant advancement in the development of our understanding of phase equilibria and will be used in the first part of this study. However, we cannot be sure of the accuracy of the databases available in the literature so there is a need to verify this data using practical experiments. High intensity *in-situ* neutron diffraction and metallographic estimations of phase fraction from thermally treated and quenched brasses in the above three groups will be used to test the ternary and quaternary calculations made using the CALPHAD approach.

As the introduction of Bi-bearing and Si-bearing brasses has gradually occurred in the potable water market, there is also a need to rediscover the metallurgy of these alloy systems under non-equilibrium conditions and therefore the expected behaviour of these alloys in later stages of processing such as machining or cold working. It is therefore the objective in the second part of Chapter 4 to more closely examine the non-equilibrium phase transformation behaviour of these two groups of Pb-free alloys (Bi, Si) with an emphasis on an in-depth characterisation of Si-bearing brass.

### 2.7.2.2 Elevated Temperature Plasticity

Traditional leaded duplex brasses have been consistently used throughout the 20th and 21st century for forging plumbing components. The exceptional workability of these alloys at elevated temperatures, which is due to the presence of the disordered BCC β phase, is well known. However, throughout many regions of the world, the ability to take advantage of this mechanism and consciously manipulate the brass microstructure for optimal forging outcomes has been lost in favour of a more empirical approach. This lost knowledge has become particularly clear with the recent implementation of 'lead-free' laws in different parts of the world. This is generally why forging is widely considered a 'black art' in comparison to other more precise processes such as machining which are completed at room temperature.

Until recently, alloy selection for forging has not been an issue, there have been a small group of leaded alloys that could simultaneously cover all of the industry requirements for contact with potable water, whilst satisfying high manufacturing efficiencies throughout the typical processing schedule (Fig. 1.3). This alloy selection remained consistent after corrosion standards came into place, such as dezincification resistance and stress corrosion cracking requirements. Two or three leaded duplex brasses with small alloying additions could be used to cover all products, and thus the empirical approach to forging had been retained. With the implementation of lead-free standards around the world, however, this is now a more complicated issue. Forging has become far more critical and now there are a significant number of 'lead-free' alloys entering the market, each with a unique composition which are expected to impact on the forgeability of the alloy, and in turn the optimal parameters and economic viability of high-volume production. Therefore, a resurgence in the knowledge behind the mechanisms of deformation during forging and the microstructural parameters required for optimal forging practices is occurring in the plumbing industry.

Although some work has been dedicated to understanding the forging of traditional leaded brasses and some binary Cu-Zn alloys, very little work is available in the literature which is focussed on the more modern lead-free brasses now available in today's market. In addition, there has been no work conducted to determine the relative effects of fabrication mode (continuous casting or extruded) on the forgeability of these brasses. It is the objective of Chapter 5 to characterise the forgeability, or elevated temperature plasticity, of a group of the more popular modern lead-free brasses, fabricated in different ways, through the use of uniaxial hot compression techniques using a range of temperatures and displacement-rates. Comparisons are drawn to the traditional leaded alloys that have been historically used in the plumbing industry.

### 2.7.2.3 Microstructure-Dezincification Relationships

Although duplex brass has excellent corrosion resistance in most potable water environments, there are specific cases where it can be susceptible to dezincification. As a result, extra steps may be required to improve the dezincification resistance of the alloy. There are two dominant approaches for improving the dezincification resistance of duplex brasses. The first involves the use of dezincification inhibitors in very low amounts (~0.10 wt. %) such as arsenic (As), phosphorus (P), or antimony (Sb). As long as they remain within solution, these elements have been found to be effective in protecting the α phase of duplex brass, but not the β' phase. The second approach involves the use of an intermediate heat treatment after hot working (~400-550$^{o}$C for 1-8 hours) to reduce the volume fraction of the susceptible β' phase, thereby transforming it into the more dezincification resistant α phase.

The above common approaches consider chemistry (inhibitors) and the volume fraction of β' as the relevant microstructural parameter. However, there are many more microstructural parameters that one may anticipate could significantly influence the dezincification behaviour: β' phase size, α grain size, interconnectivity of the β', anisotropy of the microstructure (due to different fabrication methods), etc. These microstructural features have not been explored.

The introduction of national Pb-free legislation in the United States in 2014 has led worldwide to the development of a large range of new brass compositions manufactured via different fabrication methods (e.g. continuous casting versus extrusion) and using a range a processing parameters. These new alloys and different fabrication modes give rise to significant variations in microstructure. The objective of Chapter 6 is to develop a quantitative understanding of the effect of a) β' phase fraction, b) α grain size, and c) β' interconnectivity, on the dezincification behaviour of two common low-lead duplex brasses used for the manufacture of potable water fittings.

### 2.7.2.4 Machinability of Duplex Brasses

Traditionally, lead has been utilised for its ability to improve the machinability of duplex brasses. The introduction of 'lead-free' legislation in the United States in 2014, however, has led to the wide-spread search for alternatives which can regain a level of the machinability lost due to the removal of lead, but without any other associated drawbacks to the material, be it service properties such as corrosion resistance or processing characteristics in areas such as forging or cold workability. Amongst the most notable alternatives are bismuth-bearing brasses, silicon-bearing brasses, and the deliberate formation of small intermetallics. Each of these possible solutions have been raised and researched to

various degrees using a variety of mechanical trials and turning trials, however, there remains a significant knowledge gap in three key ways:

1. No attention has been paid to the duplex brass fabrication mode, be it via extrusion or continuous casting.
2. Very little work has been completed on the effect of microstructure on machinability, namely the effects of grain size, phase fraction or Pb/Bi particle size and distribution.
3. Most prior research has been devoted to turning trials and various other mechanical trials (tensile testing, hardness testing) where in fact drilling operations are the greatest source of material removal during high volume brass machining and therefore most representative of a brass' measure of machinability.

Each of these factors is expected to have a significant impact on how we assess the machinability of lead-free alloys. It is therefore the objective of Chapter 7 to use a drilling trial to evaluate the machinability of several common industrial 'lead-free' duplex brasses compared against traditional Pb-bearing brasses which have been fabricated via both continuous casting and extrusion. The outputs of this trial, which include evaluation of feed forces, drilling torque, surface roughness, and swarf morphology, will be correlated with several key microstructural characteristics including phase fraction and Pb/Bi particle size and distribution to give us a more accurate insight into the machinability of these various duplex brasses.

# 3 Experimental Method

This chapter summarises the various experimental procedures and microstructural characterisation methods used in this thesis. In Chapter 4, a study of the effects of alloying additions on phase equilibria and phase transformations is undertaken and this serves as the platform from which the subsequent mechanical and electrochemical chapters are designed. In Chapter 5, the elevated temperature plasticity of a selection of industrially-relevant brasses is studied using uniaxial hot compression techniques. In Chapter 6, dezincification resistance is considered for a range of factors including fabrication method, extrusion direction, grain size, phase fraction, interconnectivity, and cooling rate. In Chapter 7, a study is conducted on the machinability of several industrially-relevant Pb-bearing and Pb-free brasses with a series of drilling trials, which is the machining operation which typically removes the most material in an industrial setting. Here we introduce the thermal treatments, mechanical testing, electrochemical testing, and characterisation techniques employed for the above experiments.

## 3.1 Thermal Treatments

Numerous thermal treatments were conducted in this thesis in order to generate a variety of microstructural characteristics relating to grain size, phase fraction, and phase interconnectivity. These heat treatments were all conducted in a temperature-controlled muffle furnace with an additional thermocouple for calibration. Sample surface oxidation (of Zn) could occur at elevated temperatures but did not penetrate into the bulk of the material and was therefore of no concern to the various experiments undertaken. Cooling rates, e.g. air-cooling, quenching, were each selected based on the requirements of the experiment.

## 3.2 Mechanical Testing

### 3.2.1 Vickers Hardness

Vickers hardness measurements were used to monitor the change in hardness with thermal treatment throughout both the machining trials (Chapter 7). In each case, the samples were cold mounted in epoxy resin and mechanically ground to a surface finish by 2400-grit SiC paper. Vickers testing was carried out using a Struers Duramin A300 microhardness tester with a 2kg load and a loading time of

5 seconds. A series of 6 sample measurements were completed for each alloy condition on a cross section in the transverse casting/extrusion direction to ensure a complete average was attained. The 6 indentations for each condition were averaged to form an arithmetic mean and a 95% confidence interval (CI) determined via the standard equation for student t-distribution as follows:

$$\bar{x} \pm (\acute{z} \times (\frac{\sigma}{\sqrt{n}})) \quad (3.1)$$

$\bar{x}$ is the sample mean, $\acute{z}$ is 1.96 for a 95% confidence level, σ is the standard deviation, and n is the sample size.

### 3.2.2 Tensile Testing

Tensile testing was used to measure the mechanical properties of the as-received cylindrical brass rods (10 alloys total) used for the machining trials (Chapter 7). Two samples were produced for each alloy according to the dimensions shown in Fig. 3.1 and tested on an Instron 4505 testing machine at a crosshead speed of 0.04 mm/s using a 100kN load cell, and strain recorded using a 25mm extensometer. The 0.2% proof stress, elongation % to break, and ultimate tensile strength (UTS) were measured for each sample.

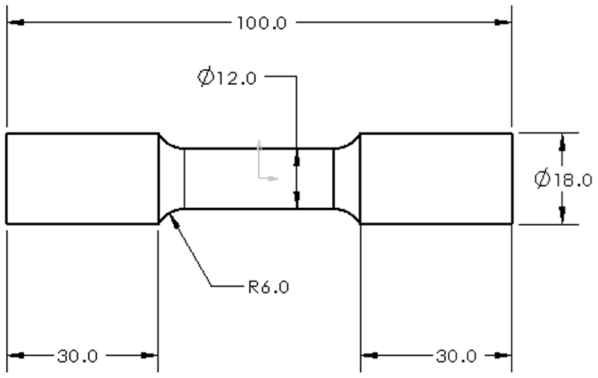


**Figure 3.1: Tensile specimen dimensions. Central gauge length of 30 mm used with a 25mm extensometer.**

### 3.2.3 Hot Compression

Uniaxial hot compression was used to assess the elevated temperature plasticity of several alloys in the elevated temperature plasticity study (Chapter 5). Samples of a range of alloys were machined into cylinders of 15 mm diameter and 25 mm length and tested under compression on a 150kN Instron Model 5984 (Fig. 3.2). A water-cooling inlet and a protective thermal plate are used to prevent overheating of the load cell, whilst two columns, the upper of which is attached to the load cell, is controlled by the Instron unit. Both columns incorporate a water-cooling inlet/outlet.

A large cylindrical furnace (digital temperature controlled) is used to encase the dies/platens and sample during testing. The cylindrical screwed die platens are made from an Inconel superalloy. This is ideal for withstanding high temperatures throughout testing. Two additional metal wire K-type thermocouples were used to monitor temperatures in the rig, the first reading ambient temperature adjacent to the sample, the other attached to the load cell to ensure the unit doesn't overheat. Finally, a ceramic block was used to place samples post-compression for cooling.

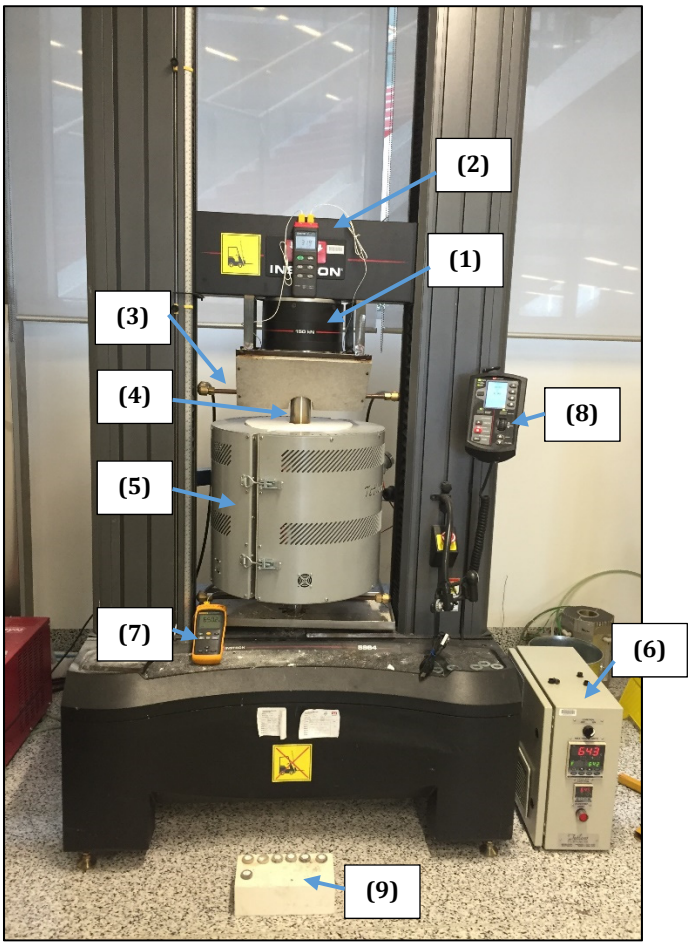


**Figure 3.2: Instron 5984 setup used for hot compression tests. (1) Load cell, (2) load cell temperature thermocouple, (3) water cooling inlet and thermal protection plate, (4) upper cooling column, (5) furnace (containing sample and two screw-in cylindrical die platens), (6) temperature controller, (7) sample temperature thermocouple, (8) Instron controller, (9) ceramic brick for sample cooling.**

Prior to hot compression, the cylindrical sample ends are tipped with a Boron Nitride coating for lubrication in order to minimise friction between the brass surfaces and platens, as well as prevent sample bonding to the platens during compression. Soak times of 10 minutes were used for each sample in order to provide adequate stabilisation time but without unnecessary time in which any α grains present may grow to excessive size. Air-cooling was used post-compression rather than

quenching to preserve the brass surface for visual assessment of any fracture formation. Examples of samples prior-to and post-compression are shown in Fig. 3.3.

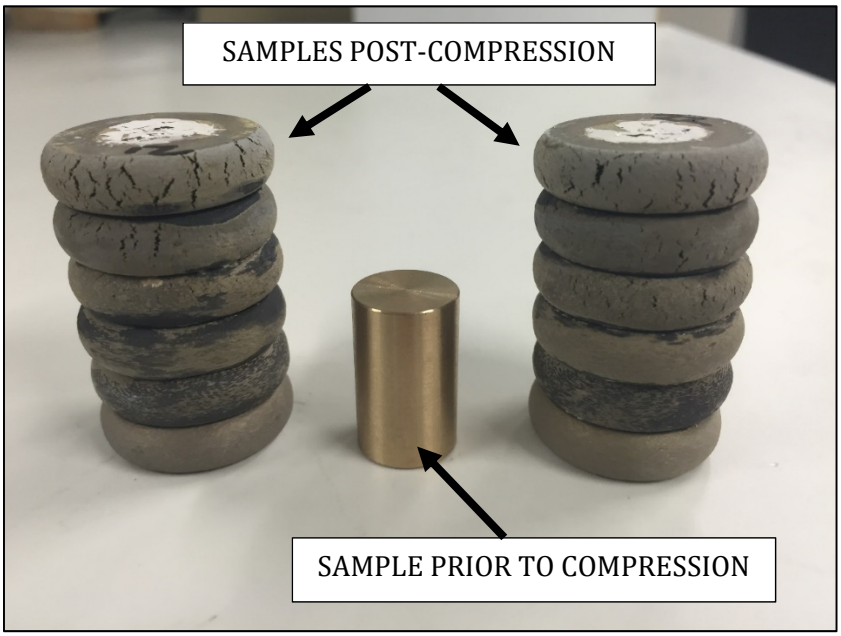


**Figure 3.3: Duplex brass cylindrical samples both before and after the hot compression process.**

For each of the alloys tested in the hot compression study, samples were compressed 72% from 25mm to 7mm. Samples were compressed over a range of temperatures in 50$^{o}$C increments from 550$^{o}$C – 800$^{o}$C and utilising constant displacement rates of 300, 540, and 720 mm/min. The equivalent strain-rate ranges for each displacement rate were subsequently 0.20-0.71, 0.36-1.29, and 0.48-1.71s$^{-1}$. A total of 525 samples were tested and data converted to true σ-ε for analysis.

### 3.2.4 Machining Experiments

There are a number of different machining operations that may be carried out on duplex brasses in order to produce a plumbing component. Drilling is often considered to be the most demanding operation as it typically removes the most material from the workpiece. In this thesis, the drilling operation for each of the duplex brass samples was conducted on a 'Spinner U-620' CNC machine in the *Deakin University Waurn Ponds School of Engineering* using a set of 10mm diameter, twin-flute solid carbide drills sourced from ISCAR Australia Pty. Ltd (Model SCD 100-035-100 AP3N) (Fig 3.4). Each alloy was allocated its own drill to avoid any issues associated with gradual tool wear. Drills were each inspected post-machining with no significant wear detected from the trials undertaken.

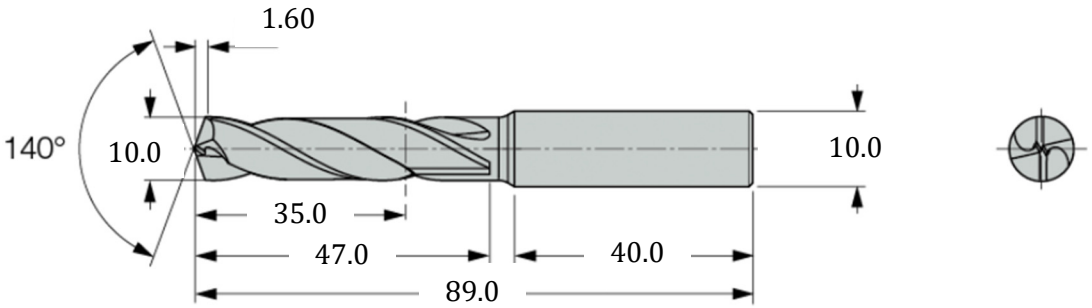


**Figure 3.4: Twin-flute solid carbide drill dimensions used for machining experiments.**

Installed on the 'Spinner U-620' machining centre (Fig. 3.5) was a Kistler multi-component drilling dynamometer (Model 9257B) used for measuring individual sample feed forces (N) and drilling torque (Nm). Readings were data-logged on a desktop computer using the associated Kistler 'DynoWare' cutting force software. Each sample underwent two drilling operations (one on each end of the sample) to test reproducibility. Each operation was completed using a cutting speed ($V_c$) of 110 m/min, a feed rate ($F_n$) of 0.22 mm/rev, and a depth of cut of 30mm. These parameters were chosen with typical industrial machining parameters for duplex brass in mind. For each drilling operation a general-purpose mineral oil-based cutting fluid emulsion with a dilution concentration of 20:1 was supplied at a flow rate of 9.9 L/min. Upon completion of each sample set, a swarf sample was retrieved for visual examination in order to determine their relative morphologies.

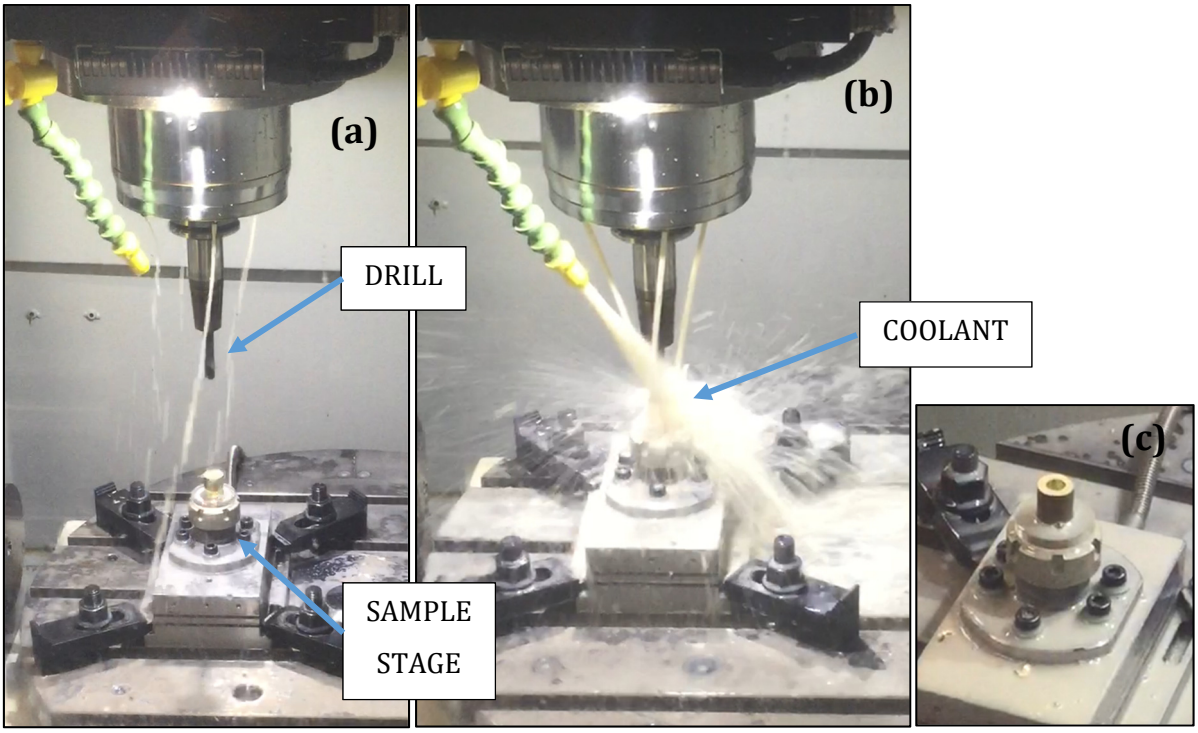


**Figure 3.5: Drilling operation on the 'Spinner U-620' CNC machine; (a) Prior to cycle commencement, (b) during drilling cycle, and (c) the sample post-machining.**

Upon completion of the drilling operations, the samples were evaluated for their surface roughness ($R_a$) along a 7.5mm length of the inner diameter generated during drilling. This was completed using a stylus measurement device (Model Talysurf Intra Series 50). The individual samples were then sectioned in the transverse direction (perpendicular to the drilling direction) and metallography used to determine the microstructural characteristics that may affect machinability (Section 3.4.1). The samples were analysed using ImageJ software in order to determine the average α grain sizes using the lineal intercept method [220] and the phase fractions of α, β', and any other present phases or intermetallics (verified using the statistical grid method [221]). Backscattered-electron imaging (Section 3.4.4) was used to analyse the Pb and Bi particle size and distribution in each alloy.

## 3.3 Electrochemical Testing

### 3.3.1 Dezincification Testing

Samples for dezincification testing and optical examination were cold mounted in clear two-part epoxy resin. A minimum spacing of 15mm was used to separate the sample from the stage (Fig 3.6) to meet the standard sample preparation requirements for the dezincification testing that would follow microstructural analysis. The samples were then ground to a flat surface finish with P4000 SiC paper and subsequently polished using a 1-micron diamond solution. Each sample was chemically etched using a solution of acidic ferric chloride to allow for optical analysis. The average α grain size was measured using the lineal intercept method [220], whilst the β' phase fraction was measured using the image analysis tool in ImageJ software and subsequently verified using the statistical grid method outlined in ASTM E562-11 [221].

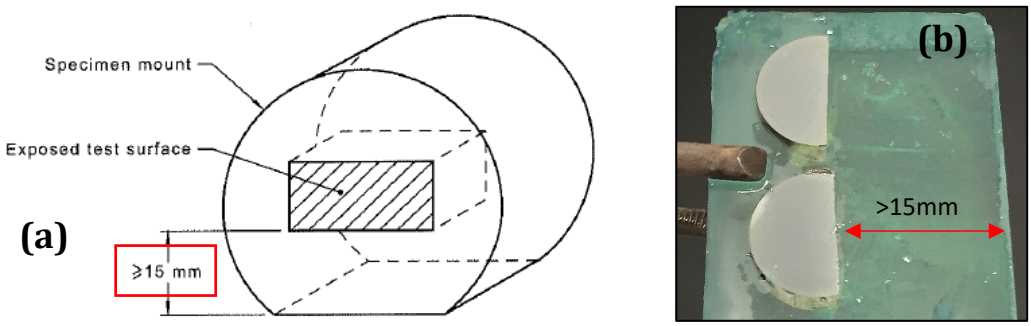


**Figure 3.6: (a) Brass sample mounting schematic and (b) examples of samples that have undergone dezincification testing according to ISO6509-1 (2014).**

After microstructural analysis, each sample was re-ground to a flat surface using P2400 SiC paper to remove any of the surface layer affected by the etching process. The samples were subsequently tested for dezincification resistance in accordance with the standard test method in ISO6509-1 (2014)

[222]. In this test, each sample is submerged (face to the side, Fig. 3.7a) in a covered solution of 12.7 g/L copper (II) chloride in demineralised water at 75±5°C for a period of 24 hours (±30 minutes) like that shown in Fig. 3.7b. Temperature stability is maintained by submerging the test chamber in an oil bath which is heated via a hot plate and measured using two temperature probes, one in the oil, the other which is intermittently placed in the copper (II) chloride solution.

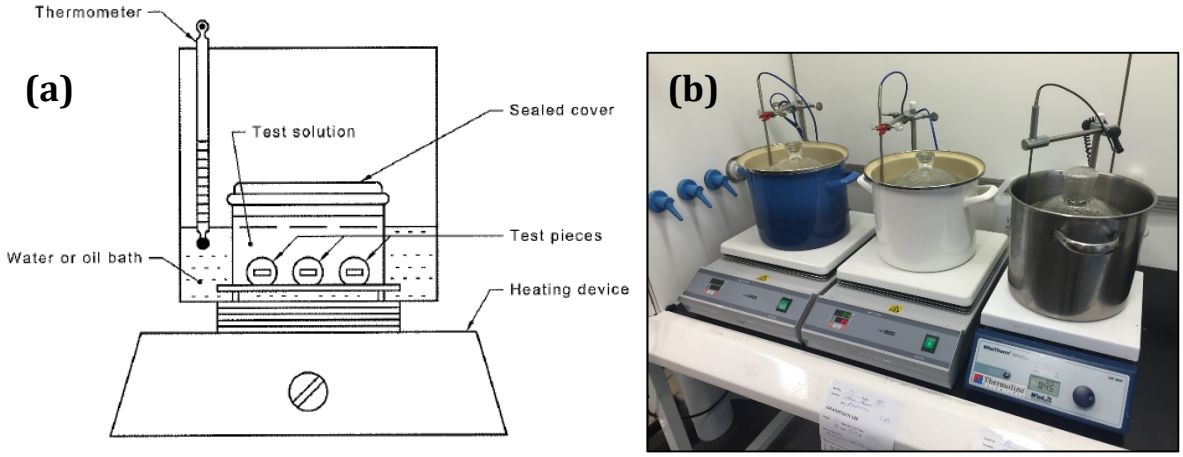


**Figure 3.7: Dezincification test rig setup (a) schematic and (b) the 3 laboratory test rigs used for testing in this study.**

After a period of 24 hours, the test samples are removed, washed in water, rinsed using ethanol, sectioned along an appropriate axis (longitudinal and/or transverse to grain direction in extruded or casting direction), re-mounted in clear two-part epoxy resin, and prepared for optical analysis to determine the average and maximum depth of dezincification. In each case, a single maximum depth of dezincification (in microns) is measured along the length of the test surface, and then an average is recorded across 25 evenly spaced measurements to provide additional confidence in the data (Figs. 3.8 and 3.9). This is taken directly from the Australian equivalent testing protocols in AS2345-06 [80]. In addition, for all of the extruded samples and hot compressed samples, testing was conducted, and results gathered in both the longitudinal and transverse directions in order to account for any anisotropy and variation in phase interconnectivity.

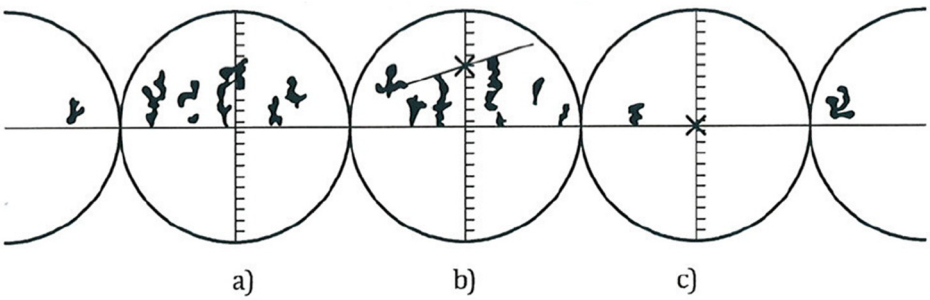


**Figure 3.8: Method for recording dezincification depths according to ISO6509-1 (2014). Each of points a), b), and c) represent an individual measurement of a dezincified samples under magnification.**

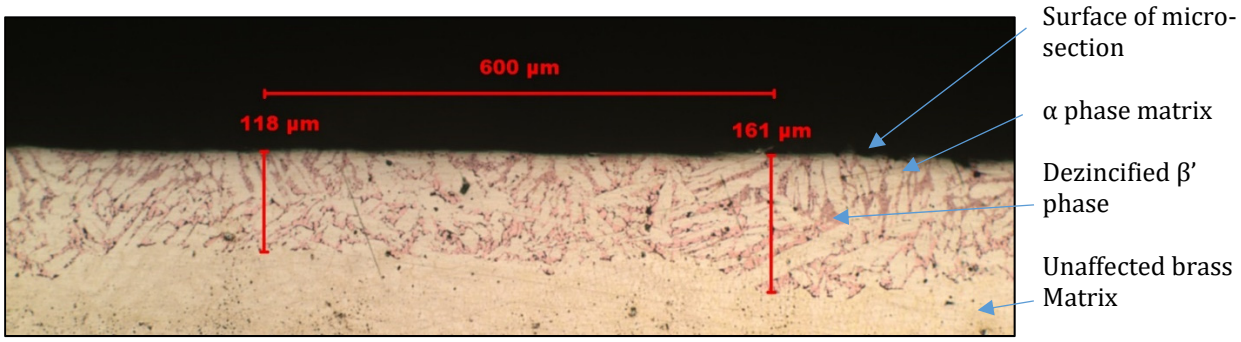


**Figure 3.9: Example of real dezincification depth measurements according to ISO6509-1 (2014).**

## 3.4 Microstructural Characterisation

### 3.4.1 Metallography

Standard metallographic preparation techniques were used to generate samples for optical microscopy in the phase equilibria (Chapter 4), dezincification behaviour (Chapter 6), and machinability (Chapter 7) sections of this work. Samples were mounted in two-part clear epoxy resin, followed by grinding to a fine surface finish with P4000-grit SiC paper. This was followed by polishing to a mirror-finish with a 1µm diamond polishing solution followed by etching with an acidic ferric chloride solution for a period of ~2-5 seconds.

At various stages throughout this thesis, there is the need to measure phase fraction and/or average grain size from metallographic images. An example of the methodology used to execute these two tasks is outlined as follows:

- **Phase Fraction:** The primary method chosen to identify the % volume fraction of a given phase in a microstructure is the statistical grid method outlined in ASTM E562-11 [221]. An etched metallographic image is loaded using ImageJ software and is superimposed with a grid of either points or hollow circles (whichever yields a more accurate reading). An example of this is shown in Fig. 3.10a. The number of test points on the grid that fall within the phase of

interest are counted and divided by the total number of test points to derive a phase %. The grid size will typically range from 16 to 100 points depending on the visually indicative % of phase fraction. This indication is determined where possible by using the colour threshold and particle analysis function built into ImageJ software (Fig. 3.10b). The lower the anticipated % of the constituent of interest, the greater the number of grid points to verify accuracy. The example shown in Fig. 3.10a would require at least 16 points (20 have been used). In each analysis throughout the thesis, at least two images are used to derive an average phase fraction.

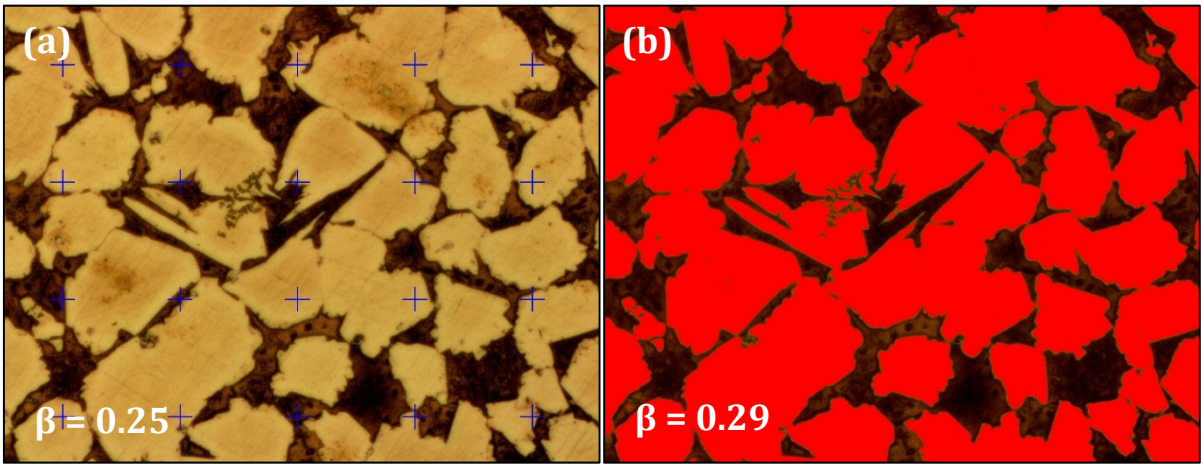


**Figure 3.10: (a) Superimposed grid (blue points) used to determine the phase fraction of BCC β' and (b) the colour threshold and particle analysis indication % used to determine the number of grid points required.**

- **Grain Size:** The primary method chosen to identify the average (typically FCC α) grain size of a duplex brass metallographic image is the lineal intercept method as outlined in ASTM E112-13 (Section 17.5) [220]. Assuming we have more than 1 phase present in the microstructure, this method involves first determining the matrix phase fraction. From here, a standard linear line sufficient to generate >50 intercepts is drawn on the image and the number of matrix grains and boundary intercepts counted. The grain size is then determined by multiplying the matrix phase fraction (%) by the length of the intercept line (µm), then divided by the number of intercepted matrix grains. In Chapter 6, the acicular nature on some of the grains requires that both a length and aspect ratio be determined of the matrix phase. Under these circumstances, a grid is superimposed onto the metallographic image of interest and the nearest neighbour to each point is individually measured until >20 grains (where possible) are recorded. Challenges can arise at times when grain boundaries are faint (Fig. 3.11a) and it is attempted under these circumstances to then '*over-etch*' (Fig. 3.11b) the same surface to further resolve the present grain boundaries. Under some circumstances, increased efforts to

discern the average grain size from microstructures can still not be adequately achieved, in these instances (for example in Chapter 7 on long intermediate heat treatments on continuous cast alloys) these measures are disregarded from the analysis.

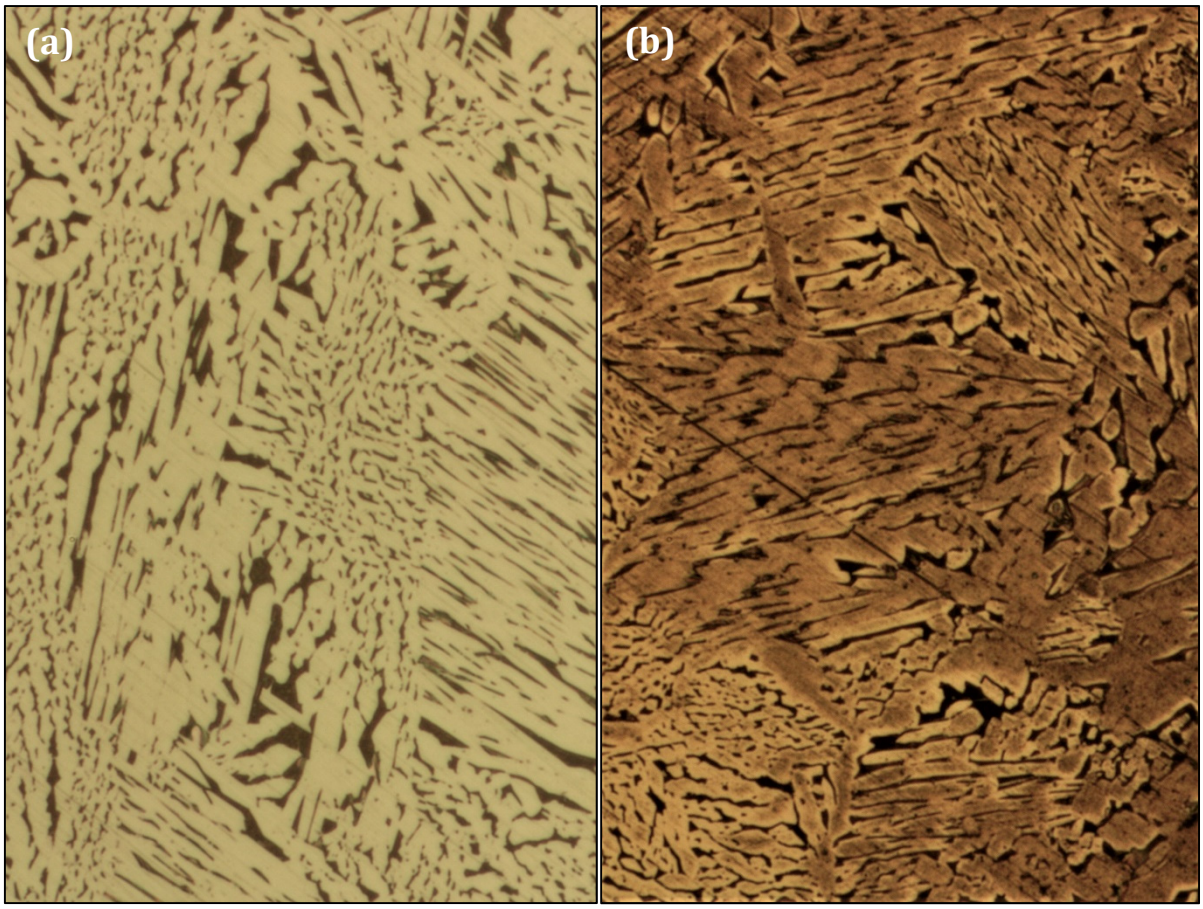


**Figure 3.11: (a) Typical continuously cast and heat treated α microstructures can be difficult to measure, and (b) example of over-etching to assist determine grain boundary locations.**

### 3.4.2 X-Ray Diffraction (XRD)

X-ray diffraction (XRD) was used for the characterisation of samples in the phase equilibria section of this work (Chapter 4). Testing was completed on two devices (due to availability), the first a Bruker D8 Advance diffractometer with a Cu Kα radiation source (λ = 1.5405Å) and Lynxeye position sensitive detector (Fig. 3.12). Scans were completed on this device with a 2θ range of 20 – 100$^{o}$, a step size of 0.02, and a time per step of 2 seconds. *In-situ* scans were also attempted on this device with the use of a HTK1200N furnace stage under a range of atmospheres (nitrogen, argon, Vacuum), however even a small presence of oxygen would influence the results and form ZnO peaks, therefore these results have been disregarded for the purposes of this study.

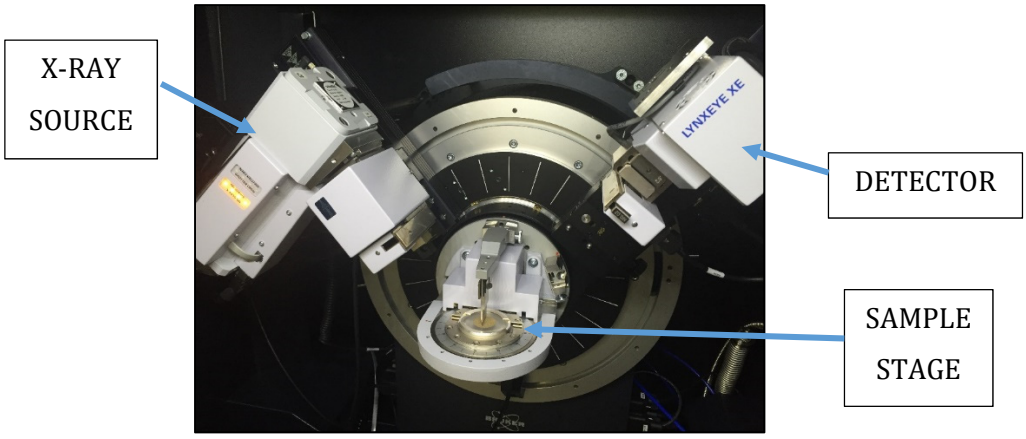


**Figure 3.12: Bruker D8 Advance - XRD powder sample setup.**

The second device used for XRD characterisation, specifically of the CuZnSi alloy samples in Chapter 4 (Section 4.2.3.5), was a Bruker D8 Discover diffractometer with a Co Kα radiation source (λ = 1.789Å). Scans were completed on this device with a 2θ range of 30-130°, a step size of 0.03 and a time per step of 2 seconds.

Rietveld refinement was completed for each of the sample scans using the software package TOPAS (version 4.2, Bruker AXS GmbH). Instrument parameters were refined from the NIST Standard Reference Material $LaB_6$. The identified phases in the various refinements include α, β', κ, Pb, Bi, η and ε with their respective space groups and lattice parameters shown in Table 3.1.

**Table 3.1: Duplex brass phases, space groups and lattice parameters [1, 223-226].**

| **Phase** | α | β' | κ | η | ε | Pb | Bi |
|---|---|---|---|---|---|---|---|
| **Space Group** | Fm-3m | Pm-3m | $P6_3/mmc$ | R-3 | I-43d | Fm-3m | C12/m1 |
| **Lattice Parameter (nm)** | a = 0.3696 | a = 0.2945 | a = 0.2561<br>c = 0.4184 | a = 0.6999<br>c = 0.7315 | a = 0.9718 | a = 0.4951 | a = 0.6673<br>b = 0.6111<br>c = 0.3300 |

Phase peak identification in each alloy was determined from the XRD spectra using the information in Table 3.1 and the Bragg equation [227]:

$$n\lambda = 2\,dsin\,\theta \qquad (3.2a)$$

$$d = \frac{a}{\sqrt{h^2 + k^2 + l^2}} \qquad (3.2b)$$

λ is the source wavelength, n is a positive integer, d is the interplane spacing, θ is the diffraction angle, a is the lattice parameter and h, k, l are miller indices.

### 3.4.3 High Intensity *In-Situ* Neutron Diffraction

Neutron diffraction was used for phase quantification of duplex brass samples under elevated temperature conditions (Chapter 4). The *in-situ* neutron diffraction was performed at the high intensity diffractometer 'Wombat' [228] at Australia's Nuclear Science and Technology Organisation (ANSTO). 5mm diameter by 50mm length cylindrical samples were placed within a 9mm diameter Vanadium tube and heated using a vacuum furnace with Nb resistance heating. A 2θ range of 22-139$^{o}$ was used with a refined monochromatic wavelength of λ = 1.47066Å. Samples were hung from a top-loading sample rod containing a C-type thermocouple directly above the sample. The samples were heated from room temperature to 835$^{o}$C at ~84$^{o}$C/minute, after which they were gradually cooled to 300$^{o}$C at ~4$^{o}$C/minute. Acquisition time for each scan was ~30 seconds and took place during both the heating and cooling stages. A temperature calibration experiment was carried out using an Fe-0.77C (wt. %) binary steel and by comparing with TTT diagrams from literature and dilatometry experiments.

Rietveld refinement was carried out on the data for quantitative analysis of α and β phase fraction using the TOPAS software package (version 4.2, Bruker AXS GmbH). The wavelength, zero error, and instrument parameters were refined from the NIST standard reference materials $LaB_6$, $Al_2O_3$ and Si. The macro used to simulate the neutron diffraction pattern in TOPAS is included in Appendix C.

### 3.4.4 Scanning Electron Microscopy (SEM) with Energy-Dispersive X-Ray Spectroscopy (EDS) and Backscattered-Electron (BSE) Imaging

An in-depth characterisation of Bi-bearing and Si-bearing brass was performed using scanning electron microscopy (SEM) and energy-dispersive x-ray spectroscopy (EDS) at the Monash Centre of Electron Microscopy (MCEM). Samples were prepared using standard metallographic procedures (Section 3.4.1) and mounted to an SEM sample stage with carbon tape for analysis with a JEOL 7001F field-emission gun SEM. Sample magnifications of 100 to 2,500 were used with standard operating conditions of a 15kV accelerating voltage and a 10mm working distance. EDS data was collected using both point spectra and map profiles and then analysed used Oxford Instruments AZtec software.

Following Section 3.2.4 on machinability of brasses, it can be difficult to determine Pb and Bi particle size and distribution using metallography alone, therefore for the samples analysed in this work it was decided to complete backscattered-electron imaging (BSE) on each of the alloys in both the 'as-received' and heat-treated states. The samples were prepared with the same surface finish as for metallography and BSE completed in cooperation with a South Korean manufacturing partner on a JEOL 7001F FEG SEM. In each case, an accelerating voltage of 20kV was used with a working distance of 10mm, and to a magnification of 500x in order to better analyse the Pb and Bi particle size and distribution.

# 4 Phase Equilibria

The thermo-mechanical processing of the new Pb-free brasses appearing on the market requires both an understanding of the temperature dependence of phase stability (for example, for choosing optimal forging temperatures), but also an understanding of the conditions under which new phases may form (for example, in the more recently developed Si-bearing brass grades).

CALPHAD evaluations of several ternary and quaternary Cu-Zn-X-Y systems are now available in the literature but their applicability to the new multicomponent Pb-free grades has not been tested. This must be completed and is the topic of Chapter 4. Although this Chapter is a short one, verification of the phase equilibria as a function of temperature is a critical ingredient for the subsequent Chapters where the effect of microstructure on elevated temperature plasticity, dezincification resistance and machinability are studied in detail.

## 4.1 Alloy Selection

Three different families of duplex brasses are considered in this Chapter; (1) Traditional Pb-bearing brass, (2) Bi-bearing brass, and (3) Si-bearing brass. These are chosen to study phase equilibria and phase transformations. In the first instance, x-ray diffraction (XRD) is used for qualitative phase identification and subsequent quantitative evaluation of phase fractions at room temperature. This was completed using Rietveld refinement for the three alloys listed in Table 4.1 (chemical composition measured by OES). All samples were initially tested in the as-received condition and as a result of the more complex microstructure, the Si-bearing samples were also tested in a range of heat-treated conditions in order to better characterise the phase transformations occurring in this alloy (Section 4.2.3.5). Each as-received sample was prepared into a powder using a filing tool with a 100µm sieve to maintain consistent particle size and to ensure good particle statistics for the quantitative Rietveld refinement.

**Table 4.1: Chemical composition (wt. %) of the investigated workpiece materials for microstructural characterisation.**

| Alloy | | Cu | Zn | Pb | Bi | Si | Sn | As | P |
|---|---|---|---|---|---|---|---|---|---|
| **CuZn36.5Pb2.3Sn** | **Pb-bearing** | 61.2 | 36.5 | 2.23 | 0.07 | <0.01 | 0.23 | 0.06 | <0.01 |
| **CuZn37.6Bi0.8Sn** | **Bi-bearing (A)** | 60.8 | 37.6 | 0.23 | 0.84 | <0.01 | 0.30 | 0.08 | 0.09 |
| **CuZn22Si3** | **Si-bearing** | 74.8 | 22.0 | 0.05 | <0.01 | 2.97 | <0.01 | <0.01 | 0.08 |

High intensity *in-situ* neutron diffraction was used to quantify the phase fractions of α and β in the alloys in Table 4.2 at elevated temperatures. There are several advantages to using this method over *in-situ* XRD, especially the ability to penetrate further into the bulk material where XRD will only penetrate close to the surface. This is very important as when this method is used under vacuum at elevated temperature it removes any concern over the formation of ZnO on the surface of the material. To prepare for high intensity *in-situ* neutron diffraction, samples were CNC machined to cylindrical dimensions of 5 mm diameter x 50 mm length. No thermal treatments were completed prior to the Neutron diffraction experiments.

**Table 4.2: Chemical composition (wt. %) of the investigated workpiece materials for Neutron diffraction experiments.**

| Alloy | | Cu | Zn | Pb | Bi | Sn |
|---|---|---|---|---|---|---|
| **CuZn36.5Pb2.3Sn** | **Pb-bearing** | Bal. | 36.5 | 2.23 | 0.07 | 0.23 |
| **CuZn36.9Bi0.8Sn** | **Bi-bearing (B)** | Bal. | 36.9 | 0.18 | 0.65 | 0.32 |

Overall, with the Pb-bearing alloy listed in Table 4.1 and 4.2 being common, a total of 4 alloys have been studied in this Chapter with the characterisation methods listed in Table 4.3. CuZn36.5Pb2.3Sn and CuZn36.9Bi0.8Sn were both fabricated via continuous casting, whilst CuZn37.6Bi0.8Sn and CuZn22Si3 were fabricated via extrusion.

**Table 4.3: Phase equilibria assessment methods undertaken for each alloy.**

| Alloy | | CALPHAD | XRD | Neutron Diffraction | Metallographic Assessment |
|---|---|---|---|---|---|
| **CuZn36.5Pb2.3Sn** | **Pb-bearing** | X | X | X | X |
| **CuZn37.6Bi0.8Sn** | **Bi-bearing (A)** | X | X | | X |
| **CuZn36.9Bi0.8Sn** | **Bi-bearing (B)** | X | | X | X |
| **CuZn22Si3** | **Si-bearing** | X | X | | X |

## 4.2 Phase Equilibria

### 4.2.1 CALPHAD Calculations

Recent developments in the use of computational thermodynamics to describe the phase equilibria of alloy systems has allowed us to generate multiple Cu-based databases using the Calphad (Calculation of Phase Diagrams) approach. Three different thermodynamic assessments have been used across the three different alloy families described in Section 4.1. Both the Pb- and Bi-brasses contain enough Sn that it needs to be considered in the assessment. The thermodynamic assessments by Miettinen [12, 28, 29] and Wang et al. [30] were used in each case (Appendix B).

In Fig. 4.1 we show the calculated isopleth generated for the alloy CuZnPb2.3Sn0.23 (Table 4.1) and the associated equilibrium phase fractions of FCC α and BCC β as a function of temperature. Of immediate note is the insoluble nature of the Pb which appears in the liquid state above ~327°C. The Sn, even only present at 0.23 wt. %, is expected to have a stabilising effect on the BCC β phase, particularly at higher temperatures where the phase boundary between the α and (α + β) phase fields bends towards the Cu-end of the diagram. With regards to phase fraction, this indicates that the BCC β will tend to commence stabilising at lower temperatures and stabilise more slowly as the temperature of the alloy is increased due to the decreased phase boundary steepness.

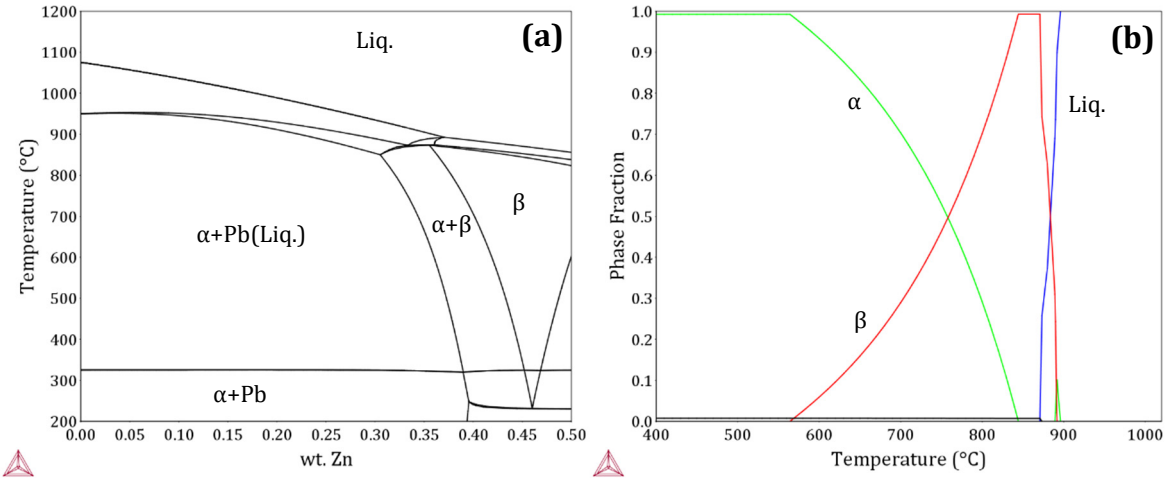


**Figure 4.1: (a) Quaternary CuZnPb2.3Sn0.23 isopleth and (b) evolution of equilibrium α (green) and β (red) phase fraction of CuZn36.5Pb2.3Sn0.23 with temperature, calculated using the CALPHAD approach in conjunction with the Cu-Zn-Pb and Cu-Zn-Sn databases developed by Miettinen [12, 28].**

The calculated isopleth for the alloy CuZnSn0.32 (Table 4.2) and the associated equilibrium phase fractions for FCC α and BCC β as a function of temperature are shown in Fig. 4.2. Given the similar nature of Bi to Pb in that it is similarly insoluble in the brass matrix, and is known to be liquid above ~271°C, it has been left out of the assessment and the remaining elements; Cu, Zn, and Sn adjusted to

maintain the same compositional ratio. Similar to CuZnPb2.3Sn0.23 (Fig. 4.1), the Sn in this Bi-bearing alloy is shown to stabilise the BCC β with the phase first appearing at a lower temperature of ~540°C and not reaching 100% β until ~850°C due to the decreased steepness of the α and β phase-field boundaries. The effect of Sn in both the Pb- and Bi-bearing alloys has important implications for elevated temperature processes such as forging or extrusion where greater processing windows (and associated margin for error) can be obtained with the minor inclusion of Sn.

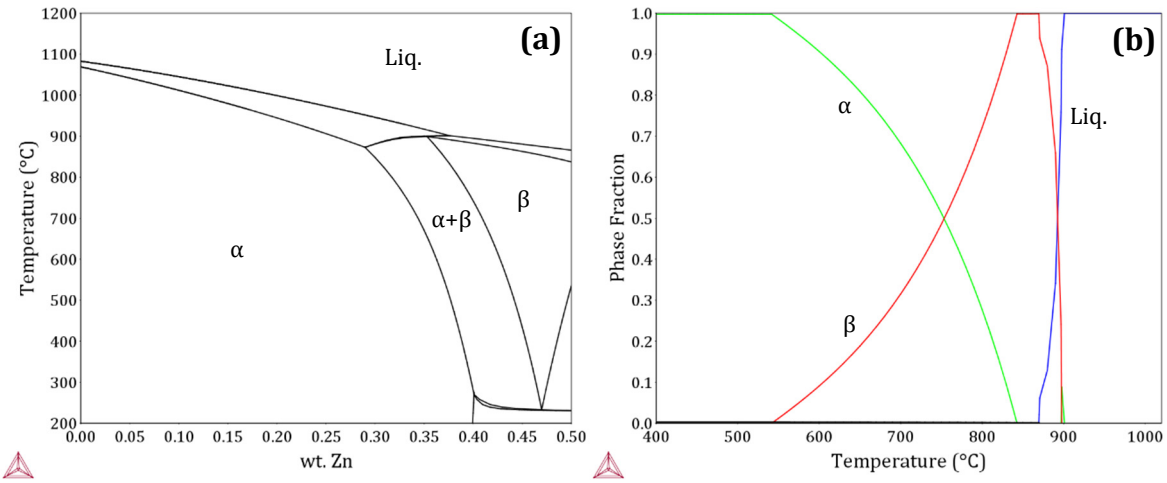


**Figure 4.2: (a) Ternary CuZnSn0.32 isopleth and (b) evolution of equilibrium α (green) and β (red) phase fraction of CuZn36.9Sn0.32 with temperature, calculated using the CALPHAD approach in conjunction with the Cu-Zn-Sn database developed by Miettinen [12].**

Three isopleths for the Cu-Zn-Si system, showing gradually increasing Si content from 2.7 wt. % to 3.4 wt. %, are shown in Fig 4.3 (a-c). Compared with the CuZn binary phase diagram, Si adds significant complexity to the phase equilibria and a strong and growing stabilisation of BCC β with increasing Si towards the Cu-rich corner. This β stabilisation is evident particularly at elevated temperatures and for significantly lower Zn compositions than standard duplex brasses. Additionally, multiple new phases appear, particularly the complex cubic γ phase and ε phase at lower temperatures and the HCP κ phase at intermediate temperatures.

The stabilisation of the β phase at a Zn content of 22 wt. % for increasing levels of Si-additions is shown in Fig. 4.3 (d). There is a clear competition between the BCC β phase and the complex cubic γ phase at ~590°C according to the CALPHAD description (Fig. 4.3d). For the temperature ranges below 590°C, the γ phase is predicted to be present at up to a phase fraction of 0.3 at equilibrium, whilst the BCC β phase is predicted to commence stabilising for 3 wt. % Si at just under 600°C and quickly reach 100% β phase fraction by 800°C. From an industrial standpoint, the predictions of stabilising BCC β at these Zn compositions would indicate this alloy should be forgeable at similar temperature ranges to

standard Pb-bearing duplex brasses. The predicted hot workability of this alloy will be explored in Chapter 5. Additionally, given the limited knowledge currently available in the literature, the presence of tertiary phases γ, κ, ε and any other potential tertiary phases formed under non-equilibrium conditions will be explored in Section 4.3.2.5 as part of a wider characterisation on this alloy.

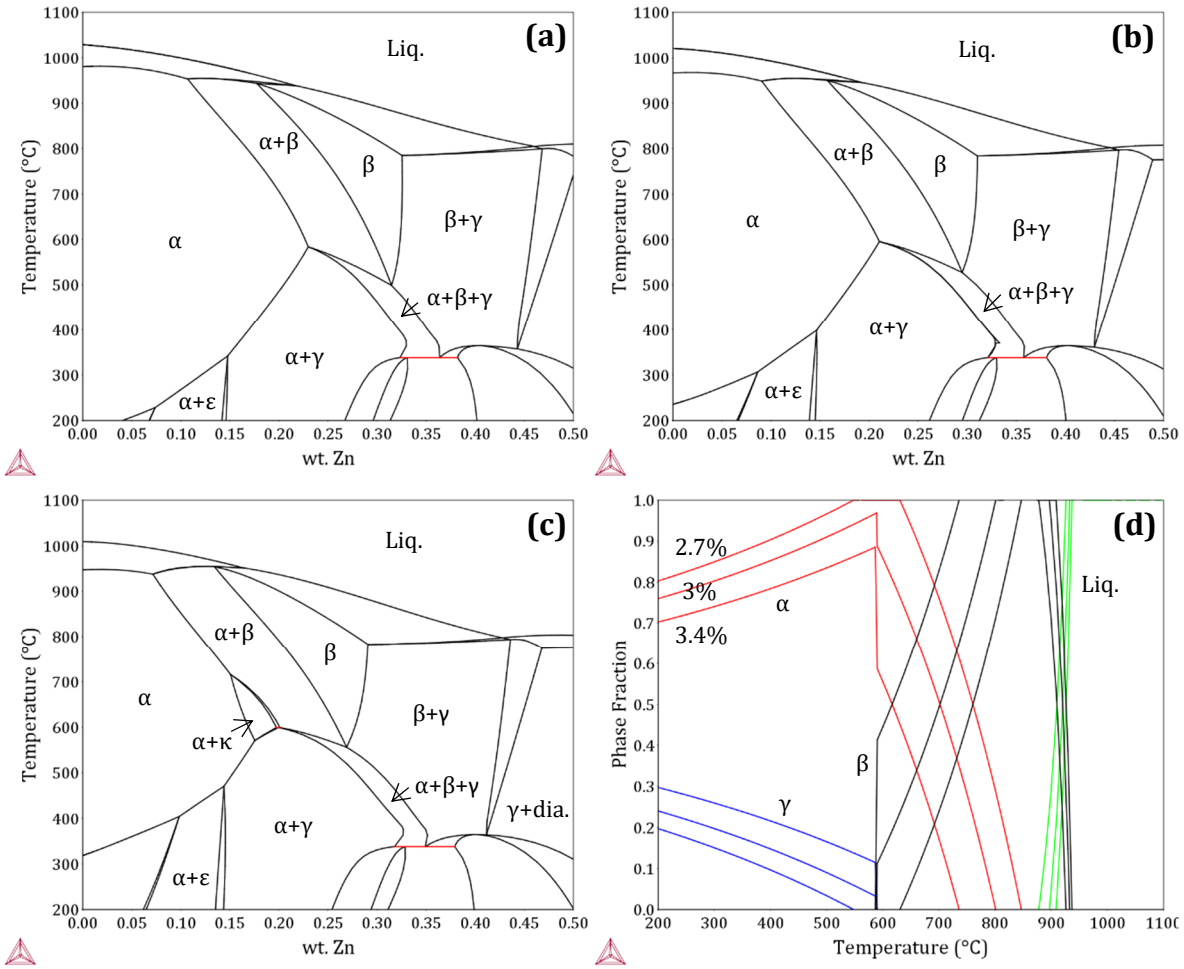


**Figure 4.3: Ternary isopleths of (a) CuZnSi2.7, (b) CuZnSi3, (c) CuZnSi3.4 and (d) the evolution of equilibrium α (red), β (black) and γ (blue) phase fraction of CuZn22Si2.7, CuZn22Si3, CuZn22Si3.4 with temperature, calculated using the CALPHAD approach in conjunction with the Cu-Zn-Si databases developed by Miettinen [29] and Wang et al. [30].**

By using the Calphad approach, the above generated ternary and quaternary isopleths give us a good starting point to experimentally examine the phase equilibria of the Pb-, Bi-, and Si-bearing alloys in Table 4.3.

### 4.2.2 X-Ray Diffraction

Powder XRD scans were performed on samples of each of the 3 brass alloy systems (Pb-, Bi-, and Si-bearing) listed in Table 4.1 to characterise their respective phases in the as-received state. After phase identification, Rietveld refinement was used to quantify the phase fractions in each alloy. Fig. 4.4 shows the room temperature XRD scan for the continuous cast CuZn36.5Pb2.3Sn in which three phases were identified using the lattice for the FCC α phase, the ordered BCC β' phase and the insoluble FCC Pb phase. The lattice parameter used for α was 0.3696nm and 0.2945nm was used for the β' phase. Rietveld refinement of the alloy shows a very high phase fraction of α (Fm-3m) above 90% with most of the remainder being ordered β' (Pm-3m). The estimated phase fraction of Pb is slightly lower than expected and likely due some removal during the mechanical filing process.

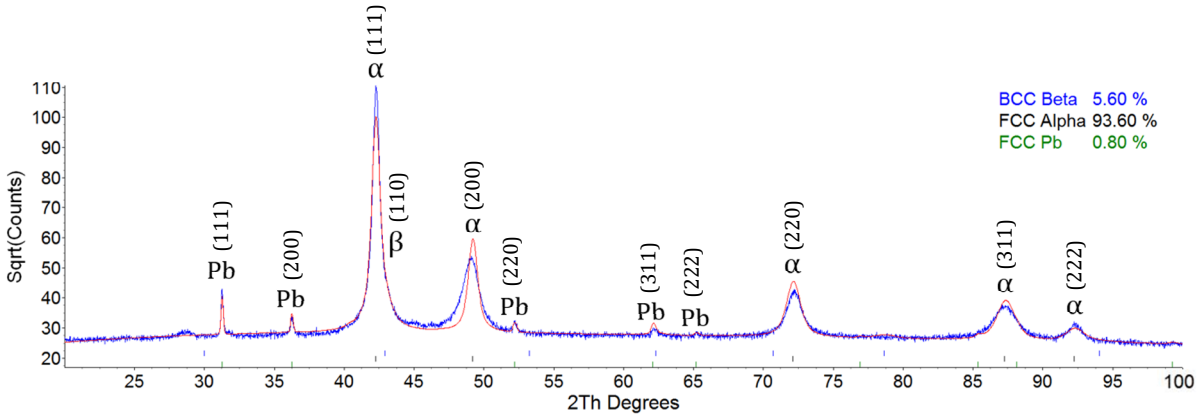


**Figure 4.4: Room temperature powder XRD scan of CuZn36.5Pb2.3Sn.**

The room temperature XRD scan for the extruded CuZn37.6Bi0.8Sn is shown in Fig. 4.5. Similar peaks and phase fractions were identified for both the FCC α phase and ordered-BCC β' phase compared to the Pb-bearing brass in Fig. 4.4, with new Bi-peaks (R3m) replacing the Pb-peaks at low 2θ. The estimated Bi phase fraction is also slightly lower than expected, likely due to the same reason highlighted for Pb in CuZn36.5Pb2.3Sn, that is the sample preparation process.

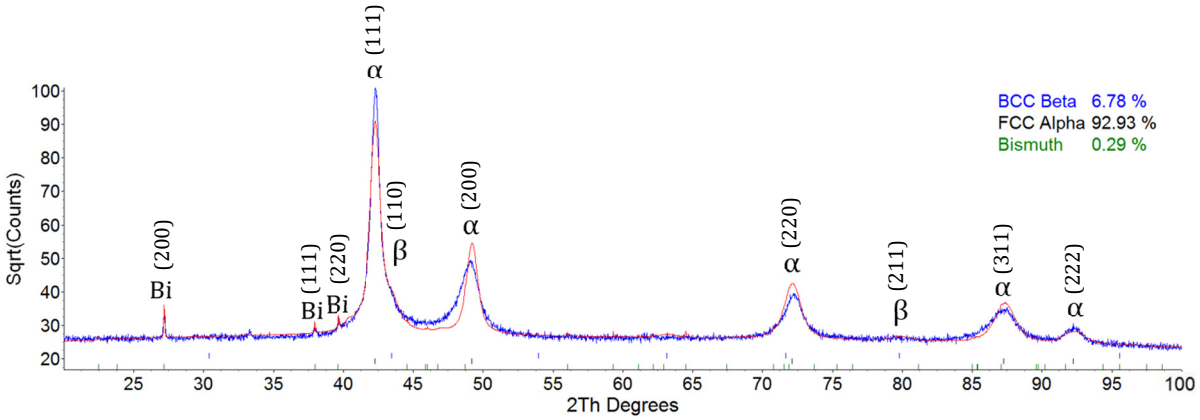


**Figure 4.5: Room temperature powder XRD scan of CuZn37.6Bi0.8Sn.**

The room temperature XRD scan for the extruded CuZn22Si3 is shown in Fig. 4.6. This alloy contains only trace amounts of the insoluble Pb (0.05 wt. %), therefore at this resolution the only contributing peaks of note are those of the base alloy matrix. Two primary peaks were identified, the FCC α phase and an HCP phase identified as κ, which is unique to Si-brasses in this compositional range. As expected, no ordered BCC β' phase was observed. However, no complex cubic γ phase was observed either as suggested by the equilibrium thermodynamic descriptions. The Rietveld fit for the scan in Fig. 4.6 does not appear as high quality as that in Fig. 4.4 and 4.5, especially in the 2θ range of 35-55. This suggests that further characterisation is required to fully understand the phases present in the alloy. Detailed characterisation of the CuZnSi system is a focus of Section 4.2.3.5.

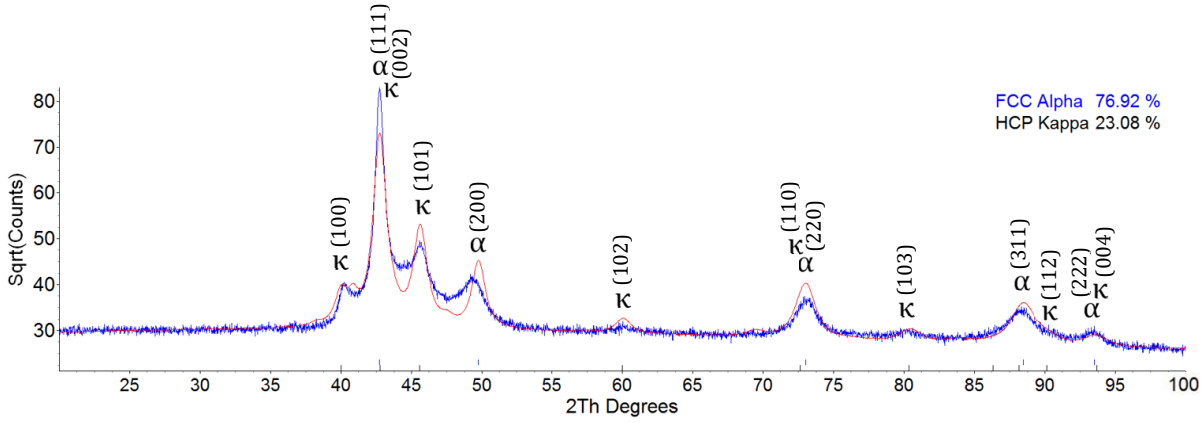


**Figure 4.6: Room temperature powder XRD scan of CuZn22Si3.**

After peak identification and Rietveld refinement were successfully employed on the as-received samples of the alloys listed in Table 4.1, the elevated temperature stability was examined. One approach is to heat-treat and water-quench samples from a range of elevated temperatures (50°C increments between 650-850°C after soak times of 30 minutes explored further in Section 4.2.3). The quenching was designed to minimise the formation of FCC α phase upon cooling. The XRD and Rietveld refinement would then be able to estimate an equivalent α and β phase fraction at the temperature used for the heat treatment. As shown in Fig. 4.7, for a heat-treated sample of CuZn37.6Bi0.8Sn0.3, quenching is ineffective at completely preventing the formation of new Widmanstätten FCC α grains. This is not surprising due to the high Zn diffusivity in the BCC β crystal structure (Section 2.2.3). Therefore, any Rietveld refinement would naturally over-estimate the α present in the microstructure. This creates a challenge in using this method. Therefore, phase fraction estimates using visual 2D metallographic techniques were used as an indicator after removing acicular α grains formed during quenching.

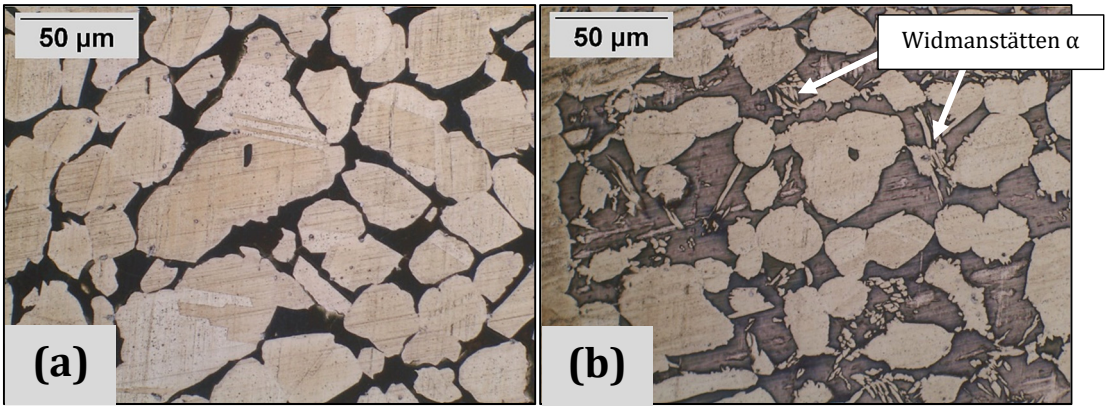


**Figure 4.7: CuZn37.6Bi0.8Sn0.3 heat treated and subsequently (a) air-cooled from 750°C and (b) quenched from 750°C. The quenched microstructure exhibits both equiaxed and Widmanstätten α grains, the latter forming on the rapid cool.**

An alternate approach is to perform *in-situ* XRD scans under controlled conditions to prevent oxidation of the alloy surface. This is important because Zn has a very strong affinity for oxygen, and therefore any oxidation of the surface will decrease the Zn content in the brass and subsequently decrease the β present in the alloy. Attempts were made to perform *in-situ* lab XRD scans on a CuZn36.5Pb2.3Sn alloy in 50°C increments from 300°C up to 750°C under various environments including nitrogen gas, argon gas and under vacuum, however each scan at elevated temperature resulted in the formation of characteristic ZnO peaks (Fig. 4.8) and a significantly lower than expected β phase fraction due to the reduction in Zn at the surface of the alloy. Attempts were made to produce scans from both powder and bulk samples, and with reduced step times (from 0.5s/step to 0.1s/step) without success. Therefore, an alternate solution to investigate the elevated temperature phase equilibria of duplex brass was pursued (Section 4.2.3).

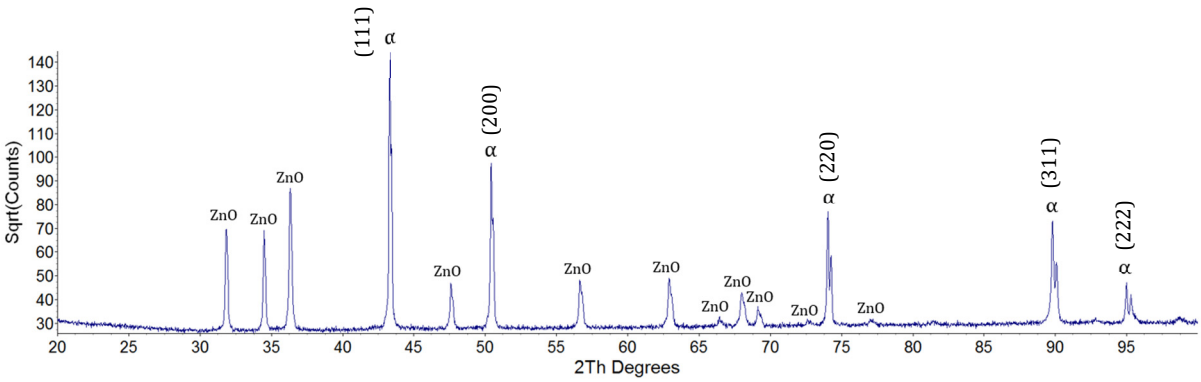


**Figure 4.8: Example of an *in-situ* XRD scan of CuZn36.5Pb2.3Sn (powder sample) performed at 700°C using a 150kPa nitrogen atmosphere and identifying several zinc oxide peaks that have formed due to surface oxidation at elevated temperatures.**

### 4.2.3 High Intensity *In-Situ* Neutron Diffraction

#### 4.2.3.1 Time-Temperature Schedule

Significant difficulties were encountered when attempting to quantify the equilibrium FCC α and BCC β phase fractions at elevated temperatures using the traditional techniques of metallography (due to the formation of small acicular α grains on rapid cooling) and *in-situ* XRD (due to surface oxidation of Zn). Although 2D visual metallography results can be used as an indicator by deliberately ignoring the small acicular α formed during quenching, another technique would need to be included in order to verify the accuracy of the Calphad phase estimates. *In-situ* neutron diffraction has a key advantage over traditional XRD in that the neutron beam passes into a significantly deeper section of a bulk sample, thereby removing concerns around surface effects such as Zn oxidation. Two samples, listed in Table 4.2, were selected for examination at the ANSTO Neutron facility under vacuum conditions using the time-temperature schedule for testing shown in Fig. 4.9. One diffraction pattern was collected every 30 seconds.

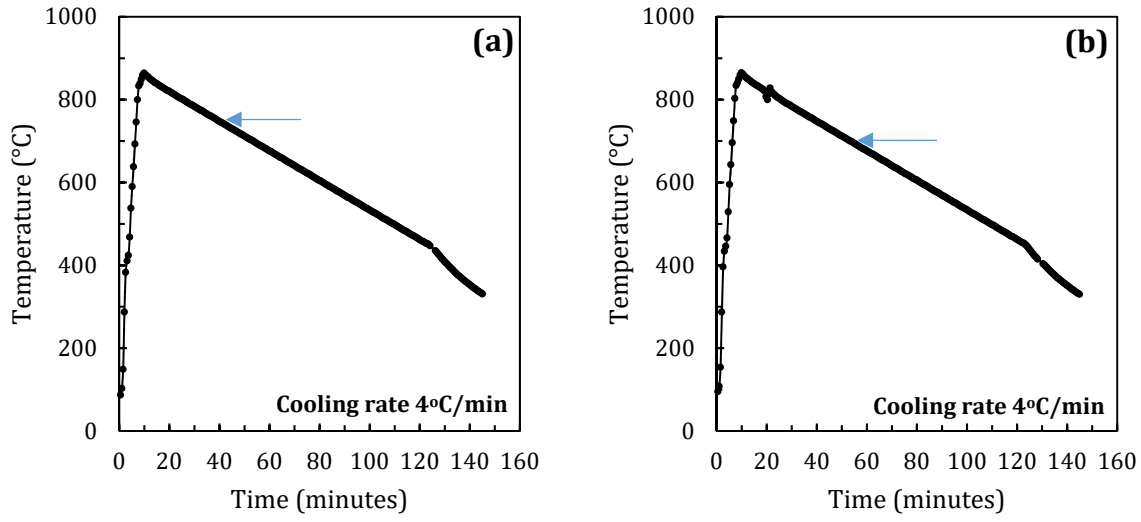


**Figure 4.9: The temperature schedule used throughout the neutron diffraction experiments for (a) the CuZn36.5Pb2.3Sn alloy and (b) the CuZn36.9Bi0.8Sn alloy. Highlighted on each figure is a temperature chosen to show an example scan in Figs. 4.10 (750°C) and 4.11 (700°C).**

Highlighted in Fig. 4.9 are two points; (1) 750°C for CuZn36.5Pb2.3Sn and (2) 700°C CuZn36.9Bi0.8Sn. The individual *in-situ* neutron diffraction patterns collected at these temperatures are shown in Figs. 4.10 and 4.11, respectively. The two key phases, FCC α and BCC β are highlighted on each scan for reference along with the Rietveld refinement. The Topas macro used for this refinement can be found in Appendix C. In each scan, an additional peak is found at 37 2θ (highlighted with a red arrow) which is due to the furnace setup and has been modelled here using a single Voigt peak.

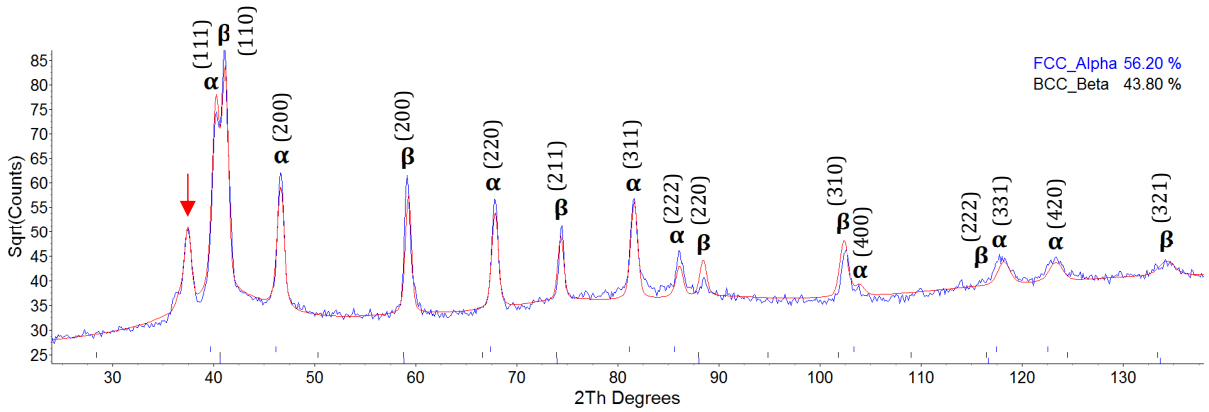


**Figure 4.10: Example of an ANSTO neutron diffraction pattern taken for the CuZn36.5Pb2.3Sn alloy at 750°C. An additional peak related to furnace setup highlighted with a red arrow.**

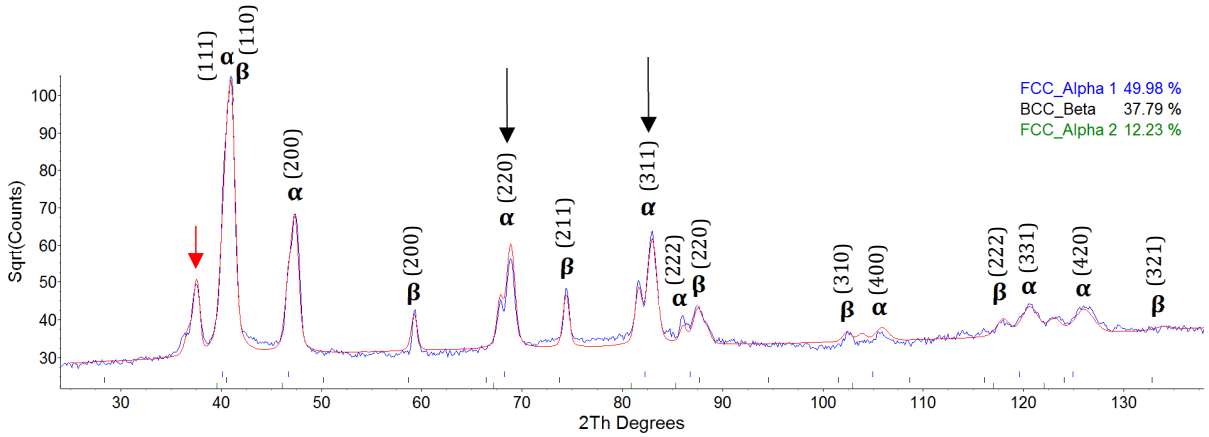


**Figure 4.11: Example of an ANSTO neutron diffraction pattern taken for the CuZn36.9Bi0.8Sn alloy at 700°C. Examples of peak splitting highlighted with black arrows.**

With respect to the use of high intensity *in-situ* neutron diffraction and metallographic examination, these experiments have been able to adequately capture the phase fraction evolution with temperature. Analysis of this (Section 4.2.3.2 – 4.3.2.5) allows us to quantify the α and β phase fractions with temperature.

An interesting observation was made for the continuous cast CuZn36.9Bi0.8Sn alloy in which peak splitting of several of the α phase peaks was found during the cool from elevated temperatures (highlighted in Fig. 4.11). It might be considered that due to the comparatively fast diffusion of Zn atoms through the more open BCC crystal structure (see Section 2.2.3) there are local regions of elevated Cu which have formed α grains first (perhaps along the β grain boundaries) with a slightly larger lattice parameter. Then as the cooling proceeds, the majority of α precipitates and grows with the smaller lattice parameter causing a larger peak to form at higher angles thus producing a peak split. To try and reproduce this peak splitting mechanism, a sample of the same Bi-bearing duplex brass was additionally heat treated in the all-β phase field at 825°C for an hour before dropping to 725°C within the α + β phase field and then water-quenching. The XRD spectra for this sample (Fig.

4.12) then showed the peak splitting occurring again, suggesting an α phase split is occurring and repeatable. Whilst not a focus for this thesis, it is an area where further work is required to understand the mechanisms behind this phenomenon.

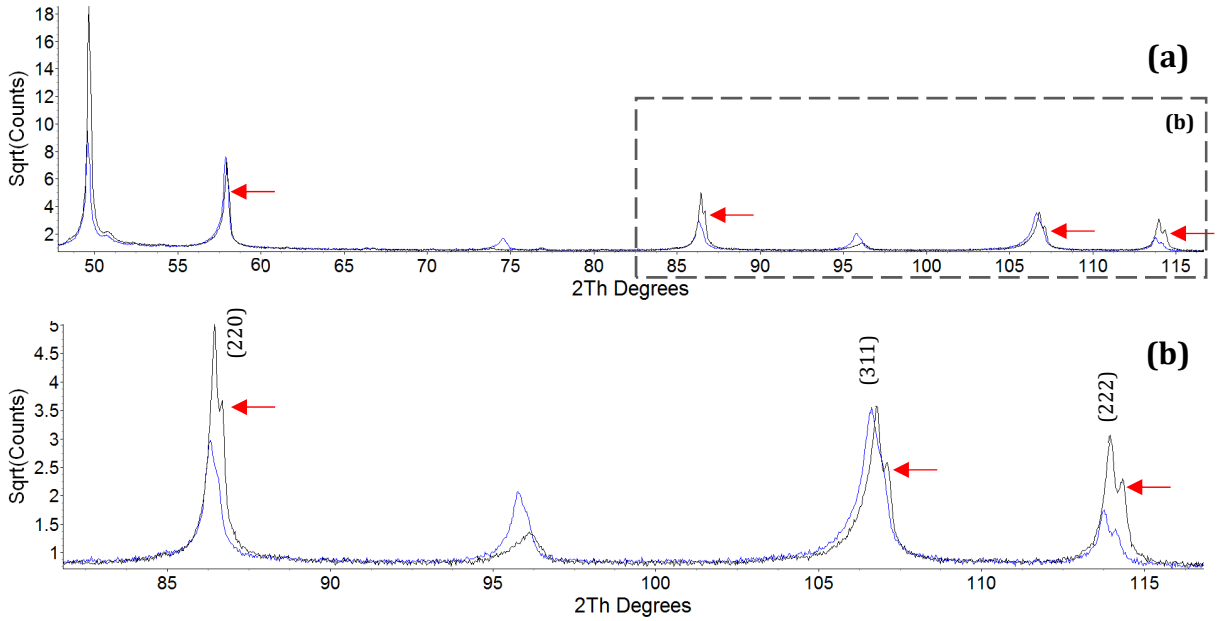


**Figure 4.12: Bulk XRD scan of CuZn36.9Bi0.8Sn before (blue scan) and after (black scan) heat treating at 825°C for 1 hour followed by a drop to 725°C for 1 hour and water-quenched. The resulting scan (a) shows the formation of α peak-splitting after heat treatment, and (b) inset view (highlighted by grey box) - increased magnification on higher-angle peaks where this is more easily observed (highlighted with red arrows).**

### 4.2.3.2 Continuous Cast CuZn36.5Pb2.3Sn

Throughout the *in-situ* neutron diffraction cooling regime, scans were collected every 30 seconds on the alloy. Each diffraction pattern was analysed for quantitative phase fraction using Rietveld refinement and the BCC β phase fraction plotted against temperature. This data for the continuously cast CuZn36.5Pb2.3Sn alloy is shown in Fig. 4.13 compared with the Calphad predictions for β phase fraction. The critical temperature range that we are most interested in is the typical *industrial* temperature range for hot working (e.g. during extrusion of rod or forging of semi-finished components) which ranges between 650-800°C. Within this temperature range we observe that the *in-situ* neutron diffraction data closely follows the Calphad predictions for BCC β phase fraction and therefore the thermodynamic description is considered quite reasonable for this alloy in this temperature range. As a result, this description will be used to calculate the equilibrium β phase fractions in subsequent Chapters of this thesis.

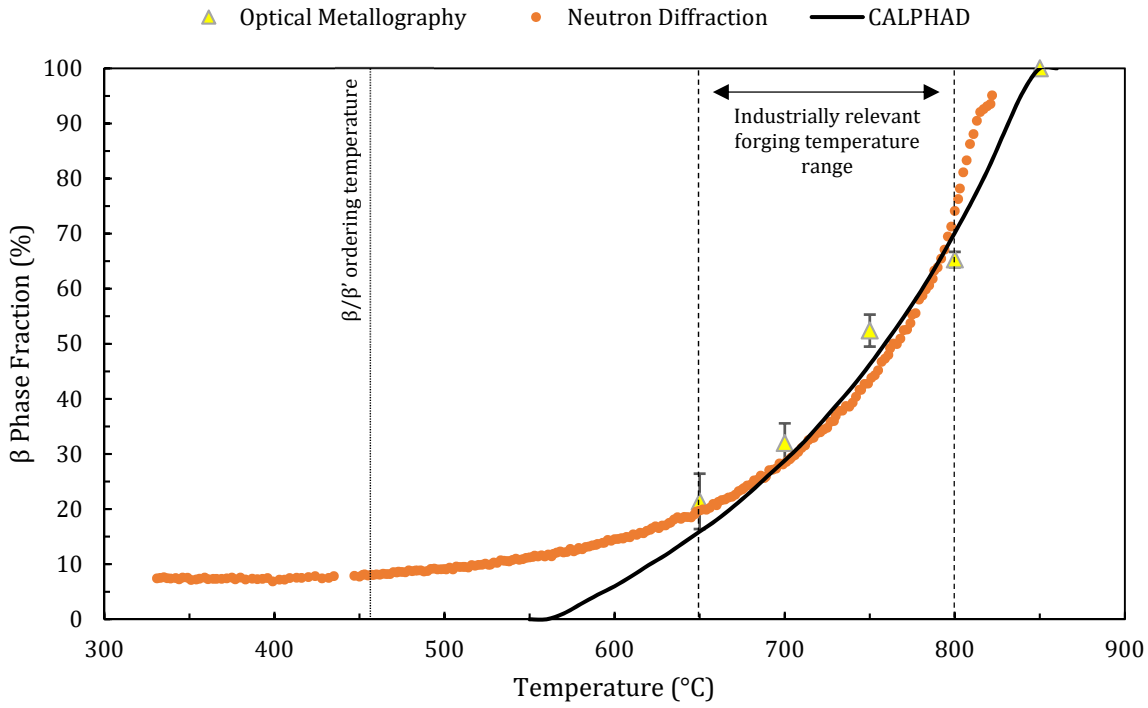


**Figure 4.13: Dependence of β phase fraction on temperature for the CuZn36.5Pb2.3Sn alloy using neutron diffraction data, CALPHAD calculations [12, 28] and optical metallography estimates. The temperature range of 650°C – 800°C has been highlighted as the most critical for elevated temperature deformation processing.**

As the temperature falls below the industrially-relevant range, the *in-situ* neutron diffraction data continues to retain a higher than Calphad-calculated β phase fraction. This is due to the slowing kinetics of phase transformations at these lower temperatures and is expected. From an industrial standpoint, duplex brasses are often heat treated at intermediate temperatures around 500°C in the

all-α phase field to yield greater resistance to corrosion, however the time required to achieve the desired changes in the microstructure is in the order of hours, not minutes.

In addition to the *in-situ* neutron diffraction data and Calphad predictions of BCC β as a function of temperature, Fig. 4.13 also presents a metallographic estimation of the β phase fraction using samples heat treated at 50°C increments between 650°C and 850°C and then rapidly quenched into water after a soak time of 30 minutes. Example microstructures from these samples are shown in Fig. 4.14. As discussed in Section 4.2.2, it is very difficult to prevent the nucleation and growth of new α grains upon rapid cooling from elevated temperatures due to the relatively fast diffusion of Zn atoms through the BCC β crystal structure. Above 700°C these α grains will present in the Widmanstätten morphology and have a significantly smaller grain size than α grains present at the elevated temperatures (Fig. 4.7b). Therefore, estimations of β phase fraction were assessed using ImageJ software as per the standard statistical grid method outlined in Section 3.4.1 for the 650°C and 700°C samples, and then treating any additional α grains of a smaller Widmanstätten morphology as β for the images collected after quenching from between 750-850°C as they are considered not to be present at these elevated temperatures. A simple example to illustrate this method is for the CuZn36.5Pb2.3Sn sample heat treated to 850°C (highlighted in Fig. 4.14e) in which all of the α present in the microstructure has formed on cooling alone and therefore must have been 100% β at this temperature and subsequently plotted in Fig. 4.13 accordingly.

The estimates for BCC β phase fraction from optical microscopy and image analysis, as a function of temperature were found to agree well with the Rietveld refinement of the Neutron diffraction data and the Calphad predictions in the critical industrial temperature range. With each incremental change in temperature there is a marked shift in the calculated β between 650°C to 850°C. Therefore, this metallographic estimation method will be used for the subsequent alloys to help verify the accuracy of the Calphad descriptions.

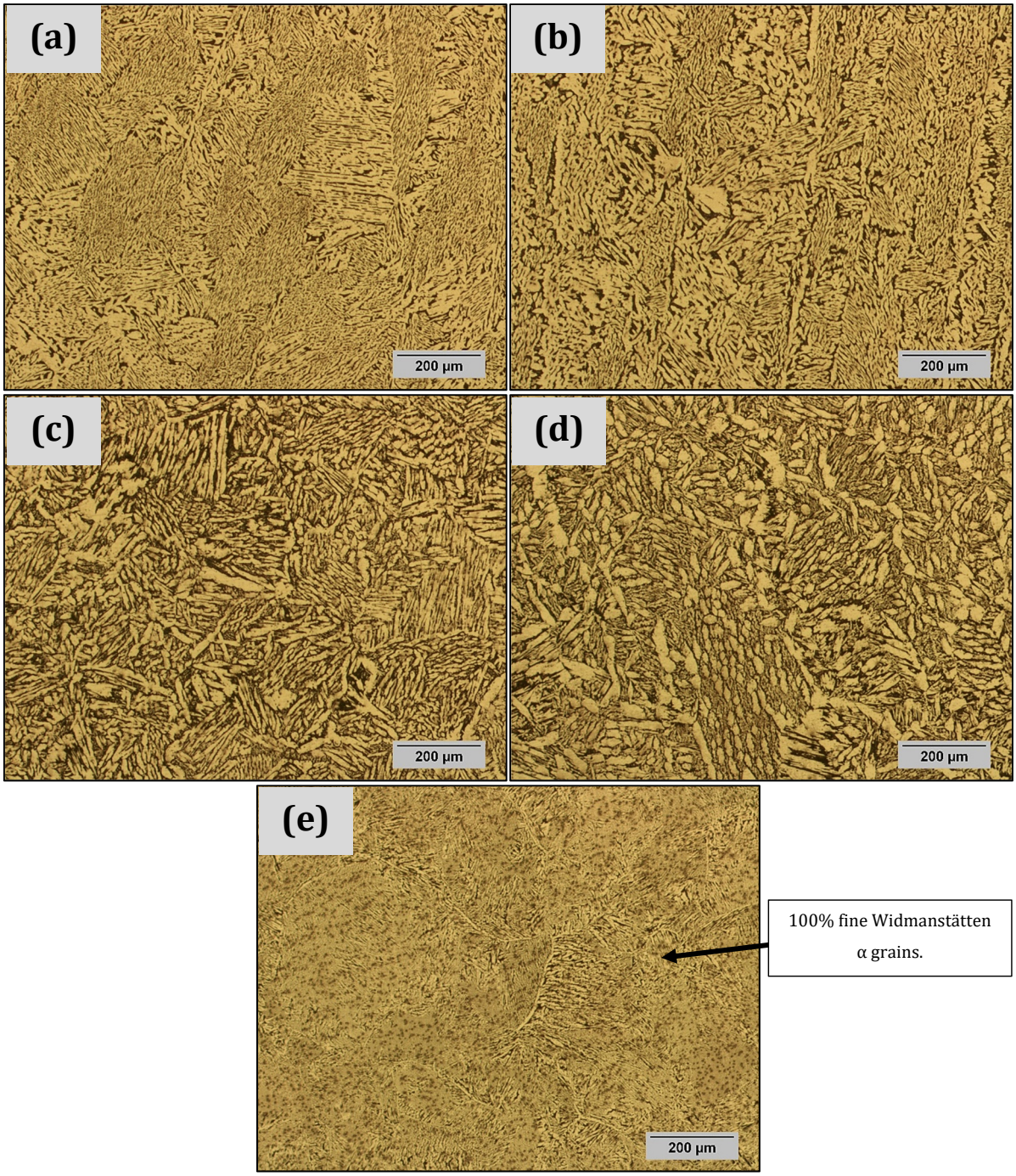


**Figure 4.14: Optical micrographs of continuous cast CuZn36.5Pb2.3Sn taken in the quenched state from (a) 650°C, (b) 700°C, (c) 750°C, (d) 800°C, (e) 850°C after a soak time of 30 minutes. The fine Widmanstätten α grains found upon cooling are highlighted in the 850°C condition.**

### 4.2.3.3 Continuous Cast CuZn36.9Bi0.8Sn

High intensity *in-situ* Neutron diffraction scans were completed every 30 seconds on the continuous cast CuZn36.9Bi0.8Sn throughout the cooling regime and then assessed for quantitative phase fraction using Rietveld refinement. The results for each scan have been plotted in Fig. 4.15 along with the Calphad predictions and metallographic estimates for BCC β as a function of temperature in 50°C heat treatment increments. If we review the data within the critical industrial temperature zone of 650-800°C, we find that between 700-800°C the data again matches the Calphad predictions and metallographic estimates well indicating good accuracy of the predictions. However, below 700°C the neutron data indicates that additional β is being retained within the microstructure.

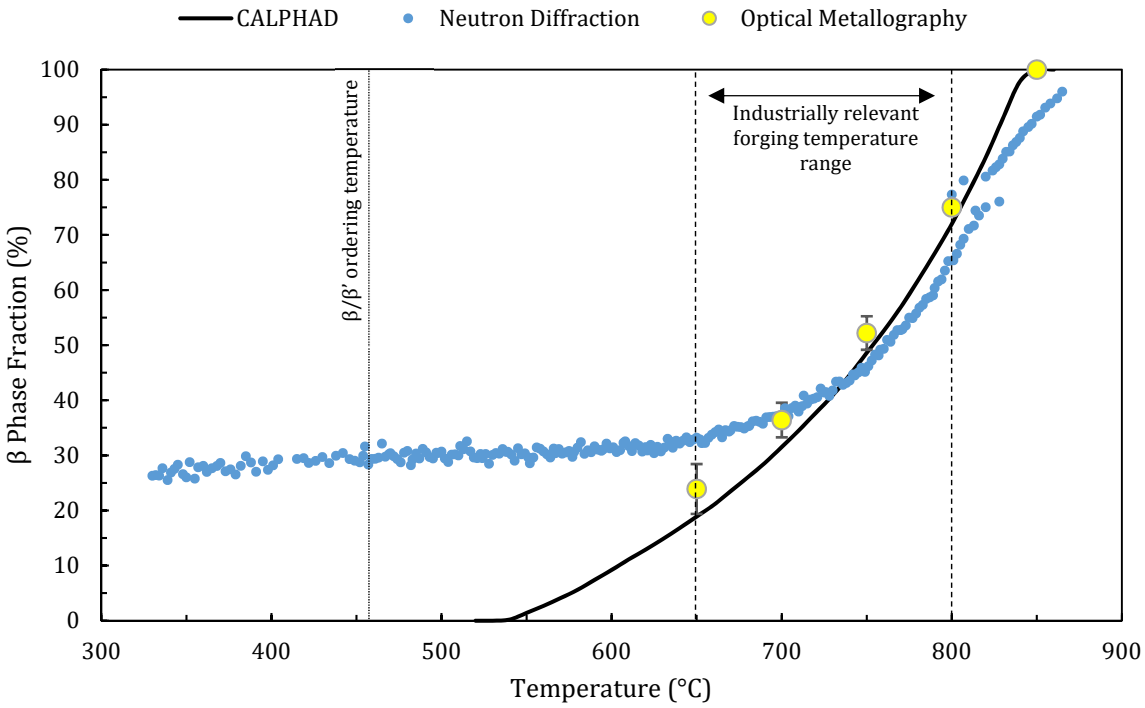


**Figure 4.15: Dependence of β phase fraction on temperature for the CuZn36.9Bi0.8Sn alloy using neutron diffraction data, CALPHAD calculations [12] and optical metallography estimates. The temperature range of 650°C – 800°C has been highlighted as the most critical for elevated temperature deformation processing.**

As with the continuous cast CuZn36.5Pb2.3Sn alloy, there is observed a significant divergence from the equilibrium phase fraction predictions as the temperature drops below 700°C associated with the slowing kinetics of phase transformation from BCC β to FCC α. The divergence is more significant in this alloy, largely due to the increased stability of β (even below 550°C). Further increases to α stabilisation could no doubt be achieved, however longer times at intermediate temperatures would be required to approach equilibrium.

Shown in Fig. 4.16 are example micrographs of each of the CuZn36.9Bi0.8Sn samples quenched from elevated temperature used for the metallographic estimations of phase fraction. With each incremental increase in soak temperature there is observed an increased competition between α grain

growth and β phase fraction stabilisation until at 750°C (Fig. 4.16c) we begin to observe the emergence of Widmanstätten α grains that have nucleated in between the larger existing α grains upon quenching (and are subsequently disregarded in the phase fraction estimates). This continues more significantly into the sample heat treated at 800°C (Fig. 4.16d) until finally we see no original α grains remaining in the 850°C micrograph (Fig. 4.16e), only newly formed Widmanstätten α, as expected.

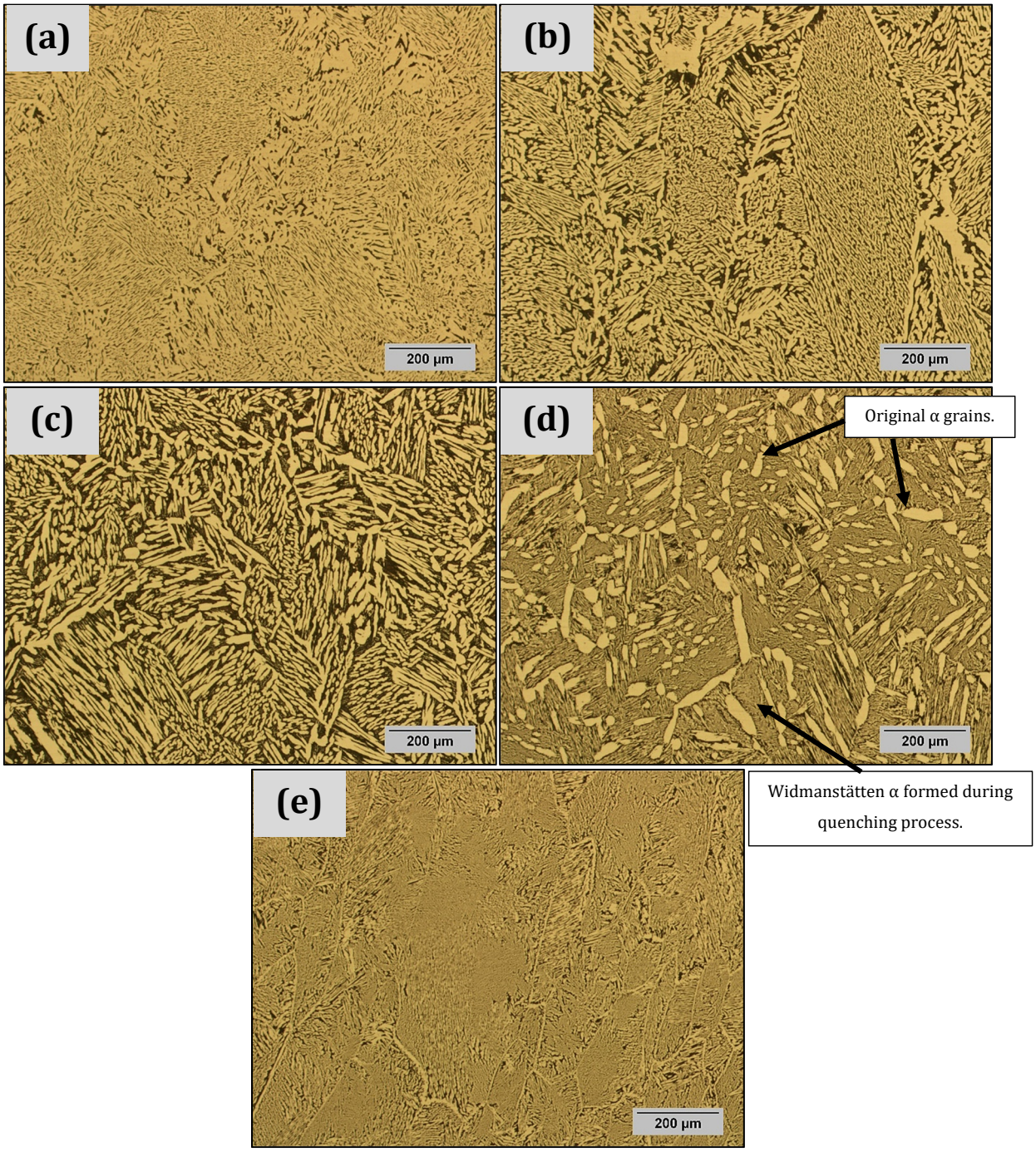


**Figure 4.16: Optical micrographs of continuous cast CuZn36.9Bi0.8Sn taken in the quenched state from (a) 650°C, (b) 700°C, (c) 750°C, (d) 800°C, (e) 850°C (soak 30 minutes). Highlighted are examples of both original α grains that are typically observed around larger β grain boundaries and Widmanstätten α formed during the quenching process and therefore not included in the equilibrium estimations of phase fraction.**

### 4.2.3.4 Extruded CuZn37.6Bi0.8Sn

Given the metallographic estimates of phase fraction proved a very good indicator of the Calphad predictions for the previous two alloys, this method was used to investigate the extruded CuZn37.6Bi0.8Sn. The estimates of BCC β in 50°C increments from 650-850°C is plotted in Fig. 4.17 against the Calphad predictions as a function of temperature. Examples of the microstructures are shown for each temperature in Fig. 4.18. As CuZn37.6Bi0.8Sn contains ~0.7 wt. % more Zn than the continuous cast CuZn36.9Bi0.8Sn (Section 4.2.3.3), it is not surprising to observe an elevated β phase fraction in the CALPHAD predictions across the range of temperatures explored. For example, at 750°C the CALPHAD prediction for β phase fraction in CuZn37.6Bi0.8Sn is 62.5%, whilst for CuZn36.9Bi0.8Sn it is 48.6%. Importantly, the metallographic estimates in the critical industrial zone are following the Calphad predictions.

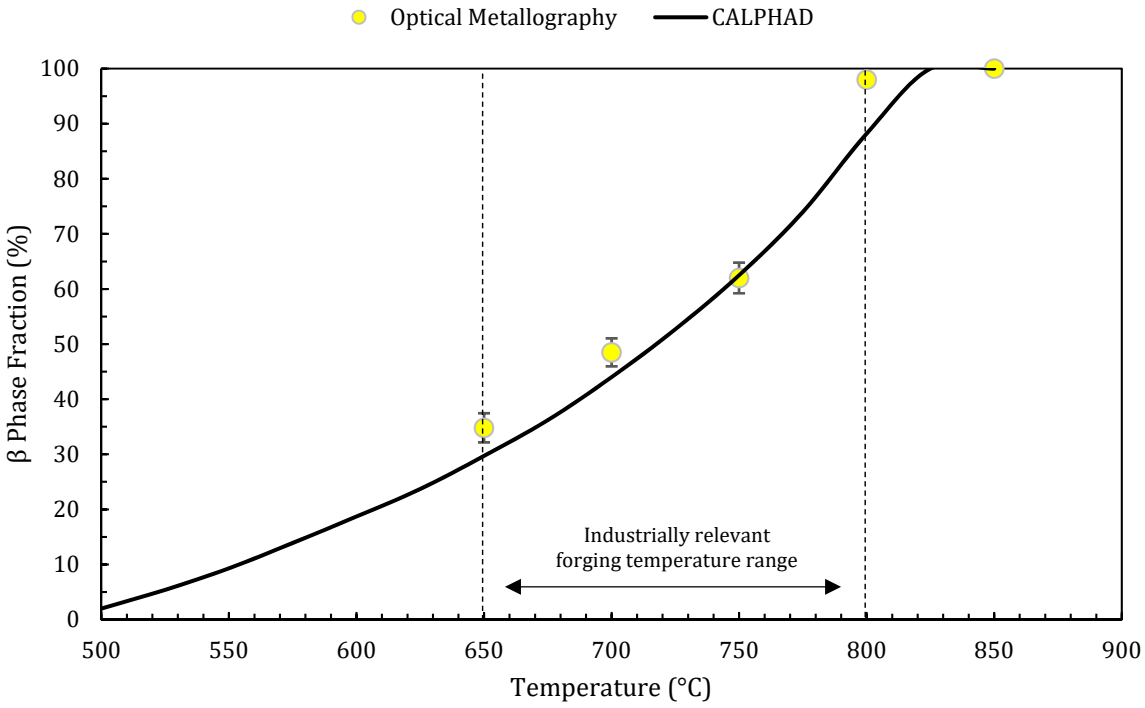


**Figure 4.17: Dependence of β phase fraction on temperature for the CuZn37.6Bi0.8Sn alloy using CALPHAD calculations [12] and optical metallography estimates.**

As can be seen in Fig. 4.18d-e for the soak temperatures of 800°C and 850°C, the α grains are observed to be entirely of the small Widmanstätten morphology, indicating 100% (or close to) β has formed at these temperatures, similar to the Calphad predictions. Significantly more of the original α is found in the sample microstructure for 750°C (~62.5% Fig. 4.18c) gradually increasing with lower soak temperatures to 34.8% (650°C, Fig. 4.18a), only marginally more than the Calphad predictions. Overall

this is a very good result, supporting the use of the Calphad thermodynamic descriptions (Appendix B) for systems including Sn in the composition.

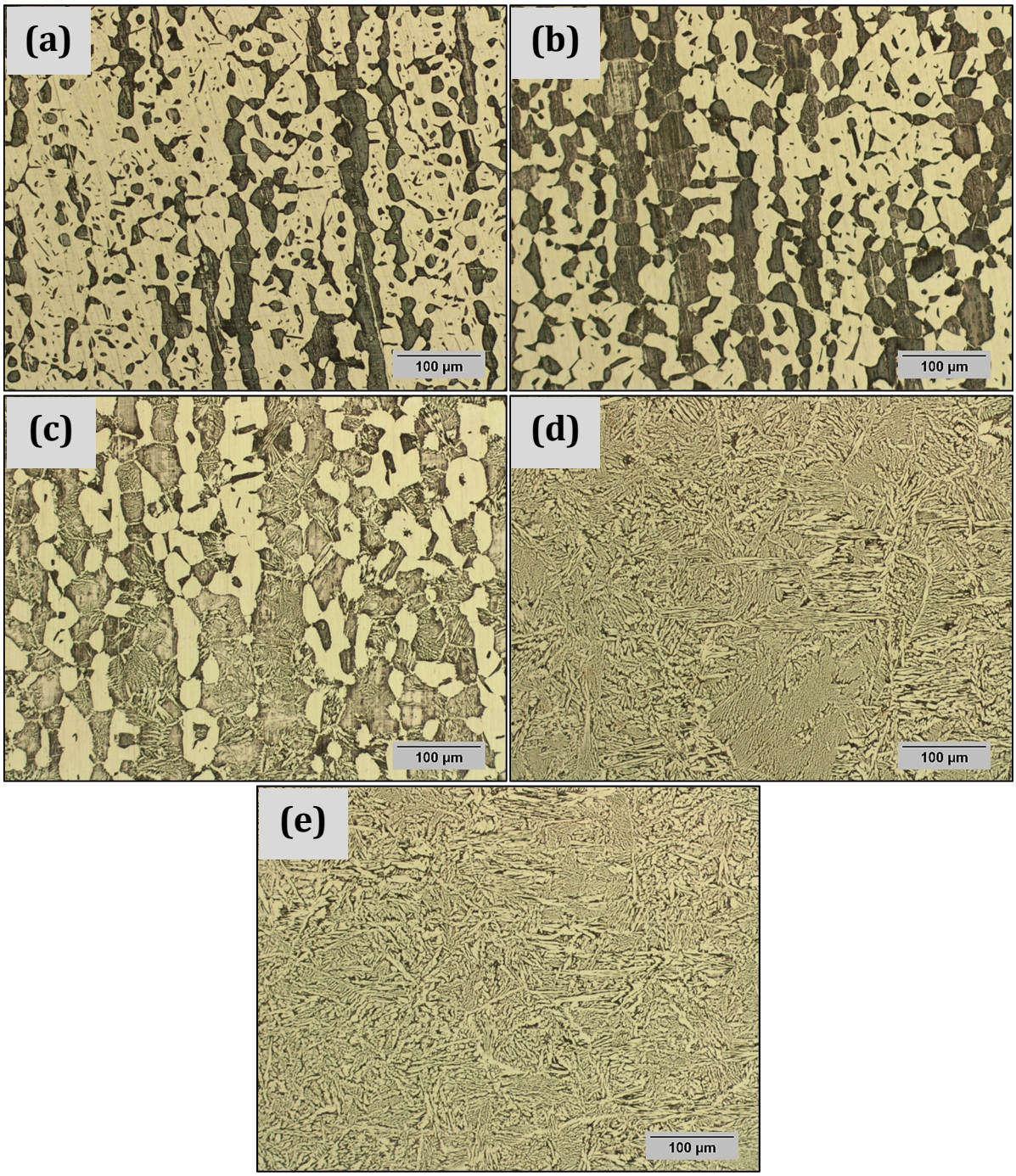


**Figure 4.18: Optical micrographs of extruded CuZn37.6Bi0.8Sn taken in the quenched state from (a) 650°C, (b) 700°C, (c) 750°C, (d) 800°C, (e) 850°C after a soak of 30 minutes.**

### 4.2.3.5 Extruded CuZn22Si3

Each of the Calphad predictions explored so far have been predominantly tied to systems including Sn, Pb and Bi with each having varying effects on the phase equilibria of CuZn alloys. In each case, the predications have agreed well with the high intensity *in-situ* Neutron diffraction and/or metallographic estimations. We now use metallographic estimates of phase fraction for a system including Si which is known to have a significantly stronger effect on the phase equilibria of brasses. This is to verify the accuracy of the developed CuZnSi Calphad database [29, 30]. Plotted in Fig. 4.19 is the estimated phase fraction of BCC β as a function of temperature using metallographic estimates, examples of which can be found in Fig. 4.20 in 50°C increments from 650-850°C covering the desired industrial temperature range. When comparing against the other alloys examined so far in this study, we note that at 750°C the predicted β phase fraction is the highest so far at 69.1%, however as the temperature is reduced, the predicted β phase fraction drops more quickly, and is predicted to reach 0% by 575°C. The steepness of this curve is indicative of a narrower processing window and will be explored further in Chapter 5. Similar to the results shown for the extruded CuZn37.6Bi0.8Sn, the CuZn22Si3 alloy exhibits good agreement between the Calphad predictions for BCC β and the metallographic estimates.

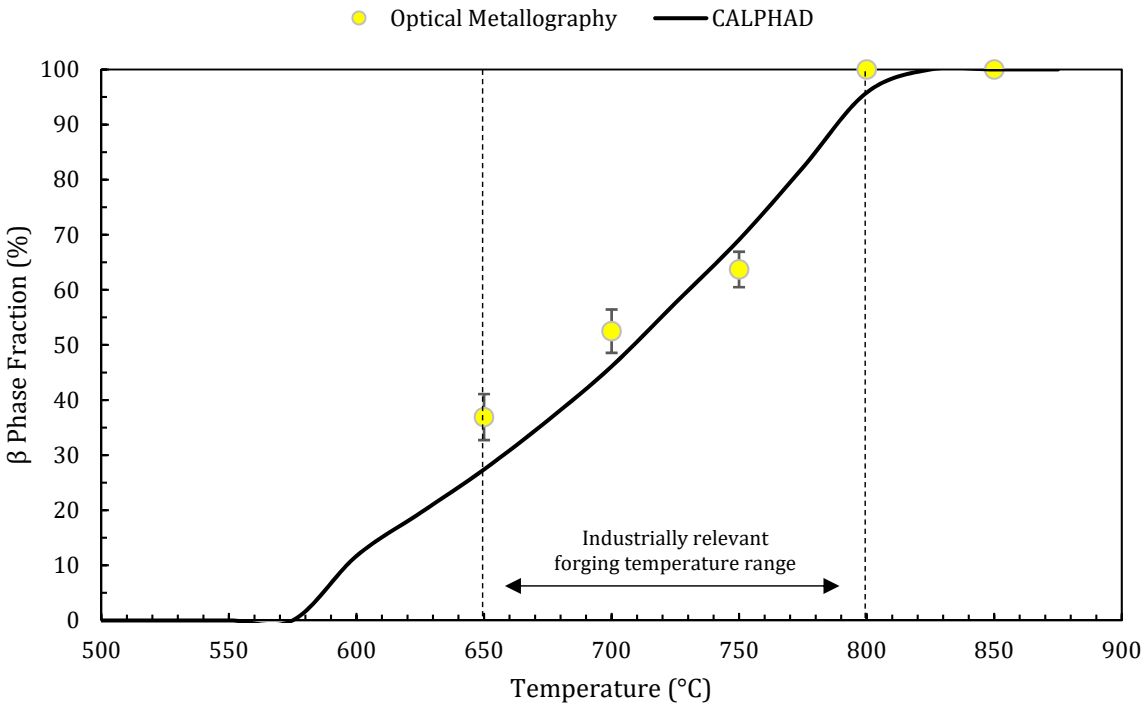


**Figure 4.19: Dependence of β phase fraction on temperature for the CuZn22Si3 alloy using CALPHAD calculations [29, 30] and optical metallography estimates.**

For the three metallographic phase fraction estimates taken between 650-750°C, the α phase gradually transforms to β at these elevated temperatures whilst the remaining α grains continue to grow. At 750°C there is a clear indication of acicular α grains forming during the quenching process which are removed from the estimate for β at temperature. Throughout this study, 750°C has

consistently been the quenching temperature at which these acicular grains have tended to form. At the highest temperature conditions of 800°C and 850°C, a similar observation of 100% β is found, however there are two additional observations made at 850°C which haven't been identified in any of the previous alloys; (1) bright spots throughout the original β grains and (2) bright areas along the prior β grain boundaries. This effect is shown more clearly in the images in Fig. 4.21.

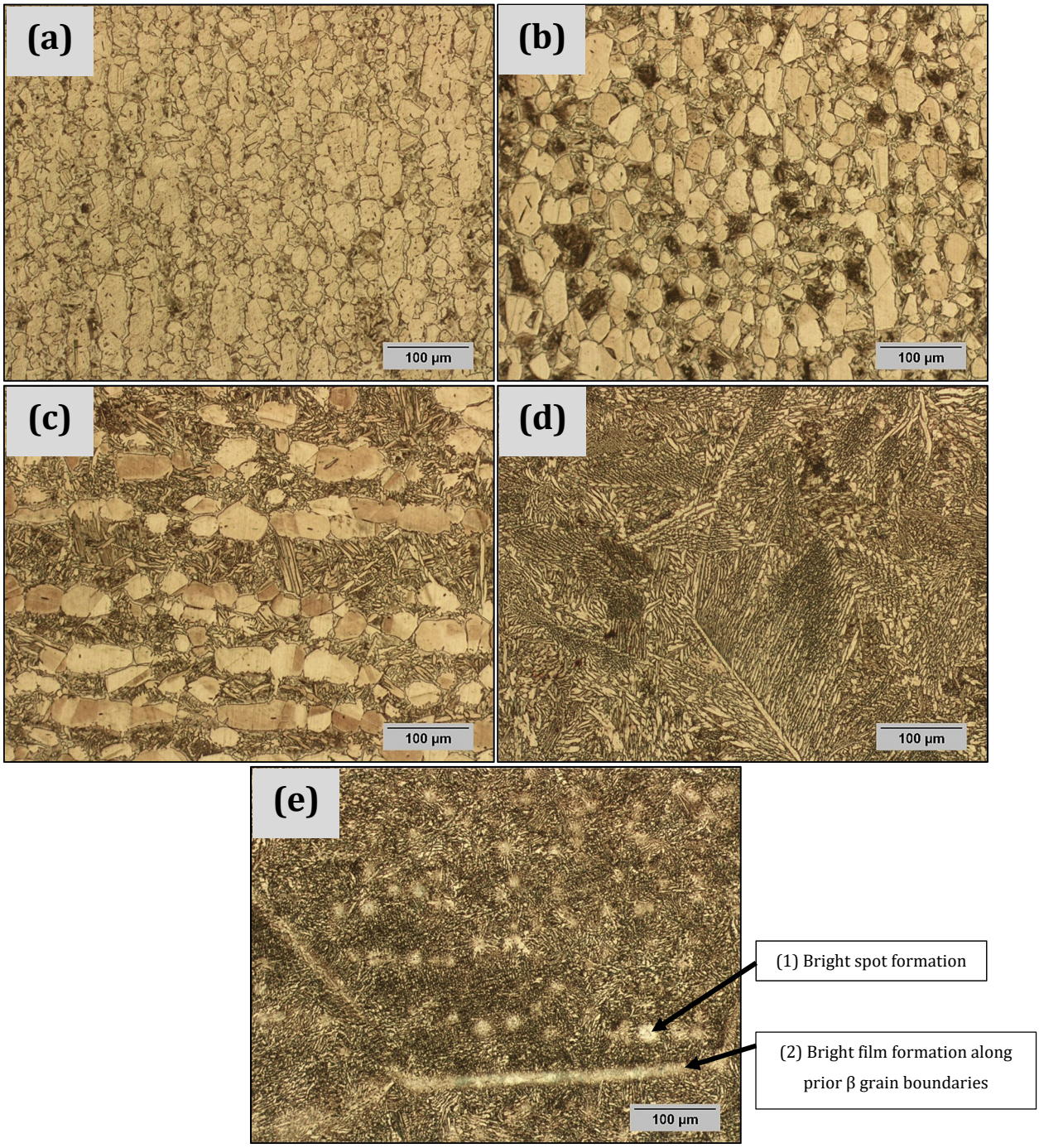


**Figure 4.20: Optical micrographs of extruded CuZn22Si3 taken in the quenched state from (a) 650°C, (b) 700°C, (c) 750°C, (d) 800°C, (e) 850°C after a soak of 30 minutes. Highlighted are abnormalities in the microstructure heat treated to 850°C (bright spot formation and prior β grain boundary film formation).**

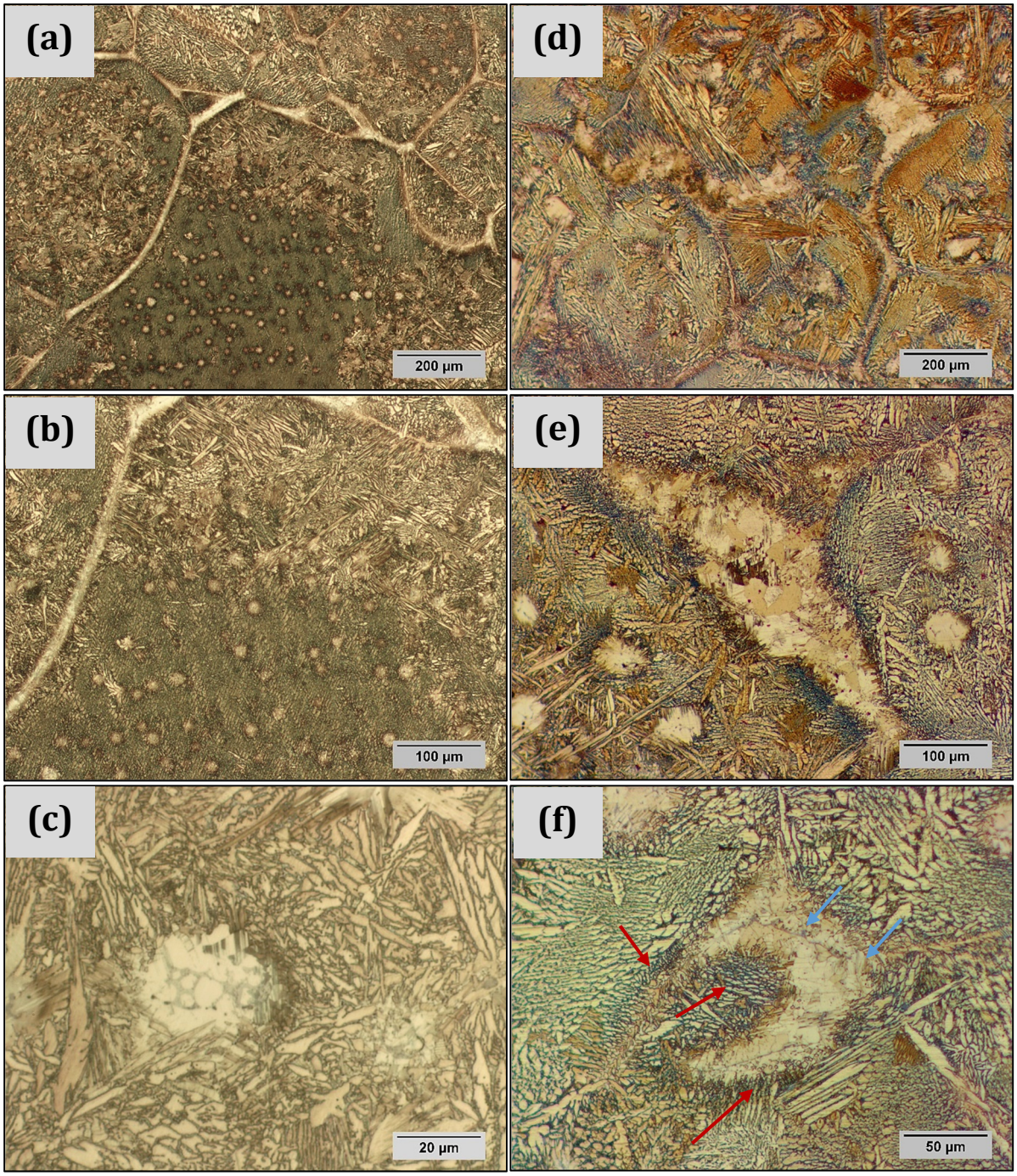


**Figure 4.21: Samples of CuZn22Si3 heat treated to 850°C for a soak time of (a-c) 30 minutes and (d-f) 45 minutes (increasing magnification). Incipient melting is occurring throughout the microstructures due to Si in composition.**

Shown in Fig. 4.21 are the microstructures of CuZn22Si3 after being heat treated at 850°C and quenched from temperature after soak times of 30 (Fig. 4.21a-c) and 45 (Fig. 4.21d-f) minutes, respectively. As the magnification of the microstructures is increased, we note that the brighter regions for the sample heat treated for 45 minutes are actually equiaxed and recrystallised α phase (some grains exhibiting mild twinning – highlighted with blue arrows Fig. 4.21f and 4.22a) which is indicative of a Zn poor region. These regions appear to be surrounded by much darker regions of

smaller grain size (highlighted with red arrows in Fig. 4.21f), likely richer in Zn. Due to the indication of chemical inhomogeneity and vastly different grain morphology, it would appear that the bright spots in the bulk microstructure and film formation along the prior BCC β grain boundaries could be associated with incipient melting of the alloy and this will now be explored.

In order to confirm the chemical inhomogeneity in the microstructures heat treated to 850°C, a sample was prepared for SEM-EDS analysis. An example of the microstructure around a grain boundary of interest is shown in Fig. 4.22a. As Zn is slightly heavier than Cu, any region in this area depleted in Zn will appear slightly darker on the BSE image, and a prior β grain boundary was located and is highlighted within the blue region in Fig. 4.22b. An EDS line scan was measured across this region (white line shown in Fig. 4.22b) and the results for Zn and Si wt. % shown in Fig. 4.23a-b.

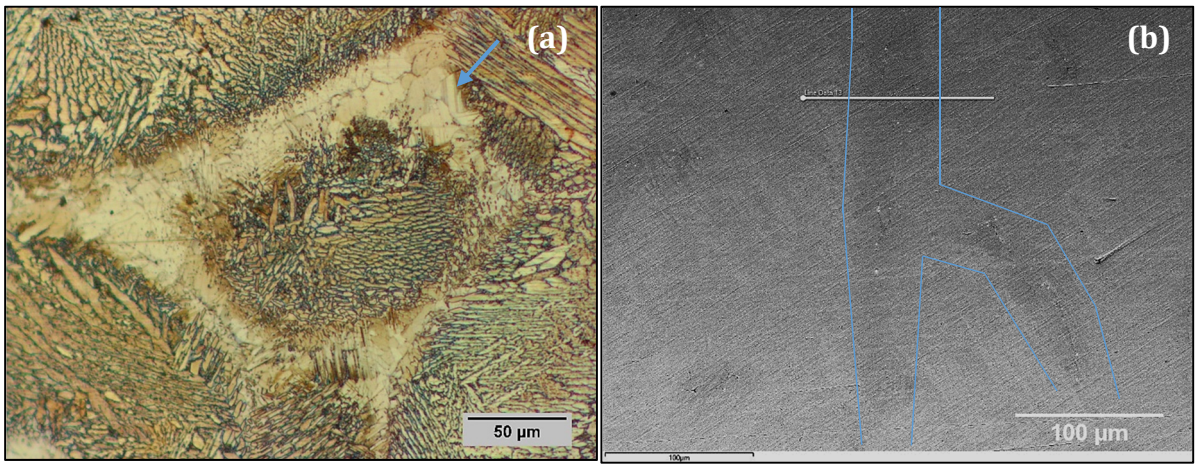


**Figure 4.22: (a) Microstructure of CuZn22Si3 heat treated to 850°C for 45 minutes adjacent to a grain boundary and (b) a low magnification BSE image of the same sample area of interest. Highlighted in the BSE image is the EDS line scan region (in white) chosen to evaluate the levels of Cu, Zn, and Si shown in Fig. 4.23 as well as the key grain boundary regions showing depleted levels of Zn (in blue).**

As can be observed in the line scans for Zn and Si in Fig. 4.23, the grain boundary region is shown to be richer in Si (and Cu) and depleted in Zn. A horizontal line is shown in each scan to denote the average wt. % of each element, whilst two black dotted lines show the region of Zn-depletion. Immediately adjacent to this grain boundary region we note an increase in the Zn content (and associated drop in the Cu content), before these elements restabilise closer to their respective averages in the bulk alloy. This is indicative of incipient melting of the grain boundary region in which the Zn is rejected into the surrounding bulk matrix, and the gradual formation of liquid which then forms into Zn-poor FCC α upon quenching.

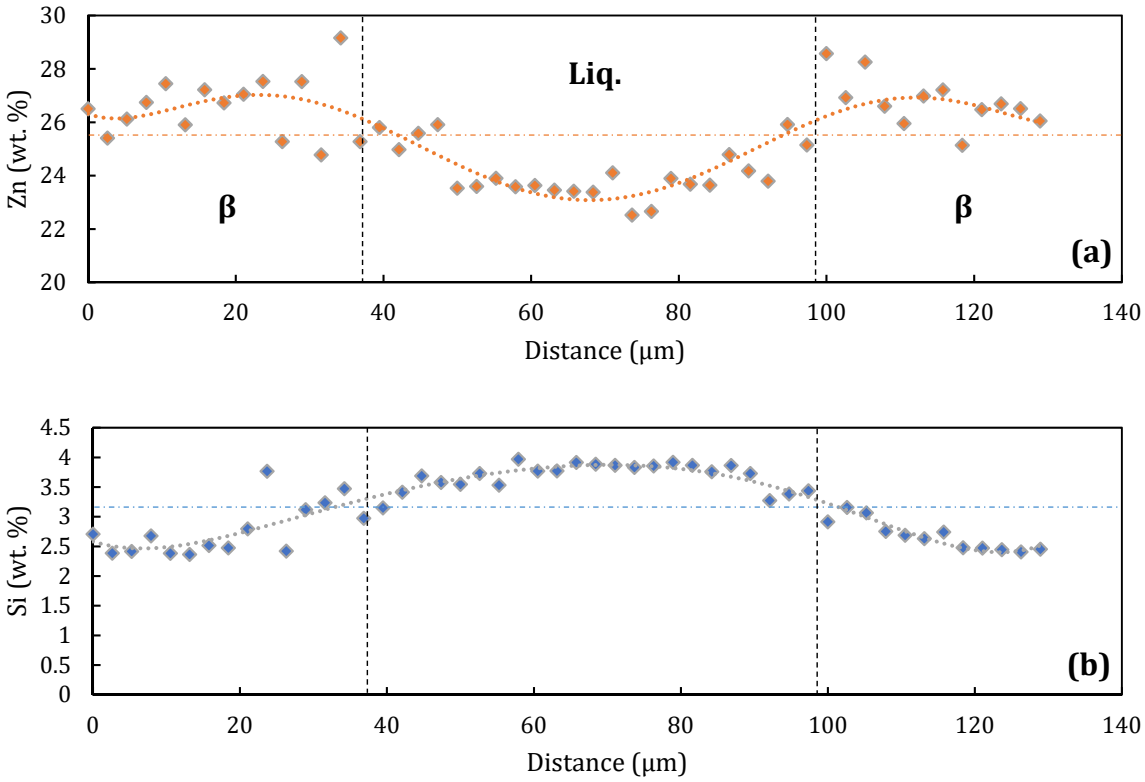


**Figure 4.23: SEM-EDS line scan of the sample in Fig. 4.22 showing the quantitative presence of (a) Zn and (b) Si. The region near the grain boundary is shown to be depleted in Zn, with higher than normal levels of Zn immediately adjacent to this region.**

A key question is then why would liquid form in these regions. It must be associated with solute segregation since liquid does not commence forming until ~890°C for this bulk composition (Fig. 4.24a). Si present in the composition will decrease the liquidus point of a brass alloy (Fig. 4.3b, to sub-800°C for standard duplex brass Cu-Zn ratios). For a homogenous composition in the bulk CuZn22Si3 alloy, the (β + L) phase field commences at ~890°C (Fig. 4.24a). However, even though the base CuZn22Si3 alloy may be stable in the all-β phase field at 850°C, any localised regions of elevated Si will be subject to incipient melting in the β + L phase field, particularly along grain boundaries. Fig. 4.24b shows that the Si composition required to bring the (β + L) phase field close to 850°C is ~3.8 wt. %, less than 1% enriched from the bulk composition and close to the experimentally measured value (Fig. 4.24b). At 850°C, there is no equilibrium α remaining in the brass microstructure and only growth of the β grains. Localised regions of elevated Si will then be susceptible to incipient melting, which leads to the formation of liquid which tends to reject Zn (Fig. 4.24c-d). Upon cooling, the liquid will form into equiaxed FCC α, poor in Zn but rich in Si and Cu.

These calculations help explain why we observe incipient melting in the microstructures shown in Fig. 4.21-4.22, and why the liquid transforms to FCC α on cooling (Zn poor). However, the question remains

as to why we observe Si segregation in the first place which leads to the liquid formation. Si segregation to the grain boundary may perhaps be expected. However, the driving force for Si enrichment at the white spots within the grains and prior β grain boundaries (Fig. 4.21b) is not known. This is an interesting area for future work.

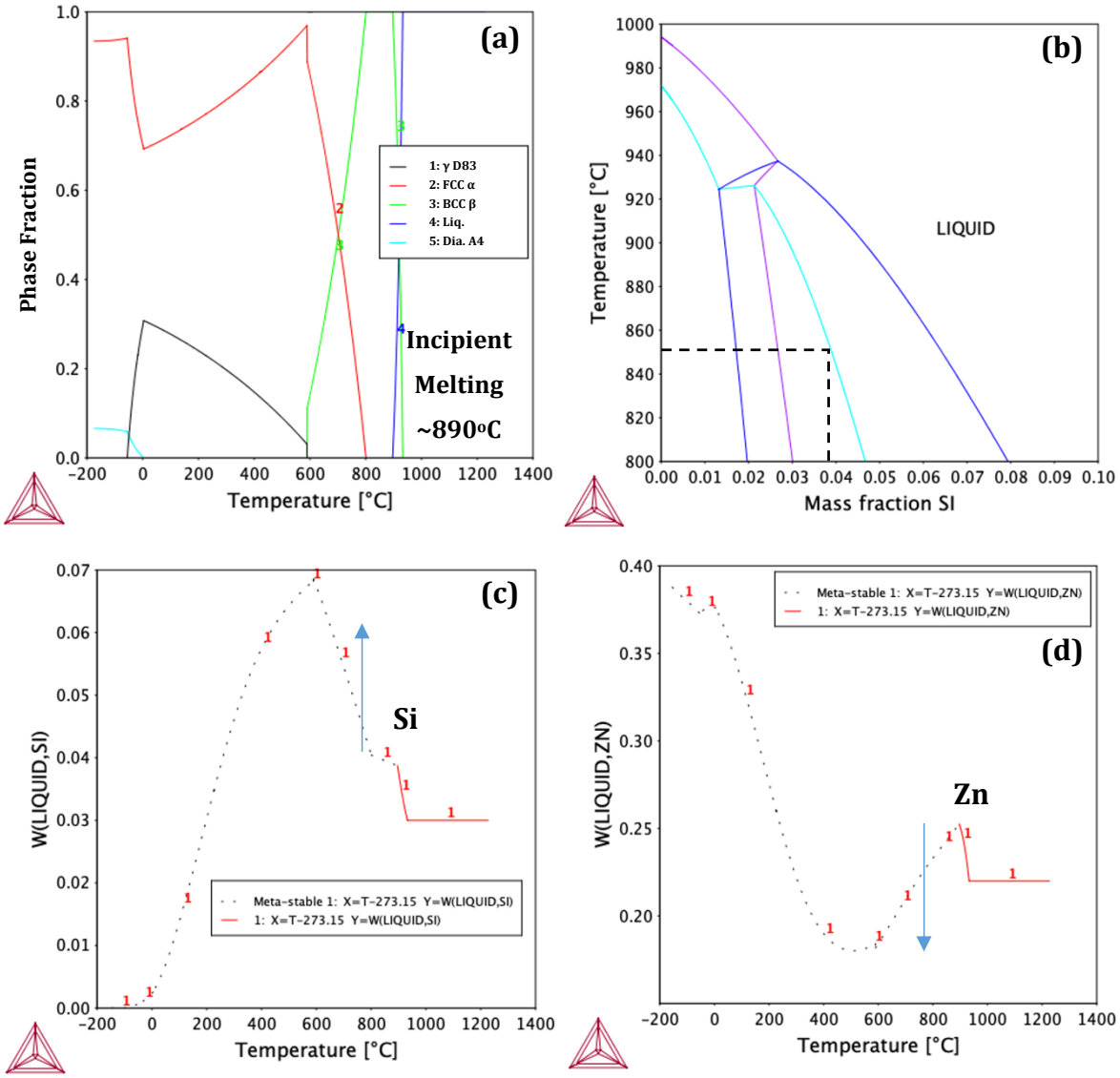


**Figure 4.24: (a) Evolution of phase fraction with temperature showing equilibrium formation of liquid for homogenous CuZn22Si3 at ~890°C, (b) CuZn22 Isopleth showing liquid formation at 850°C commences for Si content in excess of ~3.8 wt. %, (c) Increase in Si content for liquid formation, (d) decrease in Zn content for liquid formation.**

There are multiple implications to consider as a result of the observations of incipient melting in the Si-brass microstructure. Typically, a temperature range or 'window' is used in an industrial setting for the purposes of extrusion or forging, so any unexpected behaviour relating to Si segregation, particularly if it leads to incipient melting and subsequent part rejection, needs to be well understood and avoided at all costs.

In order to characterise the lower temperature microstructures of the CuZn22Si3 alloy, 5 x 15mm diameter cylindrical samples were exposed to 1-hour heat treatments in 100°C increments between 300-700°C and were then subsequently water-quenched (within 5 seconds of opening the muffle furnace). The samples then underwent metallographic preparation (at least 3mm away from any free-surface during heat treatment so as to be unaffected by oxidation) from which bulk-specimen XRD scans were completed to ascertain their respective phases present, and their phase fraction using Rietveld refinement. The XRD spectra relating to the samples heat treated at intermediate temperatures (300-500°C) is shown in Fig. 4.25.

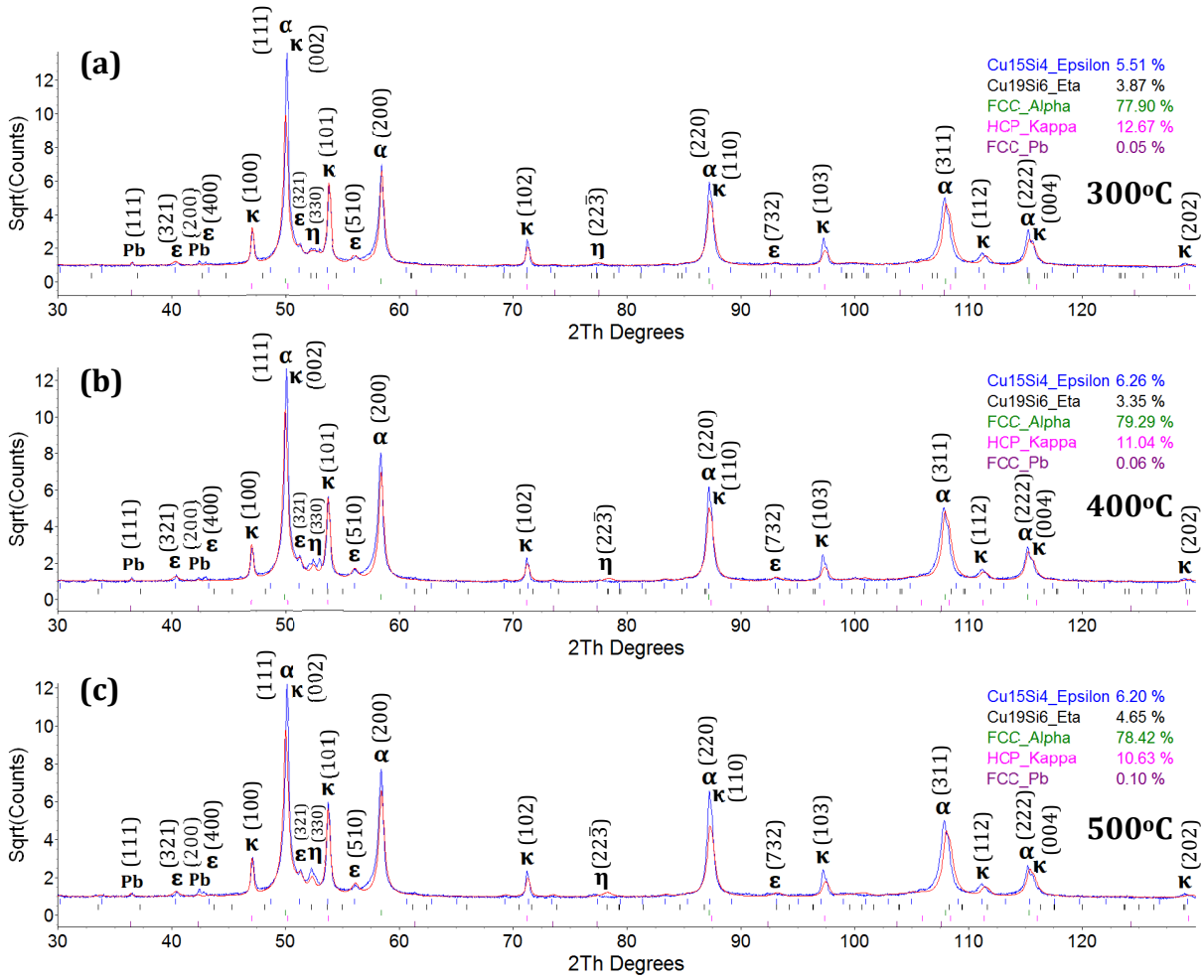


**Figure 4.25: Room-temperature bulk-specimen XRD scans (Co Kα Source – λ = 0.1789nm) of CuZn22Si3 after intermediate heat treating at (a) 300°C for 60 minutes and water-quenched, (b) 400°C for 60 minutes and water-quenched, (c) 500°C for 60 minutes and water-quenched with Rietveld refinement completed using TOPAS software.**

For each of the XRD spectra shown in Fig. 4.25 between 300-500°C, there are observed 4 different phases (in addition to the insoluble FCC Pb particles present in small amounts); FCC α, HCP κ, cubic ε, and rhombohedral η. In each case, the α phase makes up the majority of the phase fraction, with a significant contribution from κ and much smaller contributions from ε and η. The small contributions

of these phases, and weaker peak intensity, are reasons why they were not readily observed in Fig. 4.6 earlier in this Chapter where lab XRD was completed on powder (which promotes peak broadening due to strain introduced during the sample preparation process). The presence of the FCC α in large amounts is expected, however the equilibrium phase diagram (Fig. 4.3b) indicates γ should be present. This is not the case with the κ, ε, and η each absorbing varying amount of silicon present in the composition, preventing the equilibrium γ from forming. If γ is suspended in the CALPHAD calculations for CuZnSi, ε is shown to form instead (Fig. 4.26).

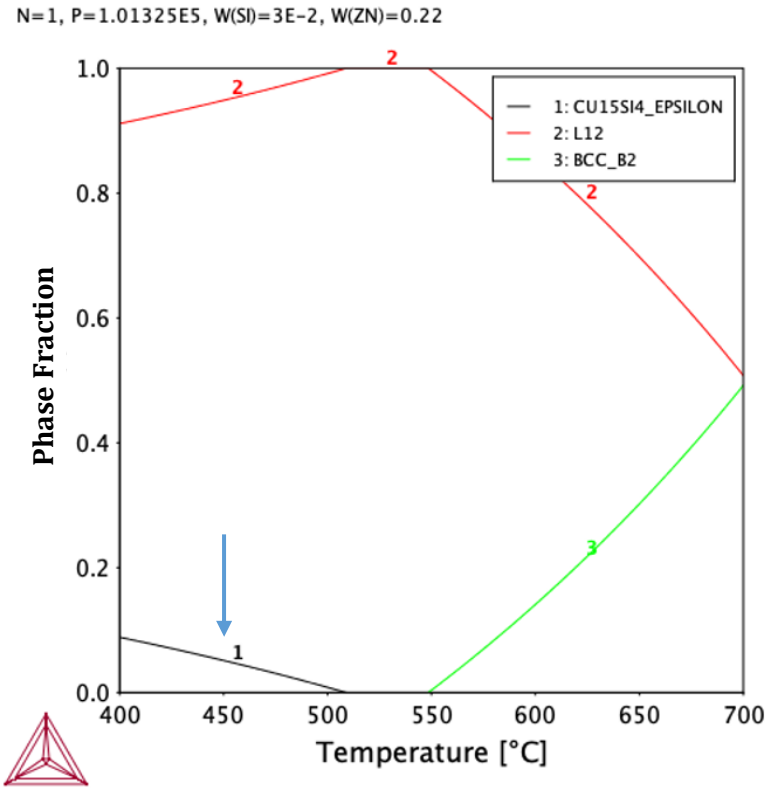


**Figure 4.26: Stabilisation of equilibrium ε (highlighted with a blue arrow) for CuZn22Si3 when γ is suspended in CALPHAD.**

The associated microstructures for these samples at 300°C, 400°C, and 500°C and SEM-EDS completed at 500°C is shown in Fig. 4.27 with each of the phases identified. It is very difficult to accurately differentiate the ε and η at these magnifications, however the EDS Si Map (Fig. 4.27d) used in combination with EDS point spectra, correlating to metallography and the XRD spectra results provide the basis for the phase identification.

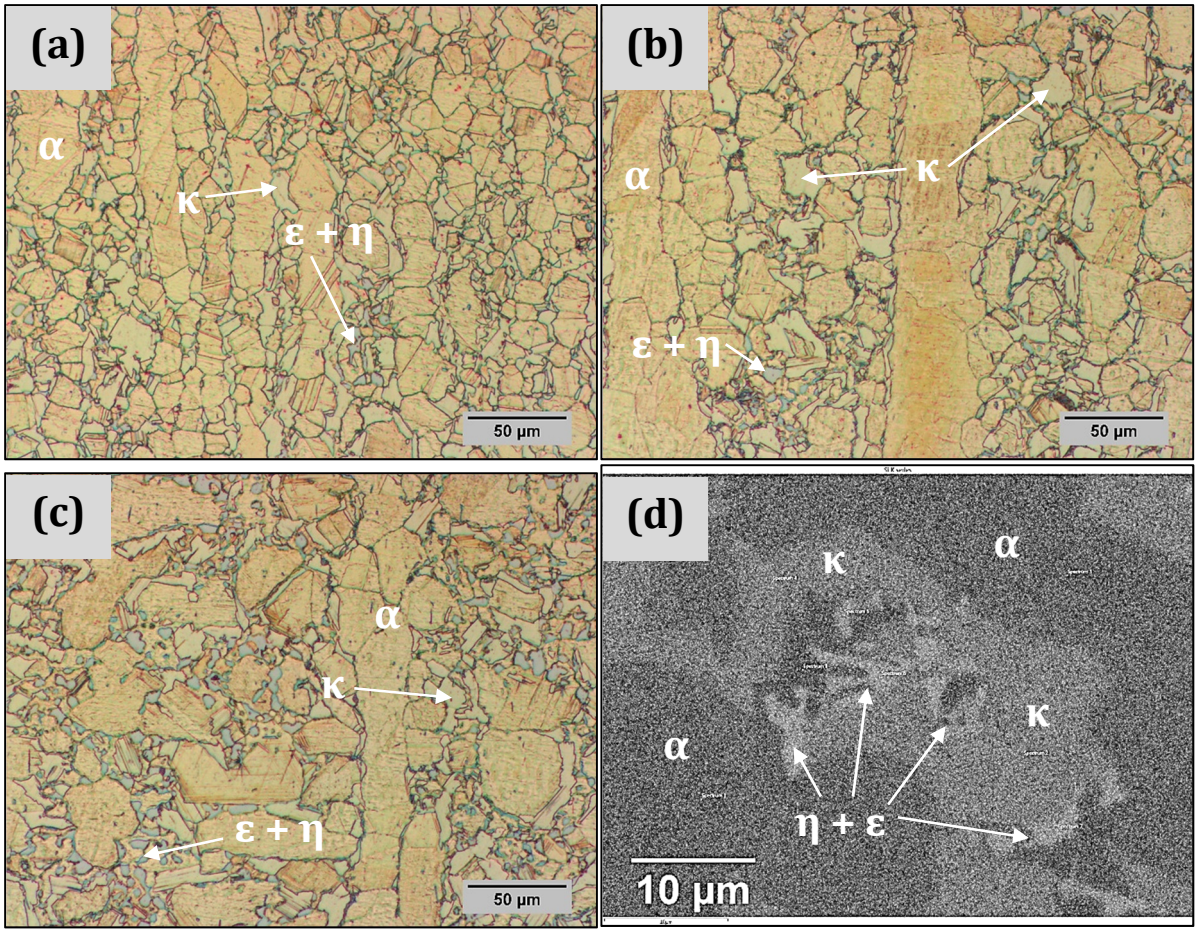


**Figure 4.27: Sample metallography of CuZn22Si3 heat treated at (a) 300°C, (b) 400°C, and (c) 500°C after a 1-hour soak time followed by water-quenching. (d) magnified SEM-EDS Si-map of the sample heat treated at 500°C in (c).**

The α phase clearly makes up the majority of the microstructures in the form of large grains with some smaller grains formed in between the other phases. The HCP κ phase appears as a lighter pale colour, a good indicator of elevated Si content as supported by the Si-map in Fig. 4.26d. Finally, the remaining small white-grey particles are very elevated in Si as shown in the EDS map, which corresponds to the ε ($Cu_{15}Si_4$) and η ($Cu_{19}Si_6$) phases.

Fig. 4.28 shows the room temperature XRD spectra of the CuZn22Si3 bulk-specimens heat treated at elevated temperatures (600-700°C). The non-equilibrium (water quenching) cooling in both of these cases has similarly led to the formation of HCP κ and rhombohedral η in the microstructure, however the cubic ε phase has not formed in either sample which indicates that it forms from the gradual migration of Si from η during intermediate heat treatment. This is supported by the additional η formed in both samples after water-quenching from these elevated temperatures (~8-11% vs. 3-5% after intermediate heat treatment). An additional difference between the phase fractions after quenching from 600-700°C is the elevated phase fraction of HCP κ at the expense of the FCC α, likely

due to the increased phase fraction of BCC β when held at these temperatures prior to quenching. This is effect is shown more strongly in the sample heat treated at 700°C with higher intensity κ peaks as it has retained ~3% more κ phase. HCP κ itself is only found at intermediate temperature ranges (550-700°C) at equilibrium (Fig. 4.3c) and this has been retained upon cooling, likely as a metastable phase.

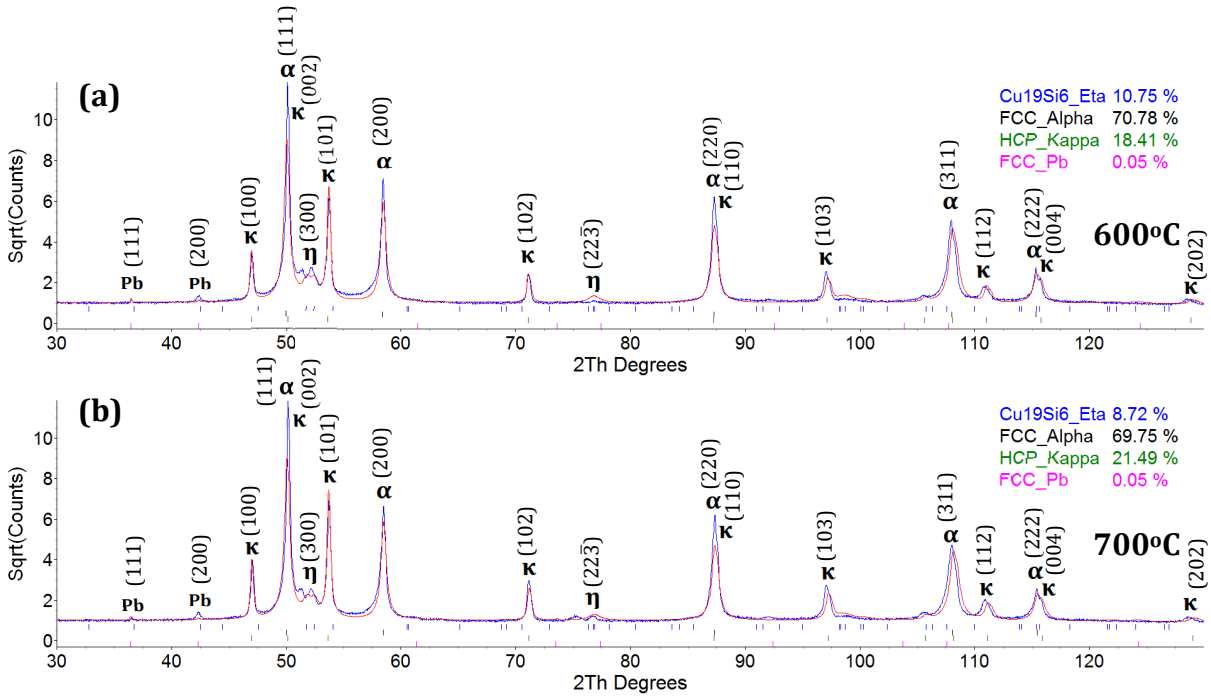


**Figure 4.28: Room-temperature bulk-specimen XRD scans (Co Kα Source) of CuZn22Si3 after elevated temperature heat treating at (a) 600°C for 60 minutes and water-quenched and (b) 700°C for 60 minutes and water-quenched with Rietveld refinement completed using TOPAS software.**

The associated microstructures for the elevated temperature (600-700°C) bulk-XRD spectra are shown in Fig. 4.29. In addition to the significantly larger α grain size compared with the intermediate temperature microstructures shown in Fig. 4.27, a mixture of the α, κ, and η grains are observed between the α. The grains of these phases are far more difficult to differentiate at this magnification, particularly the η which is very small (up to 2µm). Unlike the intermediate temperature samples (300-500°C), ε is not present in these microstructures as indicated in the XRD spectra in Fig. 4.28.

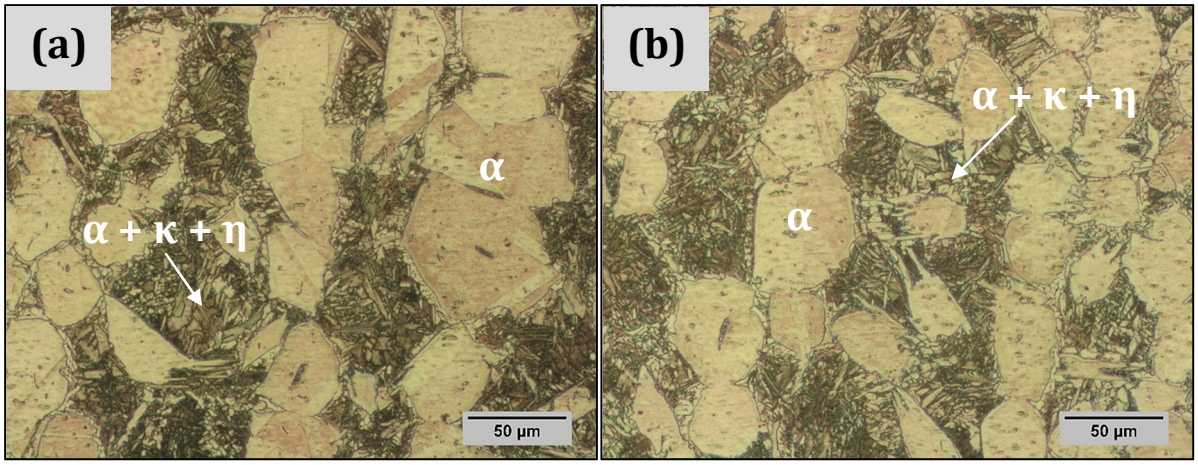


**Figure 4.29: Sample metallography of CuZn22Si3 heat treated at (a) 600°C and (e) 700°C after a 1-hour soak time followed by water-quenching.**

Compared with the other duplex brasses analysed in this Chapter, Si-bearing duplex brass is shown to have a significantly more complex phase equilibria and subsequent phase transformations, particularly under rapid cooling (water quenching) conditions. This includes:

- Observations of incipient melting after heat treatments at 850°C due to stabilisation of the β+L phase field at lower temperature as a result of Si segregation.
- The formation of several new phases after both intermediate (300-500°C) and elevated (600-700°C) temperature heat treatments. This includes ε ($Cu_{15}Si_4$), η ($Cu_{19}Si_6$) and additionally HCP κ which was previously thought to only be stable at intermediate temperatures but has been retained (perhaps as a metastable phase) at room temperature.

These complex transformations will have a significant impact on the forgeability, machinability, and cold workability of the alloy as it progresses through the processing schedule outlined in Fig. 1.3. An understanding of the above phase equilibria and transformations for duplex CuZnSi is of substantial importance given the alloy's steadily increasing use in the potable water industry.

## 4.3 Summary and Conclusions

The phase equilibria of three different families of duplex brasses; Pb-bearing, Bi-bearing, and Si-bearing, have been studied in this Chapter using a combination of the CALPHAD approach and experimental methods including x-ray diffraction for room-temperature qualitative and quantitative phase assessment, and high intensity *in-situ* Neutron diffraction to quantify the progressive equilibrium phase fractions of FCC α and BCC β at elevated temperatures.

One quaternary (CuZnSnPb) and two ternary (CuZnSn and CuZnSi) thermodynamic assessments were used to generate several isopleths to describe the three families of alloys. The insoluble nature of Pb and Bi (both liquidus above 327$^{o}$C and 271$^{o}$C respectively) made little difference to the CuZn binary phase equilibria, however Sn and Si were both shown to cause significant change. Sn inclusions were found to stabilise the BCC β, particularly at elevated temperatures, bending the (α+β) phase field towards the Cu-rich end at elevated temperatures. This has important implications for Sn-bearing duplex brass in industry which will have a larger processing window (temperature range) for optimal forging (to be explored in Chapter 5). The Si-additions add significant complexity to the phase equilibria, not only strongly stabilising BCC β, but also stabilising several new phases including cubic ε, γ and HCP κ. For a chemical ratio of CuZn21Si3, the thermodynamic description predicts the alloy should be forgeable at similar temperature ranges to standard duplex brasses available to industry.

Following the thermodynamic assessments, room-temperature XRD scans of three duplex brasses; CuZn36.5Pb2.3Sn, CuZn37.6Bi0.8Sn, and CuZn22Si3 were completed and Rietveld refinement used to quantify the phase fractions of each alloy. In both the Pb-bearing and Bi-bearing alloys, FCC α and BCC β' were observed as expected, in addition to the insoluble Pb and Bi particles in each respective case. In the Si-bearing alloy, FCC α and HCP κ were found, surprisingly without any observable complex cubic γ or ε.

Upon completion of the peak identification and Rietveld refinement at room-temperature, high intensity *in-situ* Neutron diffraction (with support from metallographic estimations) was employed to quantify the equilibrium FCC α and BCC β phase fractions of CuZn36.5Pb2.3Sn and CuZn36.9Bi0.8Sn at elevated temperatures. The method of Neutron diffraction was used due to its ability to penetrate the bulk alloy more deeply, removing any issues associated with surface effects and Zn oxidation. Within the typical industrially relevant temperature ranges of 650-800$^{o}$C, the experimentally determined phase fractions for FCC α and BCC β for both the Pb-bearing and Bi-bearing alloys were found to closely correlate to the CALPHAD calculations. By dismissing the FCC α phase fraction

contribution of Widmanstätten α grains formed during water-quenching, the metallographic estimations were also found to closely correlate with the CALPHAD calculations, and this was subsequently found to be true for two further duplex brasses; CuZn37.6Bi0.8Sn and CuZn22Si3. Phase fractions estimated from the optical metallography of these alloys produced good agreement with the CALPHAD calculations.

Detailed characterisation of CuZn22Si3 was completed to ascertain the phase equilibria of this alloy at room-temperature after a range of elevated and intermediate temperature heat treatments using lab XRD and Rietveld refinement. Several new insights can be ascertained from this characterisation:

- Heat treatment at 850$^{o}$C caused incipient melting of the microstructure, particularly along the β grain boundaries. EDS scans shows localised regions of elevated Cu and Si surrounded by regions of elevated Zn. The (β+L) phase field boundary is found at a lower temperature due to Si-segregation according to the CALPHAD calculations.
- After intermediate heat treatments (300-500$^{o}$C), 4 phases are found to form; FCC α, HCP κ, cubic ε and rhombohedral η.
- After elevated heat treatments (600-700$^{o}$C), only 3 phases are found to form; FCC α, HCP κ, and rhombohedral η. It is expected that with slower cooling rates, ε would form due to the diffusion of Si away from η, whilst Si would additionally diffuse away from the HCP κ, leading to further FCC α formation.

# 5 Elevated Temperature Plasticity

The excellent hot workability of the disordered BCC β phase is exploited during the extrusion and forging processes (Fig. 1.3) to manufacture rod and pre-form brass components with relative ease. A rule-of-thumb in the brass industry is to heat the alloy to a temperature corresponding to a phase ratio of 65% β and 35% α. However, this is not well defined in the literature for either traditional Pb-bearing brasses or the more recent 'Pb-Free' brasses entering the potable water market. The objective of Chapter 5 is to use uniaxial hot compression to determine the hot workability of several common Pb-bearing and 'Pb-Free' alloys available on the market fabricated using different methods, and at a range of temperatures and strain-rates. This evaluation will take into account an interpretation of the stress-strain curves, flow stresses, propensity to fracture, and modelling of the constitutive response using the Zener-Hollomon parameter with results being compared back to the phase equilibria studied in Chapter 4. A forgeability index is proposed for the alloys examined in this study.

## 5.1 Alloy Selection

A selection of 11 cylindrical duplex brass rods were chosen to study the effects of composition and fabrication mode on elevated temperature plasticity using uniaxial hot compression. These alloys were sourced from a variety of industry suppliers and their compositions are listed in Table 5.1 (measured using OES). The alloy composition in each case has been selected to cover a range of additions including Pb, Bi, Si, Sn, and Al (highlighted in Table 5.1) and each of these additions are expected to have an influence on the phase fraction of α and β at elevated temperatures. Cylindrical samples (dimension 15mm diameter x 25mm length) were CNC machined from each of the rods to be compressed at elevated temperatures between 550-800$^{o}$C. Three different constant crosshead displacement-rates were used of 300, 540, and 720mm/min (corresponding to an average $\dot{\varepsilon}$ of 0.35, 0.64 and 0.85$s^{-1}$ respectively) to a final height of 7mm which corresponds to a true strain of 54%. When using a constant crosshead displacement rate, the strain rate continuously increases with deformation, therefore the average strain rate was calculated and used for this study to report the true stress-strain curves.

**Table 5.1: Chemical composition (wt. %) of the investigated workpiece materials for uniaxial hot compression.**

| Alloy | U.N.S. | Cu | Zn | Pb | Bi | Si | Sn | Al | Fe | Ni | As | P |
|---|---|---|---|---|---|---|---|---|---|---|---|---|
| **CuZn39Pb2** | C37700 (CC) | 57.9 | 39.3 | 2.08 | 0.04 | <0.01 | 0.27 | 0.06 | 0.15 | 0.07 | 0.12 | <0.01 |
| **CuZn39Pb3** | C37700 (EX) | 58.1 | 38.6 | 2.85 | <0.01 | <0.01 | 0.30 | <0.01 | 0.10 | 0.10 | <0.01 | <0.01 |
| **CuZn37Pb2** | C35330 (CC) | 60.4 | 36.9 | 2.08 | 0.02 | <0.01 | 0.22 | <0.01 | 0.12 | 0.05 | 0.19 | <0.01 |
| **CuZnPb2SnFe** | *N/A Fe (EX) | 60.7 | 35.0 | 2.04 | 0.01 | 0.05 | 0.76 | 0.06 | 0.63 | 0.36 | 0.24 | <0.01 |
| **CuZnBi0.7** | C28340 (CC) | 61.5 | 37.1 | 0.17 | 0.66 | <0.01 | 0.40 | <0.01 | 0.02 | <0.01 | 0.12 | <0.01 |
| **CuZnBi0.8** | C49265 (EX) | 60.9 | 37.5 | 0.23 | 0.80 | <0.01 | 0.33 | <0.01 | 0.01 | <0.01 | 0.09 | 0.11 |
| **CuZnBi2Sn** | C49260 (EX) | 61.6 | 34.7 | 0.06 | 1.95 | <0.01 | 1.31 | <0.01 | 0.03 | 0.27 | <0.01 | 0.07 |
| **CuZnSi** | C69300 (EX) | 75.6 | 21.1 | 0.03 | <0.01 | 3.09 | <0.01 | <0.01 | 0.01 | <0.01 | <0.01 | 0.10 |
| **CuZn37** | C27451 (EX) | 62.4 | 36.9 | 0.17 | <0.01 | <0.01 | 0.10 | 0.03 | 0.02 | 0.22 | 0.14 | <0.01 |
| **CuZnSn** | C46500 (EX) | 63.1 | 35.8 | 0.15 | <0.01 | <0.01 | 0.56 | 0.04 | 0.16 | 0.05 | 0.04 | 0.03 |
| **CuZnAl** | *N/A Al (EX) | 62.4 | 36.6 | 0.17 | <0.01 | <0.01 | 0.02 | 0.56 | 0.05 | 0.10 | 0.11 | <0.01 |

***(CC) = continuous cast rod, (EX) = extruded rod, N/A = no associated UNS alloy number.**

The objectives of these hot compression experiments are to deduce:

- How strongly each alloying addition and the overall Cu-Zn ratio influences the flow stresses during compression and the subsequent susceptibility to fracture of each alloy.
- How significant the fabrication mode (continuously cast vs. extruded) is in dictating the stress-strain behaviour and subsequent susceptibility to fracture.
- The peak and steady-state stress dependence on temperature and strain-rate.
- Develop a forgeability index based on visual assessment of the samples post-compression.
- Develop a constitutive modelling approach for estimating the steady-state flow stress of a given duplex brass under compression.

Using the thermodynamic descriptions verified in Chapter 4, an estimation of the β phase present in each of the alloys listed in Table 5.1 is shown in Table 5.2 at each of the hot compression temperatures. This is important when assessing the elevated temperature properties of duplex brass given the significantly more plastic behaviour of the BCC β phase compared to the FCC α. Each of the alloys listed in Table 5.2 had Boron Nitride lubricated cylindrical samples compressed in 50$^{o}$C increments between 550$^{o}$C to 750$^{o}$C for each of the three strain-rates after holding for a soak time of 10 minutes. Samples compressed at the highest displacement-rate of 720mm/min were additionally compressed at 800$^{o}$C. True stress-strain curves are reported using an average strain-rate. A total of 525 compression tests were completed as part of this study.

**Table 5.2: Estimated BCC β phase fraction (%) of the investigated workpiece materials for uniaxial hot compression using CALPHAD calculations.**

| Alloy | U.N.S. | 550°C | 600°C | 650°C | 700°C | 750°C | 800°C |
|---|---|---|---|---|---|---|---|
| **CuZn39Pb2** | C37700 (CC) | 43.1 | 54.3 | 68.4 | 85.8 | 100 | 100 |
| **CuZn39Pb3** | C37700 (EX) | 35.5 | 46.8 | 60.3 | 77.2 | 99.0 | 100 |
| **CuZn37Pb2** | C35330 (CC) | 3.1 | 11.6 | 22.4 | 36.5 | 55.0 | 79.4 |
| **CuZnPb2SnFe** | *N/A Fe (EX) | 5.6 | 14.1 | 23.9 | 36.5 | 52.8 | 74.3 |
| **CuZnBi0.7** | C28340 (CC) | 8.1 | 16.7 | 27.0 | 40.5 | 58.4 | 82.4 |
| **CuZnBi0.8** | C49265 (EX) | 11.0 | 19.8 | 30.6 | 44.8 | 63.8 | 89.0 |
| **CuZnBi2Sn** | C49260 (EX) | 16.4 | 25.8 | 36.0 | 48.6 | 64.8 | 86.6 |
| **CuZnSi** | C69300 (EX) | 0 | 9.6 | 26.1 | 44.9 | 67.7 | 94.8 |
| **CuZn37** | C27451 (EX) | 0 | 0 | 0 | 10.1 | 28.1 | 52.3 |
| **CuZnSn** | C46500 (EX) | 0 | 6.2 | 14.6 | 25.2 | 40.2 | 60.5 |
| **CuZnAl** | *N/A Al (EX) | 17.0 | 25.0 | 36.6 | 50.6 | 69.3 | 94.5 |

***(CC) = continuous cast rod, (EX) = extruded rod, N/A = no associated UNS alloy number.**

## 5.2 Experimental Results

Experimental true stress-strain curves are reported throughout this Chapter from which peak flow stresses and steady-state flow stresses (MPa) were extracted for further analysis and modelling (Section 5.4). An example comparison of this data at 700°C and for an applied average strain rate of $0.85s^{-1}$ is shown in Table 5.3. For each temperature and applied strain rate condition used throughout this study, multiple tests were performed to show reproducibility. The peak flow stresses ($\sigma_p$) were determined for each alloy by averaging the maximum initial peak values for each curve. If multiple initial peak curves exist (for example, with cases of multiple recrystallisation waves), the largest value would be used in each case. For the steady-state flow stress ($\sigma_{ss}$), average values were derived from the curve after the softening region, that is when competition between recrystallisation and strain-hardening is equal.

**Table 5.3: Comparison of peak and steady-state flow stress (MPa) against the estimated β phase fraction (%) for each of the 11 duplex brasses at T = 700°C and $\dot{\varepsilon} = 0.85s^{-1}$.**

| Alloy | Peak Flow Stress (MPa) | Steady-State Flow Stress (MPa) | β phase fraction (%) |
|---|---|---|---|
| **CuZn39Pb2** | 13.1 | 13.0 | 85.8 |
| **CuZn39Pb3** | 16.9 | 16.7 | 77.2 |
| **CuZn37Pb2** | 25.4 | 24.2 | 36.5 |
| **CuZnPb2SnFe** | 31.3 | 30.2 | 36.5 |
| **CuZnBi0.7** | 28.3 | 26.8 | 40.5 |
| **CuZnBi0.8** | 23.0 | 22.5 | 44.8 |
| **CuZnBi2Sn** | 36.9 | 35.1 | 48.6 |
| **CuZnSi** | 27.8 | 25.9 | 44.9 |
| **CuZn37** | 48.3 | 44.0 | 10.1 |
| **CuZnSn** | 46.9 | 45.8 | 25.2 |
| **CuZnAl** | 30.3 | 30.1 | 50.6 |

## 5.2.1 Leaded Brasses

### 5.2.1.1 Traditional Continuous Cast vs. Extruded Pb-Brass

The uniaxial hot compression true stress (MPa) vs. true strain (%) curves for the continuous cast CuZn39Pb2 alloy and the extruded CuZn39Pb3 alloy are shown as a function of temperature (550-800°C) and average strain-rate ($\dot{\varepsilon}$ = 0.35, 0.64, 0.85$s^{-1}$) compressed to ε=0.54 in Fig. 5.1a-c and Fig. 5.2a-c, respectively. During compression, these curves reach an initial peak stress ($\sigma_p$) followed by a gradual decrease in flow stress. This decrease is usually attributed to dynamic recrystallisation (DRX) [58]. A steady-state stress ($\sigma_{SS}$) is achieved in which the competition between strain-hardening and softening due to DRX is equal. A final increase in flow stress is observed after 50% strain due to the increased friction between the hot compression platens and the increased surface area of the compressed sample.

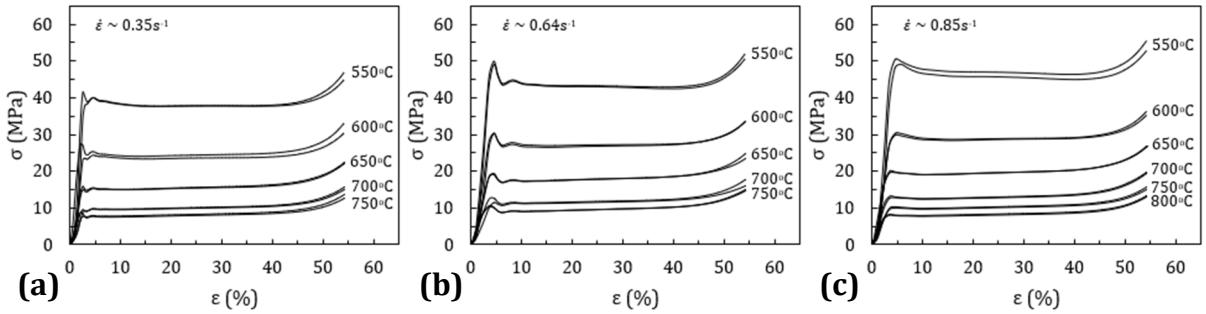


**Figure 5.1: Stress-strain curves as a function of temperature for continuous cast CuZn39Pb2 with average applied strain rates of (a) 0.35$s^{-1}$, (b) 0.64$s^{-1}$ and (c) 0.85$s^{-1}$. Multiple tests are performed at each temperature to show reproducibility.**

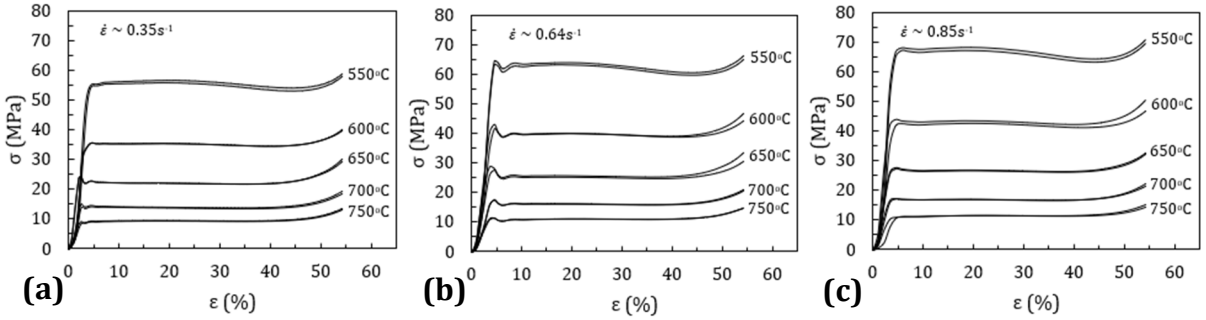


**Figure 5.2: Stress-strain curves as a function of temperature for extruded CuZn39Pb3 with average applied strain rates of (a) 0.35$s^{-1}$, (b) 0.64$s^{-1}$ and (c) 0.85$s^{-1}$.**

Due to the formation of disordered β in the CuZn39Pb2 microstructure at elevated temperatures, the peak and steady-state flow stresses of this alloy are strongly temperature dependent. This effect is particularly pronounced for 50°C increments at lower temperatures. For example, the decrease in flow stress from 550°C to 600°C is approximately 18MPa at an average strain-rate of 0.85$s^{-1}$ (estimated change from 43.1 vol. % to 54.3 vol. % β phase), while the difference observed from 700°C to 750°C for the same condition is only approximately 3MPa (estimated change from 85.8 vol. % to 100 vol. %

β phase). This indicates that a significant volume fraction of FCC α phase can remain in the microstructure whilst achieving a significant drop in the flow stress with temperature.

As expected, we observe an increase in the flow stresses with increased average strain-rate. For higher temperatures and lower strain-rates, the initial peak stress is reached more quickly, and in the case of the average strain-rates $0.35s^{-1}$ and $0.64s^{-1}$, multiple stress peaks are observed. This indicates that for these strain-rates, multiple waves of recrystallisation are occurring within the microstructure. This phenomenon is described by Luton et al. [229] who explained that if the time it takes to reach a critical strain for DRX initiation is longer than the time it takes for the alloy system to completely recrystallise, then there is a separation between recrystallisation cycles and therefore multiple oscillations in the hot compression curve are observed. At $0.85s^{-1}$, the deformation rate is too fast for multiple peaks to be observed. A similar flow stress dependence on temperature and strain-rate is observed for both the continuous cast CuZn39Pb2 and extruded CuZn39Pb3 alloys, however the effects of DRX are less pronounced in the extruded CuZn39Pb2.

Compared to the continuous cast CuZn39Pb2, the extruded CuZn39Pb3 alloy shows a significantly higher average flow stress (both $\sigma_p$ and $\sigma_{SS}$). For example, at a temperature of 650°C and an average strain-rate of $0.64s^{-1}$, the extruded brass shows a flow stress >40% greater than the continuous cast variant (Fig. 5.1b vs. Fig. 5.2b). This is likely due to a combination of CuZn39Pb3 having 0.7 wt. % less Zn (and thereby ~8.1 vol. % less β phase at 650°C) and having a grain directionality in the direction parallel to the compressive forces due to the extrusion fabrication process (Fig. 5.3). Generally speaking, these two alloys are expected to have the lowest average flow stresses of the group of brasses tested due to their high Zn content and consequently, high β phase fraction (Table 5.2).

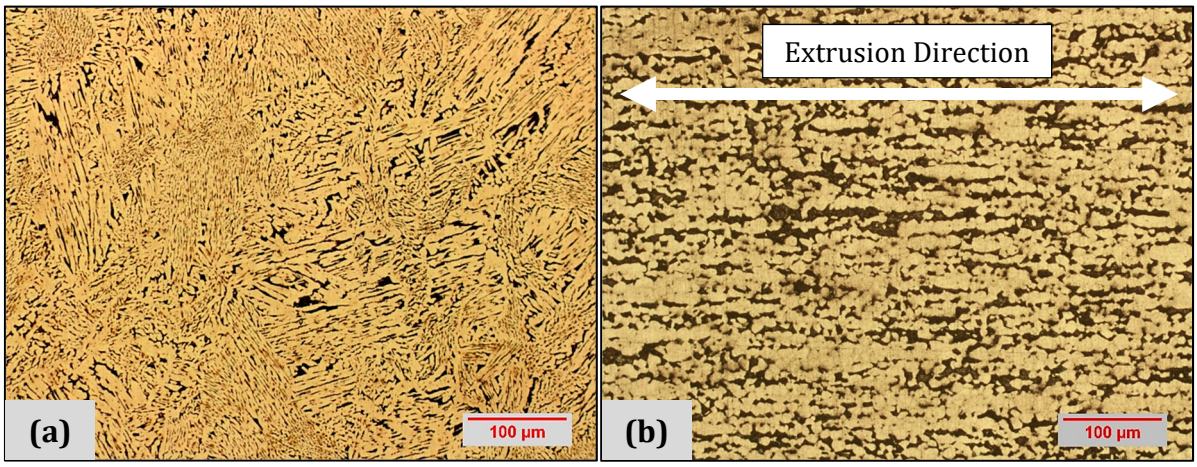


**Figure 5.3: As-fabricated (a) continuous cast CuZn39Pb2 and (b) extruded CuZn39Pb3 microstructure with highlighted grain directionality.**

### 5.2.1.2 DZR Continuous Cast vs. Extruded Pb-Brass

As a comparison to 'traditional' leaded brasses fabricated via different processes (Section 5.2.1.1), the uniaxial hot compression true stress (MPa) vs. true strain (%) curves for the continuous cast CuZn37Pb2 alloy and the extruded CuZnPb2SnFe alloy are shown as a function of temperature (550-800°C) compressed to ε=0.54 in Fig. 5.4. Higher in Cu than those alloys hot compressed in the previous Section (5.2.1.1), the CuZn37Pb2 and CuZnPb2SnFe alloys both have significantly higher peak stresses as a result of having less β vol. % in their microstructures (on average ~38% less per 50°C incremental condition). Although relatively stable at higher temperatures, the flow curves at 550°C and 600°C do not reach a steady-state stress prior to the completion of the hot compression test. Both alloys contain greater than 80 vol. % α at these temperatures.

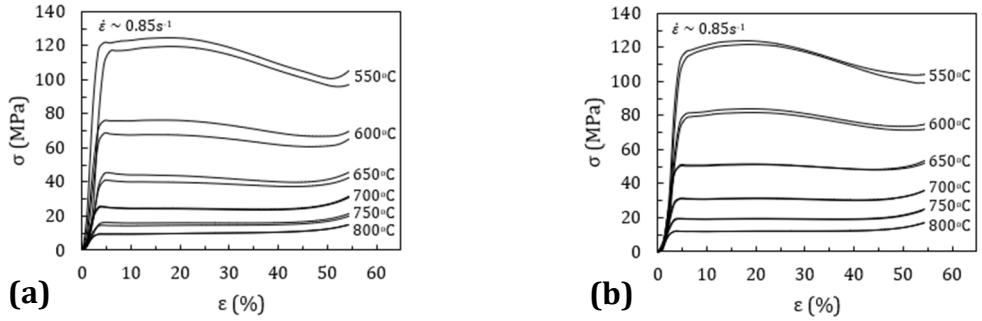


**Figure 5.4: Stress-strain curves as a function of temperature for (a) continuous cast CuZn37Pb2 and (b) extruded CuZnPb2SnFe with an average applied strain rate of 0.85s$^{-1}$.**

A comparison of these two alloys shows that the extruded CuZnPb2SnFe alloy has a slightly higher average flow stress across the range of temperatures for an average strain-rate of 0.85s$^{-1}$. Although it could be argued there is less Zn in this alloy, it does contain a significant wt. % of Sn which would be expected to have a greater β stabilising effect. Thermodynamic calculations (Table 5.2) indicate these two alloys have no more than 5% difference in β phase fraction for all of the conditions tested. The difference is likely generated by the anisotropy of the grain structure resulting from the different fabrication mode.

## 5.2.2 Bismuth Brasses

### 5.2.2.1 Continuous Cast vs. Extruded Bi-Brass

The uniaxial hot compression true stress (MPa) vs. true strain (%) curves for the continuous cast CuZnBi0.7 alloy and the extruded CuZnBi0.8 alloy are shown as a function of temperature (550-800°C) and average strain-rate ($\dot{\varepsilon}$ = 0.35, 0.64, 0.85s$^{-1}$) compressed to ε=0.54 in Fig. 5.5a-c and Fig. 5.6a-c, respectively. As was observed with each of the leaded brasses (Section 5.2.1), we note an increase in the flow stress with decreasing temperature and increasing strain-rate for these bismuth brasses. At

an average strain-rate of $0.64s^{-1}$, for example, the $\sigma_p$ of CuZnBi0.7 increases from 16 to 104 MPa for a decrease in temperature from 750°C to 550°C (coinciding with 58.4 and 8.1 vol. % β respectively), whilst at 650°C the increase in average strain-rate from $0.35s^{-1}$ to $0.85s^{-1}$ increases the $\sigma_p$ from 38.6 to 45 MPa.

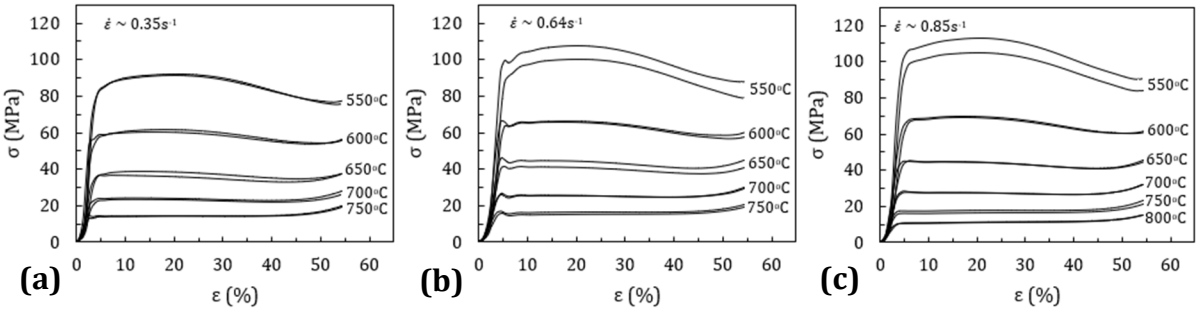


**Figure 5.5: Stress-strain curves as a function of temperature for continuous cast CuZnBi0.7 with average applied strain rates of (a) $0.35s^{-1}$, (b) $0.64s^{-1}$ and (c) $0.85s^{-1}$.**

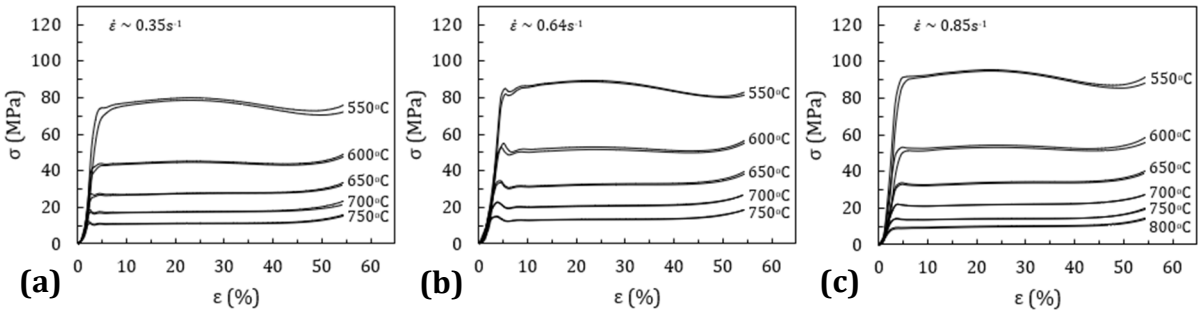


**Figure 5.6: Stress-strain curves as a function of temperature for extruded CuZnBi0.8 with average applied strain rates of (a) $0.35s^{-1}$, (b) $0.64s^{-1}$ and (c) $0.85s^{-1}$.**

As a comparison with the leaded brasses tested in Section 5.2.1, we observe a significant peak stress broadening whereby for CuZnBi0.7 the $\sigma_p$ isn't reached until approximately 18% strain at the lower temperatures. This appears to be consistent with the elevated Cu alloys in this study and is likely the result of additional strain being accommodated in the FCC α phase prior to DRX becoming the greater contributor to the flow stress softening. This is an important observation as the FCC α will experience DRX while the fast diffusion of vacancies in the BCC β will favour dynamic recovery.

If we compare the extruded CuZnBi0.8 stress-strain curves (Fig. 5.6) with the continuous cast CuZnBi0.7 (Fig. 5.5), we note a general reduction in the average flow stress for otherwise similar conditions. Whilst we would assume that the grain anisotropy of the extruded CuZnBi0.8 alloy would contribute to a higher flow stress, there is a shift in the Cu and Zn wt. % in favour of stabilising the BCC β phase at elevated temperatures for this alloy. Therefore, we observe that the average flow stress for this alloy is less than the CuZnBi0.7, in spite of the fact that it is extruded as opposed to

continuously cast. This indicates that the composition of these alloys, and therefore the α and β phase fraction, are the dominant factor in determining flow stress behaviour. Any influence of fabrication mode must be secondary in this regard.

### 5.2.2.2 Elevated Bi Alloys

The uniaxial hot compression true stress (MPa) vs. true strain (%) curves for the extruded CuZnBi2Sn alloy are shown in Fig. 5.7a-c as a function of temperature (550-800°C) and average strain-rate ($\dot{\varepsilon}$ = 0.35, 0.64, 0.85$s^{-1}$) compressed to ε=0.54. Due to the inclusion of almost 2 wt. % Bi, this alloy contains significantly less Zn wt. % than either CuZnBi0.7 or CuZnBi0.8, which has subsequently caused the average flow stress to increase substantially. At equilibrium, the inclusion of ~1.3 wt. % Sn would serve to stabilise enough β at each temperature to decrease the average flow stress. However, this is not occurring due to the interaction with the very high level of Bi (~1.95 wt. %) in the composition which causes intermetallics to form, particularly at the lower temperatures of 550°C and 600°C. Otherwise, the curves appear to generally follow the same flow stress behaviour as the other Bi alloys. Being liquid in this temperature range, we would expect the Bi to play little part in the flow stress behaviour of the material, but perhaps affect the propensity to fracture which will be explored in Section 5.3.2.

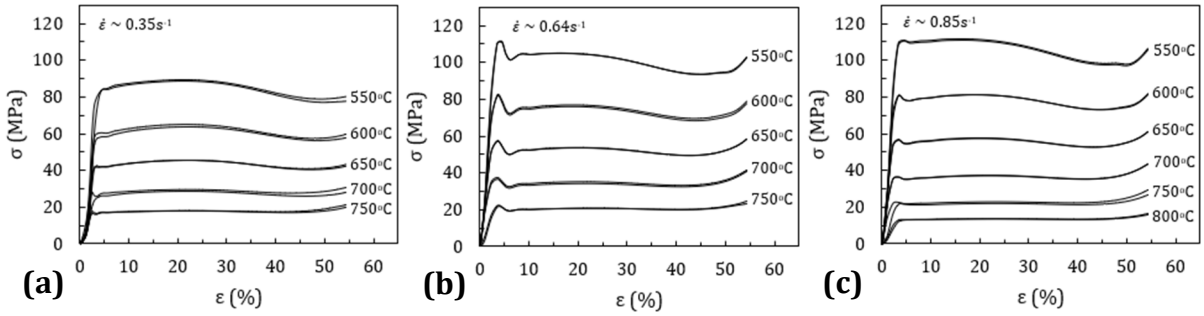


**Figure 5.7: Stress-strain curves as a function of temperature for extruded CuZnBi2Sn with average applied strain rates of (a) 0.35$s^{-1}$, (b) 0.64$s^{-1}$ and (c) 0.85$s^{-1}$.**

## 5.2.3 Silicon Brasses

The uniaxial hot compression true stress (MPa) vs. true strain (%) curves for the extruded CuZnSi alloy are shown as a function of temperature (550-800°C) and average strain-rate ($\dot{\varepsilon}$ = 0.35, 0.64, 0.85$s^{-1}$) compressed to ε=0.54 in Fig. 5.8a-c. These curves exhibit a remarkably different flow stress behaviour to any of the leaded or bismuth brasses discussed so far. One may observe the significantly higher peak stresses for lower temperatures at 550°C to 600°C. This is associated with both the presence of the very hard κ phase (~6 vol. % at 550°C) and the lack of β phase fraction due to the elevated Cu content. For example, at an average strain-rate of 0.85$s^{-1}$, the CuZn37Pb2 alloy produces a $\sigma_P$ of 122MPa at 550°C where very little β is expected to be available, whilst the CuZnSi alloy produces a $\sigma_P$

of 187MPa (53% increase) for the same experimental conditions. In practice, this would likely translate into accelerated tool wear for forging at these temperatures as much greater forces are required to allow the metal to flow through the die.

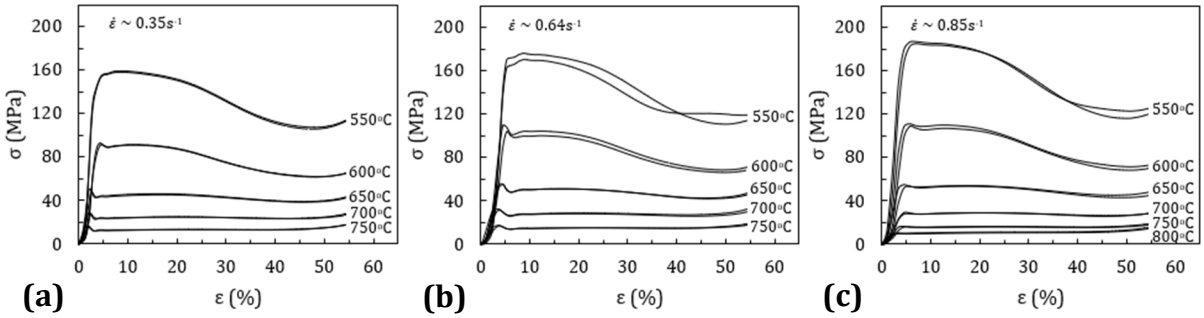


**Figure 5.8: Stress-strain curves as a function of temperature for extruded CuZnSi with average applied strain rates of (a) 0.35s$^{-1}$, (b) 0.64s$^{-1}$ and (c) 0.85s$^{-1}$.**

The more important feature in these curves is the dramatic reduction in this peak stress as the temperatures are further increased and the β phase begins to form. This stabilisation of β still occurs despite the Cu-Zn compositional ratio and is only possible due to the presence of the Si. Analysing these features from an industrial forging standpoint, if the typical temperatures used for duplex brasses (approximately 700-750°C) were applied to this Si-bearing alloy, then it would appear to show very similar flow stresses. For example, at an average strain-rate of 0.85s$^{-1}$, the CuZnBi0.8 alloy produces a $\sigma_P$ of 14.3MPa at 750°C, whilst the CuZnSi alloy produces a $\sigma_P$ of 16.0MPa for the same experimental conditions.

The observations above illustrate that although the processing window for Si-brasses may be smaller than either of the leaded brasses or bismuth brasses due to the formation of the harder κ and γ phases at lower forging temperatures, the stresses encountered at otherwise optimal forging temperatures for standard duplex brasses are much the same for the CuZnSi alloy in spite of the significant differences in Cu and Zn wt. %. This is the first time these effects on flow stress behaviour have been shown and described.

## 5.2.4 Alternative Brasses – Binary, Al-, Sn-bearing

### 5.2.4.1 Binary Cu-Zn

The focus so far has been on comparing three of the most common families of duplex brasses used in the plumbing industry (CuZnPb, CuZnBi, CuZnSi). However, it is also useful to compare these alloys against some alternatives, including a simple binary alloy CuZn37. The uniaxial hot compression true stress (MPa) vs. true strain (%) curves for the extruded CuZn37 alloy are shown as a function of temperature (550-800°C) and average strain-rate ($\dot{\varepsilon}$ = 0.35, 0.64, 0.85s$^{-1}$) compressed to ε=0.54 in Fig.

5.9a-c. This simple CuZn37 alloy tends to mirror much of the flow stress behaviour exhibited in the case of the continuous cast CuZnBi0.7 alloy except the average flow stress is somewhat higher for each condition. It can be noticed that the change in flow stress with each 50°C increment from 550°C to 700°C is roughly equal. This is because the BCC β phase is not expected to commence formation in the microstructure until just under 700°C. This is due to the Cu wt. % of 62.4 which is higher than any other alloy so far tested in this study, with the exception of CuZnSi which has β stabilised due to the presence of Si. As a result, for each condition tested, there is a significant contribution to the flow stress behaviour from the FCC α phase. From an industrial standpoint, it is expected this would be an incredibly difficult alloy to forge due to the higher temperatures required to stabilise enough β phase for the material to flow uniformly, and the anticipated acceleration in tool wear.

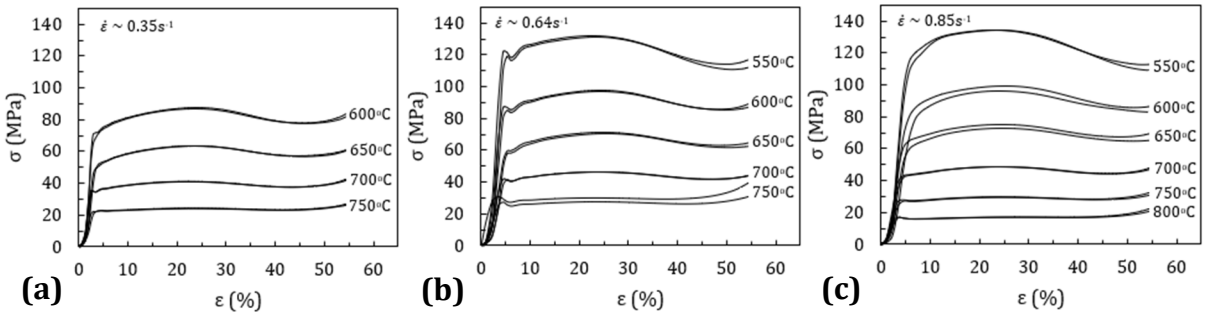


**Figure 5.9: Stress-strain curves as a function of temperature for extruded CuZn37 with average applied strain rates of (a) 0.35s$^{-1}$, (b) 0.64s$^{-1}$ and (c) 0.85s$^{-1}$.**

### 5.2.4.2 Extruded Sn-bearing vs. Extruded Al-bearing

Two other alternative alloys which are available for use in 'lead-free' markets are those that contain either Sn or Al as the tertiary constituent. The uniaxial hot compression true stress (MPa) vs. true strain (%) curves for the extruded CuZnSn alloy and the extruded CuZnAl alloy are shown as a function of temperature (550-800°C) and average strain-rate ($\dot{\varepsilon}$ = 0.35, 0.64, 0.85s$^{-1}$) compressed to ε=0.54 in Fig. 5.10a-c and Fig. 5.11a-c respectively.

Similar to the binary CuZn37 (Fig. 5.9), CuZnSn (also known as Naval Brass) has a high average flow stress compared with the other alloys so far tested. This is due to a Cu wt. % of 63.1 preventing a significant amount of β phase forming at the lower temperature conditions. The Sn present in the alloy (~0.56 wt. %) does help stabilise the BCC phase however, which prevents the average flow stresses from being significantly higher than the CuZn37 alloy. Given the normal Cu wt. % ranges for Naval Brass are 59-62 wt. % it is expected that the Sn would yield a more positive effect on the flow stress behaviour in this range.

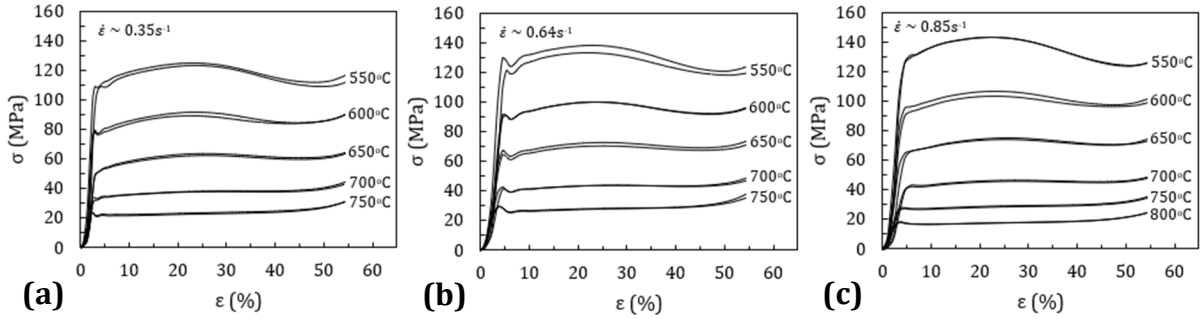


**Figure 5.10: Stress-strain curves as a function of temperature for extruded CuZnSn with average applied strain rates of (a) 0.35$s^{-1}$, (b) 0.64$s^{-1}$ and (c) 0.85$s^{-1}$.**

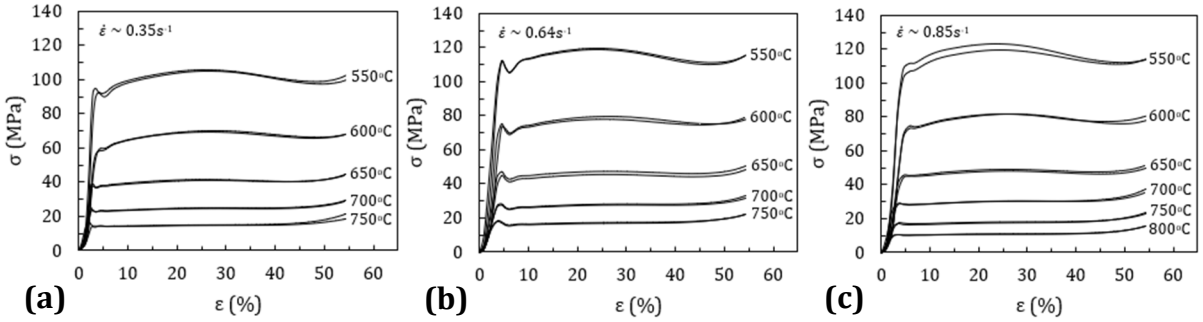


**Figure 5.11: Stress-strain curves as a function of temperature for extruded CuZnAl with average applied strain rates of (a) 0.35$s^{-1}$, (b) 0.64$s^{-1}$ and (c) 0.85$s^{-1}$.**

Al-bearing alloys are not commonly used in the potable water industry, however due to their positive effects during casting and on certain mechanical properties, they are becoming more common in niche applications. Although the CuZnAl alloy has the same Cu content (62.4 wt. %) as the binary CuZn37 alloy, the Al (0.56 wt. %) is very effective at stabilising a significant amount of the BCC β phase in the alloy, thus decreasing the average flow stress of the material. For example, at 700°C and an average strain-rate of 0.64$s^{-1}$, the CuZn37 alloy has a $\sigma_{SS}$ of ~42MPa (coinciding with 10.1 vol. % β), while the CuZnAl alloy has a $\sigma_{SS}$ of ~28MPa (coinciding with 50.6 vol. % β).

Generally speaking, it is not difficult to conclude that the duplex brasses containing a significant wt. % of Zn, thus allowing the most BCC β to form in the alloy, are the best alloys to use for the purposes of producing low flow stresses with a uniform stress-strain curve behaviour. The alloys with higher amounts of Cu and lacking any significant alloying additions such as Si or Al, will generally increase the flow stresses, which under production conditions will lead to greater power requirements, accelerated tool wear, and likely higher rejection rates for larger or more complex geometries where uniform material flow through the die is of principal importance.

## 5.3 Forgeability Index

After hot compression, the brass samples were retained for visual assessment and qualitatively ranked according to a forging index developed in this study. The index, ranked from 0 to 100, with 100 being the most ideal duplex brass for forging purposes, is determined primarily by two factors;

1. Flow stress behaviour as discussed in Section 5.2.
2. Propensity to fracture under simple uniaxial compression conditions.

In order to best observe and assess the alloy's propensity to fracture, samples compressed at an average strain-rate of $0.85s^{-1}$ were stacked in 50°C increments according to their compression testing temperature starting from 550°C to 800°C. In the following section, these compression stacks are presented and a forgeability index rating given.

Table 5.4 presents a summary of the observations of fracture for each of the duplex brasses uniaxially hot compressed in this study as a function of temperature. There was only one alloy observed to have a perfect processing window between 550°C – 800°C and that was CuZnSn. However, this same alloy was shown to have the highest flow stress which will be discussed further in Section 5.3.4.

**Table 5.4: Summary of temperature conditions vs. observation of fracture (O = No Fracture, X = Fracture, H = Hairline or Very Close to Fracture, W = Wrinkling, - = Not Tested).**

| Alloy | 550°C | 600°C | 650°C | 700°C | 750°C | 800°C |
|---|---|---|---|---|---|---|
| **CuZn39Pb2** | O | O | O | X | X | X |
| **CuZn39Pb3** | H | O | O | O | O | - |
| **CuZn37Pb2** | X | X | H | O | O | O |
| **CuZnPb2SnFe** | X | X | X | H | O | O |
| **CuZnBi0.7** | X | X | X | O | O | O |
| **CuZnBi0.8** | X | H | O | O | O | O |
| **CuZnBi2Sn** | X | X | X | X | H | H |
| **CuZnSi** | O | O | O | O | O | W |
| **CuZn37** | H | X | X | H | X | X |
| **CuZnSn** | O | O | O | O | O | O |
| **CuZnAl** | X | O | O | O | O | O |

In determining the relevant forgeability index for each of the duplex brasses, each alloy was given an initial rating of 100. For each temperature that fracture was readily observed, 10 points were removed (for a hairline or wrinkle condition 5 points removed) as this represents a reduction in the total processing window for the operator in an industrial setting. From this point the highest-ranking alloy for peak stress (i.e. the lowest peak stress during compression) was given +20 points, the next best +15 points, the next best +10 points and so on subtracting 5 points for each rank until the last alloy

was given -30 points. This closely correlates with ease of metal flow through a forging die and the power/pressure required of the forging press to complete its cycle.

Table 5.5 presents a ranking summary for each of the 11 duplex brasses examined in this study (according to peak stress ranking, fracture ranking and a combined total ranking) and subsequent forgeability index. The fracture ranking is determined by how wide the processing (i.e. temperature) window is for each alloy within the range of temperatures tested in this study (550-800°C) where signs of fracture are not exhibited. The peak stress ranking is determined by the MPa values (with the lowest value being the best) in the middle of the respective processing window for each alloy (i.e. the MPa value corresponding to the median temperature within the range where no signs of fracture are observed). The highest ranking, CuZn39Pb3, was given a forgeability index score of 100, whilst the lowest ranking, CuZn37, was given a forgeability index score of 25.

**Table 5.5: Summary of forgeability index ratings for each of the alloys tested under uniaxial hot compression.**

| Alloy | U.N.S. | Peak Stress Ranking | Fracture Ranking | Total Ranking | Forgeability Rating |
|---|---|---|---|---|---|
| **CuZn39Pb2** | C37700 (CC) | 1 | 6 | 3 | **90** |
| **CuZn39Pb3** | C37700 (EX) | 2 | 3 | 1 | **100** |
| **CuZn37Pb2** | C35330 (CC) | 4 | 7 | 5 | **80** |
| **CuZnPb2SnFe** | *N/A Fe (EX) | 8 | 9 | 9 | **50** |
| **CuZnBi0.7** | C28340 (CC) | 5 | 8 | 7 | **70** |
| **CuZnBi0.8** | C49265 (EX) | 3 | 5 | 2 | **95** |
| **CuZnBi2Sn** | C49260 (EX) | 9 | 11 | 10 | **30** |
| **CuZnSi** | C69300 (EX) | 7 | 2 | 5 | **80** |
| **CuZn37** | C27451 (EX) | 10 | 10 | 11 | **25** |
| **CuZnSn** | C46500 (EX) | 11 | 1 | 7 | **70** |
| **CuZnAl** | *N/A Al (EX) | 6 | 4 | 4 | **85** |

***(CC) = continuous cast rod, (EX) = extruded rod, N/A = no associated UNS alloy number.**

As discussed in Section 2.3.4, forgeability ratings are often used within the copper manufacturing industry to denote the ease with which a Cu-based alloy could be processed via hot working. Although this is beneficial, the existing ratings tend to be wide-ranging across many different Cu-alloy systems and with significant variation in the base Cu wt. %. As such, duplex brasses, even those which may be substantially different in composition, are typically banded within a very small range of 70-100 and the influence of the fabrication method (i.e. continuously cast or extruded) is not considered.

Therefore, it is difficult to separate the forging performance of one duplex brass from another based on the existing standard forgeability index without any supporting empirical testing. The forgeability index outlined in Table 5.5 has been developed with the aim to capture the large amount of flow stress and fracture data outlined in Sections 5.2 and 5.3 and boil this information down to one number (i.e. the forgeability rating). It focuses only on duplex brasses, and takes into account fabrication method, allowing greater resolution on this specific family of alloys. This number can then be used by the forging operators and engineers to better gauge the ease with which a duplex brass may be hot worked and the relative flexibility the operator has to adjust their forging parameters to minimise rejects whilst maximising output. For example, this could help decide the allowable temperature range for forging, the forging press used (if more power is required), the degree and uniformity of lubrication in order to ensure the brass flows through a forging die suitably, the complexity allowable for the forging design itself (that is, limiting the scope for design details that may generate stress) and essentially how forgiving the alloy is on being plastically worked.

### 5.3.1 Leaded Brasses

The hot compression sample stack of the CuZn39Pb2 alloy is shown in Fig. 5.12. This continuous cast alloy, often referred to in the manufacturing industry as '*Forging Brass'*, is found to have not only the lowest peak flow stress for all conditions tested against the other brasses in this study, but also a high resistance to fracture at the lower temperatures of 550-650°C. This is due to the relatively high BCC β phase fraction in this temperature range, estimated between 40 – 70%, allowing the alloy to compress with ease.

**Figure 5.12: Uniaxially hot compressed sample stacks of the continuous cast CuZn39Pb2 in the temperature range of 550-800°C and average strain rate of 0.85$s^{-1}$. Peak stress ($\sigma_p$) for each 50°C increment additionally labelled.**

At the higher hot compression temperatures, between 700-800°C, cracking is readily observed around the circumference of the samples, and this is likely due to a combination of two factors. Firstly, due to the composition of the alloy, the β phase fraction is estimated to be between 86 – 100% for these samples, and although the BCC phase has excellent hot workability, after 10 minutes at temperature and without any FCC α phase present along the grain boundaries of the β phase, the BCC grains will grow in an uncontrolled fashion leading to fewer grain boundaries and a resulting deterioration in strength at these temperatures. Secondly, the fabrication mode for these samples is continuous casting, and cast structures are naturally less chemically uniform (due to their solidification process) and not as mechanically strong as extruded materials. It is not surprising that we would encounter cracking under these higher temperature conditions.

Overall, this alloy has a reasonably large operating window between 550-650°C, which for older and less efficient furnaces is suitable and uses less power. The low forces required to forge this alloy are also a significant advantage for the forging press itself. This alloy is therefore given a forgeability index rating of 90 according to the approach summarised in Table 5.4.

The hot compression sample stack for CuZn39Pb3 is shown in Fig. 5.13. This extruded alloy has a similar composition with 0.7 wt. % less Zn leading to a slightly lower estimated BCC β phase fraction for each temperature condition (on average approximately 8% less for conditions between 550-700°C). The resulting peak flow stress is higher for each condition, however still significantly lower than any of the other alloys tested in this study.

**Figure 5.13: Uniaxially hot compressed sample stacks of the extruded CuZn39Pb3 in the temperature range of 550-750°C and average strain rate of 0.85$s^{-1}$. Peak stress ($\sigma_p$) for each 50°C increment additionally labelled.**

CuZn39Pb3 exhibits a strong resistance to cracking at the lower temperature ranges of 550-650°C similar to CuZn39Pb2, and this continues through to the 700°C and 750°C conditions (800°C was not tested in this study) where for the continuous cast CuZn39Pb2 alloy (Fig. 5,12), this was not the case. Given that the estimated BCC β phase fraction at 750°C for this alloy is ~99%, the extruded fabrication mode is likely playing a significant factor in preventing fracture from occurring at this higher temperature. Given this additional benefit of the fabrication mode increasing the operating window by decreasing the propensity to fracture, and the still very low forces required to compress the material, this alloy is allocated a forgeability index of 100 according to our approach. CuZn39Pb3 therefore forms the ideal duplex brass for forging by which all of the other alloys in this study are compared.

CuZn37Pb2 is the third alloy presented in this section with the hot compression stack shown in Fig. 5.14. Unlike the first two alloys presented, the continuous cast CuZn37Pb2 shows a comparatively strong resistance to fracture in the higher temperature ranges of 700-800°C, whilst at the lower temperature range of 550-650°C the propensity to cracking increases significantly. At both 550°C and 600°C, there are significant amounts of jagged or 'zig-zag' fracture occurring, and this indicates two issues; first, a lack of BCC β phase in the microstructure and second, the β phase which is present is likely accommodating far more of the plasticity than the α. It is estimated there is only 3.1 and 11.6 vol. % at each of these temperatures, respectively. As the alloy has been fabricated via continuous casting, this also limits the initial strength of alloy before compression due to a reduced dislocation density, and the likelihood of some chemical segregation inherent due to the casting process.

**Figure 5.14: Uniaxially hot compressed sample stacks of the continuous cast CuZn37Pb2 in the temperature range of 550-800°C and average strain rate of 0.85$s^{-1}$. Peak stress ($\sigma_p$) for each 50°C increment additionally labelled.**

In spite of the increased risk of fracture in the lower temperature ranges of 550-650°C, if the temperature of forging is maintained between 700-800°C, as close as possible to 750°C, then this alloy would likely forge well for a variety of more complex dimensions and with a reasonably low flow stress. This alloy is therefore given a forgeability index rating of 80 according to our approach.

The hot compression stack for the extruded CuZnPb2SnFe alloy, is shown in Fig. 5.15. This alloy shows some similar characteristics to the previous CuZn37Pb2 alloy, with a slightly elevated peak stress at each temperature, and similar β phase fractions. However, CuZnPb2SnFe presents with a smaller processing window to avoid fracture. At 550-650°C there are clear indications of fracture in the same morphology as for CuZn37Pb2 (albeit slightly less severe for 550°C and 600°C – this makes no difference in industry), with some additional mild hairline cracks appearing on the 700°C condition. It is expected that although the extrusion process has likely limited the severity of fracture for each condition compared with the continuous cast CuZn37Pb2 alloy, the increased impurity level, particularly of Fe, has led to the formation of intermetallics (Fig. 5.16), which act as stress raisers (fracture initiation sites) within the microstructure leading to an increased propensity to initiate fracture, which is shown for both the 650°C and 700°C conditions. Given this significantly decreases the available processing window for this alloy, CuZnPb2SnFe is therefore given a lower forgeability rating of 50 according to our approach in this study.

**Figure 5.15: Uniaxially hot compressed sample stacks of the extruded CuZnPb2SnFe in the temperature range of 550-800°C and average strain rate of 0.85$s^{-1}$. Peak stress ($\sigma_p$) for each 50°C increment additionally labelled.**

Three distinct compounds were identified in the CuZnPb2SnFe alloy. These have each been highlighted in Fig. 5.16a. The first and perhaps most anticipated compound are insoluble Pb particles (orange arrows) which make up ~2% of the microstructure and are relatively equiaxed in morphology. The second compound is a Sn-bearing intermetallic (green arrows) of approximate composition $Cu_4Zn_2Sn$. These intermetallics make up ~1.4% of the microstructure and similar to Pb are equiaxed in

morphology. Finally, the third compound is an iron-arsenide ($Fe_2As$ – purple arrows) which is typically spherical in particle morphology and makes up ~0.6% of the volume fraction. The presence of the last intermetallic compound ($Fe_2As$), in addition to having an adverse effect on the mechanical properties of the alloy, is likely to adversely affect the dezincification resistance of the alloy (As being a major α dezincification inhibitor – see Section 2.4.3).

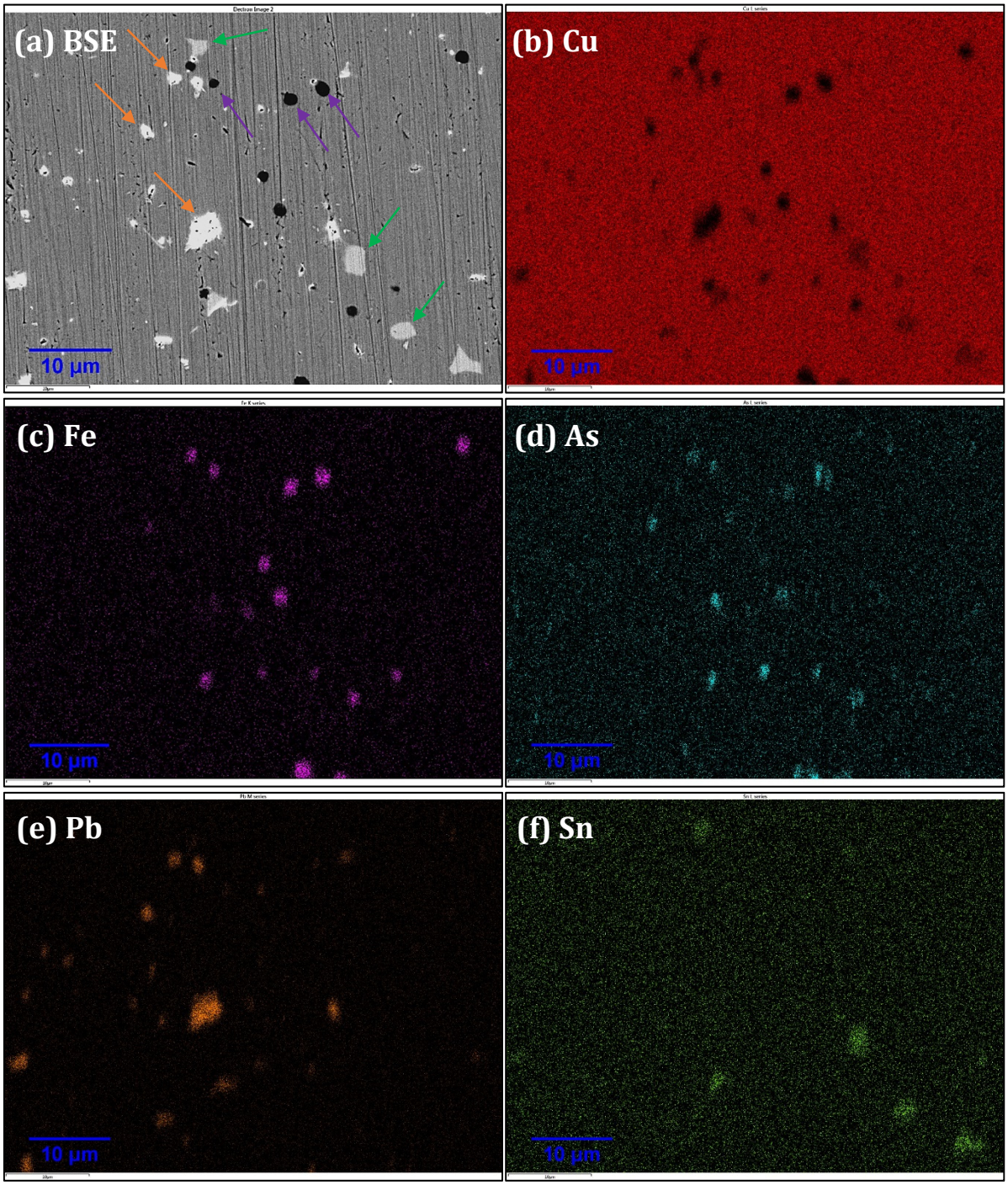


**Figure 5.16: (a) SEM-BSE image and (b) associated Cu mapping, (c) Fe mapping, (d) As mapping, (e) Pb mapping, (f) Sn mapping of CuZnPb2SnFe. There is a clear presence of intermetallic particles in the microstructure which will affect the mechanical properties of the alloy.**

### 5.3.2 Bismuth Brasses

The hot compression stack for the continuous cast CuZnBi0.7 alloy is shown in Fig. 5.17. Similar to the previous two Pb-bearing alloys CuZn37Pb2 and CuZnPb2SnFe, we readily observe fracture around the circumference of the samples in the same jagged morphology at the lower temperatures of 550-650°C with a very mild indication of fracture initiation in the 700°C samples. This is expected due to the reduced amount of workable BCC β phase at these temperatures. However, given that the CuZnBi0.7 should have slightly more β for each temperature than for example the CuZn37Pb2 alloy, and both are fabricated by the same method of continuous casting, this indicates the Bi content may have an additional negative effect on the alloy's propensity to fracture.

**Figure 5.17: Uniaxially hot compressed sample stacks of the continuous cast CuZnBi0.7 in the temperature range of 550-800°C and average strain rate of 0.85$s^{-1}$. Peak stress ($\sigma_p$) for each 50°C increment additionally labelled.**

As the peak flow stresses for the CuZnBi0.7 alloy are slightly higher than the CuZn37Pb2 alloy in the viable forging temperature window around 750°C, and the window itself is smaller leading to an increased likelihood of rejection for more complex forging geometries, this alloy is given a forgeability index rating of 70 according to our approach.

The second Bi-brass hot compression stack presented in this section is the extruded alloy CuZnBi0.8 and is shown in Fig. 5.18. Unlike the previous Bi-bearing alloy CuZnBi0.7, this alloy is resistant to fracture over a much wider temperature range, whilst maintaining a significantly lower peak stress value for each temperature tested. There are some mild hairline fractures observed to have initiated in both the 550°C and 600°C conditions, however they have not propagated into the material as readily compared with this alloy's continuous cast counterpart.

**Figure 5.18: Uniaxially hot compressed sample stacks of the extruded CuZnBi0.8 in the temperature range of 550-800°C and average strain rate of 0.85s$^{-1}$. Peak stress ($\sigma_p$) for each 50°C increment additionally labelled.**

Given the composition of the CuZnBi0.7 and CuZnBi0.8 alloys are so similar (therefore producing similar estimated β phase fractions), with significantly different propensities to fracture at the lower temperature ranges, it is concluded that the extrusion fabrication mode is clearly preferred to assist in increasing both the alloy's resistance to fracture and in turn its processing window. The extruded CuZnBi0.8 alloy is therefore given a very high forgeability index rating of 95 according to our approach.

The third Bi-brass hot compression stack is the extruded CuZnBi2Sn alloy which is shown in Fig. 5.19. In a dramatic shift from the CuZnBi0.8 alloy, which was also fabricated via extrusion, the CuZnBi2Sn alloy cracks at every temperature starting with severe fracture at the lower temperatures 550°C and 600°C and finishing with fine hairline fractures at the upper temperature conditions of 750°C and 800°C. Considering that the composition of this alloy yields an estimated 5% increase in BCC β phase compared with CuZnBi0.8 for each temperature between 550-700°C and that the alloy is extruded, it is suggested that the elevated Bi composition at 1.95 wt. % has caused a severe deleterious effect in the microstructure. Why this would be the case for Bi, and not necessarily for Pb, given both are in the liquid state at these temperatures, is not clear. A potential clue lies in the slightly different morphology of fracture, in which the cracking tends to propagate in less of a jagged way and is generally cleaner in nature.

**Figure 5.19: Uniaxially hot compressed sample stacks of the extruded CuZnBi2Sn in the temperature range of 550-800°C and average strain rate of 0.85s$^{-1}$. Peak stress ($\sigma_p$) for each 50°C increment additionally labelled.**

To better identify how the elevated Bi composition is affecting the propensity of the alloy to fracture at elevated temperatures, metallography was completed on the samples compressed at 550°C and the microstructure shown in Fig. 5.20. It is clearly observed the high density of Bi-rich particles dispersed throughout the microstructure which the fracture paths have a tendency to propagate towards, in turn leading to a higher propensity to failure.

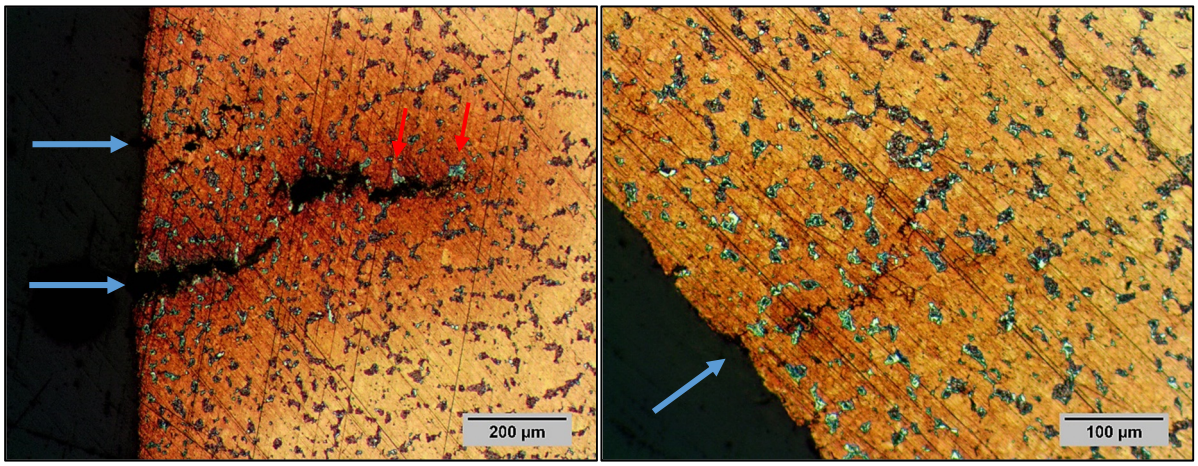


**Figure 5.20: Bi-particle-rich microstructure of CuZnBi2Sn after hot compression at 550°C. After initiation (blue arrows), the fracture paths have a tendency to propagate in directional preference to these particles (red arrows).**

Regardless of the peak stresses recorded for the CuZnBi2Sn alloy, this means little if the alloy is not capable of forging at any temperature within the assessed window. This alloy is therefore given a very low forgeability index rating of 30 according to our approach.

### 5.3.3 Silicon Brasses

The hot compression stack for the Si-bearing alloy, CuZnSi, is shown in Fig. 5.21. Compared with the duplex brasses so far investigated in this study, the extruded CuZnSi exhibits significantly higher flow stresses in the lower temperature range of 550-650°C due to the presence of the harder HCP κ and BCC η phases (Chapter 4), however the peak stresses then decrease as the temperature continues to increase to 700-800°C due to the rapid formation of the BCC β phase. In this upper temperature range the forces required to deform the material are comparable to CuZnBi0.7.

**Figure 5.21: Uniaxially hot compressed sample stacks of the extruded CuZnSi in the temperature range of 550-800°C and average strain rate of 0.85s$^{-1}$. Peak stress ($\sigma_p$) for each 50°C increment additionally labelled.**

From the perspective of identifying any fracture on the CuZnSi samples, there are no observable cracks found for any of the temperatures indicating a high resistance to crack initiation and propagation. One interesting observation was made for the 800°C condition, in which the sample surface appears more rippled or rough in texture. This indicates there has likely been some incipient melting at this temperature due to the elevated Si content (3.09 wt. %) which stabilises the BCC β + liquidus phase field at much lower temperatures than binary Cu-Zn at the same ratio (Fig. 2.12). This has been discussed in Section 4.2.

Given that a very wide temperature range can be applied to CuZnSi without any elevated risk of fracture, and that at 700°C – 750°C the flow stress behaviour and peak stresses are similar to that of CuZnBi0.7, this alloy is given a forgeability rating of 80 according to our approach.

### 5.3.4 Alternative Brasses – Binary, Al-, Sn-bearing

Within this section we explore the forgeability of 3 alternative duplex brasses; CuZn37, CuZnSn, and CuZnAl. The hot compression stack for the first alloy in this group, CuZn37, is shown in Fig. 5.22. The initial observation of this alloy is a tendency for the samples to split, rather than fracture, for each of the temperatures tested. Given the composition of the alloy, it is estimated that the workable β phase does not commence forming until 700°C, and therefore this alloy contains less β than any other alloy tested in this study. This is supported by the elevated peak flow stresses recorded for each temperature, with only the extruded CuZnSi, and CuZnSn alloys recording higher values at some temperatures.

**Figure 5.22: Uniaxially hot compressed sample stacks of the extruded CuZn37 in the temperature range of 550-800°C and average strain rate of 0.85$s^{-1}$. Peak stress ($\sigma_p$) for each 50°C increment additionally labelled.**

It is highly unlikely that this alloy, at the existing composition, would be able to accommodate a high-volume forging process without the generation of a high percentage of rejects. In addition, given the additional forces required to deform this material, the forging presses will require more power, and the forging dies would likely be worn out more quickly. Therefore, this alloy is given a low forgeability index rating of 25 according to our approach.

The hot compression stack for the second alloy in this group, CuZnSn, is shown in Fig. 5.23. This extruded alloy has the largest forging temperature window of any of the brasses tested in this study. CuZnSn exhibits no signs of fracture, splitting, or incipient melting for any of the temperatures tested between 550°C to 800°C. The reason for this is the Sn content which, particularly for higher Cu-containing alloys (in this case at 63.1 wt. %), decreases the steepness of the α / β phase field boundaries, meaning that β will begin to form at lower temperatures than a plain binary Cu-Zn alloy, and will evolve more slowly as the temperature is increased. Therefore, the probability of fracture or

splitting at the extreme lower and upper temperatures is mitigated. Where Sn has been present in other alloys in this study above 0.3 wt. %, for example in CuZnPb2SnFe, CuZnBi0.7, CuZnBi0.8, and CuZnBi2Sn, defects have been more likely to form due to impurities such as Fe or Bi, or due to the continuous cast fabrication mode which competes with the positive effect of Sn. This is an important lesson for alloy design in which a change in composition decreases the temperature sensitivity of the β phase fraction and therefore improves the processing window.

**Figure 5.23: Uniaxially hot compressed sample stacks of the extruded CuZnSn in the temperature range of 550-800°C and average strain rate of 0.85$s^{-1}$. Peak stress ($\sigma_p$) for each 50°C increment additionally labelled.**

As a result of the combined high Cu wt. % and the effect on the temperature dependence of the BCC β phase fraction due to the Sn present in the composition, the peak flow stresses recorded for this extruded alloy are undesirably high, with similar values to the extruded CuZn37. This means that the forgeability of the alloy is very good from a low propensity to fracture perspective but requires a greater amount of power to form the material into the desired geometry. Therefore, taking both of these factors into account, CuZnSn is given a forgeability index rating of 70 according to our approach.

The hot compression stack on the final alloy in this study, CuZnAl, is shown in Fig. 5.24. Like the CuZnSn alloy, CuZnAl has a very wide forging temperature window with only some mild signs of fracture at 550°C. In spite of the higher Cu content (62.4 wt. %) the Al present in the alloy shifts the α + β phase field to the Cu end therefore stabilising the more workable β phase at lower temperatures. Even at 600°C it is estimated there is approximately 25% vol. β present in the microstructure.

**Figure 5.24: Uniaxially hot compressed sample stacks of the extruded CuZnAl in the temperature range of 550-800°C and average strain rate of 0.85s$^{-1}$. Peak stress ($\sigma_p$) for each 50°C increment additionally labelled.**

The key difference between the CuZn37, CuZnSn, and CuZnAl alloys is that the CuZnAl stabilises more β at each temperature and therefore the forces required to deform the CuZnAl alloy are significantly lower, on average by ~17MPa. Therefore, the forgeability index rating for this alloy is slightly higher than CuZnSn at 85 according to our approach.

These hot-compression experiments have highlighted several key take-away messages regarding the forgeability of duplex brasses:

- Extruded alloys have a higher average forgeability rating, primarily due to their reduced propensity to fracture.
- Elevated Bi-bearing alloys and alloys with intermetallic particles are not suitable for forging purposes due to their increased propensity to fracture. This does not appear to be the case for Pb-bearing brasses. The performance of Bi-rich brasses compared with Pb-rich brasses may relate to the liquidus morphology of these elements at elevated temperatures, ranging from film-like (promoting grain boundary sliding) to remaining relatively spherical.
- Although CuZnSi has a low propensity to fracture, flow stresses rapidly increase below 650°C due to the presence of other secondary phases in the microstructure, primarily HCP κ.
- Elements such as Sn and Si decrease the steepness of the α/(α + β) phase field boundary, thus stabilising the ratio of phases within the processing window and allowing the operator greater flexibility to achieve the desired level of hot workability.
- Overall, the best performing low-Pb alloys in this study were CuZnBi0.8, CuZnSi, and CuZnAl (all extruded). Each could feasibly be considered as a potential replacement alloy for the traditional Pb-bearing alloys in industrial hot working processes.

This is the first time that each of the above points have been shown and goes a significant way to close the knowledge gap currently present in the industry between the performance of traditional Pb-bearing vs. low-Pb duplex brass alternatives entering the potable water market. The next step is to better understand the evolution of flow stress with temperature through constitutive modelling techniques and this is the topic of Section 5.4.

## 5.4 Constitutive Modelling

A large amount of data has been collected to describe the flow stress behaviour and propensity to fracture of a variety of duplex brasses under uniaxial hot compression. An opportunity to enhance our understanding of the hot working behaviour of duplex brasses now presents itself through the use of constitutive modelling. This type of modelling is often used to characterise the flow stress behaviour of alloys at elevated temperatures [48, 60, 65, 230, 231] and in this case will be specifically targeted at the response to deformation of the α and β phases.

The aim of this section to formulate a semi-empirical model which can describe the response to deformation of a duplex brass with a given composition and α/β phase ratio.

### 5.4.1 Methodology

The Zener-Hollomon parameter (Z) is often used to characterise the effects of temperature (T) and strain-rate ($\dot{\varepsilon}$) on the deformation behaviour of metals, including brasses [18, 60, 61, 70], this is expressed in Eq. (5.1).

$$Z = \dot{\varepsilon}\exp\left(\frac{Q}{RT}\right) \tag{5.1}$$

$\dot{\varepsilon}$ is the strain-rate ($s^{-1}$), T is the absolute temperature (K), R is the universal gas constant (8.3145 J/mol.K) and Q is the activation energy of deformation (kJ/mol). In order to relate flow stress to the Zener-Hollomon parameter an Arrhenius-type equation is used [18, 60, 61, 70]. This is shown by Eq. (5.2).

$$Z = A[\sinh\left(\frac{\alpha\sigma}{G}\right)]^n \tag{5.2}$$

σ is the flow stress (MPa), α and A are material parameters, *n* is the stress exponent and *G* is the shear modulus (MPa). By combining Eqs. (5.1) and (5.2) we can relate temperature and strain-rate to flow

stress as expressed in Eq. (5.3a). By rearranging Eq. (5.3a) to reflect the flow stress we are able express this as Eq. (5.3b). This allows us to calculate the steady-state flow stress of a material as a function of temperature and strain-rate if the material parameters (α, A), stress exponent (n), activation energy (Q), and shear modulus (G) are known.

$$\dot{\varepsilon} = A[\sinh\left(\frac{\alpha\sigma}{G}\right)]^{n}\exp\left(-\frac{Q}{RT}\right) \tag{5.3a}$$

$$\sigma = \frac{G}{\alpha} sinh^{-1}\left[\left(\frac{\dot{\varepsilon}}{Aexp\left(-\frac{Q}{RT}\right)}\right)^{\frac{1}{n}}\right] \tag{5.3b}$$

Using the material parameters, stress exponent, and activation energy values calculated by Spigarelli et al. [48, 60] for both the α and β phases assuming a 36 wt. % Zn FCC α phase and a 44 wt. % Zn β phase (Table 5.6), we are able to calculate the flow stress behaviour for both of these phases as individual constituents of a duplex brass using Eq. 5.3b.

**Table 5.6: Constitutive equation parameters for the α and β phases according to Spigarelli et al. [48, 60] assuming 36 wt. % Zn for FCC α and 44 wt. % Zn for BCC β.**

| Phase | A ($s^{-1}$) | α | n | Q (kJ/mol) | G (GPa) |
|---|---|---|---|---|---|
| **FCC α (hard phase)** | 6.6 x $10^{9}$ | 250 | 4.5 | 157 | 40.0 |
| **BCC β (soft phase)** | 1.44 x $10^{7}$ | 350 | 3 | 92 | 36.0 |

Given the dual-phase nature of duplex brasses, with volume fractions of each phase highly dependent on temperature and composition, the flow stress behaviour of these alloys might be described to a first approximation using the rule of mixtures shown in Eq. 5.4. In this case, the hard phase is the FCC α and the softer phase is the BCC β.

$$\bar{\sigma} = f_{\alpha}\sigma_{\alpha} + f_{\beta}\sigma_{\beta} \tag{5.4}$$

By calculating σ from Eq. 5.3b for both the α ($\sigma_{\alpha}$) and β ($\sigma_{\beta}$) phases individually and then combining using the rule of mixtures (Eq. 5.4b) to calculate $\bar{\sigma}$, we are able to compare with the values experimentally obtained in the hot compression experiments to gauge the reasonableness of this approach.

### 5.4.2 Rule of Mixtures

Using the method described in Section 5.4.1, the rule of mixtures has been used to calculate the steady-state flow stress which is then compared with the experimentally generated values for each of the 11 duplex brasses listed in Table 5.1. Examples of these comparisons are shown in Fig. 5.25 for alloys CuZn39Pb2 and CuZn37 for vastly different compositional values of Zn. Upon initial observation, the calculations of the steady-state flow stress (solid-blue lines) using the rule of mixtures show similar trends for temperature dependence to the experimental values. However, these same calculated values using the parameters proposed by Spigarelli et al. [48] consistently over-estimate the steady-state flow stress for all of the alloys tested in this study, particularly for lower temperatures (the most α-rich conditions).

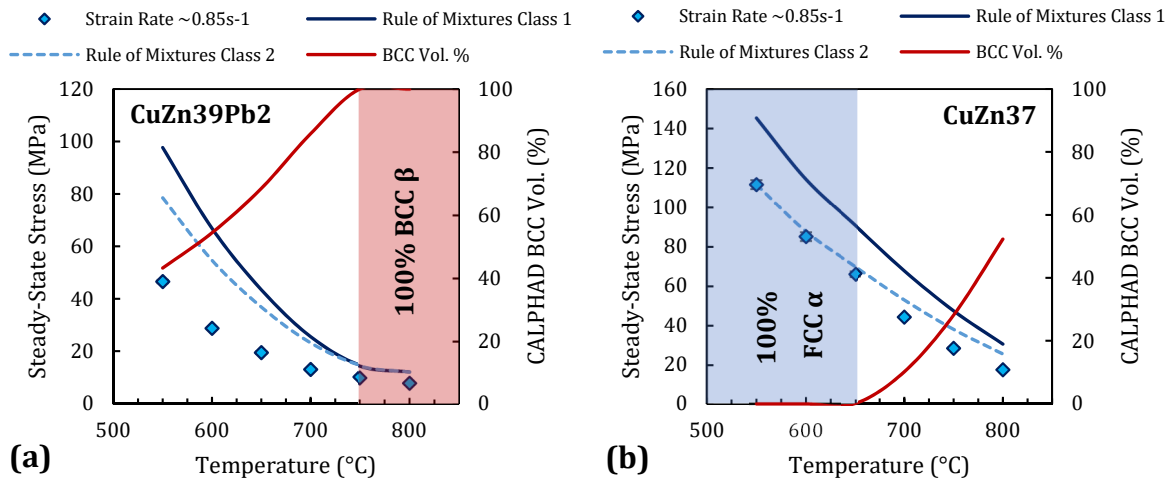


**Figure 5.25: Comparison of the steady-state flow stress determined experimentally at an average strain-rate of 0.85s$^{-1}$ against the calculation according to the rule of mixtures for (a) CuZn39Pb2 and (b) CuZn37 using the Class 1 activation energy values $Q_\alpha$ and $Q_\beta$ calculated by Spigarelli et al. [48] (solid blue line). This is compared against a recalculated rule of mixtures using the Class 2 activation energy values (dotted line).**

The comparison of the calculated and experimental steady-state flow stresses in Fig. 5.25 shows that as the volume fraction of FCC α increases, the agreement becomes significantly worse. In Fig. 5.25a, at temperatures of 750°C and 800°C, for the CuZn39Pb2 alloy, the alloy is 100% β and the agreement between the calculated and experimental flow stresses is good. This suggests that the constitutive description of the β phase reported by Spigarelli et al. [48, 60] (Table 5.6) likely works well for this study as well. However, if we consider Fig. 5.25b, the CuZn37 alloy is 100% FCC α at 550°C, 600°C, and 650°C. The calculated flow stresses are significantly higher than the experimental flow stresses. This suggests that something is not entirely correct with the constitutive response of α reported by Spigarelli et al. [48, 60] (Table 5.6) as it is applied to the alloys in this study.

To understand this better it is useful to examine more closely how Spigarelli et al. [48, 60] chose his parameters for the constitutive equation for FCC α. Fig. 5.26a shows the available activation energy and pre-exponential for Zn diffusion in FCC α from a variety of studies collected by Spigarelli. It was noted that there were two key classes of data:

- Class 1: $Q_{Zn}$ and $D_{0Zn}$ decrease and remain relatively constant, respectively, with increasing Zn content (Fig. 5.26b).
- Class 2: $Q_{Zn}$ and $D_{0Zn}$ both strongly decrease with increasing Zn content (Fig. 5.26c).

Spigarelli elected to use the Class 1 data for the purposes of his evaluation based on the larger number of sources. However, given the increased quantity of data in the Kucera et al. [232] and de Silva-Mehl [233] studies, and that the Class 2 data is inclusive up to 37% Zn (highlighted in Fig. 5.26c), which we are most interested in, we will use the Class 2 data in our calculations for Q and $D_0$ of the FCC α phase.

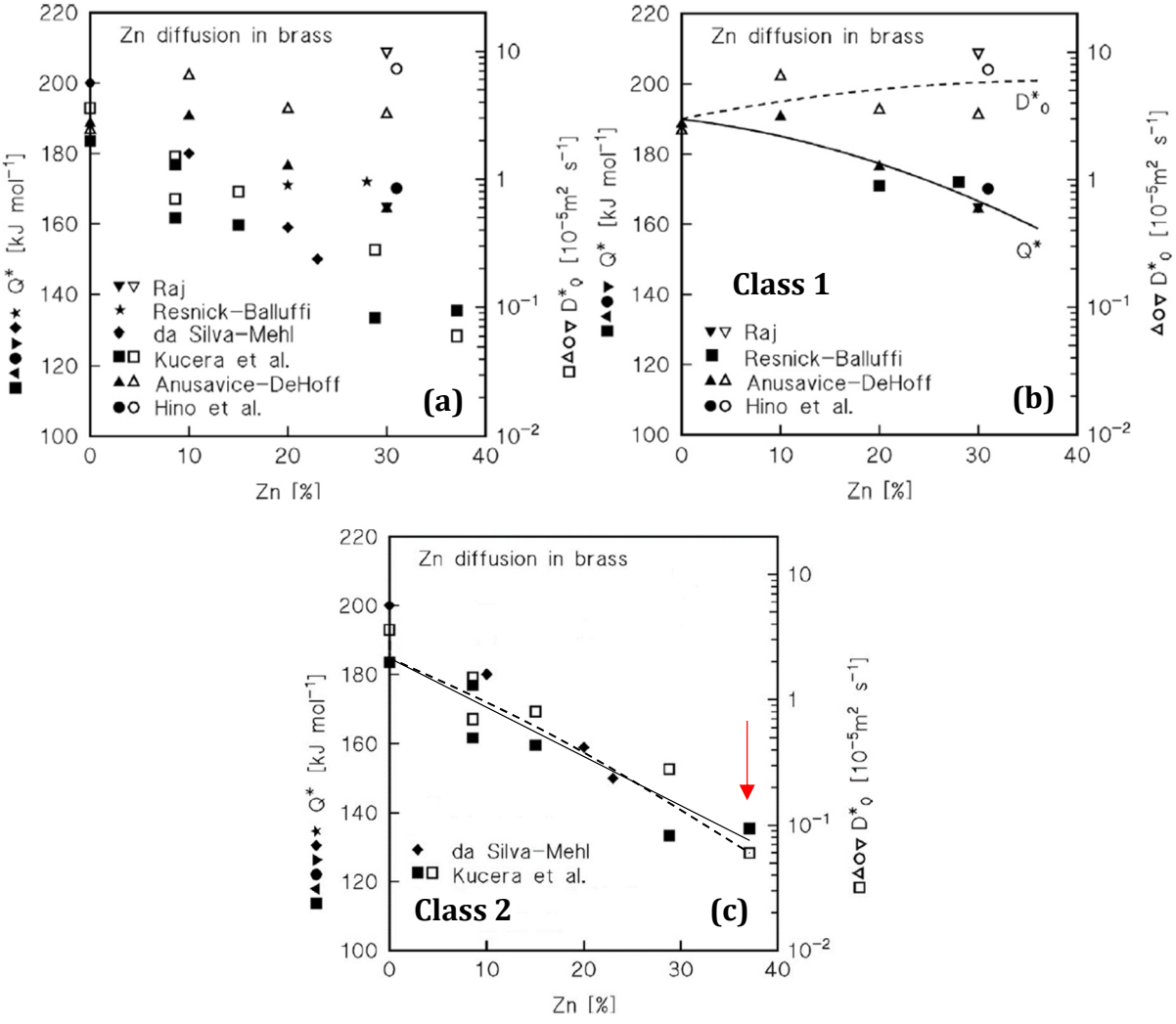


**Figure 5.26: Activation energy ($Q_{Zn}$) and frequency factor ($D_{0Zn}$) data for diffusion of Zn in brass (a) in total (b) after Class 1 selection by Spigarelli [48], and (c) Class 2 data selected for this study.**

Using the Class 2 $Q_{Zn}$ and $D_{0Zn}$ data in Fig. 5.26c, new values for $D_{Zn}$ could be calculated for a series of Zn wt. % according to Eq. 5.5:

$$D_{Zn} = D_{0Zn}\exp\left(-\frac{Q_{Zn}}{RT}\right) \quad (5.5)$$

The new values for $D_{Zn}$ are incorporated with $D_{Cu}$ to calculate the effective diffusion coefficient for dislocation climb ($D_C$) using Eq. 5.6a and then used to find the variation in the overall $Q_C$ and $D_{0C}$ using Eq. 5.6b:

$$D_C = \frac{N_{Cu}D_{Cu}+N_{Zn}D_{Zn}}{0.78} \quad (5.6a)$$

$$D_C = D_{0C}\exp\left(-\frac{Q_C}{RT}\right) \quad (5.6b)$$

The variation in $Q_C$ and $D_{0C}$ with Zn % for the FCC α phase is shown in Fig. 5.27a for Class 1 data (Fig. 5.26b) as calculated by Spigarelli et al. and in Fig. 5.27b calculated in this study using the Class 2 data (Fig. 5.26c). The new $Q_C$ value for 36 wt. % Zn using the Class 2 data has been calculated as 147.2kJ and will be used for the remainder of this study for the FCC α phase. Fig. 5.25 shows the significant improvement in agreement (dotted lines) between the experimental and calculated steady-state flow stress by using the Class 2 data.

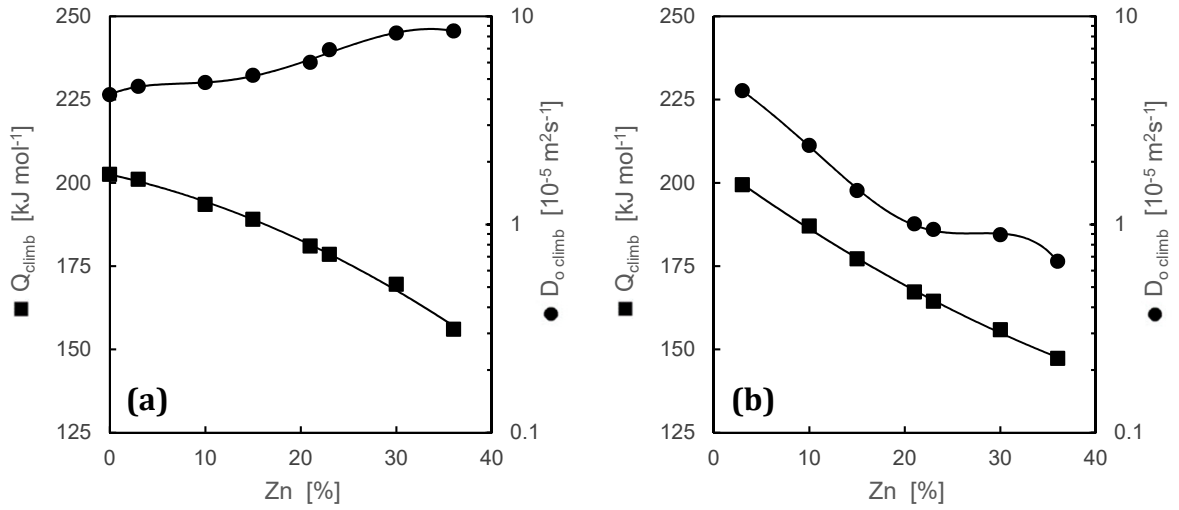


**Figure 5.27: Variation of Qc and $D_{0c}$ as (a) interpolated by Spigarelli [48] using Class 1 data and (b) as interpolated using the Class 2 data.**

Fig. 5.28 shows the CuZn39Pb2 and CuZn39Pb3 alloys using the values $Q_\alpha$ = 147.2kJ/mol and $Q_\beta$ = 92kJ/mol respectively. Due to their elevated Zn wt. %, CuZn39Pb2 and CuZn39Pb3 have the highest phase fraction of BCC β across all temperatures tested in this study, particularly at the lower temperature of 550°C and 600°C. The rule of mixtures is shown to produce reasonable agreement between 650 – 800°C for these alloys, however a difference is still observed between 550 – 650°C where the experimental values are lower than predicted by the rule of mixtures. The remaining discrepancy in these alloys occurs due to both an elevated Zn wt. % (which further reduces $Q_\alpha$), and because the rule of mixtures assumes that both phases are accommodating the same amount of strain. In reality, the softer β phase will deform preferentially to the α decreasing the experimental flow stress. This is particularly true for the continuous cast CuZn39Pb2 (Fig. 5.28a) as this alloy will have greater compositional inhomogeneity in the microstructure producing local pockets of elevated β. The average dislocation density in a cast alloy will additionally be lower than an equivalent alloy that has undergone any prior hot working (extrusion) stage. With fewer dislocations, deformation will occur more easily decreasing the experimental values.

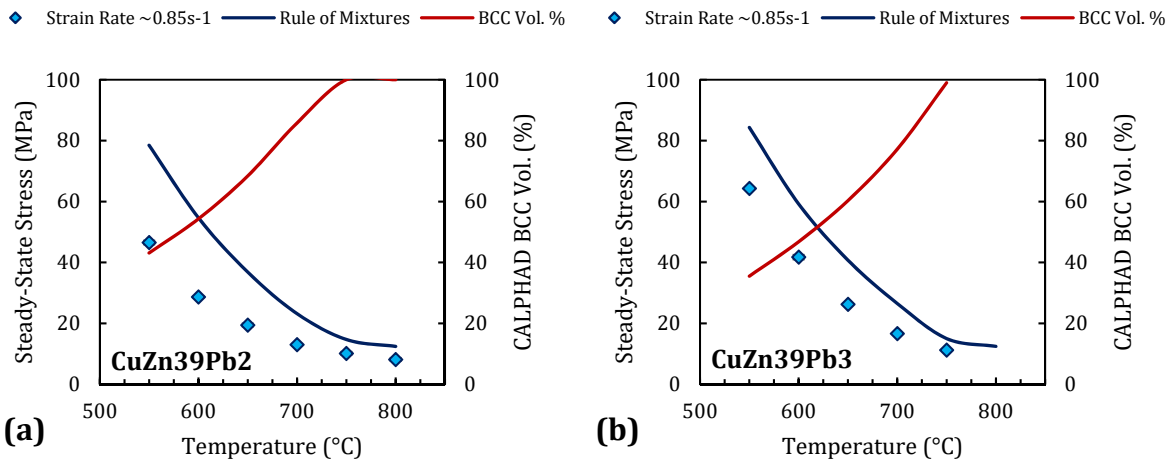


**Figure 5.28: Comparison of the steady-state stress determined experimentally at an average strain rate of 0.85s$^{-1}$ against the calculation according to the rule of mixtures for (a) CuZn39Pb2 and (b) CuZn39Pb3.**

Fig. 5.29 shows the comparison between the remaining two Pb-bearing duplex brasses, CuZn37Pb2 and CuZnPb2SnFe. In both cases and across all temperature conditions the rule of mixtures appears to work well. Overall, the two alloys align within 20 MPa for all conditions.

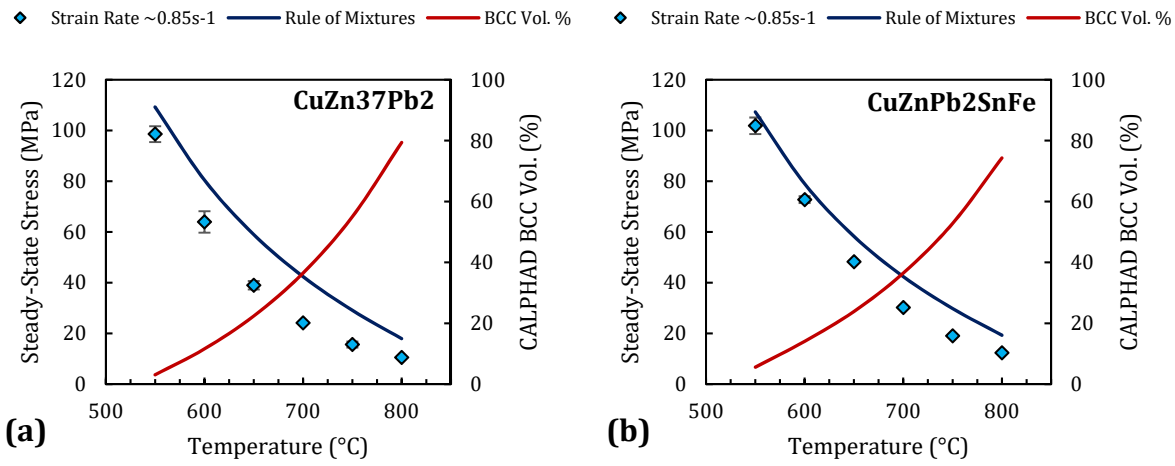


**Figure 5.29: Comparison of the steady-state stress determined experimentally at an average strain rate of 0.85s$^{-1}$ against the calculation according to the rule of mixtures for (a) CuZn37Pb2 and (b) CuZnPb2SnFe.**

In Fig. 5.30 and Fig. 5.31, we observe the comparison between the 3 Bi-bearing duplex brasses, CuZnBi0.7, CuZnBi0.8, CuZnBi2Sn and the Si-bearing duplex brass CuZnSi. Each of the three Bi-alloys are closely following the rule of mixtures approach with the largest discrepancy found between the 600-650$^{o}$C temperature conditions in the CuZnBi0.8 alloy of ~20-23MPa. Compared with the CuZn37 alloy (Fig. 5.25b), the alloys CuZnBi0.7 and CuZnBi0.8 both have elevated Zn wt. % and will naturally have a slightly lower activation energy producing this mild difference.

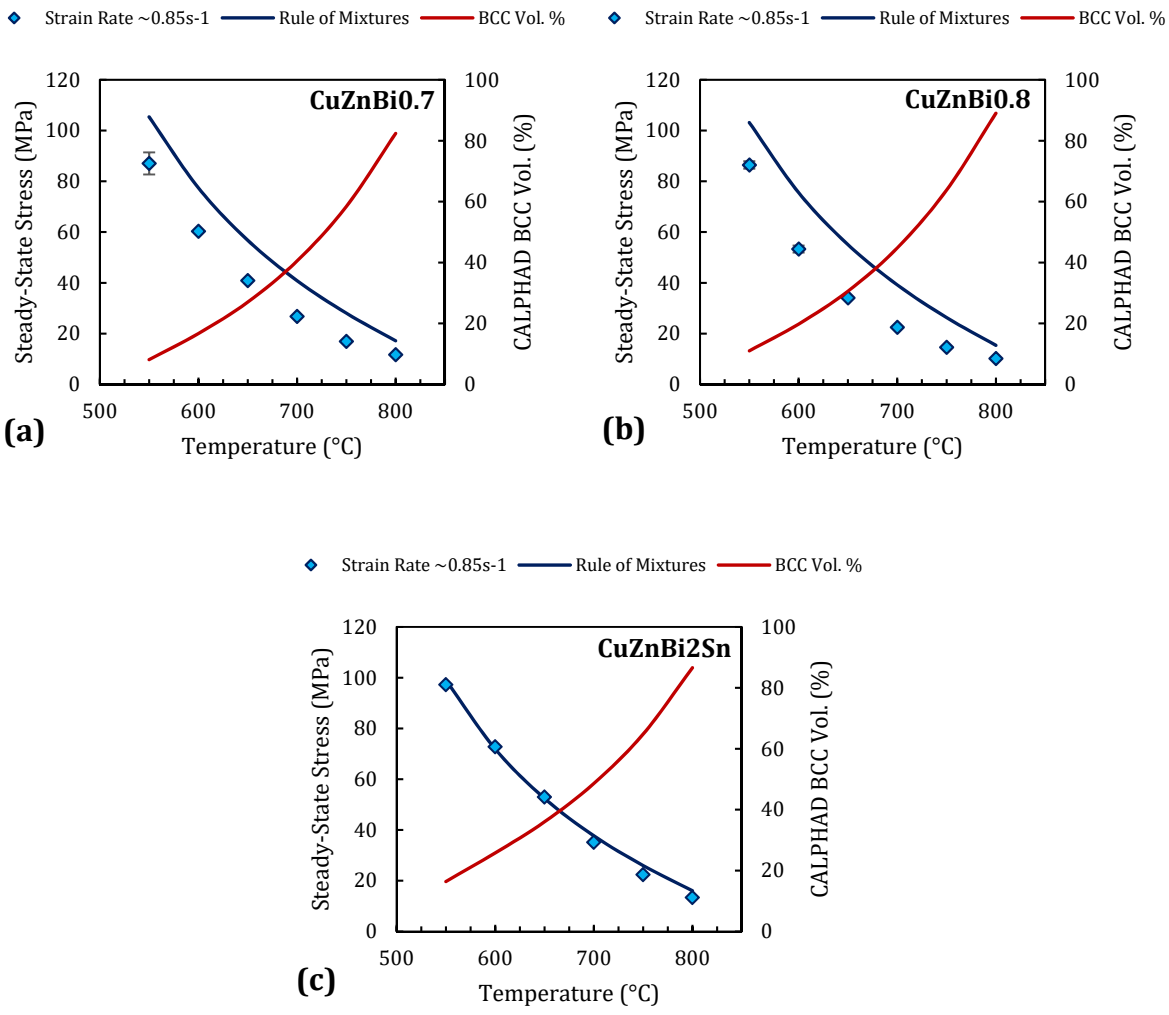


**Figure 5.30: Comparison of the steady-state stress determined experimentally at an average strain rate of 0.85s$^{-1}$ against the calculation according to the rule of mixtures for (a) CuZnBi0.7, (b) CuZnBi0.8 and (c) CuZnBi2Sn.**

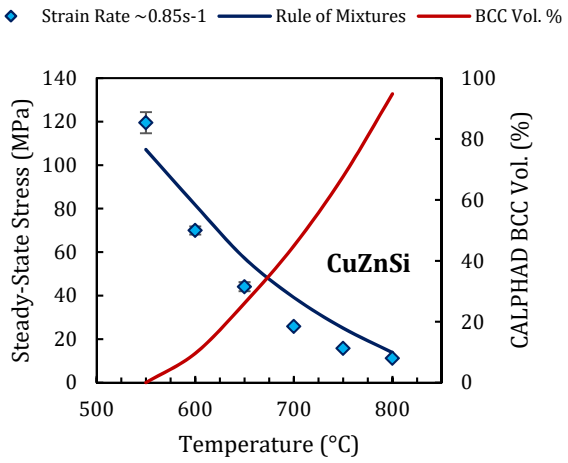


**Figure 5.31: Comparison of the steady-state stress determined experimentally at an average strain rate of 0.85s$^{-1}$ against the calculation according to the rule of mixtures for CuZnSi.**

In spite of its heavily reduced Zn wt. % against the other alloys tested in this study, the CuZnSi alloy is generally found to follow the rule of mixtures with activation energies of 147.2 and 92kJ/mol very well. The only instance in which the experimental steady-state flow stress exceeds the predicated values is for the lowest temperature condition, 550°C, where it is expected that the β phase has entirely disappeared and in addition to the α phase, harder HCP κ and cubic η will have formed in the microstructure, which are not taken into account in this approach.

In Fig. 5.32 we observe the comparison between the remaining 3 extruded duplex brass alloys, CuZn37, CuZnSn, and CuZnAl. Each of these alloys are in close agreement with the rule of mixtures predictions for flow stress. The rule of mixtures slightly under-estimates the steady-state flow stress at 550°C for CuZnSn and CuZnAl, and this may be due to a strengthening effect of the Al and Sn inclusions in the composition at this temperature.

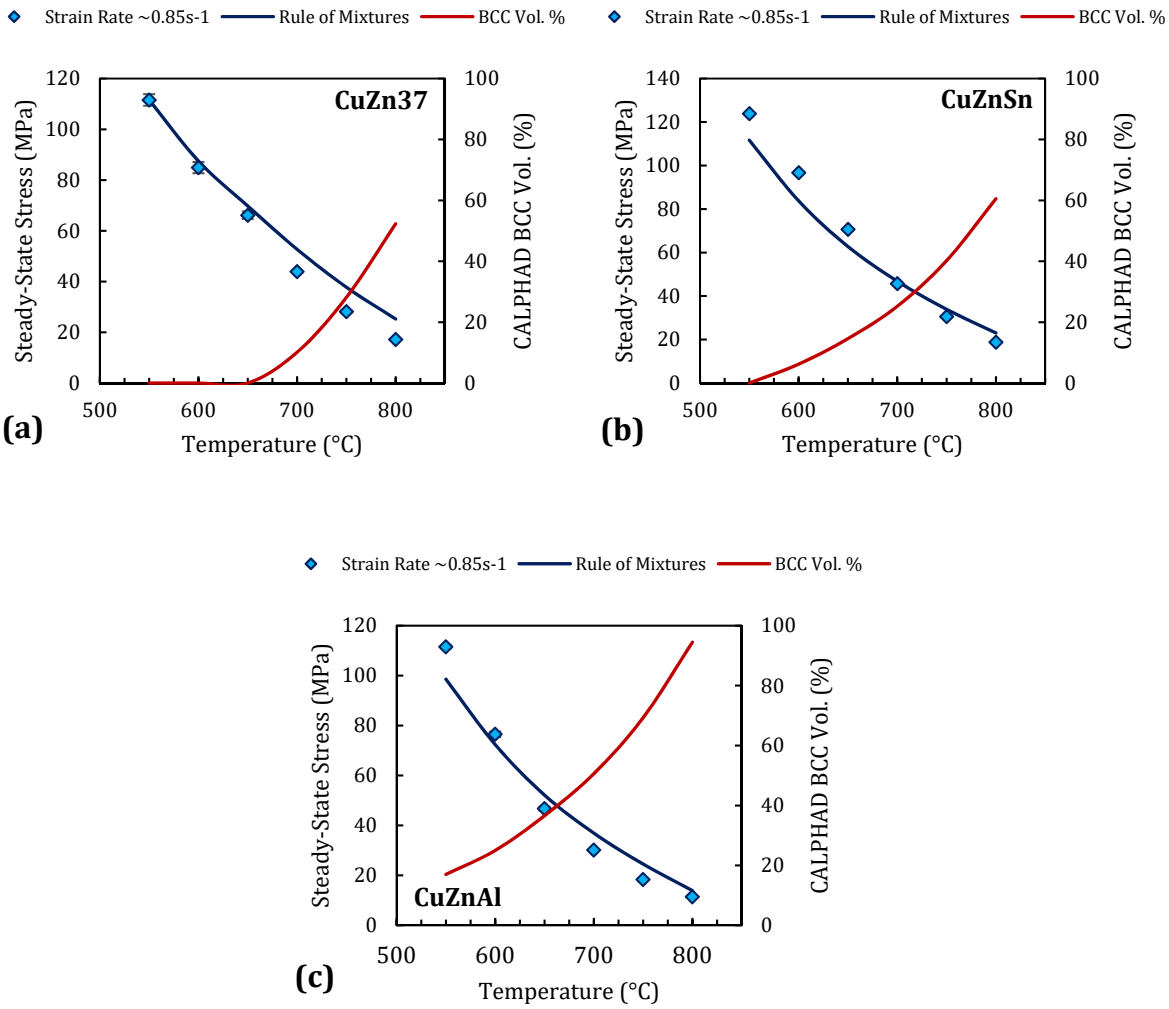


**Figure 5.32: Comparison of the steady-state stress determined experimentally at an average strain rate of 0.85s$^{-1}$ against the calculation according to the rule of mixtures for (a) CuZn37, (b) CuZnSn and (c) CuZnAl.**

Overall, the rule of mixtures is shown to work reasonably well in this study, with close agreement being attained after employing the modified approach for the activation energy values.

## 5.5 Summary and Conclusions

In this Chapter, a detailed study of the elevated temperature plasticity of 11 duplex brasses, fabricated via either continuous casting or extrusion, has been undertaken through the use of uniaxial hot compression in the range of 550-800$^{o}$C. This has occurred in 3 stages:

1) Determination of the true stress-strain curves for these alloys using 3 different strain-rates. The flow stress behaviour of each alloy was found to be strongly dependent on both the strain-rate and temperature conditions, the latter of which specifically relates to the stabilisation of the disordered BCC β phase in the microstructure. Alloying elements Si and Al were effective at stabilising additional β, particularly between 650-800$^{o}$C, although below 650$^{o}$C, the HCP κ phase is stabilised in the CuZnSi alloy producing a significantly higher flow stress. Extruded alloys produced slightly higher flow stresses on average.

2) Evaluation of the susceptibility to fracture for each of the 11 duplex brasses and the subsequent development of a forgeability index. It is demonstrated that extruded alloys have a much greater resistance to fracture than alloys fabricated via continuous casting. Alloys containing significant levels of Bi or impurities sufficient to form intermetallic particles are at greater risk of fracture. The steepness of the α/(α+β) phase field boundary is decreased with additions of Sn and Si which increases the flexibility for the forging operator in an industrial setting.

3) The formulation of a semi-empirical model to describe the steady-state flow stress of each duplex brass based on constitutive analysis. By first relating the Zener-Hollomon parameter to flow stress for both constituent phases α and β, the use of the rule of mixtures was found to be an effective tool for predicting the steady-state flow-stress of each of the 11 duplex brasses. A re-assessment of the activation energy (Q) for the FCC α as a function of Zn content was required.

# 6 Dezincification Behaviour

The corrosion resistance of potable water fittings is one of the most important considerations in alloy selection for these components. Ideally, the alloy should have excellent processing characteristics and good mechanical properties whilst simultaneously satisfying the requirements for resistance against several forms of corrosion. Duplex brasses will typically suffer from one of two major types of corrosion; Dezincification and Stress Corrosion Cracking (SCC). In many instances these two phenomena are linked. Dezincification is a mode of corrosion which has been empirically understood for some time, however with many new 'Pb-free' duplex brasses now entering the global market, there is a need to revisit the underlying science and understand not only the chemical, but also the microstructural factors at play when a duplex brass is exposed to conditions where dezincification may occur.

Currently, the industrial methods for controlling dezincification resistance of duplex brasses are centred around two strategies: (1) Chemical inhibitors such as As, P, or Sb which help to protect the FCC α phase only, and (2) Intermediate heat treatments which are designed to reduce the phase fraction of the ordered BCC β' remaining in the microstructure after hot working processing steps such as extrusion or forging (Fig. 1.3).

As new 'Pb-free' duplex brasses have entered the market, most of the attention from the literature has been placed on the effects of chemical inhibitors, be it the traditional α phase inhibitors, or new inhibitors which some claim to protect the β' phase [108, 109]. Very few systematic studies have been conducted to evaluate and interpret the dezincification resistance of duplex brasses with a focus on microstructural or processing effects (for example fabrication anisotropy or cooling rates from elevated temperature processes such as forging or extrusion). The prevailing assumption has always been simply *"more* β' *is bad"*. This chapter presents results for dezincification resistance of low-Pb brasses which have been manipulated to obtain a specific combination of microstructural features.

The primary objective is to quantitatively describe the effects of the following microstructural characteristics on dezincification resistance:

- β' phase fraction.
- β' phase interconnectivity and how it relates to the surrounding α phase morphology.
- α grain size and morphology.

## 6.1 Alloy Selection and Thermal Treatments

Cylindrical rods of two low-Pb brasses, UNS C28340 and C49265, were chosen to study the relationship between microstructure and dezincification resistance. Their compositions across four rod samples (measured using OES) are shown in Table 6.1. These alloys were sourced from a variety of industry suppliers. Alloy CuZn37.4BiAs was produced via continuous casting, whilst alloys CuZn37.2BiAs, CuZn37.6BiPAs, and CuZn37.8BiPAs were each produced via casting followed by hot extrusion. These are the two most common rod fabrication methods used in the brass industry. The chemical compositions of each of the four rod alloys are very similar with alloys CuZn37.2BiAs and CuZn37.4BiAs containing the dezincification inhibitor As, whilst alloys CuZn37.6BiPAs and CuZn37.8BiPAs contain both As and P inhibitors. The major point of difference is their manufacturing method.

**Table 6.1: Chemical composition (wt. %) of the investigated workpiece materials for microstructure-dezincification analysis. (CC) = continuous cast rod, (EX) = extruded rod.**

| Alloy | U.N.S. | Cu | Zn | Pb | Bi | Sn | As | P |
|---|---|---|---|---|---|---|---|---|
| **CuZn37.2BiAs** | C28340 (EX) | Rem. | 37.2 | 0.25 | 0.72 | 0.30 | 0.10 | <0.01 |
| **CuZn37.4BiAs** | C28340 (CC) | Rem. | 37.4 | 0.18 | 0.68 | 0.34 | 0.10 | <0.01 |
| **CuZn37.6BiPAs** | C49265 (EX) | Rem. | 37.6 | 0.23 | 0.78 | 0.29 | 0.08 | 0.10 |
| **CuZn37.8BiPAs** | C49265 (EX) | Rem. | 37.8 | 0.20 | 0.78 | 0.31 | 0.08 | 0.09 |

These alloys were selected because they are very common to the Pb-legislated North American potable water market (containing no more than 0.25 wt. % Pb). They are both Bi-bearing duplex alloys and therefore their microstructural characteristics such as α and β grain size and phase fraction can be manipulated using specific thermal treatments, and they are commonly fabricated via different processes.

The primary objective of these experiments is to develop a quantitative understanding of the effect of β' phase fraction, α grain size and morphology, and β' interconnectivity on the dezincification resistance of these alloys. In order to accomplish this objective, three sets of experiments were designed (Fig. 6.1).

1. Effect of Fabrication Anisotropy

First, samples of CuZn37.2BiAs were subject to an intermediate heat treatment temperature (508°C) in the all-α phase field for varying lengths of time and then air-cooled in order to assess the effects of β' interconnectivity and phase morphology as the result of the extrusion process.

2. Effect of Phase Fraction, Shape and Size

Second, samples of CuZn37.4BiAs and CuZn37.6BiPAs were subject to various thermal treatments (in the range of 450-850$^{o}$C) to examine the effects of the microstructural parameters by first limiting the α grain size variation whilst modifying the β' phase fraction, and then limiting the variation in the β' phase fraction whilst modifying the average α grain size. Samples were quenched into water to best preserve the microstructures present after elevated temperature annealing. Additional samples of CuZn37.4BiAs were hot compressed (in accordance with the method outlined in Section 3.2.3) in order to mimic a typical elevated temperature forging process before exposing the samples to similar heat treatment protocols followed by standard dezincification testing according to AS2345. Through each of the treatment protocols used, the interconnectivity of these phases was also monitored.

3. Effect of Cooling Rate

Finally, samples of CuZn37.8BiPAs underwent a further range of thermal treatments in the range of 650-850$^{o}$C with the intent to understand the effect of different cooling rates on both the microstructural features and subsequent dezincification resistance as this is not well understood in the literature or in industry today.

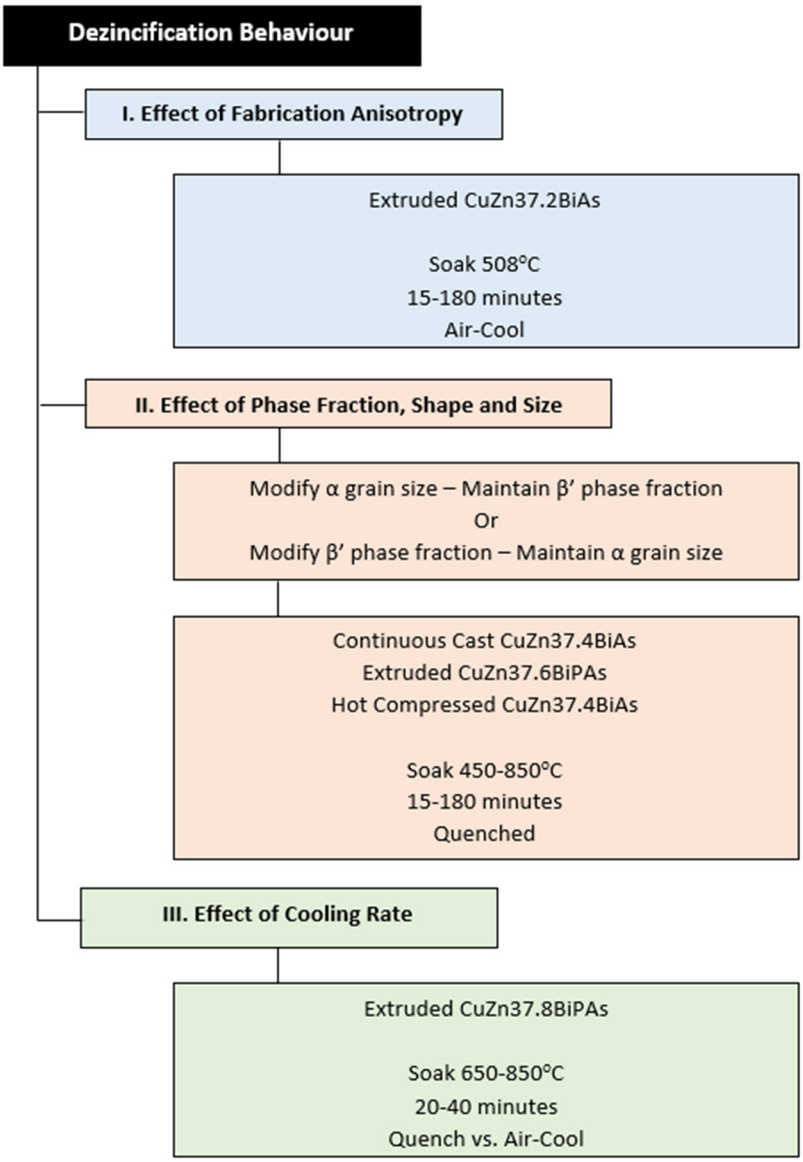


**Figure 6.1: Schematic representation of major experimental work undertaken in Chapter 6.**

## 6.2 Effect of Fabrication Anisotropy

The dezincification resistance of duplex brass is known to depend heavily on the phase fraction of β' [1, 84, 85]. Traditional commercial heat treatments are carried out at intermediate temperatures (between 400-550°C) within the 100% α phase field, in order to reduce the presence of β' and therefore the susceptibility of the alloy to dezincification [45, 81]. In this section, heat treatments are carried out on a CuZn37.2BiAs alloy at 508°C (all-α) for periods of time ranging from 15 minutes to 3 hours in order to assess the evolution of the alloy's dezincification resistance according to ISO6509-1 (2014) [222] as a function of extrusion direction (and resulting grain morphology). This has two important implications; (1) how effective are the standard intermediate heat treatments for improving the dezincification resistance of extruded CuZn37.2BiAs as a function of time and (2) how important is the β' phase interconnectivity and anisotropy for the alloy's dezincification resistance.

Fig. 6.3a-b shows the microstructure and resulting dezincification depths for an as-extruded sample of CuZn37.2BiAs brass in the transverse direction (Fig. 6.2). The dark regions present in the microstructure are β' phase, making up approximately 18.4 vol. % of the alloy, and this phase is shown to be preferentially attacked during the dezincification process (Fig. 6.3b). This alloy contains a small 0.1 wt. % of arsenic (As) which is used to protect the α phase from dezincification and as a result this phase is shown to be largely unaffected. The dezincification in this direction is shown to proceed fairly far into the alloy matrix (on average by ~122μm) due to the significant interconnectivity of the β' phase, however the corrosion path is shown to continuously change direction moving around the more resistant equiaxed α grains, and this is expected to slow the corrosion rate significantly.

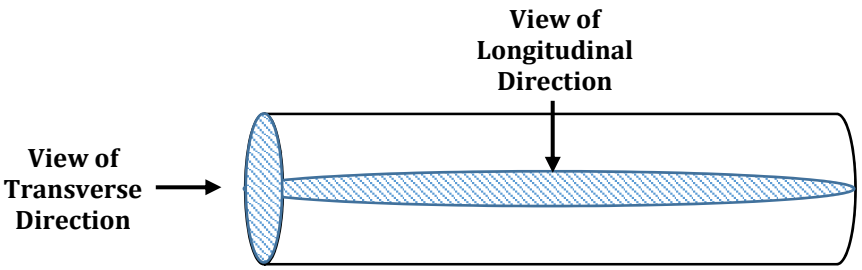


**Figure 6.2: Example of the transverse and longitudinal view for a brass rod sample.**

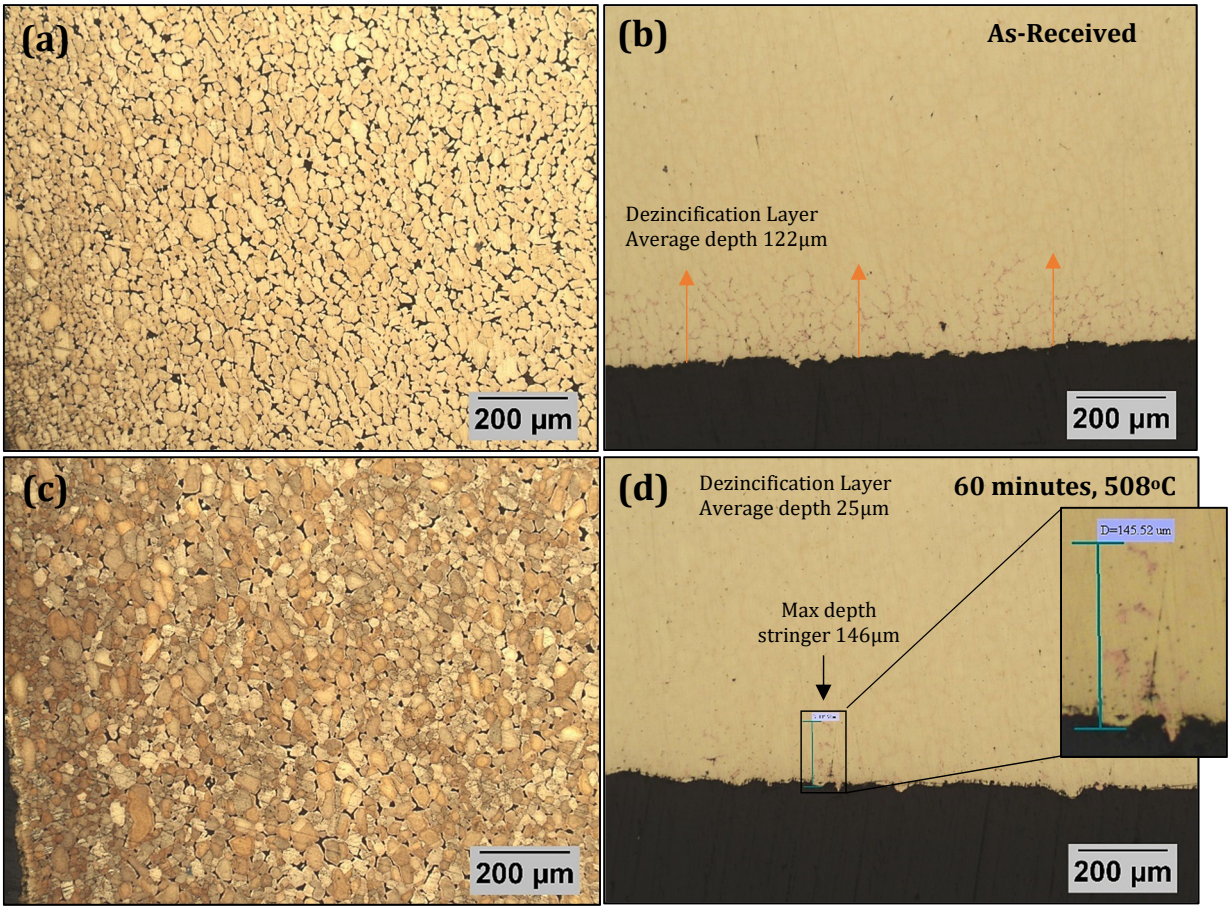


**Figure 6.3: (a) Transverse view of the as-extruded CuZn37.2BiAs microstructure and (b) resulting dezincification of this microstructure after ISO6509-1 test conditions. (c) Transverse view of the extruded CuZn37.2BiAs microstructure after 60 minutes at ~508°C and (d) resulting dezincification of this microstructure after ISO6509-1 test conditions with inset of the β 'stringer'.**

Fig. 6.3c-d shows the microstructure and resulting dezincification depths for the same extruded sample of CuZn37.2BiAs after an intermediate heat treatment has been conducted at 508°C for 60 minutes. There is a significant reduction in the phase fraction of β' from approximately 18.4 to 3.8 vol. % and an associated decrease in the average dezincification depth from 122 µm to 25 µm (inclusive of a maximum depth stringer of 146µm – arrowed Fig. 6.3d). Not only is there a reduction in the amount of β' present, but there is also a reduction in the networking of this phase which makes it more difficult for a continuous corrosion path to form within the matrix.

The evolution of dezincification depth as a function of heat treatment time at 508°C (Fig. 6.4) shows how the gradual decrease in phase fraction of β' and the associated reduction in β' interconnectivity impacts the final resistance of the alloy to this form of corrosion. Although the average dezincification depths (according to AS2345-06 [80]) are found to consistently decrease as the intermediate heat treatment time increases, the maximum individual depth is more difficult to predict. This highlights the importance of localised β' connectivity. If small clusters, also known as 'stingers' of β' are found in

the microstructure, then the corrosion path is able to progress further into the brass matrix, resulting in a higher individual dezincification measurement according to the ISO6509-1 test criteria. This is shown in particular for the CuZn37.2BiAs sample heat treated for 60 minutes (Fig. 6.3d and Fig. 6.4 arrowed 'A'). A higher individual dezincification depth is found compared with the sample heat treated for only 45 minutes and this is because of the presence of a single 'stringer' of β' which has subsequently been attacked during the test (arrowed in Fig. 6.4).

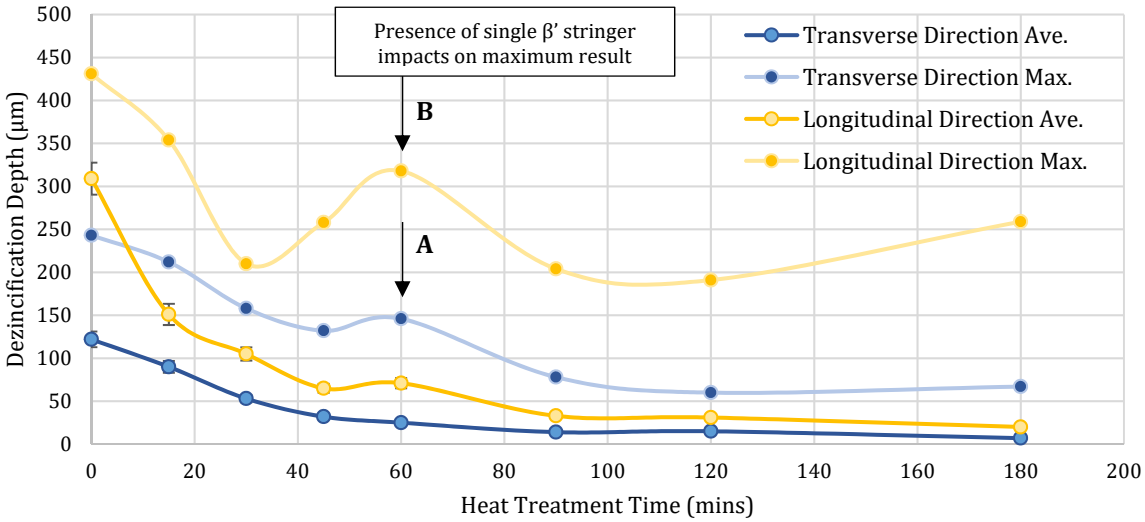


**Figure 6.4: Evolution of dezincification depths of extruded CuZn37.2BiAs as a function of intermediate heat treatment (508°C) length. Depths measured in the transverse direction (blue) and longitudinal direction (gold).**

Fig. 6.5a-b shows the microstructure and resulting dezincification depths for the as-extruded sample of CuZn37.2BiAs brass in the longitudinal (extrusion) direction. This illustrates how a duplex brass with a given phase fraction of β' (in this case ~18.4% vol.) will behave differently depending on the grain morphology and resulting interconnectivity of this phase. An average dezincification depth of 309 µm is found for the longitudinal direction (Fig. 6.5b) against 122 µm for the transverse direction (Fig. 6.3b). This is because the extrusion process tends to produce extended 'stringers' of β' which subsequently present a more linear corrosion path to follow. Therefore, the α grains in their elongated form create less of an obstacle for dezincification to progress in this direction. An intermediate heat treatment at 508°C will again cause a reduction in both the phase fraction and interconnectivity of the β' (Fig. 6.5c-d), however this will not be to the same degree as for the transverse direction, due to the partial retainment of localised β' stringers. After 60 minutes (Fig. 6.4 arrowed 'B' and Fig. 6.5d) the maximum dezincification is 318µm, and even after 180 minutes at 508°C, a maximum dezincification value of 259 µm is observed in this direction.

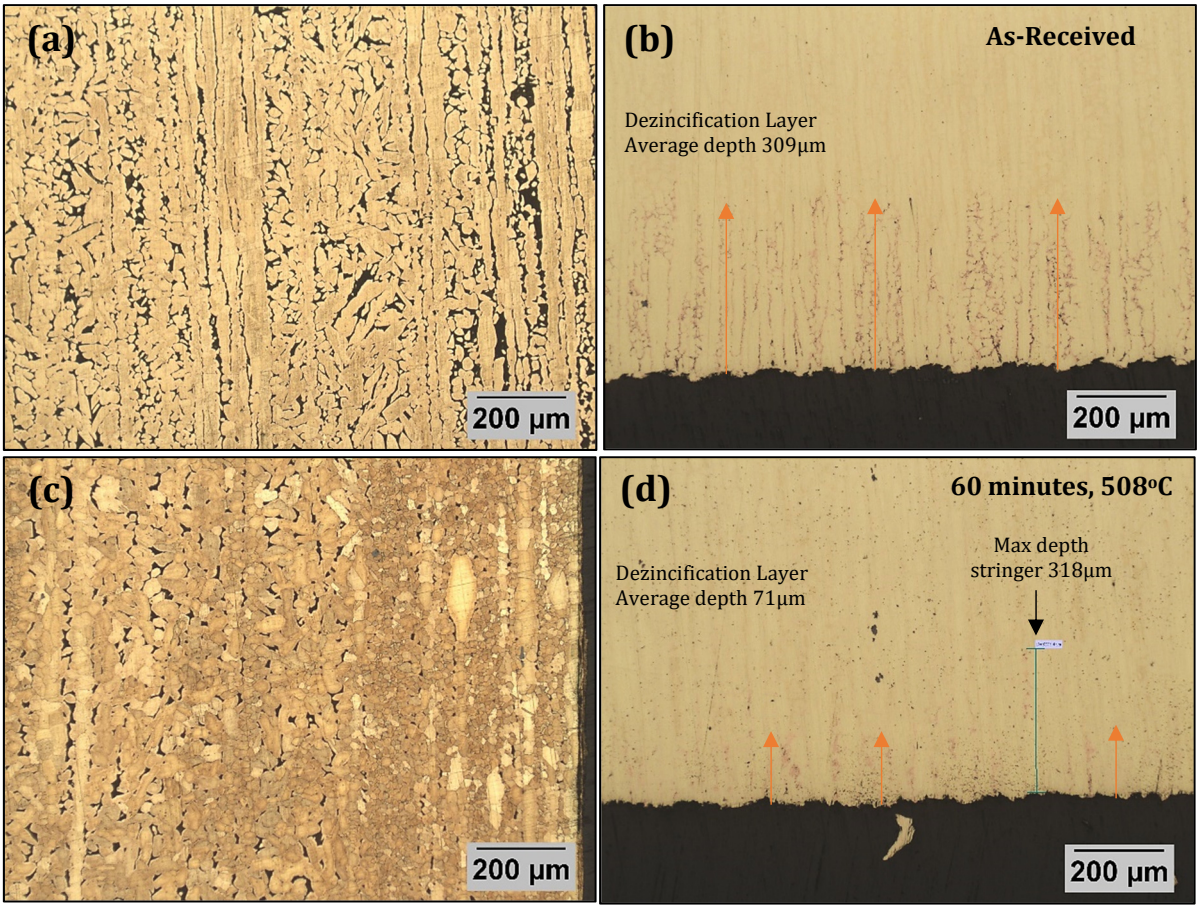


**Figure 6.5: (a) Longitudinal view of the as-extruded CuZn37.2BiAs microstructure and (b) resulting dezincification of this microstructure after ISO6509-1 test conditions. (c) Longitudinal view of the extruded CuZn37.2BiAs microstructure after 60 minutes at ~508°C and (d) resulting dezincification of this microstructure after ISO6509-1 test conditions.**

As a direct result of the interconnectivity of the β' due to the extrusion process, the evolution of the dezincification depth as a function of heat treatment time at 508°C (Fig. 6.4) shows a similar trend to that in the transverse direction, however, the dezincification depths tend to be higher for each data point, and less predictable. This is particularly true when measuring maximum individual depths, compared with averages over 25 measurements. Overall, this is a good example of an extruded duplex brass that is suitable for release in one market, but not another. In this case, after a heat treatment time of 15 minutes the alloy would be deemed suitable for use in the Australian plumbing market as the average dezincification depth drops below 100 µm in the transverse direction and 300 µm in the longitudinal direction. However, it would be deemed unsuitable in the North American market as the maximum dezincification depth remains in excess of 200 µm for the majority of heat treatments, even though the average is very low after 1 hour. This shows how critical the interconnectivity of β' is, in particular for resistance to localised dezincification.

## 6.3 Effect of Phase Fraction, Size and Shape

### 6.3.1 Effect of Fabrication Mode

Samples of the continuous cast CuZn37.4BiAs and extruded CuZn37.6BiPAs raw materials were examined in the as-received condition. Example optical micrographs of both materials are shown in Fig. 6.6.

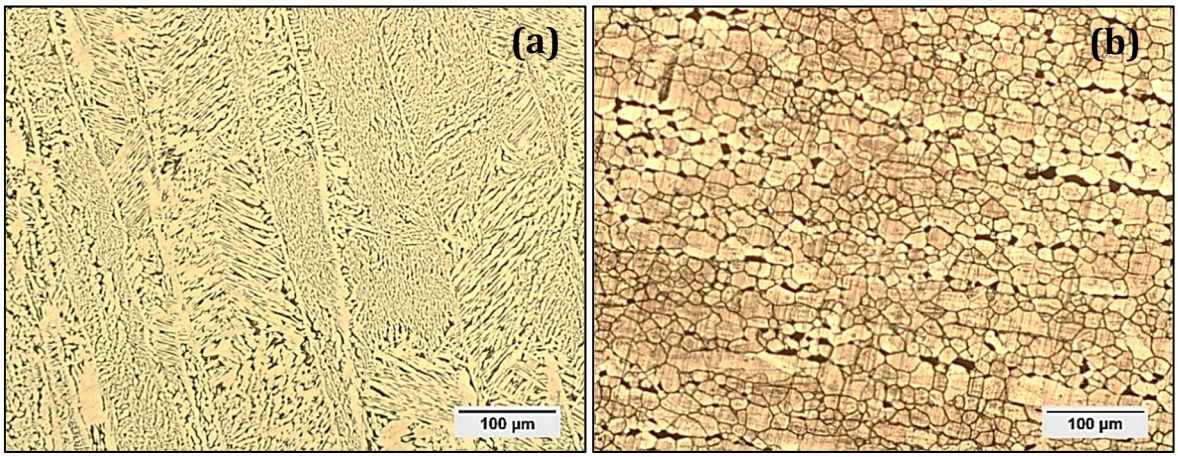


**Figure 6.6: Optical micrographs of a) as-received continuous cast CuZn37.4BiAs brass microstructure, and (b) as-received extruded CuZn37.6BiPAs brass microstructure.**

The continuous casting process involves direct casting (typically in a horizontal orientation) into a rod for subsequent forging and machining. Being a continuous process, raw materials are periodically fed into the brass molten mixture, with ongoing chemical composition checks performed to ensure consistency within the melt and therefore the outgoing cast rod. The casting involves rapid solidification through die-cooling and water spray, and as a result the final grain sizes are typically very small (e.g. Fig. 6.6a compared with Fig. 6.6b). Due to the rapid solidification, the α grains also tend to form with a Widmanstätten plate or needle shape nucleated from the prior β grain boundaries (Fig. 6.6a). The microstructure of the as-received, continuously cast CuZn37.4BiAs (Fig. 6.6a) exhibits an average Widmanstätten α grain length of 19.7 microns with an aspect ratio of 7.57 and a β' phase fraction of 20.0 vol. % (Table 6.2).

Considering this alloy contains over 15% β' and appears to have a level of interconnectivity within the microstructure, the average dezincification depth of 29 µm (Table 6.2) may be considered low for such a high β' phase fraction, and this speaks to the important effect of the α grain size and morphology and this will be further explored in subsequent sections. Dezincification tends to follow the prior β grain boundaries. This makes sense given this is where the first α grains form on cooling during continuous casting and provides the greatest 'wall-like' barriers for the corrosion to progress. An example is shown in Fig. 6.7.

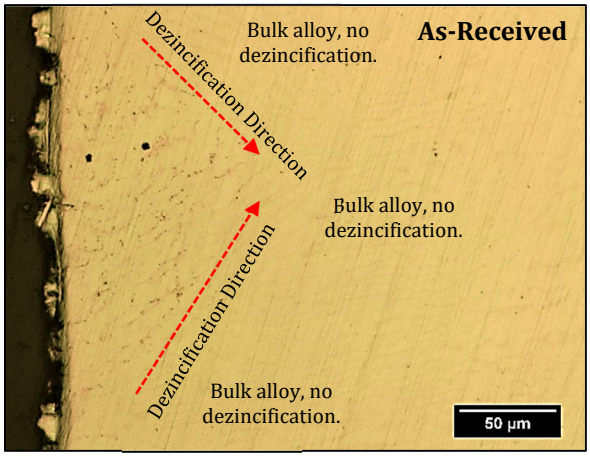


**Figure 6.7: Observation of the tendency for dezincification to follow prior β grain boundaries in the continuous cast CuZn37.4BiAs, likely due to orientation of acicular α grains.**

The extrusion process involves multiple stages beginning with the casting of significantly larger diameter ingots in a similar way to continuous casting. These ingots are then subsequently reheated to forging temperatures (within the α+β phase field) and extruded through a set of dies to achieve the desired rod dimensions. As a result, the α grain size tends to be significantly larger due to reheating/working within the dual phase region, and the individual α grains are much more equiaxed (Fig. 6.6b) than the finer Widmanstätten α produced in the continuously cast product. The other notable effect is that extrusion introduces significant directionality into the structure (e.g. aligned β' in Fig. 6.6b) which causes anisotropic dezincification resistance as demonstrated in Section 6.2. Even though the β' phase fraction is lower in this alloy (~7 vol. %) (Table 6.2) compared with the as-received continuous cast alloy (~20 vol. %), the β' networking in the longitudinal direction tends to form connected lines known as 'stringers', which allows significantly larger depths of dezincification to be achieved (57 µm compared to 29 µm in the continuous cast material, Table 6.2).

In Fig. 6.4 we showed the importance of the β' phase fraction on dezincification, however, from this simple comparison of two brasses, with nominally the same compositions but different fabrication methods, one can see that the β' phase fraction alone is not necessarily a good guide to expected dezincification resistance.

**Table 6.2: Dezincification resistance of the two as-received rod sections according to ISO6509-1.**

| U.N.S. Alloy /Direction | α grain size (µm) length | α grain aspect ratio | β' phase fraction (vol. %) | Average Dezincification Depth (µm) | Maximum Dezincification Depth (µm) |
|---|---|---|---|---|---|
| **CuZn37.4BiAs - Transverse** | 19.7±3.56 | 7.57±0.44 | 20.0 | 29 | 57 |
| **CuZn37.6BiPAs – Transverse** | 17.36±2.03 | ~1 | 7.22 | 8 | 30 |
| **CuZn37.6BiPAs – Longitudinal** | | | | 57 | 168 |

### 6.3.2 Effect of β' Phase Fraction on Dezincification Resistance

#### 6.3.2.1 Continuous Cast and Hot Compressed CuZn37.4BiAs – Effect of β' Phase Fraction

Six samples of the continuous cast rod were annealed at temperatures between 450-675°C for soak times ranging from 15 – 30 min and subsequently water quenched. This annealing step was designed to change the β' phase fraction whilst keeping the α grain size as constant as possible. The β' phase fraction can easily be controlled simply by temperature and the equilibrium phase fractions can be calculated using computational thermodynamics (Chapter 4). However, during annealing the α grain size and shape will also change due to grain growth and phase fraction changes. As a result, different times were used at the different temperatures to manipulate the microstructures to have relatively constant α grain sizes with different β' phase fractions. An example of the microstructures produced by these heat treatments is shown in Figs. 6.8a (450°C 15min) and b (500°C 30min). Increasing the annealing times within the single α phase region have decreased the phase fraction of β' without significantly modifying the average α grain size and shape. In Fig. 6.8a the average α length and aspect ratio is 26.9±2.7µm and 6.8±0.3. In Fig. 6.8b the average α length and aspect ratio is 32.5±3.4µm and 6.6±0.3.

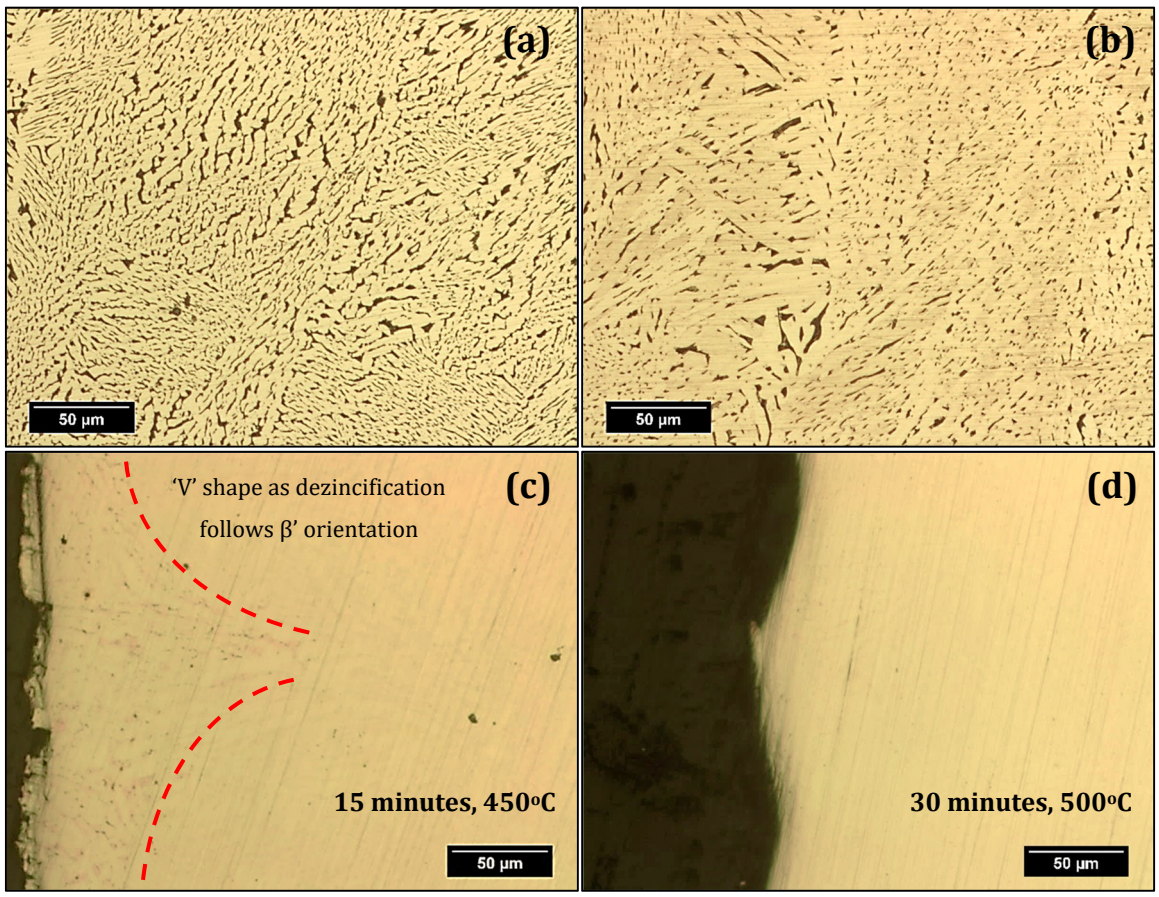


**Figure 6.8: (a) CuZn37.4BiAs microstructure post-heat treatment at 450°C for 15 minutes, (b) CuZn37.4BiAs microstructure post-heat treatment at 500°C for 30 minutes, (c-d) resulting dezincification of these microstructures after testing to ISO6509-1.**

The average α grain length (µm) and aspect ratios of the six continuously cast samples after annealing treatment between 450 – 675°C are shown in Fig. 6.9 to illustrate the consistency of the overall grain size. The acicular grain length is held between 26.8-34.3µm, whilst the aspect ratio shifts mildly between 4.3 – 6.8.

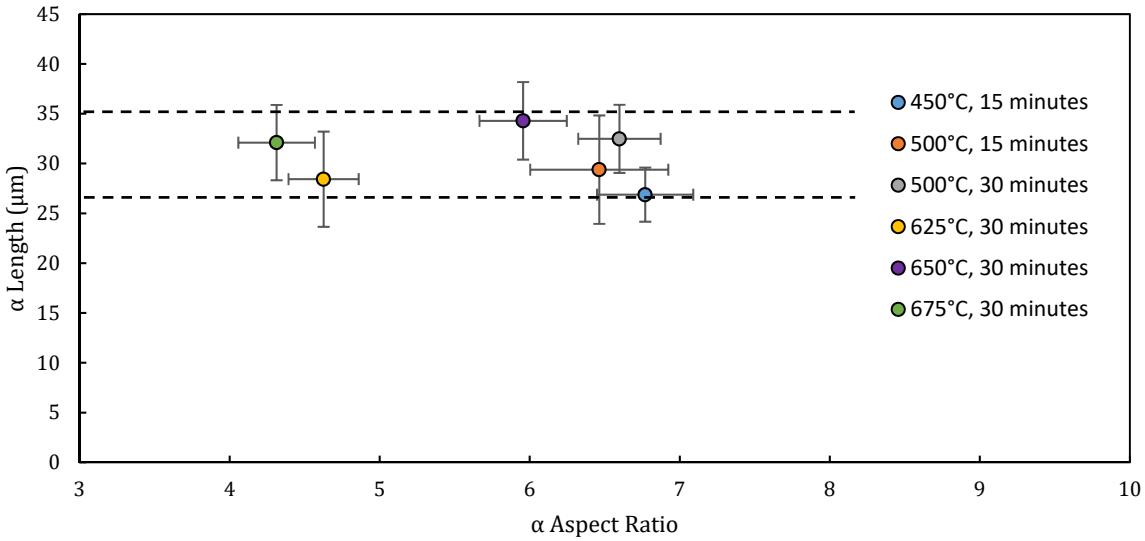


**Figure 6.9: Average α grain length (µm) vs. aspect ratio of continuously cast CuZn37.4BiAs samples annealed between 450-675°C.**

Six dezincification tests were performed in accordance with ISO6509-1 on these continuously cast samples annealed to produce different β' phase fractions at relatively constant α grain length. The results are summarised in Fig. 6.10.

The average α grain length was maintained between 26.8 – 34.3 microns with the β' phase fraction ranging from 12 – 25 vol. %. As initial testing on the as-received, continuously cast samples shows a negligible effect of the sample orientation, only the transverse direction was tested for dezincification resistance in this case. Fig. 6.10 shows a steady increase in the average and maximum dezincification depths as the β' phase fraction increases. This strong dependence of dezincification resistance on the β' phase fraction is well known and represents one of the two strategies used in industry to improve the dezincification resistance of duplex brasses (the other being the use of alloying inhibitors).

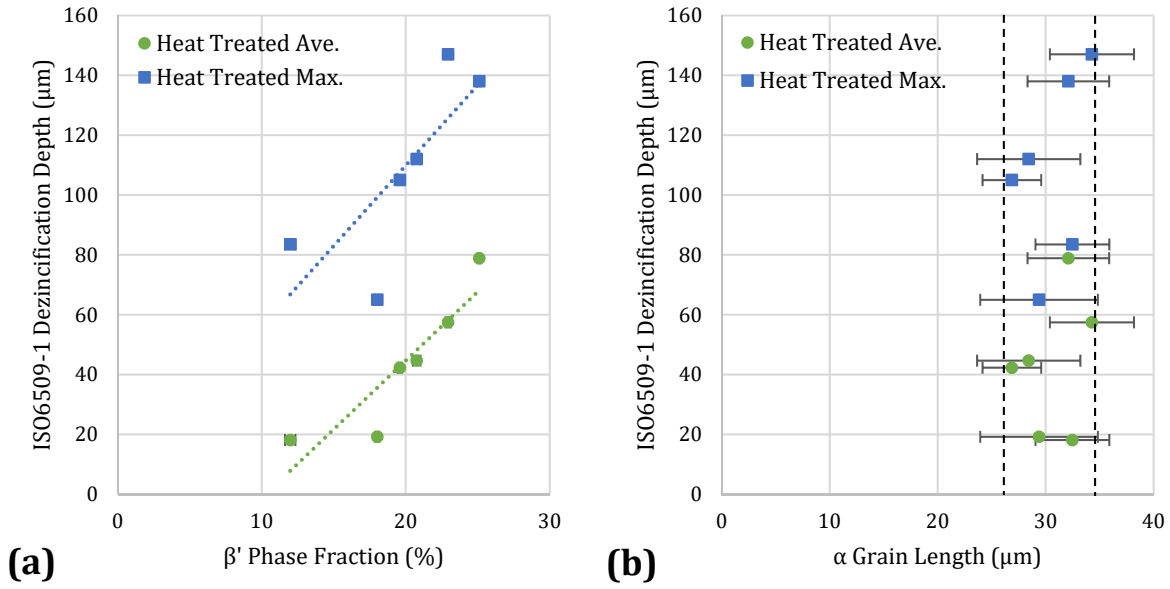


**Figure 6.10: Continuous cast CuZn37.4BiAs Dezincification (ISO6509-1) dependency on (a) β' phase fraction while (b) α grain size is maintained.**

Optical micrographs showing the dezincification depths of the continuously cast samples annealed for 15 minutes at 450°C and 30 minutes at 500°C are shown in Figs. 6.8c and d in the unetched state. The dezincification attack is preferentially targeting the thin β' phase present in the form of 'stringers' in the microstructure. A distinctive 'V' shape of dezincification is formed in the first sample (Fig. 6.8c) due to the Widmanstätten shape of the α grains (aspect ratio ~6.8) producing a maximum depth of ~105µm. This is then almost totally absent for the second sample (Fig. 6.8d) as the β' phase has decreased significantly, and the β' that is still present is not well networked, so dezincification cannot proceed to any significant degree (average depth <20µm).

Samples of the continuous cast brass were additionally hot compressed at 750°C at a strain-rate of $0.85s^{-1}$ in order to mimic a forging process. The hot-compressed samples were then subjected to annealing for 30 minutes at temperatures ranging from 450 – 750°C. These samples were subsequently water quenched in order to preserve the β' phase fraction, with minimal impact on the α grain size. This difference in β' phase fraction is clearly observed in Fig. 6.11a (13.6%) and b (58.0%). The heat treatment at 750°C has produced a greater volume fraction of β' (Fig. 6.11b) without significantly impacting the average α grain size (24.3±2.8µm) compared with a sample heat treated at 550°C for the same duration (Fig. 6.11a, 25.9±1.9µm). In this case, one can see that the α is much more equiaxed after hot compression and annealing than for the case without hot compression (Fig. 6.8).

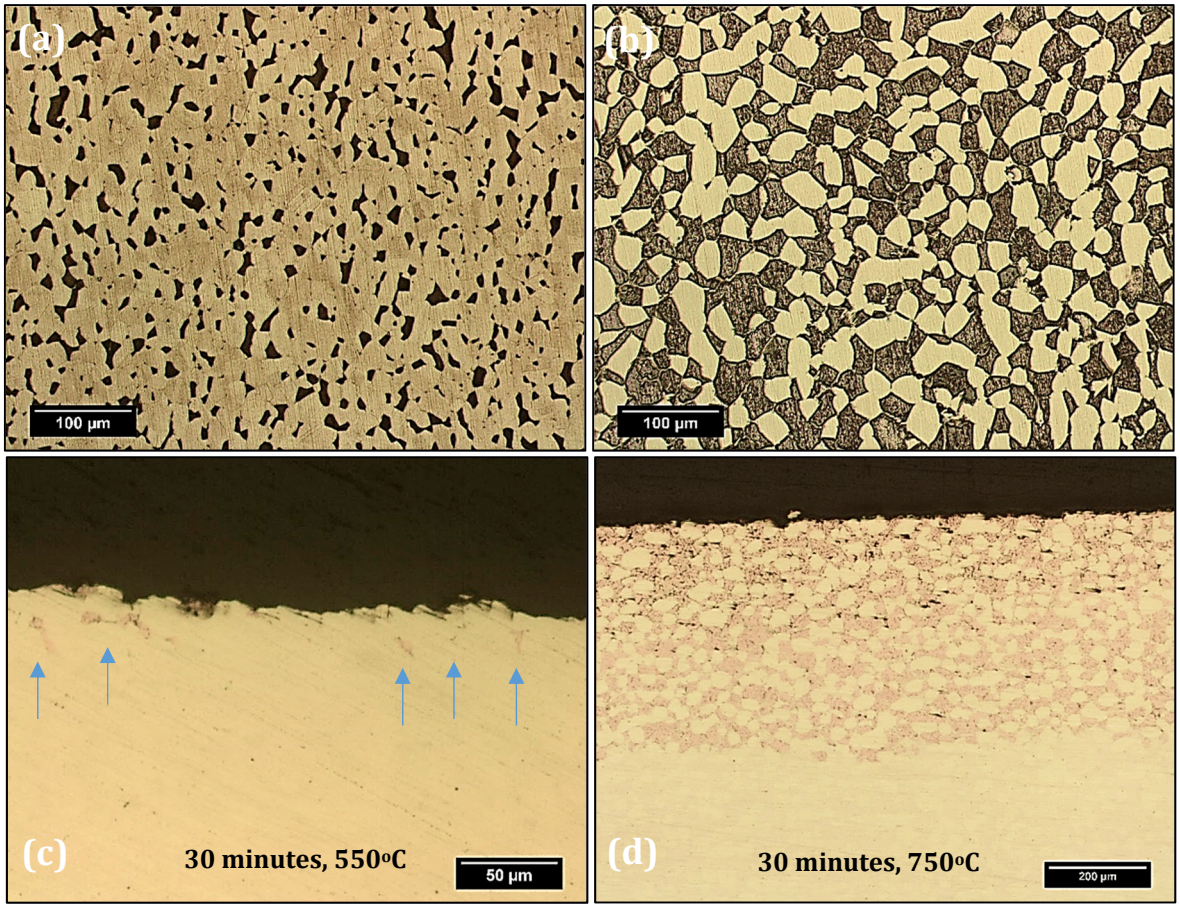


**Figure 6.11: (a) Hot compressed CuZn37.4BiAs microstructure post-heat treatment at 550°C for 30 minutes, (b) Hot compressed CuZn37.4BiAs microstructure post-heat treatment at 750°C for 30 minutes, (c-d) resulting dezincification of these microstructures after testing to ISO6509-1.**

Seven continuously cast, then hot compressed and subsequently annealed samples with varying β' phase fractions were tested for dezincification resistance in accordance with ISO6509-1. The average α grain size was maintained between 23.2 – 32.2µm (with an aspect ratio between 1-2 – an equiaxed morphology) with a β' phase fraction range of 14-60%. As the samples were hot compressed, this can introduce a degree of directionality into the microstructure and therefore dezincification testing was carried out in both the transverse and longitudinal directions in order to observe any anisotropy in dezincification behaviour. The average dezincification depths are summarised in Fig. 6.12. The results in Fig. 6.12 show an increase in dezincification depth for both the transverse (from 15 to 374 µm) and longitudinal directions (from 13 to 471 µm) as the β' phase fraction increases. However, this trend is not as clear as it was for the as-received continuously cast material subject to annealing (Fig. 6.10). Fig. 6.12 shows that there was little difference between the longitudinal and transverse directions, with a slightly higher average dezincification depth recorded for the longitudinal direction. Even though one could predict the increasing dezincification depth with increasing β' phase fraction, the dependence is non-linear and suggests that other factors are also important.

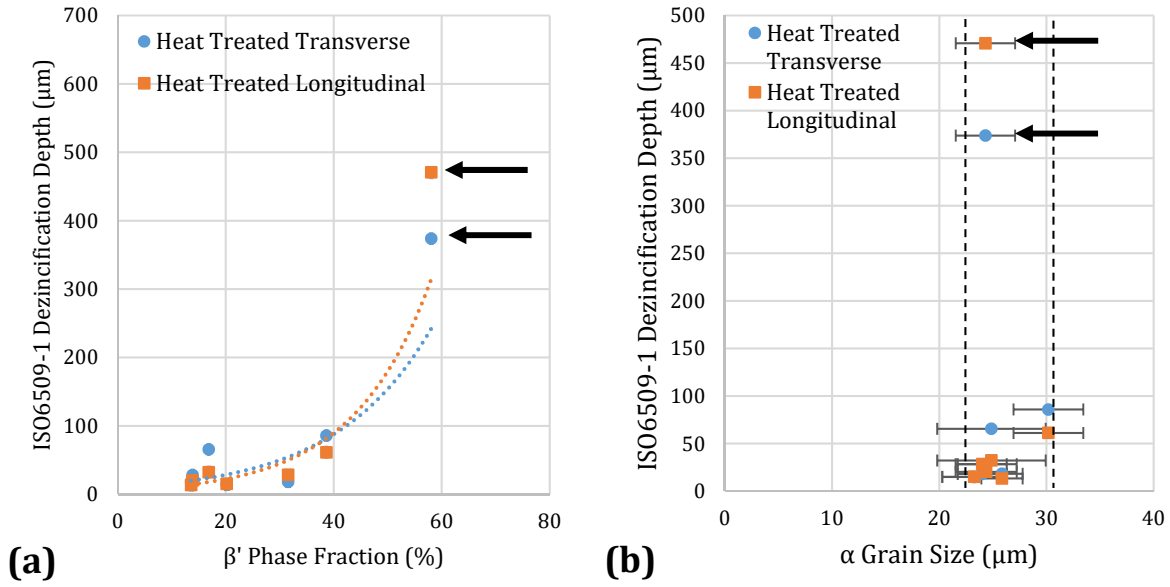


**Figure 6.12: Hot compressed continuous cast CuZn37.4BiAs Dezincification (ISO6509-1 average depth) dependency on (a) β' phase fraction while (b) α grain size is maintained.**

A large increase in the dezincification depth is shown for the arrowed data points in Fig. 6.12. These samples contain 58% β', and this microstructure is shown in Fig. 6.11b. The microstructure in Fig. 6.11a has a β' phase fraction of 14% and as a result of the anneal at 550°C after hot compression, the α grains have recrystallised and disrupted the interconnectivity of the β' (blue arrows Fig. 6.11c). Even though the α grains in Fig. 6.11b have also become equiaxed (aspect ratio 1.59), enough β' has formed that the interconnectivity of the β' has been restored. This allows the dezincification process to proceed more easily through the matrix as shown in Fig. 6.11d for an average depth of 374 microns and a maximum individual depth of 440 microns in the transverse direction, and an average depth of 471 microns and a maximum individual depth of 515 microns in the longitudinal direction. The abrupt change in dezincification depth from a β volume fraction of 40% to one of 58% in Fig. 6.12 is indicative of a percolation threshold [234]. This represents a critical β volume fraction above which a relatively linear interconnected path (and hence corrosion path) through the microstructure can be identified. Indeed, for equiaxed phases, the percolation threshold lies between 40-60% depending on the assumptions of the percolation model [234]. In Section 6.5 we will examine these effects using percolation simulations.

### 6.3.2.2 Extruded CuZn37.6BiPAs - Effect of β' phase fraction

Samples of extruded CuZn37.6BiPAs were similarly heat treated for different times at temperatures ranging from 450 – 750°C to manipulate the β' phase fraction whilst maintaining a relatively constant α grain size. An example of this change in β' phase fraction is shown in Fig. 6.13a (500°C 15min) and b (625°C 30min). In both of these cases the α grains have retained their original equiaxed morphology with sizes of 18.6±2.0µm and 19.9±1.6µm respectively, whilst the β volume fraction changes from 9.2% to 36.4%.

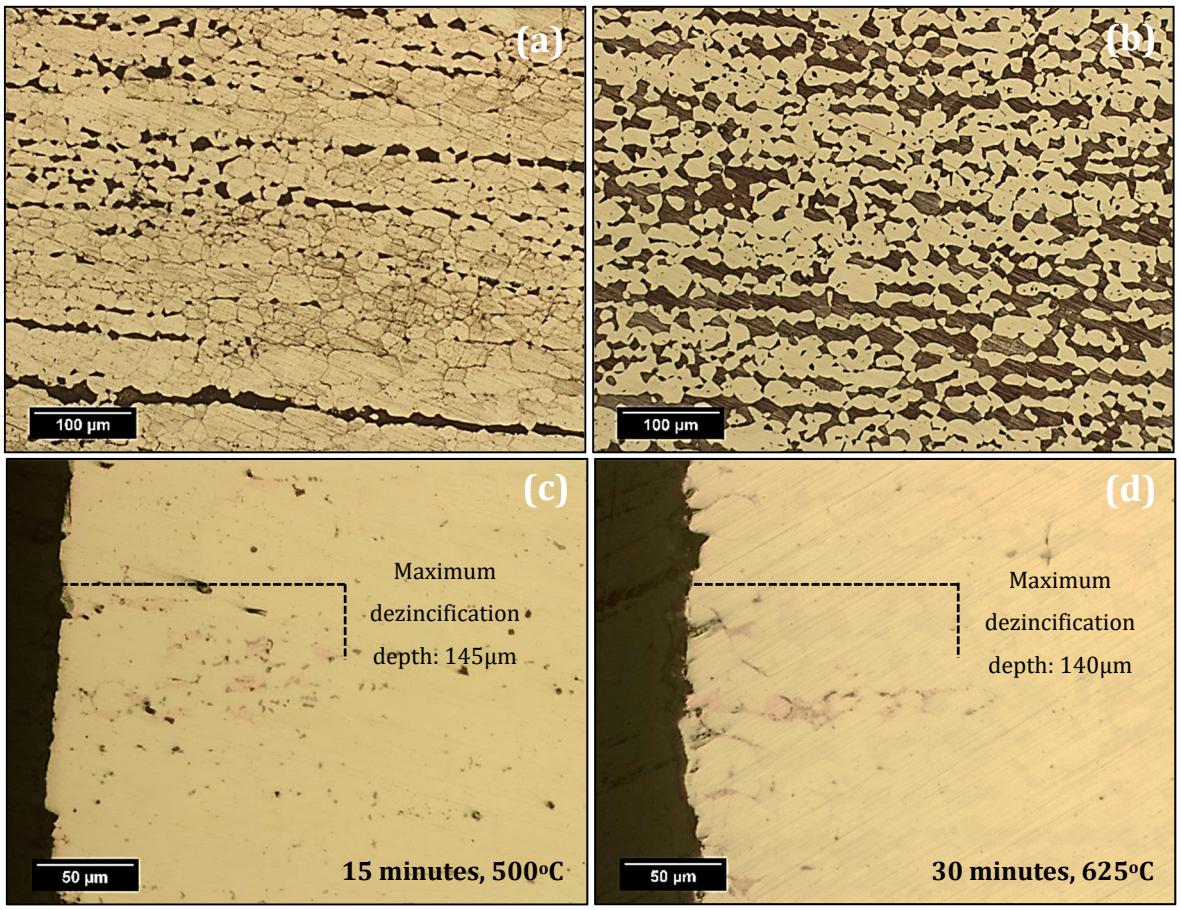


**Figure 6.13: (a) CuZn37.6BiPAs microstructure in the longitudinal direction post-heat treatment at 500°C for 15 minutes, (b) CuZn37.6BiPAs microstructure in the longitudinal direction post-heat treatment at 625°C for 30 minutes, and (c-d) the resulting dezincification of these microstructures after ISO6509-1 test conditions.**

Seven samples of the extruded brass with a varying phase fractions of β' were tested for dezincification resistance in accordance with ISO6509-1. The samples had an average α grain size between 17.2 – 24.5 µm with a β' phase fraction range of 7 – 52 vol. %. Dezincification testing was carried out in both the transverse and longitudinal directions to probe the anisotropic behaviour.

The average and maximum dezincification depths are summarised in Fig. 6.14, along with a direct comparison to the continuous cast sample data (Section 6.3.2.1). The extruded samples show only a

weak increase in dezincification depths in the transverse direction (from 4 to 28 µm) and no significant dependence of dezincification depths in the longitudinal direction with increasing β' phase fraction. This is unexpected because the β' phase fraction is higher for 4 of the extruded samples compared with the continuous cast data set (Section 6.3.2.1). Differences are observed, however, between the average α grain size for the equiaxed extruded samples (average of 20.6µm) and the acicular α of the continuous cast samples (30.6µm average α grain length with an aspect ratio of 5.8).

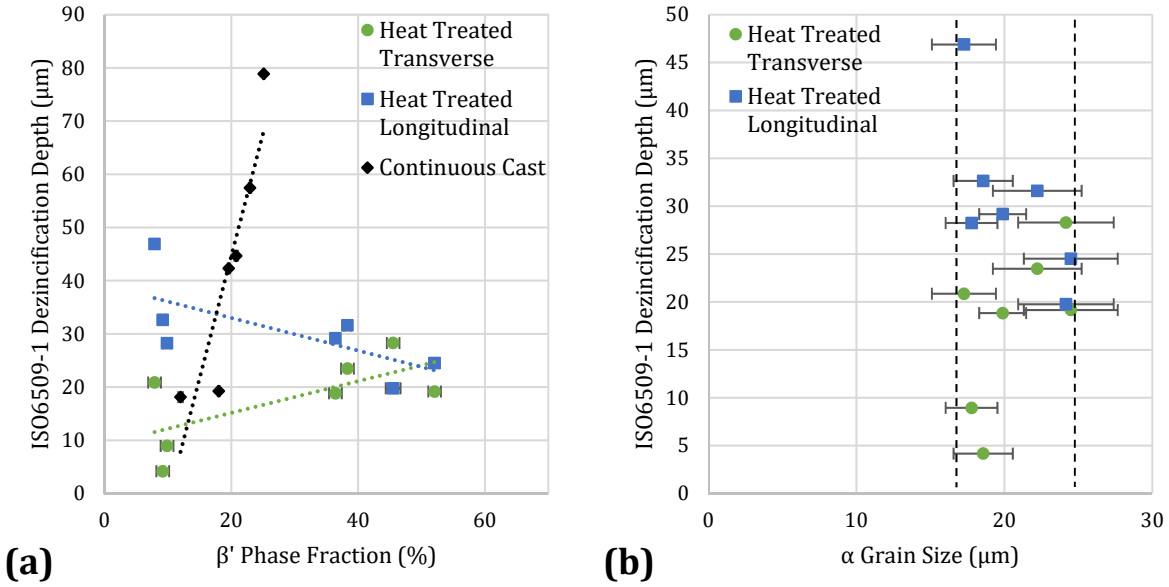


**Figure 6.14: Extruded CuZn37.6BiPAs Dezincification (ISO6509-1 average depth) dependency on (a) β' phase fraction while (b) α grain size is maintained.**

Using a direct comparison of the microstructures and resulting dezincification depths found in Fig. 6.13a and c (500°C, 15 minutes) and Fig. 6.13b and d (625°C, 30 minutes), a significant increase in the β' phase fraction for the extruded sample heat treated at 625°C is observed. However, both the average and maximum individual dezincification depths are very similar for both samples. As a result of the equiaxed α grain morphology (aspect ratio 1.55 and 1.38 respectively) one would assume a greater depth of dezincification would be achieved in the sample containing greater β', however the interconnectivity of the β' may still be limited thereby impeding the corrosion path throughout the 24-hour accelerated test conditions. This will be explored further in Section 6.3.3.2 and Section 6.4. It should also be noted that the extruded CuZn37.6BiPAs samples tested in this section contain small amounts of phosphorus (P – 0.10 wt. %) which is a known α phase dezincification inhibitor. This inclusion in the chemical composition may be aiding in the overall dezincification resistance of these components, however it has never been identified in prior literature that phosphorus is capable of also protecting the β' phase under certain microstructural conditions.

### 6.3.3 Effect of α Grain Size and Shape on Dezincification Resistance

#### 6.3.3.1 Continuous Cast and Hot Compressed CuZn37.4BiAs – Effect of α Grain Size

Seven samples of the continuous cast CuZn37.4BiAs brass were heat treated at a temperature of 700°C for soak times ranging from 30 – 180 minutes in order to manipulate the α grain size and shape whilst maintaining a relatively constant β' phase fraction. In addition, selected samples were heat treated at 800°C and 850°C for various times between 20-60 minutes to accelerate the α grain growth before furnace cooling to 700°C to set the β' phase fraction and then water quenching to preserve the microstructures for dezincification testing. Example microstructures are shown in Fig. 6.15a-c. It is clear from Fig. 6.15 that the α grains adopt a Widmanstätten morphology, initially with a high aspect ratio, but during annealing both their shape and size evolve.

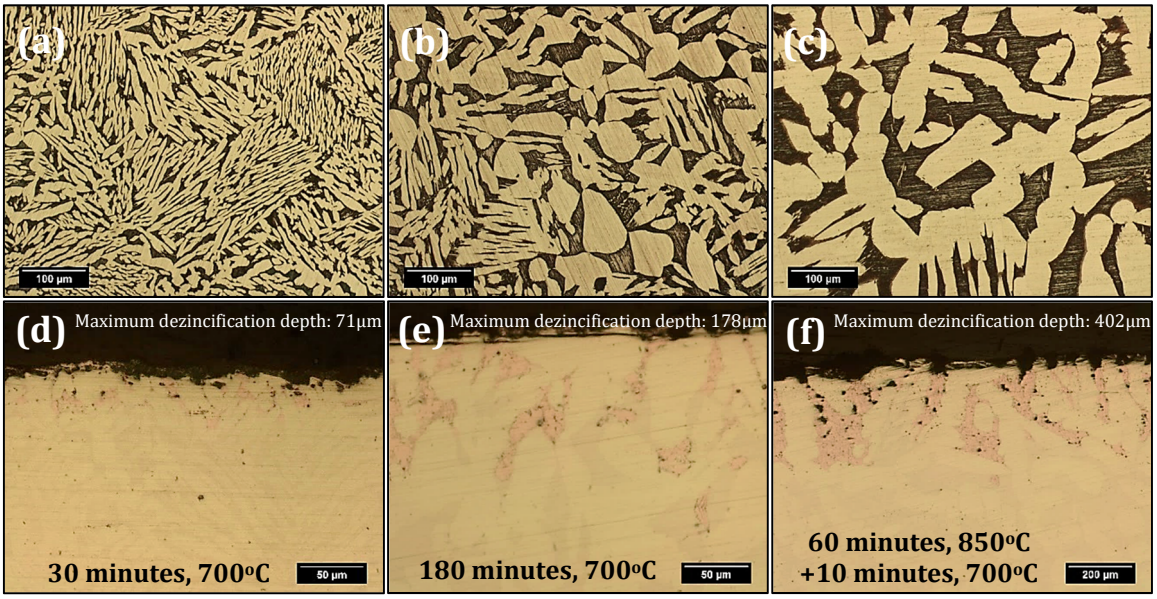


**Figure 6.15: (a) CuZn37.4BiAs microstructure post-heat treatment at 700°C for 30 minutes, (b) at 700°C for 180 minutes, (c) at 850°C for 60 minutes and ramped down to 700°C for 10 minutes, and (d-f) resulting dezincification of these microstructures after testing to ISO6509-1.**

The average α grain length (µm) and aspect ratios of the as-received and seven continuously cast samples after annealing treatment between 700-800°C are shown in Fig. 6.16 to illustrate the evolution of the grain size and shape seen in the microstructures of Fig. 6.15a-c. The acicular grain length increases from an as-received 19.7µm to a range of 64 – 226µm with increasing heat treatment time. The aspect ratio initially increases from the as-received 7.57 to 7.98 for 700°C after 30 minutes, and then subsequently decreases to 6.21, whilst the 800°C heat treatments increase up to 8.76 before the 850°C heat treatments decrease to 4.51. This can be explained though the process of self-coarsening [235]. The original smaller Widmanstätten α grains grow initially via lengthening of the plates, before they eventually coarsen and become more equiaxed with annealing time. This is highlighted in Fig. 6.16 for both the 700°C (A) and 800/850°C (B) heat treatments.

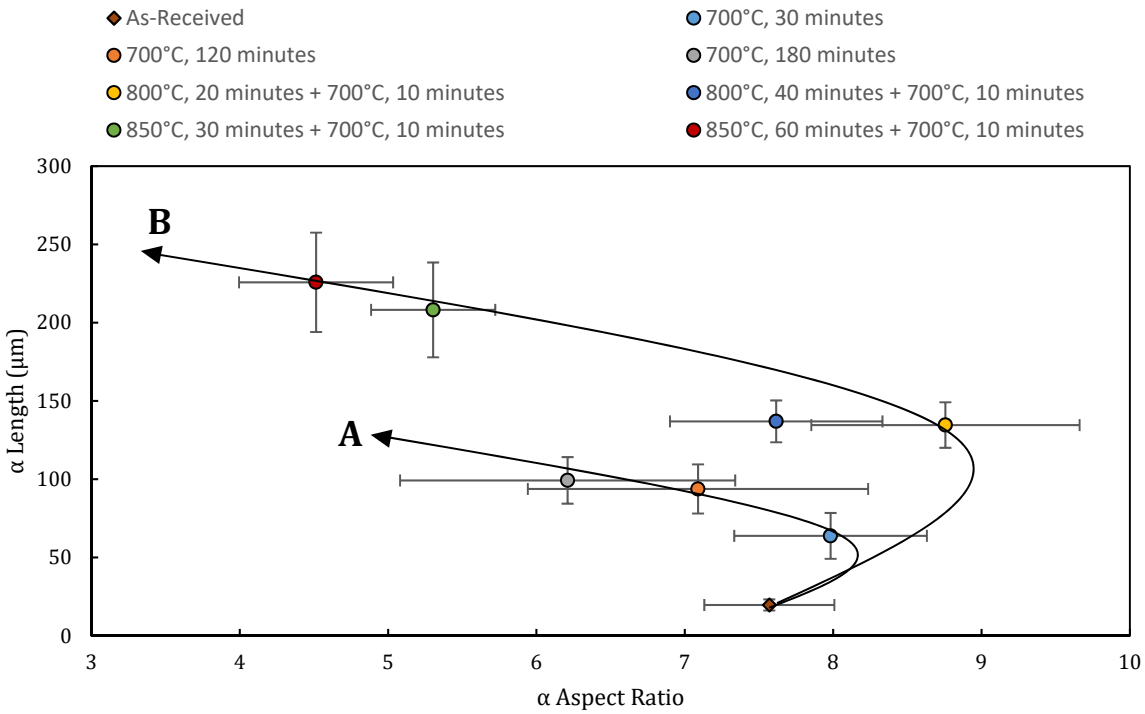


**Figure 6.16: Average α grain length (µm) vs. aspect ratio of continuously cast CuZn37.4BiAs samples annealed between 700-800°C. The self-coarsening trend is highlighted (black curves A and B).**

The seven annealed continuously cast samples with a range of average α grain sizes (64-226µm α length and ave. aspect ratio of 6.78), at relatively constant β' phase fraction (34-44%)) were tested in accordance with ISO6509-1 and the results are summarised in Fig. 6.17. As initial testing on the as-received samples shows little difference in test direction for the continuous cast fabrication method, only the transverse direction was tested for dezincification resistance. In Fig. 6.17 we observe a strong increase in both the average (from 37 to 365 µm) and maximum (from 59 to 465 µm) dezincification depths as the average α grain length increases and the aspect ratio simultaneously decreases. This has very important implications on any percolation limit found for β' phase fraction as an increase in α grain size will likely reduce the percolation limit of β required.

Compared to the effect of β' phase fraction on dezincification depth (Figs. 6.10, 6.12 and 6.14), the combined effect of increasing α grain length and decreasing the aspect ratio is shown to be significantly stronger in this range of β' phase fraction and this is the first time this effect has been reported. It highlights that at least as much attention should be applied to maintaining a fine α grain size as to minimising the β' phase fraction. Considering the very important effect that β' has on properties such as machining (Chapter 7), it may actually be preferable in practice to maintain some β' in the matrix and use the α grain size to bring the dezincification behaviour to an appropriate level. The α grain size is an important lever that the brass metallurgist may use to manipulate the dezincification resistance.

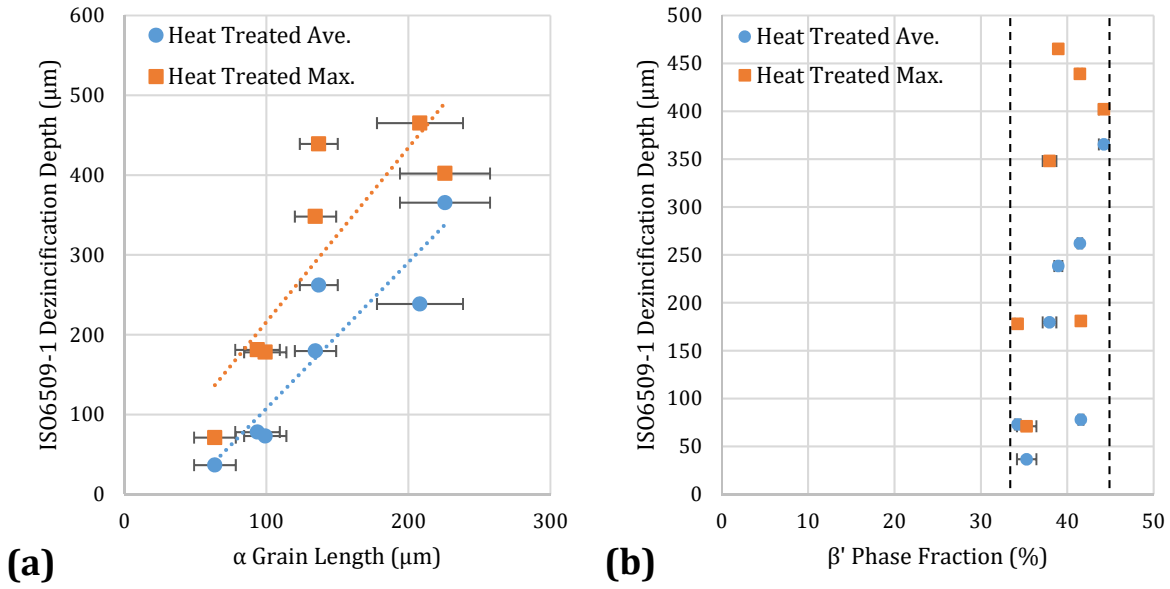


**Figure 6.17: Continuous cast CuZn37.4BiAs Dezincification (ISO6509-1) dependency on (a) α grain size while (b) β' phase fraction is maintained.**

The microstructures shown in Figs. 6.15a-c are continuously cast samples annealed at 700°C for 30 and 180 minutes, and at 850°C for 60 minutes followed by a furnace cool to 700°C for 10 minutes, respectively. They illustrate the evolution of the α grain size and morphology with annealing time. As the α grains in the continually cast brass grow, they change morphology into a more equiaxed shape in this case from aspect ratios of 7.98 to 6.21 to 4.51, and this in turn alters the interconnectivity of the β' phase. This is particularly evident in Fig. 6.15c, where the α grains allow the dezincification path to proceed much further into the brass matrix, attacking the susceptible β' phase. The dezincification of these microstructures is shown in the corresponding dezincification images (Fig. 6.15d-f), where very high depths are obtained for α grain lengths in excess of 100 µm causing more rapid percolation. It is shown that both the size and aspect ratio are important in this case.

Samples of the continuous cast CuZn37.4BiAs were also hot compressed at 750°C to mimic a typical hot working process, air-cooled and subsequently annealed at 700°C for a range of annealing times to again manipulate the α grain size at relatively constant β' phase fraction. The microstructures shown in Figs. 6.18a and b illustrate some of the differences observed. In Fig. 6.18a the average α grain size is 40.1±2.5µm, whilst in Fig. 6.18b the average α grain size is 166.7±29.8µm. Both microstructures show equiaxed conditions similar to the hot compressed samples in Section 6.3.2.1, with increasing heat treatment increasing the rate of grain growth.

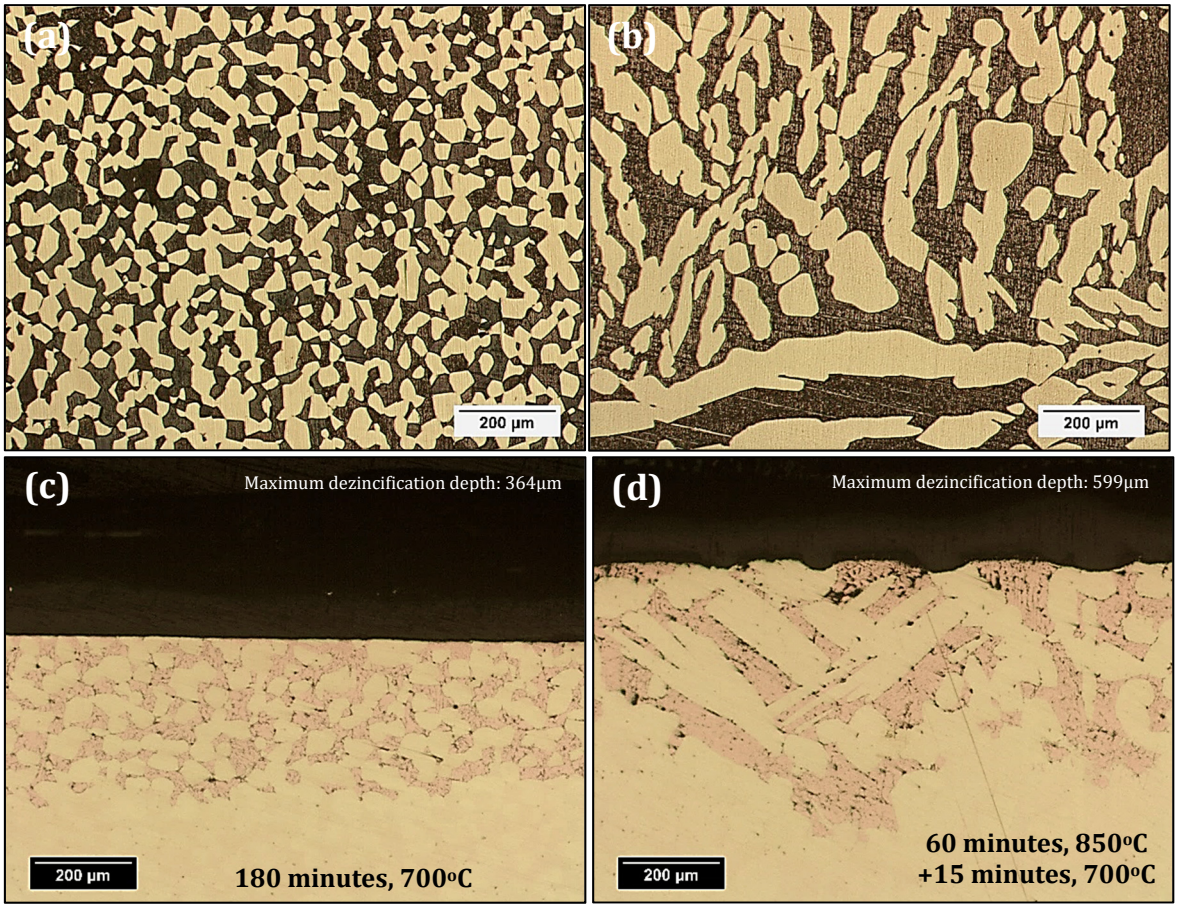


**Figure 6.18: (a) Hot compressed CuZn37.4BiAs microstructure post-heat treatment at 700°C for 180 minutes, (b) at 850°C for 60 minutes and ramped down to 700°C for 15 minutes, and (c-d) the resulting dezincification of these microstructures after ISO6509-1 test conditions.**

Six dezincification tests were completed with the β' phase fraction maintained between 38-46 % and an average α grain size range of 30 – 167µm. Dezincification testing was carried out in both the transverse and longitudinal directions. The average and maximum dezincification depths are summarised in Fig. 6.19.

Similar to the reports of the effect of α grain size on dezincification depths in the previous section, we observe a strong increase in the recorded average dezincification depths for both the transverse (from 86 to 554 µm) and longitudinal directions (from 61 to 542 µm) as the average α grain size increases, however in this case the α grains are equiaxed so this shows an intrinsic effect of α grain size without the compound effect of aspect ratio. Similar to the findings for hot compressed CuZn37.4BiAs tested for dezincification resistance as a function of β' phase fraction, the trends observed for this data set are less consistent than that for the continuous cast-only samples and this is strongly related to the interconnectivity of the β' phase in the microstructure as a function of grain size. This data supports the earlier observation that the effect of increasing α grain size and its role on increasing interconnectivity (and improving the subsequent percolation path) is shown to be a significant

microstructural factor, even more so than the effect of increasing β' phase fraction. In Fig. 6.19 it appears that there is a critical α grain size (~35µm) below which dezincification is greatly reduced. This will be explored in Section 6.5 using percolation simulations.

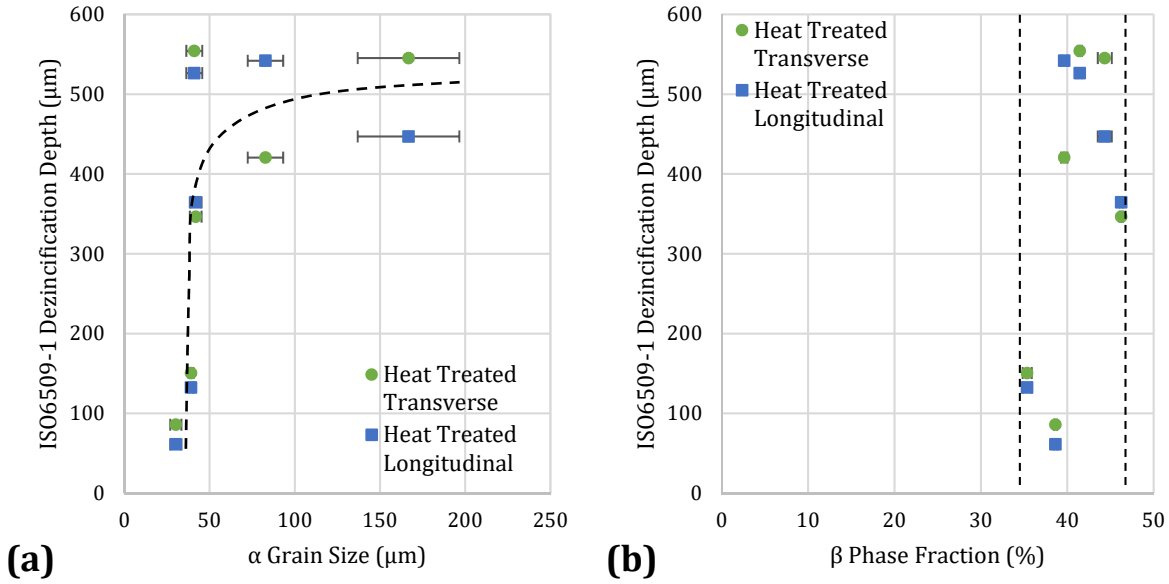


**Figure 6.19: Hot compressed continuous cast CuZn37.4BiAs Dezincification (ISO6509-1 average depth) dependency on (a) α grain size while (b) β' phase fraction is maintained.**

With respect to the increasing trends observed in Fig. 6.19, the corresponding microstructures in Figs. 6.18a and b, which are of the hot compressed CuZn37.4BiAs samples heat treated for 180 minutes at 700°C (Fig. 6.18a) and for 60 minutes at 850°C before furnace cooling to 700°C (Fig. 6.18b), highlights how important the interconnectivity of the β' phase is for dezincification to proceed into the brass matrix. In both cases the strong networking of this phase has produced average dezincification depths well in excess of 300 microns, and both of these brasses would be unfit for potable water service in their given microstructural state. As a direct result of the significantly larger α grain size (166.7±29.8 µm) for the sample in Fig. 6.18b, large regions of β' are freely available for preferential attack without any α grains available to impede the dezincification process.

### 6.3.3.2 Extruded CuZn37.6BiPAs - Effect of α Grain Size

Samples of the extruded CuZn37.6BiPAs were heat treated at a temperature of 700°C for soak times ranging from 30 – 180 minutes in order to manipulate the α grain size, with minimal impact on the β' phase fraction. In addition to this, further samples were heat treated at 850°C for a range of soak times between 30 - 60 minutes in order to further accelerate the rate of α grain growth before furnace cooling to 700°C and water quenching to preserve the microstructures for dezincification testing. An example of the gradual progression in increasing average α grain size with increasing heat treatment soak times and temperatures is shown below in Fig. 6.20a-c. This also illustrates the gradual increase in β' interconnectivity as the α grains increase in size. In this case, starting from the extruded state the α grains remain relatively equiaxed.

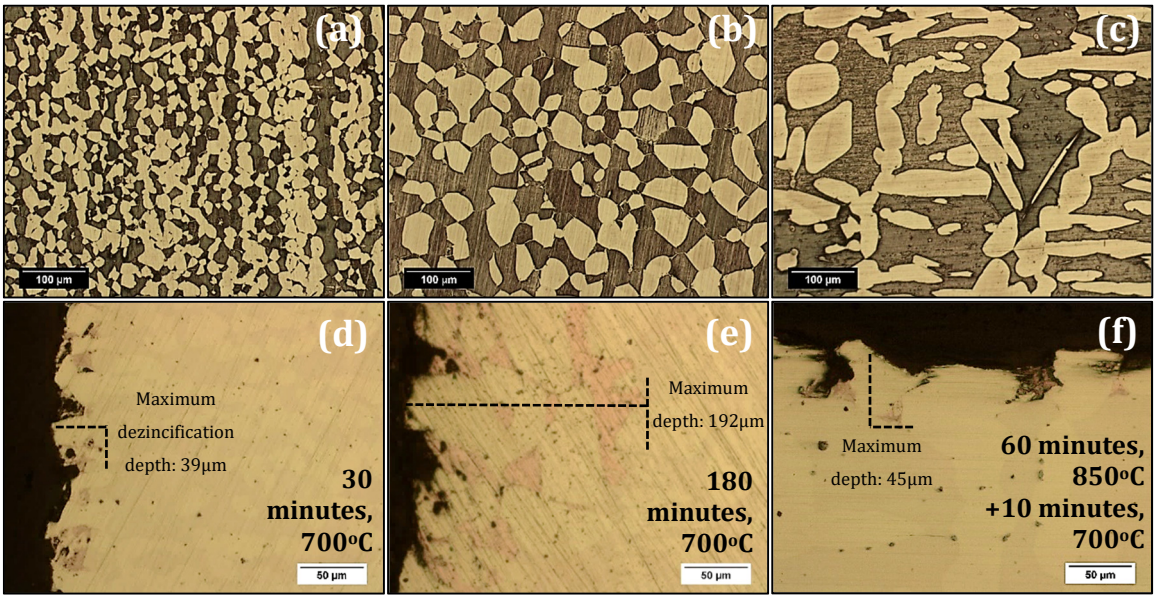


**Figure 6.20: (a) CuZn37.6BiPAs microstructure in the longitudinal direction post-heat treatment at 700°C for 30 minutes, (b) CuZn37.6BiPAs microstructure in the longitudinal direction post-heat treatment at 700°C for 180 minutes, (c) CuZn37.6BiPAs microstructure in the longitudinal direction post-heat treatment at 850°C for 60 minutes and ramped down to 700°C for 10 minutes, (d-f) the resulting dezincification of these microstructures after ISO6509-1 test conditions.**

A total of 6 tests were completed with the β' phase fraction maintained between 48.7 –56.4 vol. % and an average α grain size range of 13.8 – 37.0 microns. As these samples were fabricated via extrusion, this has introduced a degree of grain directionality into the brass matrix, therefore dezincification testing was carried out in both the transverse and longitudinal directions to account for any differences. The average dezincification depths over 25 measurements for this sample set are shown in Fig. 6.21 with a comparison to the continuous cast sample data taken in Section 6.3.3.1. Similar to the results obtained in Section 6.3.2.2., Fig. 6.21 shows a negligible trend for both the transverse and longitudinal directions with only one single average measurement in excess of 50

microns (sample heat treated at 700°C for 180 minutes – Fig. 6.20b). This is a surprising outcome considering almost every sample contains more than 50 vol. % β' and that the average α grain size appears to be having little effect. This is in stark contrast to the continuous cast data set from Section 6.3.3.1.

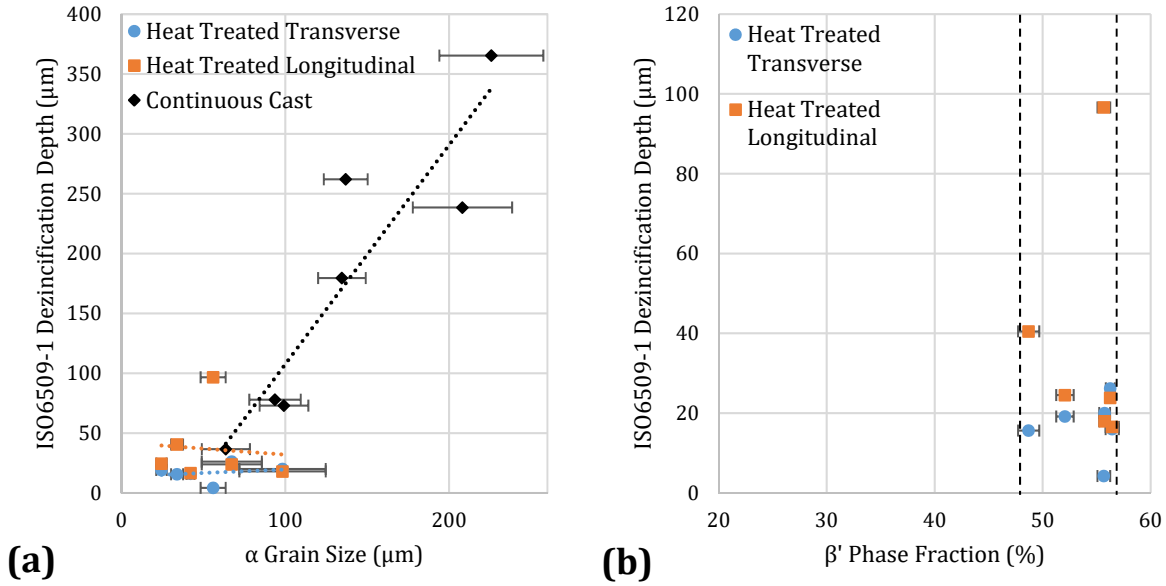


**Figure 6.21: Extruded CuZn37.6BiPAs Dezincification (ISO6509-1 average depth) dependency on (a) α grain size while (b) β' phase fraction is maintained.**

A direct comparison of the microstructures and resulting dezincification depths found in Figs. 6.20a (700°C, 30 minutes), b (700°C, 180 minutes), and c (850°C, 60 minutes, followed by 700°C for 10 minutes) reveals a large increase in the average α grain size as the soak time at 700°C is increased, and another large increase when elevated temperatures at 850°C are used to speed up the grain growth kinetics. As the α grains continue to grow, large localised regions of β are also forming. Upon quenching from 700°C, any β grain boundary which is absent of α at high temperature has a tendency to form allotriomorphic coatings of α which then sympathetically nucleate Widmanstätten α upon cooling. An example of this is shown in Fig. 6.22 for CuZn37.6BiPAs heat treated to 700°C for 120 minutes and quenched. These Widmanstätten α grains may be impeding the dezincification path in the short-term, particularly given their inclusion of two α inhibitors (As and P) in the composition and this is likely to be one factor contributing to the lower than expected dezincification depths produced in this data set. In addition, any sample cooled from the all-β phase field at 850°C down to 700°C will produce the majority of α grains along the β grain boundaries which will gradually grow in size at 700°C producing long walls of α grains. In spite of the high β' phase fraction, these α walls then significantly slow down the percolation of dezincification from β' grain to the next also contributing to the low dezincification depths in the short term.

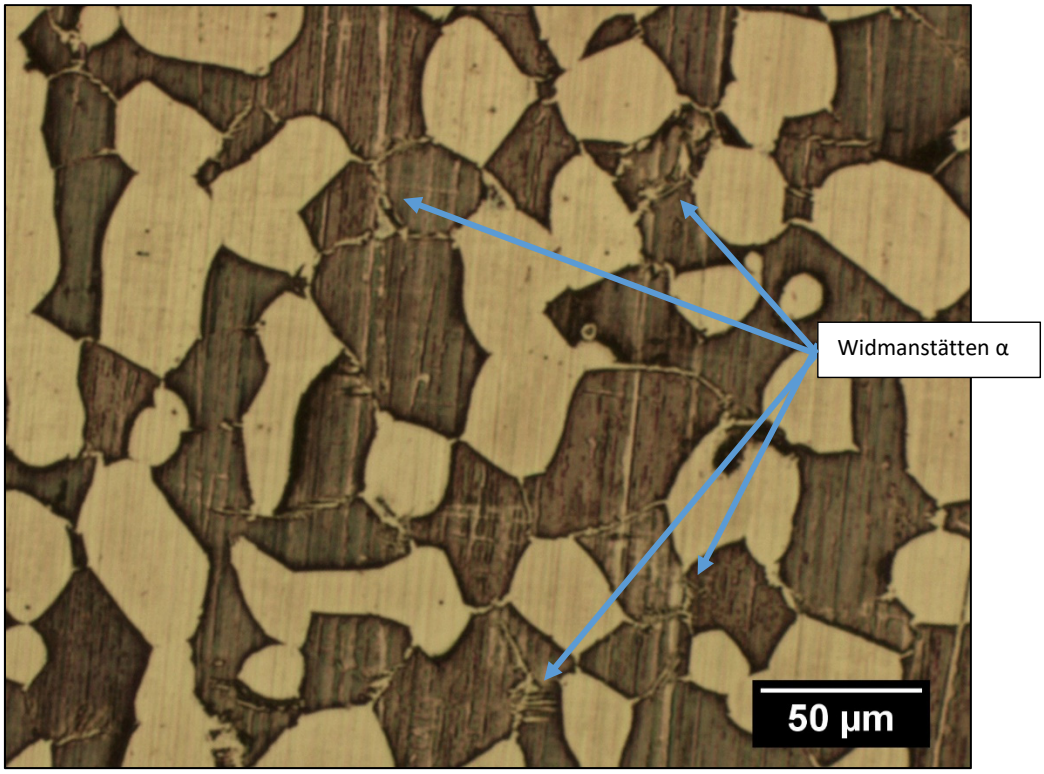


**Figure 6.22: Observation of Widmanstätten α forming along β grain boundaries in CuZn37.6BiPAs post-quenching from 700°C after a soak time of 120 minutes.**

As outlined in Section 6.3.2.2., this CuZn37.6BiPAs alloy also contains 0.10 wt. % phosphorus which may be additionally contributing to the lower than expected dezincification depths due to its known ability to protect the α phase from this form of corrosion. It is extremely difficult to prevent the nucleation of very small grains of α within large regions of β when quenching is used, and it is therefore hypothesised that the phosphorus is helping to protect any small Widmanstätten α grains which have formed along the large β' grain boundaries in the quenched microstructure, thus preventing any significant dezincification depths being produced over the 24-hour test period utilised for ISO6509-1.

In order to better understand the mechanism by which low dezincification depths are being achieved for this extruded CuZn37.6BiPAs brass, two samples; (1) an as-received and (2) a heat treated (850°C, 60 minutes, followed by 700°C for 10 minutes) sample were both subjected to the dezincification test conditions outlined in ISO6509-1 but for an extended period of 120 hours (as opposed to the standard 24 hours). The results, taken in the longitudinal direction, are shown in Fig. 6.23 and Table 6.3a and b. Looking at the microstructures in Fig. 6.23, it is immediately evident there is a difference in resistance between the two samples after 120 hours, and this is the opposite to the results obtained after 24 hours.

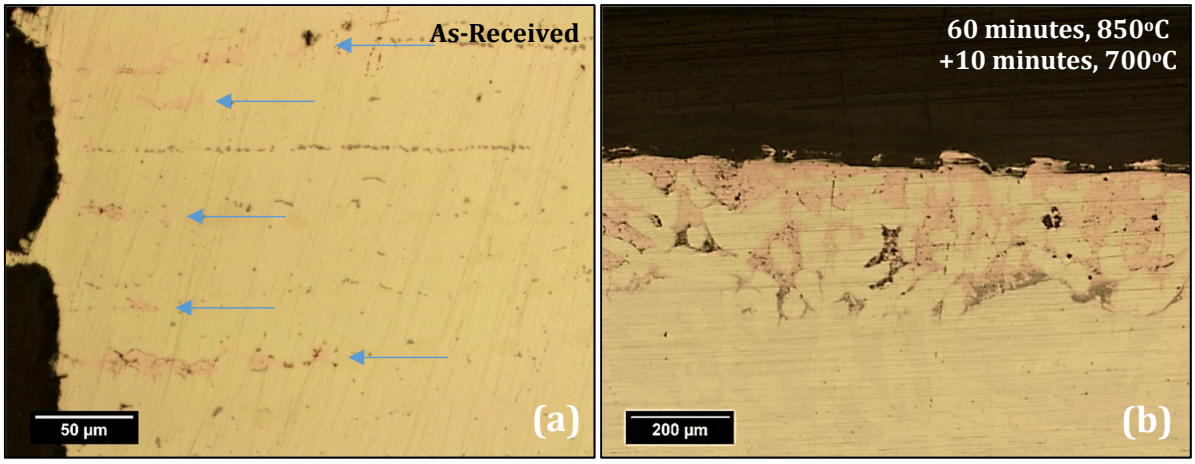


**Figure 6.23: Dezincification results of: (a) as-received CuZn37.6BiPAs and (b) CuZn37.6BiPAs heat treated at 850°C for 60 minutes and ramped down to 700°C for 10 minutes after being subject to ISO6509-1 conditions for 120 hours (5 days). Results in longitudinal direction.**

**Table 6.3 (a) Heat treatment conditions and microstructural parameters used for extended dezincification testing according to ISO6509-1.**

| Alloy – Heat Treatment | α Grain Size (µm) | β' Phase Fraction (vol. %) |
|---|---|---|
| **(1) As-Received** | 13.5 | 7.22 |
| **(2) 850°C-60 mins + 700°C-10 mins** | 32.8 | 56.3 |

**Table 6.3 (b) Dezincification results after 24 hours and 120 hours – Longitudinal Direction.**

| Alloy | Average Depth – 24 Hours | Maximum Depth – 24 Hours | Average Depth – 120 Hours | Maximum Depth – 120 Hours |
|---|---|---|---|---|
| **(1)** | 57 µm | 168 µm | 80 µm | 198 µm |
| **(2)** | 24 µm | 45 µm | 244 µm | 362 µm |

After 120 hours, the results in Table 6.3b show that the as-received sample has produced a small increase in both the average and maximum dezincification depths. The dezincification tends to follow the small β' stringers in the microstructure and this is expected for a duplex brass in the as-received condition as it contains both a low average α grain size and a low β' phase fraction. The heat treated CuZn37.6BiPAs sample, however, shows a significantly higher dezincification depth with the average increasing by an order of magnitude. This is consistent with the expected dezincification resistance, similar to the continuous cast sample results in Sections 6.3.2.1. and 6.3.3.1. There is not only a significantly greater phase fraction of β', but a higher average α grain size, and a subsequent increase in β' interconnectivity. Overall, these results support the hypothesis that there is a short-term inhibition of the dezincification process for the extruded CuZn37.6BiPAs in the quenched state due to the formation of thin Widmanstätten α along prior β' grain boundaries and these Widmanstätten α may be significantly assisted by the addition of 0.1 wt. % phosphorus into the chemical composition. The additional time required to observe the actual resistance of the heat treated alloy suggests the existing standard time period of 24 hours in both ISO6509-1 [222] and AS2345 [80] may not be sufficient to validate the dezincification resistance status of a duplex brass once in the field.

## 6.4 Dezincification of Extruded CuZn37.8BiPAs – Effect of Cooling Rate

The previous sections of this chapter have been focussed on the dezincification resistance of continuous cast CuZn37.4BiAs and extruded CuZn37.6BiPAs duplex brass in the heat treated and quenched state. The primary reason was to preserve the microstructural characteristics obtained at elevated temperatures, particularly the β' phase fraction, α grain size, morphology, and subsequent phase interconnectivity. The results from this work yielded important new insight, particularly with respect to the major effect of α grain size and shape and the dezincification resistance of extruded CuZn37.6BiPAs with a high β' phase fraction and a range of α grain sizes producing a strong short-term resistance under ISO6509-1 test conditions. However, in industrial processes we do not quench samples, we continuously cool them. The focus of this section is to look more closely at the effects of cooling rate from elevated temperatures, specifically the differences obtained in the dezincification resistance of extruded CuZn37.8BiPAs when either air-cooled or water quenched from elevated temperatures.

A study has been conducted in which samples of the extruded CuZn37.8BiPAs have been heat treated in 50$^{o}$C increments over a temperature range of 650 – 850$^{o}$C and then either water quenched after soak times of 20 minutes and 30 minutes or air-cooled after soak times of 20 minutes and 40 minutes for a total of 4 sets of data. A plot of the resulting variation in room temperature β' phase fraction with heat treatment temperature is shown in Fig. 6.24 in addition to the estimated equilibrium β' phase fractions at elevated temperatures according to the CALPHAD approach. As expected, the samples which have been air-cooled have a consistent β' phase fraction within a range of ~25 – 30 vol. % over the range of heat treatment temperatures (highlighted blue Fig. 6.24). This consistency in β' phase fraction is the result of adequate time provided for α grain growth during the air-cooling process. However, this cooling time is not available to the quenched brass samples (highlighted orange Fig. 6.24) and therefore we find the β' phase fractions are higher for the equivalent temperatures in this state with the highest average β' phase fraction being retained from 700$^{o}$C and gradually decreasing as the temperature increases to 850$^{o}$C.

The samples cooled from 800$^{o}$C and 850$^{o}$C are fairly close in their β' phase fraction regardless of whether they are quenched or air-cooled from these temperatures. This is largely because these temperatures are within the 100% β phase region so any α that forms on cooling must first nucleate from the β. As the diffusion kinetics within the BCC β grain are very fast (See Section 2.2.3), the nucleation of new α grains occurs very readily, the major difference between the two cooling rates

being the resulting α grain size. This will be explored further later in this section. Between 650 – 750°C on the other hand, there are still α grains remaining in the microstructure at these temperatures which then contribute to the larger difference in β' phase fraction post-cooling.

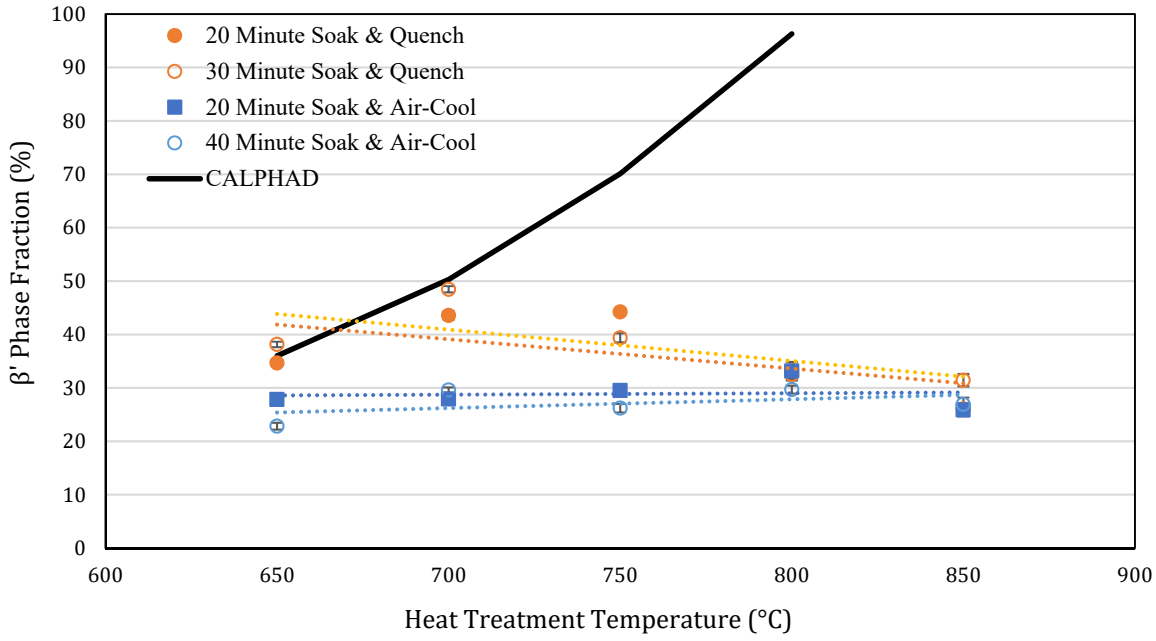


**Figure 6.24: β' phase fraction (calculated using ImageJ analysis) of extruded CuZn37.8BiPAs brass after either water-quenching (orange) or air cooling (blue) from elevated temperatures as well as the estimated equilibrium β phase fraction at temperature using the CALPHAD approach [12].**

Examples of the microstructures produced by 50°C incremental increases in heat treatment temperature are shown in Fig. 6.25a, c, e, g, i in the quenched state after 30 minutes soak time, and b, d, f, h, j in the air-cooled state after 20 minutes soak time. For those quenched, we first note the significant increase in β' phase fraction from Fig. 6.25a (650°C quenched) to c (700°C quenched) as the BCC β becomes more stable at higher temperatures. This is then followed by a different reaction in Fig. 6.25e (750°C quenched) in which a bimodal α structure is produced consisting of large equiaxed α grains which were present at 750°C and newly nucleated Widmanstätten α grains which form along the prior β grain boundaries and in a smaller average grain size within the β' grains, indicating they were produced during the quenching process. The Widmanstätten α grains are again observed when quenching from both 800°C and 850°C, however as this is in the all-β phase field, there are no longer any equiaxed α grains remaining in the microstructure leaving a relatively small average acicular α grain length of 11µm (aspect ratio 7.0) and 13µm (aspect ratio 7.5) respectively.

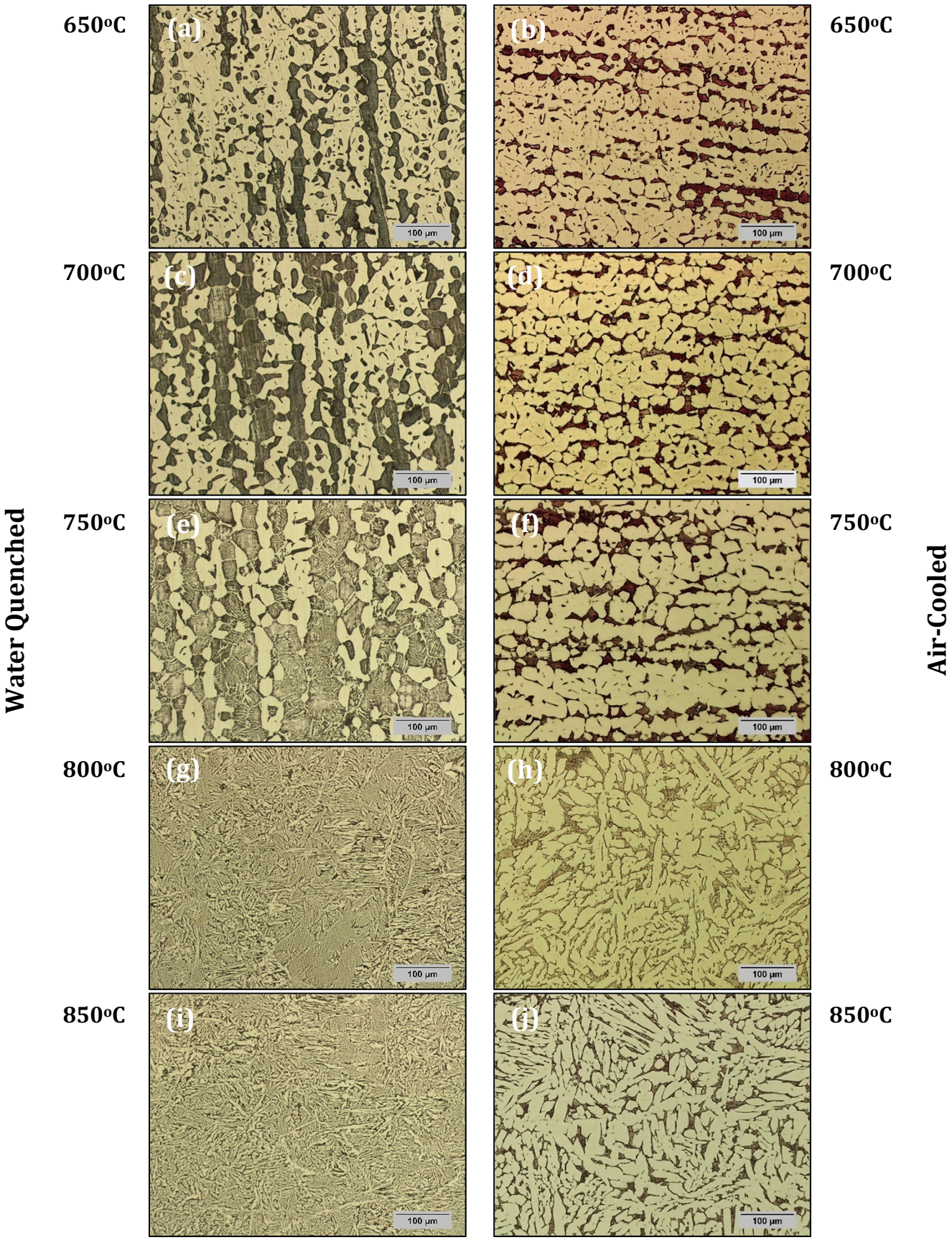


**Figure 6.25: Extruded CuZn37.8BiPAs microstructures post-heat treatment annealing for 30 minutes soak and quenched (column 1), and 20 minutes soak and air-cooled (column 2) from (a-b) 650°C, (c-d) 700°C, (e-f) 750°C, (g-h) 800°C, and (i-j) 850°C. All images at same magnification.**

When compared with the quenched microstructures (Fig. 6.25a,c,e,g,i), the air-cooled microstructures (Fig. 6.25b,d,f,h,j) appear relatively consistent in β' phase fraction across the range of soak temperatures used (measured as 27.8% after air-cooling from 650°C to 25.9% after air-cooling from 850°C). In Fig. 6.25b (650°C air-cooled) we still observe some directionality in the horizontal direction, which is a remnant from the extrusion process, with approximately 28 vol. % β phase fraction and a reasonably consistent α grain size across the microstructure. A similar microstructure remains in Fig. 6.25d (700°C air-cooled) however with a slight reduction in directionality and greater separation between the α grains leading to an increased β' interconnectivity. In Fig. 6.25f (750°C air-cooled) as the grain growth kinetics increase with elevated temperature, the equiaxed α grains have become comparatively larger. By 800°C and 850°C we see a significant shift in the α grain morphology (Fig. 6.25h and j), which is consistent with cooling from the 100% β phase field. Although the β' phase fraction is shown to be quite similar between the quenched and air-cooled states from these temperatures (Fig. 6.24), there is obviously a substantial difference between the average α grain size and the subsequent β' interconnectivity.

A comparison of the average (across 25 measurements to ISO6509-1) and maximum individual dezincification depths is shown in Figs. 6.26 and 6.27, respectively. For both the water quenched and air-cooled samples, regardless of the soak time at elevated temperatures, the dezincification resistance of the extruded CuZn37.8BiPAs decreases with increasing heat treatment temperature. For the air-cooled samples from 650°C – 750°C, this is primarily due to an increase in average α grain size, subsequently increasing the connectivity of the β' phase. At 800°C and 850°C there is a change in the α morphology into an elongated shape, but still of relatively similar grain size to the other air-cooled samples. This creates inconsistency in the average readings for dezincification as shown in Fig. 6.26, however we expect to see an increase in the maximum individual reading dependent on the orientation of the α grains at the corrosion front (as found in Fig. 6.27). If the α grains provide a long straight path for dezincification, this allows for greater depths to be achieved over a 24-hour period, while for equiaxed α grains, the corrosion path must consistently manoeuvre around the less-susceptible α.

Between the various soak times, it is also generally found that samples treated for 40 minutes and air-cooled have a lower resistance than for the samples only treated for 20 minutes and air-cooled (Fig. 6.26). Again, this effect may be attributed to the gradual increase in average α grain size for each individual temperature condition as soak times increase, leading to a subsequent increase in β' interconnectivity with increasing soak time. For example, for the 700°C air-cooled condition, the

difference in average α grain size is 28µm after a soak time of 20 minutes and 35µm after a soak time of 40minutes. There appears to be little difference between the dezincification resistance of the quenched samples held for 20- or 30-minute soak times.

In spite of the higher β' phase fractions retained in the quenched samples for each heat treatment temperature used (Fig. 6.24), the quenched samples have a significantly higher dezincification resistance compared to the air-cooled samples. As the trend lines show in Figs. 6.26 and 6.27, this effect worsens with increasing soak temperature, particularly for measurements of the maximum individual dezincification depths.

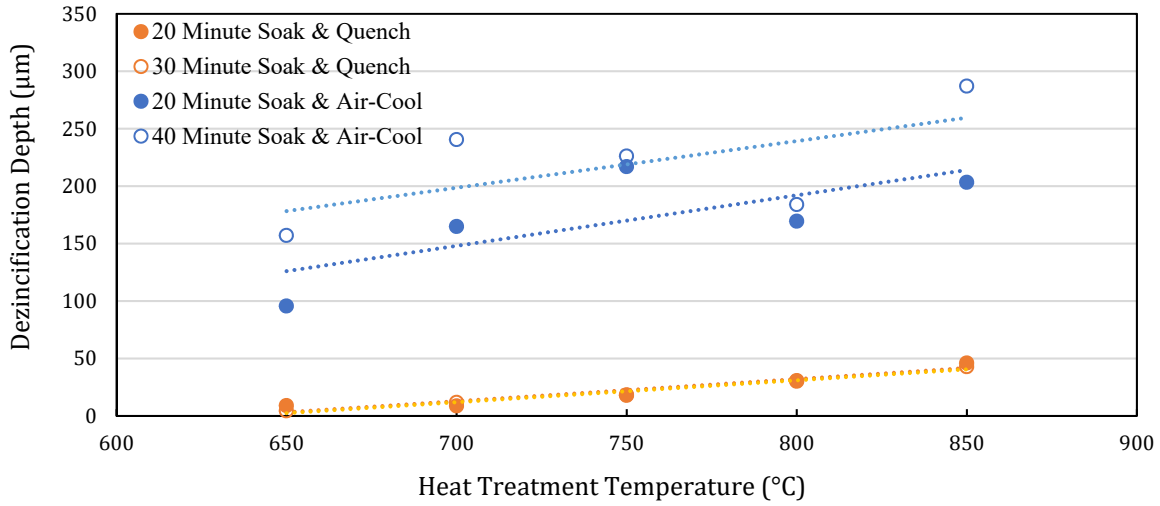


**Figure 6.26: The evolution of <u>average</u> dezincification depth of extruded CuZn37.8BiPAs to ISO6509-1 as a function of heat treatment temperature. Samples have been either air-cooled or water quenched from elevated temperatures. Depths measured in transverse direction.**

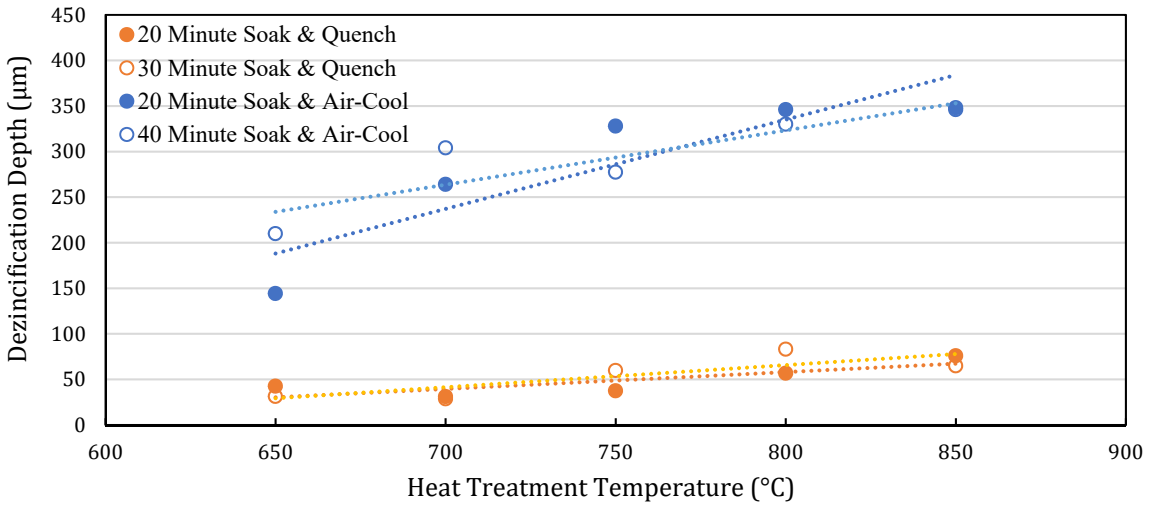


**Figure 6.27: The evolution of <u>maximum</u> dezincification depth of extruded CuZn37.8BiPAs to ISO6509-1 as a function of heat treatment temperature. Samples have been either air-cooled or water quenched from elevated temperatures. Depths measured in transverse direction.**

Example micrographs exhibiting the dezincification of extruded CuZn37.8BiPAs after various heat treatments and exposure to ISO6509-1 test conditions are shown in Fig. 6.28. In all cases it is clear that the β' phase is being preferentially targeted by the dezincification process for each heat treatment condition, regardless of microstructural state. What we do observe for each sample is an indication of how difficult it is for the corrosion front to penetrate into the alloy matrix. The air-cooled samples, as shown in Fig. 6.28f, not only provide a significant β' vol. % to preferentially attack, but also have a higher degree of interconnectivity (relative to the water-quenched samples) due to the larger average α grain size. This is the same for all of the air-cooled sample conditions in this study.

For the samples quenched above the Widmanstätten α soak temperatures (Fig. 6.28c-e for 750°C, 800°C, and 850°C) we are able to observe the complex corrosion paths taken through the brass matrix. As the Widmanstätten α is comparatively small, produced in a higher density due to the fast diffusion in the BCC β grains upon cooling (Section 2.2.3), and protected by multiple corrosion inhibitors (As and P), the dezincification cannot proceed in a simple linear path as was the case for the air-cooled samples. As such, the dezincification proceeds more slowly over the 24-hour period outlined in the standard.

For the microstructural conditions shown in Figs. 6.25a and c corresponding to the dezincification micrographs in Fig. 6.28a (650°C) and b (700°C) it becomes more difficult to observe any Widmanstätten α, certainly not to the extent where it is clearly inhibiting the dezincification path as is the case for higher soak temperatures. From these dezincification micrographs, we tend to see the dezincification follow a simpler path, similar to the air-cooled samples, however this stops abruptly at β' grain boundaries or where two α grains form together. At the lower heat treatment soak temperatures of 650°C and 700°C, many α grains are still present and this in turn inhibits the growth of β, which in turn leaves a higher density of β grain boundaries. As there is a lower β' phase fraction at 650°C and 700°C, upon quenching there are lower driving forces for Widmanstätten α to form, however new α still readily forms along the β grain boundaries and this appears to impede the dezincification path over 24 hours, again particularly as it is inhibited by P and As, but perhaps not for longer periods, e.g. after 120 hours as indicated at the end of Section 6.3.3.2.

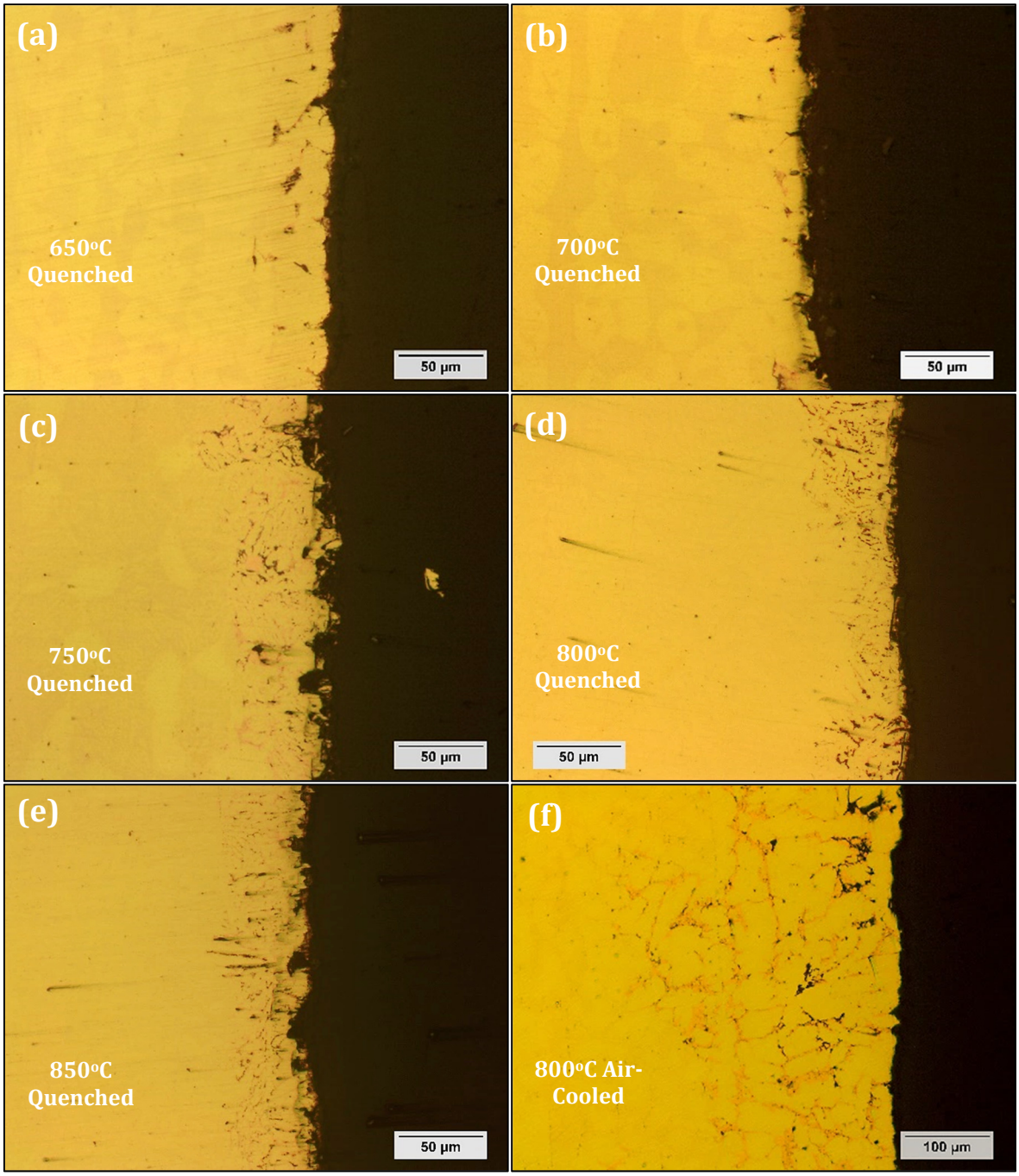


**Figure 6.28: ISO6509-1 Dezincification micrographs for the (a) 650°C quenched, (b) 700°C quenched, (c) 750°C quenched, (d) 800°C quenched, (e) 850°C quenched conditions after 30-minute soak and for the (f) 800°C air-cooled condition after 20 minutes soak. Dezincification depths shown in the transverse direction.**

Fig. 6.29 plots the correlation between dezincification resistance and β' phase fraction for this series of CuZn37.8BiPAs alloys, both quenched and air-cooled. The dominant microstructural feature dictating the dezincification resistance of the air-cooled samples appears to be the larger α grain size and morphology allowing for an increased β' interconnectivity and simplified corrosion path (as the β' phase fraction remains relatively consistent, see Fig. 6.29). On the other hand, the dominant microstructural feature dictating the dezincification resistance of the quenched samples appears to

be the β' interconnectivity as it relates to either (a) the formation of Widmanstätten α and at higher temperatures (>~750°C), or (b) grain boundary α at sub-acicular temperatures (<~750°C). We find that for these samples, as the β' phase fraction is increasing, the dezincification resistance is improving in direct contradiction to traditional theory and industrial knowledge. This is the first systematic trial to observe these microstructural observations and why they account for differences in dezincification resistance between air-cooled and quenched duplex brass.

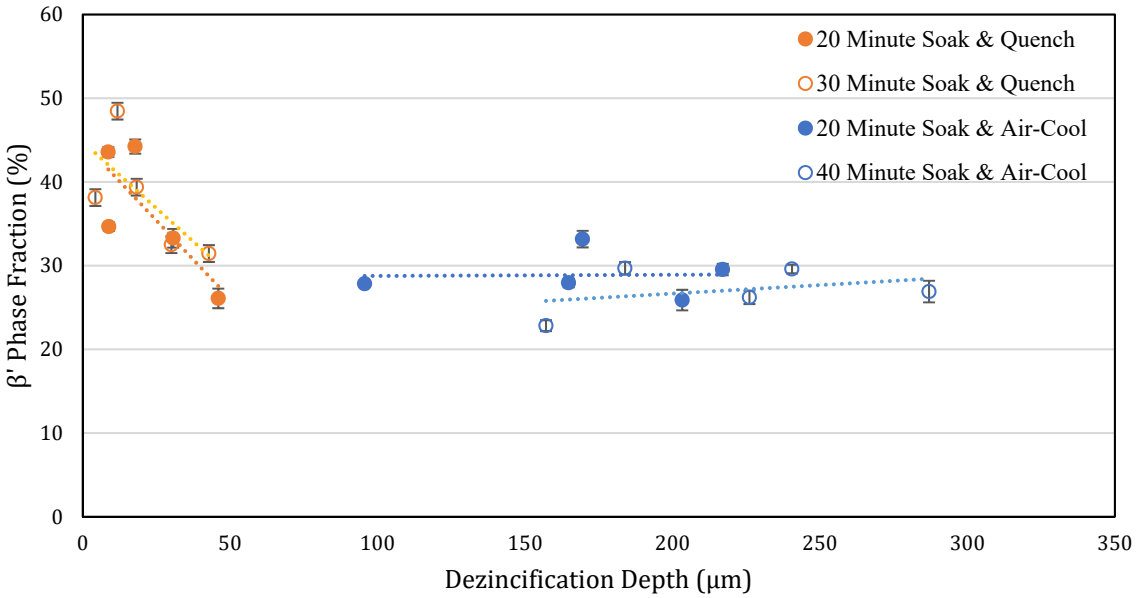


**Figure 6.29: Average dezincification depth results of extruded CuZn37.8BiPAs to ISO6509-1 as a function of β' phase fraction. Depths measured in transverse direction.**

## 6.5 Percolation Simulations of the Effect of Phase Fraction, Size and Morphology on Dezincification

The dezincification process involves at least two levels of complexity. The first is with regard to the details of the selective dissolution process and the development of a porous network of the β' phase, which involves electrolyte leaching the less noble elements (Zn). This is an electrochemistry effect and some understanding of these processes exists in the literature, e.g. as considered in the framework of computer simulations of selective dissolution in binary alloys [236]. The second level of complexity considers the larger time and length scale regarding the microstructural dependence of dealloying kinetics in multiphase systems, including phase fractions, grain size, morphology, etc. The characterisation and manipulation of these microstructural variables on controlling dezincification kinetics is seldom discussed.

As shown by the systematic experiments reported in this Chapter, the measured dezincification kinetics correlates strongly with the microstructural variations in the same alloy chemistry. This leads to the hypothesis that the topology effect regarding microstructural variables in the duplex brass can be just as important as the alloy chemistry effect. Of course, the topology and chemistry effects can be coupled. The critical question is whether the observed dependence of dezincification on microstructural variables can be explained simply by topology – the effect of α grain size, shape and fraction acting as a barrier to the progression of the dezincification front. To test this hypothesis, we provide a percolation analysis to examine the effect of microstructural connectivity on the dezincification kinetics, to see if the experimental dezincification kinetics can be qualitatively compared with the simulations with only topology considerations.

### 6.5.1 Percolation-Simulation Methodology

To simplify the problem, we shall describe the microstructure of duplex brass with 4 internal variables: β' phase fraction (f), effective α phase grain size (d), tilt angle of the acicular α phase (modelled as ellipses) with respect to the free surface (θ) and aspect ratio of the elliptic (acicular) α grains (k).

The simulation consists of two steps. The first is microstructure initialisation, and here we employ a 2D 100x100 square lattice model, which includes 3 classes of identities representing the microstructural evolution during the dezincification process: α phase, dissolved β' phase and undissolved β' phase (Fig. 6.30). The α grains are simplified as elliptic grains (including the spherical cases). These α grains are expanded from seeds (Fig. 6.30), of which the site coordinates are generated as pseudorandom numbers in MATLAB. Spiral matrices centred from the seeds are marked clockwise

to be α phase with the counts of specified grain area (i.e. $d^2$ pixels). In the generation of a spiral matrix, it is masked in respect to the ellipse shape based on the specified θ and k, and only the site in the spiral matrix leading to the specified ellipse shape are marked as α phase. Fig. 6.30a-b are two examples of applying different masking leading to spherical α and elongated elliptical α, respectively. In the case that the lattice site has been pre-occupied as α phase, the current site is skipped and the next unoccupied site in the masked spiral matrix will be counted and marked. The initial empty square lattice sites are first occupied by elliptic α phase (black circles in Fig. 6.30). The rest of the square lattice sites are marked as β' phase, in which the left boundary sites are marked as the dissolved β' phase (red circles in Fig. 6.30). This simulates the onset of dezincification of the β' phase at the free surface exposed to an electrolyte. The rest of the lattice sites for undissolved β' phase are indicated as blue circles in Fig. 6.30.

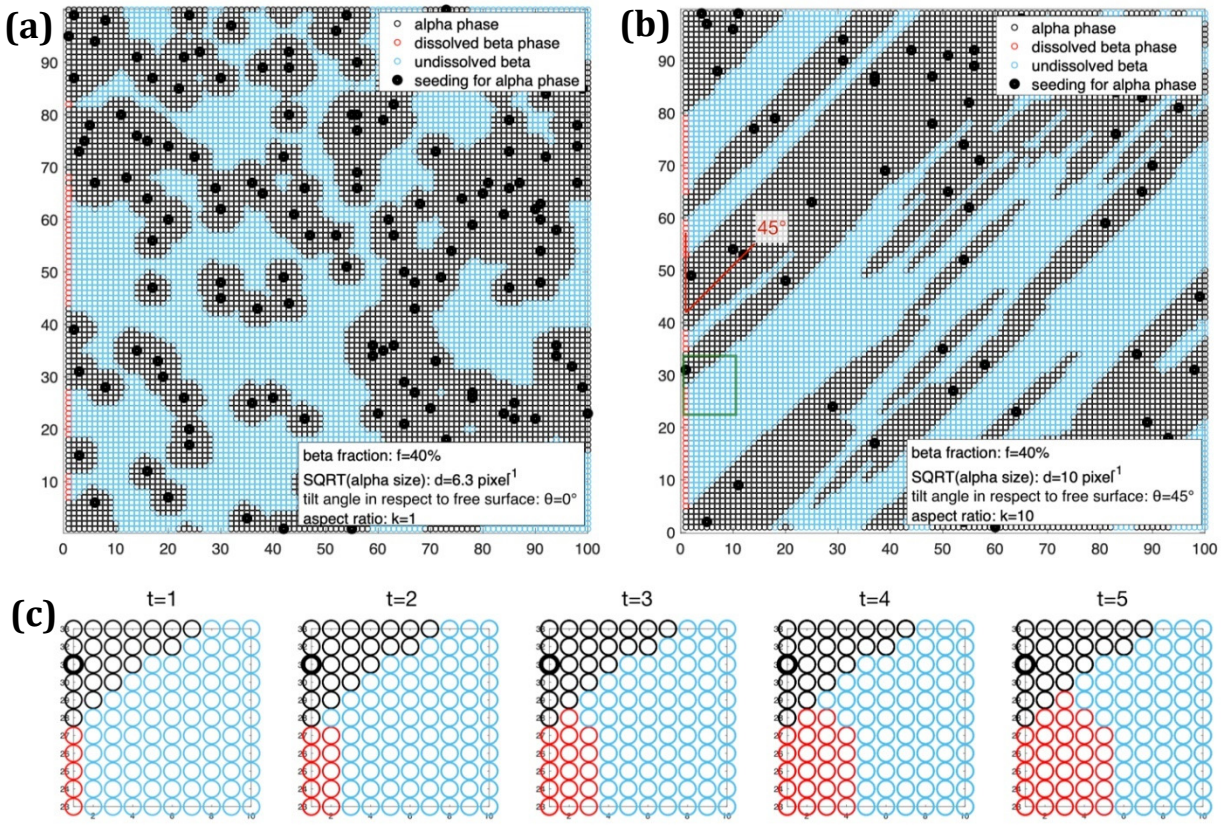


**Figure 6.30: Square lattice model initialised based on microstructural variables f (β vol. fraction), d (α grain size), θ (tilt angle) and k (α aspect ratio) – (a) spherical shape, (b) elliptical shape and (c) the lattice evolution of dissolved β' (red circles), undissolved β' (blue circles) and resistant α (black circles) phases in the first 5 time-steps in the simulation. The magnified region shown in (c) is highlighted in (b).**

The second part of the simulation is the site-switching criterion to evolve the microstructure. The site-switching is applied to the undissolved β' phase in the neighbourhood to the dissolved β' phase. We use the Von Neumann neighbourhood, for which the state of site with coordinate (i,j) in the next time

step depends on the states of the nearest neighbours in the current time step, i.e. $S_{i,j}^{t+\Delta t}=f(S_{i-1,j}^{t}, S_{i+1,j}^{t}, S_{i,j-1}^{t}, S_{i,j+1}^{t})$. In the site switching criterion, as long as there is a minimum one dissolved β' phase in the nearest neighbourhood, the undissolved β' phase $S_{i,j}^{t}$ in the current time step becomes dissolved β' phase $S_{i,j}^{t+\Delta t}$ in the next time step. In each time step, all the current undissolved β' phase sites with neighbouring dissolved β' phase are scanned based on the above site switching criterion, and the lattice evolution of the first 5 time steps (based on initial lattice model of Fig. 6.30b) is shown in Fig. 6.30c, highlighting the evolution of β' phase dissolution in each step. In this algorithm, we do not consider the stochastic nature of diffusion in the β' phase, and we assume that the α phase is not dissolved. In general, this represents the scenario that the percolation of dissolved β' phase dominates the dezincification kinetics where the kinetics of local mass transport is less important. In this way, we design these calculations to understand the geometric effect of microstructure variables on the dezincification kinetics. In the simulation, periodic boundary conditions are used on the top and bottom boundary. The lattice sites of the dissolved β' phase at the left boundary starts to propagate until it percolates to the right boundary or is completely arrested by the non-dissolving α phase (not able to reach the right boundary). Such percolation analyses have been performed as a function of the microstructural variables f, d, θ and k using the randomly generated square lattice model in Fig. 6.30. To reduce the statistical scattering of the simulation results based on the random square lattice, we have averaged 100 repeat simulations for each set of the microstructural variables. To compare quantitatively with the measured dezincification depth under constant time, we use the percolation depth (in pixels) from the left boundary projected along the horizontal direction at $99^{th}$ step as a comparison. For the employed 2D 100x100 square lattice, it takes a minimum of 99 steps to create a dezincification path across the square lattice. It is important to emphasise that there is no physical length scale in this simulation.

To validate the methodology, we first compare the simulation results with classic percolation theory. In contrast to the classic percolation analysis defining the occupation probabilities for each lattice site, we probabilistically seed some lattice sites but deterministically expand the surrounding lattice sites. This naturally increases the chance of creating dezincification paths, as occupied sites of α phase are aggregated leading to improved connectivity of the β' phase. In Fig. 6.31, the probability of percolation occurrence is plotted as a function of β' phase fraction, and this is used to resolve the percolation threshold when plotted against occupation probability. For the classic percolation analysis, one should simulate a Heaviside step function with the sharp step at x=0.593 as the percolation threshold for the case of percolation with 4 nearest site neighbours [234]. We describe that the way we define the occupied sites will lead to improved connectivity in unoccupied sites (β' phase), as compared to what

would be expected from classic percolation theory. This makes the simulated curves of probability of percolation occurrence against β' fraction deviate from the step function in Fig. 6.31.

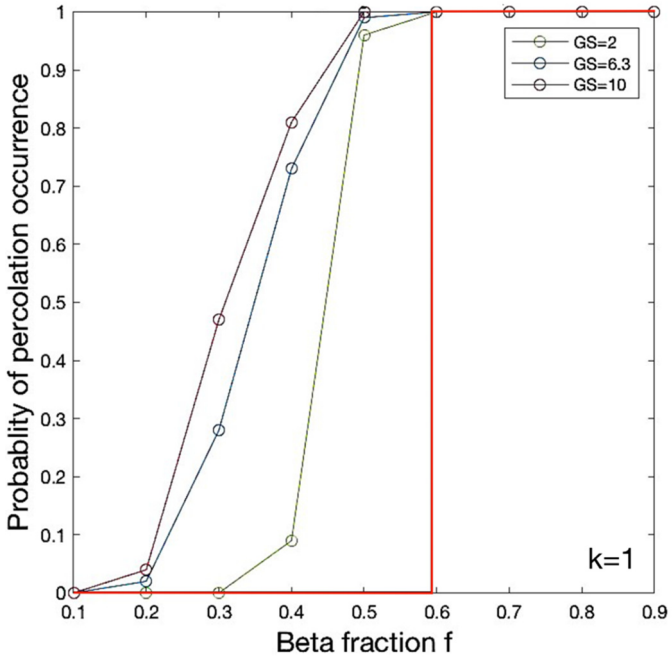


**Figure 6.31: Probability of percolation occurrence (determined from 100 repeats) as a function of β' phase fraction for 3 different α grain sizes. The site percolation threshold at 0.593 for the case of nearest neighbour in square lattice is labelled (red).**

When comparing the effects of 3 different α grain sizes (in pixels$^{-1}$) in Fig. 6.31, smaller α grain sizes (with the same phase fraction) approach the step function with the percolation threshold at 0.593. In these simulations, we only use a 2D 100x100 square lattice, and larger lattice (e.g. 500x500) is normally required to further resolve the steep percolation threshold [234]. From the justification by Fig. 6.31, the simulation results seem rather reasonable as compared to the classic percolation theory, and the deviation can be well understood. We expect that comparisons can be made from the calculations using the low-cost simple 2D 100x100 square lattice consistently. In the following sections (6.5.2 and 6.5.3), we simulate a range of percolation processes as a function of microstructure (f, d, θ and k), and in particular extract the percolation depth along the horizontal direction as a proxy for dezincification depth. In Section 6.5.2 we start with the discussion on the effect of β' phase fraction and α grain size on dezincification kinetics based on spherical α grains (e.g. Fig. 6.30a).

### 6.5.2 Effect of β' Phase Fraction and α Grain Size on Percolation

In practice, the control of the Zn-rich β' phase fraction is considered of primary importance to control dezincification. The important effect of β' phase fraction is highlighted in Fig. 6.32, where the percolation depth varies by a factor of ~4 between a β' phase fraction f=0.1 and f=0.4. At low β' fraction, more α phase blocks the percolation path development in β' phase. It is when β' fraction is large enough (up to ~0.7) that a path spanning across the lattice could exist in 99 time-steps, while low β' fraction (high α fraction) provide less switchable sites from undissolved β' to dissolved β'. This observation supports the findings of Section 6.3.2, and industry knowledge in general, that as the β' phase fraction increases, particularly from low to moderate phase fraction, so too will the susceptibility to greater dezincification depths.

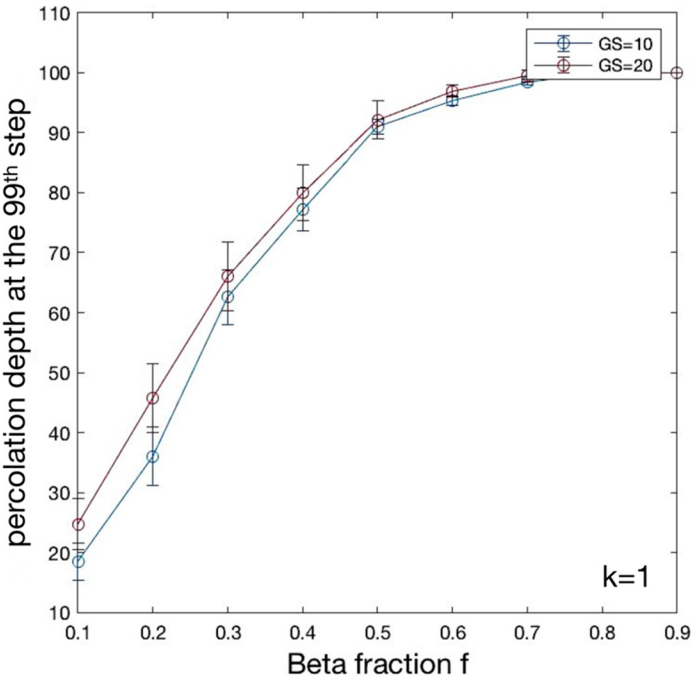


**Figure 6.32: Percolation depth at the 99th step as a function of β' phase fraction for 2 different α grain sizes. Error bars represent the 95% confidence interval calculated from 100 repeats.**

It is experimentally observed in Section 6.3.3 that a smaller α grain size has a large and (perhaps) surprising effect on slowing down dezincification kinetics. In Fig. 6.33, the dependence of percolation depth on α grain size is simulated with a controlled β' phase fraction. The α grain size is calculated as the square root of the pixel counts used to expand the α seed during microstructure initialisation, which wound dimensionally correlate with actual grain size and to some extent mimic the aggregation of α grains in a real microstructure. In Fig. 6.33, it is clear that the simulated percolation depth decreases with smaller α grain size, and this dependence is more pronounced for smaller β' phase fractions. It is also intriguing that there appears to exist a critical grain size (~10 pixels$^{-1}$) separating

the dependence into 2 regimes: above the critical grain size, the dependence of percolation depth on α grain size is less sensitive, while below the critical grain size, the percolation depth changes more steeply with grain size. Importantly, the manipulation of α grain size could lead to a comparable effect on percolation depth as the phase fraction: the decrease of α grain size from 10 to 2 (a factor of 5) can yield a 3 times difference in percolation depth. This is in accordance with the experimental observations of Section 6.3.3 where for the hot compressed CuZn37.4BiAs (Fig. 6.19), there was a readily observable dual-regime behaviour with respect to dezincification depths. Whilst a very steep increase was initially observed, this then tapered off above roughly 70μm. The rationale behind the α grain size effect is that more distributed α phase with smaller grain sizes can break down the connectivity of β' phase and lead to more hindrance for the propagation of the dissolving β' phase, and this slows down the dezincification kinetics.

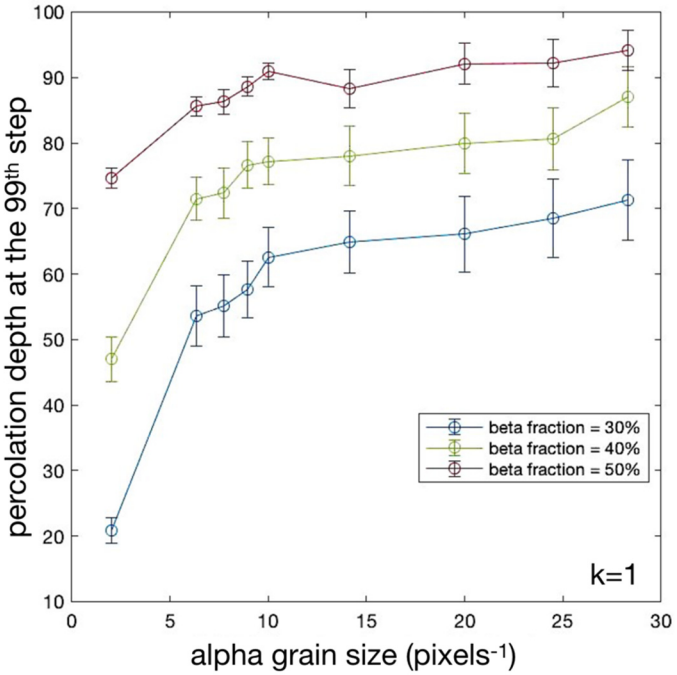


**Figure 6.33: Percolation depth at the 99th step as a function of α grain size (pixel$^{-1}$) for 3 different β' phase fractions. Error bars represent the 95% confidence interval calculated from 100 repeats.**

To illustrate the more complete picture of the dependence of percolation depth on both β' fraction and α grain size, a contour plot with both factors as axes is shown in Fig. 6.34. Clearly, the β' phase fraction has the dominating effect on percolation depth, but for the duplex brass studied earlier in this Chapter, which has both strength and ductility requirements, the window of β' fraction manipulation to control dezincification becomes smaller. For a β' fraction less than 50%, the further decrease of percolation depth by a factor of 2 can be readily achieved by grain refinement. A larger range of the percolation depth dependence on grain size can be further examined by larger lattice models (e.g. 500x500). In practice, a smaller average α grain size may be realised by reducing elevated temperature

soak times prior to hot working, as well as using faster cooling after these same hot working processes (e.g. extrusion or forging) as discussed in Section 6.4.

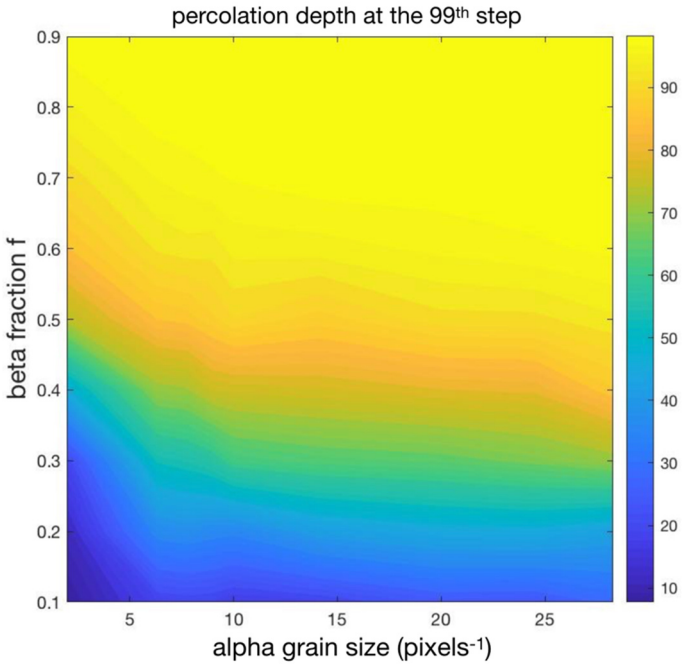


**Figure 6.34: Contour plot showing the dependence of percolation depth at the 99th step on the β' phase fraction and α grain size. The colour bar (right) shows the extent of the percolation depth.**

### 6.5.3 Effect of α Aspect Ratio and Orientation on Percolation

We have so far discussed the effect of β' phase fraction and α grain size based on spherical α grains, and now we extend the discussion to understand the morphological contribution to the dezincification kinetics at controlled β' fraction f=0.4 and α grain size d=10. We use elliptic grains to represent the observed Widmanstätten-like α, and a further simplification is that all the elliptic α grains are tilted at the same angle to the free surface (e.g. Fig. 6.30b) to avoid extra complexities in examining the tilt angle effect. The evolution of percolation depth as a function of aspect ratio and tilt angle is shown in Fig. 6.35. There are 2 major observations from the simulation results. The first is that once the α grain becomes elliptic (k>1), a smaller tilt angle (more parallel to the free surface) can reduce the percolation depth effectively. For an aspect ratio k=10, the difference in percolation depth between θ=30° and θ=75° can be by a factor of ~2 (Fig. 6.35). These simulations represent the intermediate states between, θ=0° where elliptic α grains parallel to the free surface could completely block the percolation path in β' phase, and, θ=90° where elliptic α grains aligned perpendicular to free surface could easily allow the horizontally spanning path exist without detouring vertically with more steps. For low tilt angles θ=30° and θ=45° (Fig. 6.35), the percolation depth decreases with aspect ratio monotonically, and the α grains are effectively elongated when resolved along the vertical direction

and block the horizontal percolation in β' phase. For higher tilt angles θ=60° and θ=75° both above 45° (Fig. 6.35), the percolation depth initially increases and then decreases very slightly with aspect ratio. For the cases of high tilt angle (θ>45°), an increased aspect ratio (from spherical to elliptic) initially leads to smaller resolved length along vertical direction facilitating percolation, leading to initially increased percolation depth with aspect ratio.

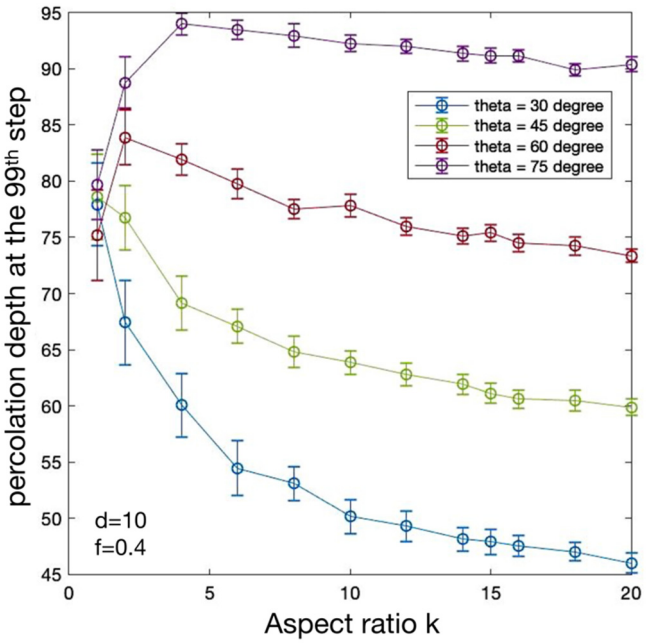


**Figure 6.35: Percolation depth at the 99th step as a function of aspect ratio for 4 different tilt angles. Error bars represent the 95% confidence interval calculated from 100 repeats.**

The overall effect of aspect ratio and tilt angle on percolation depth is summarised in Fig. 6.36. The tilt angle has a very strong effect on the percolation depth for elliptic α grains (k>1), and this can vary from almost being unable to percolate (with percolation depth ~ 10) to percolating the spanning path in 99 steps. The tilt angle is purely defined for illustration, and in real brass microstructures the tilt angles are statically a combination of both positive and negative values, which would more effectively decrease the percolation depth. An increased aspect ratio also has an important effect on reducing the percolation depth for the tilt angle θ<45°, and a further reduction of percolation depth by a factor of >2 can be introduced by controlling aspect ratio. The aspect ratio here is simulated up to 20 and this range is generally what we observe from the current metallography earlier in this Chapter. Therefore, we do not need to design this simulation for high aspect ratios. To obtain larger aspect ratios of α phase, one will usually consider very rapid cooling from the liquidus or all-β phase fields.

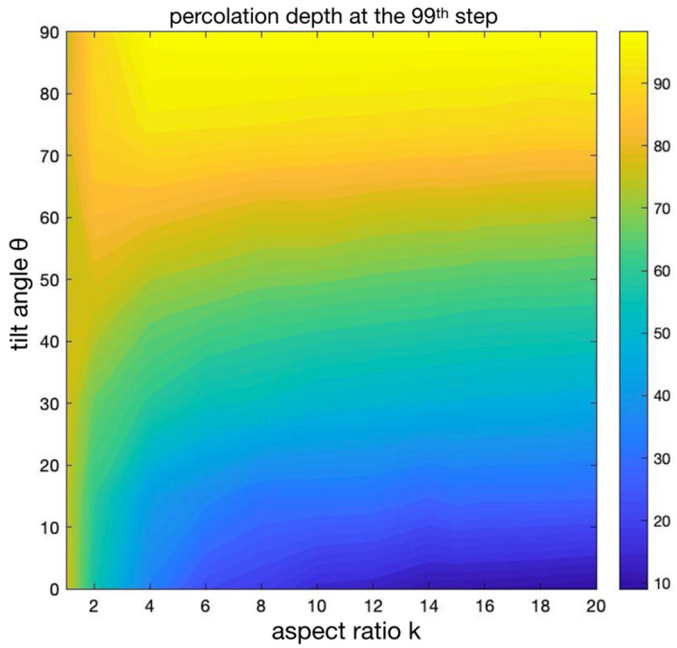


**Figure 6.36: Contour plot showing the dependence of percolation depth at the 99th step on aspect ratio and tilt angle. The colour bar (right) shows the extent of the percolation depth.**

### 6.5.4 Percolation Simulations on Real Microstructures

The discussion so far has revolved around exploring the effect of topology considerations on percolation for an artificially generated 2D 100 x 100 square lattice model. The α grains have been simplified to range from spherical to elliptical with various aspect ratios and all with a consistent orientation. This has effectively shown the anticipated effects of β' phase fraction, α grain size, aspect ratio and orientation on the dezincification percolation in a duplex brass microstructure. The next question one might ask would be whether these same percolation simulation principles could be applied to a real microstructure and then correlated against real dezincification test results. To explore this, we will take some examples from earlier in Chapter 6 for percolation analysis.

If we were to first focus on the effects of β' phase fraction and use the examples shown earlier in Fig. 6.11 for a hot compressed CuZn37.4BiAs, one could take the microstructural images (Fig. 6.37a and Fig. 6.38a), apply a binary effect using ImageJ (Fig. 6.37b), convert this image into a grid lattice model (in this case 297 x 225, Fig. 6.37c), and subsequently test for percolation using the minimum number of time-steps required for a perfect horizontal percolation, that is run the simulation for 297 time-steps and compare the relative depth of percolation (Fig. 6.37d and Fig. 6.38b). An increase in percolation depth of 1 is approximately equal to a dezincification depth of 2µm. Observing the resulting percolation depth of 227 ≈ 454µm in Fig. 6.37d compared with the real dezincification depth

of 440µm for the hot compressed CuZn37.4BiAs samples heat treated for 30 minutes at 750°C, this appears an appropriate starting point for comparison against a standard 24-hour test.

A direct comparison between the examples containing a β' phase fraction of 58% (Fig. 6.37) and 13.6% (Fig. 6.38) shows that the simulation has yielded a significant difference in percolation depth (220 ≈ 440µm) in a similar range to the difference between the real dezincification result (382µm). A simulated percolation depth of 7 ≈ 14µm is a lower value than the real maximum value of 58µm in Fig. 6.38, however the cross-sectional area used to extract the real result was wider and therefore the simulation would likely yield a closer result if an equal data set was used. This effectively supports the general trend of finding an increased percolation depth with increasing β' phase fraction.

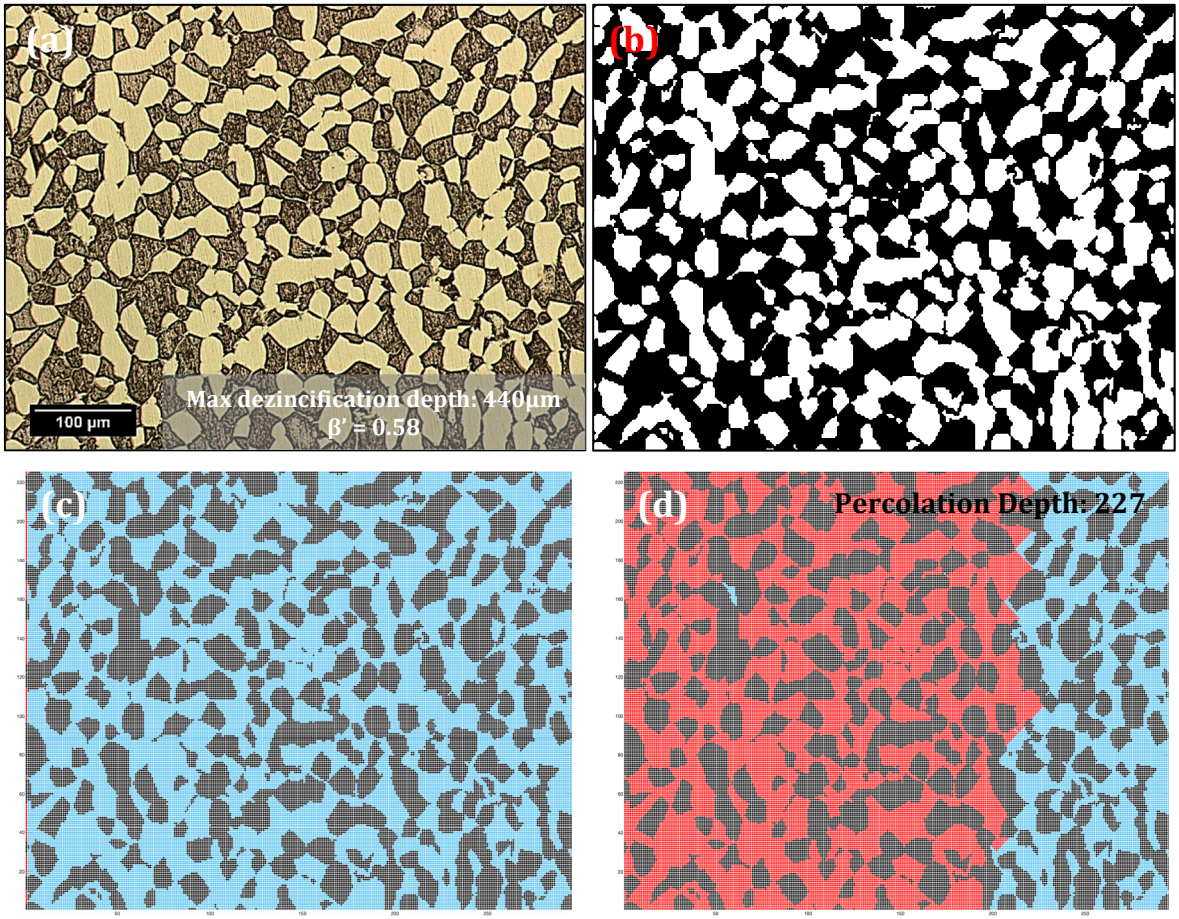


**Figure 6.37: (a) Hot compressed CuZn37.4BiAs microstructure post heat treatment at 750°C for 30 minutes, (b) in binary form, (c) converted to a 297 x 225 grid lattice model, and (d) the resulting percolation after the 297th time-step.**

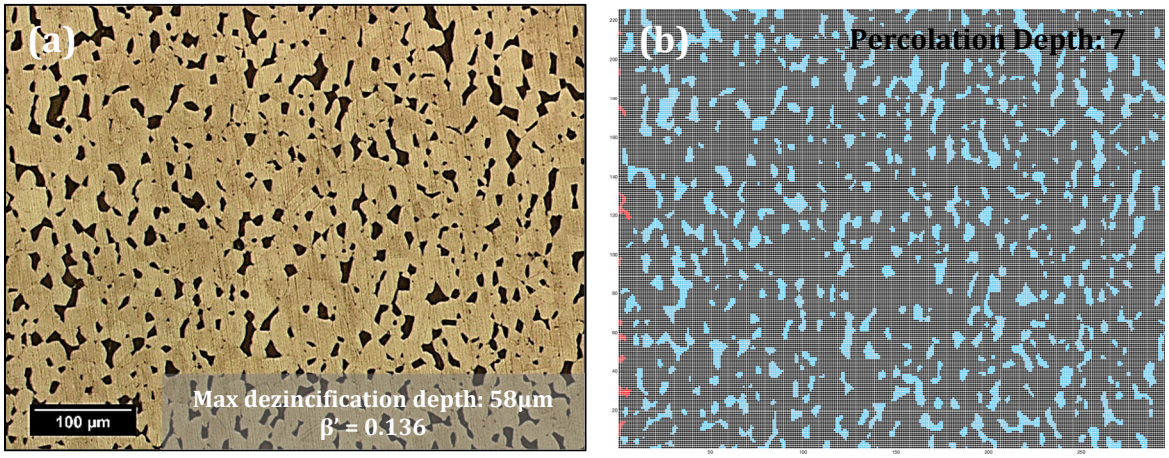


**Figure 6.38: (a) Hot compressed CuZn37.4BiAs microstructure post heat treatment at 550°C for 30 minutes, (b) 297 x 225 grid lattice model and resulting percolation after the 297th time-step.**

The example microstructures and real dezincification results shown earlier in Chapter 6 in Fig. 6.18 are used in Fig. 6.39 to show the effect of α grain size on simulated percolation. Here, samples of hot compressed CuZn37.4BiAs with an average grain size of 40µm and 167µm are compared using inset images (highlighted in Fig. 6.39a, c) to create the same 297 x 225 lattice grid. The simulated percolation depths of 201 ≈ 402µm and 272 ≈ 544µm are again comparable with the real dezincification depths of 364µm and 599µm. We can easily see the effects of having a clear path for percolation along the bottom of Fig. 6.39d, whilst a more complicated percolation path is required in Fig. 6.39b. Overall, the ratios between the two samples effectively show the anticipated differences in dezincification depth due to the average α grain size.

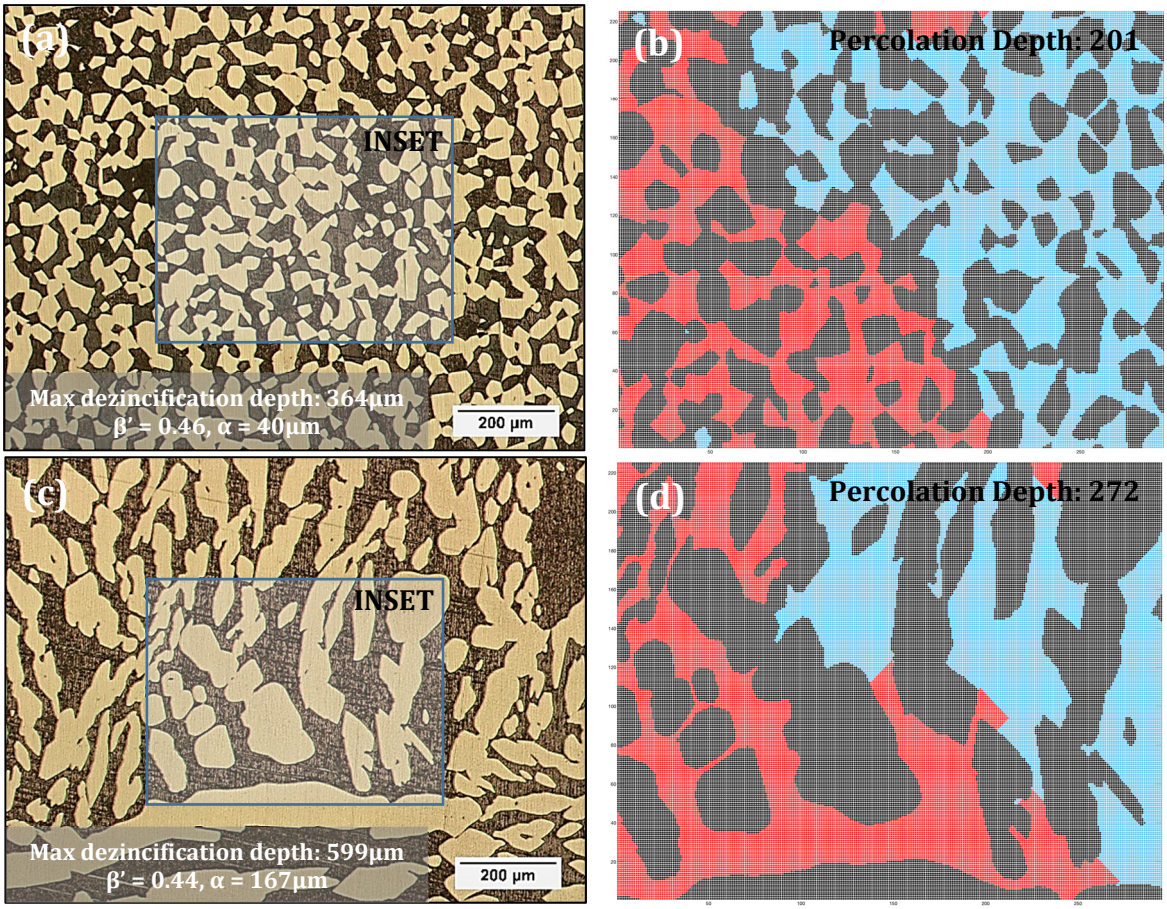


**Figure 6.39: (a) Hot compressed CuZn37.4BiAs microstructure post heat treatment at 700°C for 180 minutes, (b) inset 297 x 225 grid lattice model and resulting percolation after the 297th time-step, (c) hot compressed CuZn37.4BiAs microstructure post heat treatment at 850°C for 60 minutes and ramped down to 700°C for 15 minutes, and (d) inset 297 x 225 grid lattice model and resulting percolation after the 297th time-step.**

### 6.5.5 Perspectives on Microstructural Effects on Dezincification

If one were to generalise the effect of the microstructural variables on dezincification resistance, the β' phase fraction is analogous to a percolation threshold and strongly influences the percolation kinetics. This is recognised in industry and is appreciated to be the major way to control dezincification. In this contribution, α grain size and morphology are additionally recognized to be of comparable importance as the β' fraction, as supported by the percolation simulation with pure topology considerations. Smaller α grain sizes causes the β' phase to be statistically less interconnected and thus a more complex path is needed for percolation. The morphology of α grains more directly deals with the relationship between the percolation direction and α grain arrangement. A small tilt angle with high aspect ratio effectively distributes the α phase more effectively across the microstructure, leading to a larger barrier more resistant to percolation. Reduced α grain size (at constant β' fraction) acts in the same way and increases the resolved barrier resisting percolation.

## 6.6 Summary and Conclusions

A detailed investigation into the effect of microstructure on the dezincification resistance of continuous cast CuZn37.4BiAs, and extruded CuZn37.6BiPAs 'lead-free' duplex brass has been undertaken. This has focused on the effects of the average α grain size (μm), aspect ratio, and the β' phase fraction (vol. %) and how these factors, in addition to the fabrication mode, will affect the interconnectivity of the β' phase, and subsequent dezincification resistance of the alloy.

The β' phase fraction is of strong importance to the final dezincification resistance of the continuous cast CuZn37.4BiAs alloy, and this is an expected trend based on industry knowledge and available literature. More surprisingly, for certain ranges of β'phase fraction, the average α grain size actually plays a more significant role in determining the final dezincification resistance of the continuous cast CuZn37.4BiAs alloy. This is the first time this has been shown and has important implications for the brass industry. Probably, the findings in this Chapter are the most important in this thesis.

For the CuZn37.4BiAs alloys, hot compressed to simulate the forging process, similar trends were found for the influence of β' phase fraction and average α grain size, however these tended to be less consistent and depended strongly upon the aspect ratio and subsequent interconnectivity of the β' phase. This was influenced not only by the grain size, but also the α grain morphology post-recrystallisation and has been further explained using the percolation simulations.

The extruded CuZn37.6BiPAs showed remarkably different characteristics to the CuZn37.6BiAs, in part due to its prior processing history. Weak trends were shown for β' phase fraction and α grain size, and in some cases the dezincification resistance actually decreased for higher phase fractions of β'. It was shown that this effect is only present in the short-term, as longer testing times (120 hours vs. 24 hours) show significantly higher dezincification depths, which is more consistent with the available literature and industry understanding. Subsequent testing of CuZn37.8BiPAs after various cooling rates also shows that quenching of these alloys is able to inhibit dezincification due to the formation of fine Widmanstätten α grains in the microstructure which, when supported by both As and P dezincification inhibitors, impedes the dezincification process over the standard 24-hour test period. These microstructural explanations for changes in dezincification resistance according to cooling rate are the first time this has been shown and brings into question the reliability of the existing time period used in the accelerated dezincification testing protocols (ISO6509-1 and AS2345) considering the expected life-span of these brasses once in the field.

# 7 Machinability

One of the major reasons why duplex brass is used so extensively in the plumbing industry is due to its versatility. Installations may require a variety of different fitting and valve connection types (for example barb, push-to-connect, threaded, compression, solder, press) and in a wide range of sizes from mm to cm scale, all whilst maintaining tight design tolerances to produce a secure connection with optimal potable water flow. Casting or forging alone cannot achieve the desired dimensional requirements, therefore machining is a critical step in the processing schedule. Machining encompasses a wide range of operations, including turning, drilling, boring, milling, threading, parting and grooving, each of which has specific tooling types and parameters to achieve the final desired dimensions of the component in an economical manner. Tooling considerations are critically important but only form part of the equation. The workpiece material itself is a key factor in the ease of machining and traditional leaded duplex brasses have been widely regarded as one of the best materials to work with for their 'free machining' characteristics. The 'free-machining' property is predominantly due to the inclusion of Pb particles which are thought to simultaneously break up machining chips (swarf) and lubricate the machining surfaces of both the workpiece and the tooling interface.

With the evolution away from traditional leaded duplex brasses due to health concerns around Pb-leaching into potable water, several new 'lead-free' alloys have entered the market, many with claims of regaining a level of the machinability lost due to the removal of Pb. Machinability is measured using multiple indicators, such as tooling life, swarf morphology, component aesthetic, power consumption or cycle times, and although improvements may have been shown in one or more of these indicators, there are yet to be any of these 'lead-free' brasses shown in the literature that satisfy all of the 'free-machining' properties that were once achieved by leaded duplex brasses. Machining trials in the literature typically focus on compositional influence only and tend to use either basic mechanical testing or turning operations which aren't necessarily the most robust way to determine the machinability of a workpiece material.

The objective of this Chapter is to characterise the machinability of several modern 'Pb-free' duplex brasses available in the market today and compare with traditional Pb-bearing brasses as a function of (1) chemical composition, (2) mechanical properties, and (3) microstructural characteristics. This is completed using Drilling operations which in an industrial setting tends to remove the most material in the shortest period of time.

## 7.1 Alloy Selection and Thermal Treatments

Ten different duplex brasses sourced from various industrial suppliers are used in this machining study. A drilling operation is performed to evaluate common measures of machinability such as the average feed forces ($F_Z$), drilling torque ($M_Z$), surface roughness ($R_a$), and swarf morphology.

The compositions of each alloy were determined using optical emission spectroscopy (OES model Thermo Fisher Scientific ARL3460) and are shown in Table 7.1. Each alloy was chosen specifically to ascertain differences in machinability based on:

1. The presence of various alloying additions known to affect machinability such as Pb (CuZn39Pb3, CuZn37Pb2, CuZnPb2SnFe), Bi (CuZnBi0.7, CuZnBi0.8, CuZnBi2Sn), and Si (CuZnSi). The level of addition is consistent with common duplex brasses used in industry today.
2. The presence of various alloying additions for which machinability has not been explored in detail in the literature such as Sn (CuZnPb2SnFe, CuZnBi2Sn, CuZnSn) and Al (CuZnAl).
3. A binary Cu-Zn alloy with no significant alloying additions or impurities (CuZn37).
4. Fabrication method. Alloys produced via either continuous casting (CC) or extrusion (EX) as indicated in Table 7.1.

It is expected that the microstructural state in each of these alloys will vary based on the points described above and this will have an impact on the machinability of each alloy.

**Table 7.1: Chemical composition (wt. %) of the investigated workpiece materials for machinability evaluations.**

| Alloy | U.N.S. | Cu | Zn | Pb | Bi | Si | Sn | Al | Fe | Ni | As | P |
|---|---|---|---|---|---|---|---|---|---|---|---|---|
| **CuZn39Pb3** | C37700 (EX) | 58.1 | 38.6 | 2.85 | <0.01 | <0.01 | 0.30 | <0.01 | 0.10 | 0.10 | <0.01 | <0.01 |
| **CuZn37Pb2** | C35330 (CC) | 60.4 | 36.9 | 2.08 | 0.02 | <0.01 | 0.22 | <0.01 | 0.12 | 0.05 | 0.19 | <0.01 |
| **CuZnPb2SnFe** | *N/A Fe (EX) | 60.7 | 35.0 | 2.04 | 0.01 | 0.05 | 0.76 | 0.06 | 0.63 | 0.36 | 0.24 | <0.01 |
| **CuZnBi0.7** | C28340 (CC) | 61.5 | 37.1 | 0.17 | 0.66 | <0.01 | 0.40 | <0.01 | 0.02 | <0.01 | 0.12 | <0.01 |
| **CuZnBi0.8** | C49265 (EX) | 60.9 | 37.5 | 0.23 | 0.80 | <0.01 | 0.33 | <0.01 | 0.01 | <0.01 | 0.09 | 0.11 |
| **CuZnBi2Sn** | C49260 (EX) | 61.6 | 34.7 | 0.06 | 1.95 | <0.01 | 1.31 | <0.01 | 0.03 | 0.27 | <0.01 | 0.07 |
| **CuZnSi** | C69300 (EX) | 75.6 | 21.1 | 0.03 | <0.01 | 3.09 | <0.01 | <0.01 | 0.01 | <0.01 | <0.01 | 0.10 |
| **CuZn37** | C27451 (EX) | 62.4 | 36.9 | 0.17 | <0.01 | <0.01 | 0.10 | 0.03 | 0.02 | 0.22 | 0.14 | <0.01 |
| **CuZnSn** | C46500 (EX) | 63.1 | 35.8 | 0.15 | <0.01 | <0.01 | 0.56 | 0.04 | 0.16 | 0.05 | 0.04 | 0.03 |
| **CuZnAl** | *N/A Al (EX) | 62.4 | 36.6 | 0.17 | <0.01 | <0.01 | 0.02 | 0.56 | 0.05 | 0.10 | 0.11 | <0.01 |

***(CC) = continuous cast rod, (EX) = extruded rod, N/A = no associated UNS alloy designation.**
***Highlighted in grey are inclusions of elements known to affect machinability of Cu-Zn alloys.**
***Highlighted in green are alloys which were tested both as-received and after heat treatments.**

There is currently no universally accepted methodology for measuring machinability. Furthermore, quantitative relationships between the machinability and the microstructure do not yet exist and are not fully understood. Qualitatively, the first order material properties affecting machinability are thought to be the following [237, 238]:

- Ductility – It is thought that materials with high ductility will exhibit greater adhesion to the cutting tool and be detrimental to machining. Lower ductility values are therefore thought to be better for machining.
- Hardness – The hardness of a ductile brass is related to its yield strength. Higher hardness means greater resistance to cutting and this is thought to be bad for machining. Lower hardness is considered better for machinability, except for extremely ductile materials that adhere to the cutting tool. Hardness is thought to be the most important factor affecting cutting forces.
- Thermal conductivity – Machining generates heat and it is desirable to have a workpiece that is able to dissipate that heat effectively. Metals with high thermal conductivity are expected to exhibit better machinability, everything else held constant. It must be kept in mind that large solute additives may decrease the thermal conductivity significantly.
- Strain-hardening capacity – the strain hardening of a material is related to the difference between its yield strength and ultimate tensile strength (UTS). A large strain hardening means that greater energy is required to cut the material and this will translate to large cutting forces.

Each of these properties can be very significantly affected by both compositional and microstructural changes in a brass. Unfortunately, a proper quantitative understanding of the relative importance of each material property for different machining conditions in not known.

One would expect the hardness to increase and the ductility to decrease as the volume fraction of β' increases. The strain hardening behaviour may show a complicated dependence on the β' phase fractions depending on any composite strengthening effects. The ductility should depend also on the presence of particles in the microstructure, whether they are Pb, Bi, or other particles such as those observed in Si brass. One would also expect the thermal conductivity to increase, with increases in FCC α fraction and decrease in solute content. Alloys such as the Si brass (containing multiple covalently bonded phases) are expected to exhibit a lower thermal conductivity than most of the other alloys examined in this Chapter.

To assist in the exploration of the above, alloys CuZn37Pb2, CuZnBi0.7, CuZnBi0.8, CuZnBi2Sn, CuZnSi (highlighted green in Table 7.1) were exposed to the machining operation in both the 'as-received'

state and after various heat-treatments. Solid cylindrical rod samples of 80mm length and 18-22mm diameter were prepared from each of the 10 alloys listed in Table 7.1 in the as-received condition. Additional samples of alloys CuZn37Pb2, CuZnBi0.7, CuZnBi0.8, CuZnBi2Sn, CuZnSi were heat treated in a muffle furnace for soak times ranging from 30 minutes – 2 hours, at temperatures ranging from 500°C - 800°C, and using both air-cooling and water quenching to create different microstructures. These heat treatments are described in Table 7.2. The resulting material properties for each alloy in the as-received state and after various heat treatment conditions are described in Section 7.2.

**Table 7.2: Heat-treatment parameters applied to CuZn37Pb2, CuZnBi0.7, CuZnBi0.8, CuZnBi2Sn and CuZnSi.**

| HEAT TREATMENT | TEMPERATURE | SOAK TIME | COOLING METHOD |
|---|---|---|---|
| As-received | - | - | - |
| HT1 | 500°C | 30 minutes | Air-cooled |
| HT2 | 500°C | 120 minutes | Air-cooled |
| HT3 | 500°C | 30 minutes | Water Quenched |
| HT4 | 600°C | 30 minutes | Air-cooled |
| HT5 | 600°C | 30 minutes | Water Quenched |
| HT6 | 700°C | 30 minutes | Air-cooled |
| HT7 | 700°C | 120 minutes | Air-cooled |
| HT8 | 700°C | 30 minutes | Water Quenched |
| HT9 | 800°C | 30 minutes | Air-cooled |
| HT10 | 800°C | 30 minutes | Water Quenched |

## 7.2 Sample Material Properties

Each of the 10 selected duplex brasses have been allocated into one of 4 sub-groups and their material properties measured in the as-received state and, if applicable, any heat-treated conditions. These four sub-groups are as follows:

- Leaded brass: CuZn39Pb3, CuZnPb2SnFe, CuZn37Pb2
- Bismuth brass: CuZnBi0.7, CuZnBi0.8, CuZnBi2Sn
- Silicon brass: CuZnSi
- Other Alternative brasses: CuZn37, CuZnSn, and CuZnAl

Each of the 10 duplex brasses was subject to room temperature tensile testing. Their respective tensile properties including yield strength (MPa), ultimate tensile strength (MPa) and elongation (%) are shown in Table 7.3.

**Table 7.3: Room temperature tensile data for each of the alloy sample compositions shown in Table 7.1.**

| Alloy | U.N.S. | 0.2% Yield Strength (MPa) | Ultimate Tensile Strength (MPa) | Elongation (%) |
|---|---|---|---|---|
| **CuZn39Pb3** | C37700 (EX) | 267 | 553 | 24.8 |
| **CuZn37Pb2** | C35330 (CC) | 172 | 506 | 25.6 |
| **CuZnPb2SnFe** | *N/A Fe (EX) | 236 | 460 | 32.3 |
| **CuZnBi0.7** | C28340 (CC) | 166 | 392 | 15.3 |
| **CuZnBi0.8** | C49265 (EX) | 127 | 518 | 39.6 |
| **CuZnBi2Sn** | C49260 (EX) | 280 | 459 | 23.1 |
| **CuZnSi** | C69300 (EX) | 448 | 795 | 26.3 |
| **CuZn37** | C27451 (EX) | 289 | 546 | 37.2 |
| **CuZnSn** | C46500 (EX) | 167 | 563 | 41.0 |
| **CuZnAl** | *N/A Al (EX) | 156 | 583 | 42.0 |

***(CC) = continuous cast rod, (EX) = extruded rod, N/A = no associated UNS alloy designation.**
***Alloy data points coloured orange represent the minimum for the data set, green represents the maximum for the data set in each of the 3 properties recorded.**

### 7.2.1 Leaded Brass

The as-received microstructures of the Pb-bearing duplex brasses, CuZn39Pb3, CuZnPb2SnFe and CuZn37Pb2 are shown in Fig. 7.1. Their average Vickers hardness values and associated tensile properties (Fig. 7.1d) are also shown. The first alloy in this group, the extruded CuZn39Pb3 (Fig. 7.1a), has the highest Vickers hardness (116.7 Hv) as well as the highest yield strength (267 MPa) and tensile strength (553 MPa). These values are higher than either of the other two Pb-bearing alloys due primarily to two factors. The first is that CuZn39Pb3 has the highest Zn wt. % and therefore the lowest α phase fraction at ~64%, with the remainder of the microstructure being made up of the harder BCC β' phase (in addition to some Pb-particles). The second is that the material has been extruded rather than continuously cast. This second factor contributes to a relatively small α grain size of ~8µm.

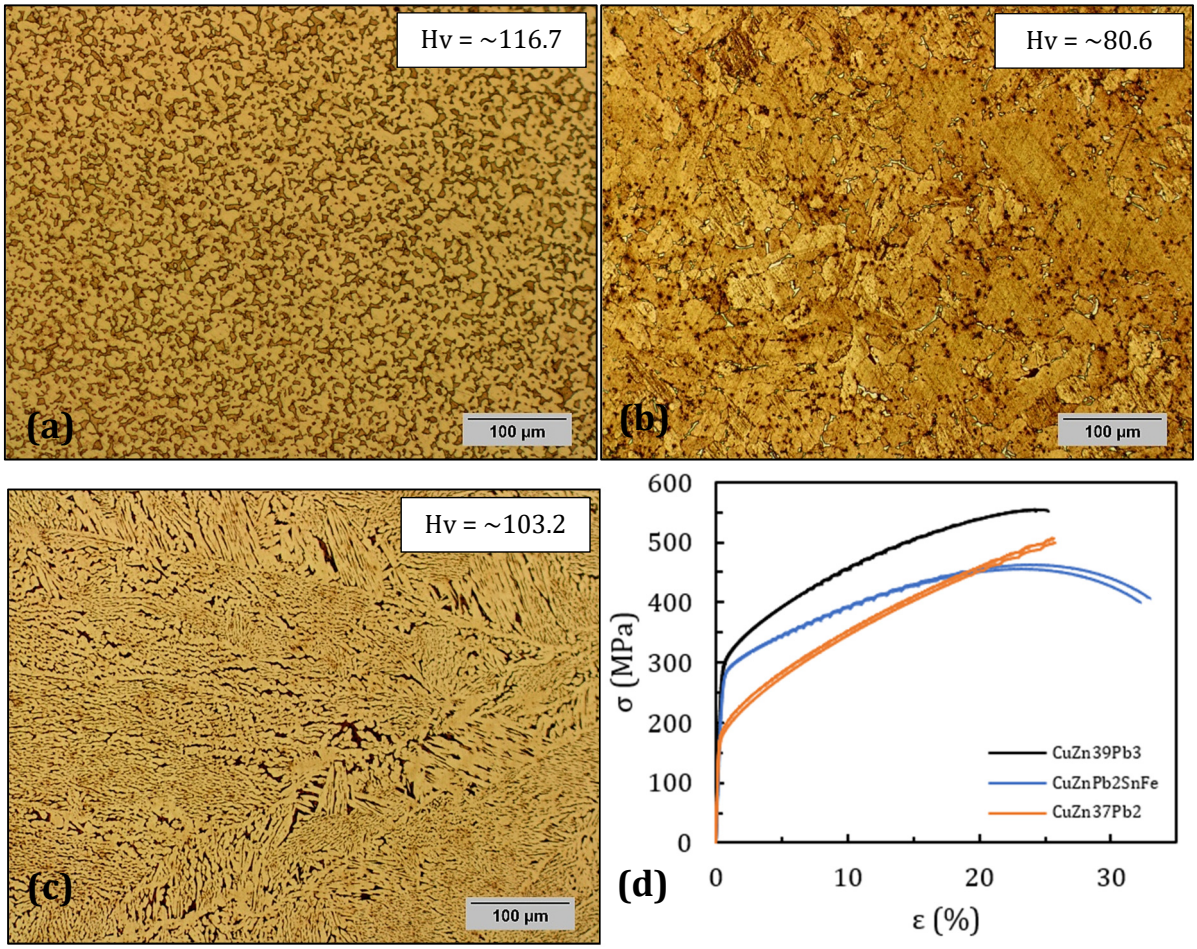


**Figure 7.1: The as-received microstructures and average Vickers hardness values for (a) CuZn39Pb3, (b) CuZnPb2SnFe, (c) CuZn37Pb2, and (d) their respective tensile stress-strain curves (x2).**

The second alloy in this group, CuZnPb2SnFe (Fig. 7.1b), exhibits the lowest Vickers hardness (80.6 Hv) and tensile strength (460 MPa), however retains a relatively high yield strength of 236 MPa and the highest elongation to fracture (32.3%). Given that the alloy contains a phase fraction of ~96.9% FCC α,

which is softer and more ductile at room temperature than β', and a significantly larger average α grain size of 34.9µm (the largest as-received α grain size in this study), the hardness value is not surprising. The inclusion of Fe and Sn in the composition is likely increasing the yield strength through intermetallic formation. Noted on both sets of tensile curves at approximately 10% elongation is serrated yielding. This is known as the Portevin - Le Chatelier (PLC) effect and is the result of the dynamic interaction between diffusing solute atoms and mobile dislocations, i.e. the solute has a diffusivity such that its rate of mass transfer is similar to the rate of dislocation motion during straining [239]. This is also known as dynamic strain ageing (DSA).

The third alloy in this group, the continuously cast CuZn37Pb2 (Fig. 7.1c), has both a moderate hardness (103.2 Hv) and tensile strength (506 MPa), but with the lowest yield strength (172 MPa) by a significant margin. With a very small average FCC α grain size of ~3.2µm and a moderate α phase fraction (~74.4%) this suggests that the material should have a higher yield strength, however due to its fabrication mode being continuous casting the material has a low dislocation density and is prone to localised chemical inhomogeneity and therefore weaker than its wrought counterpart. This also results in the highest strain hardening rate of the 3 Pb-bearing alloys.

Additional samples (10) of the continuous cast CuZn37Pb2 (Fig. 7.1c) alloy were produced and subjected to various heat treatments to generate a series of microstructures for the machining experiments. Fig. 7.2 shows the evolution in Vickers hardness (7.2a), α grain size and phase fraction (7.2b) for each of these samples as a function of their respective soak temperature ranging between 500°C to 800°C. Three series are shown to represent samples air-cooled after 30 minutes at temperature, air-cooled after 120 minutes at temperature and water quenched after 30 minutes at temperature.

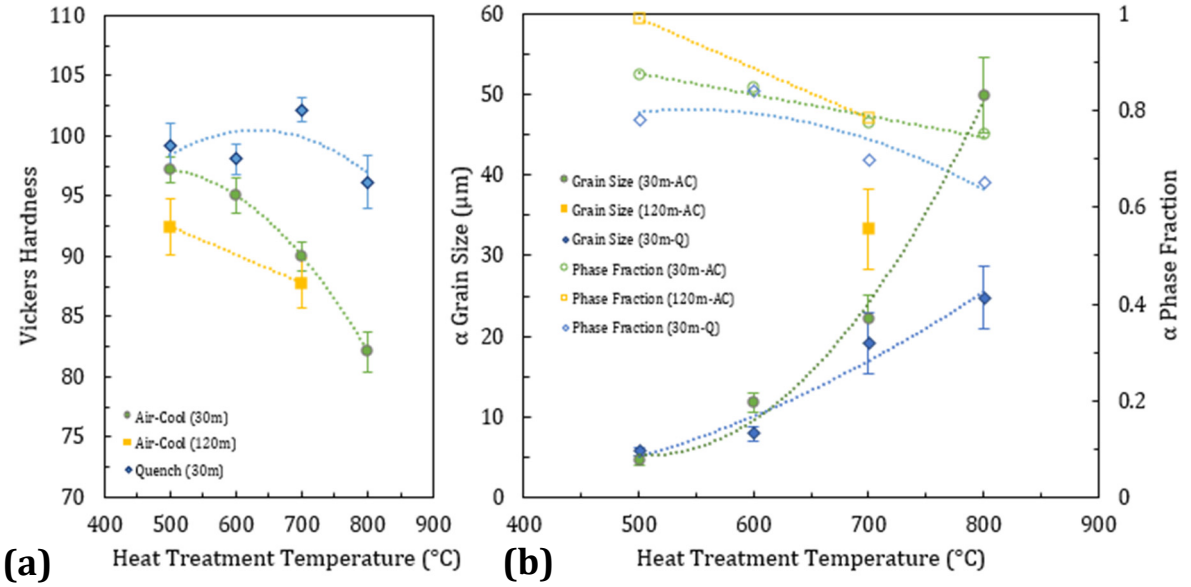


**Figure 7.2: The evolution of (a) Vickers hardness and (b) α grain size and phase fraction with applied heat treatment temperature for CuZn37Pb2.**

Significant differences are observed between the quenched and air-cooled CuZn37Pb2 samples heat treated at 800°C (Fig. 7.2). Examples of the resulting microstructures for these particular samples are shown in Fig. 7.3. As the heat treatment temperature is increased, the hardness of the air-cooled samples is generally found to decrease whilst for the quenched samples the hardness remains comparatively stable. This can be explained by the convergence of the two data sets for grain size and α phase fraction. As the temperature is increased, grain growth of the FCC α occurs more quickly, and while air-cooling provides time for α phase stabilisation and growth on cooling (Fig. 7.3a), the quenched samples (Fig. 7.3b) have less time available for this to occur. Therefore, the hardness decreases more readily in the air-cooled samples.

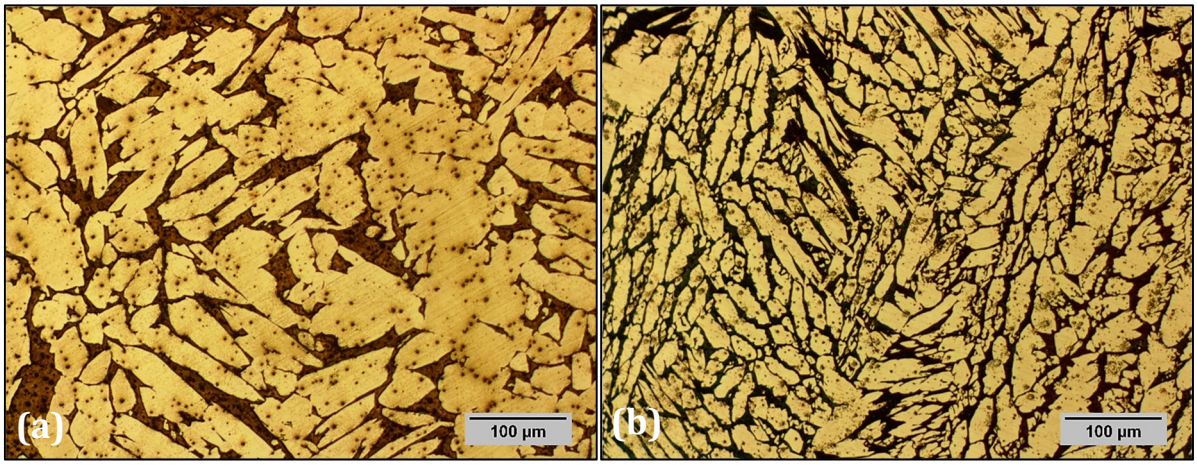


**Figure 7.3: CuZn37Pb2 microstructures post heat treatment at (a) 800°C for 30 minutes followed by air-cooling and (b) 800°C for 30 minutes followed by water-quenching.**

### 7.2.2 Bismuth Brass

The as-received microstructures and associated Vickers hardness and stress-strain tensile curves for the second alloy group, Bi-bearing CuZnBi0.8, CuZnBi2Sn and CuZnBi0.7 are shown in Fig. 7.4. The first alloy in this group, the extruded CuZnBi0.8, exhibits a moderate Vickers hardness (104.6 Hv) with the highest tensile strength (518 MPa) and elongation to fracture (39.6%) for any of the Bi-bearing alloys. However, its yield strength (127 MPa) is the lowest within this same group. The microstructure of this alloy shows equiaxed α grains of an average size of ~13.6µm and a BCC β phase fraction of ~6.6% indicating the alloy has either been cooled very slowly post-extrusion or exposed to subsequent annealing at intermediate temperatures which has led to an increased ductility and reduced yield.

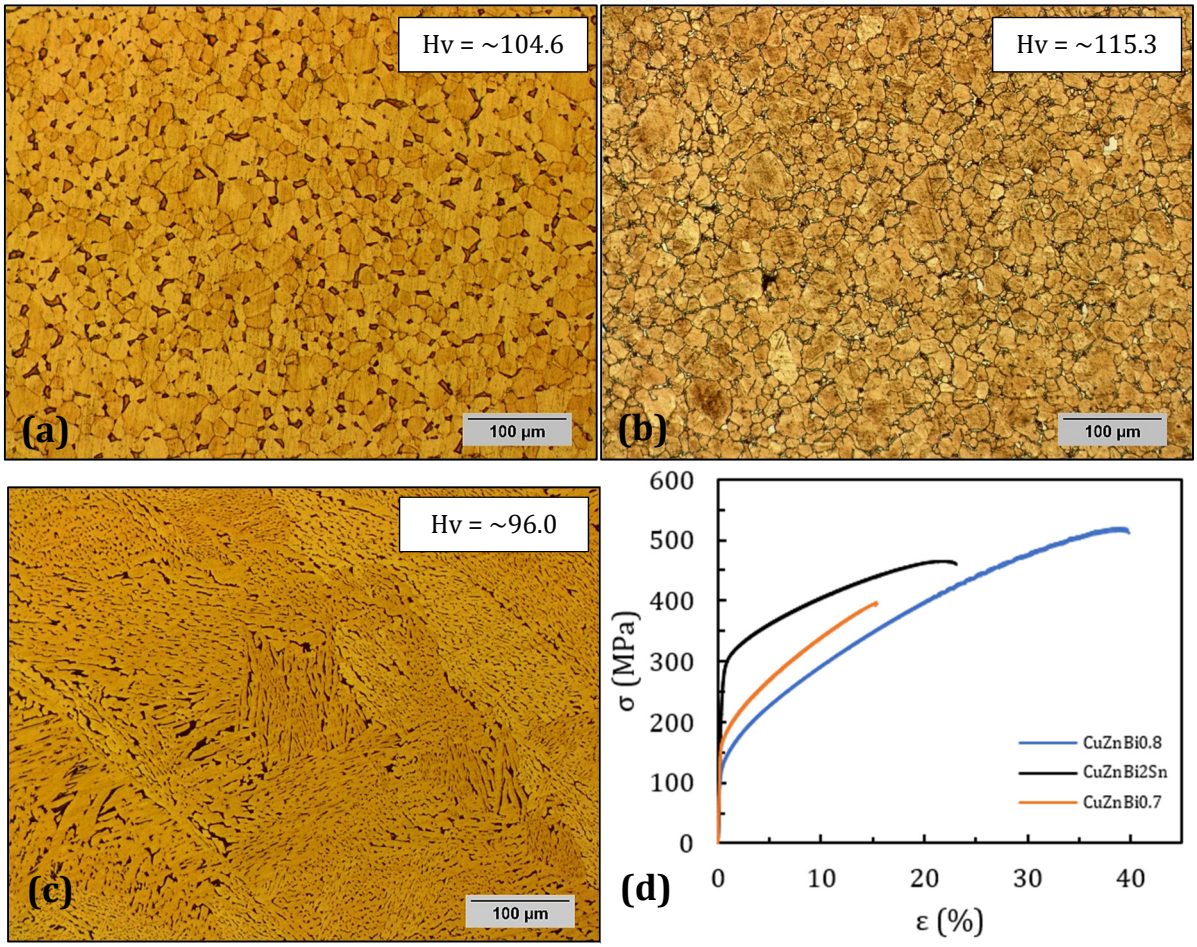


**Figure 7.4: The as-received microstructures and average Vickers hardness values for (a) CuZnBi0.8, (b) CuZnBi2Sn, (c) CuZnBi0.7, and (d) their respective tensile stress-strain curves (x2).**

The second alloy in this group, extruded CuZnBi2Sn (from the same industry supplier, Fig. 7.4b), appears to have a very similar microstructure to CuZnBi0.8, with an average α grain size of ~11.9µm and α phase fraction of ~95.7%. The alloy has a slightly higher Vickers hardness (115.3 Hv), however a significant difference in both yield strength and tensile strength. This is largely in part to the inclusion of ~1.31 wt. % Sn which can form hard intermetallics at these concentrations. This leads to a higher

yield and reduced ductility. The contribution of brittle bismuth particles in higher concentrations (~1.95 wt. %) can also not be ruled out as a contributing factor to the reduced ductility in this case.

The third alloy in this group, the continuously cast CuZnBi0.7 (Fig. 7.4c), has many similar characteristics to the continuously cast Pb-bearing CuZn37Pb2. Both have a moderate hardness (96.0 Hv vs. 103.2 Hv) and low yield strengths (166 MPa vs. 172 MPa). Both have a small average FCC α grain size (~3.4µm vs. ~3.2µm) and a relatively moderate α phase fraction (~78.8% vs. ~74.4%) and is due to both alloys being continuously cast and therefore absent of any prior strain history. The CuZnBi0.7 alloy also has the highest strain hardening rate of ~15.3 dσ/dε and a very low elongation to fracture (15.3%) which is the least ductile alloy tested in this entire study. This low elongation also prevents the tensile strength reaching higher than 400 MPa. One possible reason for the reduction in ductility compared with the Pb-bearing continuously cast alloy, is that bismuth is both brittle and a stress raiser at room temperature due to its expansion upon solidification by ~3.32% [73]. Bismuth also has a tendency to form in a film-like morphology along grain boundaries causing embrittlement [74-77, 147, 148].

Additional samples (10) of each of the extruded CuZnBi0.8 alloy, the extruded CuZnBi2Sn alloy and the continuous cast CuZnBi0.7 alloy were produced and subjected to various heat treatments to generate a series of microstructures for the machining experiments. In Fig. 7.5 the evolution in Vickers hardness (7.6a), α grain size and phase fraction (7.6b) for each of the CuZnBi0.8 samples are shown as a function of their respective soak temperatures between 500°C to 800°C. Three series are shown in Fig. 7.5 to represent samples air-cooled after 30 minutes at temperature, air-cooled after 120 minutes at temperature and water quenched after 30 minutes at temperature.

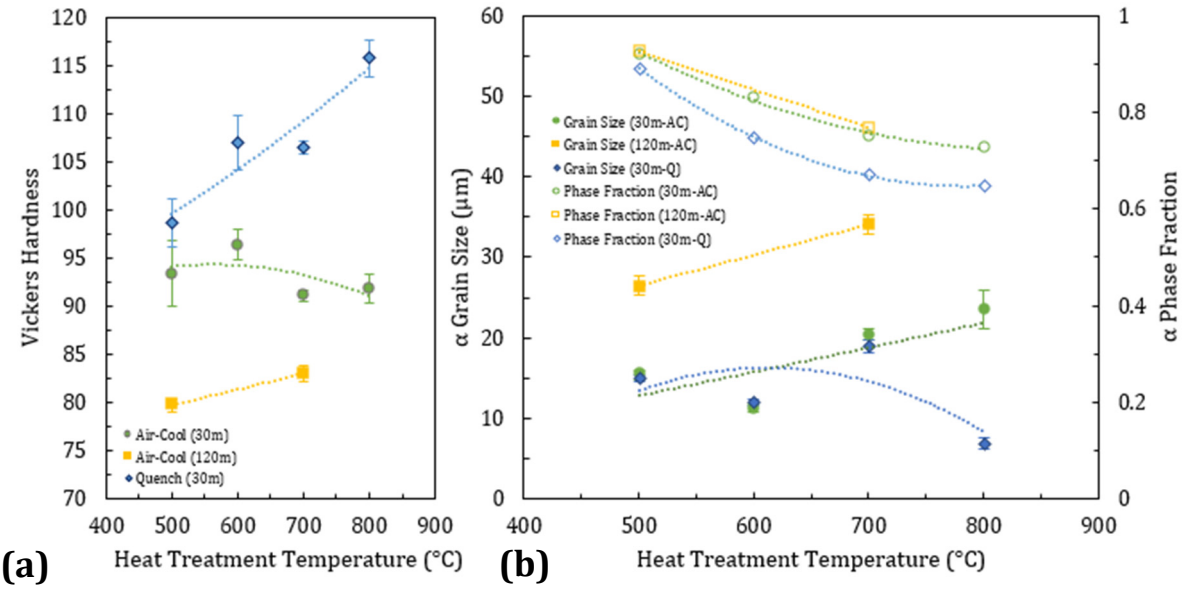


**Figure 7.5: The evolution of (a) Vickers hardness and (b) α grain size and phase fraction with applied heat treatment temperature for CuZnBi0.8.**

For the CuZnBi0.8 samples soaked at 500°C there was a decrease in hardness associated with an increase in average α grain size (from ~13.6µm to above 26.5µm) whilst maintaining the α phase fraction (from ~93.4% to above 92.7%). The hardness values then either stabilised (decreased slightly for 700°C) for the air-cooled samples or increased again in the water-quenched samples due to the gradual stabilisation of more β phase as temperatures increased, and for the case of the 800°C water-quenched sample, this produced a very small α grain size of ~6.9µm. This very small grain size can be achieved when quenching a duplex brass that is heated in the all-β phase field. This difference in grain size for samples heated to 800°C can be observed in Fig. 7.6b and c, compared with a sample heated to lower temperatures (700°C – Fig. 7.6a) for reference. This also shows the indicative change in grain morphology dependent on what temperature cooling commences. For a sample cooled from 700°C, the equiaxed structure from the as-received sample still remains, whilst the samples cooled from 800°C, despite their vast difference in grain size, both have a very acicular α grain structure.

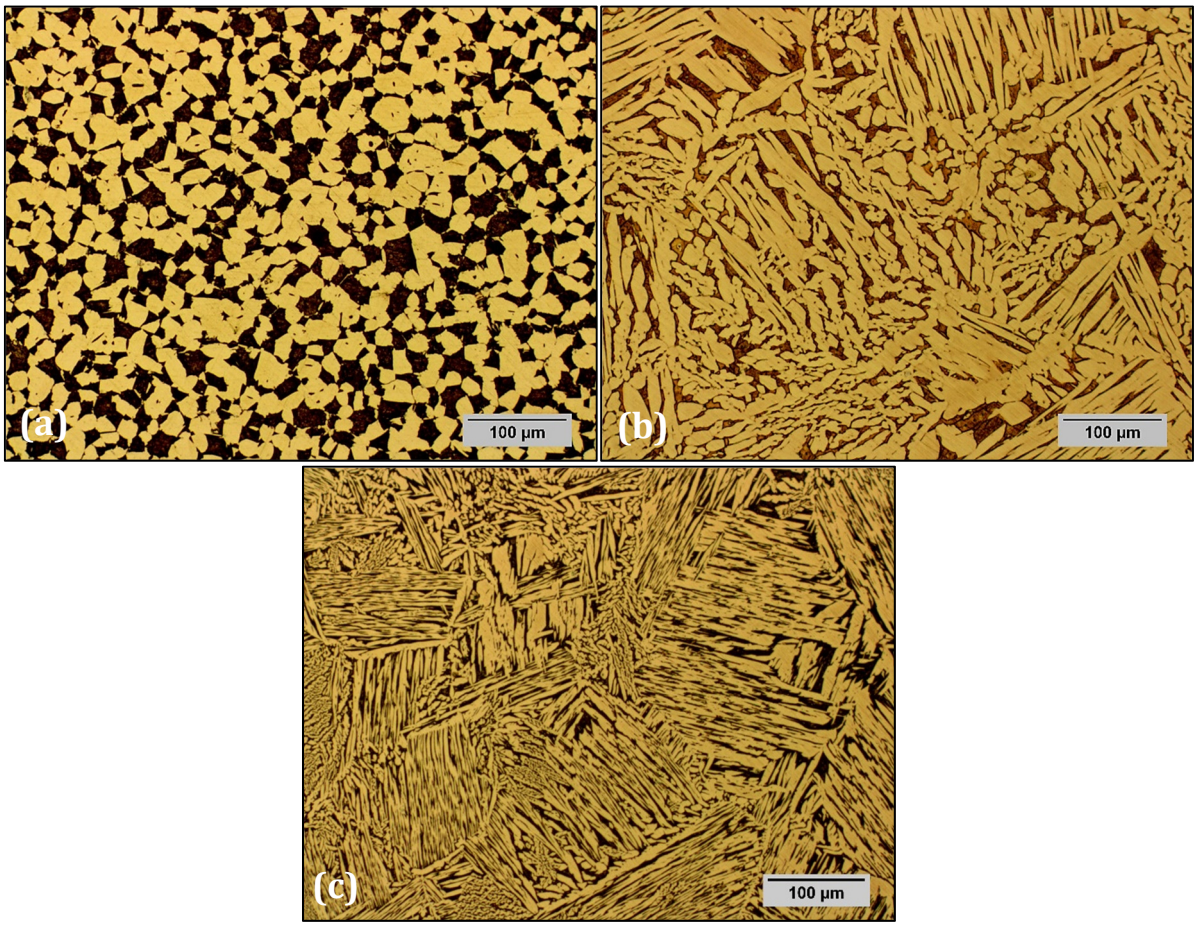


**Figure 7.6: CuZnBi0.8 microstructures post heat treatment at (a) 700°C for 30 minutes followed by water quenching, (b) 800°C for 30 minutes followed by air-cooling, and (c) 800°C for 30 minutes followed by water quenching.**

The evolution in Vickers hardness, α grain size and phase fraction for the extruded CuZnBi2Sn alloy samples heat treated at various temperatures are shown in Fig. 7.7a-b. Given the stability of the FCC α phase due to the significantly lower Zn wt. %, the hardness varies primarily as a function of the average grain size and Sn/Bi distribution for both the air-cooled and water-quenched samples. As the soak temperature is increased, there is an additional observation made that more small acicular α grains form between the significantly larger α grains as the Bi and Sn particles begin to coalesce together along grain boundaries as either large spherical particles, or in a film like manner along the α grain boundaries. This is particularly prevalent for the 800°C air-cooled condition (microstructure shown in Fig. 7.8) in which there is a clear formation of small acicular grains alongside the significantly larger equiaxed grains and particles of Bi. This apparent effect on the hardness and the various outputs for machinability will be explored further later in this Chapter.

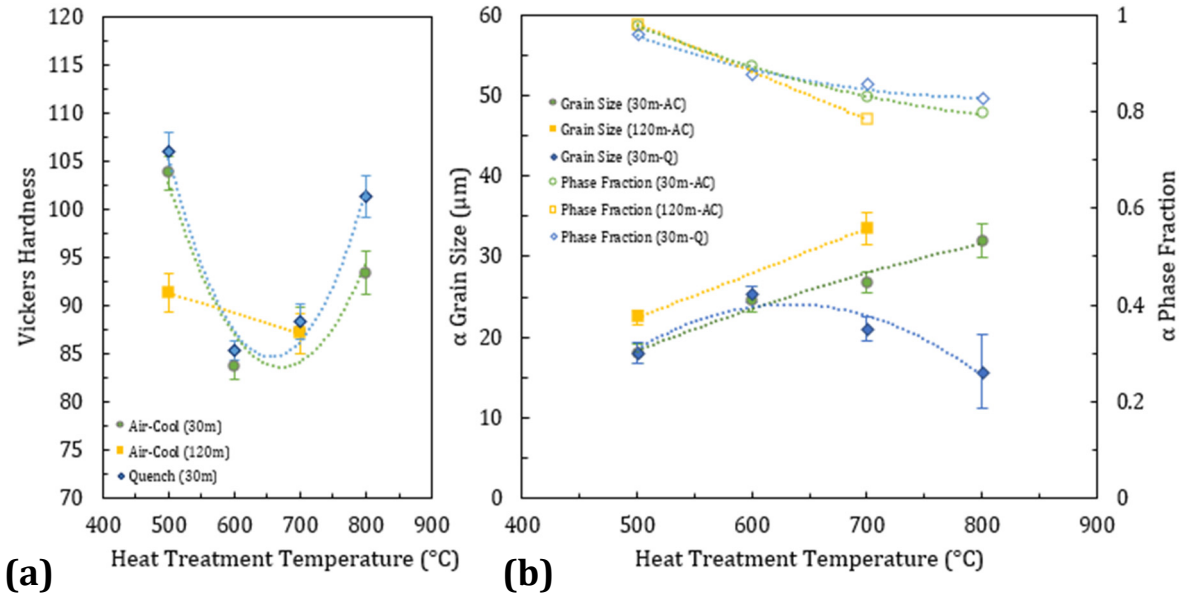


**Figure 7.7: The evolution of (a) Vickers hardness and (b) α grain size and phase fraction with applied heat treatment temperature for CuZnBi2Sn.**

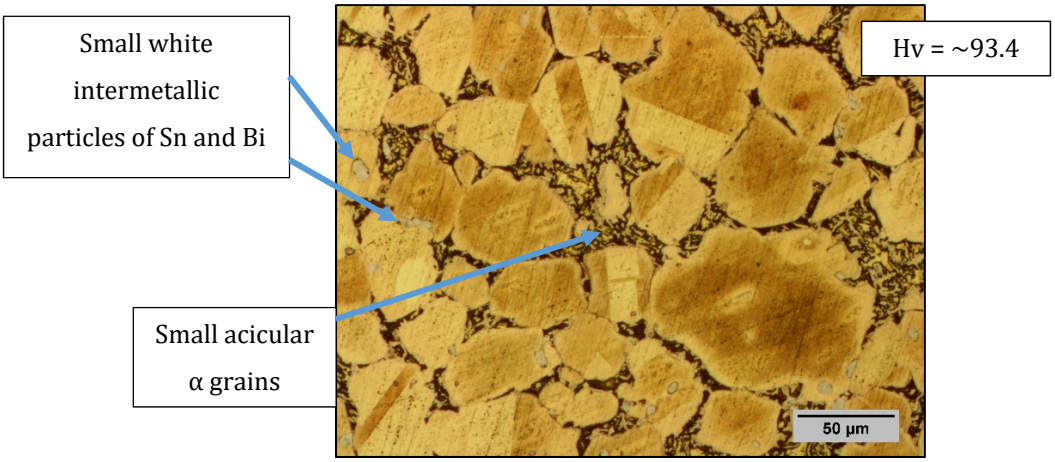


**Figure 7.8: CuZnBi2Sn microstructure post heat treating at 800°C for 30 minutes followed by air-cooling.**

The evolution in Vickers hardness, α grain size and phase fraction for the continuous cast CuZnBi0.7 alloy samples heat treated at various temperatures are shown in Fig. 7.9a-b. Exhibiting very similar behaviour to the continuously cast CuZn37Pb2 alloy, the dominant evolution with increasing heat treatment temperature is an increase in average α grain size and a gradual decrease in α phase fraction, the latter being due to greater amounts of BCC β being stabilised at elevated temperatures, followed by limited time available for α precipitation and growth. The increase in grain size and change in β' phase fraction has a direct impact on the Vickers hardness, and this is evident for the 30m air-cooled series in which the hardness drops from 96.0 Hv to 78.8 Hv with an 15x increase in grain size. The quenched samples exhibit a similar evolution in microstructure up to 700°C, however at 800°C there is a significant difference to the air-cooled samples generated by finer acicular α grains and a greater phase fraction of β'.

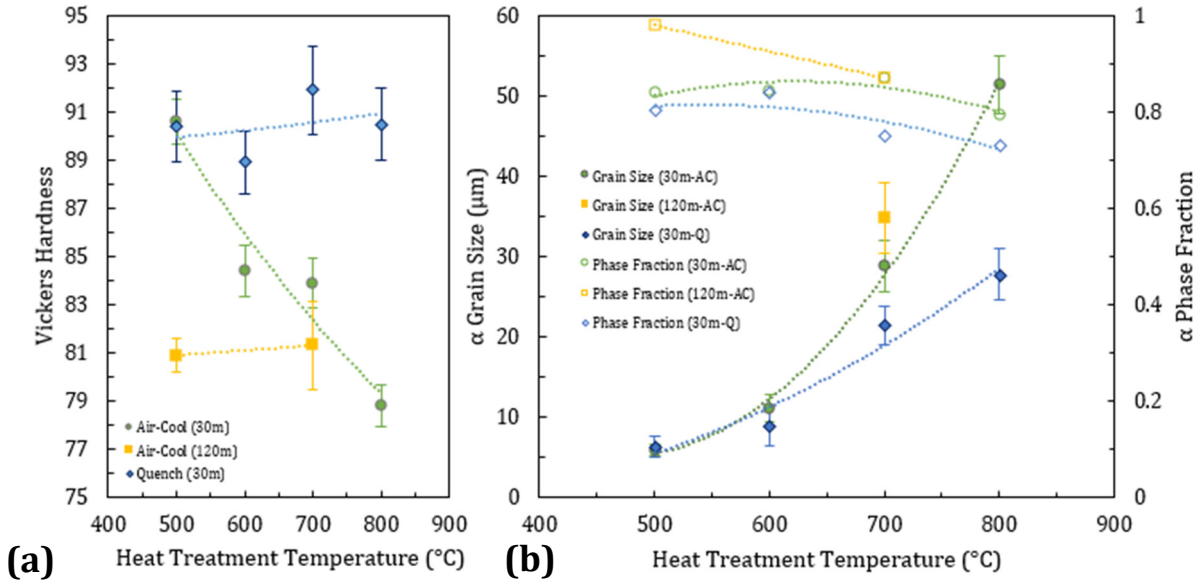


**Figure 7.9: The evolution of (a) Vickers hardness and (b) α grain size and phase fraction with applied heat treatment temperature for CuZnBi0.7.**

### 7.2.3 Silicon Brass

The as-received microstructure for the extruded Si-bearing alloy CuZnSi, as well as its associated Vickers hardness and tensile stress-strain curves are shown in Fig. 7.10. Compared with the other alloys studied in this work, CuZnSi presents with the highest values of Vickers hardness (143.1 Hv), yield strength (448 MPa) and tensile strength (795 MPa). This increase in the hardness and tensile strength is due to the formation of the harder HCP κ, BCC ε, and rhombohedral η phases which are observed between the FCC α grains shown in Fig. 7.10a and are expected to have an effect on the machinability of the alloy.

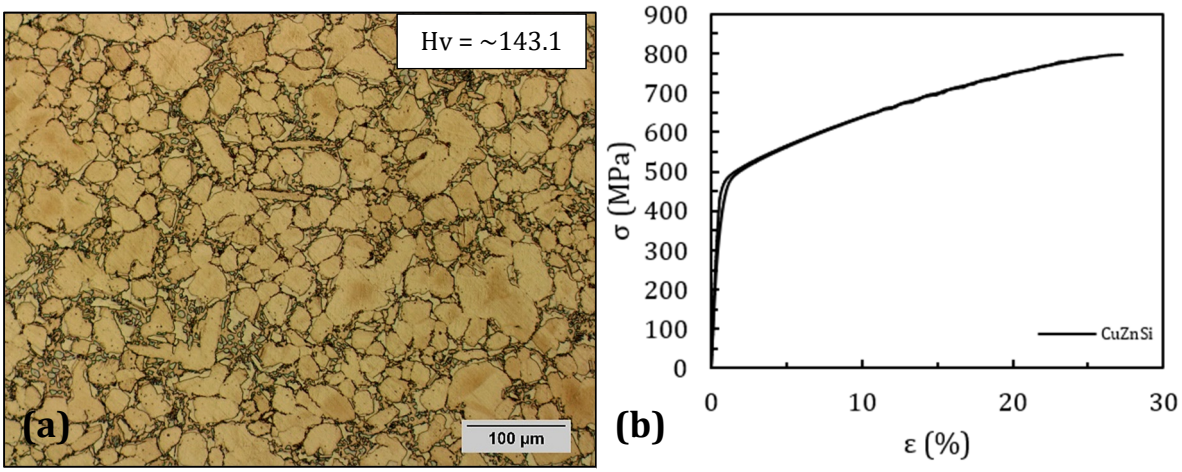


**Figure 7.10: (a) The as-received microstructure and average Vickers hardness value for CuZnSi and (b) the resulting tensile stress-strain curves (x2) for this same alloy.**

Additional samples (10) of the extruded CuZnSi alloy were produced and subjected to various heat treatments to generate a series of microstructures for the machining experiments. In Fig. 7.11 the evolution in Vickers hardness (7.12a), α grain size and phase fraction (7.12b) for each of the CuZnSi samples are shown as a function of the respective soak temperature ranging between 500°C to 800°C. Three series are shown in Fig. 7.11 to represent samples air-cooled after 30 minutes at temperature, air-cooled after 120 minutes at temperature and water quenched after 30 minutes at temperature.

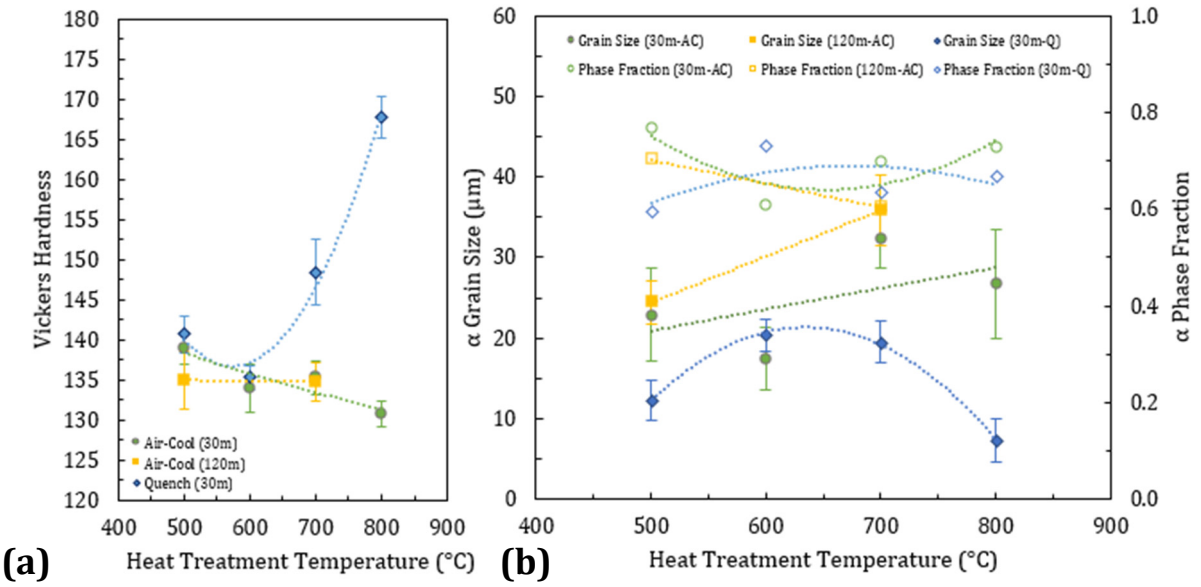


**Figure 7.11: The evolution of (a) Vickers hardness and (b) α grain size and phase fraction with applied heat treatment temperature for CuZnSi.**

Compared with the other alloys tested in this study, CuZnSi tends to exhibit a lower average phase fraction of FCC α through each of the heat treatments. However, as opposed to the typical BCC β' phase present in the other duplex brasses in this study, other phases are present in the form of either HCP κ, BCC ε or Rhombohedral η. Examples of how the microstructures evolve are shown in Fig 7.12 in which samples have been air-cooled after a 120-minute soak and quenched after a 30-minute soak from 700°C. We see equiaxed FCC α grains, typically larger on average in the air-cooled samples, and with a combination of κ, small η and ε, and acicular α grains having formed upon cooling. Air-cooling allows additional time for the ε and η to transform and grow, thus making clear observation of the ε and η grains simpler. In the quenched sample, there is less time for the ε and η to grow, thus the distinction is more difficult with the majority still remaining the α and κ phases. The retention of a much greater κ phase fraction additionally leads to a significant increase in hardness.

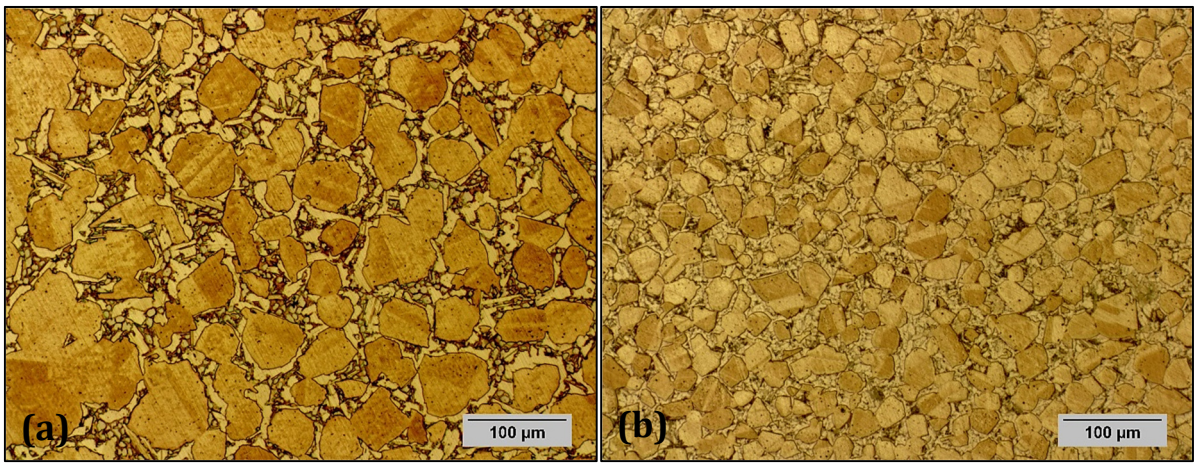


**Figure 7.12: CuZnSi microstructures post heat treatment at (a) 700°C for 120 minutes followed by air-cooling and (b) 700°C for 30 minutes followed by water quenching.**

### 7.2.4 Alternative Brasses – Binary, Al-, Sn-bearing

The as-received microstructures, associated Vickers hardness values and tensile stress-strain curves for the final alloy group in the series, CuZnSn, CuZnAl and CuZn37 are shown in Fig. 7.13. The first alloy in this group, CuZnSn (Fig. 7.13a) has a near-100% FCC α microstructure in which the α grains are recrystallised and of a consistent grain size (~15 µm) and equiaxed shape. The resulting yield strength (167 MPa) is relatively low, whilst the tensile strength (563 MPa) and elongation (41%) are significantly higher than the average of the other alloys tested in this study.

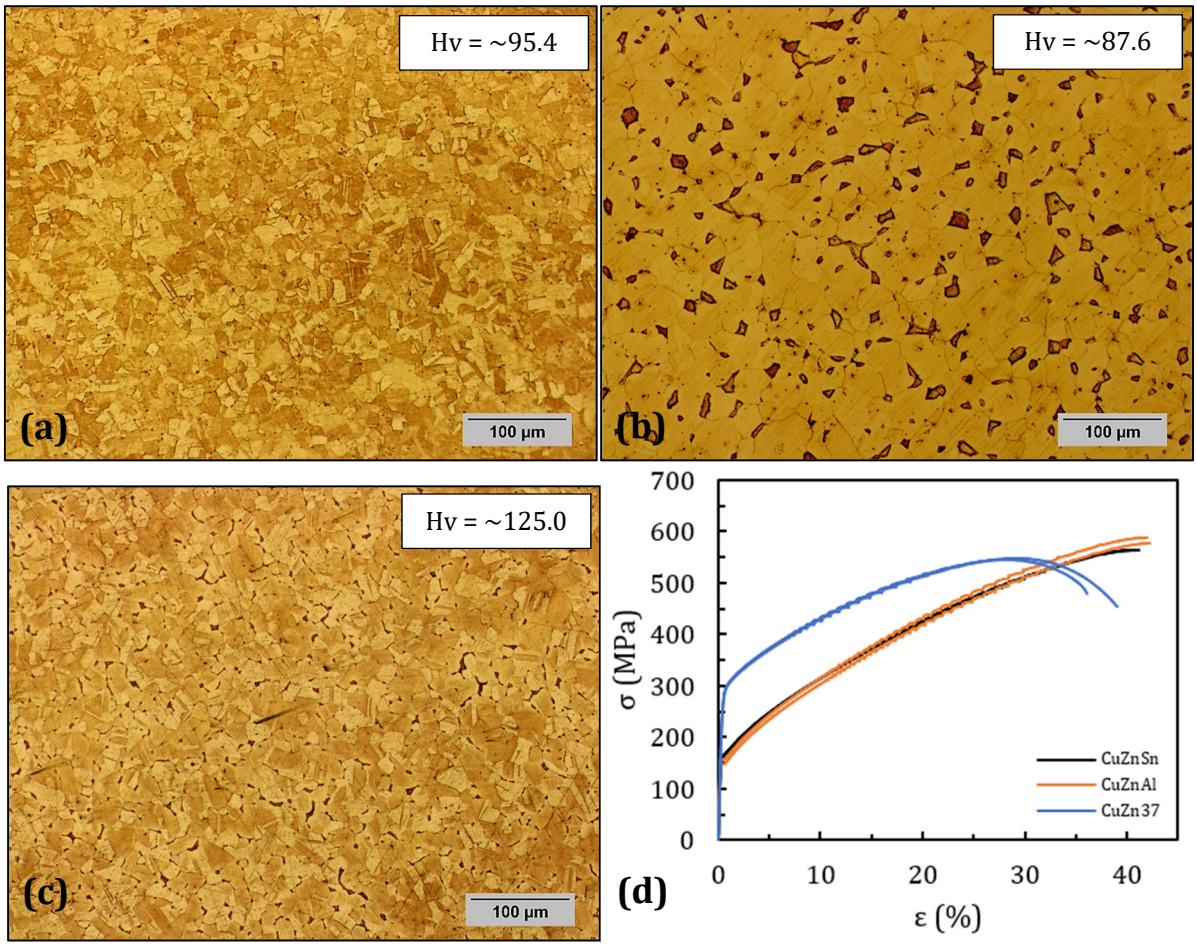


**Figure 7.13: The as-received microstructures and average Vickers hardness values for (a) CuZnSn, (b) CuZnAl, (c) CuZn37 and (d) their respective tensile stress-strain curves (x2).**

The second alloy in this group, CuZnAl (Fig. 7.13b), contains approximately 11.5% BCC β' in the microstructure as a result of the stabilising effect of the Al (0.56 wt. %). This would normally lead to an increase in Vickers hardness, however in this case, given the average FCC grain size is over 30 µm and highly equiaxed, the Vickers (87.6 Hv) and yield strength (156 MPa) are both low compared with the other alloys tested in this study, whilst the tensile strength (583 MPa) and elongation (42%) are similar to the CuZnSn alloy.

The third alloy in this group, CuZn37 (Fig. 7.13c), exhibits a different mechanical behaviour to either CuZnSn or CuZnAl, particularly an elevated yield strength (289 MPa) and Vickers hardness (125.0 Hv). Given this essentially binary alloy has an average α grain size of ~17μm and a β' phase fraction of only 4.5%, this elevated hardness and yield values are not expected.

## 7.3 Machining Experimental Results

The machining experiments involved drilling cylindrical samples of each alloy (in both the as-received state and in their heat-treated conditions) using a 10mm solid carbide drill at a cutting speed ($V_C$) of 110m/min, a feed rate ($F_n$) of 0.22mm/rev and a depth of cut ($A_P$) of 30mm. Each alloy was allocated a new drill. For each operation a dynamometer was used to measure an output feed force ($F_Z$) and drilling torque ($M_Z$), both critical in determining the power consumption of the machine and the overall forces required to machine the material which cannot be measured using a turning operation alone. A total of 145 drilling operations were completed in this study after which swarf samples were collected for analysis and the sample bores were measured for surface roughness (Ra). Each drill was inspected after machining was completed with no reportable wear detected in any case.

### 7.3.1 As-Received Experimental Results

Throughout each drilling operation the feed force ($F_Z$) and torque ($M_Z$) was recorded as a function of time. An example of a $F_Z$ and $M_Z$ measurement is shown in Fig. 7.14 and 7.15, respectively, for the CuZnSi alloy. Each measurement for $F_Z$ and $M_Z$ is split into two segments; the segment labelled A is the drill being slowly positioned into the face of the cylindrical sample, whilst segment B is the live $F_Z$ and $M_Z$ using the desired machining parameters described in the experimental method.

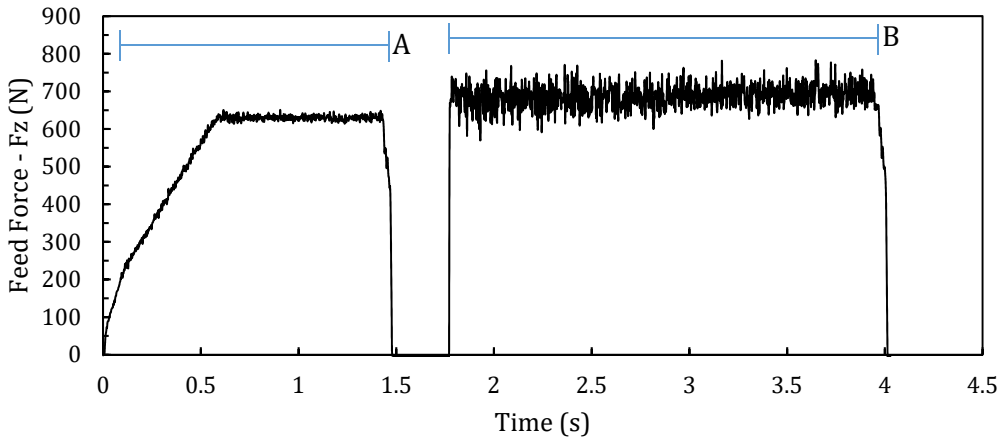


**Figure 7.14: An example of drilling feed force ($F_Z$) measurement as a function of time for as-received CuZnSi for the program set on the Spinner U-620. Segment A – Drill positioning, Segment B – Full Testing.**

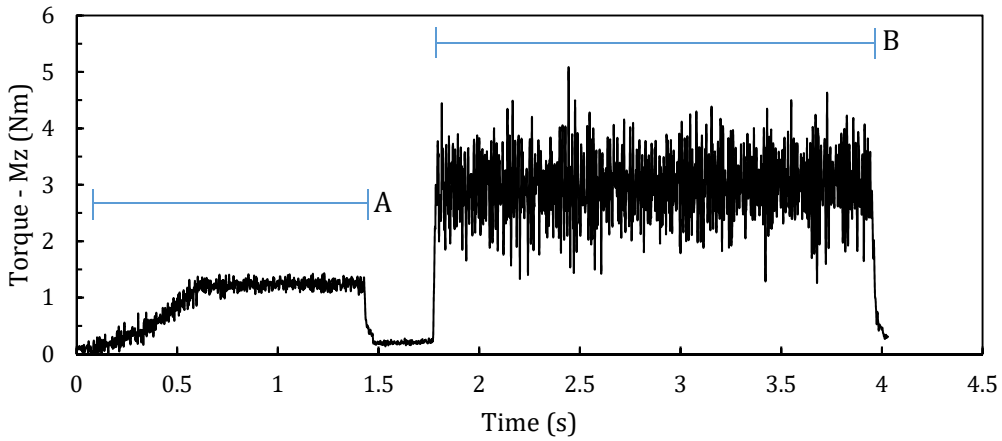


**Figure 7.15: An example of drilling torque ($M_z$) measurement as a function of time for as-received CuZnSi for the program set on the Spinner U-620. Segment A – Drill positioning, Segment B – Full Testing.**

For each measurement of the feed force ($F_z$, Fig. 7.14) and drilling torque ($M_z$, Fig. 7.15), the average reading of segment B was extracted, and the standard deviation computed. The average $F_z$ and $M_z$ for each of the 10 alloys tested in the as-received state are shown in Fig. 7.16, with the standard deviation used to calculate the standard error.

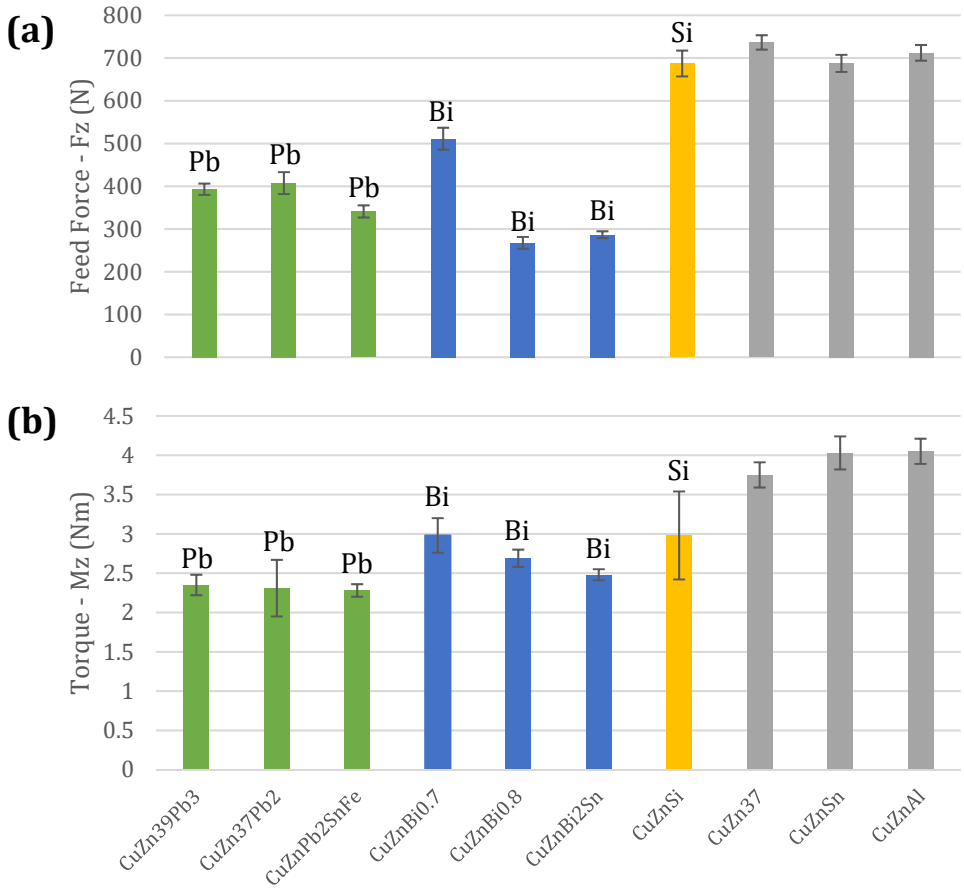


**Figure 7.16: (a) Average feed force ($F_z$) and (b) drilling torque ($M_z$) for each of the CuZn alloys tested in the as-received condition.**

The 4 sub-groups (Pb-, Bi-, Si-, and other duplex brasses) in Fig. 7.16 have been categorised by colour. The Pb-bearing alloys (green) provide the benchmark for traditional alloys used in the plumbing industry with an $F_Z$ in the range of 300-400 N, with CuZnPb2SnFe producing the lowest average value likely due to its lower hardness (Hv ~80.6). There is a similar finding for $M_Z$ with a very consistent measurement in the range of 2-2.5 Nm.

Looking at the $F_Z$ for the Bi-bearing alloys (blue, Fig. 7.16a), the continuous cast CuZnBi0.7 produced a higher $F_Z$ of 500 N, and the extruded Bi-bearing alloys both produced an average $F_Z$ in the range of 200-300 N. Therefore, in both the Pb- and Bi-sub-groups, the continuous cast alloys produce a markedly higher average $F_Z$ reading. The very low $F_Z$ results for CuZnBi0.8 are likely due to the low $\sigma_y$ of 127 MPa, whilst for CuZnBi2Sn, this is hypothesised to be due to the much higher content of Bi in the composition and almost no BCC β'. With respect to the $M_Z$ measurements for the Bi-sub-group (Fig. 7.16b), the continuous cast CuZnBi0.7 produced yet again the higher value with an $M_Z$ of 3 Nm, with the extruded Bi-bearing alloys both producing a gradual step-down to ~2.7 Nm and ~2.45 Nm average $M_Z$ respectively. Given the CuZnBi0.7 alloy contains the least Bi, this would be an important factor in producing the highest $M_Z$ for the group. Note that for each of the Pb and Bi alloy families, the continuous cast alloys CuZn37Pb2 and CuZnBi0.7 had the highest fluctuations which is translated into the standard error. Unlike the measurements taken for $F_Z$, all of the Bi-bearing alloys yielded higher values than their Pb-bearing counterparts suggesting that the type of particle and level in the composition plays a more critical role on torque than it does on feed force.

The $F_Z$ measurement for the CuZnSi alloy (yellow, Fig. 7.16a), in addition to the $F_Z$ for each of the alloys in the fourth sub-group (without any contribution from known chemical inclusions for machinability coloured grey) each produced much higher average $F_Z$ readings in the range of 650-750 N. On face value, there is a clear benefit of including Pb or Bi in the composition as it appears to reduce the $F_Z$ in each alloy, however there are clearly additional mechanical and microstructural factors at play. The CuZnSi alloy (yellow), produced an average $M_Z$ value similar to the CuZnBi0.7 alloy (Fig. 7.16b), whilst each of the alloys in the fourth sub-group each produced higher average $M_Z$ readings in the range of 3.5-4.1 Nm. The result from the CuZnSi alloy, considering the large gap to the Bi-bearing alloys in $F_Z$, and the narrow gap to $M_Z$ indicates that inclusions of Si in the composition can produce a more beneficial effect on some aspects of machinability. It is hypothesised that whilst the phases generated by Si additions (κ, ε, η) may assist in reducing torque due to their brittle particle-like nature, as the hardness increases due to their presence, the feed forces will naturally increase as well. Of additional note was a larger standard deviation in the average result for CuZnSi against the other samples. None

of the alloys in the 4th group (grey) contain any Pb, Bi, or Si, and each produced comparatively high readings for $M_Z$. This is a reflection of the absence of stress-raising particles to help fracture during drilling and chip formation.

A key question from the initial results for $F_Z$ and $M_Z$ (Fig. 7.16) is how do they correlate with the room temperature mechanical properties reported in Section 7.2. The workpiece hardness is thought to be a key property in determining machinability forces. Correlations between the Vickers hardness, ultimate tensile strength (UTS) and the $F_Z$ and $M_Z$ values are shown in Fig. 7.17.

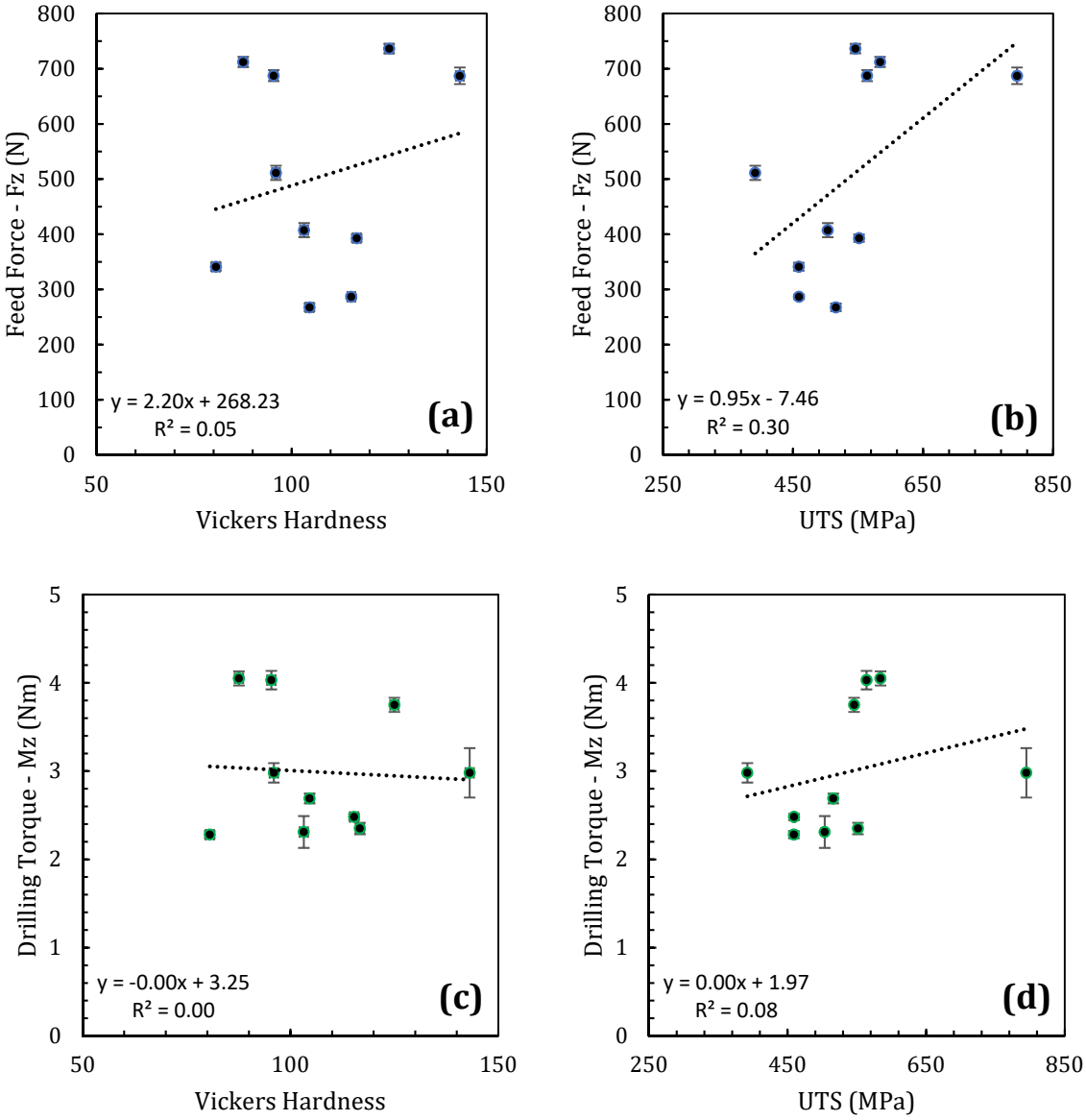


**Figure 7.17: Correlations observed between (a) Vickers hardness and feed force, (b) UTS and feed force, (c) Vickers hardness and drilling torque and (d) UTS and drilling torque for each of the alloys in the 'as-received' condition. The feed forces ($F_Z$) are significantly more affected by the mechanical properties of the alloy, whilst there are only weak or negligible correlations for drilling torque ($M_Z$).**

None of the plots shown in Fig. 7.17 is especially well correlated, although it must be kept in mind that each of the alloys all have different compositions and microstructures and hence similar Hardness, or UTS, may be associated with very different microstructures. The strongest correlation in Fig. 7.17 is between the feed force ($F_z$) and the UTS. The UTS would be one of the key determinants for releasing brass chips into the drill flutes, thus allowing the drill to drive further into the bulk material. The Vickers hardness appears to have a negligible effect on $M_Z$, with a weak correlation found for UTS. One should expect the $F_Z$ to be affected by mechanical properties such as hardness given it would increase the resistance to plunging the drill into the brass. This will be revisited in Section 7.4 on multiple samples of the same alloy heat treated to various extents and therefore with a range of $H_V$ values.

Fig. 7.18 presents the correlation for $F_Z$ and $M_Z$ with elongation. As perhaps expected, the $M_Z$ values are indeed shown to increase as the ductility is increased. This is closely related to adherence of the cutting chips to the drill edge and the strain required to fracture the sample. The elongation of the samples will be affected by the presence of Pb, Bi or Sn containing particles and these are likely having a strong effect on the $M_Z$ behaviour observed.

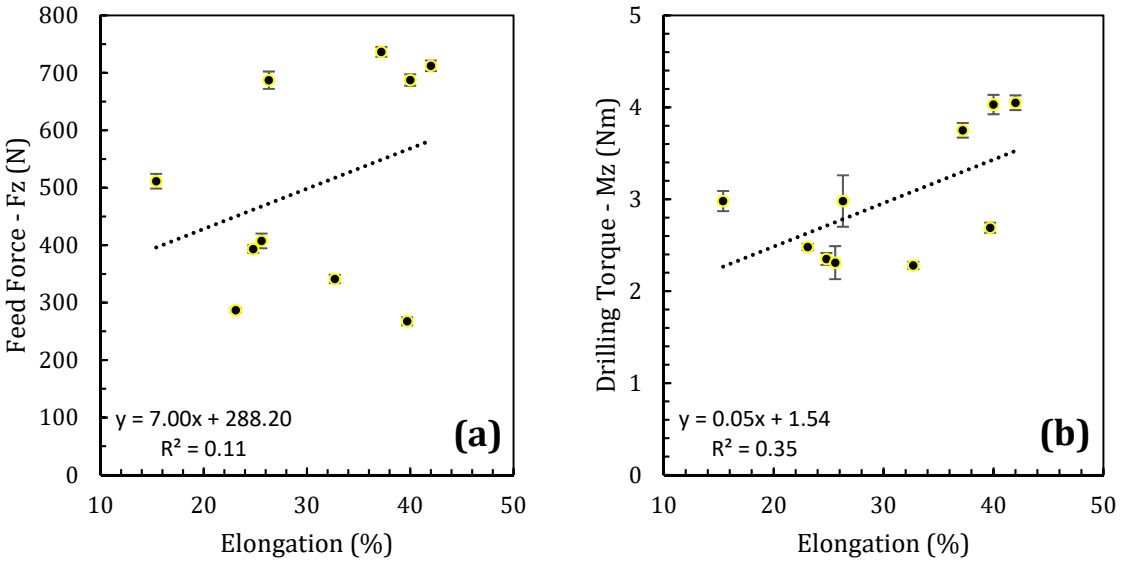


**Figure 7.18: Correlations observed between (a) elongation and feed force and (b) elongation and drilling torque. An increase in the ductility of the alloy is shown to be detrimental to both forms of machinability.**

Upon completion of the drilling operations, the newly machined surface of each sample was characterised using a profilometer to determine their average surface roughness ($R_a$). The resulting average $R_a$ and standard error for each of the 10 alloys studied in this work are shown in Fig. 7.19. In contrast to the $F_Z$ or $M_Z$ outputs (Fig. 7.16), the $R_a$ averages show that the Pb-bearing alloys (green) performed the worst with measurements in the range of 1.2-1.4µm. This indicates that while a high number of Pb-particles may be helpful to reduce the $F_Z$ and $M_Z$, the effect on surface roughness is an area of weakness and will be explored further in Section 7.4. The Bi-bearing (blue, Fig. 7.17) and other alloys (grey) each fared better with the extruded CuZnBi0.8 alloy producing the best value of the two groups at ~0.43µm. Given that CuZnBi2Sn contains almost as much Bi as two of the alloys that contain Pb, with significantly better results, this indicates that Bi particles are not as severe in deteriorating the $R_a$ of the alloy and therefore must fracture differently to Pb-particles under the same machining conditions. Finally, CuZnSi (yellow) was shown to have the best overall $R_a$ at ~0.26µm. The nature of the other phases present, the lack of Pb or Bi, and the higher Cu in this base-matrix are each likely to contribute to this effect.

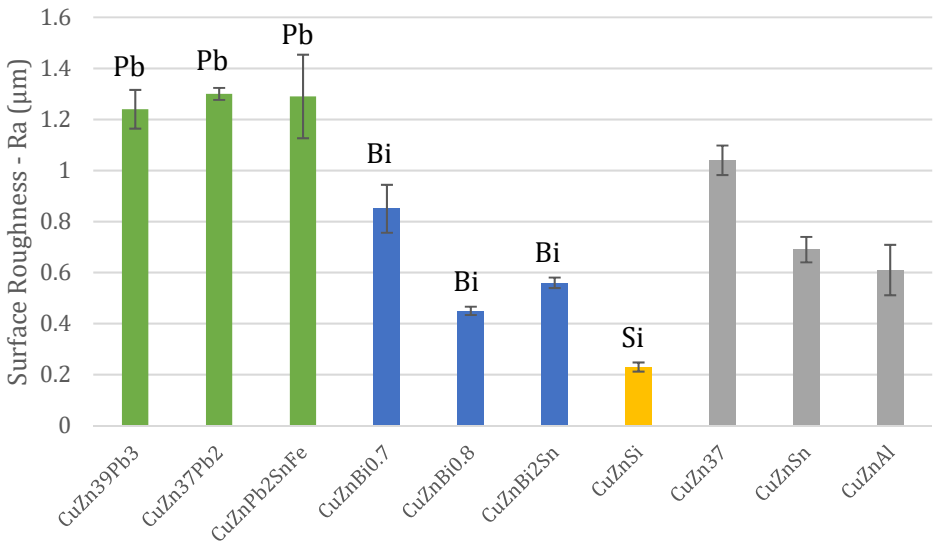


**Figure 7.19: Average drilled surface roughness ($R_a$) for each of the CuZn alloys tested in the as-received condition.**

In Fig. 7.20, correlations between the surface roughness and the Vickers hardness and elongation are shown. Whilst a weak trend is observed between the ductility and surface roughness, there is an indication that the Vickers hardness could be playing a role affecting the final $R_a$. That is, a harder duplex brass may be better able to produce a smoother surface finish. This is primarily shown by CuZnSi (highlighted with a blue arrow), which contains little Pb or Bi, and additionally has a very high workpiece hardness compared with the alternative alloys CuZn37, CuZnSn and CuZnAl. This is explored in Section 7.4.

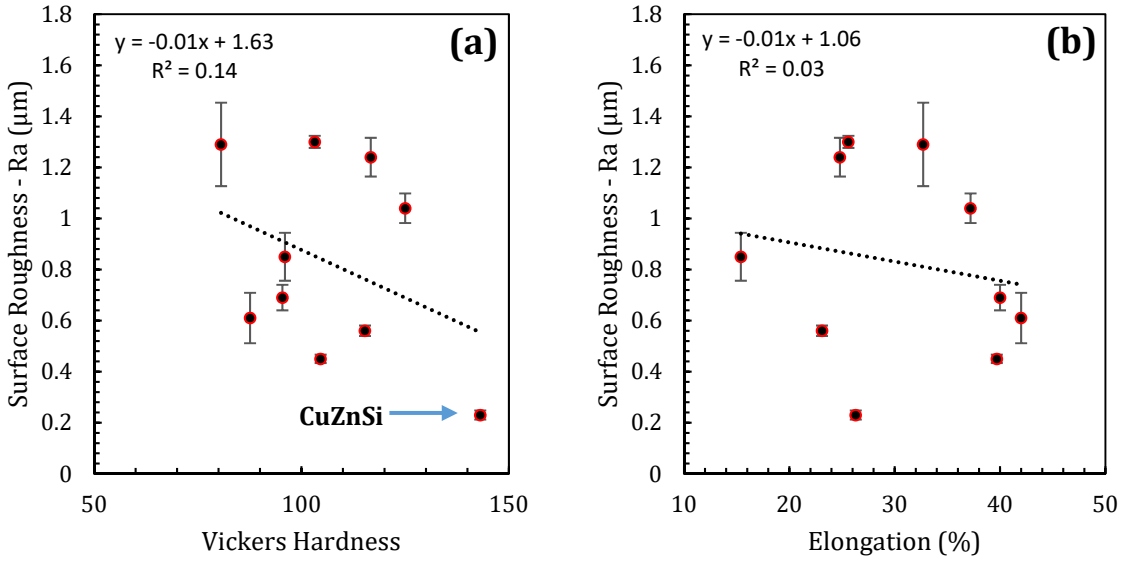


**Figure 7.20: Correlations observed between (a) Vickers hardness and (b) elongation and surface roughness for each of the alloys in the 'as-received' condition. Whilst a weak correlation is noted for ductility, the surface roughness does appear to be moderately impacted by the Vickers hardness.**

### 7.3.2 Swarf Morphology

As each of the as-received cylindrical workpieces were removed from the Spinner-U620 CNC post-drilling, a swarf sample was retrieved from the bore of the workpiece and kept for later visual assessment. The swarf samples for each of the 10 as-received brasses tested in this study are shown in Fig. 7.21 ranked from the finest grade to the most coarse. A grade, from I to IV, has been given to each alloy depending on the level of chipping and this is also marked in Fig. 7.18.

**Grade I:** The grade I brasses, CuZnPb2SnFe, CuZn37Pb2 and CuZnBi0.8 each exhibited excellent chipping characteristics, that is a very fine chip size with no significant spiral formation. This makes the swarf easy to contain, with minimal machine stoppages likely and therefore each of the alloys would be desirable for standard industrial machining operations. It is not surprising that the alloys within this grade contain significant levels of either Pb or Bi particles, both known to improve swarf chipping.

**Grade II:** The grade II brasses, CuZnSi, CuZnBi0.7 and CuZnBi2Sn are each observed to show similar free-cutting characteristics in comparison to the grade I alloys, however not to the same degree with slightly larger chip sizes and some mild spiral formation. The CuZnSi alloy (Fig. 7.21d) fractures readily along the chip surfaces, however as they do not entirely reach through the chip length, the larger chips remain intact. The Bi-bearing alloys are generally accepted to have free cutting behaviours, but they are not as effective as their Pb-bearing counterparts.

**Grade III:** Only one alloy was allocated as a grade III brass, CuZn39Pb3, due to its blend of very fine grade 1 chips, partially fractured grade 2 chips (similar to CuZnSi), and some significant grade 4 spirals. Whilst the inclusion of Pb has helped to produce much of the grade 1 and 2 chipping behaviour, the very small grain size (7.95µm) and high tensile strength (>550MPa) is expected to be the reason for the grade 4 spiral behaviour. This inconsistency of the chip size therefore lowers the overall grade of the material.

**Grade IV:** The grade IV alloys, CuZn37, CuZnSn and CuZnAl, are all absent of any Pb or Bi particles, and have no other significant means of generating a free-cutting swarf behaviour (for example through alternate phase formation like CuZnSi). Therefore, the observation of significantly larger average chip size and varying spiral lengths is expected. Each of these alloys would be expected to have issues by causing machine stoppages when operating in an industrial setting at high volume.

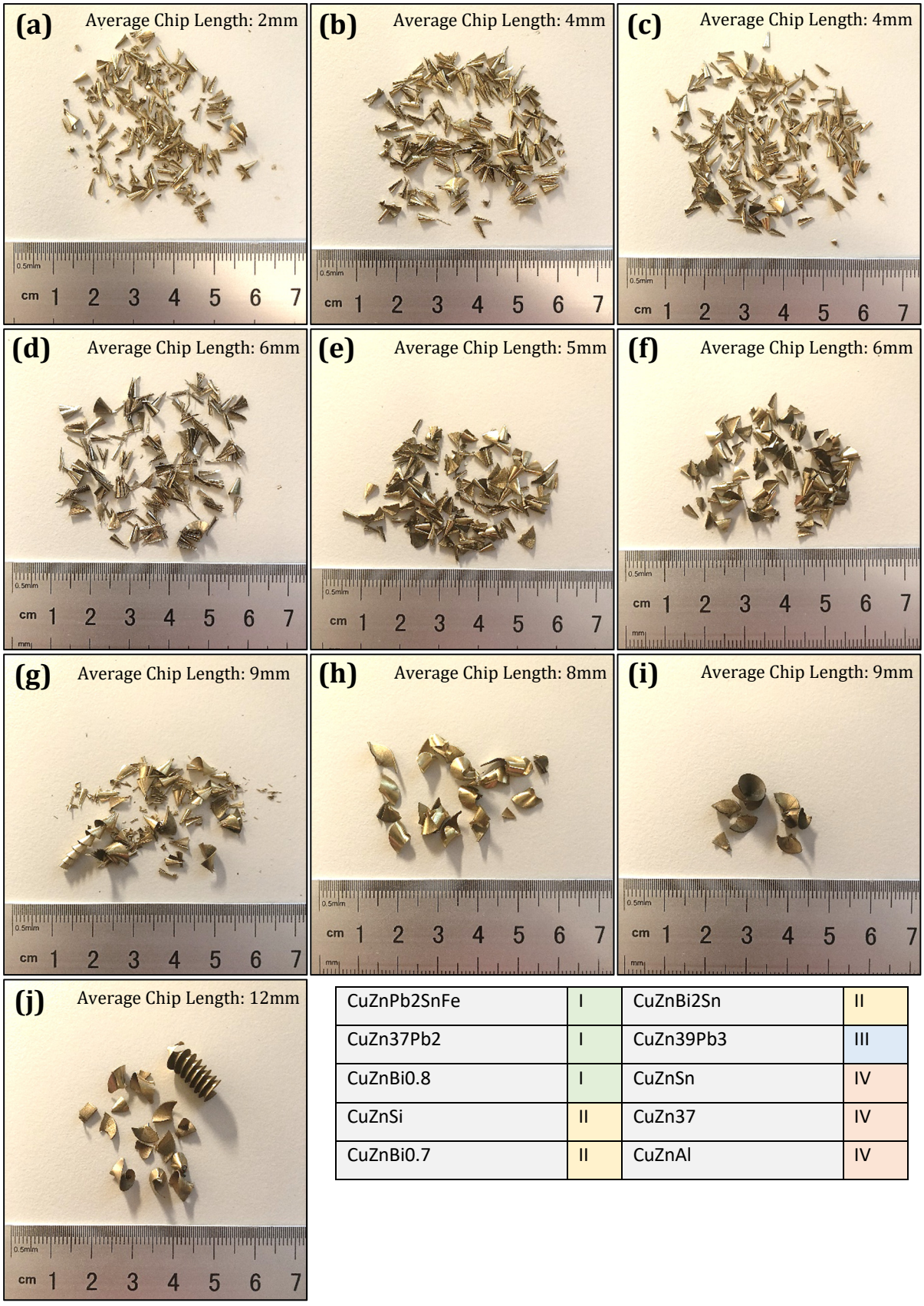


| | | | |
|---|---|---|---|
| CuZnPb2SnFe | I | CuZnBi2Sn | II |
| CuZn37Pb2 | I | CuZn39Pb3 | III |
| CuZnBi0.8 | I | CuZnSn | IV |
| CuZnSi | II | CuZn37 | IV |
| CuZnBi0.7 | II | CuZnAl | IV |

**Figure 7.21: Swarf morphology of (a) CuZnPb2SnFe, (b) CuZn37Pb2, (c) CuZnBi0.8, (d) CuZnSi, (e) CuZnBi0.7, (f) CuZnBi2Sn, (g) CuZn39Pb3, (h) CuZnSn, (i) CuZn37, (j) CuZnAl and a grading summary of each.**

## 7.4 Microstructure-Machinability Correlations

The machining experiments reported in Section 7.3, and the correlations with some mechanical properties were made for the 10 different alloys in the as-received state. These alloys have significant differences in microstructures, even for similar values of some mechanical properties and this must be kept in mind when considering the strength of the correlations observed. To examine relationships between machinability measures and the properties or microstructures of these brasses, in this section we examine the machinability of each alloy as a function of subsequent heat treatments to modify the microstructure. In this way, the effect of bulk compositional variations between each alloy can be separated from changes to the microstructure. The objective is to identify the first- and second-order influences of microstructural parameters such as particle size and distribution, α grain size and phase fraction on machinability.

### 7.4.1 Feed Force ($F_Z$)

In Section 7.3 the $F_Z$ results for the 'as-received' duplex brasses (Figs. 7.16a and 7.17a-b) revealed several interesting correlations with the base material properties. One of these is related to the workpiece hardness which is thought to affect the cutting resistance and subsequently increase the machining feed forces. To examine in more detail, data was collected from samples of the CuZn37Pb2, CuZnBi0.7, CuZnBi0.8, CuZnBi2Sn and CuZnSi alloys which were each additionally heat treated according to Table 7.2. The results are shown in Fig. 7.22.

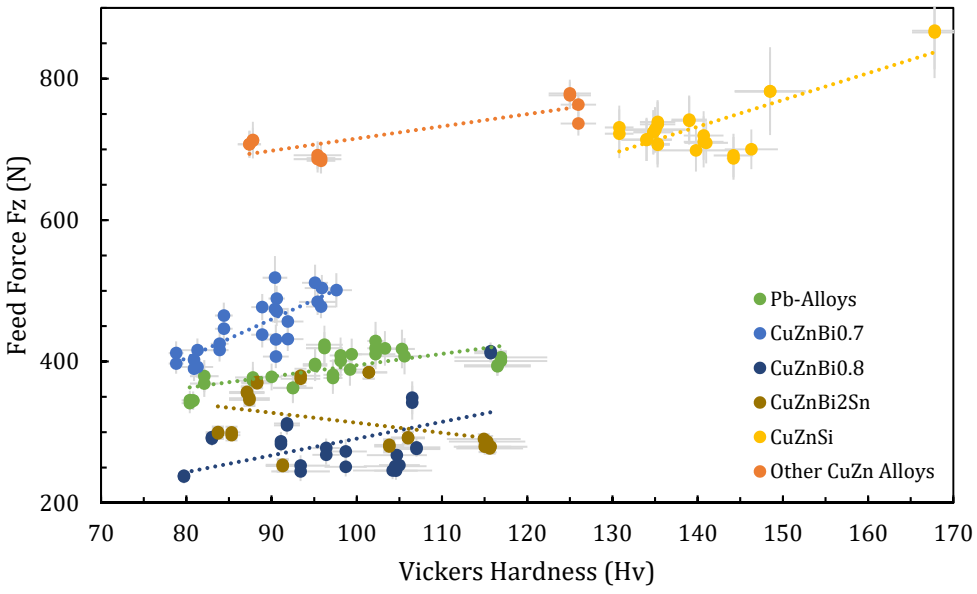


**Figure 7.22: The evolution of Feed Force ($F_Z$) with increasing Vickers hardness segregated by colour into key groups (Pb-Alloys, each of the individual Bi-Alloys, CuZnSi and other CuZn alloys).**

The results in Fig. 7.22 provide further confirmation that the workpiece hardness is linked somewhat closely with the feed forces with all except the CuZnBi2Sn alloy showing increasing trends for $F_Z$ with Hv. The plots do not fall on a master curve so other factors obviously also influence the feed force, but for a given alloy composition, an increase in hardness will increase the feed force. Changes to grain size, grain morphology, phase fraction, intermetallic formation, and new phase formation are all expected to influence the hardness and are therefore capable of affecting the machinability of the brasses tested in this study, particularly the $F_Z$.

In Fig. 7.23, the changes to $F_Z$ as a function of FCC α grain size and phase fraction are shown. These microstructural parameters are both directly related to the material hardness. It is shown in Section 7.2 that as the α grain size or α phase fraction increases, the hardness of the workpiece will decrease. It is important to compare these two microstructural characteristics simultaneously as they are often competing with each other at elevated temperatures, particularly for heat treatments in the range of 700-800°C where more β is stable and the kinetics of α grain growth are higher.

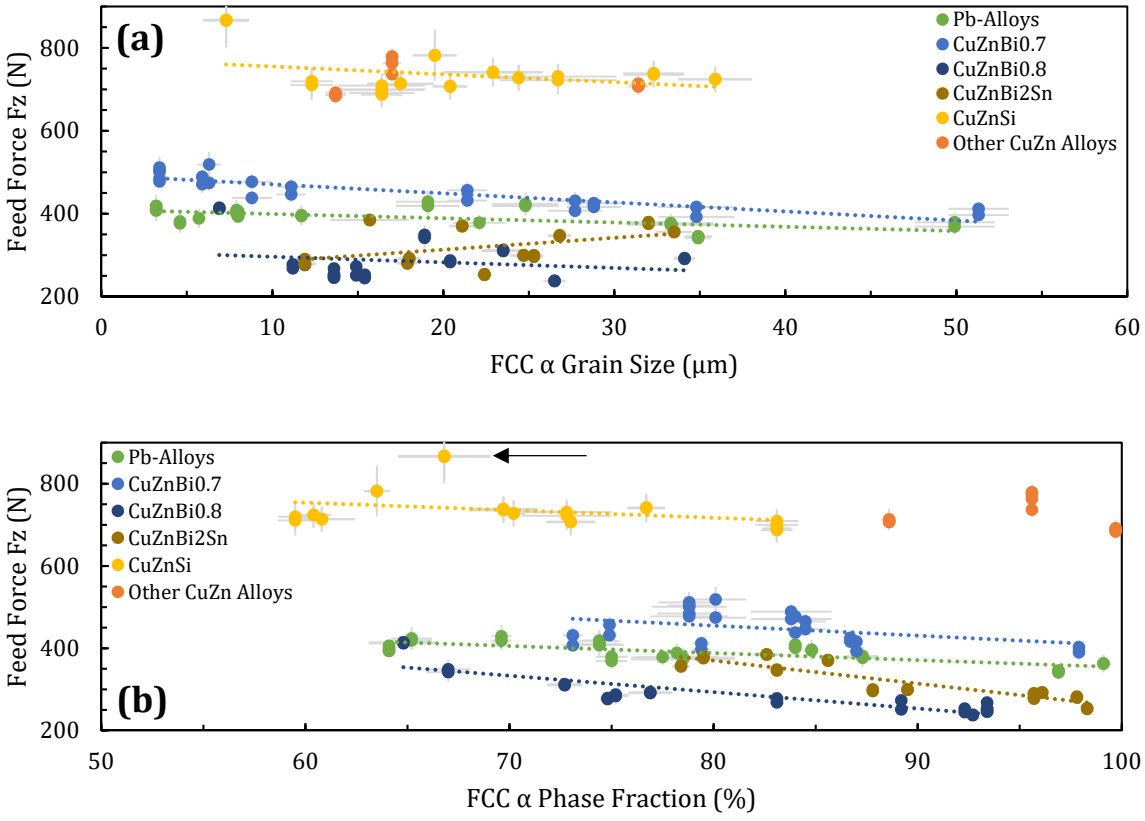


**Figure 7.23: The evolution of Feed Force ($F_Z$) with increasing FCC α (a) grain size and (b) phase fraction segregated by colour into key groups (Pb-Alloys, each of the individual Bi-Alloys, CuZnSi and other CuZn alloys).**

A general trend is observed for both sets of data in that the $F_Z$ will decrease as both the average FCC α grain size and phase fraction increase. In the most basic sense, this indicates that as the softer α phase forms in the microstructure or the grains of this phase grow and provide a reduced density of grain boundaries to dislocation motion, the microstructure becomes easier to penetrate and therefore the feed forces decrease. Whilst this may seem self-evident, this is the first time this connection has been shown between these microstructural parameters and the resulting $F_Z$ during drilling operations. Such systematic experiments, that couple microstructural characterization, drilling operations and mechanical property measurements are rare.

If we examine more closely the Pb-bearing alloys (Fig. 7.23a-b, highlighted in green), we observe that the downward trends for $F_Z$ are present for both increases in α grain size and phase fraction. Given that heat treatments of the continuously cast CuZn37Pb2 were completed using both air-cooling and water-quenching, this naturally produced some variation, particularly for those samples that were water-quenched. For example, heat treating at 800$^o$C produced a difference in $F_Z$ after 30 minutes from the as-received value of 413N to 374N after air-cooling and 421N after quenching. In both samples there was a significant increase in α grain size (by 46.7 and 21.6μm respectively), and in the quenched sample there was an additional increase in the phase fraction of the harder and more brittle BCC β' (by ~9.2%). As a direct result, the samples with an elevated β' phase fraction due to quenching tend to sit above the trend line in the plot for grain size which neutralises the full effect or trend due to increasing grain size, whilst the same neutralising effect can be found in the phase fraction plot where samples with a smaller grain size tend to sit above the trend line.

For the Bi-bearing alloys in Fig. 7.23 (CuZnBi0.7, CuZnBi0.8 and CuZnBi2Sn), similar trends were found to the Pb-bearing alloys with the exception of the extruded CuZnBi2Sn (highlighted brown). It was found that this alloy, which on average contained significantly more α phase compared with the other alloys, was far more heavily affected by the introduction of intermetallic particles (Fig. 7.8). These intermetallic particles form upon heat treatment between the growing α grains due to the significantly higher composition of Sn and Bi. As a result, we see a reduction in the bulk average hardness, however the particles significantly increase the overall cutting resistance of the alloy. In other words, if we compare the direct effects of which effect is stronger for dictating the $F_Z$ in these Bi-bearing alloys, α grain size or phase fraction, the phase fraction appears to be the first-order effect. This is also supported by the Pb-bearing alloys already discussed.

Finally, if we examine the evolution in $F_Z$ for the CuZnSi alloy, in spite of the alternate phases (HCP κ and complex cubic γ) present not being the BCC β', there is again a consistent decrease in $F_Z$ with increased average α grain size or phase fraction. The largest outlier observed in Fig. 7.23b (highlighted with a black arrow) is the water-quenched sample from 800°C in which both the smallest grain size (~7.3µm) and a low α phase fraction (~66.8%) work in tandem to produce a very high $F_Z$.

The correlations shown in Fig. 7.23 between the α grain size, phase fraction and resulting $F_Z$ values which directly translates to workpiece hardness, is an incredibly important tool for the industrial machinist to understand. Being able to have levers to manipulate the machinability of a duplex brass through means other than the inclusion of Pb is very important in an industrial setting.

### 7.4.2 Drilling Torque ($M_Z$)

In Section 7.3, the drilling torque for the 10 'as-received' duplex brasses was summarised, and some correlations sought. As shown in Fig. 7.17c-d, the workpiece hardness and UTS, whilst significant for their effects on the $F_Z$ of the alloys, was very weak or even negligible for their effect on the $M_Z$ values. In order to verify this, further data was collected from samples of the CuZn37Pb2, CuZnBi0.7, CuZnBi0.8, CuZnBi2Sn and CuZnSi alloys which were each additionally heat treated according to Table 7.2. The results are shown in Fig. 7.24.

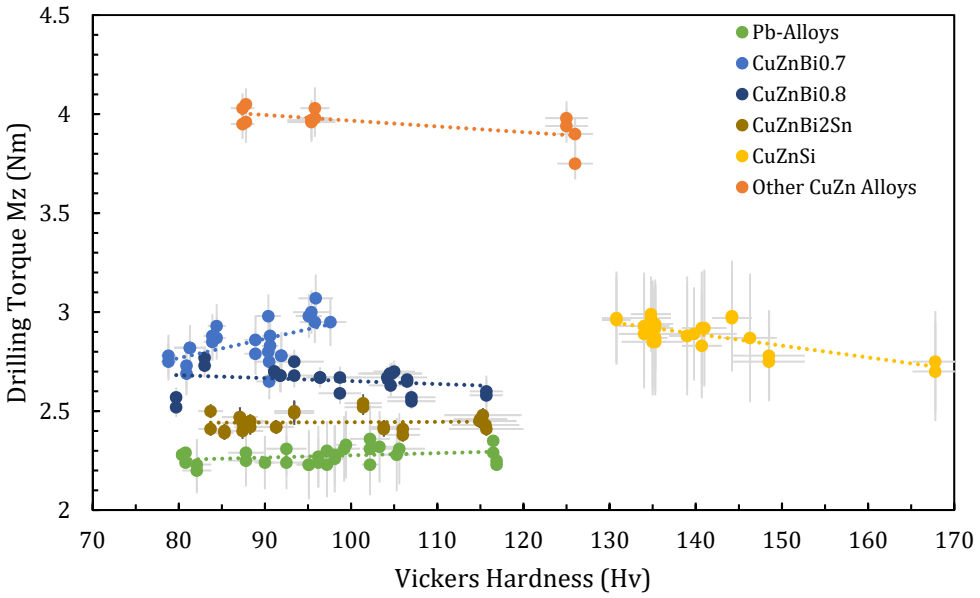


**Figure 7.24: The evolution of Drilling Torque ($M_Z$) with increasing Vickers hardness segregated by colour into key groups (Pb-Alloys, each of the individual Bi-Alloys, CuZnSi and other CuZn alloys).**

While some mild effects can be observed for the CuZnSi (decreasing) and CuZnBi0.7 (increasing) with increasing hardness, there are relatively minor effects with all of the other alloys exhibiting minimal change in $M_Z$ with Hv.

In addition to the data in Fig. 7.24, plots showing the evolution of $M_Z$ with the average α grain size and phase fraction are shown in Fig. 7.25. It is clear from the neutral trends in each alloy that these microstructural characteristics of the brass, with the exception perhaps of the presence of HCP κ in the CuZnSi microstructure, do not have significant effects on the average drilling torque. It is more likely that for the continuous cast alloys (CuZn37Pb2 and CuZnBi0.7), which both encounter mild reductions in $M_Z$ from elevated temperature heat treatments, the increasing Pb and/or Bi particle size is playing the primary role of reducing the $M_Z$ rather than any other microstructural contribution.

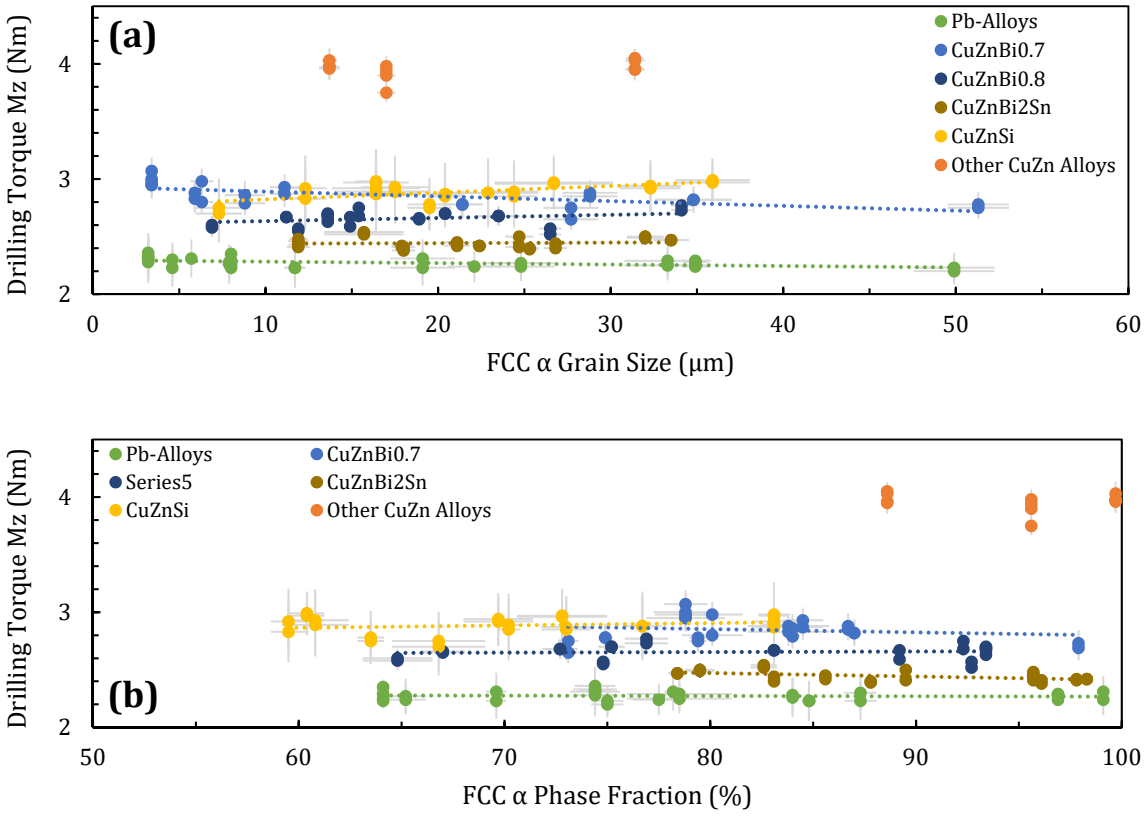


**Figure 7.25: The evolution of Drilling Torque ($M_Z$) with increasing FCC α (a) grain size and (b) phase fraction segregated by colour into key groups (Pb-Alloys, each of the individual Bi-Alloys, CuZnSi and other CuZn alloys).**

The key point in assessing the correlations between $M_Z$ and the base-material properties is to identify how strongly the wt. % of free-machining elements Pb and Bi affect the $M_Z$. In Section 7.3, the $M_z$ was most closely correlated with the elongation, and whilst full tensile behaviour as not been measured as a function of heat treatment condition for all the alloys considered in this section, the ductility is

strongly affected by stress-raising 2nd phase particles. All of the brasses trialled within this study contain some Pb, 3 of which are high Pb-brasses with greater than 2 wt. % each, whilst the remainder are classed as “low-Pb” alloys according to North American definitions with less than 0.25 wt. % [6]. Three of the alloys additionally contain varying levels of Bi from 0.66 to 1.95 wt. %.

In Fig. 7.26, the average $M_Z$ for each duplex brass is plotted as a function of compound composition, that is the Pb + Bi wt. %, with three distinct groupings found and coloured accordingly.

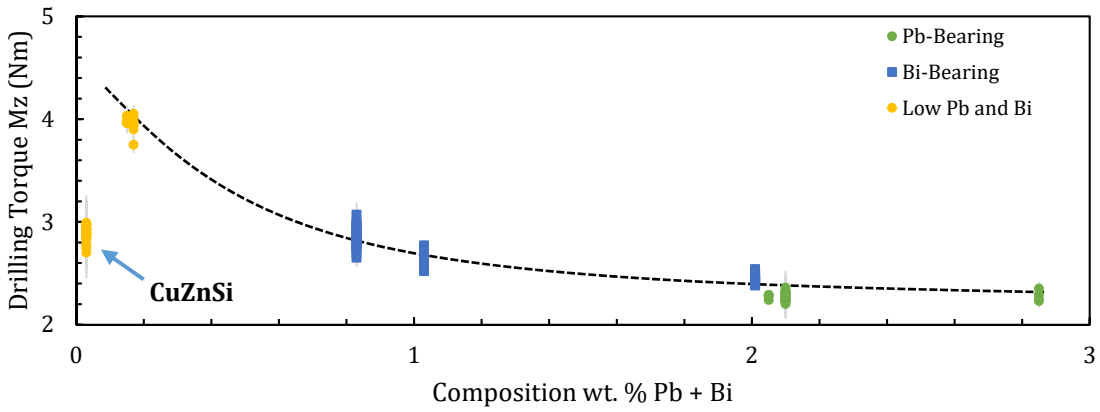


**Figure 7.26: Compound composition of Pb + Bi wt. % vs. the average drilling torque ($M_Z$) for all of the brasses tested in the machinability study.**

For the average $M_Z$ shown in Fig. 7.26, we observe a decrease in $M_Z$ as the Pb and Bi wt. % are increased and this would be expected based on industry knowledge and the general machinability index [1]. In addition, 3 key observations can be made: a) there is a greater advantage to the Pb-bearing alloys in this data set with all producing lower values (range of 2.2-2.4 Nm) than the Bi-bearing alloys, b) each of the alloys is producing a relatively tight tolerance range for $M_Z$ output indicating that the wt. % of elemental additions has a first-order effect on $M_Z$, c) the third observation is for the group of data points at 0.03 wt. % Pb + Bi which coincides with the CuZnSi alloy. Although this alloy contains no significant inclusion of Pb or Bi, its performance is comparatively very good for $M_Z$, far better than any of CuZn37, CuZnSn or CuZnAl, which is indicative of the influence of other intermetallic, stress-raising particles present in this alloy (HCP κ, BCC ε).

In Fig. 7.26 it is shown that with compositional inclusions of Pb and Bi, first-order changes to $M_Z$ can be obtained. However, the raw composition is not the only factor affecting these key outputs. One would anticipate that the effects of particle size and distribution in the microstructure may also affect the $M_Z$ (and perhaps $R_a$) values. In order to assess this, samples of each of the 10 duplex brasses tested using the drilling operations were analysed using SEM-BSE. This technique allows us to identify the Pb

and Bi particles present in the microstructure due to their different atomic weights and subsequently quantify their relative size and number per unit area. Table 7.4 summarises each of the samples assessed using SEM-BSE for both particle size (µm) and particle density (per $mm^2$). This is inclusive of all of the as-received samples in addition to 3 heat treated samples for CuZn37Pb2, CuZnBi0.7, CuZnBi0.8, CuZnBi2Sn and CuZnSi.

**Table 7.4: CuZn alloy samples submitted for BSE analysis and their resulting average particle size and density as measured using ImageJ analysis.**

| ALLOY DESIGNATION | HEAT TREATMENT CONDITION | AVERAGE PARTICLE SIZE (µm) | PARTICLE DENSITY (Particles/$mm^2$) |
|---|---|---|---|
| **CuZn39Pb3** | As Received | 1.2 ± 0.4 | 14,151 |
| **CuZn37Pb2** | As Received | 0.6 ± 0.1 | 50,621 |
| | 500°C, 120m, AC | 0.7 ± 0.1 | 45,582 |
| | 700°C, 120m, AC | 1.7 ± 0.3 | 9,511 |
| | 800°C, 30m, Q | 2.5 ± 0.3 | 8,167 |
| **CuZnPb2SnFe** | As Received | 2.3 ± 0.3 | 8,209 |
| **CuZnBi0.7** | As Received | 0.7 ± 0.2 | 11,338 |
| | 500°C, 120m, AC | 1.2 ± 0.3 | 7,790 |
| | 700°C, 120m, AC | 2.1 ± 0.3 | 4,493 |
| | 800°C, 30m, Q | 3.0 ± 0.5 | 2,666 |
| **CuZnBi0.8** | As Received | 1.3 ± 0.1 | 5,438 |
| | 500°C, 120m, AC | 2.9 ± 0.2 | 3,254 |
| | 700°C, 120m, AC | 3.1 ± 0.3 | 1,050 |
| | 800°C, 30m, Q | 3.6 ± 0.6 | 2,058 |
| **CuZnBi2Sn** | As Received | 4.4 ± 1.7 | 3,716 |
| | 500°C, 120m, AC | 6.2 ± 1.8 | 2,646 |
| | 700°C, 120m, AC | 12.1 ± 2.9 | 1,323 |
| | 800°C, 30m, Q | 9.1 ± 2.5 | 1,260 |
| **CuZnSi** | As Received | 0.7 ± 0.1 | 1,512 |
| | 500°C, 120m, AC | 0.8 ± 0.1 | 1,281 |
| | 700°C, 120m, AC | 0.9 ± 0.1 | 420 |
| | 800°C, 30m, Q | 0.6 ± 0.1 | 420 |
| **CuZn37** | As Received | 0.5 ± 0.1 | 1,743 |
| **CuZnSn** | As Received | 0.5 ± 0.1 | 2,352 |
| **CuZnAl** | As Received | 1.0 ± 0.1 | 1,659 |

The SEM-BSE images for each of the samples summarised in Table 7.4 are shown in Fig. 7.27 (CuZn39Pb3, CuZn37Pb2 and CuZnPb2SnFe), Fig. 7.28 (CuZnBi0.7 and CuZnBi0.8), Fig. 7.29 (CuZnBi2Sn), Fig. 7.30 (CuZnSi) and Fig. 7.31 (CuZn37, CuZnSn and CuZnAl).

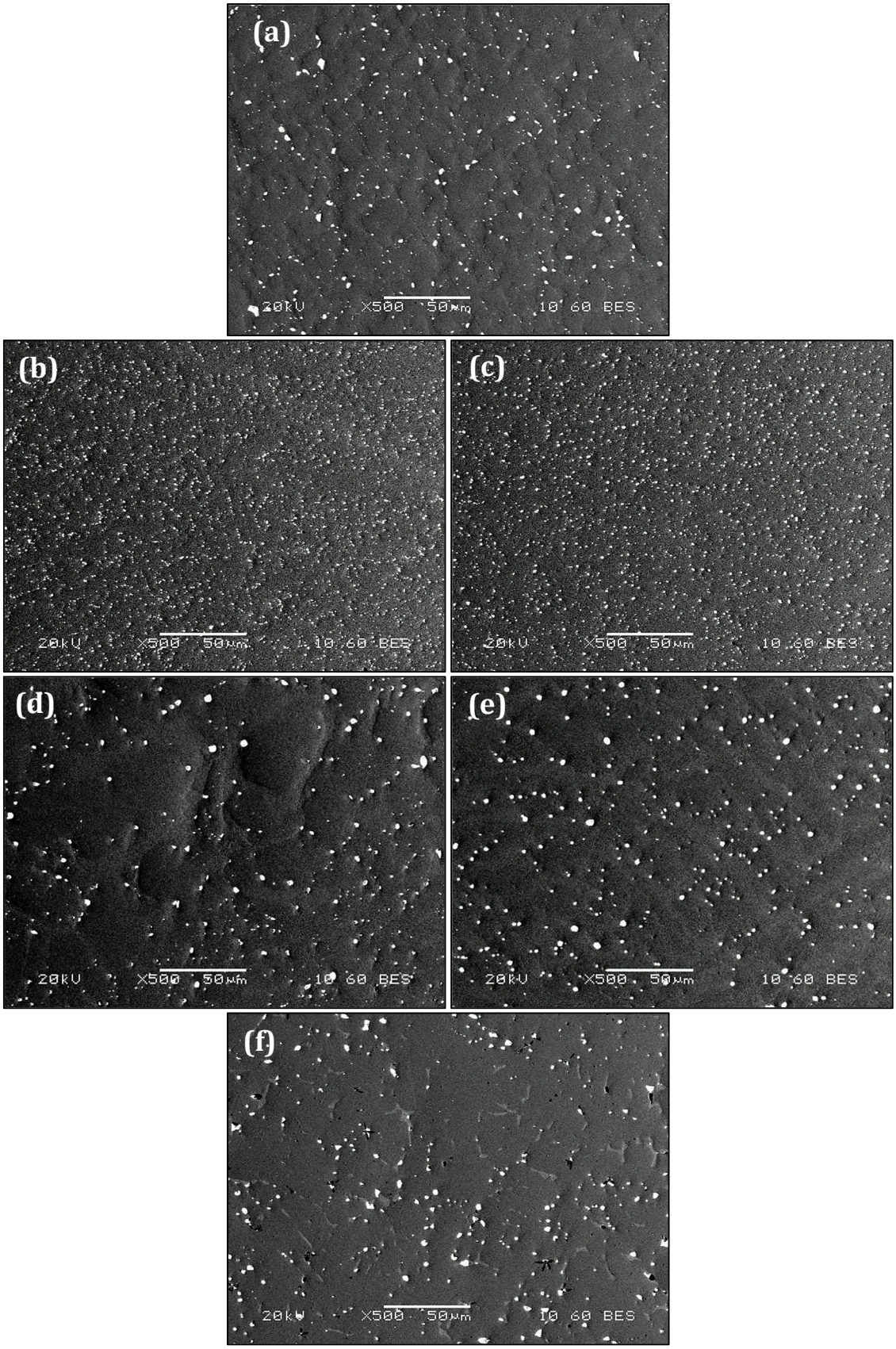


**Figure 7.27: BSE images (500x) of (a) CuZn39Pb3 as received, (b) CuZn37Pb2 as received, (c) after soaking at 500°C for 120 minutes and air-cooled, (d) after soaking at 700°C for 120 minutes and air-cooled, (e) after soaking at 800°C for 30 minutes and water quenching and (f) CuZnPb2SnFe as received.**

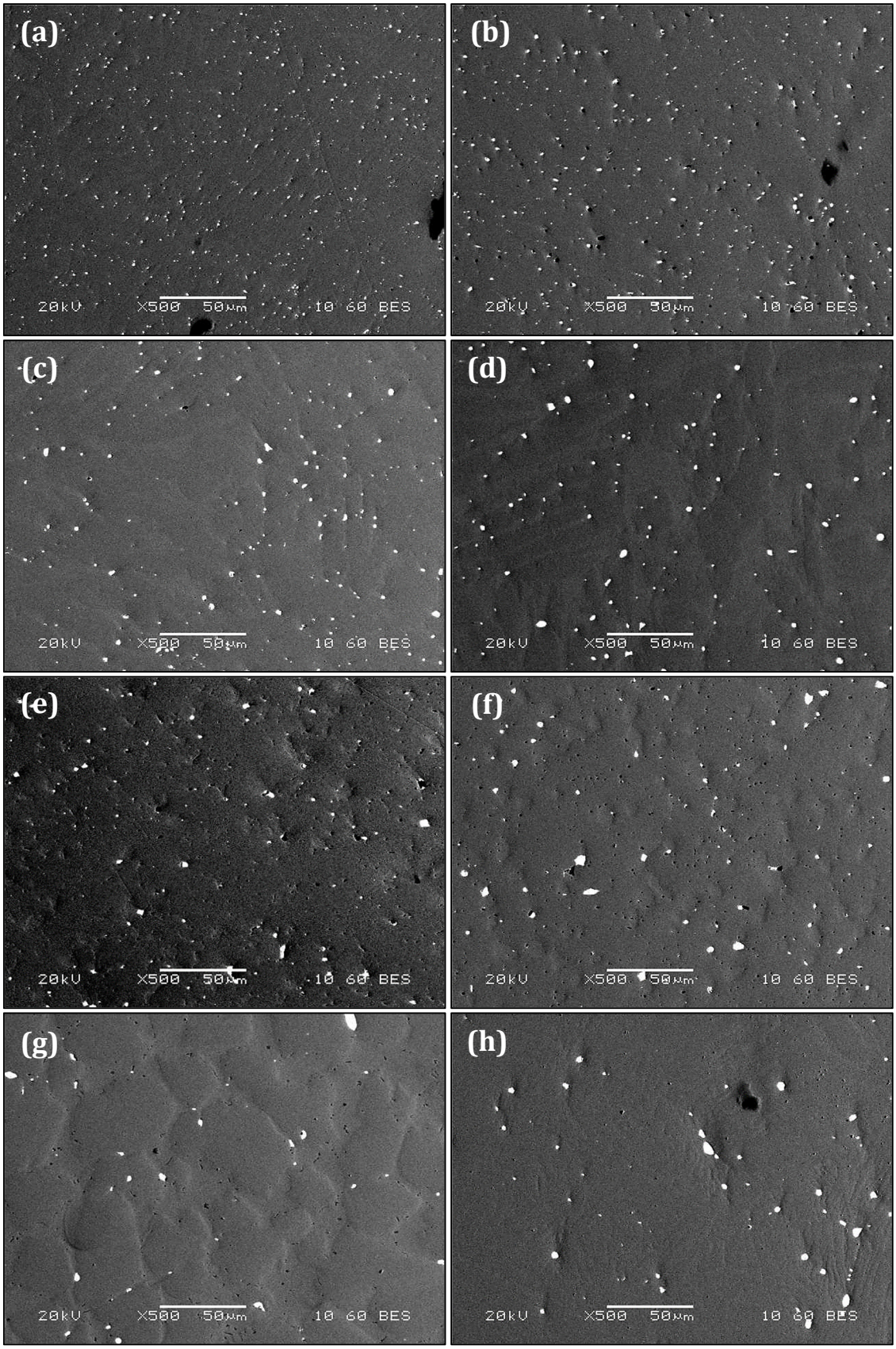


**Figure 7.28: BSE images (500x) of (a) CuZnBi0.7 as received, (b) after soaking at 500°C for 120 minutes and air-cooled, (c) after soaking at 700°C for 120 minutes and air-cooled, (d) after soaking at 800°C for 30 minutes and water quenching and (e-h) as for images a-d but with CuZnBi0.8.**

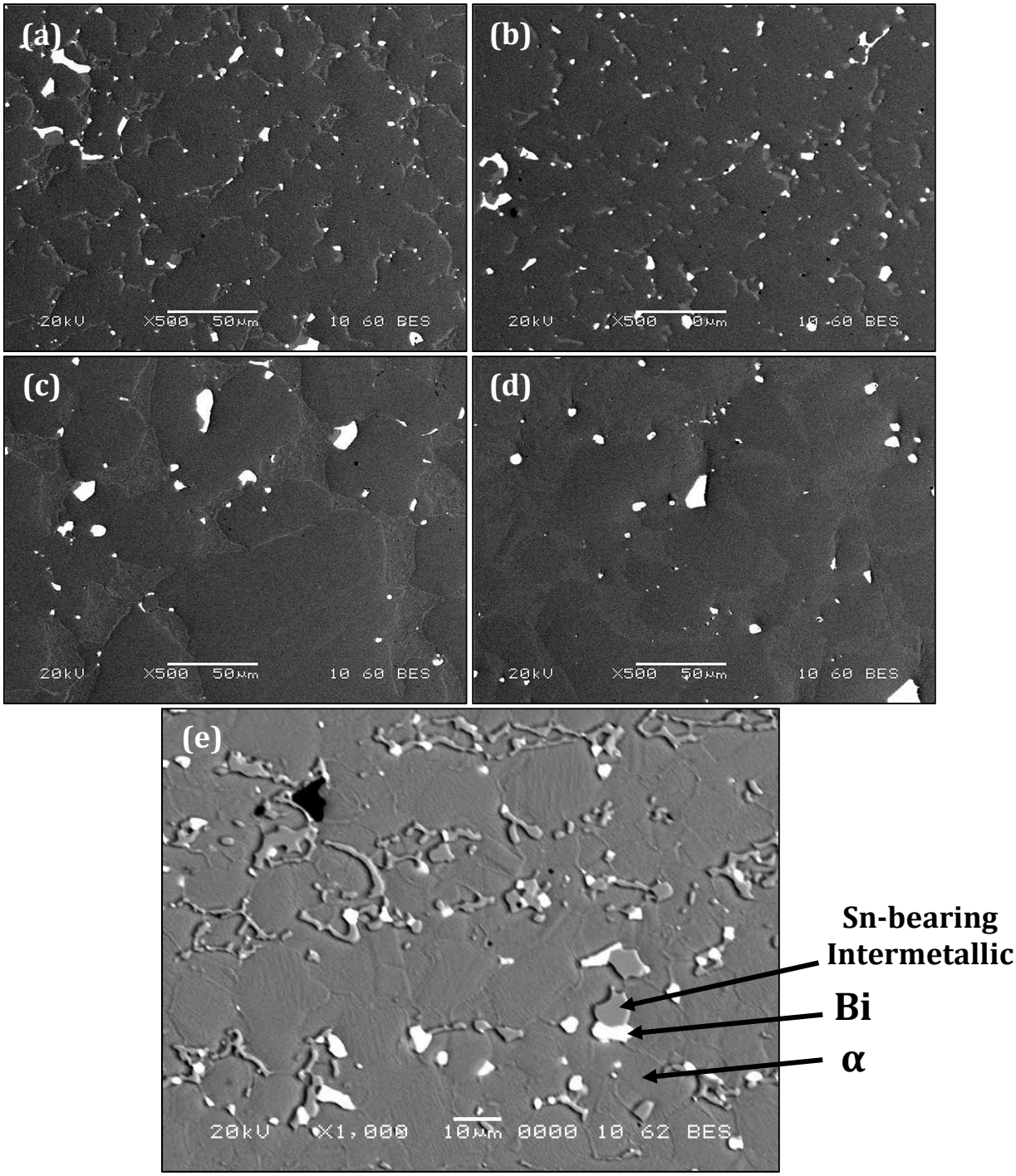


**Figure 7.29: BSE images (500x) of (a) CuZnBi2Sn as received, (b) after soaking at 500°C for 120 minutes and air-cooled, (c) after soaking at 700°C for 120 minutes and air-cooled, (d) after soaking at 800°C for 30 minutes and water quenching and (e) magnified view of as received sample to show Sn-bearing intermetallics.**

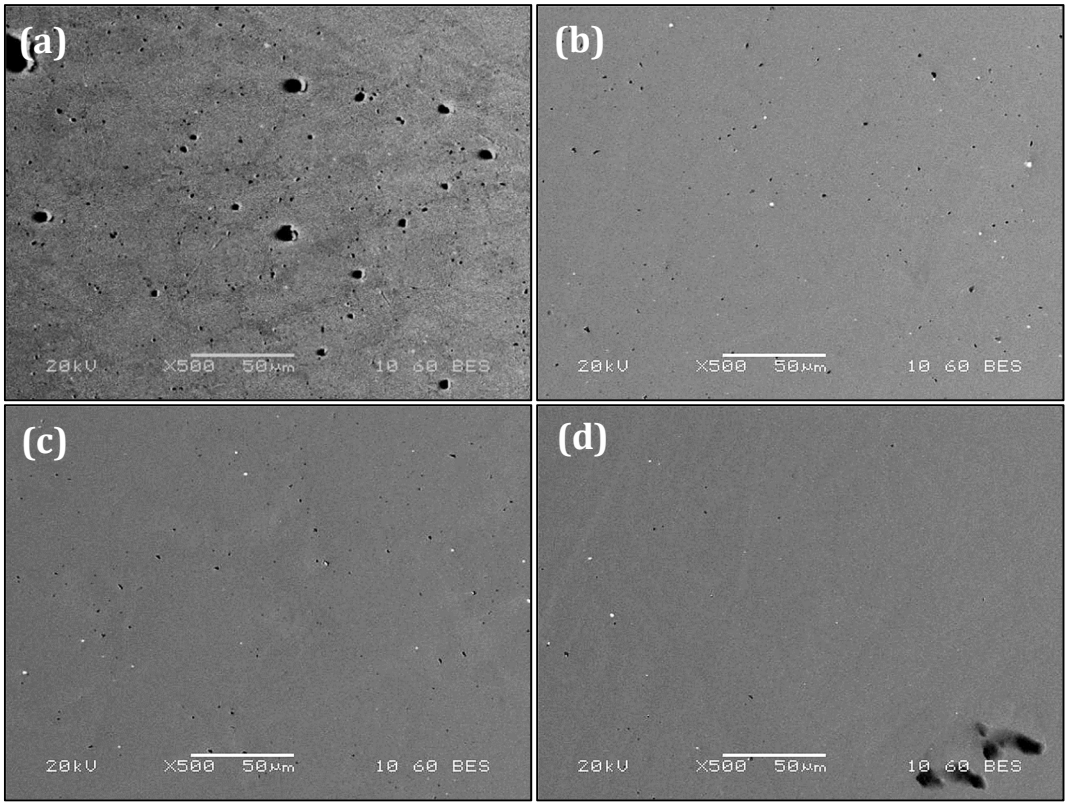


**Figure 7.30: BSE images (500x) of (a) CuZnSi as received, (b) after soaking at 500°C for 120 minutes and air-cooled, (c) after soaking at 700°C for 120 minutes and air-cooled, (d) after soaking at 800°C for 30 minutes and water quenching.**

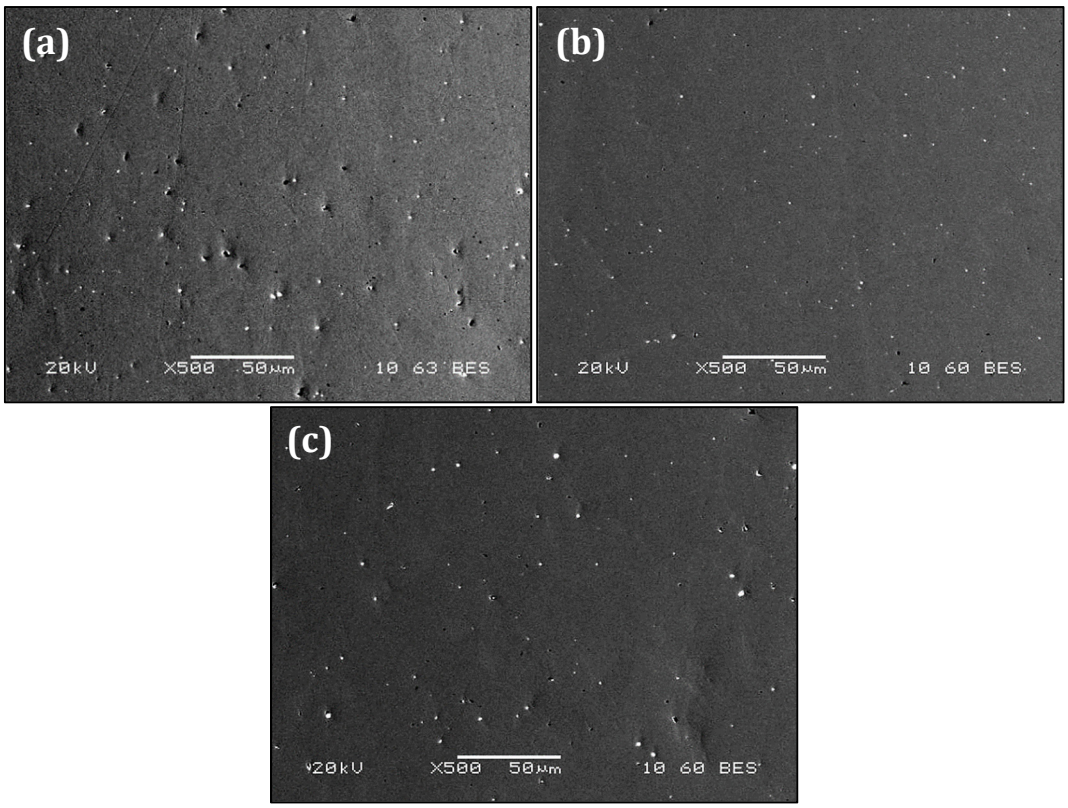


**Figure 7.31: BSE images (500x) of (a) CuZn37 as received, (b) CuZnSn as received and (c) CuZnAl as received.**

Of the three Pb-bearing alloys examined in the as-received state, CuZn39Pb3, CuZn37Pb2 and CuZnPb2SnFe, the continuous cast CuZn37Pb2 (Fig. 7.27b) has both the smallest particle size (~0.6µm) and largest number of particles per unit area (>50,000/mm$^2$). This is due to the fabrication process of continuous casting in which there is no secondary high temperature processing step (as with extrusion) to allow the Pb particles to melt and begin coalescing together. The same observation is made for the Bi-bearings alloys in which the continuous cast CuZnBi0.7 alloy (Fig. 7.28a) records the lowest particle size (0.65µm) and highest number of particles (>11,000/mm$^2$) in spite of having less than half of the wt. % Bi compared with the extruded CuZnBi2Sn alloy (Fig. 7.29a). It might be argued that the extruded alloys CuZnSi, CuZn37, CuZnAl and CuZnSn (Fig. 7.30-7.31) also have a very small particle size in spite of their extruded fabrication mode, however the low wt. % of Pb or Bi prevents any significantly large particles from forming within the microstructure in spite of the multiple elevated temperature processing steps during fabrication.

The most readily observable change in particle size and distribution with heat treatment in the CuZn37Pb2, CuZnBi0.7, CuZnBi0.8, CuZnBi2Sn and CuZnSi alloys is a general increase in Pb and Bi particle size and an associated decrease in the number of particles present in the microstructure with increasing soak temperature. Given that these elements are liquid above 327$^o$C and 271$^o$C respectively, the particles will tend to coalesce at the elevated temperatures used in this study. The only exceptions are for CuZnBi2Sn (Fig. 7.29d) and CuZnSi (Fig. 7.30d) after quenching from 800$^o$C after 30 minutes vs. air-cooling after 120 minutes at 700$^o$C. The increased soak time at 700$^o$C and slower cooling rate has allowed the particles to grow larger in both of these cases by 34% and 50% respectively.

By far, the largest particle sizes are recorded for the extruded CuZnBi2Sn alloy (Fig. 7.29) ranging between 4.4µm to 12.2µm in size. Not only are large Bi particles exhibited and shown to increase in size with increasing temperature and soak time, there are additional areas between the FCC α grain boundaries which are observed to have Sn-bearing intermetallics. These are observed as narrow areas of darker colour than the Bi-particles, but brighter than the surrounding matrix due to their atomic weight between that of Cu/Zn and Bi (magnified view in Fig. 7.29e). This phenomenon is also observed in the next highest Sn-bearing alloy CuZnPb2SnFe (Fig. 7.27f).

The alloys CuZnSi, CuZn37, CuZnAl and CuZnSn (Figs. 7.30-7.31), each have very little occurring by way of changes to particle size and distribution due to their low chemical composition of the key elements Pb and Bi. Little else is observed in their SEM-BSE images of note with the exception of some porosity in the as-received CuZnSi sample (Fig. 7.30a).

In Fig. 7.32, we show the evolution of $M_Z$ as a function of the number of Pb and Bi particles present in the microstructure per $mm^2$ and the corresponding average particle size (in µm). It is important to understand if any trends are present in order to determine if the wt. % inclusion of free-machining elements Pb and Bi (ie. volume fraction of particles) is the first order effect on drilling torque, or if the particle size and distribution is also a significant factor. The continuously cast CuZn37Pb2 appears to show negligible change with increasing particle density and in this case only a minor decrease in $M_Z$ with increasing particle size. Particle size is found to have some effect in the Bi-bearing alloys, particularly CuZnBi0.7 and CuZnBi0.8 in which both show significant downward trends for $M_Z$ with size. This is the most obvious for the continuous cast alloy CuZnBi0.7 for particle sizes in excess of 0.65µm.

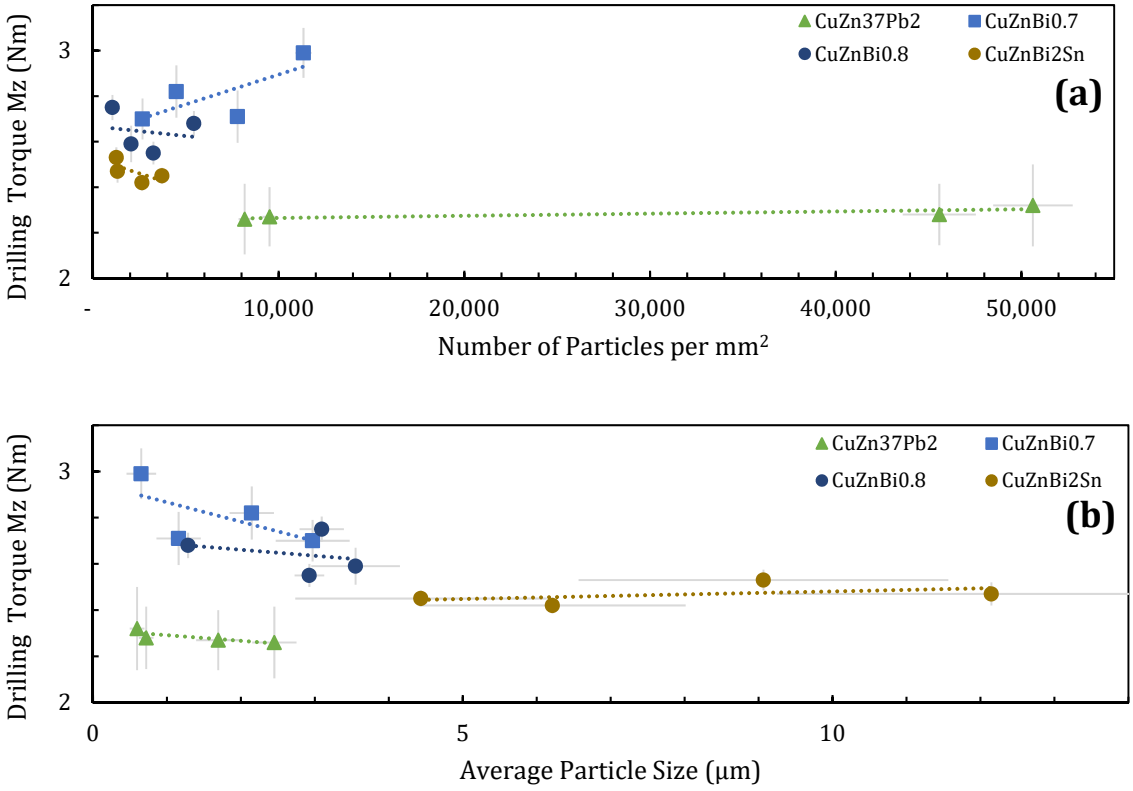


**Figure 7.32: The evolution of drilling torque ($M_Z$) with increasing (a) Pb + Bi particle density and (b) average particle size segregated into the 4 heat-treated alloys (CuZn37Pb2, CuZnBi0.7, CuZnBi0.8, CuZnBi2Sn).**

Overall, although the effects of particle size on drilling torque shown in Fig. 7.32 are weak by comparison to the first order effect of wt. % Pb and Bi and to a lesser extent, the ductility as shown in Fig. 7.18. However, the effect of particle size and distribution is shown to have some effect on the surface roughness, Section 7.4.3.

### 7.4.3 Surface Roughness ($R_a$)

It was observed in Fig. 7.20 that the Vickers hardness of brass workpiece may have an underlying effect on the surface roughness of the machined component. In order to examine this in greater detail, data was collected from samples of the CuZn37Pb2, CuZnBi0.7, CuZnBi0.8, CuZnBi2Sn and CuZnSi alloys which were each heat treated according to Table 7.2. The results are shown in Fig. 7.33.

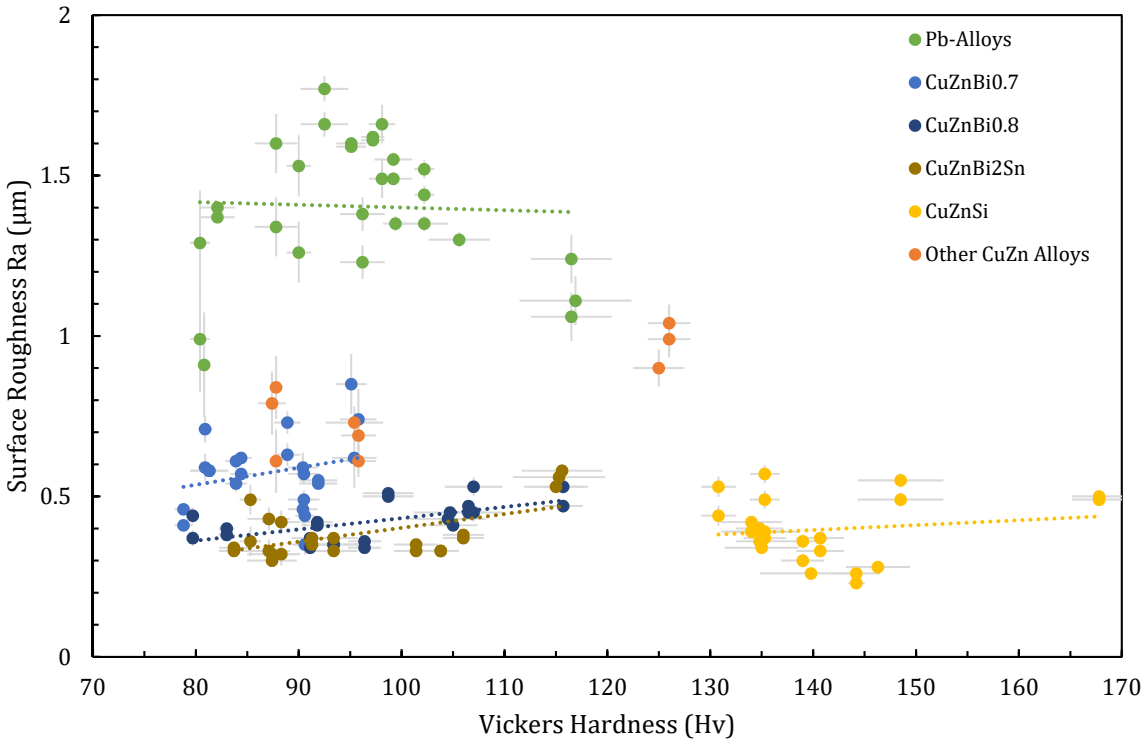


**Figure 7.33: The evolution of Surface Roughness ($R_a$) with increasing Vickers hardness segregated by colour into key groups (Pb-Alloys, each of the individual Bi-Alloys, CuZnSi and other CuZn alloys).**

Whilst the surface roughness of the CuZnSi brass (highlighted yellow Fig. 7.33) is very low, this is more likely due to the presence of other secondary phases, in particular the ε and κ phases. Other brasses, which much lower hardness, also exhibit similarly low roughness (e.g. CuZnBi2Sn and CuZnBi0.8) Most of the alloys tested in this study show negligible trends for $R_a$ with Hv.

The evolution of the surface roughness ($R_a$) as a function of average FCC α grain size and phase fraction are shown in Fig. 7.37. In this case there are again observed only weak trends with the $R_a$ decreasing mildly as the average α grain size increases and for the continuously cast samples as the α phase fraction decreases or for CuZnSi as the α phase fraction increases.

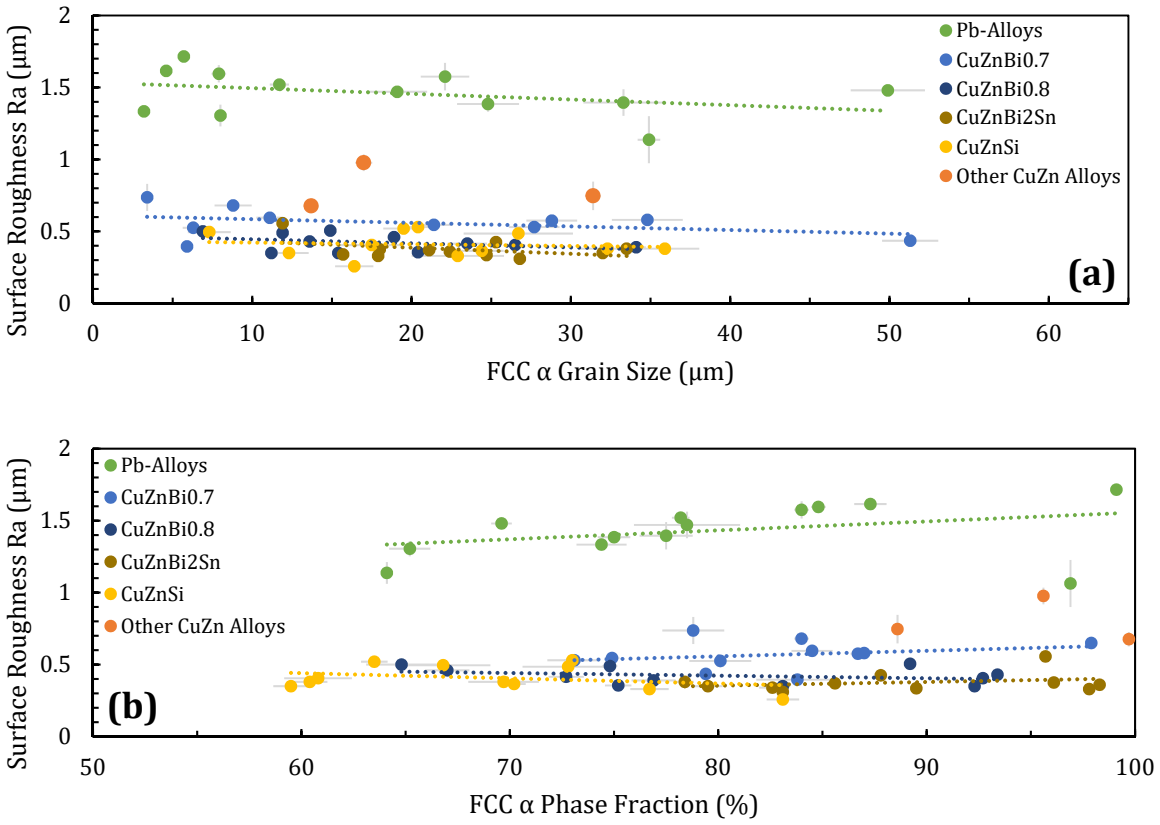


**Figure 7.34: The evolution of Surface Roughness ($R_a$) with increasing FCC α (a) grain size and (b) phase fraction segregated by colour into key groups (Pb-Alloys, each of the individual Bi-Alloys, CuZnSi and other CuZn alloys).**

It was noted that for the CuZnSi alloy a slight increase in $R_a$ was discovered with elevated temperature heat treatments starting at 600°C and differentiating depending on the cooling rate. This also happened to coincide with the presence, or lack thereof of BCC ε (Fig. 7.35) and this is supported somewhat by the downward trend in $R_a$ for increasing α phase fraction.

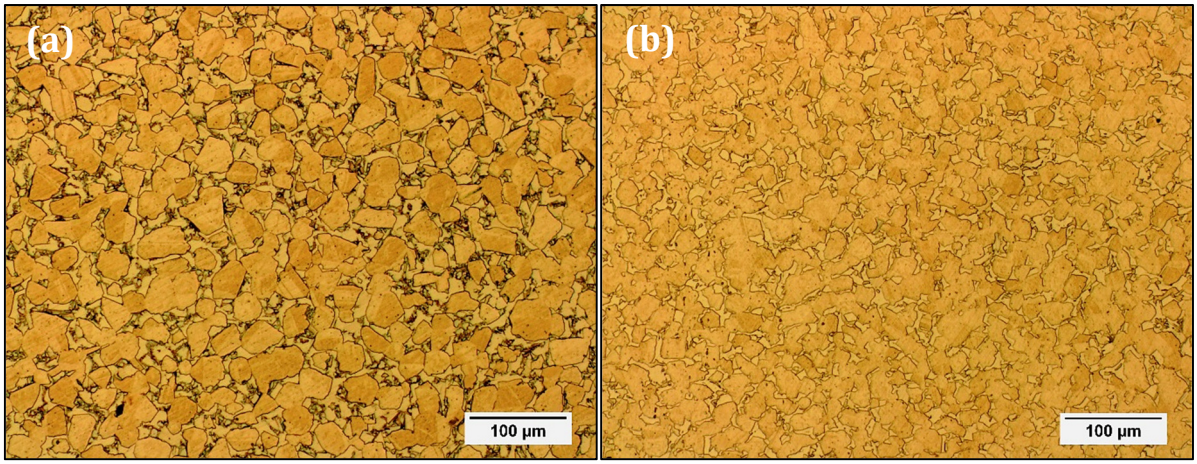


**Figure 7.24: CuZnSi microstructures for the (a) air-cooled and (b) quenched state after soaking at 600°C for 30 minutes. The BCC ε forms at lower temperatures upon air-cooling but does not have adequate time to form during quenching.**

The $R_a$ for each of the 10 duplex brasses is shown as a function of Pb + Bi wt. % in Fig. 7.36. Interestingly it is the high Pb-bearing alloys with greater than 2 wt. % which produce the highest (and least desirable) $R_a$ output. Between the alloys with minimal inclusions (with the exception of CuZnSi) and those which include Bi particles there is a slight decrease in $R_a$ with increasing wt. %, with particularly good values for the CuZnBi2Sn alloy, but this is relatively mild. Whilst the CuZnSi alloy produced very good $M_Z$ readings and might be assumed to follow the Pb-bearing alloys with a poor $R_a$, it actually produces the lowest overall $R_a$ measurements for the study in the range of 0.23-0.57µm. In all cases there is a relatively wide range of output $R_a$ values for individual composition points, indicating the presence of Pb and Bi in the composition certainly affects the $R_a$, however the raw composition is not the only factor which determines the final measure. For example, CuZn37Pb2 produces a very wide $R_a$ range of 1.23-1.77µm with the highest value occurring after one of the longest heat treatments (500°C for 120 minutes). The next step is to identify how changes to the Pb and Bi particles within the microstructure (density and size) affect the $R_a$ values.

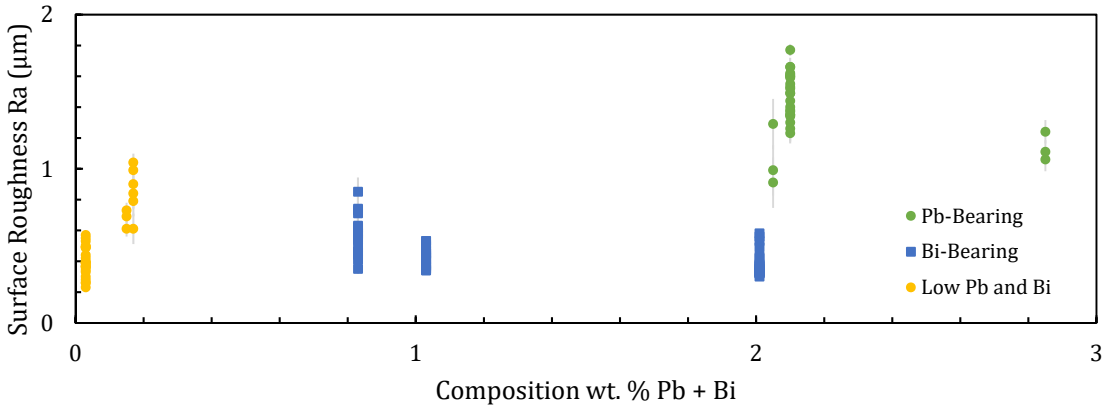


**Figure 7.36: Compound composition of Pb + Bi wt. % vs. the average surface roughness ($R_a$) for all of the brasses tested in the machinability study.**

Fig. 7.37 shows the evolution of $R_a$ as a function of the number of Pb and Bi particles present within the microstructure per $mm^2$ and the corresponding average particle size (in µm) using the SEM-BSE data in Table 7.3. While the continuous cast CuZn37Pb2 clearly shows the worst performance of each of the 4 heat treated brasses, there is a very clear trend that with increasing the number of particles and similarly decreasing the average particle size, the $R_a$ increases. This is indicative of the drilling operation progressively fracturing the particles in the brass matrix, leaving behind a comparatively rough surface. The higher the particle density, the higher percentage chance of the drill cutting edge hitting the particle and in turn the greater the surface area of a rougher surface at the end of the machining operation. The comparative performance of the Pb-particles against Bi indicates a different mode of particle fracture.

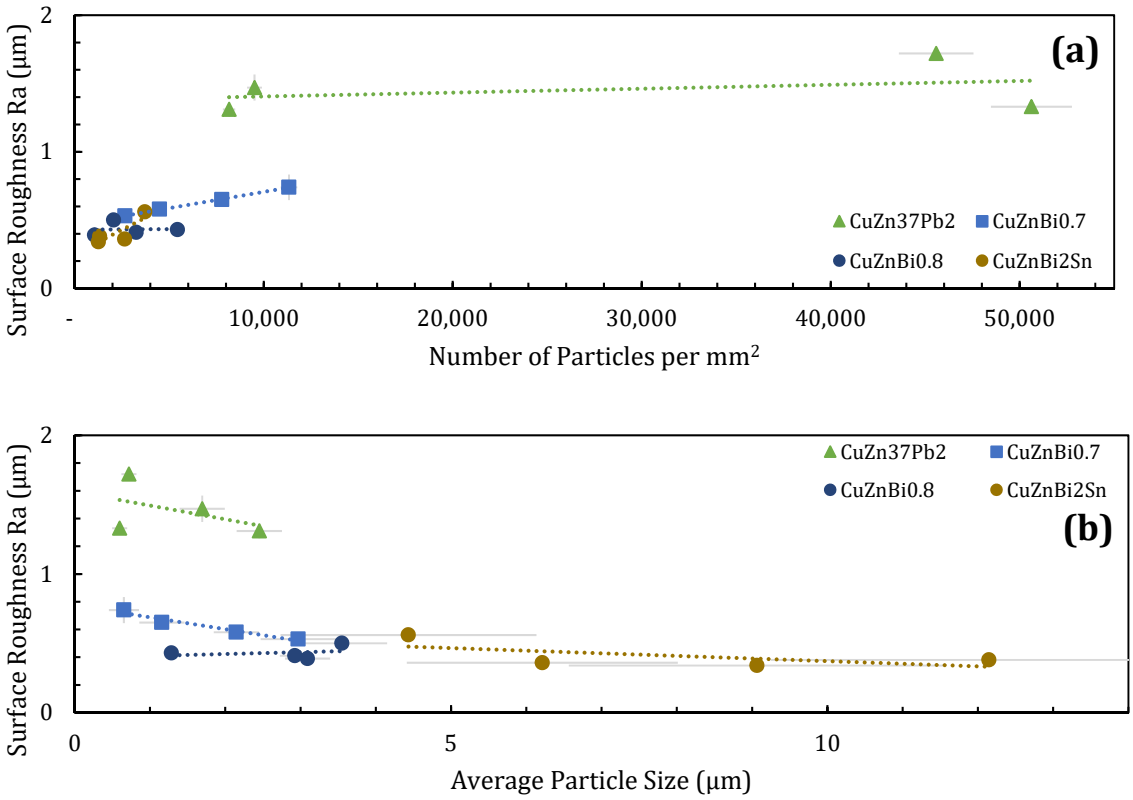


**Figure 7.37: The evolution of drilling surface roughness ($R_a$) with increasing (a) Pb + Bi particle density and (b) average particle size segregated into the 5 heat-treated alloys (CuZn37Pb2, CuZnBi0.7, CuZnBi0.8, CuZnBi2Sn).**

A focus for this thesis has been on the effects of microstructure on the processing of brass. This includes effects on elevated temperature plasticity, dezincification behaviour and machinability. Studies of machinability are usually part of the field of manufacturing engineering and whilst there are some limited examples of collaborations with Materials Science, the overwhelming majority do not link with the microstructure. Similarly, there are a range of effects at modelling the machining process. These tend to fall in one of two categories: studies using Finite Element models to example the paths of material flow during large strain deformation, or empirical models such as Neural Networks trying to find relationships between machining and compositions to help guide the choice of machining parameters. In neither case, is microstructure, or its effect on the elasto-plastic, and damage, properties of a brass considered. This Chapter is designed to start that investigation and to understand the first order effects of microstructure and properties on the machinability in a systematic and well controlled way.

Of the three machining parameters monitored ($F_Z$, $M_Z$ and $R_a$), first order effects can be identified.

- The $F_Z$ is shown to be predominantly influenced by mechanical properties such as workpiece hardness and UTS.
- The $M_Z$ is primarily affected by the compositional wt. % of Pb, Bi or Si (which corresponds with the volume fraction of stress-raising 2$^{nd}$ phase particles), with second-order effects of ductility (although these are of course connected).
- The surface roughness ($R_a$) is shown to be the most heavily affected by Pb or Bi particle density and associated particle size.

Understanding these first order effects for each of these machinability outputs is of high significance to the industrial machinist.

## 7.5 Summary and Conclusions

In this Chapter, a comprehensive study of the machinability of 10 duplex brasses (Pb-, Bi-, Si-bearing and alternative Sn-, Al-bearing and binary), both as-received and in a range of heat-treated conditions, has been undertaken through the use of a series of drilling operations. These experiments have occurred in 3 stages:

1. Identification of the room-temperature mechanical properties of each duplex brass using tensile testing and Vickers hardness, in addition to the evolution of Vickers and microstructural parameters (α grain size and phase fraction) in a range of heat-treated conditions (Table 7.2).

2. Correlations between the identified properties in point 1 and the machining outputs $F_Z$, $M_Z$, $R_a$ and swarf morphology for the 'as-received' alloy samples using a series of drilling operations.
    a. Feed force ($F_Z$): Whilst the Pb- and Bi-bearing brasses were found to produce the lowest average $F_Z$ values, this was found to be strongly dependent on both the workpiece hardness (closely associated with cutting resistance) and the UTS (as it relates to both the ductility and strain-hardening capacity).
    b. Drilling torque ($M_Z$): The Pb-bearing alloys produced the lowest output $M_Z$ values, closely related to the inclusion of fine Pb particles, however the Si-bearing alloy also performed significantly better relative to the alternative Sn-, Al- and binary alloys. This is likely due to the presence of fine secondary phases such as HCP κ and BCC ε. A relatively close correlation was observed between the ductility and $M_Z$ output across the 10 alloys associated with adherence to the cutting tool.
    c. Surface roughness ($R_a$): Unlike the results found for the $F_Z$ and $M_Z$ outputs, the Pb-bearing alloys produced the worst $R_a$ followed by the Bi-bearing alloys. This is closely related to the particle density of the alloys. Given the very good $R_a$ value produced by the Si-bearing brass, there is some indication that workpiece hardness may also assist in reducing $R_a$.
    d. Swarf morphology: Unsurprisingly, the alloys containing 'free-machining' alloying inclusions Pb and Bi in the composition also tended to produce the finest swarf morphology. The Si-bearing alloy was also able to produce a finer swarf morphology through the presence of alternative phases (κ, ε) which help to break up the chips.

3. Further verification of the correlations identified in point 2 using a wider range of heat-treated duplex brass samples.
    a. Feed force ($F_Z$): The workpiece hardness was shown to be a key factor in determining the forces required to plunge the drill into the alloy. This is heavily determined by both the α grain size (a smaller grain size produces a harder material) and the phase fraction of FCC α (softer) and ordered BCC β (harder). The only exception was the extruded CuZnBi2Sn alloy which was more significantly influenced by the presence of intermetallic particles associated with the high Sn in the composition produced only after certain heat treatments.
    b. Drilling torque ($M_Z$): Workpiece hardness and the associated microstructural parameters α grain size and phase fraction were shown to have little effect on the drilling torque. A clear correlation was found between the $M_Z$ and the alloying additions of Pb and Bi by wt. %. The exception in this regard was the extruded CuZnSi alloy which consistently produced a much smaller $M_Z$ across a range of heat treatments due to the presence of secondary phases which act in a similar manner to Pb and Bi. BSE-SEM images were collected for each alloy and the particle size and distributions summarised. Generally speaking, there was some indication that a larger particle size (particularly for the continuously cast CuZnBi0.7) may reduce the $M_Z$ values, however this was a second-order effect relative to the wt. % in the composition.
    c. Surface roughness ($R_a$): A correlation was observed for the as-received alloys that an increased hardness may assist to reduce the surface roughness of a duplex brass workpiece. The data collected from the heat-treated samples shows minimal change with this material property and the associated α grain size and phase fraction. For the extruded CuZnSi this has been shown to be more heavily associated with the presence, or lack thereof, of the cubic ε phase which only forms under certain cooling conditions (typically air-cooling from elevated temperatures). It was very clearly shown from the SEM-BSE data that as the particle density (of Pb and Bi) increases, and as the particle size decreases, the surface roughness deteriorates. This is the first time this conclusion has been identified.

# 8 Conclusions and Future Work

## 8.1 Conclusions

In this thesis, a variety of the metallurgical issues associated with the recent global movement from leaded to lead-free duplex brass have been studied, including variations to phase equilibria with alloying additions, assessment of the hot workability and machinability of several market-available lead-free duplex brasses, and an in-depth look at the microstructural mechanisms that influence the most common form of corrosion in duplex brasses in potable water environments; dezincification.

The primary conclusions in this work may be summarised as follows:

1. The phase equilibria of 3 families of duplex brass; Pb-bearing(+Sn), Bi-bearing (+Sn) and Si-bearing, were studied using a combination of thermodynamic descriptions according to CALPHAD and using experimental methods including XRD and high intensity *in-situ* Neutron diffraction. Sn and Si were found to exhibit the strongest effects on the CuZn phase equilibria, with Sn bending the (α+β) phase field towards the Cu-rich end at elevated temperatures. This has important implications to the otherwise steep nature of the α/(α+β) phase-field boundary and allow the forging operator more margin for area in hot working operations. The Si had a much stronger effect on the phase equilibria of CuZn, sharply stabilising β and additionally stabilising several other phases including HCP κ and cubic ε. High intensity *in-situ* Neutron diffraction was used effectively to quantify the elevated temperature equilibrium phase fractions of FCC α and BCC β in a Pb-bearing and Bi-bearing duplex brass. The experimental data agreed well with the CALPHAD calculations (in the industrially relevant temperature zone of 650-800$^{o}$C) and thus these thermodynamic descriptions would be used for the further Chapters in this thesis. Further room temperature XRD characterisation of the CuZn22Si3 was undertaken after several heat treatments and after intermediate heat treatment (300-500$^{o}$C) 4 phases were identified; FCC α, HCP κ, cubic ε and rhombohedral η. After elevated heat treatments (600-700$^{o}$C) only 3 phases were identified; FCC α, HCP κ, and rhombohedral η. The water quenching from elevated temperatures is expected to have limited Si migration away from the η to form ε and the κ to stabilise further α.
2. The elevated temperature plasticity of 11 duplex brasses was evaluated using uniaxial hot compression at a range of temperatures (550-800$^{o}$C) and average strain rates (0.35-0.85$s^{-1}$). From the true stress-strain curves it was found that the flow stress behaviour was heavily

dependent on the phase fraction of disordered BCC β, and this was particularly important for the alloys containing β stabilisers Al and Si. The Si-bearing alloy produced particularly high flow stresses below 650°C in which other phases (HCP κ) begin to form. Evaluation for cracking of the hot compressed surfaces post-compression readily demonstrated that extruded alloys have a greater resistance to fracture than those fabricated via continuous casting. Additionally, those containing significant levels of insoluble bismuth or impurities sufficient to form intermetallic particles had a greater susceptibility to fracture. Using alloying additions such as Sn and Si decrease the steepness of the α\(α+β) phase boundary and as such afford a forging operator greater margin for error (temperature range) for hot working. The combined evaluation of the fracture data and flow stress behaviour was used to produce a forgeability index in which the extruded CuZnBi0.8 was found to have the highest rating (95) for a Pb-Free duplex brass. Constitutive analysis was used to create a semi-empirical model to describe the steady-state flow stress of each alloy by relating the Zener-Hollomon parameter to flow stress for both the constituent α and β phases. The rule of mixtures was an effective tool for predicting steady-state stress in duplex brasses. A re-assessed activation energy (Q) value of 147.2kJ/mol was used for the FCC α phase.

3. Dezincification resistance of duplex brass is a very important consideration for plumbing components. Whilst dezincification is empirically understood in terms of chemical inhibitors and heat treating to minimise β’ phase fraction, there was a significant knowledge gap in connecting key microstructural factors such as α grain size and morphology to the resulting dezincification resistance of a standard low-Pb duplex brass. A series of dezincification experiments was undertaken on two Bi-bearing duplex brasses which were heat treated in such a way as to manipulate the β’ phase fraction, α grain size and α aspect ratio. This was completed on an (a) alloy fabricated via continuous casting, (b) the same alloy after uniaxial hot compression to mimic the hot forging process and (c) another similar alloy fabricated via extrusion. As anticipated, the β’ phase fraction played a significant role in controlling the dezincification resistance of the continuous cast alloy, however the α grain size was also found to have a large impact, in some cases more strongly than for the phase fraction of β’. For the same alloy post-hot compression, the β’ phase fraction had a similar effect on the dezincification resistance, but this was not as consistent and was highly dependent on the final α grain aspect ratio which has been further explained through the use of percolation simulations. Finally, for the extruded Bi-bearing duplex brass, much weaker trends were found for β’ phase fraction and α grain size, however upon further testing the elevated resistance to dezincification was shown to be a short-term effect only and tied heavily to the cooling rate

post elevated heat treatment. Fast cooling through water quenching can increase the short-term dezincification resistance of duplex brasses through the formation of small Widmanstätten α within the microstructure. Over a 24-hour period this can artificially slow down dezincification progression. Percolation studies were subsequently completed to further enhance our understanding of the dezincification behaviour of duplex brasses with varying β phase fraction and α grain size and aspect ratio (plus tilt angle). The β' phase fraction strongly influences the percolation kinetics and is recognised in industry to be the major way to control dezincification. The α grain size and aspect ratios are additionally recognized to be of comparable importance as the β' fraction, as supported by the percolation simulation with purely geometric considerations. Smaller α grain size causes the β' phase to be statistically less interconnected, while the morphology of α grains more directly deals with the relationship between the percolation direction and α grain arrangement. A small tilt angle with high aspect ratio effectively distributes the α phase with greater breadth, leading to greater percolation resistance. Reduced α grain size acts in the same way and increases the resolved breadth resisting the percolation front.

4. The machinability of 10 different duplex brasses, both as-received and after a range of heat treatments, were evaluated using a series of drilling operations. The outputs included in the analysis were feed force ($F_Z$), drilling torque ($M_Z$), swarf morphology, and the resulting surface roughness ($R_a$) of the machined workpiece. Several key correlations between the base material properties, their associated microstructural parameters, and the machinability outputs were identified. Of note, the $F_Z$ of a brass workpiece is largely determined by its hardness (closely related to the resistance to cutting) and UTS (closely related to a combination of tool adherence and strain-hardening), which are in turn heavily associated with the alloy's α grain size and phase fraction. The $M_Z$ was not heavily affected by the alloy's hardness or UTS, but more strongly dependent on the baseline composition of 'free-machining' particles Pb and Bi or secondary phases as present in the Si-bearing brass. Ductility was also found to be a significant factor in the as-received alloys given it can impact on the tool adherence. The $R_a$ values were found to also be heavily dependent on the presence of 'free-machining' alloying additions Pb and Bi, however in this case it is strongly dependent on the particle size and distribution within the alloy, with a smaller particle size and higher distribution producing a significantly increased $R_a$ value.

If one were to holistically consider the requirements of a brass alloy that follows the standard processing schedule outlined in the introduction (Chapter 1, Fig. 1.3), it is not difficult to observe why

Pb-bearing duplex brass has for so long dominated the plumbing industry. Compared with several low-Pb alternatives now entering the market, Pb-bearing brasses have a relatively simple phase equilibria (where Pb makes little impact as an insoluble element) as shown in Chapter 5, they are generally readily forgeable as shown in Chapter 6 with forging ratings between 80-100, they are adaptable to become dezincification resistant in the field, and are excellent at reducing machining forces (as shown in Chapter 8) allowing high volume, economical manufacturing to take place.

If we consider what might be the most appropriate alternative alloy solution to follow Pb-bearing brasses into a Pb-free industry, the work in this thesis essentially boils the answer down to 5 sub-types of duplex brass (and various hybrids in between). That is, CuZn binary, CuZnBi, CuZnSn, CuZnAl and CuZnSi. Whilst a binary CuZn alloy may appeal due to its simplicity (both in composition and phase equilibria) and likely lower raw material cost, the implications (as shown in Chapters 6 and 8) are that this is not favourable from an elevated temperature deformation or machining point of view and in essence will likely cost the manufacturer more to produce.

The CuZnBi alternative has several key advantages over the other alloy families, namely it retains much of the elevated temperature deformation properties (particularly when using extruded raw material stock) and machinability characteristics as CuZnPb. This is essentially because Bi and Pb share many similar attributes, at the forefront being that they are both insoluble in duplex brass. However, as shown in Chapters 6 and 8, Bi is simply not as effective on a 1 to 1 basis with Pb and cannot be added to the same degree as typically found in CuZnPb alloys due to likely embrittlement during elevated temperature deformation (see example CuZnBi2Sn). One additional advantage of CuZnBi, however, is It is also shown from Chapter 7 that these alloys can be microstructurally tuned to meet dezincification requirements.

CuZnSn and CuZnAl both have the same key advantage and the same key disadvantage. Both sub-types have the ability to perform relatively well during elevated temperature deformation (as shown in Chapter 6), in the case of CuZnSn by decreasing the steepness of the $\alpha/(\alpha+\beta)$ phase field boundary, and in the case of CuZnAl by stronger stabilisation of the $\beta$ phase. However, both sub-types have also shown in Chapter 8 that additional care needs to be taken during machining due to typically higher machining forces and by extension reduced tool life. Along with binary CuZn, these alloy sub-types are far less cooperative for high-volume repetitive machining.

Finally, if we consider the CuZnSi sub-type, one might comment on the complexity of the phase equilibria of these alloys (Chapter 5), the likely need to increase Cu wt. % (and by extension the raw material cost) in order to accommodate the Si in the composition, or the unknowns about this sub-type still being relatively new to industry. However, one cannot ignore the obvious advantages shown first in elevated temperature forgeability (Chapter 6) with Si both having the ability to strongly stabilise β and simultaneously decrease the α/(α+β) phase field boundary in the key hot working zone. Secondly, the likely increase in dezincification resistance and other forms of corrosion resistance due to the higher Cu wt. %. Third, the exceptional room temperature mechanical properties far surpassing standard duplex brasses (Chapter 8), and finally the adequately low machining forces and very good surface roughness garnered in the machining operations (Chapter 8).

As legislation limiting the wt. % of Pb in duplex brasses becomes more common globally, the alternative alloy solutions are now coming under the spotlight. It's clear that so far no single alloy has produced a perfect combination of properties on par with the traditional duplex CuZnPb alloys used in the plumbing industry, however it is the author's view, based on the research completed in this thesis, that Si-bearing duplex brass bears the most promise for the future of high-volume plumbing manufacturing.

## 8.2 Future Work

The works contained within this thesis have identified a number of key future projects that could be undertaken to better understand the behaviour and optimal processing conditions of lead-free duplex brasses. A summary of the most important points is outlined below for each section of this thesis.

### 8.2.1 Phase Equilibria

1. Thermodynamic assessments for several CuZn-based ternary systems now readily exist, including CuZnSn, CuZnPb, CuZnAl, and CuZnSi. Whilst these are very useful for calculating the equilibrium phase fractions of FCC α and BCC β at elevated temperatures and subsequent stabilisation of new phases such as HCP κ at low to intermediate temperatures for said ternary alloys, many new alloys are being developed with more complex combinations of alloying additions, for example CuZnSiSn and CuZnSiAl, for which quaternary thermodynamic descriptions would be very useful.
2. The XRD and high intensity *in-situ* Neutron diffraction experiments revealed a new phenomenon with respect to peak splitting of the FCC α peaks in Bi-bearing duplex brass. This has not been observed or reported previously in the literature and would be ideal to understand the mechanisms behind its existence upon cooling from the all-β phase field.
3. High intensity *in-situ* Neutron diffraction was carried out on both a traditional Pb-bearing duplex brass and a Bi-bearing (Pb-free) duplex brass with close agreement to the CALPHAD calculations for equilibrium FCC α and BCC β within the industrially relevant temperature zone of 650-800$^{o}$C. It would be useful to conduct this same exercise on a Si-bearing duplex brass to develop a greater understanding of this alloy system at the same relevant elevated temperatures.
4. Further work needs to be undertaken to better understand Si-segregation in CuZnSi alloys as it relates to the hot workability and potential incipient melting of the alloy. Typical industrial practices utilise a temperature range for forging and extrusion, so any potential for part rejection as a result of incipient melting needs to be well understood.

### 8.2.2 Elevated Temperature Plasticity

1. A series of 11 duplex brasses of varying composition and fabrication mode were uniaxially hot compressed in order to develop the forgeability index presented in Section 5.3. Whilst more than 500 data points were recorded in this study, further studies on duplex brasses containing tiered amounts of Al, Sn, and Si (all β stabilisers of varying strength), or even better a

combination of these elements would be appropriate to further alloy development for application in the growing global lead-free market.

2. The use of uniaxial hot compression is the simplest method for identifying the elevated temperature plasticity of each duplex brass. In reality, industrial forging processes are substantially more severe and involve a combination of compressive, tensile and shear forces in order to generate the desired pre-form topology. Developing a more robust method and subsequent standard to incorporate a combination of forces would be a logical next step in this space.
3. Whilst the use of the Zener-Hollomon parameter and Rule of Mixtures approach to develop a semi-empirical model to describe the flow stress of a duplex brass proved to work fairly well in Section 5.4, further development of the constitutive model by using an IsoWork contribution and other physically-based phenomena such as the Avrami and Estrin-Mecking equations could further increase the accuracy of this approach.

### 8.2.3 Dezincification Behaviour

1. Dezincification experiments were conducted on two different Bi-bearing duplex brasses fabricated via continuous casting and extrusion respectively. These alloys, whilst very similar in composition had some key differences in results which could be further explored:
    a. The extruded alloy contained a small wt. % of phosphorus inhibitor which is traditionally thought to only protect the α phase. Whilst this may be the case, the mechanism by which P works for different microstructural parameters is not well understood.
    b. A key outcome of the extruded alloy testing was the identification of temporarily increased dezincification resistance due to rapid quenching of the alloy from elevated temperatures. This has been identified as due to the formation of very small Widmanstätten α predominantly along the β grain boundaries, which slows the progress of dezincification through the microstructure over a short-term period (which may be supported by the inclusion of P). This mechanism of quenching to increase dezincification resistance could be further explored, particularly as it relates to the percolation threshold.
2. The dezincification experiments in this study were limited to Bi-bearing duplex brass of a relatively standard Cu:Zn ratio to suit the normal processing schedule of plumbing components. Several other Pb-free duplex brasses (containing Si for example), which may contain alternate phases (e.g. HCP κ) or different Cu:Zn ratios should be studied in a similar

manner to determine their relative percolation thresholds and subsequent dezincification resistance.

3. Dezincification has been identified in the literature to be closely related to several other forms of corrosion which may impact a plumbing components performance in the field. This includes stress corrosion cracking (SCC) in particular. Further evaluation of the resistance of duplex brass to SCC (in accordance with ISO6957 [206] exposing the brass to a controlled-pH environment of ammonia for 24 hours), once optimised for dezincification resistance, should be undertaken with respect to this direct link.

### 8.2.4 Machinability

1. Throughout the machining study, over 145 drilling operations were conducted for 10 duplex brass alloys. Each alloy was machined with a new drill to prevent any wear affecting the output results for $F_Z$, $M_Z$, $R_a$ and no tool wear was observed after the study was completed. Tool wear is a key indicator of machinability in an industrial setting and this typically begins to occur in duplex brass components after thousands of operations have been completed. It would be beneficial to conduct a study on similar duplex brasses containing Pb, Bi, Si etc. to determine their relative effects on tool wear.
2. The CuZnSi alloy produced very interesting results across a range of outputs. It had a very high $F_Z$, moderate $M_Z$ and very good $R_a$. It would be useful to explore how alterations in the composition, and therefore the phase equilibria, would impact on these various outputs for future development of this alloy system, whether beneficial or if the composition trialled is the preferred embodiment for machinability.
3. It was found that several key tensile properties, namely the ultimate tensile strength and the elongation had significant effects on the resulting machinability (particularly $F_Z$ and $M_Z$) of the 'as-received' duplex brasses tested in this study. It would be useful to conduct a deeper study on these properties (through the use of heat treatments) to better verify how closely they impact the final machinability of the alloy workpiece.
4. There is very little literature available that explores the physical modelling of machinability. Modelling today typically consists of either:
    a. FEM analysis, which looks at material flow during cutting but completely discounts microstructural effects and several other key factors important to industry.
    b. Neural networks, which seek to empirically fit various base material properties (for example hardness, strain hardening, ductility) to machinability outputs (e.g. cutting forces).

    It would be highly useful for future studies to include a physical modelling approach that connects the key material inputs and machinability of the duplex brass.

# Appendix A – U.N.S. Alloy Designations

Covered in this Appendix are a list of the known compositional ranges of the alloys used in the research chapters of this thesis which are set according to the U.N.S. alloy designation system [2]. Some of the custom alloys researched in this thesis do not have an associated U.N.S. designation, their specific wt. % values can be found in the alloy selection section of each Chapter in this thesis.

**Table A1: U.N.S. Chemical Composition Ranges (wt. %) of commonly found alloys in this thesis.**

| Alloy | Cu | Zn | Pb | Bi | Si | Sn | Fe | Ni | As | P |
|---|---|---|---|---|---|---|---|---|---|---|
| C27451 | 61.0 – 65.0 | Rem | 0.25 max. | - | - | - | 0.35 max. | - | - | 0.05 – 0.20 |
| C28340 | 61.0 – 62.0 | Rem | 0.17 – 0.25 | 0.65 – 0.75 | - | 0.30 – 0.40 | 0.12 max. | 0.20 max. | 0.07 – 0.17 | - |
| C35330 | 59.5 – 64.0 | Rem | 1.5 – 3.5 | - | - | - | - | - | 0.02 – 0.25 | - |
| C37700 | 58.0 – 61.0 | Rem | 1.5 – 2.5 | - | - | - | 0.30 max. | - | - | - |
| C37710 | 56.5 – 60.0 | Rem | 1.0 – 3.0 | - | - | - | 0.30 max. | - | - | - |
| C46500 | 59.0 – 62.0 | Rem | 0.20 max. | - | - | 0.50 – 1.0 | 0.10 max. | - | 0.02 – 0.06 | - |
| C49260 | 58.0 – 63.0 | Rem | 0.09 max. | 0.50 – 1.8 | - | 0.50 max. | 0.50 max. | - | - | 0.05 – 0.15 |
| C49265 | 58.0 – 62.0 | Rem | 0.09 – 0.25 | 0.50 – 1.3 | - | 0.50 max. | 0.30 max. | - | - | 0.05 – 0.12 |
| C69300 | 73.0 – 77.0 | Rem | 0.09 max. | - | 2.7 – 3.4 | 0.20 max. | 0.10 max. | 0.10 max. | - | 0.04 – 0.15 |

# Appendix B – CALPHAD .tdb Files

The detailed code used for the thermodynamic descriptions of the ternary CuZnPb, CuZnSn, CuZnAl and CuZnSi systems as well as the combined quaternary system CuZnPbSn are shown in this Appendix using data extracted from Wang et al. [30] and Miettinen [29].

## Cu-Zn-Pb .tdb file

```
$
 ELEMENT /-   ELECTRON_GAS          0.0000E+00  0.0000E+00  0.0000E+00!
 ELEMENT VA   VACUUM                0.0000E+00  0.0000E+00  0.0000E+00!
 ELEMENT CU   FCC_A1                6.3546E+01  5.0041E+03  3.3150E+01!
 ELEMENT PB   FCC_A1                2.0720E+02  6.8785E+03  6.4785E+01!
 ELEMENT ZN   HCP_ZN                6.5380E+01  5.6567E+03  4.1631E+01!


 FUNCTION GHSERCU    2.98000E+02  -7770.458+130.485235*T-24.112392*T*LN(T)
    -.00265684*T**2+1.29223E-07*T**3+52478*T**(-1);  1.35777E+03  Y
     -13542.026+183.803828*T-31.38*T*LN(T)+3.64167E+29*T**(-9);
    3.20000E+03  N !
 FUNCTION GBCCCU     2.98150E+02  +4017-1.255*T+GHSERCU#;   6.00000E+03   N !

 FUNCTION GHSERPB    2.98000E+02  -7650.085+101.715188*T-24.5242231*T*LN(T)
    -.00365895*T**2-2.4395E-07*T**3;  6.01000E+02  Y
     -10531.115+154.258155*T-32.4913959*T*LN(T)+.00154613*T**2
    +8.05644E+25*T**(-9);  1.20000E+03  Y
     +4157.596+53.154045*T-18.9640637*T*LN(T)-.002882943*T**2
    +9.8144E-08*T**3-2696755*T**(-1)+8.05644E+25*T**(-9);  2.10000E+03  N !

 FUNCTION GHSERZN    2.98000E+02  -7285.787+118.470069*T-23.701314*T*LN(T)
    -.001712034*T**2-1.264963E-06*T**3;  6.93000E+02  Y
     -11070.559+172.34566*T-31.38*T*LN(T)+4.70514E+26*T**(-9);  1.70000E+03
     N !
 FUNCTION GBCCZN     2.98150E+02  +2886.96-2.5104*T+GHSERZN#;   6.00000E+03
     N !
 FUNCTION GFCCZN     2.98150E+02  +2969.82-1.56968*T+GHSERZN#;   6.00000E+03
      N !

 FUNCTION L0FCUPB    2.98150E+02  +45684+5.151*T;   6.00000E+03   N !
 FUNCTION L0FPBZN    2.98150E+02  32873;   6.00000E+03   N !
 FUNCTION L0BCT      2.98150E+02  50000;   6.00000E+03   N !
 FUNCTION L0HCP      2.98150E+02  50000;   6.00000E+03   N !
 FUNCTION L0GAM      2.98150E+02  50000;   6.00000E+03   N !
 FUNCTION ZERO       298.15 0.0; 6000.00  N !
 FUNCTION UN_ASS 298.15 0; 3000 N !

 TYPE_DEFINITION % SEQ *!
 DEFINE_SYSTEM_DEFAULT SPECIE 2 !
 DEFAULT_COMMAND DEF_SYS_ELEMENT VA !

$ PHASE 1
 PHASE LIQ:L % 1  1.0  !
    CONSTITUENT LIQ:L :CU,PB,ZN :  !

   PARAMETER G(LIQ,CU;0)  2.98000E+02  +5194.277+120.973331*T
  -24.112392*T*LN(T)-.00265684*T**2+1.29223E-07*T**3+52478*T**(-1)
  -5.8489E-21*T**7;  1.35777E+03  Y
   -46.545+173.881484*T-31.38*T*LN(T);  3.20000E+03  N REF:0 !
   PARAMETER G(LIQ,PB;0)  2.98000E+02  -2977.961+93.949561*T
  -24.5242231*T*LN(T)-.00365895*T**2-2.4395E-07*T**3
  -6.019E-19*T**7;  6.01000E+02  Y
  -5677.958+146.176046*T-32.4913959*T*LN(T)+.00154613*T**2;  1.20000E+03  Y
  +9010.753+45.071937*T-18.9640637*T*LN(T)-.002882943*T**2
```

```
 +9.8144E-08*T**3-2696755*T**(-1);  2.10000E+03  N REF:0 !
  PARAMETER G(LIQ,ZN;0)  2.98000E+02  -128.574+108.177079*T
 -23.701314*T*LN(T)-.001712034*T**2-1.264963E-06*T**3-3.58958E-19*T**7;
 6.92680E+02  Y
  -3620.391+161.608594*T-31.38*T*LN(T);  1.70000E+03  N REF:0 !
  PARAMETER G(LIQ,CU,PB;0)  2.98150E+02  +31008-7.195*T;   6.00000E+03   N
 REF:0 !
  PARAMETER G(LIQ,CU,PB;1)  2.98150E+02  +15345-10.826*T;   6.00000E+03   N
 REF:0 !
  PARAMETER G(LIQ,CU,PB;2)  2.98150E+02  -6493+5.947*T;   6.00000E+03   N
 REF:0 !
  PARAMETER G(LIQ,CU,PB;3)  2.98150E+02  -18416+13.16*T;   6.00000E+03   N
 REF:0 !

  PARAMETER G(LIQ,CU,ZN;0)  2.98150E+02  -40696+12.653*T;   6.00000E+03   N
 REF:0 !
  PARAMETER G(LIQ,CU,ZN;1)  2.98150E+02  +4403-6.554*T;   6.00000E+03   N
 REF:0 !
  PARAMETER G(LIQ,CU,ZN;2)  2.98150E+02  +7818-3.254*T;   6.00000E+03   N
 REF:0 !

  PARAMETER G(LIQ,PB,ZN;0)  2.98150E+02  +23259-3.687*T;   6.00000E+03   N
 REF:0 !
  PARAMETER G(LIQ,PB,ZN;1)  2.98150E+02  -44-2.962*T;   6.00000E+03   N
 REF:0 !
  PARAMETER G(LIQ,PB,ZN;2)  2.98150E+02  -4987+6.818*T;   6.00000E+03   N
 REF:0 !
  PARAMETER G(LIQ,PB,ZN;3)  2.98150E+02  -9978+8.2*T;   6.00000E+03   N
 REF:0 !
  PARAMETER G(LIQ,PB,ZN;4)  2.98150E+02  +13275-10.2*T;   6.00000E+03   N
 REF:0 !

  PARAMETER G(LIQ,CU,PB,ZN;0)  2.98150E+02  +37000;   6.00000E+03   N
 REF:0 !
  PARAMETER G(LIQ,CU,PB,ZN;1)  2.98150E+02  +40000-50*T;   6.00000E+03   N
 REF:0 !
  PARAMETER G(LIQ,CU,PB,ZN;2)  2.98150E+02  +30*T;   6.00000E+03   N
 REF:0 !

$ PHASE 2

 TYPE_DEFINITION ' GES A_P_D FCC_A1 MAGNETIC  -3.0    2.80000E-01 !
 PHASE FCC_A1  %'  2 1   1 !
   CONSTITUENT FCC_A1  :CU,PB,ZN : VA :  !

  PARAMETER G(FCC_A1,CU:VA;0)  2.98150E+02  +GHSERCU#;  6.00000E+03   N
 REF:0 !
  PARAMETER G(FCC_A1,PB:VA;0)  2.98000E+02  +GHSERPB#;  2.10000E+03  N
 REF:0 !
  PARAMETER G(FCC_A1,ZN:VA;0)  2.98150E+02  +GFCCZN#;  6.00000E+03   N
 REF:0 !
  PARAMETER G(FCC_A1,CU,PB:VA;0)  2.98150E+02  +L0FCUPB#;  6.00000E+03   N
 REF:0 !
  PARAMETER G(FCC_A1,CU,ZN:VA;0)  2.98150E+02  -42804+10.023*T;
 6.00000E+03   N REF:0 !
  PARAMETER G(FCC_A1,CU,ZN:VA;1)  2.98150E+02  +2936-3.053*T;   6.00000E+03
   N REF:0 !
  PARAMETER G(FCC_A1,CU,ZN:VA;2)  2.98150E+02  +9034-5.393*T;   6.00000E+03
   N REF:0 !
  PARAMETER G(FCC_A1,PB,ZN:VA;0)  2.98150E+02  +L0FPBZN#;  6.00000E+03   N
 REF:0 !
  PARAMETER G(FCC_A1,CU,PB,ZN:VA;0)  2.98150E+02  +50000;   6.00000E+03   N
 REF:0 !

$ PHASE 3
 TYPE_DEFINITION & GES A_P_D BCC_A2 MAGNETIC  -1.0    4.00000E-01 !
 PHASE BCC_A2  %&  2 1   3 !
   CONSTITUENT BCC_A2  :CU,PB,ZN : VA :  !

  PARAMETER G(BCC_A2,CU:VA;0)  2.98150E+02  +GBCCCU#;   6.00000E+03   N
 REF:0 !
```

```
  PARAMETER G(BCC_A2,PB:VA;0)  2.98000E+02  +2400-1.1*T+GHSERPB#;
 2.10000E+03  N REF:0 !
  PARAMETER G(BCC_A2,ZN:VA;0)  2.98150E+02  +GBCCZN#;   6.00000E+03   N
 REF:0 !
  PARAMETER G(BCC_A2,CU,PB:VA;0)  2.98150E+02  +L0FCUPB#;   6.00000E+03   N
 REF:0 !
  PARAMETER G(BCC_A2,CU,ZN:VA;0)  2.98150E+02  -51596+13.064*T;
 6.00000E+03   N REF:0 !
  PARAMETER G(BCC_A2,CU,ZN:VA;1)  2.98150E+02  +7562-6.454*T;   6.00000E+03
   N REF:0 !
  PARAMETER G(BCC_A2,CU,ZN:VA;2)  2.98150E+02  +30744-29.915*T;
 6.00000E+03   N REF:0 !
  PARAMETER G(BCC_A2,PB,ZN:VA;0)  2.98150E+02  +L0FPBZN#;   6.00000E+03   N
 REF:0 !

  PARAMETER G(BCC_A2,CU,PB,ZN:VA;0)  2.98150E+02  +20000;   6.00000E+03   N
 REF:0 !

$ PHASE 4

 PHASE HCP_A3  %  2 1   .5 !
   CONSTITUENT HCP_A3  :CU,PB,ZN : VA :  !

  PARAMETER G(HCP_A3,CU:VA;0)  2.98150E+02  +600+.2*T+GHSERCU#;
 6.00000E+03   N REF:0 !
  PARAMETER G(HCP_A3,PB:VA;0)  2.98000E+02  +300+T+GHSERPB#;  2.10000E+03
 N REF:0 !
  PARAMETER G(HCP_A3,ZN:VA;0)  2.98150E+02  +2970-1.57*T+GHSERZN#;
 6.00000E+03   N REF:0 !
  PARAMETER G(HCP_A3,CU,PB:VA;0)  2.98150E+02  +L0HCP#;   6.00000E+03   N
 REF:0 !
  PARAMETER G(HCP_A3,CU,ZN:VA;0)  2.98150E+02  -36475+4.896*T;
 6.00000E+03   N REF:0 !
  PARAMETER G(HCP_A3,CU,ZN:VA;1)  2.98150E+02  +24790-10.135*T;
 6.00000E+03   N REF:0 !
  PARAMETER G(HCP_A3,PB,ZN:VA;0)  2.98150E+02  +L0HCP#;   6.00000E+03   N
 REF:0 !

$ PHASE 5
 PHASE GAMSOL  %  1  1.0  !
   CONSTITUENT GAMSOL  :CU,ZN :  !

  PARAMETER G(GAMSOL,CU;0)  2.98150E+02  +10+GHSERCU#;   6.00000E+03   N
 REF:0 !
  PARAMETER G(GAMSOL,ZN;0)  2.98150E+02  +10+GHSERZN#;   6.00000E+03   N
 REF:0 !
  PARAMETER G(GAMSOL,CU,ZN;0)  2.98150E+02  -39470+9.436*T;   6.00000E+03
 N REF:0 !
  PARAMETER G(GAMSOL,CU,ZN;1)  2.98150E+02  +36675-5.196*T;   6.00000E+03
 N REF:0 !
  PARAMETER G(GAMSOL,CU,ZN;2)  2.98150E+02  +90163-32.62*T;   6.00000E+03
 N REF:0 !

$ PHASE 6
 PHASE HCP_ZN  %  1  1.0  !
   CONSTITUENT HCP_ZN  :CU,PB,ZN :  !

  PARAMETER G(HCP_ZN,CU;0)  2.98150E+02  +600+.2*T+GHSERCU#;   6.00000E+03
  N REF:0 !
  PARAMETER G(HCP_ZN,PB;0)  2.98000E+02  +300+T+GHSERPB#;  2.10000E+03
  N REF:0 !
  PARAMETER G(HCP_ZN,ZN;0)  2.98150E+02  +GHSERZN#;   6.00000E+03   N REF:0 !
  PARAMETER G(HCP_ZN,CU,ZN;0)  2.98150E+02  -14432-10.781*T;   6.00000E+03
  N REF:0 !
  PARAMETER G(HCP_ZN,CU,PB;0)  2.98150E+02  +50000;   6.00000E+03 N REF:0 !
  PARAMETER G(HCP_ZN,PB,ZN;0)  2.98150E+02  +39436;   6.00000E+03 N REF:0 !
```

# Cu-Zn-Sn .tdb file

```
$
 ELEMENT /-   ELECTRON_GAS          0.0000E+00  0.0000E+00  0.0000E+00!
 ELEMENT VA   VACUUM                0.0000E+00  0.0000E+00  0.0000E+00!
 ELEMENT CU   FCC_A1                6.3546E+01  5.0041E+03  3.3150E+01!
 ELEMENT SN   BCT_A5                1.1869E+02  6.3230E+03  5.1180E+01!
 ELEMENT ZN   HCP_ZN                6.5380E+01  5.6567E+03  4.1631E+01!


 FUNCTION GHSERCU    2.98000E+02  -7770.458+130.485235*T-24.112392*T*LN(T)
    -.00265684*T**2+1.29223E-07*T**3+52478*T**(-1);  1.35777E+03  Y
    -13542.026+183.803828*T-31.38*T*LN(T)+3.64167E+29*T**(-9);
    3.20000E+03  N !
 FUNCTION GBCCCU     2.98150E+02  +4017-1.255*T+GHSERCU#;   6.00000E+03   N !

 FUNCTION GHSERSN    1.00000E+02  -7958.517+122.765451*T-25.858*T*LN(T)
    +.51185E-03*T**2-3.192767E-06*T**3+18440*T**(-1);  2.50000E+02  Y
    -5855.135+65.443315*T-15.961*T*LN(T)-18.8702E-03*T**2
    +3.121167E-06*T**3-61960*T**(-1);  5.05078E+02  Y
    +2524.724+4.005269*T-8.2590486*T*LN(T)-16.814429E-03*T**2
    +2.623131E-06*T**3-1081244*T**(-1)-1.2307E+25*T**(-9);  8.00000E+02  Y
    -8256.959+138.99688*T-28.4512*T*LN(T)-1.2307E+25*T**(-9);  3.00000E+03
     N !

 FUNCTION GHSERZN    2.98000E+02  -7285.787+118.470069*T-23.701314*T*LN(T)
    -.001712034*T**2-1.264963E-06*T**3;  6.93000E+02  Y
     -11070.559+172.34566*T-31.38*T*LN(T)+4.70514E+26*T**(-9);  1.70000E+03
     N !
 FUNCTION GBCCZN     2.98150E+02  +2886.96-2.5104*T+GHSERZN#;   6.00000E+03
     N !
 FUNCTION GFCCZN     2.98150E+02  +2969.82-1.56968*T+GHSERZN#;   6.00000E+03
      N !



 TYPE_DEFINITION % SEQ *!
 DEFINE_SYSTEM_DEFAULT SPECIE 2 !
 DEFAULT_COMMAND DEF_SYS_ELEMENT VA !

$ PHASE 1
 PHASE LIQ:L %  1  1.0  !
   CONSTITUENT LIQ:L :CU,SN,ZN :  !

  PARAMETER G(LIQ,CU;0)  2.98000E+02  +5194.277+120.973331*T
 -24.112392*T*LN(T)-.00265684*T**2+1.29223E-07*T**3+52478*T**(-1)
 -5.8489E-21*T**7;  1.35777E+03  Y
 -46.545+173.881484*T-31.38*T*LN(T);  3.20000E+03  N REF:0 !
  PARAMETER G(LIQ,SN;0)  1.00000E+02  -855.425+108.677684*T-25.858*T*LN(T)
 +.51185E-03*T**2-3.192767E-06*T**3+18440*T**(-1)+1.47031E-18*T**7;
 2.50000E+02  Y
 1247.957+51.355548*T-15.961*T*LN(T)-18.8702E-03*T**2
 +3.121167E-06*T**3-61960*T**(-1)++1.47031E-18*T**7;  5.05078E+02  Y
 +9496.31-9.809114*T-8.2590486*T*LN(T)-16.814429E-03*T**2
 +2.623131E-06*T**3-1081244*T**(-1);  8.00000E+02  Y
 -1285.372+125.182498*T-28.4512*T*LN(T);  3.00000E+03  N
 REF:0 !
  PARAMETER G(LIQ,ZN;0)  2.98000E+02  -128.574+108.177079*T
 -23.701314*T*LN(T)-.001712034*T**2-1.264963E-06*T**3-3.58958E-19*T**7;
 6.92680E+02  Y
  -3620.391+161.608594*T-31.38*T*LN(T);  1.70000E+03  N REF:0 !
  PARAMETER G(LIQ,CU,SN;0)  2.98150E+02  -8124-6.553*T;   6.00000E+03   N
 REF:0 !
  PARAMETER G(LIQ,CU,SN;1)  2.98150E+02  -23970+7.037*T;   6.00000E+03   N
 REF:0 !
  PARAMETER G(LIQ,CU,SN;2)  2.98150E+02  -25124+13.566*T;   6.00000E+03   N
 REF:0 !
  PARAMETER G(LIQ,CU,SN;3)  2.98150E+02  -10213+10.042*T;   6.00000E+03   N
 REF:0 !

  PARAMETER G(LIQ,CU,ZN;0)  2.98150E+02  -40696+12.653*T;   6.00000E+03   N
```

```
 REF:0 !
  PARAMETER G(LIQ,CU,ZN;1)  2.98150E+02  +4403-6.554*T;   6.00000E+03   N
 REF:0 !
  PARAMETER G(LIQ,CU,ZN;2)  2.98150E+02  +7818-3.254*T;   6.00000E+03   N
 REF:0 !

  PARAMETER G(LIQ,SN,ZN;0)  2.98150E+02  +19315-75.899*T+8.7514*T*LN(T);
 6.00000E+03   N REF:0 !
  PARAMETER G(LIQ,SN,ZN;1)  2.98150E+02  -5696+4.202*T;   6.00000E+03   N
 REF:0 !
  PARAMETER G(LIQ,SN,ZN;2)  2.98150E+02  +1037+0.984*T;   6.00000E+03   N
 REF:0 !

  PARAMETER G(LIQ,CU,SN,ZN;0)  2.98150E+02  -60000+50*T;   6.00000E+03   N
 REF:0 !
  PARAMETER G(LIQ,CU,SN,ZN;1)  2.98150E+02  +40000;    6.00000E+03   N
 REF:0 !
  PARAMETER G(LIQ,CU,SN,ZN;2)  2.98150E+02  +60000;   6.00000E+03   N
 REF:0 !

$ PHASE 2

 TYPE_DEFINITION ' GES A_P_D FCC_A1 MAGNETIC  -3.0    2.80000E-01 !
 PHASE FCC_A1  %'  2 1   1 !
    CONSTITUENT FCC_A1  :CU,SN,ZN : VA :  !

  PARAMETER G(FCC_A1,CU:VA;0)  2.98150E+02  +GHSERCU#;   6.00000E+03   N
 REF:0 !
  PARAMETER G(FCC_A1,SN:VA;0)  2.98150E+02  +4150-5.2*T+GHSERSN#;
 3.00000E+03  N REF:0 !
  PARAMETER G(FCC_A1,ZN:VA;0)  2.98150E+02  +GFCCZN#;   6.00000E+03   N
 REF:0 !
  PARAMETER G(FCC_A1,CU,SN:VA;0)  2.98150E+02  -10672-1.484*T;
 6.00000E+03   N REF:0 !
  PARAMETER G(FCC_A1,CU,SN:VA;1)  2.98150E+02  -15331+6.954*T;
 6.00000E+03   N REF:0 !
  PARAMETER G(FCC_A1,CU,ZN:VA;0)  2.98150E+02  -42804+10.023*T;
 6.00000E+03   N REF:0 !
  PARAMETER G(FCC_A1,CU,ZN:VA;1)  2.98150E+02  +2936-3.053*T;   6.00000E+03
   N REF:0 !
  PARAMETER G(FCC_A1,CU,ZN:VA;2)  2.98150E+02  +9034-5.393*T;   6.00000E+03
   N REF:0 !
  PARAMETER G(FCC_A1,SN,ZN:VA;0)  2.98150E+02  +80*T;   6.00000E+03   N
 REF:0 !
  PARAMETER G(FCC_A1,CU,SN,ZN:VA;0)  2.98150E+02  -25000;   6.00000E+03   N
 REF:0 !
  PARAMETER G(FCC_A1,CU,SN,ZN:VA;1)  2.98150E+02  +10000;   6.00000E+03   N
 REF:0 !
  PARAMETER G(FCC_A1,CU,SN,ZN:VA;2)  2.98150E+02  +10000;   6.00000E+03   N
 REF:0 !

$ PHASE 3
 TYPE_DEFINITION & GES A_P_D BCC_A2 MAGNETIC  -1.0    4.00000E-01 !
 PHASE BCC_A2  %&  2 1   3 !
    CONSTITUENT BCC_A2  :CU,SN,ZN : VA :  !

  PARAMETER G(BCC_A2,CU:VA;0)  2.98150E+02  +GBCCCU#;   6.00000E+03   N
 REF:0 !
  PARAMETER G(BCC_A2,SN:VA;0)  2.98150E+02  +4400-6.0*T+GHSERSN#;
 3.00000E+03  N REF:0 !
  PARAMETER G(BCC_A2,ZN:VA;0)  2.98150E+02  +GBCCZN#;   6.00000E+03   N
 REF:0 !
  PARAMETER G(BCC_A2,CU,SN:VA;0)  2.98150E+02  -44822+51.216*T;
 6.00000E+03   N REF:0 !
  PARAMETER G(BCC_A2,CU,SN:VA;1)  2.98150E+02  -6877-56.427*T;
 6.00000E+03   N REF:0 !
  PARAMETER G(BCC_A2,CU,ZN:VA;0)  2.98150E+02  -51596+13.064*T;
 6.00000E+03   N REF:0 !
  PARAMETER G(BCC_A2,CU,ZN:VA;1)  2.98150E+02  +7562-6.454*T;   6.00000E+03
   N REF:0 !
  PARAMETER G(BCC_A2,CU,ZN:VA;2)  2.98150E+02  +30744-29.915*T;
```

```
 6.00000E+03   N REF:0 !
  PARAMETER G(BCC_A2,SN,ZN:VA;0)  2.98150E+02  +80*T;   6.00000E+03   N
 REF:0 !

  PARAMETER G(BCC_A2,CU,SN,ZN:VA;0)  2.98150E+02  -5000-100*T;
 6.00000E+03   N REF:0 !
  PARAMETER G(BCC_A2,CU,SN,ZN:VA;1)  2.98150E+02  +420000;
 6.00000E+03   N REF:0 !
  PARAMETER G(BCC_A2,CU,SN,ZN:VA;2)  2.98150E+02  +90000-130*T;
 6.00000E+03   N REF:0 !

$ PHASE 4
 PHASE GAMMA  %  1  1.0  !
   CONSTITUENT GAMMA  :CU,SN,ZN :  !

  PARAMETER G(GAMMA,CU;0)  2.98150E+02  +10+GHSERCU#;   6.00000E+03   N
 REF:0 !
  PARAMETER G(GAMMA,SN;0)  2.98150E+02  +10+GHSERSN#;   3.00000E+03   N
 REF:0 !
  PARAMETER G(GAMMA,ZN;0)  2.98150E+02  +10+GHSERZN#;   6.00000E+03   N
 REF:0 !
  PARAMETER G(GAMMA,CU,SN;0)  2.98150E+02  +40039-32.912*T;
 6.00000E+03   N REF:0 !
  PARAMETER G(GAMMA,CU,SN;1)  2.98150E+02  -232532+135.367*T;
 6.00000E+03   N REF:0 !
  PARAMETER G(GAMMA,CU,SN;2)  2.98150E+02  +210180-129.043*T;
 6.00000E+03   N REF:0 !
  PARAMETER G(GAMMA,CU,ZN;0)  2.98150E+02  -39470+9.436*T;   6.00000E+03
 N REF:0 !
  PARAMETER G(GAMMA,CU,ZN;1)  2.98150E+02  +36675-5.196*T;   6.00000E+03
 N REF:0 !
  PARAMETER G(GAMMA,CU,ZN;2)  2.98150E+02  +90163-32.62*T;   6.00000E+03
 N REF:0 !
  PARAMETER G(GAMMA,SN,ZN;0)  2.98150E+02  +50000;   6.00000E+03
 N REF:0 !
  PARAMETER G(GAMMA,CU,SN,ZN;0)  2.98150E+02  -315000;   6.00000E+03
 N REF:0 !
  PARAMETER G(GAMMA,CU,SN,ZN;1)  2.98150E+02  -65000;   6.00000E+03
 N REF:0 !
  PARAMETER G(GAMMA,CU,SN,ZN;2)  2.98150E+02  +95000;   6.00000E+03
 N REF:0 !

$ PHASE 5

 PHASE CU41SN11_DELTA  %  2 .788   .212 !
   CONSTITUENT CU41SN11_DELTA  :CU : SN :  !

  PARAMETER G(CU41SN11_DELTA,CU:SN;0)  2.98150E+02  -6323.5-1.2808*T
 +0.788*GHSERCU#+0.212*GHSERSN#;   3.00000E+03   N REF:0 !

$ PHASE 6

 PHASE CU3SN_EPSILON  %  2 .75   .25 !
   CONSTITUENT CU3SN_EPSILON  :CU : SN :  !

  PARAMETER G(CU3SN_EPSILON,CU:SN;0)  2.98150E+02  -8194.2-0.2034*T
 +0.75*GHSERCU#+0.25*GHSERSN#;   3.00000E+03   N REF:0 !

$ PHASE 7

 PHASE CU10SN3_ZETA  %  2 .769   .231 !
   CONSTITUENT CU10SN3_ZETA  :CU : SN :  !

  PARAMETER G(CU10SN3_ZETA,CU:SN;0)  2.98150E+02  -6353-1.8*T
 +0.769*GHSERCU#+0.231*GHSERSN#;   3.00000E+03   N REF:0 !
```

# Cu-Zn-Al .tdb file

```
$
 ELEMENT /-   ELECTRON_GAS          0.0000E+00  0.0000E+00  0.0000E+00!
 ELEMENT VA   VACUUM                0.0000E+00  0.0000E+00  0.0000E+00!
 ELEMENT CU   FCC_A1                6.3546E+01  5.0041E+03  3.3150E+01!
 ELEMENT AL   FCC_A1                2.6982E+01  4.5400E+03  2.8300E+01!
 ELEMENT ZN   HCP_ZN                6.5380E+01  5.6567E+03  4.1631E+01!


 FUNCTION GHSERCU    2.98000E+02  -7770.458+130.485235*T-24.112392*T*LN(T)
    -.00265684*T**2+1.29223E-07*T**3+52478*T**(-1);  1.35777E+03  Y
    -13542.026+183.803828*T-31.38*T*LN(T)+3.64167E+29*T**(-9);
    3.20000E+03  N !
 FUNCTION GBCCCU     2.98150E+02  +4017-1.255*T+GHSERCU#;   6.00000E+03   N !

 FUNCTION GHSERAL    2.98150E+02  -7976.15+137.093038*T-24.3671976*T*LN(T)
    -1.884662E-03*T**2-.877664E-06*T**3+74092*T**(-1);  7.00000E+02  Y
    -11276.24+223.048446*T-38.5844296*T*LN(T)+18.531982E-03*T**2
    -5.764227E-06*T**3+74092*T**(-1);  9.33470E+02  Y
    -11278.378+188.684153*T-31.748192*T*LN(T)-1.231E+28*T**(-9);
  2.90000E+03  N !

 FUNCTION GHSERZN    2.98000E+02  -7285.787+118.470069*T-23.701314*T*LN(T)
    -.001712034*T**2-1.264963E-06*T**3;  6.93000E+02  Y
     -11070.559+172.34566*T-31.38*T*LN(T)+4.70514E+26*T**(-9);  1.70000E+03
     N !
 FUNCTION GBCCZN     2.98150E+02  +2886.96-2.5104*T+GHSERZN#;   6.00000E+03
     N !
 FUNCTION GFCCZN     2.98150E+02  +2969.82-1.56968*T+GHSERZN#;   6.00000E+03
      N !



 TYPE_DEFINITION % SEQ *!
 DEFINE_SYSTEM_DEFAULT SPECIE 2 !
 DEFAULT_COMMAND DEF_SYS_ELEMENT VA !

$ PHASE 1

 PHASE LIQ:L %  1  1.0  !
   CONSTITUENT LIQ:L :AL,CU,ZN :  !

   PARAMETER G(LIQ,CU;0)  2.98000E+02  +5194.277+120.973331*T
  -24.112392*T*LN(T)-.00265684*T**2+1.29223E-07*T**3+52478*T**(-1)
  -5.8489E-21*T**7;  1.35777E+03  Y
  -46.545+173.881484*T-31.38*T*LN(T);  3.20000E+03  N REF:0 !
   PARAMETER G(LIQ,AL;0)  2.98150E+02  +3028.879+125.251171*T
  -24.3671976*T*LN(T)-1.884662E-03*T**2-.877664E-06*T**3
  +74092*T**(-1)+7.934E-20*T**7;  7.00000E+02  Y
  -271.21+211.206579*T-38.5844296*T*LN(T)+18.531982E-03*T**2
  -5.764227E-06*T**3+74092*T**(-1)+7.934E-20*T**7;  9.33470E+02  Y
  -795.996+177.430178*T-31.748192*T*LN(T);  2.90000E+03  N REF:0 !
   PARAMETER G(LIQ,ZN;0)  2.98000E+02  -128.574+108.177079*T
  -23.701314*T*LN(T)-.001712034*T**2-1.264963E-06*T**3-3.58958E-19*T**7;
  6.92680E+02  Y
   -3620.391+161.608594*T-31.38*T*LN(T);  1.70000E+03  N REF:0 !
   PARAMETER G(LIQ,AL,CU;0)  2.98150E+02  -66622+8.1*T;   6.00000E+03   N
  REF:0 !
   PARAMETER G(LIQ,AL,CU;1)  2.98150E+02  +46800-90.8*T+10*T*LN(T);
  6.00000E+03   N REF:0 !
   PARAMETER G(LIQ,AL,CU;2)  2.98150E+02  -2812;   6.00000E+03   N
  REF:0 !


   PARAMETER G(LIQ,CU,ZN;0)  2.98150E+02  -40696+12.653*T;   6.00000E+03   N
  REF:0 !
   PARAMETER G(LIQ,CU,ZN;1)  2.98150E+02  +4403-6.554*T;   6.00000E+03   N
  REF:0 !
   PARAMETER G(LIQ,CU,ZN;2)  2.98150E+02  +7818-3.254*T;   6.00000E+03   N
  REF:0 !
```

```
  PARAMETER G(LIQ,AL,ZN;0)  2.98150E+02  +10466-3.393*T;
 6.00000E+03   N REF:0 !


  PARAMETER G(LIQ,AL,CU,ZN;0)  2.98150E+02  +20000;   6.00000E+03   N
 REF:0 !
  PARAMETER G(LIQ,AL,CU,ZN;1)  2.98150E+02  -20000;   6.00000E+03   N
 REF:0 !
  PARAMETER G(LIQ,AL,CU,ZN;2)  2.98150E+02  +40000;   6.00000E+03   N
 REF:0 !


$ PHASE 2

 TYPE_DEFINITION ' GES A_P_D FCC_A1 MAGNETIC  -3.0    2.80000E-01 !
 PHASE FCC_A1  %'  2 1   1 !
   CONSTITUENT FCC_A1  :AL,CU,ZN : VA :  !

  PARAMETER G(FCC_A1,CU:VA;0)  2.98150E+02  +GHSERCU#;   6.00000E+03   N
 REF:0 !
  PARAMETER G(FCC_A1,AL:VA;0)  2.98150E+02  +GHSERAL#;
 2.90000E+03  N REF:0 !
  PARAMETER G(FCC_A1,ZN:VA;0)  2.98150E+02  +GFCCZN#;   6.00000E+03   N
 REF:0 !
  PARAMETER G(FCC_A1,AL,CU:VA;0)  2.98150E+02  -64400+10*T;
 6.00000E+03   N REF:0 !
  PARAMETER G(FCC_A1,AL,CU:VA;1)  2.98150E+02  +34000;
 6.00000E+03   N REF:0 !
  PARAMETER G(FCC_A1,CU,ZN:VA;0)  2.98150E+02  -42804+10.023*T;
 6.00000E+03   N REF:0 !
  PARAMETER G(FCC_A1,CU,ZN:VA;1)  2.98150E+02  +2936-3.053*T;   6.00000E+03
   N REF:0 !
  PARAMETER G(FCC_A1,CU,ZN:VA;2)  2.98150E+02  +9034-5.393*T;   6.00000E+03
   N REF:0 !
  PARAMETER G(FCC_A1,AL,ZN:VA;0)  2.98150E+02  +7297+.475*T;
 6.00000E+03   N REF:0 !
  PARAMETER G(FCC_A1,AL,ZN:VA;1)  2.98150E+02  +6613-4.591*T;
 6.00000E+03   N REF:0 !
  PARAMETER G(FCC_A1,AL,ZN:VA;2)  2.98150E+02  -3097+3.306*T;
 6.00000E+03   N REF:0 !
  PARAMETER G(FCC_A1,AL,CU,ZN:VA;0)  2.98150E+02  +78000-80*T;
 6.00000E+03   N REF:0 !
  PARAMETER G(FCC_A1,AL,CU,ZN:VA;1)  2.98150E+02  +78000-80*T;
 6.00000E+03   N REF:0 !
  PARAMETER G(FCC_A1,AL,CU,ZN:VA;2)  2.98150E+02  +60000;   6.00000E+03   N
 REF:0 !

$ PHASE 3

 TYPE_DEFINITION & GES A_P_D BCC_A2 MAGNETIC  -1.0    4.00000E-01 !
 PHASE BCC_A2  %&  2 1   3 !
   CONSTITUENT BCC_A2  :AL,CU,ZN : VA :  !

  PARAMETER G(BCC_A2,CU:VA;0)  2.98150E+02  +GBCCCU#;   6.00000E+03   N
 REF:0 !
  PARAMETER G(BCC_A2,AL:VA;0)  2.98150E+02  +10083-4.813*T+GHSERAL#;
 2.90000E+03  N REF:0 !
  PARAMETER G(BCC_A2,ZN:VA;0)  2.98150E+02  +GBCCZN#;   6.00000E+03   N
 REF:0 !
  PARAMETER G(BCC_A2,AL,CU:VA;0)  2.98150E+02  -104600+27.5*T;
 6.00000E+03   N REF:0 !
  PARAMETER G(BCC_A2,AL,CU:VA;1)  2.98150E+02  +9800+20*T;
 6.00000E+03   N REF:0 !
  PARAMETER G(BCC_A2,CU,ZN:VA;0)  2.98150E+02  -51596+13.064*T;
 6.00000E+03   N REF:0 !
  PARAMETER G(BCC_A2,CU,ZN:VA;1)  2.98150E+02  +7562-6.454*T;   6.00000E+03
   N REF:0 !
  PARAMETER G(BCC_A2,CU,ZN:VA;2)  2.98150E+02  +30744-29.915*T;
 6.00000E+03   N REF:0 !
  PARAMETER G(BCC_A2,AL,ZN:VA;0)  2.98150E+02  +7297+.475*T;
```

```
 6.00000E+03   N REF:0 !
  PARAMETER G(BCC_A2,AL,ZN:VA;1)  2.98150E+02  +6613-4.591*T;
 6.00000E+03   N REF:0 !
  PARAMETER G(BCC_A2,AL,ZN:VA;2)  2.98150E+02  -3097+3.306*T;
 6.00000E+03   N REF:0 !

  PARAMETER G(BCC_A2,AL,CU,ZN:VA;0)  2.98150E+02  -57000+30*T;
 6.00000E+03   N REF:0 !
  PARAMETER G(BCC_A2,AL,CU,ZN:VA;1)  2.98150E+02  +20000;
 6.00000E+03   N REF:0 !
  PARAMETER G(BCC_A2,AL,CU,ZN:VA;2)  2.98150E+02  -5000;
 6.00000E+03   N REF:0 !


$ PHASE 4

 PHASE GAMMA  %  1  1.0  !
   CONSTITUENT GAMMA  :AL,CU,ZN :  !

  PARAMETER G(GAMMA,CU;0)  2.98150E+02  +10+GHSERCU#;   6.00000E+03   N
 REF:0 !
  PARAMETER G(GAMMA,AL;0)  2.98150E+02  +10+GHSERAL#;   3.00000E+03   N
 REF:0 !
  PARAMETER G(GAMMA,ZN;0)  2.98150E+02  +10+GHSERZN#;   6.00000E+03   N
 REF:0 !
  PARAMETER G(GAMMA,AL,CU;0)  2.98150E+02  -53150+18.6*T;
 6.00000E+03   N REF:0 !
  PARAMETER G(GAMMA,AL,CU;1)  2.98150E+02  +236000-27.8*T;
 6.00000E+03   N REF:0 !
  PARAMETER G(GAMMA,AL,CU;2)  2.98150E+02  +364000-88.3*T;
 6.00000E+03   N REF:0 !
  PARAMETER G(GAMMA,CU,ZN;0)  2.98150E+02  -39470+9.436*T;   6.00000E+03
 N REF:0 !
  PARAMETER G(GAMMA,CU,ZN;1)  2.98150E+02  +36675-5.196*T;   6.00000E+03
 N REF:0 !
  PARAMETER G(GAMMA,CU,ZN;2)  2.98150E+02  +90163-32.62*T;   6.00000E+03
 N REF:0 !
 PARAMETER G(GAMMA,AL,ZN;0)  2.98150E+02  +50000;   6.00000E+03
 N REF:0 !
 PARAMETER G(GAMMA,AL,CU,ZN;0)  2.98150E+02  +106000;   6.00000E+03
 N REF:0 !
 PARAMETER G(GAMMA,AL,CU,ZN;1)  2.98150E+02  -354000;   6.00000E+03
 N REF:0 !
 PARAMETER G(GAMMA,AL,CU,ZN;2)  2.98150E+02  +8000+48*T;   6.00000E+03
 N REF:0 !
```

# Cu-Zn-Pb-Sn .tdb file

```
$ From database: CUSNZN
 ELEMENT /-   ELECTRON_GAS          0.0000E+00  0.0000E+00  0.0000E+00!
 ELEMENT VA   VACUUM                0.0000E+00  0.0000E+00  0.0000E+00!
 ELEMENT CU   FCC_A1                6.3546E+01  5.0041E+03  3.3150E+01!
 ELEMENT PB   FCC_A1                2.0720E+02  6.8785E+03  6.4785E+01!
 ELEMENT SN   BCT_A5                1.1869E+02  6.3230E+03  5.1180E+01!
 ELEMENT ZN   HCP_ZN                6.5380E+01  5.6567E+03  4.1631E+01!


 FUNCTION GHSERCU    2.98000E+02  -7770.458+130.485235*T-24.112392*T*LN(T)
    -.00265684*T**2+1.29223E-07*T**3+52478*T**(-1);  1.35777E+03  Y
     -13542.026+183.803828*T-31.38*T*LN(T)+3.64167E+29*T**(-9);
    3.20000E+03  N !
 FUNCTION GHSERSN    1.00000E+02  -7958.517+122.765451*T-25.858*T*LN(T)
    +5.1185E-04*T**2-3.192767E-06*T**3+18440*T**(-1);  2.50000E+02  Y
     -5855.135+65.443315*T-15.961*T*LN(T)-.0188702*T**2+3.121167E-06*T**3
    -61960*T**(-1);  5.05070E+02  Y
     +2524.724+4.005269*T-8.2590486*T*LN(T)-.016814429*T**2
    +2.623131E-06*T**3-1081244*T**(-1)-1.2307E+25*T**(-9);  8.00000E+02  Y
     -8256.959+138.99688*T-28.4512*T*LN(T)-1.2307E+25*T**(-9);  3.00000E+03
     N !
 FUNCTION GFCCZN     2.98150E+02  +2969.82-1.56968*T+GHSERZN#;   6.00000E+03
      N !
 FUNCTION GBCCCU     2.98150E+02  +4017-1.255*T+GHSERCU#;   6.00000E+03   N !
 FUNCTION GBCCZN     2.98150E+02  +2886.96-2.5104*T+GHSERZN#;   6.00000E+03
     N !
 FUNCTION GHSERZN    2.98000E+02  -7285.787+118.470069*T-23.701314*T*LN(T)
    -.001712034*T**2-1.264963E-06*T**3;  6.93000E+02  Y
     -11070.559+172.34566*T-31.38*T*LN(T)+4.70514E+26*T**(-9);  1.70000E+03
     N !
 FUNCTION GHSERPB    2.98000E+02  -7650.085+101.715188*T-24.5242231*T*LN(T)
    -.00365895*T**2-2.4395E-07*T**3;  6.01000E+02  Y
     -10531.115+154.258155*T-32.4913959*T*LN(T)+.00154613*T**2
    +8.05644E+25*T**(-9);  1.20000E+03  Y
     +4157.596+53.154045*T-18.9640637*T*LN(T)-.002882943*T**2
    +9.8144E-08*T**3-2696755*T**(-1)+8.05644E+25*T**(-9);  2.10000E+03  N !
 FUNCTION L0FCUPB    2.98150E+02  +45684+5.151*T;   6.00000E+03   N !
 FUNCTION L0FPBZN    2.98150E+02  32873;   6.00000E+03   N !
 FUNCTION L0HCP      2.98150E+02  50000;   6.00000E+03   N !
 FUNCTION UN_ASS 298.15 0; 300 N !

 TYPE_DEFINITION % SEQ *!
 DEFINE_SYSTEM_DEFAULT ELEMENT 2 !
 DEFAULT_COMMAND DEF_SYS_ELEMENT VA /- !


 PHASE LIQ:L %  1  1.0  !
   CONSTITUENT LIQ:L :CU,PB,SN,ZN :  !

  PARAMETER G(LIQ,CU;0)  2.98000E+02  +5194.277+120.973331*T
 -24.112392*T*LN(T)-.00265684*T**2+1.29223E-07*T**3+52478*T**(-1)
 -5.8489E-21*T**7;  1.35777E+03  Y
  -46.545+173.881484*T-31.38*T*LN(T);  3.20000E+03  N REF0 !
  PARAMETER G(LIQ,PB;0)  2.98000E+02  -2977.961+93.949561*T
 -24.5242231*T*LN(T)-.00365895*T**2-2.4395E-07*T**3-6.019E-19*T**7;
 6.01000E+02  Y
  -5677.958+146.176046*T-32.4913959*T*LN(T)+.00154613*T**2;  1.20000E+03  Y
  +9010.753+45.071937*T-18.9640637*T*LN(T)-.002882943*T**2+9.8144E-08*T**3
 -2696755*T**(-1);  2.10000E+03  N REF0 !
  PARAMETER G(LIQ,SN;0)  1.00000E+02  -855.425+108.677684*T-25.858*T*LN(T)
 +5.1185E-04*T**2-3.192767E-06*T**3+18440*T**(-1)+1.47031E-18*T**7;
 2.50000E+02  Y
  +1247.957+51.355548*T-15.961*T*LN(T)-.0188702*T**2+3.121167E-06*T**3
 -61960*T**(-1)+1.47031E-18*T**7;  5.05070E+02  Y
  +9496.31-9.809114*T-8.2590486*T*LN(T)-.016814429*T**2+2.623131E-06*T**3
 -1081244*T**(-1);  8.00000E+02  Y
  -1285.372+125.182498*T-28.4512*T*LN(T);  3.00000E+03  N REF0 !
  PARAMETER G(LIQ,ZN;0)  2.98000E+02  -128.574+108.177079*T
 -23.701314*T*LN(T)-.001712034*T**2-1.264963E-06*T**3-3.58958E-19*T**7;
```

```
6.92680E+02  Y
 -3620.391+161.608594*T-31.38*T*LN(T);  1.70000E+03  N REF0 !
 PARAMETER G(LIQ,CU,SN;0)  2.98150E+02  -8124-6.553*T;   6.00000E+03   N
REF0 !
 PARAMETER G(LIQ,CU,SN;1)  2.98150E+02  -23970+7.037*T;   6.00000E+03   N
REF0 !
 PARAMETER G(LIQ,CU,SN;2)  2.98150E+02  -25124+13.566*T;   6.00000E+03   N
REF0 !
 PARAMETER G(LIQ,CU,SN;3)  2.98150E+02  -10213+10.042*T;   6.00000E+03   N
REF0 !
 PARAMETER G(LIQ,CU,SN,ZN;0)  2.98150E+02  -60000+50*T;   6.00000E+03   N
REF0 !
 PARAMETER G(LIQ,CU,SN,ZN;1)  2.98150E+02  40000;   6.00000E+03   N REF0 !
 PARAMETER G(LIQ,CU,SN,ZN;2)  2.98150E+02  60000;   6.00000E+03   N REF0 !
 PARAMETER G(LIQ,CU,ZN;0)  2.98150E+02  -40696+12.653*T;   6.00000E+03   N
REF0 !
 PARAMETER G(LIQ,CU,ZN;1)  2.98150E+02  +4403-6.554*T;   6.00000E+03   N
REF0 !
 PARAMETER G(LIQ,CU,ZN;2)  2.98150E+02  +7818-3.254*T;   6.00000E+03   N
REF0 !
 PARAMETER G(LIQ,CU,PB;0)  2.98150E+02  +31008-7.195*T;   6.00000E+03   N
REF0 !
 PARAMETER G(LIQ,CU,PB;1)  2.98150E+02  +15345-10.826*T;   6.00000E+03   N
REF0 !
 PARAMETER G(LIQ,CU,PB;2)  2.98150E+02  -6493+5.947*T;   6.00000E+03   N
REF0 !
 PARAMETER G(LIQ,CU,PB;3)  2.98150E+02  -18416+13.16*T;   6.00000E+03   N
REF0 !
 PARAMETER G(LIQ,CU,PB,ZN;0)  2.98150E+02  37000;   6.00000E+03   N REF0 !
 PARAMETER G(LIQ,CU,PB,ZN;1)  2.98150E+02  +40000-50*T;   6.00000E+03   N
REF0 !
 PARAMETER G(LIQ,CU,PB,ZN;2)  2.98150E+02  +30*T;   6.00000E+03   N REF0 !
 PARAMETER G(LIQ,PB,ZN;0)  2.98150E+02  +23259-3.687*T;   6.00000E+03   N
REF0 !
 PARAMETER G(LIQ,PB,ZN;1)  2.98150E+02  -44-2.962*T;   6.00000E+03   N
REF0 !
 PARAMETER G(LIQ,PB,ZN;2)  2.98150E+02  -4987+6.818*T;   6.00000E+03   N
REF0 !
 PARAMETER G(LIQ,PB,ZN;3)  2.98150E+02  -9978+8.2*T;   6.00000E+03   N
REF0 !
 PARAMETER G(LIQ,PB,ZN;4)  2.98150E+02  +13275-10.2*T;   6.00000E+03   N
REF0 !
 PARAMETER G(LIQ,SN,ZN;0)  2.98150E+02  +19315-75.899*T+8.7514*T*LN(T);
6.00000E+03   N REF0 !
 PARAMETER G(LIQ,SN,ZN;1)  2.98150E+02  -5696+4.202*T;   6.00000E+03   N
REF0 !
 PARAMETER G(LIQ,SN,ZN;2)  2.98150E+02  +1037+.984*T;   6.00000E+03   N
REF0 !

TYPE_DEFINITION & GES A_P_D BCC_A2 MAGNETIC  -1.0    4.00000E-01 !
PHASE BCC_A2  %&  2 1   3 !
  CONSTITUENT BCC_A2  :CU,PB,SN,ZN : VA :  !

 PARAMETER G(BCC_A2,CU:VA;0)  2.98150E+02  +GBCCCU#;   6.00000E+03   N
REF0 !
 PARAMETER G(BCC_A2,PB:VA;0)  2.98000E+02  +2400-1.1*T+GHSERPB#;
2.10000E+03  N REF0 !
 PARAMETER G(BCC_A2,SN:VA;0)  2.98150E+02  +4400-6*T+GHSERSN#;
3.00000E+03  N REF0 !
 PARAMETER G(BCC_A2,ZN:VA;0)  2.98150E+02  +GBCCZN#;   6.00000E+03   N
REF0 !
 PARAMETER G(BCC_A2,CU,SN:VA;0)  2.98150E+02  -44822+51.216*T;
6.00000E+03   N REF0 !
 PARAMETER G(BCC_A2,CU,SN:VA;1)  2.98150E+02  -6877-56.427*T;
6.00000E+03   N REF0 !
 PARAMETER G(BCC_A2,CU,SN,ZN:VA;0)  2.98150E+02  -5000-100*T;
6.00000E+03   N REF0 !
 PARAMETER G(BCC_A2,CU,SN,ZN:VA;1)  2.98150E+02  420000;   6.00000E+03   N
REF0 !
 PARAMETER G(BCC_A2,CU,SN,ZN:VA;2)  2.98150E+02  +90000-130*T;
6.00000E+03   N REF0 !
```

```
 PARAMETER G(BCC_A2,CU,ZN:VA;0)  2.98150E+02  -51596+13.064*T;
6.00000E+03   N REF0 !
 PARAMETER G(BCC_A2,CU,ZN:VA;1)  2.98150E+02  +7562-6.454*T;   6.00000E+03
  N REF0 !
 PARAMETER G(BCC_A2,CU,ZN:VA;2)  2.98150E+02  +30744-29.915*T;
6.00000E+03   N REF0 !
 PARAMETER G(BCC_A2,CU,PB:VA;0)  2.98150E+02  +L0FCUPB#;   6.00000E+03   N
REF0 !
 PARAMETER G(BCC_A2,CU,PB,ZN:VA;0)  2.98150E+02  20000;   6.00000E+03   N
REF0 !
 PARAMETER G(BCC_A2,PB,ZN:VA;0)  2.98150E+02  +L0FPBZN#;   6.00000E+03   N
REF0 !
 PARAMETER G(BCC_A2,SN,ZN:VA;0)  2.98150E+02  +80*T;   6.00000E+03   N
REF0 !

PHASE CU10SN3_ZETA  %  2 .769   .231 !
  CONSTITUENT CU10SN3_ZETA  :CU : SN :  !

 PARAMETER G(CU10SN3_ZETA,CU:SN;0)  2.98150E+02  -6353-1.8*T+.769*GHSERCU#
+.231*GHSERSN#;  3.00000E+03  N REF0 !

PHASE CU3SN_EPSILON  %  2 .75   .25 !
  CONSTITUENT CU3SN_EPSILON  :CU : SN :  !

 PARAMETER G(CU3SN_EPSILON,CU:SN;0)  2.98150E+02  -8194.2-.2034*T
+.75*GHSERCU#+.25*GHSERSN#;  3.00000E+03  N REF0 !

PHASE CU41SN11_DELTA  %  2 .788   .212 !
  CONSTITUENT CU41SN11_DELTA  :CU : SN :  !

 PARAMETER G(CU41SN11_DELTA,CU:SN;0)  2.98150E+02  -6323.5-1.2808*T
+.788*GHSERCU#+.212*GHSERSN#;  3.00000E+03  N REF0 !

TYPE_DEFINITION ' GES A_P_D FCC_A1 MAGNETIC  -3.0    2.80000E-01 !
PHASE FCC_A1  %'  2 1   1 !
  CONSTITUENT FCC_A1  :CU,PB,SN,ZN : VA :  !

 PARAMETER G(FCC_A1,CU:VA;0)  2.98150E+02  +GHSERCU#;   6.00000E+03   N
REF0 !
 PARAMETER G(FCC_A1,PB:VA;0)  2.98000E+02  +GHSERPB#;  2.10000E+03  N REF0 !
 PARAMETER G(FCC_A1,SN:VA;0)  2.98150E+02  +4150-5.2*T+GHSERSN#;
3.00000E+03  N REF0 !
 PARAMETER G(FCC_A1,ZN:VA;0)  2.98150E+02  +GFCCZN#;   6.00000E+03   N
REF0 !
 PARAMETER G(FCC_A1,CU,SN:VA;0)  2.98150E+02  -10672-1.484*T;
6.00000E+03   N REF0 !
 PARAMETER G(FCC_A1,CU,SN:VA;1)  2.98150E+02  -15331+6.954*T;
6.00000E+03   N REF0 !
 PARAMETER G(FCC_A1,CU,SN,ZN:VA;0)  2.98150E+02  -25000;   6.00000E+03   N
REF0 !
 PARAMETER G(FCC_A1,CU,SN,ZN:VA;1)  2.98150E+02  10000;   6.00000E+03   N
REF0 !
 PARAMETER G(FCC_A1,CU,SN,ZN:VA;2)  2.98150E+02  10000;   6.00000E+03   N
REF0 !
 PARAMETER G(FCC_A1,CU,ZN:VA;0)  2.98150E+02  -42804+10.023*T;
6.00000E+03   N REF0 !
 PARAMETER G(FCC_A1,CU,ZN:VA;1)  2.98150E+02  +2936-3.053*T;   6.00000E+03
  N REF0 !
 PARAMETER G(FCC_A1,CU,ZN:VA;2)  2.98150E+02  +9034-5.393*T;   6.00000E+03
  N REF0 !
 PARAMETER G(FCC_A1,CU,PB:VA;0)  2.98150E+02  +L0FCUPB#;   6.00000E+03   N
REF0 !
 PARAMETER G(FCC_A1,CU,PB,ZN:VA;0)  2.98150E+02  50000;   6.00000E+03   N
REF0 !
 PARAMETER G(FCC_A1,PB,ZN:VA;0)  2.98150E+02  +L0FPBZN#;   6.00000E+03   N
REF0 !
 PARAMETER G(FCC_A1,SN,ZN:VA;0)  2.98150E+02  +80*T;   6.00000E+03   N
REF0 !

PHASE GAMMA  %  1  1.0  !
  CONSTITUENT GAMMA  :CU,SN,ZN :  !
```

```
 PARAMETER G(GAMMA,CU;0)  2.98150E+02  +10+GHSERCU#;   6.00000E+03   N
REF0 !
 PARAMETER G(GAMMA,SN;0)  2.98150E+02  +10+GHSERSN#;  3.00000E+03  N REF0 !
 PARAMETER G(GAMMA,ZN;0)  2.98150E+02  +10+GHSERZN#;   6.00000E+03   N
REF0 !
 PARAMETER G(GAMMA,CU,SN;0)  2.98150E+02  +40039-32.912*T;   6.00000E+03
N REF0 !
 PARAMETER G(GAMMA,CU,SN;1)  2.98150E+02  -232532+135.367*T;   6.00000E+03
 N REF0 !
 PARAMETER G(GAMMA,CU,SN;2)  2.98150E+02  +210180-129.043*T;   6.00000E+03
 N REF0 !
 PARAMETER G(GAMMA,CU,SN,ZN;0)  2.98150E+02  -315000;   6.00000E+03   N
REF0 !
 PARAMETER G(GAMMA,CU,SN,ZN;1)  2.98150E+02  -65000;   6.00000E+03   N
REF0 !
 PARAMETER G(GAMMA,CU,SN,ZN;2)  2.98150E+02  95000;   6.00000E+03   N REF0 !
 PARAMETER G(GAMMA,CU,ZN;0)  2.98150E+02  -39470+9.436*T;   6.00000E+03
N REF0 !
 PARAMETER G(GAMMA,CU,ZN;1)  2.98150E+02  +36675-5.196*T;   6.00000E+03
N REF0 !
 PARAMETER G(GAMMA,CU,ZN;2)  2.98150E+02  +90163-32.62*T;   6.00000E+03
N REF0 !
 PARAMETER G(GAMMA,SN,ZN;0)  2.98150E+02  50000;   6.00000E+03   N REF0 !

PHASE GAMSOL  %  1  1.0  !
  CONSTITUENT GAMSOL  :CU,ZN :  !

 PARAMETER G(GAMSOL,CU;0)  2.98150E+02  +10+GHSERCU#;   6.00000E+03   N
REF0 !
 PARAMETER G(GAMSOL,ZN;0)  2.98150E+02  +10+GHSERZN#;   6.00000E+03   N
REF0 !
 PARAMETER G(GAMSOL,CU,ZN;0)  2.98150E+02  -39470+9.436*T;   6.00000E+03
N REF0 !
 PARAMETER G(GAMSOL,CU,ZN;1)  2.98150E+02  +36675-5.196*T;   6.00000E+03
N REF0 !
 PARAMETER G(GAMSOL,CU,ZN;2)  2.98150E+02  +90163-32.62*T;   6.00000E+03
N REF0 !

PHASE HCP_A3  %  2 1   .5 !
  CONSTITUENT HCP_A3  :CU,PB,ZN : VA :  !

 PARAMETER G(HCP_A3,CU:VA;0)  2.98150E+02  +600+.2*T+GHSERCU#;
6.00000E+03   N REF0 !
 PARAMETER G(HCP_A3,PB:VA;0)  2.98000E+02  +300+T+GHSERPB#;  2.10000E+03
N REF0 !
 PARAMETER G(HCP_A3,ZN:VA;0)  2.98150E+02  +2970-1.57*T+GHSERZN#;
6.00000E+03   N REF0 !
 PARAMETER G(HCP_A3,CU,PB:VA;0)  2.98150E+02  +L0HCP#;   6.00000E+03   N
REF0 !
 PARAMETER G(HCP_A3,CU,ZN:VA;0)  2.98150E+02  -36475+4.896*T;
6.00000E+03   N REF0 !
 PARAMETER G(HCP_A3,CU,ZN:VA;1)  2.98150E+02  +24790-10.135*T;
6.00000E+03   N REF0 !
 PARAMETER G(HCP_A3,PB,ZN:VA;0)  2.98150E+02  +L0HCP#;   6.00000E+03   N
REF0 !

PHASE HCP_ZN  %  1  1.0  !
  CONSTITUENT HCP_ZN  :CU,PB,ZN :  !

 PARAMETER G(HCP_ZN,CU;0)  2.98150E+02  +600+.2*T+GHSERCU#;   6.00000E+03
 N REF0 !
 PARAMETER G(HCP_ZN,PB;0)  2.98000E+02  +300+T+GHSERPB#;  2.10000E+03  N
REF0 !
 PARAMETER G(HCP_ZN,ZN;0)  2.98150E+02  +GHSERZN#;   6.00000E+03   N REF0 !
 PARAMETER G(HCP_ZN,CU,ZN;0)  2.98150E+02  -14432-10.781*T;   6.00000E+03
 N REF0 !
 PARAMETER G(HCP_ZN,CU,PB;0)  2.98150E+02  50000;   6.00000E+03   N REF0 !
 PARAMETER G(HCP_ZN,PB,ZN;0)  2.98150E+02  39436;   6.00000E+03   N REF0 !
```

# Cu-Zn-Si .tdb file

```
ELEMENT /-   ELECTRON_GAS              0.0000E+00  0.0000E+00  0.0000E+00!
 ELEMENT VA   VACUUM                   0.0000E+00  0.0000E+00  0.0000E+00!
 ELEMENT CU   FCC_A1                   6.3546E+01  5.0041E+03  3.3150E+01!
 ELEMENT SI   DIAMOND_A4               2.8085E+01  3.2175E+03  1.8820E+01!
 ELEMENT ZN   HCP_A3                   6.5380E+01  5.6567E+03  4.1631E+01!

 SPECIES CU2                    CU2!
 SPECIES SI1                    SI!
 SPECIES SI2                    SI2!
 SPECIES SI3                    SI3!

 FUNCTION UCUSI     298.15 0.0;        6000   N !
 FUNCTION GCU3SI    298.15  +3*UCUSI#;  6000   N !
 FUNCTION GCUSI3    298.15  +3*UCUSI#;  6000   N !
 FUNCTION GCU2SI2   298.15  +4*UCUSI#;  6000   N !
 FUNCTION LCUSI0    298.15 0.0;        6000   N !
 FUNCTION LCUSI1    298.15 0.0;        6000   N !
 FUNCTION UCUZN     298.15 0.0;        6000   N !
 FUNCTION GCU3ZN    298.15  +3*UCUZN#;  6000   N !
 FUNCTION GCUZN3    298.15  +3*UCUZN#;  6000   N !
 FUNCTION GCU2ZN2   298.15  +4*UCUZN#;  6000   N !
 FUNCTION LCUZN0    298.15 0.0;        6000   N !
 FUNCTION LCUZN1    298.15 0.0;        6000   N !
 FUNCTION USIZN     298.15 0.0;        6000   N !
 FUNCTION SIZN3     298.15  +3*USIZN#;  6000   N !
 FUNCTION SI2ZN2    298.15  +4*USIZN#;  6000   N !
 FUNCTION SI3ZN     298.15  +3*USIZN#;  6000   N !
 FUNCTION LSIZN0    298.15 0.0;        6000   N !
 FUNCTION LSIZN1    298.15 0.0;        6000   N !

 FUNCTION GB2ZNVA   2.98150E+02  25222.7027;  6.00000E+03   N !
 FUNCTION LB2ZNVA   2.98150E+02  -2257.4895;  6.00000E+03   N !

 FUNCTION GHSERCU   298.15  -7770.458+130.485235*T-24.112392*T*LN(T)
   -.00265684*T**2+1.29223E-07*T**3+52478*T**(-1);  1.35777E+03  Y
    -13542.026+183.803828*T-31.38*T*LN(T)+3.64167E+29*T**(-9);
   3.20000E+03  N !
 FUNCTION GHSERSI   298.15  -8162.609+137.236859*T-22.8317533*T*LN(T)
   -.001912904*T**2-3.552E-09*T**3+176667*T**(-1);  1.68700E+03  Y
    -9457.642+167.281367*T-27.196*T*LN(T)-4.20369E+30*T**(-9);
   3.60000E+03  N !
 FUNCTION GHSERZN   298.15  -7285.787+118.470069*T-23.701314*T*LN(T)
   -.001712034*T**2-1.264963E-06*T**3;  6.92680E+02  Y
    -11070.559+172.34566*T-31.38*T*LN(T)+4.70514E+26*T**(-9);  1.70000E+03
    N !
 FUNCTION GLIQCU    298.15  +5194.277+120.973331*T-24.112392*T*LN(T)
   -.00265684*T**2+1.29223E-07*T**3+52478*T**(-1)-5.8489E-21*T**7;
   1.35777E+03  Y
    -46.545+173.881484*T-31.38*T*LN(T);  3.20000E+03  N !
 FUNCTION GLIQSI    298.15  +42533.751+107.13742*T-22.8317533*T*LN(T)
   -.001912904*T**2-3.552E-09*T**3+176667*T**(-1)+2.0931E-21*T**7;
   1.68700E+03  Y
    +40370.523+137.722298*T-27.196*T*LN(T);  3.60000E+03  N !
 FUNCTION GLIQZN    298.15  -128.574+108.177079*T-23.701314*T*LN(T)
   -.001712034*T**2-1.264963E-06*T**3-3.58958E-19*T**7;  6.92680E+02  Y
    -3620.391+161.608594*T-31.38*T*LN(T);  1.70000E+03  N !

 FUNCTION GBCCCU    298.15  +4017-1.255*T+GHSERCU#;  6000   N !
 FUNCTION GHCPCU    298.15  +600+.2*T+GHSERCU#;      6000   N !

 FUNCTION GBCCSI    298.15  +47000-22.5*T+GHSERSI#;  3.60000E+03  N !
 FUNCTION GFCCSI    298.15  +51000-21.8*T+GHSERSI#;  3.60000E+03  N !
 FUNCTION GHCPSI    298.15  +49200-20.8*T+GHSERSI#;  3.60000E+03  N !

 FUNCTION GBCCZN    298.15  +2886.96-2.5104*T+GHSERZN#;  6000   N !
 FUNCTION GFCCZN    298.15  +2969.82-1.56968*T+GHSERZN#;  6000   N !
 FUNCTION GHCPZN    298.15  +2970-1.57*T+GHSERZN#;       6000   N !

 TYPE_DEFINITION % SEQ *!
```

```
 DEFINE_SYSTEM_DEFAULT SPECIE 2 !
 DEFAULT_COMMAND DEF_SYS_ELEMENT VA !
$
 PHASE HCP_ZN  %  2 1   .5 !
   CONSTITUENT HCP_ZN  :CU,SI,ZN% : VA% :  !

  PARAMETER G(HCP_ZN,CU:VA;0)  298.15  +600+.2*T+GHSERCU#;     6000   N  !
  PARAMETER G(HCP_ZN,SI:VA;0)  298.15  +49201-20.8*T+GHSERSI#;  6000   N  !
  PARAMETER G(HCP_ZN,ZN:VA;0)  298.15  +GHSERZN#;            6000   N !
  PARAMETER G(HCP_ZN,CU,SI:VA;0)  298.15  1E-04;             6000   N  !
  PARAMETER G(HCP_ZN,CU,ZN:VA;0)  298.15  -14432.17-10.7814*T;  6000   N  !
  PARAMETER G(HCP_ZN,SI,ZN:VA;0)  298.15  +80*T;             6000   N  !
$
 PHASE DIAMOND_A4  %  1  1.0  !
   CONSTITUENT DIAMOND_A4  :SI%,ZN :  !

  PARAMETER G(DIAMOND_A4,SI;0)  298.15  +GHSERSI#;      6000   N  !
  PARAMETER G(DIAMOND_A4,ZN;0)  298.15  +30*T+GHSERZN#;  6000   N  !
  PARAMETER G(DIAMOND_A4,SI,ZN;0)  298.15  +100*T;       6000   N  !
$
 PHASE LIQUID  %  1  1.0  !
   CONSTITUENT LIQUID  :CU,SI,ZN :  !

  PARAMETER G(LIQUID,CU;0)  298.15  +5194.277+120.973331*T
 -24.112392*T*LN(T)-.00265684*T**2+1.29223E-07*T**3+52478*T**(-1)
 -5.8489E-21*T**7;  1.35777E+03  Y
  -46.545+173.881484*T-31.38*T*LN(T);  3.20000E+03  N  !
  PARAMETER G(LIQUID,SI;0)  298.15  +50696.4-30.0994*T
 +2.09307E-21*T**7+GHSERSI#;  1.68700E+03  Y
  +49828.2-29.5591*T+4.20369E+30*T**(-9)+GHSERSI#;        6000  N  !
  PARAMETER G(LIQUID,ZN;0)  298.15  -128.574+108.177079*T
 -23.701314*T*LN(T)-.001712034*T**2-1.264963E-06*T**3-3.58958E-19*T**7;
 6.92680E+02  Y
  -3620.391+161.608594*T-31.38*T*LN(T);  1.70000E+03  N  !
  PARAMETER G(LIQUID,CU,SI;0)  298.15  -38763.5+12*T;       6000   N  !
  PARAMETER G(LIQUID,CU,SI;1)  298.15  -52431.2+27.4571*T;   6000   N  !
  PARAMETER G(LIQUID,CU,SI;2)  298.15  -29426.5+14.775*T;    6000   N  !

  PARAMETER G(LIQUID,CU,ZN;0)  298.15  -8.96870901E+04+369.491938*T
     -44.5741924*T*LN(T);  6000   N  !
  PARAMETER G(LIQUID,CU,ZN;1)  298.15  -4.75592380E+03+2.19826283*T; 6000 N !
  PARAMETER G(LIQUID,CU,ZN;2)  298.15  1.05130673E+04-6.77908806*T;  6000 N !

  PARAMETER G(LIQUID,SI,ZN;0)  298.15  +7829.25;          6000   N  !
  PARAMETER G(LIQUID,SI,ZN;1)  298.15  -3338.18;          6000   N  !
  PARAMETER G(LIQUID,SI,ZN;2)  298.15  -891.33;           6000   N  !
$
 TYPE_DEFINITION * GES A_P_D FCC_A1 MAGNETIC  -3.0    2.80000E-01 !
 PHASE FCC_A1  %*  2 1   1 !
   CONSTITUENT FCC_A1  :CU%,SI,ZN : VA% :  !

  PARAMETER G(FCC_A1,CU:VA;0)  298.15  +GHSERCU#;            6000   N  !
  PARAMETER G(FCC_A1,SI:VA;0)  298.15  +51000-21.8*T+GHSERSI#;  6000   N  !
  PARAMETER G(FCC_A1,ZN:VA;0)  198.15  +2969.82-1.56968*T+GHSERZN#;
 1.70000E+03  N  !
  PARAMETER G(FCC_A1,CU,SI:VA;0)  298.15  -42203.5+13.89137*T;  6000   N  !
  PARAMETER G(FCC_A1,CU,SI:VA;1)  298.15  -1102.2-18.177912*T;  6000   N  !

  PARAMETER G(FCC_A1,CU,ZN:VA;0)  298.15  -42803.75+10.02258*T; 6000   N  !
  PARAMETER G(FCC_A1,CU,ZN:VA;1)  298.15  +2936.39-3.05323*T;   6000   N  !
  PARAMETER G(FCC_A1,CU,ZN:VA;2)  298.15  +9034.2-5.39314*T;    6000   N  !
  PARAMETER G(FCC_A1,SI,ZN:VA;0)  298.15  +80*T;              6000   N  !

$ THIS PHASE HAS A DISORDERED CONTRIBUTION FROM FCC_A1
 TYPE_DEFINITION ) GES AMEND_PHASE_DESCRIPTION L12 DIS_PART FCC_A1,,,!
 PHASE L12  %)  3 .75   .25   1 !
   CONSTITUENT L12  :CU%,SI,ZN : CU%,SI,ZN : VA% :  !

     PARA G(L12,CU:CU:VA;0) 298.15 0; 6000 N!
     PARA G(L12,SI:CU:VA;0) 298.15 0; 6000 N!
     PARA G(L12,ZN:CU:VA;0) 298.15 0; 6000 N!
```

```
     PARA G(L12,CU:SI:VA;0) 298.15 0; 6000 N!
     PARA G(L12,SI:SI:VA;0) 298.15 0; 6000 N!
     PARA G(L12,ZN:SI:VA;0) 298.15 0; 6000 N!
     PARA G(L12,CU:ZN:VA;0) 298.15 0; 6000 N!
     PARA G(L12,SI:ZN:VA;0) 298.15 0; 6000 N!
     PARA G(L12,ZN:ZN:VA;0) 298.15 0; 6000 N!
  PARAMETER G(L12,SI,ZN:CU:VA;0)  298.15  +6*USIZN#;   6000   N  !
  PARAMETER G(L12,CU,ZN:SI:VA;0)  298.15  +6*UCUZN#;   6000   N  !
  PARAMETER G(L12,CU,SI:ZN:VA;0)  298.15  +6*UCUSI#;   6000   N  !
$
 TYPE_DEFINITION ' GES A_P_D BCC_A2 MAGNETIC  -1.0    4.00000E-01 !
 PHASE BCC_A2  %'  2 1   3 !
   CONSTITUENT BCC_A2  :CU,SI,VA,ZN : VA :  !

  PARAMETER G(BCC_A2,CU:VA;0)  298.15  +GBCCCU#;             6000   N  !
  PARAMETER G(BCC_A2,SI:VA;0)  298.15  +47000-22.5*T+GHSERSI#;  6000   N  !
     PARA G(BCC_A2,VA:VA;0)  298.15 0;                  6000   N  !
  PARAMETER G(BCC_A2,ZN:VA;0)  298.15  +GBCCZN#;             6000   N  !

  PARAMETER G(BCC_A2,CU,VA:VA;0)  298.15  100000;            6000   N  !
  PARAMETER G(BCC_A2,CU,SI:VA;0)  298.15  -26447.3+10.21623*T;  6000   N  !
  PARAMETER G(BCC_A2,CU,SI:VA;1)  298.15  -47275.11-8.517323*T; 6000   N  !

  PARAMETER L(BCC_A2,CU,ZN:VA;0)  298.15  -51932.7966+13.481258*T; 6000 N !
  PARAMETER G(BCC_A2,CU,ZN:VA;1)  298.15  +7562.12-6.45432*T;   6000   N  !
  PARAMETER G(BCC_A2,CU,ZN:VA;2)  298.15  +30743.74-29.915*T;   6000   N  !

  PARAMETER G(BCC_A2,SI,VA:VA;0)  298.15  60000;   6000   N  !
  PARAMETER G(BCC_A2,SI,ZN:VA;0)  298.15  +80*T;   6000   N  !
  PARAMETER G(BCC_A2,VA,ZN:VA;0)  298.15  +GB2ZNVA#+LB2ZNVA#;   6000   N  !

$ THIS PHASE HAS A DISORDERED CONTRIBUTION FROM BCC_A2
 TYPE_DEFINITION & GES AMEND_PHASE_DESCRIPTION BCC_B2 DIS_PART BCC_A2,,,!
 PHASE BCC_B2  %&  3 .5   .5   3 !
   CONSTITUENT BCC_B2  :CU,SI,VA,ZN : CU,SI,VA,ZN : VA :  !

     PARA G(BCC_B2,CU:CU:VA;0) 298.15 0; 6000 N!
     PARA G(BCC_B2,SI:CU:VA;0) 298.15 0; 6000 N!
     PARA G(BCC_B2,VA:CU:VA;0) 298.15 0; 6000 N!
 PARAMETER G(BCC_B2,ZN:CU:VA;0) 298.15  -6170;   6000   N  !
     PARA G(BCC_B2,CU:SI:VA;0) 298.15 0; 6000 N!
     PARA G(BCC_B2,SI:SI:VA;0) 298.15 0; 6000 N!
     PARA G(BCC_B2,VA:SI:VA;0) 298.15 0; 6000 N!
     PARA G(BCC_B2,ZN:SI:VA;0) 298.15 0; 6000 N!
     PARA G(BCC_B2,CU:VA:VA;0) 298.15 0; 6000 N!
     PARA G(BCC_B2,SI:VA:VA;0) 298.15 0; 6000 N!
     PARA G(BCC_B2,VA:VA:VA;0) 298.15 0; 6000 N!
 PARAMETER G(BCC_B2,ZN:VA:VA;0) 298.15 +.5*GB2ZNVA#-.5*LB2ZNVA#; 6000 N!
 PARAMETER G(BCC_B2,CU:ZN:VA;0) 298.15  -6170;   6000   N  !
     PARA G(BCC_B2,SI:ZN:VA;0) 298.15 0; 6000 N!
     PARA G(BCC_B2,VA:ZN:VA;0) 298.15 +.5*GB2ZNVA#-.5*LB2ZNVA#; 6000 N!
     PARA G(BCC_B2,ZN:ZN:VA;0) 298.15 0; 6000 N!

$
 TYPE_DEFINITION + GES A_P_D HCP_A3 MAGNETIC  -3.0    2.80000E-01 !
 PHASE HCP_A3  %+  2 1   .5 !
   CONSTITUENT HCP_A3  :CU,SI,ZN% : VA% :  !

  PARAMETER G(HCP_A3,CU:VA;0)  298.15  +600+.2*T+GHSERCU#;     6000   N  !
  PARAMETER G(HCP_A3,SI:VA;0)  298.15  +49200-20.8*T+GHSERSI#;  6000   N  !
  PARAMETER G(HCP_A3,ZN:VA;0)  298.15  +2970-1.57*T+GHSERZN#;   6000   N  !
  PARAMETER G(HCP_A3,CU,SI:VA;0)  298.15  -26798.8-.731518*T;   6000   N  !
  PARAMETER G(HCP_A3,CU,SI:VA;1)  298.15  -28064.75-.028889*T;  6000   N  !
  PARAMETER G(HCP_A3,CU,ZN:VA;0)  298.15  -36475+4.896*T;      6000   N  !
  PARAMETER G(HCP_A3,CU,ZN:VA;1)  298.15  +24790-10.135*T;     6000   N  !
  PARAMETER G(HCP_A3,SI,ZN:VA;0)  298.15  +80*T;             6000   N  !
$
 PHASE CU15SI4_EPSILON  %  2 .789474   .210526 !
   CONSTITUENT CU15SI4_EPSILON  :CU%,ZN : SI :  !

  PARAMETER G(CU15SI4_EPSILON,CU:SI;0)  298.15  +.789474*GHSERCU#
```

```
 +.210526*GHSERSI#+1240.9639-6.7191165*T;  6000  N !
$
 PHASE CU33SI7_DELTA  %  2 .825  .175 !
   CONSTITUENT CU33SI7_DELTA  :CU%,ZN : SI :  !

  PARAMETER G(CU33SI7_DELTA,CU:SI;0)  298.15  +.825*GHSERCU#
 +.175*GHSERSI#+1972.382-6.9663933*T;  6000  N !

$
 PHASE CU56SI11_GAMMA  %  2 .835821  .164179 !
   CONSTITUENT CU56SI11_GAMMA  :CU%,ZN : SI :  !

  PARAMETER G(CU56SI11_GAMMA,CU:SI;0)  298.15  +.835821*GHSERCU#
 +.164179*GHSERSI#+1046.4873-5.8746832*T;  6000  N !
$
 PHASE CUSI_ETA  %  2 .76  .24 !
   CONSTITUENT CUSI_ETA  :CU%,ZN : SI :  !

  PARAMETER G(CUSI_ETA,CU:SI;0)  298.15  +.76*GHSERCU#+.24*GHSERSI#
 +1367.6622-7.1976229*T;  6000  N !
$
 PHASE GAMMA_D83  %  3 4  1  8 !
   CONSTITUENT GAMMA_D83  :ZN,SI : CU,ZN : CU,ZN :  !

  PARAMETER G(GAMMA_D83,ZN:CU:CU;0)  298.15  -5.71302472E+04+1.02562226E+01*T
  +4*GHSERZN#+9*GHSERCU#;  6000  N !
  PARAMETER G(GAMMA_D83,ZN:ZN:CU;0)  298.15  -2.99360592E+04+0*T+5*GHSERZN#
 +8*GHSERCU#;  6000  N !
  PARAMETER G(GAMMA_D83,ZN:CU:ZN;0)  298.15  2.80988568E+04+0*T+12*GHSERZN#
 +GHSERCU#;  6000  N !
  PARAMETER G(GAMMA_D83,ZN:ZN:ZN;0) 298.15  +118432.549+13*GHSERZN#; 6000 N !
$  PARAMETER G(GAMMA_D83,ZN:CU,ZN:CU;0)  298.15  -2.21318711E+05;  6000  N !
  PARAMETER G(GAMMA_D83,ZN:*:CU,ZN;0)  298.15  -4.88548579E+05;  6000  N !
$$
$$
  PARAMETER G(LIQUID,CU,SI,ZN;0)  298.15  +9500;      6000  N !
  PARAMETER G(LIQUID,CU,SI,ZN;1)  298.15  +45535.6149; 6000  N !
  PARAMETER G(LIQUID,CU,SI,ZN;2)  298.15  0;        6000  N !

  PARAMETER G(FCC_A1,CU,SI,ZN:VA;0)  298.15  -93014.29845-65.058687*T;
      6000  N !
  PARAMETER G(FCC_A1,CU,SI,ZN:VA;1)  298.15  196879.031;   6000  N !
  PARAMETER G(FCC_A1,CU,SI,ZN:VA;2)  298.15  0;   6000  N !

  PARAMETER G(BCC_A2,CU,SI,ZN:VA;0)  298.15  -188361.4392+19.8831715*T;
    6000  N !
  PARAMETER G(BCC_A2,CU,SI,ZN:VA;1)  298.15  220413.937;
    6000  N !
  PARAMETER G(BCC_A2,CU,SI,ZN:VA;2)  298.15  0;
    6000  N !

  PARAMETER G(HCP_A3,CU,SI,ZN:VA;0)  298.15  -4.06335688E+05;   6000  N !
  PARAMETER G(HCP_A3,CU,SI,ZN:VA;1)  298.15  1.05957578E+06;   6000  N !
  PARAMETER G(HCP_A3,CU,SI,ZN:VA;2)  298.15  -6.87958658E+04;   6000  N !
$
 PARAMETER G(CU56SI11_GAMMA,ZN:SI;0)  298.15  +.835821*GHSERZN#
 +.164179*GHSERSI#+1.00000000E+04;                      6000  N !
 PARAMETER G(CU56SI11_GAMMA,CU,ZN:SI;0)  298.15  -34279.06+8.42725575*T;
  6000  N !

 PARAMETER G(CU15SI4_EPSILON,ZN:SI;0)  298.15  +.789474*GHSERZN#
 +.210526*GHSERSI#+1.00000000E+04;                      6000  N !
 PARAMETER G(CU15SI4_EPSILON,CU,ZN:SI;0)  298.15  -41972.27
  +23.2043396*T; 6000  N !

 PARAMETER G(CUSI_ETA,ZN:SI;0)  298.15  +.76*GHSERZN#+.24*GHSERSI#
 +1.00000000E+04;                                  6000  N !
 PARAMETER G(CUSI_ETA,CU,ZN:SI;0)  298.15  7.64113763E+04;      6000  N !

 PARAMETER G(CU33SI7_DELTA,ZN:SI;0)  298.15  +.825*GHSERZN#
 +.175*GHSERSI#+1.00000000E+04;  6000  N !
```

```
 PARAMETER G(CU33SI7_DELTA,CU,ZN:SI;0)  298.15 -20202.2993;   6000   N  !
$
 PARAM G(GAMMA_D83,SI:CU:CU;0)    298.15 4*GHSERSI+1*GHSERCU+8*GHSERCU
  +1.87832703E+04-6.14304500E+01*T; 6000 N !
 PARAM G(GAMMA_D83,SI:ZN:CU;0)    298.15 4*GHSERSI+1*GHSERZN+8*GHSERCU
  +64622.0585; 6000 N !
 PARAM G(GAMMA_D83,SI:CU:ZN;0)    298.15 4*GHSERSI+1*GHSERCU+8*GHSERZN
  +211157.998; 6000 N !
 PARAM G(GAMMA_D83,SI:ZN:ZN;0)    298.15 4*GHSERSI+1*GHSERZN+8*GHSERZN
  +56606.2041; 6000 N !
$
 PARAM L(GAMMA_D83,SI,ZN:CU:CU;0)  298.15  -104070.674-100*T; 6000  N !
```

# Appendix C – TOPAS Macro for Rietveld Refinement of Neutron Diffraction Data

The attached input file in this Appendix is an example of the TOPAS macro developed for Rietveld-based parametric refinement of the neutron diffraction data in Chapter 1. It has been modified to realise the sequential batch processing of large data sets collected at the high-intensity powder diffractometer – 'Wombat' at ANSTO.

## Neutron Diffraction TOPAS Macro

```
iters 300
no_LIMIT_warnings
chi2_convergence_criteria 0.00001
do_errors
continue_after_convergence

 #ifndef BATCH
    macro file1 ["C:15]
    macro seqno
                macro type { KEEP }
                macro Temp { 400 }
                macro Composition { 1022 }
                macro Time { 30 }

    macro temp_HSD {capillary_x1}
    macro temp_VSD {capillary_y1}

                #define FCC_alpha
    #define BCC_beta_order
    '#define BCC_beta_disorder
    #define FCC_alpha2

               '#define EXCLUSION
                #define OUTPUT
 #endif
'-------------------------------------------------------------------------------
xdd file1
  r_wp   6.27211603  r_exp   2.6016211  r_p   4.87989808  r_wp_dash   18.9625134  r_p_dash   23.4222208  r_exp_dash   7.86549146
weighted_Durbin_Watson  0.331176584 gof  2.41084915
            bkg @  1164.52216`_3.92373529  285.957471`_5.81517491 -0.367290348`_4.81149914  40.5581428`_4.71496319
            HSD(!temp_HSD,  4.49374_0.64843 min -2.0 max 8 ) ' -0.07897_0.00068 and -0.09119_0.00113 and -0.10404
            VSD(!temp_VSD, -1.35666_0.31601 min -5.0 max 2.0 ) ' -0.02827_0.00086 and -0.01360_0.00152 for LaB6
  start_X  25
  finish_X 140

'********** FCC_alpha str-----------------------------------------------
            #ifdef FCC_alpha
  str ' FCC_alpha
    r_bragg  2.94380867
    phase_MAC  45.5198933
    phase_name "FCC_alpha"
    MVW( 254.184, 51.369`_0.024, 32.638`_1.291)
    scale scale_fcc  10.4126608`_0.5003 min 0.00000001 val_on_continue = Rand(5, 10);
    space_group "Fm-3m"
    Phase_LAC_1_on_cm( 374.02239`_0.17629)
    Phase_Density_g_on_cm3( 8.21668`_0.00387)
    Cubic(a_fcc  3.717353`_0.000584 min =3.65; max =3.75; val_on_continue = Rand(3.65, 3.75);)  '3.646816_0.000476 #120
    site Cu1 num_posns  4 x 0 y 0 z 0  occ Cu  !occ_fcc_Cu  1 min =0.5; max =1.0;   beq  beq_fcc_Cu   2.76261`_0.10786 min =0.3; max =6.0;
              site Zn1 num_posns  4 x 0 y 0 z 0  occ Zn  occ_fcc_Zn =1-occ_fcc_Cu;:  0.00000 beq  beq_fcc_Zn  0.30000`_2.41085 min =0.3;
max =6.0;
```

```
            '------------------------------------------------------------------------
    str_hkl_angle ang_fcc 2 1 1 ' The crystallographic direction
                                    lor_fwhm = (0.1 Rad Lam / (Cos(Th) csl_fcc)) Multiplicities_Sum(((march_fcc_cs^2 Cos(ang_fcc)^2 +
Sin(ang_fcc)^2 / march_fcc_cs)^(-1.5)));
                                    gauss_fwhm = (0.1 Rad Lam / (Cos(Th) csg_fcc)) Multiplicities_Sum(((march_fcc_cs^2 Cos(ang_fcc)^2 +
Sin(ang_fcc)^2 / march_fcc_cs)^(-1.5)));
                                    lor_fwhm   = msl_fcc Tan(Th) Multiplicities_Sum(((march_fcc_ms^2 Cos(ang_fcc)^2 + Sin(ang_fcc)^2 /
march_fcc_ms)^(-1.5)));
                                    gauss_fwhm = msg_fcc Tan(Th) Multiplicities_Sum(((march_fcc_ms^2 Cos(ang_fcc)^2 + Sin(ang_fcc)^2
/ march_fcc_ms)^(-1.5)));
    prm  !march_fcc_cs  1 min = 0.1; max = 2; val_on_continue = Rand(0.7, 1.2); ' March parameter for crystalline size
                        prm  !march_fcc_ms  1 min = 0.1; max = 1; val_on_continue = Rand(0.5, 0.9); ' March parameter for strain
                        prm  csl_fcc  50.00000`_10.11353 min =50; max =5000; val_on_continue = Rand(50, 150);
                        prm  !csg_fcc  5000 min =20; max =5000;
                        prm  !msl_fcc  0.0001 min =0.0001; max =0.9; val_on_continue = Rand(0.0001, 0.5);
                        prm  msg_fcc  0.65416`_0.06998 min =0.0001; max =0.9;              val_on_continue = Rand(0.0001, 0.0005);
                        prm  LVol_IB_fcc = 1.0 / IB_from_CS(csg_fcc, csl_fcc);:  31.91443`_6.46723 ' The reportable crystallite size
                        prm  e0_fcc = Voigt_FWHM_GL(msg_fcc, msl_fcc)/4 * Pi/360;:  0.00143`_0.00015 ' The reportable microstrain
    '------------------------------------------------------------------------
    'Preferred_Orientation(po_fcc, 0.81422_0.01863, ang_po_fcc, 1 1 1)

                        #ifdef OUTPUT
            Out_Quant(occ_fcc_Cu, beq_fcc_Cu, beq_fcc_Zn, LVol_IB_fcc, e0_fcc)
    #endif

  #endif


'********** BCC_beta str----------------------------------------------
            #ifdef BCC_beta_order
  str ' BCC_beta
    r_bragg  1.73216354
    phase_MAC  48.1599141
    phase_name "BCC_beta_order"
    MVW( 128.955, 27.107`_0.008, 64.252`_1.377)
    scale scale_bcc  76.5691852`_2.513 min 0.00000001 val_on_continue = Rand(15, 20);
    space_group "Pm-3m"
    Phase_LAC_1_on_cm(  380.43797`_0.10865)
    Phase_Density_g_on_cm3( 7.89947`_0.00226)
    Cubic(a_bcc  3.003976`_0.000286 min =2.81; max =3.1; val_on_continue = Rand(2.85, 2.95);)

    site Cu1 num_posns  1 x 0 y 0 z 0      occ  Cu !occ_bcc_Cu  0.5 min 0.5 max 1.0        beq  beq_bcc_Cu    5.70129`_156.64466 min =0.3;
max = 10;
    site Zn1 num_posns  1 x 0 y 0 z 0      occ  Zn occ_bcc_Zn  =1 - occ_bcc_Cu;:  0.50000 beq  =beq_bcc_Cu;:  5.70129`_156.64466
    site Cu1 num_posns  1 x 0.5 y 0.5 z 0.5 occ  Cu =1 - occ_bcc_Cu;:  0.50000 beq  =beq_bcc_Zn;:  5.70466`_156.76219
    site Zn1 num_posns  1 x 0.5 y 0.5 z 0.5 occ  Zn =1 - occ_bcc_Zn;:  0.50000 beq  beq_bcc_Zn    5.70466`_156.76219 min =0.3; max =10 ;

            'site  Zn1  num_posns    2  x  0  y  0  z  0  occ  Zn  occ_bcc_Zn  =1-occ_bcc_Cu;:    0.12915_3753080.31691          beq  @
3.00000_58532409.59627 min =0.3; max =3;

            '------------------------------------------------------------------------
    str_hkl_angle ang_bcc 0 3 1 ' The crystallographic direction
                                    lor_fwhm = (0.1 Rad Lam / (Cos(Th) csl_bcc)) Multiplicities_Sum(((march_bcc^2 Cos(ang_bcc)^2 +
Sin(ang_bcc)^2 / march_bcc)^(-1.5)));
                                    gauss_fwhm = (0.1 Rad Lam / (Cos(Th) csg_bcc)) Multiplicities_Sum(((march_bcc^2 Cos(ang_bcc)^2 +
Sin(ang_bcc)^2 / march_bcc)^(-1.5)));
                                    lor_fwhm   = msl_bcc Tan(Th) Multiplicities_Sum(((march_bcc2^2 Cos(ang_bcc)^2 + Sin(ang_bcc)^2 /
march_bcc2)^(-1.5)));
                                    gauss_fwhm = msg_bcc Tan(Th) Multiplicities_Sum(((march_bcc2^2 Cos(ang_bcc)^2 + Sin(ang_bcc)^2 /
march_bcc2)^(-1.5)));
    prm  !march_bcc  1 min = 1; max = 2; val_on_continue = Rand(0.7, 1.2); ' March parameter for crystalline size
    prm  !march_bcc2  1 min = 0.1; max = 1; val_on_continue = Rand(0.5, 0.9); ' March parameter for strain
                        prm  csl_bcc  107.21550`_24.94443 min =20; max =5000; val_on_continue = Rand(50, 150);
                        prm  !csg_bcc  5000 min =20; max =5000;
                        prm  !msl_bcc  0.00010 min =0.0001; max =0.9; val_on_continue = Rand(0.0001, 0.5);
                        prm  msg_bcc  0.00010`_306.57796 min =0.0001; max =0.9;          val_on_continue = Rand(0.0001, 0.0005);
                        prm  LVol_IB_bcc = 1.0 / IB_from_CS(csg_bcc, csl_bcc);:  68.51707`_15.95496 ' The reportable crystallite size
                        prm  e0_bcc = Voigt_FWHM_GL(msg_bcc, msl_bcc)/4 * Pi/360;:  0.00000`_0.62153 ' The reportable microstrain

                        #ifdef OUTPUT
```

```
            Out_Quant(occ_bcc_Cu, beq_bcc_Cu, beq_bcc_Zn, LVol_IB_bcc, e0_bcc)
   #endif

  #endif

 /*
'********** BCC_beta disorder str----------------------------------------------
            #ifdef BCC_beta_disorder
  str ' BCC_beta_disorder
    r_bragg  3.90992777
    phase_MAC  48.1599141
    phase_name "BCC_beta_disorder"
    MVW( 128.955, 25.977_0.013, 27.663_1.805)
    scale scale_bcc  26.6898268_2.351 min 0.00000001 val_on_continue = Rand(15, 20);
    space_group "Im-3m"
    Phase_LAC_1_on_cm( 396.99382_0.19998)
    Phase_Density_g_on_cm3( 8.24324_0.00415)
    Cubic(a_bcc  2.961623_0.000497 min =2.9; max =3.1; val_on_continue = Rand(2.90, 3.10);)
    site Cu1 num_posns  2 x 0 y 0 z 0  occ Cu  !occ_bcc_Cu  0.5 min 0.3 max 1       beq  beq_bcc_disorder_Cu   2.63073_3.16807 min =0.3;
max =6;
             site Zn1 num_posns  2 x 0 y 0 z 0  occ Zn  occ_bcc_Zn =1-occ_bcc_Cu;:  0.50000   beq  beq_bcc_disorder_Zn   1.69423_3.07175
min =0.3; max =6;

    '-------------------------------------------------------------------------
    str_hkl_angle ang_bcc 0 0 2 ' The crystallographic direction
                                        lor_fwhm  = (0.1 Rad  Lam  /  (Cos(Th)  csl_bcc))  Multiplicities_Sum(((march_bcc^2  Cos(ang_bcc)^2  +
Sin(ang_bcc)^2 / march_bcc)^(-1.5)));
                                        gauss_fwhm = (0.1 Rad Lam / (Cos(Th) csg_bcc)) Multiplicities_Sum(((march_bcc^2 Cos(ang_bcc)^2 +
Sin(ang_bcc)^2 / march_bcc)^(-1.5)));
                                        lor_fwhm    = msl_bcc Tan(Th) Multiplicities_Sum(((march_bcc2^2 Cos(ang_bcc)^2 + Sin(ang_bcc)^2 /
march_bcc2)^(-1.5)));
                                        gauss_fwhm = msg_bcc Tan(Th) Multiplicities_Sum(((march_bcc2^2 Cos(ang_bcc)^2 + Sin(ang_bcc)^2 /
march_bcc2)^(-1.5)));
    prm  !march_bcc  1 min = 1; max = 2; val_on_continue = Rand(0.7, 1.2); ' March parameter for crystalline size
    prm  !march_bcc2  1 min = 0.1; max = 1; val_on_continue = Rand(0.5, 0.9); ' March parameter for strain
                            prm  csl_bcc  50.00000_13.92544 min =50; max =5000; val_on_continue = Rand(50, 150);
                            prm  !csg_bcc  5000.00000_30609078.47973 min =20; max =5000;
                            prm  !msl_bcc  0.00010_0.06422 min =0.0001; max =0.9; val_on_continue = Rand(0.0001, 0.5);
                            prm  msg_bcc  0.00010_520.06635 min =0.0001; max =0.9;           val_on_continue = Rand(0.0001, 0.0005);
                            prm  LVol_IB_bcc = 1.0 / IB_from_CS(csg_bcc, csl_bcc);:  31.91443_8.90480 ' The reportable crystallite size
                            prm  e0_bcc = Voigt_FWHM_GL(msg_bcc, msl_bcc)/4 * Pi/360;:  0.00000_1.05433 ' The reportable microstrain
    '-------------------------------------------------------------------------

                            #ifdef OUTPUT
            Out_Quant(occ_bcc_Cu, beq_bcc_disorder_Cu, beq_bcc_disorder_Zn, LVol_IB_bcc, e0_bcc)
    #endif

  #endif
  */
'********** FCC_alpha2 str----------------------------------------------
  #ifdef FCC_alpha2
  str ' FCC_alpha
    r_bragg  2.4625221
    phase_MAC  45.5198933
    phase_name "FCC_alpha2"
    MVW( 254.184, 53.466`_0.121,  3.110`_0.851)
    scale scale_fcc2  0.953260221`_0.2679 min 0.00000001 val_on_continue = Rand(5, 10);
    space_group "Fm-3m"
    Phase_LAC_1_on_cm( 359.35363`_0.80999)
    Phase_Density_g_on_cm3( 7.89443`_0.01779)
    Cubic(a_fcc2  3.767260`_0.002831 min =a_fcc; max =3.80; val_on_continue = Rand(a_fcc, 3.8);)  '3.646816_0.000476 #120
    site Cu1 num_posns  4 x 0 y 0 z 0  occ Cu  !occ_fcc2_Cu  1 min =0.5; max =1.0;   beq  beq_fcc2_Cu   0.46413`_0.41380 min =0.3; max
=10.0;
             site Zn1 num_posns  4 x 0 y 0 z 0  occ Zn  occ_fcc2_Zn =1-occ_fcc_Cu;:  0.00000  beq  beq_fcc2_Zn   0.30000`_2.41085 min =0.3;
max =10.0;

            '-------------------------------------------------------------------------
    str_hkl_angle ang_fcc2 2 1 1 ' The crystallographic direction
                                        lor_fwhm = (0.1 Rad Lam / (Cos(Th) csl_fcc2)) Multiplicities_Sum(((march_fcc2_cs^2 Cos(ang_fcc2)^2 +
Sin(ang_fcc2)^2 / march_fcc2_cs)^(-1.5)));
```

```
                                    gauss_fwhm = (0.1 Rad Lam / (Cos(Th) csg_fcc2)) Multiplicities_Sum(((march_fcc2_cs^2
Cos(ang_fcc2)^2 + Sin(ang_fcc2)^2 / march_fcc2_cs)^(-1.5)));
                                    lor_fwhm = msl_fcc2 Tan(Th) Multiplicities_Sum(((march_fcc2_ms^2 Cos(ang_fcc2)^2 +
Sin(ang_fcc2)^2 / march_fcc2_ms)^(-1.5)));
                                    gauss_fwhm = msg_fcc2 Tan(Th) Multiplicities_Sum(((march_fcc2_ms^2 Cos(ang_fcc2)^2 +
Sin(ang_fcc2)^2 / march_fcc2_ms)^(-1.5)));
    prm !march_fcc2_cs 1 min = 0.1; max = 2; val_on_continue = Rand(0.7, 1.2); ' March parameter for crystalline size
    prm !march_fcc2_ms 1 min = 0.1; max = 1; val_on_continue = Rand(0.5, 0.9); ' March parameter for strain
                        prm csl_fcc2 50.00000`_54.25861 min =50; max =5000; val_on_continue = Rand(50, 150);
                        prm !csg_fcc2 5000.00000_26913408.03492 min =20; max =5000;
                        prm !msl_fcc2 0.00010_0.09021 min =0.0001; max =0.9; val_on_continue = Rand(0.0001, 0.5);
                        prm msg_fcc2 0.90000`_0.30107 min =0.0001; max =0.9; val_on_continue = Rand(0.0001, 0.0005);
                        prm LVol_IB_fcc2 = 1.0 / IB_from_CS(csg_fcc2, csl_fcc2);: 31.91443`_34.69638 ' The reportable crystallite size
                        prm e0_fcc2 = Voigt_FWHM_GL(msg_fcc2, msl_fcc2)/4 * Pi/360;: 0.00196`_0.00066 ' The reportable microstrain
    '------------------------------------------------------------------------

                        #ifdef OUTPUT
            Out_Quant(occ_fcc2_Cu, beq_fcc2_Cu, beq_fcc2_Zn, LVol_IB_fcc2, e0_fcc2)
    #endif

  #endif

'*****************************Instrument Functions**************************************
for xdds {
  neutron_data
            Lorentz_Factor

  lam
                        'ymin_on_ymax 0.0001
                        la 1 lo !bwave_len 1.4706631_8.54415032e-005 val_on_continue = Rand(1.46, 1.48); min 1.45 max 1.5 lg
3.92895_0.80749 min 0.00001

            x_calculation_step = 0.01; 'Yobs_dx_at(Xo);
            'weighting = If(SigmaYobs < 1, 1, 1/SigmaYobs^2);

            Zero_Error(!z_error, 1.14433_0.00173 val_on_continue = Rand(1.1, 1.25); min =-2; max =2;) '0.98985

            Rs 728
            Rp 2100

  Finger_et_al(!finger1 0.07967_0.58478, !finger2 151.29362_2.15066)
            'Simple_Axial_Model(axial_1, 0.00179_862813.73925)
  ' Empirical instrumental width/shape
   'User_Defined_Dependence_Convolution(gauss_fwhm,      1/Cos(Th) ,  UDDC_gfwhm_cos  , 0.00010_42295212.00690)
    User_Defined_Dependence_Convolution(gauss_fwhm,      Tan(Th)  , !UDDC_gfwhm_tan  , 0.60317_0.00449 min 0 max 2)
   'User_Defined_Dependence_Convolution(gauss_fwhm,           , UDDC_gfwhm_con  , 0.00000_888197005.30452 min 0 max 2)
    User_Defined_Dependence_Convolution(gauss_fwhm,      Cos(2 Th) , !UDDC_gfwhm_cos2 , 0.51980_0.01224 min 0 max 2)
   'User_Defined_Dependence_Convolution(lor_fwhm,       Sin(Th)  ,  UDDC_lfwhm_sin  , 0.00010_5.69100)
   'User_Defined_Dependence_Convolution(lor_fwhm,       1/Cos(Th) ,  UDDC_lfwhm_cos  , 0.13176_0.00608)
   'User_Defined_Dependence_Convolution(lor_fwhm,       Tan( Th)  ,  UDDC_lfwhm_tan  , 0.07232_0.01339)
    User_Defined_Dependence_Convolution(lor_fwhm,          , !UDDC_lfwhm_con  , 0.12348_0.00593)
   'User_Defined_Dependence_Convolution(circles_conv,    Sin(Th)  ,  UDDC_cconv_sin  , 0.00010_0.06801)
   'User_Defined_Dependence_Convolution(circles_conv,    Cos(Th)  ,  UDDC_cconv_cos  , 0.00010_0.06434)
   'User_Defined_Dependence_Convolution(circles_conv,    Tan(Th)  ,  UDDC_cconv_tan  , 0.00010_0.18653)
   'User_Defined_Dependence_Convolution(circles_conv,          ,  UDDC_cconv_con  , 0.00010_586.83209)
    User_Defined_Dependence_Convolution(exp_conv_const,  Cos(2 Th) , !UDDC_exp_cosn  , -1.44901_0.03376 min -3 max 0)
   'User_Defined_Dependence_Convolution(hat,          Cos(2 Th) ,  UDDC_hat_cos  , 0.00007_4.78660 min 0 max 2)
   'User_Defined_Dependence_Convolution(hat       ,  Th      ,  UDDC_hat_Th   , 0.01311_0.00199) ' 0.009139
             'User_Defined_Dependence_Convolution(hat       ,  Sin(2 Th) ,  UDDC_hat_sin  , 0.00014_1.46344) ' 0.01589
   'User_Defined_Dependence_Convolution(one_on_x_conv,          ,  UDDC_on_x_con  , 0.00001_0.82756 min 0 max 2)

            '********** Furnace Peaks----------------------------------------------
    xo_Is
      xo fur_hump_1 36.12`_0.0665376731 min 36.12 max 36.5 val_on_continue = Rand(36.12, 36.98); '11.7900718
      I I_fur_hump_1 27.53029`_3.81945 min 0
'     peak_type fp
'           pv_lor fur_hump_lor_1 0.650671076_12027.01 min 0.001 'max 1.5 'val_on_continue = Rand(0.6, 0.8);
'           pv_fwhm fur_hump_fwhm_1 0.0151627778_3.9999031 min 0.001 'max 0.3 'val_on_continue = Rand(10, 20);

    xo_Is
             xo fur_hump_2 36.9279456`_0.0176376906 min 35.7 max 38.1 val_on_continue = Rand(37.1, 38.1); '11.7900718
```

```
            I  I_fur_hump_2  120.14738`_4.91665 min 0
            peak_type fp
 '                  pv_lor   fur_hump_lor_2  0.389278418_5398.33949 min 0.001 'max 0.99  val_on_continue = Rand(0.6, 0.8);
 '                  pv_fwhm  fur_hump_fwhm_2  0.01_3.97737083 min 0.001 'max 0.3 'val_on_continue = Rand(10, 20);

} ' End of for xdds
'*****************************************************************************

' Output Macro ----------------------------------------------------------------
macro Out_Quant(pm1, pm2, pm3, pm4, pm5)
            { out Output_Topas_Brass1_LCL_ebrass.txt append

' Parameters being output to text file
' FileName SeqNo     SetTemp  Time       SetTemp  TCTemp   P1         P2         P3         P4         StartCurr  BeamP1
            BeamP2   BeamP3   BeamP4     Disp1    Disp1Err Disp2      Disp2Err   Cyl_ur     Cyl_urErr  PhaseName            Wt%
            Errwt%   Scale    ErrScale   A        ErrA     B          ErrB       C          Errc       CellVol    ErrCellVol
            XtalSize ErrXtalSize MicroStrain          ErrMicroStrain        Elem1Beq   ErrElem1Beq        OxBeq      ErrOxBeq
            Mix_MAC  Rwp       Type

Out_String("\n")        ' \n means do new line
            Out_String( file1 )
  'Out_String("\t")  ' \t means insert a Tab
  'Out_String("\t")
            Out( seqno                                                              , "\t%10.3f")
            Out( Composition                        , "\t%10.1f")
            Out( Get(phase_name)                , "\t%15s " )  ' \s means a string
            Out( Time                                                   , "\t%10.6f")
            Out( Temp                                                   , "\t%10.1f")
            Out( Get(scale)         , "\t%15.9f","\t%15.9f")
            Out( Get(a)             , "\t%10.6f","\t%10.8f")
            Out( Get(b)             , "\t%10.6f","\t%10.8f")
            Out( Get(c)             , "\t%10.6f","\t%10.8f")
            Out( Get(al)            , "\t%10.4f","\t%10.6f")
            Out( Get(be)            , "\t%10.4f","\t%10.6f")
            Out( Get(ga)            , "\t%10.4f","\t%10.6f")
            Out( Get(cell_volume)   , "\t%10.6f","\t%10.8f")
            Out( Get(cell_mass)     , "\t%10.6f","\t%10.8f")
            Out( Get(weight_percent) , "\t%8.2f","\t%8.3f")         ' the second field is for the parameter error (if do_errors is defined)
            Out( pm1                , "\t%10.6f","\t%10.8f") ' calculated volume fraction
            Out( pm2                , "\t%10.6f","\t%10.8f")
            Out( pm3                , "\t%10.6f","\t%10.8f")
            Out( pm4                , "\t%10.6f","\t%10.8f")
            Out( pm5                , "\t%10.6f","\t%10.8f")
'           Out( pm7                , "\t%10.4f","\t%10.3f")
'           Out( pm8                , "\t%10.4f","\t%10.3f")
            Out( Get(mixture_MAC)   , "\t%10.2f")
            Out( Get(r_wp)          , "\t%10.2f")
            Out_String("\t")
  Out_String(type)
            }

'*************************User-defined macro************************************
   ' Capillary Sample Displacement-----------------------------------------
    macro Horizontal_Sample_Displacement { HSD }
    macro HSD(hd_v) { HSD(,hd_v) }
    macro HSD(hd, hd_v)
    {
      #m_argu hd 'offset of the sample from the centre of the gonio
                  ' +ve displacement = closer to the detector
            If_Prm_Eqn_Rpt(hd, hd_v, min =-Rs/10; max =Rs/10;) 'max offset of a tenth of a radius


            th2_offset = -ArcSin(CeV(hd, hd_v) Sin(2 Th) / Rs ) Rad;
    }

    macro Vertical_Sample_Displacement { VSD }
    macro VSD(hd_v) { VSD(,hd_v) }
    macro VSD(hd, hd_v)
    {
      #m_argu hd 'offset of the sample from the centre of the gonio
                  ' +ve displacement = closer to the detector
```

```
        If_Prm_Eqn_Rpt(hd, hd_v, min =-Rs/10; max =Rs/10;) 'max offset of a tenth of a radius

        th2_offset = ArcSin(CeV(hd, hd_v) * Cos(2 Th) / Rs ) Rad;
    }


C_matrix_normalized
{
                 1  2  3  4  5  6  7  8  9 10 11 12 13 14 15 16 17 18 19 20 21 22 23 24 25 26
bkgeea898        1:  100  18  30  11  -9  18   7  -2   5   0   8   5  -4  -7  20 -20   1  16   8   1  12   0   3  -7   0  -5
bkgeea938        2:   18 100  12  32   7  -5  -5   1  12   0   4  -2  -3  -1   4  -4   7  -7  -7  -0  13   0  -3   7   1   6
bkgeea9d8        3:   30  12 100  12  -3   2   5  -1  -6   0  -6   4   7  -1  -6   6   7  -9  -6   1   5   0   2  -6  -1  -5
bkgeeaa78        4:   11  32  12 100 -10  10   6  -1  -8   0   5   0  -2  -1  -0   0  -6  10  10   1 -12   0   0  -1   0  -0
scale_fcc        5:   -9   7  -3 -10 100 -78 -42  29  67   0 -46  33  19   3 -10  10 -69  30  11  23 -64   0  -1   0  -1  -0
csl_fcc          6:   18  -5   2  10 -78 100  69 -18 -42   0  32 -31 -22 -26  11 -10  58 -31 -16  -3  55   0   1   0   2   1
msg_fcc          7:    7  -5   5   6 -42  69 100  27 -52   0  23 -22 -15 -15   3  -3  14 -26 -37  41  28   0   0   0   1   1
a_fcc            8:   -2   1  -1  -1  29 -18  27 100 -20   0   2  13   8   6  -5   5 -50  -7 -44  69 -26   0  -0  -1  -1  -1
beq_fcc_Cu       9:    5  12  -6  -8  67 -42 -52 -20 100   0 -39  24  12  -9  -1   1 -17  15  34 -27 -34   0  -0   0  -0  -0
beq_fcc_Zn      10:    0   0   0   0   0   0   0   0   0 100   0   0   0   0   0   0  -0   0   0  -0   0   0   0  -0   0   0
scale_bcc       11:    8   4  -6   5 -46  32  23   2 -39   0 100 -53 -42  18 -16  16   7   4  -1   3  11   0   0  -0   0   0
csl_bcc         12:    5  -2   4   0  33 -31 -22  13  24   0 -53 100  74  -9   3  -3  -5  -4  -4   2  -3   0   0   1   1   1
msg_bcc         13:   -4  -3   7  -2  19 -22 -15   8  12   0 -42  74 100   0  -0   0  -2  -5  -3   1  -1   0   0   1   1   1
a_bcc           14:   -7  -1  -1  -1   3 -26 -15   6  -9   0  18  -9   0 100  -4   4 -16   8   1   3 -14   0  -0  -1  -1  -1
beq_bcc_Cu      15:   20   4  -6  -0 -10  11   3  -5  -1   0 -16   3  -0  -4 100-100  14  -5   6   3  10   0   0  -1  -0  -1
beq_bcc_Zn      16:  -20  -4   6   0  10 -10  -3   5   1   0  16  -3   0   4-100 100 -14   5  -6  -3 -10   0  -0   1   0   1
scale_fcc2      17:    1   7   7  -6 -69  58  14 -50 -17  -0   7  -5  -2 -16  14 -14 100 -63 -19 -50  86   0  -1   0  -1  -1
csl_fcc2        18:   16  -7  -9  10  30 -31 -26  -7  15   0   4  -4  -5   8  -5   5 -63 100  74   7 -55   0   1   2   4   3
msg_fcc2        19:    8  -7  -6  10  11 -16 -37 -44  34   0  -1  -4  -3   1   6  -6 -19  74 100 -34 -37   0   1   1   3   3
a_fcc2          20:    1  -0   1   1  23  -3  41  69 -27  -0   3   2   1   3   3  -3 -50   7 -34 100 -26   0   0   0   0   0
beq_fcc2_Cu     21:   12  13   5 -12 -64  55  28 -26 -34   0  11  -3  -1 -14  10 -10  86 -55 -37 -26 100   0  -0   0  -1  -0
beq_fcc2_Zn     22:    0   0   0   0   0   0   0   0   0   0   0   0   0   0   0   0   0   0   0   0   0   0 100   0  -0   0   0
fur_hump_1      23:    3  -3   2   0  -1   1   0  -0  -0   0   0   0   0  -0   0  -0  -1   1   1   0  -0   0 100  31  45 -39
l_fur_hump_1    24:   -7   7  -6  -1   0   0   0  -1   0  -0  -0   1   1  -1  -1   1   0   2   1   0   0  -0  31 100  42 -32
fur_hump_2      25:    0   1  -1   0  -1   2   1  -1  -0   0   0   1   1  -1  -0   0  -1   4   3   0  -1   0  45  42 100 -26
l_fur_hump_2    26:   -5   6  -5  -0  -0   1   1  -1  -0   0   0   1   1  -1  -1   1  -1   3   3   0  -0   0 -39 -32 -26 100
}
```

# References


1. Davis, J.R., ASM Specialty Handbook; Copper and Copper Alloys, ed. A.I.H. Committee. 2010, OH, USA.
2. Copper-Development-Association. https://www.copper.org/resources/. 2018.
3. Reliance-Worldwide-Corporation. http://www.sharkbite.com/. 2018.
4. Reliance-Worldwide-Corporation. http://www.rmc.com.au/. 2018.
5. NSF-International-Standard/American-National-Standard, NSF/ANSI 61: Drinking Water System Components - Health Effects. 2015.
6. NSF-International-Standard/American-National-Standard, NSF/ANSI 372: Drinking Water System Components - Lead Content. 2016.
7. American-Society-of-Mechanical-Engineers-and-Canadian-Standards-Association, ASME A112.18.1-2012/CSA B125.2-12 Plumbing Supply Fittings. 2012 (R2017).
8. World-Health-Organisation, http://www.who.int/ipcs/assessment/public_health/lead/en/. 2018.
9. Molino, P., Bentham, R., Higgins, M., Hinds, J., Whiley, H., Public Health Risks Associated with Heavy Metal and Microbial Contamination of Drinking Water in Australia. International Journal of Environmental Research and Public Health, 2019. 16.
10. 4MS-Joint-Management-Committee. Acceptance of Metallic Materials used for Products in Contact with Drinking Water, Part A: Procedure for Acceptance, https://www.umweltbundesamt.de/en/topics/water/drinking-water/distributing-drinking-water/approval-harmonization-4ms-initiative. 2019.
11. ASM-International, ASM Handbook: Volume 3 - Alloy Phase Diagrams. 1992.
12. Miettinen, J., Thermodynamic description of the Cu-Al-Zn and Cu-Sn-Zn systems in the copper-rich corner. Calphad: Computer Coupling of Phase Diagrams and Thermochemistry, 2002. 26(1): p. 119-139.
13. ASM-International, ASM Handbook: Volume 9 - Metallography and Microstructures. 2004.
14. Porter D., E.K., Sherif M., Phase Transformations in Metals and Alloys, Third Edition. 2009.
15. Murch, G.E. and C.M. Bruff, Diffusion in Solid Metals and Alloys · Co-Pd - Fe-Mo: Datasheet from Landolt-Börnstein - Group III Condensed Matter · Volume 26: "Diffusion in Solid Metals and Alloys" in SpringerMaterials (https://dx.doi.org/10.1007/10390457_58), H. Mehrer, Editor., Springer-Verlag Berlin Heidelberg.
16. Dieter, E.G., Mechanical Metallurgy. SI Metric ed. 1988, UK: McGraw-Hill Book Company.
17. Heidenreich, R.D., Shockley, W., Report on Strength of Solids. 1948, Physical Society: London. p. 37.
18. Xiao, Y.-H., C. Guo, and X.-Y. Guo, Constitutive modeling of hot deformation behavior of H62 brass. Materials Science and Engineering A, 2011. 528(21): p. 6510-6518.
19. Keating, D.T. and B.E. Warren, Long-range order in beta-brass and Cu3Au. Journal of Applied Physics, 1951. 22: p. 286-290.
20. Ayers, J.D. Disordering kinetics of ' phase Cu-Zn and Ag-Zn alloys. in 5th Spring Meeting of the Metallurgical Society of AIME, 29 May-1 June 1973. 1973. New York, NY, USA: Metallurgical Soc. AIME.
21. Neishi, K., Z. Horita, and T.G. Langdon, Achieving superplasticity in ultrafine-grained copper: influence of Zn and Zr additions. Materials Science & Engineering A (Structural Materials: Properties, Microstructure and Processing), 2003. A352(1-2): p. 129-35.
22. Lin, F.-Y., Y.-H. Huang, and F. Ruan, STUDY ON THE SUPERPLASTICITY OF BRASS AND ITS APPLICATIONS. International journal of machine tool design & research, 1986. 26(1): p. 51-60.

23. Khezri-Yazdan, A. and K.N. Subramanian, Elevated temperature deformation behaviour of alpha-beta brass bicrystals. I. Ordered beta. Journal of Materials Science, 1984. 19(10): p. 3185-90.
24. Khezri-Yazdan, A. and K.N. Subramanian, Elevated temperature deformation behaviour of alpha-beta brass bicrystals. II. Disordered beta. Journal of Materials Science, 1984. 19(10): p. 3191-5.
25. Khezri-Yazdan, A. and K.N. Subramanian, Elevated temperature deformation behaviour of alpha-beta brass bicrystals. III. Supporting studies. Journal of Materials Science, 1984. 19(10): p. 3196-200.
26. Davis, D.D., Copper Development Association Inc. - A Note on the Dezincification of Brass and the Inhibiting Effect of Elemental Additions, www.copper.org/applications/rodbar/pdf/7013.pdf. 1993.
27. Guillet, L., Portevin, A., Ternary alloys and the equivalence coefficients. Revue de Metallurgie, 1920. 17: p. 561-567.
28. Miettinen, J., V. Gandova, and G. Vassilev, Thermodynamic description of the Cu-Pb-Zn system. Calphad: Computer Coupling of Phase Diagrams and Thermochemistry, 2010. 34(3): p. 377-383.
29. Miettinen, J., Thermodynamic description of the Cu-Si-Zn system in the copper-rich corner. CALPHAD: Computer Coupling of Phase Diagrams and Thermochemistry, 2007. 31(4): p. 422-7.
30. Wang, J., H. Xu, S. Shang, L. Zhang, Y. Du, W. Zhang, S. Liu, P. Wang, and Z.-K. Liu, Experimental investigation and thermodynamic modeling of the Cu-Si-Zn system with the refined description for the Cu-Zn system. Calphad: Computer Coupling of Phase Diagrams and Thermochemistry, 2011. 35(2): p. 191-203.
31. Miettinen, J., Thermodynamic description of the Cu-Ni-Zn system above 600C. Calphad: Computer Coupling of Phase Diagrams and Thermochemistry, 2003. 27(3): p. 263-274.
32. Miettinen, J., Thermodynamic description of the Cu- Mn- Zn system in the copper-rich corner. CALPHAD: Computer Coupling of Phase Diagrams and Thermochemistry, 2004. 28(3): p. 313-20.
33. Miettinen, J., Thermodynamic description of the Cu-Fe-Zn system. CALPHAD: Computer Coupling of Phase Diagrams and Thermochemistry, 2008. 32(3): p. 514-19.
34. Sadayappan, M., Thompson, J.P., Elboujdaini, M., Ping Gu, G., Sahoo, M. Grain Refinement of Permanent Mold Cast Copper Base Alloys - Copper Development Association, NY & United States Dept. of Energy. 2004.
35. CES EduPack 2016 Granta Design Ltd. 2016.
36. Baker, H. and H. Okamoto, ASM Handbook, Volume 03 - Alloy Phase Diagrams. 1992.
37. Vilarinho, C., D. Soares, and F. Castro, Contribution to the knowledge of the Cu-Sn-Zn system for compositions close to brass alloys. Journal of Alloys and Compounds, 2004. 379(1-2): p. 161-5.
38. Vilarinho, C., D. Soares, and F. Castro, Phase equilibria of the Al-Cu-Zn system for compositions close to brass alloys. Journal of Phase Equilibria, 2003. 24(3): p. 236-239.
39. Taha, M.A., N.A. E-Mahallawy, T.M. Mousa, R.M. Hamouda, and A.F.A.G. Yousef, Microstructure and castability of lead-free silicon brass alloys. Materialwissenschaft und Werkstofftechnik, 2012. 43(8): p. 699-704.
40. Puathawee, S., S. Rojananan, and S. Rojananan. Lead-free Cu-Si-Zn brass with tin addition. in International Conference on Engineering, Applied Sciences, and Technology, ICEAST 2013, August 21, 2013 - August 24, 2013. 2013. Bangkok, Thailand: Trans Tech Publications Ltd.
41. Doostmohammadi, H. and H. Moridshahi, Effects of Si on the microstructure, ordering transformation and properties of the Cu60Zn40 alloy. Journal of Alloys and Compounds, 2015. 640: p. 401-7.

42. Oishi, K., Free-cutting copper alloy containing very low lead, US Patent 11420623, L. Mitsubishi Shindoh Co, Editor. 2011: US.
43. Klocke, F., C. Nobel, and D. Veselovac, Influence of Tool Coating, Tool Material, and Cutting Speed on the Machinability of Low-Leaded Brass Alloys in Turning. Materials and Manufacturing Processes, 2016. 31(14): p. 1895-903.
44. Altan T., N.G., Shen G., ASM Handbook, Cold and Hot Forging; Fundamentals and Applications. 2004.
45. Bowers, J.E., P.W.R. Oseland, and G.C. Davies, Development of a hot-stamping brass resistant to dezincification. British Corrosion Journal, 1978. 13(4): p. 177-85.
46. Padmavardhani, D. and Y.V.R.K. Prasad, Effect of zinc content on processing map for hot deformation of brass. Materials Science and Technology, 1991. 7(10): p. 947-953.
47. Suarez, L., P. Rodriguez-Calvillo, J.M. Cabrera, A. Martinez-Romay, D. Majuelos-Mallorquin, and A. Coma, Hot working analysis of a CuZn40Pb2 brass on the monophasic () and intercritical (+) regions. Materials Science and Engineering: A (Structural Materials: Properties, Microstructure and Processing), 2015. 627: p. 42-50.
48. Spigarelli, S., M. El Mehtedi, M. Cabibbo, F. Gabrielli, and D. Ciccarelli, High temperature processing of brass: Constitutive analysis of hot working of Cu-Zn alloys. Materials Science and Engineering: A (Structural Materials: Properties, Microstructure and Processing), 2014. 615: p. 331-9.
49. Savitskii, E.M., The Influence of Temperature on the Mechanical Properties of Metals and Alloys. 1962: Stanford University Press.
50. http://www.hydromec.it/?lang=en#. 2018.
51. http://www.autind.com/. 2018.
52. Momeni, A., Application of a self-consistent model to study the flow behavior of CuZn39Pb3 at elevated temperatures. Journal of Materials Research, 2015. 30(22): p. 3453-3460.
53. ASM-International, Dictionary of Metals. 2012.
54. Pantazopoulos, R.G. and A. Vazdirvanidis, Failure Analysis of a Fractured Leaded-Brass (CuZn39Pb3) Extruded Hexagonal Rod. Journal of Failure Analysis and Prevention, 2008. 8(3): p. 218-22.
55. Pantazopoulos, G. and A. Vazdirvanidis, Fracture analysis and embrittlement phenomena of machined brass components. Procedia Structural Integrity, 2017. 5: p. 476-83.
56. Yano, T., X. Ling, K. Higashida, and R. Onodera, Improvement of formability of leaded brass during hot working. Materials Science and Technology, 1999. 15(1): p. 67-72.
57. Kchaou, M., R. Elleuch, Y. Desplanques, X. Boidin, and G. Degallaix, Failure mechanisms of H13 die on relation to the forging process - A case study of brass gas valves. Engineering Failure Analysis, 2010. 17(2): p. 403-415.
58. Humphreys F., H.M., Recrystallisation and Related Annealing Phenomena. 1st ed. 1995.
59. Cram, D., Dynamic Recrystallisation of Pure Copper and Copper-Tin Alloys. 2012, PhD Thesis, Department of Materials Engineering - Monash University.
60. Spigarelli, S., M. El Mehtedi, and M. Cabibbo. Characterization of hot deformation of CW602N brass, Acta Physica Polonica A - Vol. 128. 2015. Polish Academy of Sciences.
61. Momeni, A., G.R. Ebrahimi, and H.R. Faridi, Effect of chemical composition and processing variables on the hot flow behavior of leaded brass alloys. Materials Science and Engineering: A (Structural Materials: Properties, Microstructure and Processing), 2015. 626: p. 1-8.
62. Farabi, E., A. Zarei-Hanzaki, M.H. Pishbin, and M. Moallemi, Rationalization of duplex brass hot deformation behavior: the role of microstructural components. Materials Science and Engineering: A (Structural Materials: Properties, Microstructure and Processing), 2015. 641: p. 360-8.
63. Tamura, I., Y. Tomota, and M. Ozawa, Strength and ductility of Fe-Ni-C alloys composed of austenite and martensite with various strength. Institute of Metals (London), Monograph and Report Series, 1973. 1(3): p. 611-615.

64. Bouaziz, O. and P. Buessler, Iso-work increment assumption for heterogeneous material behavior modelling. Advanced Engineering Materials, 2004. 6(1-2): p. 79-83.
65. Haghdadi, N., D. Martin, and P. Hodgson, Physically-based constitutive modelling of hot deformation behavior in a LDX 2101 duplex stainless steel. Materials and Design, 2016. 106: p. 420-427.
66. Yakovtseva, O.A., A.V. Mikhailovskaya, A.D. Kotov, and V.K. Portnoi, Effect of alloying on superplasticity of two-phase brasses. Physics of Metals and Metallography, 2016. 117(7): p. 742-8.
67. Yakovtseva, O.A., A.V. Mikhaylovskaya, A.V. Pozdniakov, A.D. Kotov, and V.K. Portnoy, Superplastic deformation behaviour of aluminium containing brasses. Materials Science and Engineering A, 2016. 674: p. 135-143.
68. Drozda, T., C. Wick, J.T. Benedict, R.F. Veilleux, R. Bakerjian, P.J. Mitchell, and E. Society of Manufacturing, Tool and manufacturing engineers handbook : a reference book for manufacturing engineers, managers, and technicians. 4th ed. / revised under the supervision of the SME Publications Committee in cooperation with the SME Technical Divisions. ed. 1983, Dearborn, Mich.: Dearborn, Mich. : Society of Manufacturing Engineers.
69. Vaandrager, B.L. and G.M. Pharr, Creep of alpha brass containing a liquid grain boundary phase. Scripta Metallurgica, 1984. 18(11): p. 1337-9.
70. Blaz, L., Z. Konior, and T. Majda, Structural aspects of alpha/beta transformation in hot deformed CuZn-39Pb3 alloy. Journal of Materials Science, 2001. 36(15): p. 3629-35.
71. Nes, E., N. Ryum, and O. Hunderi, On the Zener Drag. Acta Metallurgica, 1985. 33(1): p. 11-22.
72. Li, W.B. and K.E. Easterling, Influence of particle shape on Zener drag. Acta Metallurgica, 1990. 38(6): p. 1045-1052.
73. Suzuki H., M.Y., Organobismuth Chemistry; Elsevier Science. 1st ed. 2001, Japan.
74. Li, L., Y. Chen, Q. Li, and G. Huang, Study on the Microstructures and Properties of the Lead-free Easy-cutting BiAl-brass. Advanced Materials Research, 2012. 463-464(2): p. 1057-61.
75. Joseph, B., F. Barbier, and M. Aucouturier, Embrittlement of copper by liquid bismuth. Scripta Materialia, 1999. 40(8): p. 893-897.
76. Joseph, B., F. Barbier, G. Dagoury, and M. Aucouturier, Rapid penetration of liquid Bi along Cu grain boundaries. Scripta Materialia, 1998. 39(6): p. 775-781.
77. Jang, Y., S. Kim, and S. Han, Effect of Misch metal on elevated temperature tensile ductility of the Cu-Zn-Bi alloy. Metallurgical and Materials Transactions A: Physical Metallurgy and Materials Science, 2005. 36(4): p. 1060-1065.
78. Parikh, P.D.C.T., Modification of leaded brasses to improve hot workability, US patent 918333, C. Olin, Editor. 1979: US.
79. Atsumi, H., H. Imai, S. Li, K. Kondoh, Y. Kousaka, and A. Kojima. Microstructural and mechanical properties of the extruded - duplex phase brass Cu-40Zn-Ti alloy. in Advances in Materials Science for Environmental and Energy Technologies - Materials Science and Technology 2011 Conference and Exhibition, MS and T 2011, October 16, 2011 - October 20, 2011. 2012. Columbus, OH, United states: American Ceramic Society.
80. Australian-Standard, AS2345: Dezincification resistance of copper alloys. 2006.
81. Tuck C.D.S., P.C.A., Nuttall J., Shrier's Corrosion; Vol. 3 Corrosion and Degradation of Engineering Materials. 2010.
82. Seungman, S. and K. Tak, The effects of tin and nickel on the corrosion behavior of 60Cu-40Zn alloys. Journal of Alloys and Compounds, 2002. 335: p. 281-9.
83. Krampe-Harex. https://www.krampeharex.com/en/abrasive-media/. 2018.
84. Zhang, Y., Dezincification and Brass Lead Leaching in Premise Plumbing Systems: Effects of Alloy, Physical Conditions and Water Chemistry, Masters Thesis. 2009, Virginia Polytechnic Institute and State University.

85. Sarver, E., Insights into Non-Uniform Copper and Brass Corrosion in Potable Water Systems, Masters Thesis. 2010, Department of Civil and Environmental Engineering - Virginia Polytechnic Institute and State University.
86. Kenworthy, L., O'Driscoll, W.G., Dezincification of Brasses. Anti-Corrosion Methods and Materials, 1955. 2(8): p. 247-249.
87. Langenegger, E.E. and B.G. Callaghan, Use of an empirical potential shift technique for predicting dezincification rates of alpha beta Brasses in chloride media. Corrosion (Houston), 1972. 28(7): p. 245-254.
88. Langenegger, E.E. and F.P.A. Robinson, Effect of polarization technique on dezincification rates and physical structure of dezincified zones. Corrosion, 1968. 24(12): p. 411-417.
89. Langenegger, E.E. and F.P.A. Robinson, Study of mechanism of dezincification of brasses. Corrosion, 1969. 25(2): p. 59-66.
90. Newman, R.C., T. Shahrabi, and K. Sieradzki, Direct electrochemical measurement of dezincification including the effect of alloyed arsenic. Corrosion Science, 1988. 28(9): p. 873-86.
91. Lucey, V.F., The mechanism of dezincification and the effect of arsenic. I. British Corrosion Journal, 1969. 1: p. 9-14.
92. Lucey, V.F., The mechanism of dezincification and the effect of arsenic II. British Corrosion Journal, 1969. 1: p. 53-59.
93. Zhou, P., M.J. Hutchison, J.W. Erning, J.R. Scully, and K. Ogle, An in situ kinetic study of brass dezincification and corrosion. Electrochimica Acta, 2017. 229: p. 141-154.
94. Heidersbach, R., Clarification of the Mechanism of the Dealloying Phenomenon. Corrosion, 1968. 24(2): p. 38-44.
95. Horton, R.M., New metallographic evidence for dezincification of Brass by redeposition of Copper. Corrosion, 1970. 26(6): p. 160-163.
96. Polunin, A.V., A.P. Pchelnikov, V.V. Losev, and I.K. Marshakov, Electrochemical studies of the kinetics and mechanism of Brass dezincification. Electrochimica Acta, 1982. 27(4): p. 467-475.
97. Sugawara, H. and H. Ebiko, Dezincification of brass. Corrosion Science, 1967. 7(8): p. 513-523.
98. Dinnappa, R.K. and S.M. Mayanna, Dezincification of Brass and its inhibition in acidic chloride and sulphate solutions. Corrosion Science, 1987. 27(4): p. 349-361.
99. Heidersbach Jr, R.H. and E.D. Verink Jr, Dezincification of alpha and beta Brasses. Corrosion (Houston), 1972. 28(11): p. 397-418.
100. Claesson, E. and O. Rod, The effect of alloying elements on the corrosion resistance of brass. Materials Science and Technology, 2016. 32(17): p. 1794-803.
101. Hutchinson, B., Oliver, J., Lindh-Ulmgren, E., Symniotis, E. Investigations into the Dezincification of alpha-Brass. in International Conference Copper '06. 2006.
102. Mazza, F. and S. Torchio, Factors influencing the susceptibility to intergranular attack, stress corrosion cracking and de-alloying attack of aluminium brass. Corrosion Science, 1983. 23(10): p. 1053-72.
103. Fink, F.W., Dezincification of alpha brass with special reference to arsenic. Metal Industry (London), 1939. 54(18): p. 489-491.
104. Seuss, F., N. Gaag, and S. Virtanen, Corrosion mechanism of CuZn21Si3P in aggressive tap water. Materials and Corrosion, 2017. 68(1): p. 42-49.
105. Karpagavalli, R. and R. Balasubramaniam, Influence of arsenic, antimony and phosphorous on the microstructure and corrosion behavior of brasses. Journal of Materials Science, 2007. 42(15): p. 5954-8.
106. Sundberg, R., Hertzman, S., Linder, M. Intergranular Corrosion (IGA) of Brass. in International Conference Copper '06. 2006.
107. Langenegger, E.E. and F.P.A. Robinson, Role of arsenic in preventing dezincification of a-brass. Corrosion, 1969. 25(3): p. 137-143.

108. Wu, W.-T. and C.-Y. Hung, Method for inhibiting dezincification of Brass, U. National Chung-Hsing, Editor. 2017: US.
109. Chang-Yu, H., L. Chi-Ming, H. Chih-Chun, L. Chia-Chun, W. Paxon Ti-Yuan, C. Kuan-Ting, and W. Weite, A novel approach to improving resistance to dezincification of diphasic brass. Journal of Alloys and Compounds, 2016. 671: p. 502-8.
110. Balasubramaniam, R. and R. Karpagavalli, Development of novel brasses to resist dezincification. Corrosion Science, 2007. 49(3): p. 963-79.
111. Mannheim, R.L., O.L. Bustos, and J. Garin. Study on segregation-dezincification relationship in Bi-Se-bearing brasses. in Thermec 2003 Processing and Manufacturing of Advanced Materials. 2003. Madrid, Spain: Trans Tech Publications Ltd.
112. Suksongkarm, D., S. Rojananan, and S. Rojananan. Microstructure and hardness of Cu-Zn-Si-Al-Sn brasses with antimony addition. in International Conference on Engineering, Applied Sciences, and Technology, ICEAST 2013, August 21, 2013 - August 24, 2013. 2013. Bangkok, Thailand: Trans Tech Publications Ltd.
113. Vilarinho, C., D. Soares, J. Barbosa, and F. Castro. Leaching of brasses in long-term direct contact with water. in Advanced Materials Forum II: Proceedings of the II International Materials Symposium: Materials 2003 and XI Encontro da Sociedade Portugesa de Materials, 2003 ATERIAIS, April 14, 2003 - April 16, 2003. 2004. Caparica, Portugal: Trans Tech Publications Ltd.
114. Stalnacke, E., E. Claesson, C. Obitz, M. Lilja, J. Odqvist, J. Hagstrom, and O. Rod, Corrosion-microstructure interrelations in new low-lead and lead-free brass alloys. Material Science and Technology, 2018: p. 1-8.
115. Yohai, L., W.H. Schreiner, M. Vazquez, and M.B. Valcarce, Surface characterization of copper, zinc and brass in contact with tap water inhibited with phosphate ions. Applied Surface Science, 2011. 257(23): p. 10089-10095.
116. Yohai, L., W.H. Schreiner, M. Vazquez, and M.B. Valcarce, Phosphate ions as inhibiting agents for copper corrosion in chlorinated tap water. Materials Chemistry and Physics, 2013. 139(2-3): p. 817-824.
117. Yohai, L., W.H. Schreiner, M. Vazquez, and M.B. Valcarce, Brass corrosion in chlorinated tap water inhibited by phosphate ions. Journal of Solid State Electrochemistry, 2015. 19(5): p. 1559-68.
118. Wolley, D.J. and A.G. Fox, The embrittlement of leaded and unleaded + (60-40) brasses in the temperature range 300 to 500C. Journal of Materials Science Letters, 1988. 7(7): p. 763-5.
119. Schultheiss, F., D. Johansson, V. Bushlya, Z. Jinming, K. Nilsson, and J.E. Stahl, Comparative study on the machinability of lead-free brass. Journal of Cleaner Production, 2017. 149: p. 366-77.
120. Schultheiss, F., D. Johansson, M. Linde, P.L. Tam, V. Bushlya, J. Zhou, L. Nyborg, and J.E. Stahl, Machinability of CuZn21Si3P brass. Materials Science and Technology, 2016. 32(17): p. 1744-50.
121. Nobel, C., F. Klocke, D. Lung, and S. Wolf. Machinability enhancement of lead-free brass alloys, Procedia CIRP. 2014. Elsevier.
122. Toulfatzis, A.I., G.A. Pantazopoulos, G.J. Besseris, and A.S. Paipetis, Machinability evaluation and screening of leaded and lead-free brasses using a non-linear robust multifactorial profiler. International Journal of Advanced Manufacturing Technology, 2016. 86(9-12): p. 3241-3254.
123. Davim, J.P., C. Vilarinho, D. Soares, F. Castro, and J. Barbosa, Influence of the chemical composition on the machinability of brasses. Journal of Materials Processing Technology, 2005. 170(1-2): p. 441-7.
124. Gane, N., The effect of lead on the friction and machining of brass. Philosophical Magazine A (Physics of Condensed Matter, Defects and Mechanical Properties), 1981. 43(3): p. 545-66.

125. Nomani, J., A. Pramanik, T. Hilditch, and G. Littlefair, Machinability study of first generation duplex (2205), second generation duplex (2507) and austenite stainless steel during drilling process. Wear, 2013. 304(1-2): p. 20-8.
126. Sandvik-Coromant-Academy, Metal Cutting Technology: Training Handbook. 1st ed. 2013.
127. Nobel, C., U. Hofmann, F. Klocke, and D. Veselovac, Experimental investigation of chip formation, flow, and breakage in free orthogonal cutting of copper-zinc alloys. International Journal of Advanced Manufacturing Technology, 2016. 84(5-8): p. 1127-40.
128. Toulfatzis, A.I., G.A. Pantazopoulos, and A.S. Paipetis, Fracture Behavior and Characterization of Lead-Free Brass Alloys for Machining Applications. Journal of Materials Engineering and Performance, 2014. 23(9): p. 3193-206.
129. Toulfatzis, A.I., G.A. Pantazopoulos, and A.S. Paipetis, Microstructure and properties of lead-free brasses using post-processing heat treatment cycles. Materials Science and Technology, 2016. 32(17): p. 1771-81.
130. Gan, C., K. Zheng, H. Wang, and N. Zhou, Effect of Magnesium Content on Machinability of Cu-Zn-Bi-Sb Alloy. Materials Science Forum, 2016. 850: p. 544-8.
131. Nobel, C., U. Hofmann, F. Klocke, D. Veselovac, and H. Puls, Application of a new, severe-condition friction test method to understand the machining characteristics of Cu-Zn alloys using coated cutting tools. Wear, 2015. 344-345: p. 58-68.
132. 4MS-Joint-Management-Committee, Acceptance of Metallic Materials used for Products in Contact with Drinking Water - Part B: 4MS Common Composition List. 2017.
133. Kramer, K.D.U.S., T.R.U.S. Hoesly, and F.F.U.S. Treul, Brass alloys US patent 471006, I. Starline Mfg. Co, Editor. 1997: US.
134. Atsumi, H., H. Imai, L. Shufeng, K. Kondoh, Y. Kousaka, and A. Kojima, High-strength, lead-free machinable - duplex phase brass Cu-40Zn-Cr-Fe-Sn-Bi alloys. Materials Science & Engineering: A (Structural Materials: Properties, Microstructure and Processing), 2011. 529: p. 275-81.
135. Breedis, J.F.U.S., J.C.U.S. Fister, A.J.U.S. Brock, R.N.U.S. Caron, F.N.U.S. Mandigo, J. Crane, D.D.U.S. McDevitt, and M.N.U.S. Pearman, Corrosion-resistant bismuth brass, US Patent 277928, C. Olin, Editor. 1997: US.
136. Peng, F., B. Xia, J. Liu, B. Feng, C. Zheng, and W. Liu, Lead-free free-cutting corrosion-resistant silicon-bismuth brass alloy, US patent app 13243754, L.A.N.M.M.C.L. Ningbo Xingaoda Advanced Metallic Materials Co, Editor. 2013: US.
137. Kang, C.-S., S.-W. Yeh, and C.-H. Shih, Brass alloy and method for manufacturing the same, US patent 14160941, R. Metal Industries and C. Development, Editors. 2015: US.
138. Cheerla, M.K.U.S. and R.O.U.S. Learmont, Plumbing fixture made of bismuth brass alloy, US patent 13218553, C. Brasscraft Manufacturing, Editor. 2013: US.
139. Cheerla, M.K.U.S. and R.O.U.S. Learmont, Method of processing a bismuth brass article, US patent 13218582, C. BrassCraft Manufacturing, Editor. 2012: US.
140. Uchida, T., Lead-free free-machining brass having improved castability, US patent 12308966, L. Toto, Editor. 2015: US.
141. Yamamoto, H., T. Hoshino, K. Nakajima, M. Ueno, and T. Matsuhashi, Lead-free Brass alloy for hot working, US patent 14127212, C. Joetsu Bronz, Editor. 2014: US.
142. Tang, T., Low-Lead Brass alloy, US patent 14324249, k. Zhuhai seagull and l. bath products co, Editors. 2015: US.
143. Yamagishi, Y., Copper-based alloy excellent in dezincing resistance, US patent 694792, L. Dowa Mining Co, Editor. 2005: US.
144. Singh, A.R.U.S., Plumbing fixtures and fittings employing copper-bismuth casting alloys, US patent 471908, I. Federalloy, Editor. 1999: US.
145. Atsumi, H., H. Imai, S. Li, K. Kondoh, Y. Kousaka, and A. Kojima. The characteristics of high strength and lead-free machinable - duplex phase brass Cu-40Zn-Cr-Fe-Sn-Bi alloy. in Advances in Materials Science for Environmental and Energy Technologies - Materials Science

and Technology 2011 Conference and Exhibition, MS and T 2011, October 16, 2011 - October 20, 2011. 2012. Columbus, OH, United states: American Ceramic Society.
146. Han, H., X. Huang, Y. Wu, Y. Qin, and J. Cao. Microstructure and properties of a bismuth-brass. in 2012 International Conference on Nanotechnology Technology and Advanced Materials, ICNTAM 2012, April 12, 2012 - April 13, 2012. 2012. Hong Kong, Hong kong: Trans Tech Publications.
147. Martinez-Hernandez, M., A. Juarez-Hernandez, C. Gonzalez-Rivera, and M.A.L. Hernandez-Rodriguez, Bismuth segregation and crack formation on a free lead yellow brass tap. Engineering Failure Analysis, 2013. 28: p. 63-68.
148. Li, J., Lead-free Bismuth-free Silicon-free Brass, US patent 14354958, I.D.C.P. JiaXing and L. Heating Technology Ltd.ZheJiang Idc Fluid Control Co, Editors. 2016: US.
149. European-Copper-Institute Recommendation on the non-use of bismuth for lead substitution, https://copperalliance.eu/uploads/2018/01/bismuthnonsuitability3c80c8107bd124e19f48e60e.pdf. 2007.
150. Lansell, L.V. and C.V. Lansell, Brass alloy, US patent app. 13638412, L.T.D. Lclip Pty, Editor. 2013: US.
151. Podany, P. and P. Slama. Free machining brasses with minimized lead content. in International Symposium on Metallography, Metallography 2013, April 24, 2013 - April 26, 2013. 2014. Stara Lesna, Slovakia: Trans Tech Publications Ltd.
152. Copper-Development-Association-Inc. Alloy Data Sheet: EnviroBrass (SeBiLOY); Non-Leaded* Red Brass and Yellow Brass Casting Alloys, https://www.copper.org/applications/industrial/PDF_files/sebiloy.PDF.
153. King, M.G.U.S. and T. Li, Method for making machinable lead-free copper alloys with additive, US patent 493337, A. Incorporated, Editor. 1997: US.
154. Lazarus, N.M., Lead-Free Brass Alloy, US patent 15289580, B. National and I. Metals, Editors. 2017: US.
155. Goris, D., The application of bismuth versus silicon in copper alloys from a sustainability perspective, Report 2013, Metallo-Chimique NV.
156. Munce, B., Lead free dezincification alloy and method of making same, US patent 14227385, I. Mueller Industries, Editor. 2016: US.
157. Zhang, M., Lead-Free Free-Cutting Copper-Antimony Alloys, Patent. 2009, Ningbo Powerway Alloy Material Co., Ltd.
158. Tameda, H., H. Terui, K. Ito, and T. Ozasa, Brass alloys and processed part and wetted part, US patent 14439505, C. Kitz, Editor. 2015: US.
159. Kuhn, H.-A., A. Kaeufler, and S. Gross, Copper alloy, US patent 14235884, A.G. Wieland-Werke, Editor. 2016: US.
160. Svenningsson, I. and J. Nilsson, Brass Alloy Comprising Ceramic Alumina Nanoparticles And Having Improved Machinability, US patent 15036138, A.B. Nordic Brass Gusum, Editor. 2016: US.
161. Lee, B.J., W.H. Kim, C.M. Park, Y.R. Cho, and M.J. Jeong, Leadless free-cutting copper alloy and method for producing the same, US patent 14347214, C. Poongsan, Editor. 2017: US.
162. Zhu, S., B. Shen, and M. Wilson, Brass alloys for use in turbocharger bearing applications, US patent 13838736, I.N.C. Honeywell International, Editor. 2014: US.
163. Ruchel, P. and L. Hofmann, Brass alloy, US patent 750543, H. Diehl Gmb and Co, Editors. 1987: US.
164. Xu, C., Z. Hu, and S. Zhang, Lead-free, bismuth-free free-cutting phosphorous brass alloy, US patent 12644750, L. Xiamen Lota International Co, Editor. 2012: US.
165. Li, L., B. Ma, Q. Li, and G. Huang, Study on the lead-free easy-cutting Mg-Sb brass. Advanced Materials Research, 2011. 239-242(2): p. 1670-3.

166. Zhu, Q., W.-D. Wu, K.-Z. Liu, G. Chen, and W.-P. Chen, Study on microstructure and properties of brass containing Sb and Mg. Science in China Series E: Technological Sciences, 2009. 52(8): p. 2172-4.
167. Pantazopoulos, G.A. and A.I. Toulfatzis, Fracture Modes and Mechanical Characteristics of Machinable Brass Rods. Metallography, Microstructure, and Analysis, 2012. 1(2): p. 106-114.
168. Hofmann, U., W. Dannenmann, l.r.D. Humpenoeder-Boegel, M. Breu, G. Schmid, and J. Seeger, Lead-free copper alloy and a method of manufacture, US patent 10788037, A.G. Wieland-Werke, Editor. 2008: US.
169. Xu, C., Z. Hu, and S. Zhang, Lead-free, bismuth-free free-cutting silicon brass alloy, US patent 12651723, L. Xiamen Lota International Co, Editor. 2012: US.
170. Gaag, N. and P. Ruchel, Copper-zinc alloy, US patent 580536, H. Diehl Gmb and Co, Editors. 1997: US.
171. Song, I., Copper Corrosion Resistant, Machinable Brass Alloy, US patent 12957259. 2012: US.
172. Hirayama, M., T. Watakabe, and K. Okubo, High-strength brass alloy for sliding member, and sliding member, US patent 14549937, C. Oiles, Editor. 2017: US.
173. Xu, C., Z. Hu, N. Zhou, S. Zhang, J. Long, and H. Zhang, Lead-free easy-to-cut corrosion-resistant Brass alloy with good thermoforming performance, US patent 14765305, L.T.D. Xiamen Lota International Co, Editor. 2016: US.
174. Kuhn, H.-A. and R. Liebsch, Copper-nickel-zinc alloy containing silicon, US patent 15278448, A.G. Wieland-Werke, Editor. 2017: US.
175. Gulbrandsen Dahl, S. and J. Ivar Moe, Brass alloy comprising silicon and arsenic and a method of manufacturing thereof, US patent 13822267, W. Raufoss and A.S. Gas, Editors. 2015: US.
176. Hehemann Frederick, H., Silicon brass rod, US patent 388339. 1943: US.
177. Oishi, K., Lead-free free-cutting copper alloys, US patent 987173, L. Sambo Copper Alloy Co, Editor. 2002: US.
178. Oishi, K., Copper/zinc alloys having low levels of lead and good machinability, US patent 09983029, L. Sambo Copper Alloy Co, Editor. 2006: US.
179. Oishi, K., Copper alloy, L. Mitsubishi Shindoh Co, US patent 10597454, Editor. 2011: US.
180. Oishi, K., Copper/zinc alloys having low levels of lead and good machinability, US patent 11094815, L. Mitsubishi Shindoh Co, Editor. 2013: US.
181. Schultheiss, F., C. Windmark, S. Sjostrand, M. Rasmusson, and J.-E. Stahl, Machinability and manufacturing cost in low-lead brass. International Journal of Advanced Manufacturing Technology, 2018. 99(9-12): p. 2101-2110.
182. Hentati, N., A. Makni, and R. Elleuch, Study of Failure Modes Affecting a Crimped Nut Related to Forging Process. Journal of Failure Analysis and Prevention, 2012. 12(2): p. 130-8.
183. Pola, A., M. Gelfi, L. Eleonora Depero, and R. Roberti, Study of annealing temperature effect on stress-corrosion cracking of aluminum brass heat-exchangers tubes by microdiffraction experiments. Engineering Failure Analysis, 2007. 15(1-2): p. 54-61.
184. The-Home-Depot. https://www.homedepot.com/s/push%20to%20connect?NCNI-5. 2018.
185. Lowes-Home-Improvement. https://www.lowes.com/search?searchTerm=push+to+connect. 2018.
186. Bunnings-Warehouse, https://www.bunnings.com.au/our-range/bathroom-plumbing/plumbing/pipe-fittings/pushfit-pip-fittings. 2018.
187. Miranda-Medina, M.L., P. Somkuti, D. Bianchi, U. Cihak-Bayr, D. Bader, M. Jech, and A. Vernes, Characterisation of orange peel on highly polished steel surfaces. Surface Engineering, 2015. 31(7): p. 519-25.
188. Rittel, D. and I. Roman, Tensile deformation of coarse-grained cast austenitic manganese steels. Materials Science & Engineering A (Structural Materials: Properties, Microstructure and Processing), 1989. A110: p. 77-87.
189. Dyer, M.S. and E.P. Guyer, Plumbing Hardware Failure Analyses. Journal of Failure Analysis and Prevention, 2017. 17(1): p. 23-29.

190. Chou, T.C., Stress corrosion cracking of leaded brass in a sulphuric acid environment. Journal of Materials Science, 1998. 33(14): p. 3585-3590.
191. Bobby Kannan, M. and P.K. Shukla, Stress corrosion cracking (SCC) of copper and copper-based alloys. 2011, Elsevier Ltd. p. 409-426.
192. Rebak, R.B., R.M. Carranza, and J.R. Galvele, The stress corrosion cracking mechanism of -brass in NaNO2 solutions. Corrosion Science, 1988. 28(11): p. 1089-106.
193. Loto, C.A., Stress corrosion cracking: characteristics, mechanisms and experimental study. International Journal of Advanced Manufacturing Technology, 2017. 93(9-12): p. 3567-3582.
194. Torchio, S., The stress corrosion cracking of Admiralty brass in sulphate solutions. Corrosion Science, 1986. 26(2): p. 133-5.
195. Qiao, L.J. and J.L. Luo, Effect of ammonia concentrations on SCC of -brass under mode III loading. Scripta Materialia, 1996. 35(12): p. 1475-80.
196. Shahrabi, T., R.C. Newman, and K. Sieradzki, Stress-corrosion cracking of alpha-brass without copper oxidation. Journal of the Electrochemical Society, 1993. 140(2): p. 348-52.
197. Du, X.S., Y.J. Su, J.X. Li, L.J. Qiao, and W.Y. Chu, Inhibitive effects and mechanism of phosphates on the stress corrosion cracking of brass in ammonia solutions. Corrosion Science, 2012. 60: p. 69-75.
198. Newman, R.C., T. Shahrabi, and K. Sieradzki, Film-induced cleavage of alpha-brass. Scripta Metallurgica, 1989. 23(1): p. 71-4.
199. Allam, N.K., A.A. Nazeer, and E.A. Ashour, Effect of annealing on the stress corrosion cracking of -brass in aqueous electrolytes containing aggressive ions. Industrial and Engineering Chemistry Research, 2010. 49(19): p. 9529-9533.
200. Mo, M., Y. Tan, B. Cao, and M. Chen, Fracture analysis on the faucet valve of HPb59-1. Applied Mechanics and Materials, 2013. 401-403: p. 163-6.
201. Yu, J., R.N. Parkins, Y. Xu, G. Thompson, and G.C. Wood, Stress corrosion crack initiation in -brass exposed to sodium nitrite solutions. Corrosion Science, 1987. 27(2): p. 141-57.
202. Fernandez, S.A. and M.G. Alvarez, Passivity breakdown and stress corrosion cracking of -brass in sodium nitrate solutions. Corrosion Science, 2011. 53(1): p. 82-8.
203. Lee, C.K. and H.C. Shih, Determination of the critical potentials for pitting, protection, and stress corrosion cracking of 67-33 brass in fluoride solutions. Journal of the Electrochemical Society, 1995. 142(3): p. 731-7.
204. Rao, T.S. and K.V.K. Nair, Microbiologically influenced stress corrosion cracking failure of admiralty brass condenser tubes in a nuclear power plant cooled by freshwater. Corrosion Science, 1998. 40(11): p. 1821-1836.
205. Australian-Standard, AS2136: Method for Detecting the Susceptibility of Copper and its Alloys to Stress Corrosion Cracking using the Mercurous Nitrate Test. 1977.
206. International-Standard, ISO6957: Copper alloys - Ammonia test for stress corrosion resistance. 1988.
207. ASTM-International-Standard, ASTM B858: Standard Test Method for Ammonia Vapor Test for Determining Susceptibility to Stress Corrosion Cracking in Copper Alloys. 2006 (R2012).
208. ASTM-International-Standard, ASTM G37: Standard Practice for Use of Mattsson's Solution of pH 7.2 to Evaluate the Stress-Corrosion Cracking Susceptibility of Copper-Zinc Alloys. 1998 (R2011).
209. Du, X.S., Y.J. Su, C. Zhang, J.X. Li, L.J. Qiao, W.Y. Chu, W.G. Chen, Q.S. Zhang, and D.X. Liu, Pre-strain enhances film rupture to promote SCC of brass in Mattsson's solution - A proposal for a film-rupture-induced SCC mechanism. Corrosion Science, 2013. 69: p. 302-10.
210. Asabe, T., M. Rifai, M. Yuasa, and H. Miyamoto, Effect of Grain Size on the Stress Corrosion Cracking of Ultrafine Grained Cu-10 wt% Zn Alloy in Ammonia. International Journal of Corrosion, 2017. 2017: p. 2893276 (8 pp.).

211. El-Amoush, A.S., A. Zamil, D. Jaber, and N. Ismail, Stress corrosion cracking of the pre-immersed tin brass heat exchanger tube in an ammoniacal solution. Materials and Design, 2014. 56: p. 842-847.
212. You, S.-J., Y.-S. Choi, J.-G. Kim, H.-J. Oh, and C.-S. Chi, Stress corrosion cracking properties of environmentally friendly unleaded brasses contaning bismuth in Mattson's solution. Materials Science and Engineering A, 2003. 345(1-2): p. 207-214.
213. Leidheiser Jr, H. and R. Kissinger, Chemical analysis of the liquid within a propagating stress corrosion crack in 70:30 Brass immersed in concentrated ammonium hydroxide. Corrosion (Houston), 1972. 28(6): p. 218-221.
214. Giordano, C.M., G.S. Duffo, and J.R. Galvele, The effect of Cu2+ concentration on the stress corrosion cracking susceptibility of -brass in cupric nitrate solutions. Corrosion Science, 1997. 39(10-11): p. 1915-23.
215. Farina, S.B., G.S. Duffo, and J.R. Galvele, Stress corrosion cracking of copper and silver, specific effect of the metal cations. Corrosion Science, 2005. 47(1): p. 239-245.
216. Syrett, B.C. and R.N. Parkins, The effect of Sn and As on the stress corrosion of Cu-Zn alloys. Corrosion Science, 1970. 10(4): p. 197-210.
217. Luo, X. and J. Yu. The inhibition of the stress corrosion cracking of 70/30 brass in nitrite solution with additions of alloying arsenic and arsenic anions. in International Conference on Environment-Sensitive Cracking: Mechanisms and Industrial Applications, 4-9 Sept. 1994. 1996. UK: Elsevier.
218. Brandl, E., R. Malke, T. Beck, A. Wanner, and T. Hack, Stress corrosion cracking and selective corrosion of copper-zinc alloys for the drinking water installation. Materials and Corrosion, 2009. 60(4): p. 251-8.
219. Torchio, S., The influence of arsenic and phosphorus on the stress corrosion cracking of aluminium brass in chloride-citrate solution. Corrosion Science, 1981. 21(6): p. 425-37.
220. ASTM-International-Standard, ASTM E112: Standard Test Methods for Determining Average Grain Size. 2013.
221. ASTM-International-Standard, ASTM E562: Standard Test Methods for Determining Volume Fraction by Systematic Manual Point Count. 2011.
222. International-Standard, ISO6509-1; Corrosion of metals and alloys - Determination of dezincification resistance of copper alloys with zinc - Part 1: Test method. 2014.
223. Mizutani, U., Hume-Rothery Rules for Structurally Complex Alloy Phases. 2011: CRC Press.
224. Akselrud, L.G., M. Hanfland, and U. Schwarz, Refinement of the crystal structure of Bi-II, at 2.54 GPa. Zeitschrift fur Kristallographie - New Crystal Structures, 2003. 218(4): p. 415-416.
225. Mattern, N., R. Seyrich, L. Wilde, C. Baehtz, M. Knapp, and J. Acker, Phase formation of rapidly quenched Cu-Si alloys. Journal of Alloys and Compounds, 2007. 429(1-2): p. 211-215.
226. Solberg, J.K., The crystal structure of η-Cu3/Si precipitates in silicon. Acta Crystallographica Section A, 1978. 34(5): p. 684-698.
227. Brandon, D., . Kaplan, W,, Microstructural Characterization of Materials. 2nd ed. 2008: Wiley.
228. Studer, A.J., M.E. Hagen, and T.J. Noakes, Wombat: The high-intensity powder diffractometer at the OPAL reactor. Physica B: Condensed Matter, 2006. 385-386: p. 1013-1015.
229. M J Luton, C.M.S., Dynamic recrystallisation in nickel and nickel-iron alloys during high temperature deformation. Acta Metallurgica, 1969. 17.
230. Pu, E.-X., H. Feng, M. Liu, W.-J. Zheng, H. Dong, and Z.-G. Song, Constitutive Modeling for Flow Behaviors of Superaustenitic Stainless Steel S32654 during Hot Deformation. Journal of Iron and Steel Research International, 2016. 23(2): p. 178-184.
231. Samantaray, D., S. Mandal, U. Borah, A.K. Bhaduri, and P.V. Sivaprasad, A thermo-viscoplastic constitutive model to predict elevated-temperature flow behaviour in a titanium-modified austenitic stainless steel. Materials Science and Engineering A, 2009. 526(1-2): p. 1-6.
232. Kucera, J., B. Million, and J. Plskova, Diffusion of Zinc in Cu and in Cu-Zn solid solutions. Physica Status Solidi (A) Applied Research, 1972. 11(1): p. 361-366.

233. Correa da Silva, L.C. and R.F. Mehl, Interface and marker movements in diffusion in solid solutions of metals. American Institute of Mining and Metallurgical Engineers -- Journal of Metals, 1951. 191(2): p. 155-173.
234. D. Stauffer, A.A., Introduction to Percolation Theory. 2nd ed, ed. Taylor and Francis. 1992.
235. J.W.Martin, R.D.D., B.Cantor, Stability of microstructure in metallic systems. 2nd ed. 1997.
236. Sieradzki, K., R.R. Corderman, K. Shukla, R.C. Newman, and K. Sieradzki, Computer simulations of corrosion: Selective dissolution of binary alloys. Philosophical Magazine A: Physics of Condensed Matter, Structure, Defects and Mechanical Properties, 1989. 59(4): p. 713-746.
237. Andersson, M. and J.-E. Stahl. Polar Machinability Diagrams - A Model to Predict the Machinability of a Work Material. in 1st Swedish Production Symposium. 2007. Gothenborg, Sweden: Lund University.
238. Xu, L., F. Schultheiss, M. Andersson, and J.-E. Stahl, General conception of polar diagrams for the evaluation of the potential machinability of workpiece materials. International Journal of Machining and Machinability of Materials, 2013. 14.
239. Kubin, L.P. and Y. Estrin, Evolution of dislocation densities and the critical conditions for the Portevin-Le Chatelier effect. Acta Metallurgica, 1990. 38(5): p. 697-708.